astrium

LISA

Study of the Laser Interferometer Space Antenna

Final Technical Report

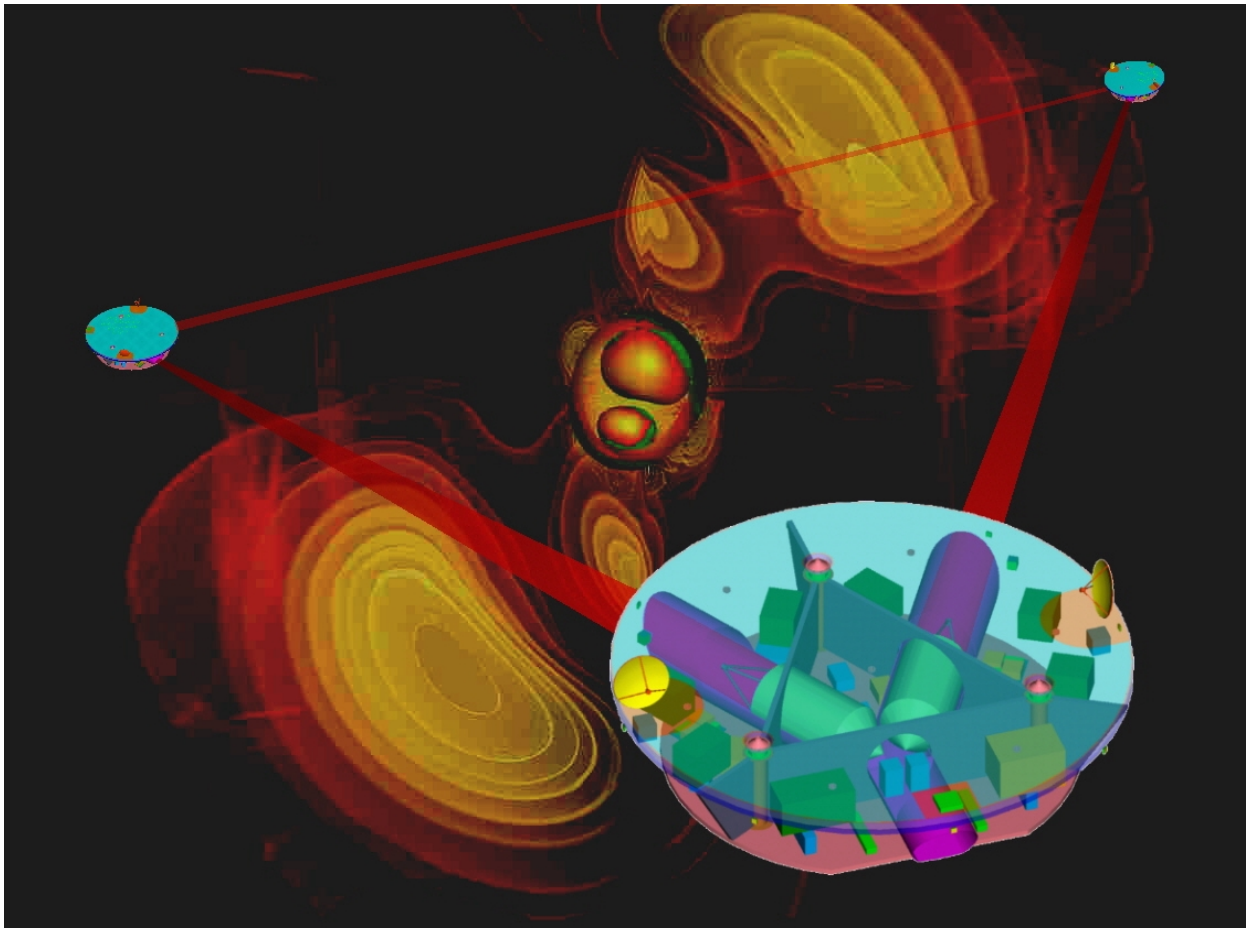

Dornier Satellitensysteme GmbH - Matra Marconi Space - Alenia Aerospazio

Austrian Research Centre Seibersdorf - Centrospazio Italy - LABEN S.p.A. - Laser Zentrum Hannover - Max-Planck Institut für Quantenoptik - ONERA France - University of Birmingham University of Glasgow - University of Trento

ESTEC Contract no. 13631/99/NL/MS

Report No. LI-RP-DS-009 **April 2000**

Study of Laser Interferometer Space Antenna

Final Technical Report

Prepared by:	Dornier Satellitensysteme GmbH
	Alenia Aerospazio
	Matra Marconi Space
	Austrian Research Centre Seibersdorf
	Centrospazio
	ESOC
	LABEN S.p.A.
	Laser Zentrum Hannover
	Max-Planck Institut für Quantenoptik
	ONERA
	Rutherford Appleton Laboratory
	University of Birmingham
	University of Glasgow
	University of Trento

Study Managers:

Customer	Trefor Edwards, Rutherford Appleton Laboratory
Contractor	Axel Hammesfahr, Dornier Satellitensysteme GmbH

DSS Report No. LI-RP-DS-009 **April 2000**

This report has been compiled from contributions of the following study team members:

Dornier Satellitensysteme GmbH	Henry Faulks, Kurt Gehbauer, Dr. Axel Hammesfahr, Karl Honnen, Dr. Ulrich Johann, Dr. Günther Kahl, Michael Kersten, Dr. Lutz Morgenroth, Matthias Riede, Dr. Hans-Reiner Schulte.
Alenia Aerospazio	Marco Bisi Stefano Cesare.
Matra Marconi Space	Olivier Pierre, Xavier Sembely, Ludovic Vaillon.
ESOC	Dr. José Rodríguez-Canabal.
Austrian Research Centre Seibersdorf	Prof. Friedrich Ruedenauer
Centrospazio	Salvo Marcuccio, Davide Nicolini.
LABEN S.p.A.	Luca Maltecca
Laser Zentrum Hannover	Dr. Michael Peterseim
ONERA	Dr. Manuel Rodrigues
Rutherford Appleton Laboratory	David Hayoun, Sam Heys, Bary J. Kent.
University of Birmingham	Dr. Iain Butler
University of Glasgow	Dr. David Robertson
University of Trento	Prof. Stefano Vitale

Table of Contents

ANNEX

1 INTRODUCTION

1.1 Study Objectives

1.1.1 Background

The primary objective of the Laser Interferometer Space Antenna (LISA) mission is to detect gravitational waves from massive black holes and galactic binaries in the frequency range 10^{-4} to 10^{-1} Hz. This low-frequency range is inaccessible to ground-based interferometers as they are limited in dimension to a few kilometres and disturbed by local gravitational noise.

Early conceptual studies for a space-borne gravitational wave observatory began already in the mid 1980's in the USA at the Joint Institute for Laboratory Astrophysics. In 1993 LISA was first time proposed by a European science team to ESA as a candidate for the third medium-size project (M3) within the ESA space science programme Horizon-2000. The scientists proposed a mission with four spacecraft in a heliocentric orbit forming an interferometer with a baseline of $5x10^6$ km.

Based on this proposal ESA performed an assessment study in the M3 cycle combining this concept with another similar mission called 'Sagittarius', proposing six spacecraft in a geocentric orbit. The ESA study team adopted the heliocentric option as the baseline, as it has the advantage to provide for nearly constant interferometer arm lengths and for a stable disturbance environment generating low noise forces to the proof masses. Also it provides the superiority of clear separation between sunlight and the laser light because the spacecraft form a relative plane constantly inclined versus the ecliptic.

Because of the cost, then estimated to be far beyond the M3 budget, LISA was proposed as a cornerstone project of the 'Horizon 2000 Plus' programme, involving six spacecraft in a heliocentric orbit. As it was considered that a realistic launch date would not be before 2017 the LISA science team investigated several essential design modifications and proposed them in 1997 for reduction of the mission cost without compromising the science goals. These included -

- reduction from six to three spacecraft, each containing now two instruments
- defining the drag-free control as part of the payload
- reduction of the aperture of the telescope from 38 to 30 cm
- use of solar-electric ion engines for main propulsion function.

By these changes the total estimated mission cost could essentially be lowered. Also the launch mass could be reduced to about 1400 kg, enabling now cheaper launch options (Delta II). It was then also proposed by the science team and the ESA Fundamental Physics Advisory Group to carry out the mission in collaboration with NASA. Now the LISA mission could well be considered for a launch in about 2009, which would also draw full advantage of the benign radiation environment during the solar minimum in that period.

This modified concept has then been studied in more detail both by the European LISA Science Team and by NASA's JPL documented in the two summary reports 'LISA Pre-Phase A Report' and 'JPL - LISA Mission Concept Study'. Those reports in conjunction with the system requirements and the payload definition documents have formed the starting point of this industrial phase A study.

1.1.2 Content of Study

This study of the Laser Interferometer Space Antenna (LISA) has been performed from June 1999 to February 2000. It was split in three sub-phases:

- Phase 1 – System Concept Review and Trade-off
  included a critical review of the design concepts proposed in previous study reports and the proposals and trade-off of alternative options. The results were presented and discussed at the Preliminary Concept Review and used to confirm a preliminary system baseline.
- Phase 2 – System Concept Development
  comprised all tasks defining and analysing the major system and payload design aspects necessary to achieve a profound technical basis for the final assessment of mission cost, technical feasibility and risk involved.
- Phase 3 – System Concept Consolidation
  included tasks to refine the system design, to complete schedule, risk and cost assessments, and to prepare the final report.

As the instrument design concept had already in the past been defined and studied to a reasonable degree of detail, this was taken as a fixed starting point. The major attention of this industrial study was given to the detailed implication of this instrument concept and the resulting performance requirements both on the overall spacecraft design and on the individual subsystems and instrument components. Based on the various results of unit design and performance characteristics the predicted system performance with respect to the science measurement requirements were evaluated (sec. 5.1).

As the instrument puts by far the highest requirements on technology and development risk, major emphasis was given to the preliminary design and analysis of the critical instrument subsystems. Those will certainly involve the primary development risks and form the major part of the mandatory technology programme.

1.2 Study Team and Organisation

Dornier Satellitensysteme was the prime contractor for the system study also covering the majority of the spacecraft standard subsystems. The fact that the instrument subsystems involve the major development risks and drive the technology programme is reflected in the unusual broad reflection of related specific expertise in the industrial consortium and in the consulting science institutes. For the payload design, performance, and accommodation experts from Dornier, Alenia Aerospazio and Matra Marconi Space have been involved in this study. For the aspects of space qualification of instrument electronics, and of future developments in the on-board data handling domain experts from Laben S.p.A. were engaged as consultants.

Regarding instrument engineering, a large number of institutes hitherto involved in the LISA Science Team have been involved, as requested in the ITT. They were either directly integrated into the team for dedicated instrument tasks and/or supported the system and instrument trade-off and design in the fields of scientific advise and specific instrument technologies.

In direct contractual relation to ESA further support was given by the engineering team at the Rutherford Appleton Laboratory (RAL), UK and by ESOC.

For mission and orbit analyses and operations major analytical data have been generated by ESOC. Major functional support was given by the RAL engineers on the final thermal and gravitational analyses involving the detailed instrument models derived from the models already generated during the pre-phase A activities.

The task allocation within the industrial/consulting team is presented in Figure 1-1. Reduced teams were involved in the phases 1 and 3.

All recommended science team experts, except Zeiss, have been engaged for consultative support to the critical detailed payload and system work packages. Thus, the study will take full advantage of the specific experience and knowledge gained at those institutes in former studies. The key persons within this group of science team experts are listed below with their primary work scope.

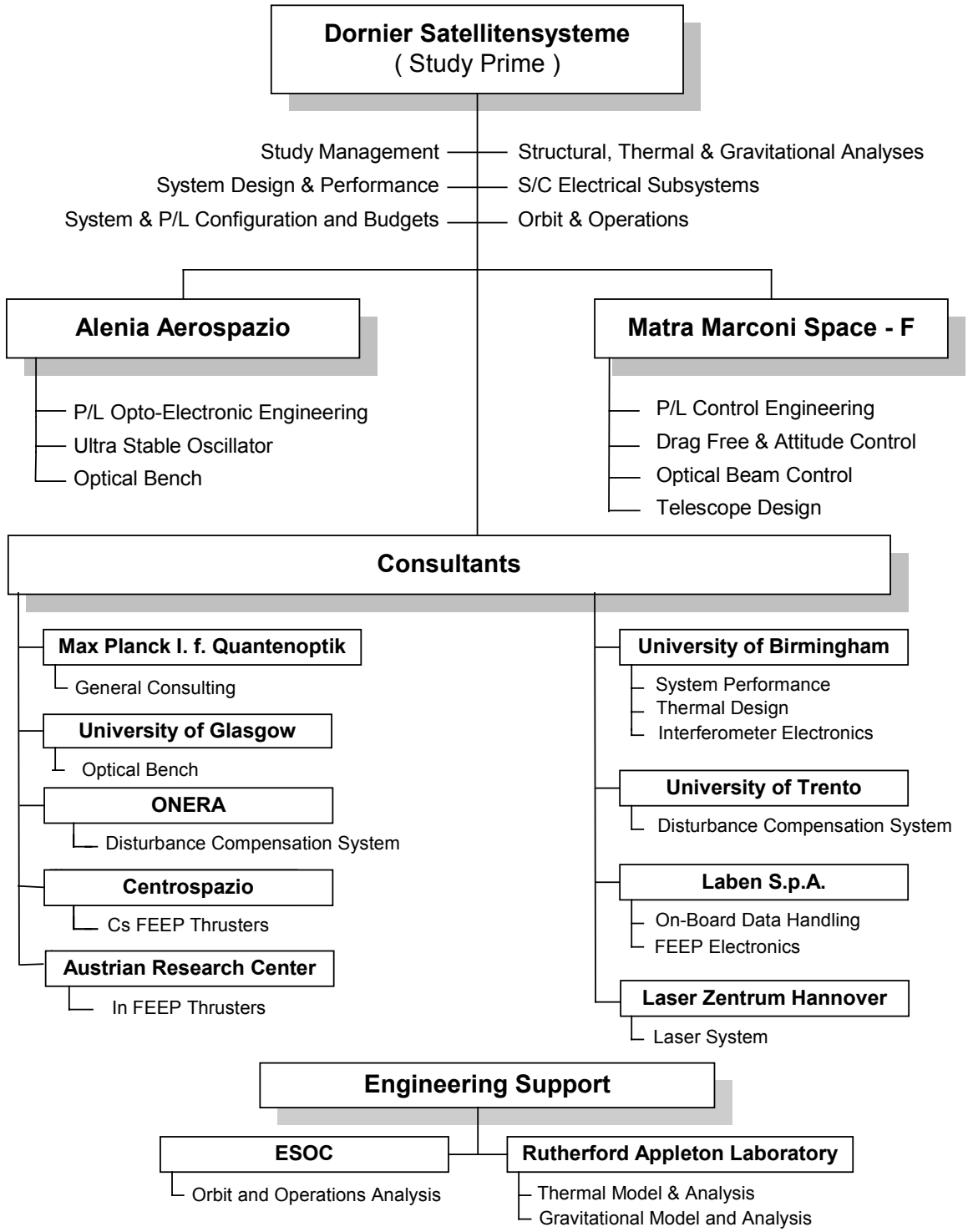

Figure 1-1: Work Distribution within the Study Team in Phase 2

2 Mission Objectives

2.1 Scientific Mission Goals

The primary objective of the Laser Interferometer Space Antenna (LISA) mission is to detect and observe gravitational waves from massive black holes (MBH) and galactic binaries in the frequency range 10^{-4} to 10^{-1} Hz.

This low-frequency range is inaccessible to ground-based interferometers because of the unshieldable background of local gravitational noise and because ground-based interferometers are limited in length to a few kilometres. The ground-based interferometers LIGO, VIRGO, TAMA 300 and GEO 600 and the LISA interferometer in space complement each other in an essential way. It is considered very important to complement the gravitational wave observations on ground in the high-frequency regime of10 to 1000 Hz with observations in space in the low-frequency regime (10^{-4} to 10^{-1} Hz). This is in analogy to the importance of space observations at sub-millimetre, infrared, ultraviolet, X-ray and gamma-ray wavelengths as complements to earth based optical and radio observations.

Ground-based interferometers can observe the bursts of gravitational radiation emitted by galactic binaries during the final stages (minutes and seconds) of coalescence when the frequencies are high and both the amplitudes and frequencies increase quickly with time. At low frequencies, which can only be observed in space, the orbital radii of the binary systems are larger and the frequencies are stable over millions of years. Coalescence of MBHs is only observable from space. Both ground- and space-based detectors will also search for a cosmological background of gravitational waves. Since both kinds of detectors have similar energy sensitivities their different observing frequencies are ideally complementary: observations can provide crucial spectral information.

2.2 Measurement Methods and Features

The LISA mission comprises three identical spacecraft located $5 \cdot 10^6$km apart forming an equilateral triangle. LISA is basically a giant Michelson interferometer placed in space, with a third arm added to give independent information on the two gravitational wave polarisations, and for redundancy. The distance between the spacecraft - the interferometer arm length - determines the frequency range in which LISA can make observations: it was carefully chosen to allow for the observation of most of the interesting sources of gravitational radiation. The centre of the triangular formation is in the ecliptic plane, 1 AU from the Sun and 20° behind the Earth. The plane of the triangle is inclined at 60° with respect to the ecliptic. These particular heliocentric orbits for the three spacecraft were chosen such that the triangular formation is maintained throughout the year with the triangle appearing to rotate about the centre of the formation once per year.

While LISA can be described as a big Michelson interferometer, the actual implementation in space is very different from a laser interferometer on the ground and is much more reminiscent of the technique called spacecraft tracking, but here realised with infrared laser light instead of radio waves. The laser light going out from the centre spacecraft to the other corners is not directly reflected back because very little light intensity would be left over that way. Instead, in complete analogy with a RF transponder scheme, the laser on the distant spacecraft is phase-locked to the incoming light providing a return beam with full intensity again. After being emitted back from the far spacecraft to the centre spacecraft,

the light is superposed with the on-board laser light serving as local oscillator in a heterodyne detection scheme. This gives information on the length of one arm modulo the laser frequency. The other arm is treated the same way, giving information on the length of the other arm modulo the same laser frequency. The difference between these two signals will thus give the difference between the two arm lengths (i.e. the gravitational wave signal). The sum will give information on laser frequency fluctuations. The technique used by LISA for laser spatial and spectral /phase acquisition and tracking has much in common to emerging coherent free-space laser communication links.

Each spacecraft contains two optical assemblies. The two assemblies on one spacecraft are each pointing towards an identical assembly on each of the other two spacecraft to form a Michelson interferometer. A frequency stable 1 W infrared laser beam at 1μm wavelength is transmitted to the corresponding remote spacecraft via a 30-cm aperture f/1 Cassegrain telescope. The same telescope is used to focus the very weak beam (a few pW) coming from the distant spacecraft and to direct the light to a sensitive photodetector where it is superimposed with a fraction of the original local light (optical heterodyne receiver).

At the heart of each assembly is a vacuum enclosure containing a free-flying polished platinum-gold cube, 4 cm in size, referred to as the proof mass, which serves as an optical reference ("mirror") for the light beams. A passing gravitational wave will change the length of the optical path between the proof masses of one arm of the interferometer relative to the other arm. The distance fluctuations are measured to sub-Angstrom precision which, when combined with the large separation between the spacecraft, allows LISA to detect gravitational-wave strains down to a level of order $\Delta l / l = 10^{-23}$ in one year of observation, with a signal-to-noise ratio of 5.

The spacecraft mainly serve to shield the proof masses from the adverse effects due to the solar radiation pressure, and the spacecraft position does not directly enter into the measurement. It is nevertheless necessary to keep all spacecraft moderately accurately (10^{-8} m/$\sqrt{Hz}$ in the measurement band) centred on their respective proof masses to reduce spurious local noise forces. This is achieved by a "drag-free" control system, consisting of an accelerometer (or inertial sensor) and a system of electrical thrusters. Capacitive sensing in three dimensions is used to measure the displacements of the proof masses relative to the spacecraft. These position signals are used in a feedback loop to command micro-Newton ion-emitting proportional thrusters to enable the spacecraft to follow its proof masses precisely. The thrusters are also used to control the attitude of the spacecraft relative to the incoming optical wavefronts, using signals derived from quadrant photodiodes. As the three-spacecraft constellation orbits the Sun in the course of one year, the observed gravitational waves are Doppler-shifted by the orbital motion. For periodic waves with sufficient signal-to-noise ratio, this allows the direction of the source to be determined (to arc minute or degree precision, depending on source strength).

Each of the three LISA spacecraft has a launch mass of about 400 kg (plus margin) including the payload, ion drive all propellants and the spacecraft adapter. The ion drives are used for the transfer from the Earth orbit to the final position in interplanetary orbit. All three spacecraft can be launched by a single Delta II 7925H. Each spacecraft carries in the baseline concept a 30 cm steerable antenna used for transmitting the science and engineering data, stored on board for two days, at a rate of 7 kBps in the Ka-band to the 34-m network of the DSN. Nominal mission lifetime is two years with a possible extension to 10 years.

LISA is envisaged as a possible ESA Horizon 2000 cornerstone. Further, it may evolve into a collaborative ESA / NASA project, with NASA providing the launch vehicle, the on-board communication subsystem, mission and science operations and 50% of the payload. In this scenario ESA would provide

three spacecraft including propulsion module and ion drive. European institutes and industry would provide the other 50 % of the payload presumably nationally funded. A collaborative LISA mission would be aimed at a launch in the 2008 to 2010 time frame.

3 Mission and Operations Analyses

3.1 Launch Phase

3.1.1 Launcher and Launcher Payload

As the baseline launcher for the mission has been foreseen the Delta II as produced by the Boeing Corporation. The version originally proposed was the 7925H with a 9.5ft diameter metal fairing, but has been superseded by the same model equipped with the composite 10ft fairing.

The payload for this launcher is shown in Fig. 3.1-1, consists of 3 composite satellite assemblies stacked on top of each other, and is installed in the launcher fairing as illustrated. The total mass of the stack should not exceed 1380Kg, to enable the mission launch profile to be executed.

Further information in relation to the satellite configuration and the launcher accommodation is given in sections 5.2 and 5.4.

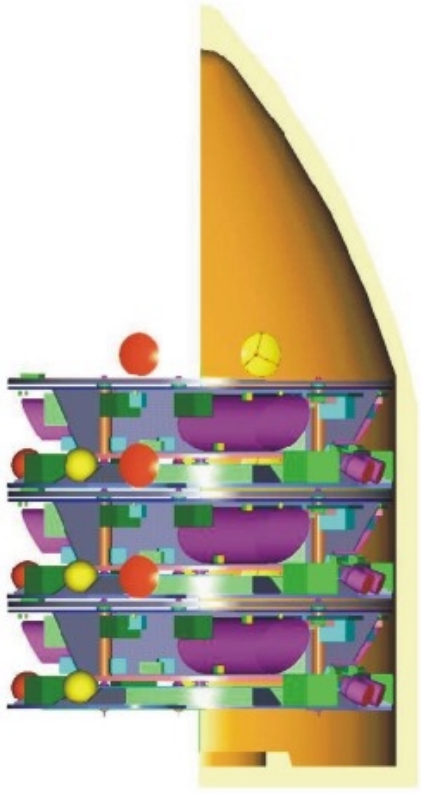

Fig. 3.1-1: 3 LISA Composite Spacecraft in the Delta II10ft Fairing

3.1.2 Analysis of Launch Phase

The stack of three LISA composite spacecraft will be launched on a single Delta II 7925H three-stage vehicle from the Eastern Launch Site. The best mass performances are obtained for a launch flight azimuth of 95°, leading to an orbital inclination of 28.7°, and a perigee altitude of 185 km.

The first part of the ascent phase (main engine of Stage I and the strap-on solid rockets) is followed by a first ignition of Stage II to achieve a circular orbit. Payload fairing separation is performed in this phase. After a coast arc, Stage II is ignited again up to second engine cut-off. The third stage, based on the STAR 48B solid rocket motor, is spun-up, separated, and fired to inject into the final orbit. The injection orbit is an Earth-escape trajectory with an escape velocity, V∞, of about 1 km/s (the normalised excess energy $C_3 = V\infty^2$). The third stage can have a yo-yo de-spin system to leave the spacecraft with the required spin velocity which is supposed to be zero.

The three LISA composite spacecraft will be separated one by one and will autonomously perform any required attitude manoeuvres to enter into a safe Sun pointing mode. Each spacecraft consists of a Science Module (S/M) and of an attached Propulsion Module (P/M) that provides the capability to individually manoeuvre the composite spacecraft into the required operational orbit. The P/M uses electrical propulsion (one ion engine active, the other one in cold redundancy) with a thrust of about 20 mN.

The mass performance of the launcher depends on the required V∞ (near 1km/s the change is less than 3 kg of payload mass per 100 m/s). The precise conditions of Earth-escape will be selected as function of the launch date and the final S/M and P/M characteristics.

All three composite spacecraft leave the Earth such that after 2 weeks the distance to the Earth is 1.5 million km, and the relative velocity about 1 km/s when leaving the sphere of influence of the Earth, Fig. 3.1-2.

Orbit determination during this phase is a standard task of DSN.

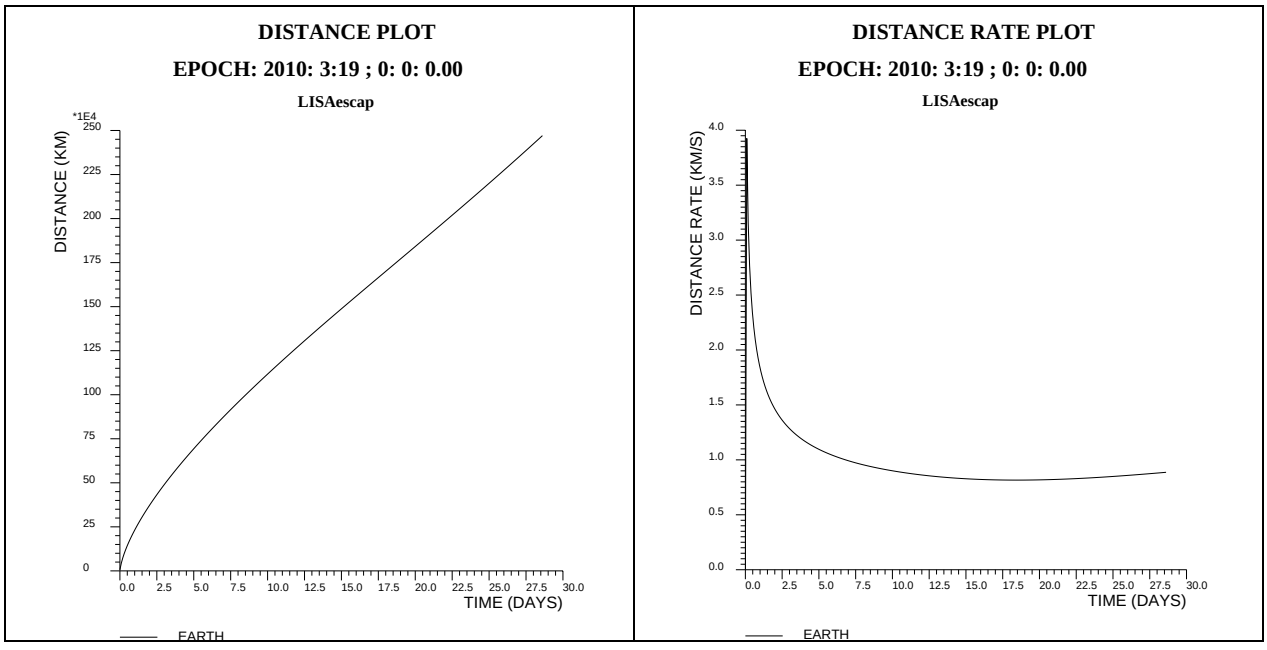

Fig. 3.1-2: Distance and distance rate of change to the Earth during the first 4 weeks after launch

After injection by the launcher, the conditions of spacecraft illumination by the Sun, and the relative geometry of the spacecraft, Earth and Sun are very similar for launch on any day of the year ensuring the possibility of launch at any day of the year.

3.2 Operational Orbit Injection and Composite Separation

3.2.1 Composite Spacecraft

The composite satellite consists of a Science Module (S/M) and a separable Propulsion Module (P/M), as illustrated in Fig. 3.2-1. In this figure the upper two elements are the composite, and are shown attached to the next lower Science Module. The total size of the composite is 2700mm diameter and 800mm depth. A more detailed description is provided in sections 5.2 and 5.4.

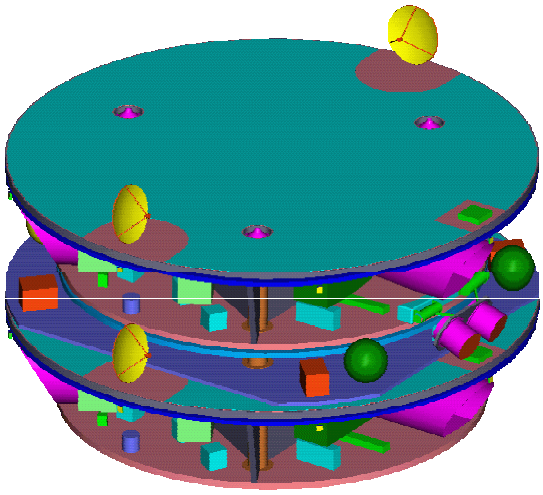

Fig. 3.2-1: LISA Composite (attached to the next lower Science Module)

3.2.2 Analysis of Injection into Operational Orbit

The desired operational orbit configuration for the LISA spacecraft is such that the three spacecraft are positioned at the vertices of a quasi-equilateral triangle with centre in the ecliptic plane, about 20° behind the Earth. The side of the triangle, d, is initially 5 million-km. This configuration is achieved by selecting the following orbital elements for the spacecraft orbits:

semi-major axis	a = 1 AU,
eccentricity	e = d / (2 a $\sqrt{3}$),
inclination with respect to the ecliptic	i = d / (2 a),
argument of pericentre	90° or as 270°.

The ecliptic longitude of the ascending node, Ω, and the mean anomaly, M, of the three spacecraft differ by 120°:

for S/C 1	(Ω, M)
for S/C 2	(Ω+120°, M-120°)
for S/C 3	(Ω−120°, M+120°)

For a given date, Ω and M are selected such that the centre of the triangle at that epoch is 20° behind the Earth and with the required triangle orientation. When propagating the orbits to a different date the quasi-equilateral triangular configuration is maintained and the orientation of the triangle rotates in a plane that is inclined 60° with respect to the ecliptic.

After spacecraft separation from the launcher the spacecraft will autonomously enter into a safe Sun pointing mode and slowly drift away from the Earth. Ground control will initiate the operation of the spacecraft, and control the ion engine to establish the transfer to the operational orbit.

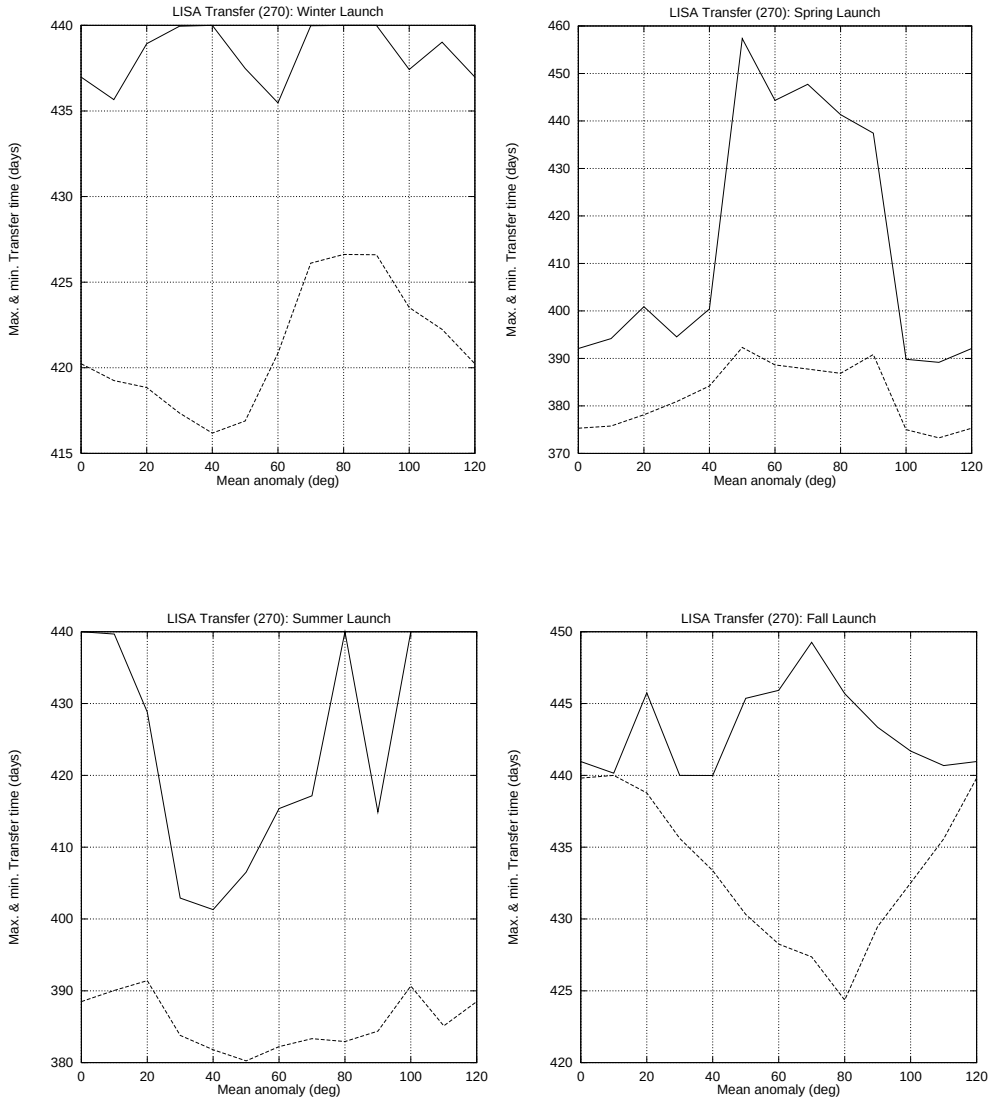

Fig. 3.2-2: Maximum and minimum transfer time for launch in winter, spring, summer, and fall to all possible triangular configuration. For each configuration the max. and min. transfer time for the 3 spacecraft is shown.

The general characteristics of the transfer trajectories for each spacecraft were analysed as follows: For launch dates in Winter, Spring, Summer, and Fall the period and direction of thrust of the ion-engines

has been optimised to generate trajectories to transfer one spacecraft from the Earth to the operational orbit. In this optimisation one has left fixed the parameters D_0, $V\infty$, $\delta\infty$, θ, where D_0 is the day of launch, $V\infty$ the module of the escape velocity, $\delta\infty$ the declination of $\mathbf{V\infty}$ with respect to the ecliptic, and θ, defines the triangle orientation at D_0. The direction of $\mathbf{V\infty}$ in the ecliptic plane, the sequence and duration of thrust and coast arcs, the arrival date, and the variable thrust direction are left as free parameters to be optimised. The ion engine is either working at full power with 18 mN thrust or switched off. The initial mass of the composite spacecraft is taken as 430 kg.

The results of the optimisation show that:

- The longest transfer time is always less than 15 months, and the difference in time of injection into the operational of the 3 spacecraft is about 1 month, Fig. 3.2-2.
- The propellant mass required for the transfer varies between 12.5 kg and 20 kg, Fig. 3.2-3.

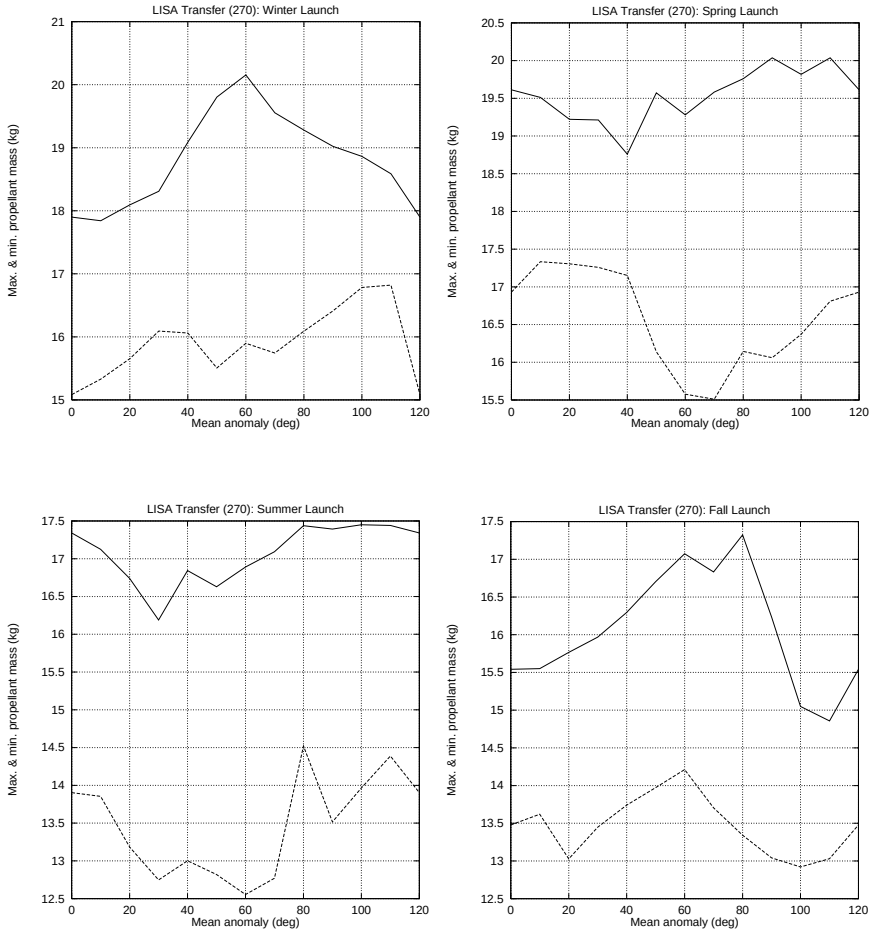

Fig. 3.2-3: Maximum and minimum propellant mass for launch in winter, spring, summer, and fall to all possible triangular configuration. For each configuration the max. and min. propellant mass for the 3 spacecraft is shown.

- The angle between the thrust direction and the direction to the Sun, if it is not constrained in the optimisation process, will vary so that the fixed solar array will not always be pointing

orthogonal to the Sun but may go up to 55° away. However, the solar aspect angle can be constrained to any desirable value at a modest increase of the propellant mass, Fig. 3.2-4. This angle can be restricted to less than 25° without propellant mass penalty, and to 15° with a penalty of less than 0.5 kg. The loss of solar power is 10% , and 3.5%, respectively.

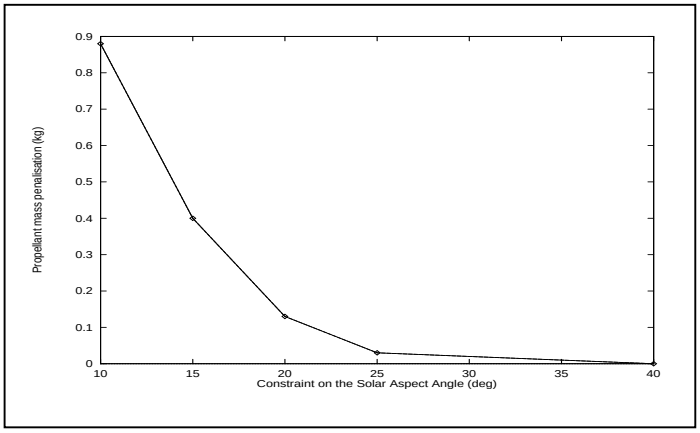

Fig. 3.2-4: Propellant mass penalisation as function of the Solar Aspect Angle constraint. A SAA of 0° provides full illumination of the solar array.

The design of the LISA composite spacecraft should support a transfer time of up to 15 months, and have a propellant capability of 20 kg for an initial mass of 430 kg and a 18 mN ion engine. If seasonal launch restrictions are acceptable, this propellant allocation can be reduced to about 16 kg.

For a particular launch day a triangular configuration will be selected from the general characteristics of the transfer trajectories, and the trajectories for the 3 spacecraft can be re-optimised for a common launch with the same vehicle. As an example, Fig. 3.2-5 presents the evolution of the orbital elements for the three spacecraft during the transfer phase for launch in summer. The transfer types are either a sequence of coast-thrust-coast-thrust arcs or a sequence thrust-coast-thrust. Depending on each spacecraft, the first thrust arc can start very early after leaving the sphere of influence of the Earth (a minimum limit of 10 days from launch has been allocated for spacecraft commissioning), or after a coast arc of up to 3 months. In all cases, the thrust direction is such that the orbital semi-major axis increases, producing a larger drift velocity of the spacecraft with respect to the Earth, and then start to decrease and reaches zero when the spacecraft is on station.

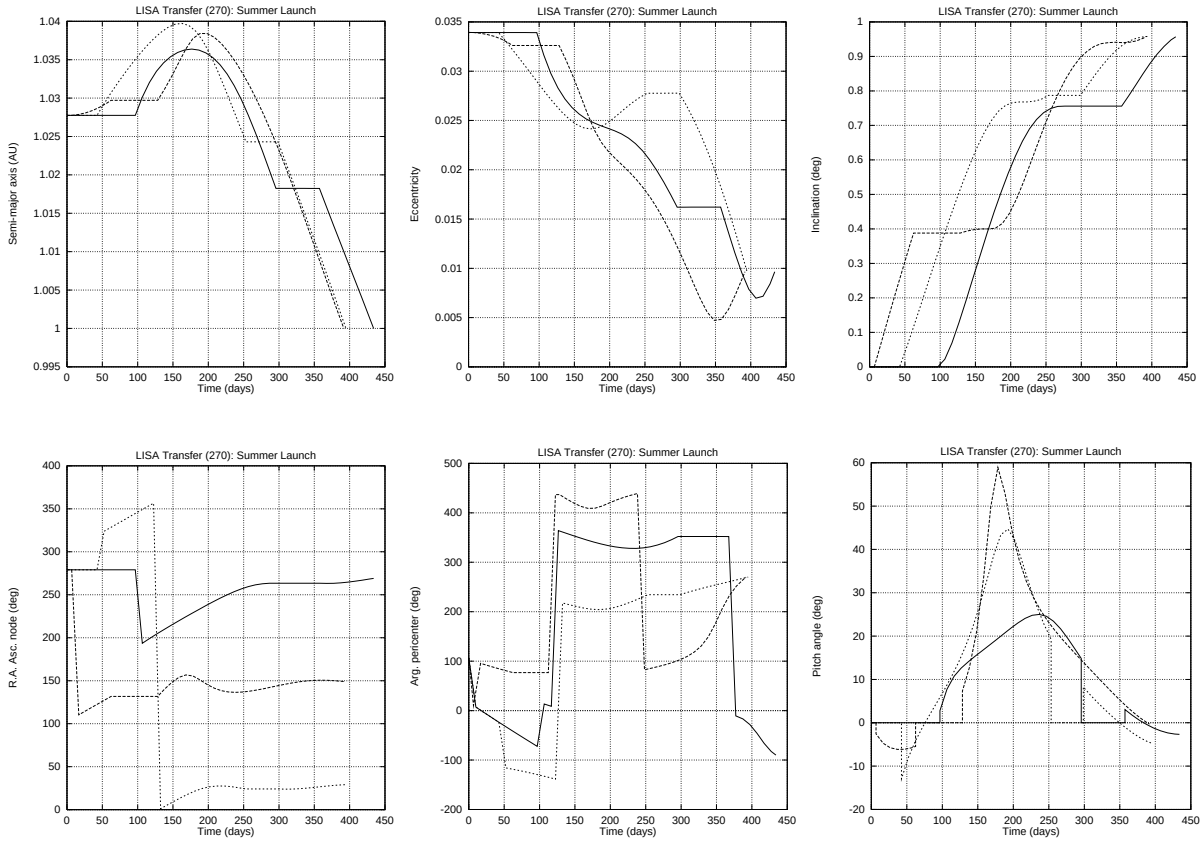

Fig. 3.2-5: Evolution history of orbital elements and unconstrained pitch angle (angle between the thrust direction and the plane normal to the Sun direction) for launch in summer.

3.2.3 Analysis of Composite Separation

The Propulsion Module will deliver the composite spacecraft very accurately to the operational orbit and, before separation from the spacecraft, it will perform an attitude slew manoeuvre to leave it in the proper attitude for operation. A high accuracy of orbit insertion is needed because after the Science Module has been separated from the Propulsion Module it has very limited manoeuvre capabilities due to the very low thrust levels of the FEEPs. The required orbital delivery accuracy depends on the tolerable errors in the evolution of the orbital triangular configuration, in particular on the variation of the interferometer arm length change and on the arm length change rate. It has been shown that, using standard X-band radio tracking, delivery errors of 10 km in position and of less than 2 mm/s in velocity are possible and these values are acceptable in view of the evolution of the triangular configuration for periods of several years.

The Propulsion Module will separate from the Science Module by means of a two-stage separation system. This system needs to produce a small relative velocity of separation between the S/M and the P/M ensuring that the two craft will separate safely without risk of collision. The mechanisation error of the separation must, however, not be so big that it takes a long time to correct resulting S/M position

and attitude errors with the FEEPs. For a S/M of 250 kg, it takes about 14 hrs to correct 1 cm/s with a thrust of 50 μN. The current baseline is to separate the P/M from the spacecraft at a relative velocity of 3 cm/s. This velocity ensures that the distance of the P/M to the plane formed by the 3 S/Ms is continuously increasing to about 55 km in 2 month. This period is larger than the time required for commissioning of the spacecraft and beginning of drag-free control, and it ensures that the Field of View of the telescope will be unobstructed, Fig. 3.2-6. After the drag-free control is activated the distances between the P/Ms and the triangular plane spanned by the three S/Ms will continuously increase to more than 30000 km after one year without any risk of collision between craft.

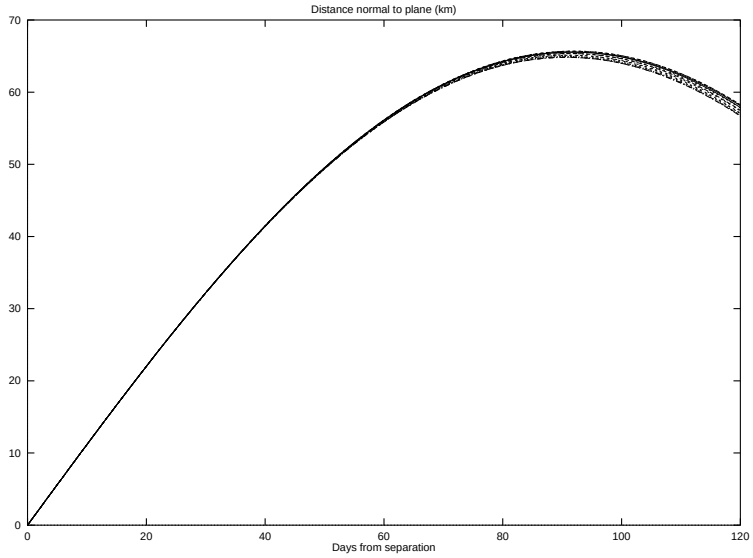

Fig. 3.2-6: Distance of Propulsion Module to the triangular plane after separation.

Another matter of importance for the separation is the angular rate imparted to the S/M during separation. Since there is presently no battery foreseen onboard the S/M, this rate must be small enough so that it can be countered by the FEEPs before the solar aspect angle w.r.t. the S/M solar array gets so large that no longer enough power is generated to drive the FEEPs.

3.3 Evolution of the Operational Orbit

The operational orbits of the 3 S/Ms are selected to maintain these spacecraft at the vertices of a quasi-equilateral triangle with centre in the ecliptic plane, about 20° behind the Earth and with sides of 5 million km length, Fig. 3.3-1.

The orientation of the triangle rotates once a year on a plane that makes an angle of 60° with the ecliptic, and the line of intersection with the ecliptic is orthogonal to the line connecting the Sun with the centre of triangle. The 20° trailing angle to the Earth results from a trade-off between radio communication links and the orbital perturbation due to Earth and Moon. The distances between spacecraft are dictated by the requirements of the scientific measurements that will be performed by LISA.

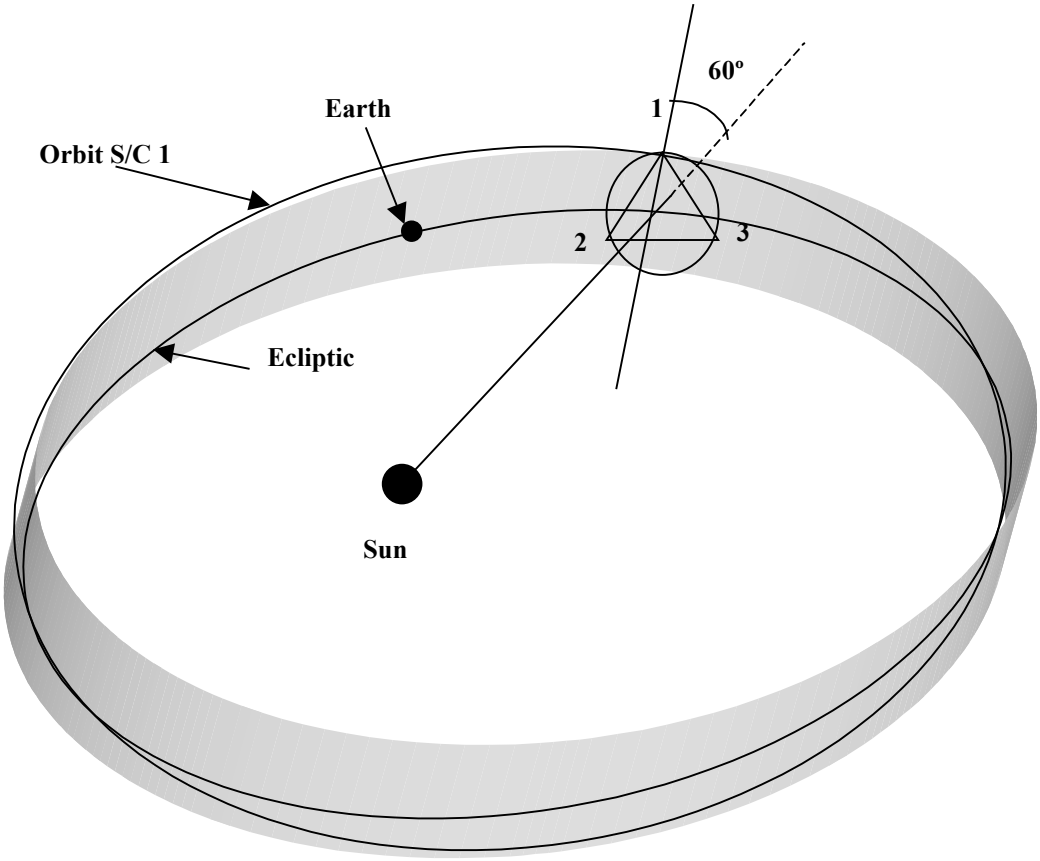

Fig. 3.3-1: Operational orbit configuration of the 3 Science Modules

Once in Science Mode operations the S/Ms are controlled in drag-free mode, and, therefore, it is only the gravitational forces of the Sun, planets, and other bodies of the solar system that determine the trajectory of each spacecraft.

Starting with the orbits as described in sect. 3.2.2, the initial distance between spacecraft is 5 million km, but this distance periodically varies over one year. Different strategies have been investigated to reduce this variation:

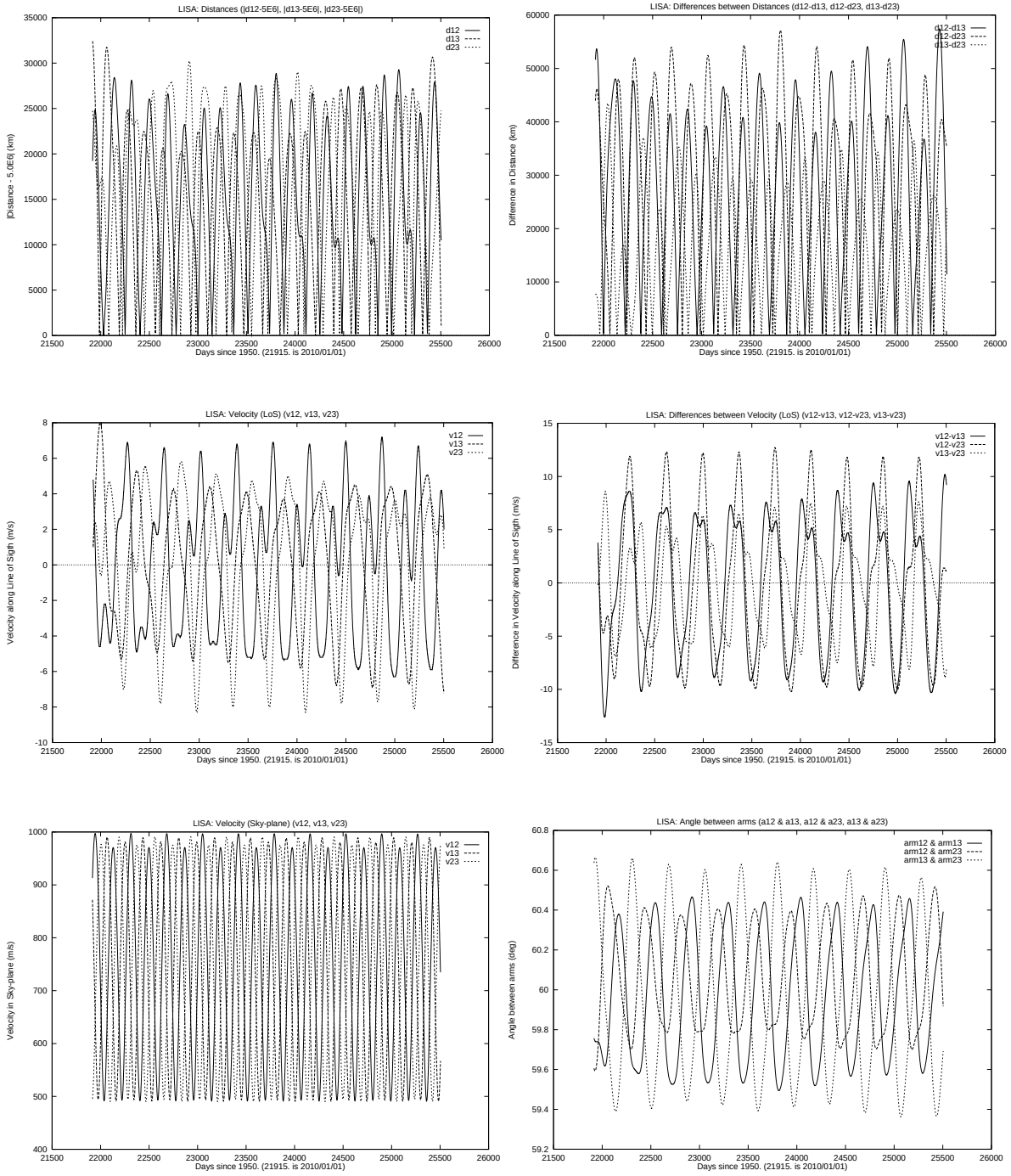

Fig. 3.3-2: Evolution for a period of 10 years of: arm length with respect to the desired 5 million km; difference between arm lengths; velocity between spacecraft along the instrument Line of

Sight; difference between the LOS velocity in different arms; velocity normal to the Line of Sight; angle between arms.

- Passively, by selecting the initial conditions to minimise the variations of one, two, or three arms of the triangle;
- Actively, by performing orbital corrections with the FEEPs. In this case, the analysis shows that it is not possible to stabilise the rate of change of all three arms, but only of one or two arms for a period of a few years. The active control requires as well that manoeuvres may need to be performed for several days every month, with a possible disruption of the scientific measurements.

Therefore, the current baseline is to select the initial orbital conditions so as to minimise the average rate of change of the distance between the three pairs of spacecraft, to let the orbits freely evolve and to avoid orbit control manoeuvres. Fig. 3.3-2 presents the evolution over 10 years of the parameters of such a configuration.

The distances between S/M spacecraft, i.e. the interferometer arm length, will oscillate around the nominal value of 5 million km with an amplitude of less than 30000 km, and the difference between the different arm lengths can be up to 60000 km. The velocity along the line of sight of the telescope introduces a measurement noise caused by the Doppler shift that will be corrected by modulating the laser beams. This Doppler compensation is able to cope with the predicted rate of maximum 8 m/s, and with the predicted rate differences between each arm of less than 12 m/s.

The angle between any two S/Ms as seen from the third one changes periodically through the year with variations around 60° with an amplitude of less than 0.6°. This is due to a velocity in the sky plane for each spacecraft as observed by any of the other spacecraft that oscillates between 500 m/s to 1000 m/s. The velocity in the sky plane of spacecraft 2 with respect to spacecraft1 is the projection on a plane orthogonal to the line from S/C 1 to S/C 2 of the relative velocity of S/C 2 with respect to S/C 1. This velocity necessitates in addition the application of a point-ahead angle between the transmitted and received laser beams. The point-ahead angle can be split into two components: in-plane and out-of-plane w.r.t. the plane spanned by the three spacecraft. It has been quantified as follows:

In-plane point-ahead angle	Bias	3.3 μrad
	Variation	±55 nrad
Out-of-plane point-ahead angle	Bias	85 nrad
	Variation	±5.75 μrad

The considerable out-of-plane variation is nicely sinusoidal.

3.4 Operational Strategy

3.4.1 Nominal Operations Concept

The general concept for operating LISA is that all activities will be performed according to a master schedule on-board each spacecraft, which will be kept updated and harmonised from ground. This on-board master schedule performs the time-tagged commanding of On-Board Control Procedures (OBCPs) which are to be written in an On-Board Control Procedure Language. The OBCPs will be defined in a way that they are continued autonomously after simple failures.

All parameters used for autonomous operation including fault management, orbit, drag-free and attitude control etc. will be updateable by telecommand and be available in telemetry.

Time-tagged commands will be applied for scheduled automatic tasking in Routine Phase as well as for event driven procedures. Event driven procedures have to be analysed, a forecast of schedule events from Earth has to be commanded as timeline or in real-time under ground contact.

3.4.2 Advanced Operations Concept

The operations concept briefly outlined in the previous section requires a significant man-power effort for elaborating timelines, since the operation of the three spacecraft is closely interrelated.

The application of an Advanced Timeline Generator on ground (e.g. the TINA 5.0 system developed by DSS and already applied in two ESTEC studies) allows to generate timelines which contain time windows for the execution of an OBCP with starting and ending times and which contain required key parameter values, required system state and required available resource information. The TINA timeline generator kernel performs the timeline computation based on the commercial ILOG constraint propagation libraries.

The on-board complement for the application of “event driven timeline execution” is already existing as demonstrator application at DSS under the label “System Autonomy Testbed”.

This Autonomy Testbed is based on a modular on-board software architecture which has been developed by DSS in the frame of the project “MARCO” (Modular Architecture for Robotics Control) under DARA contract. It features a modular Ada software concept based on VxWorks real-time operating system.

The controlling component of the architecture is called the Supervisor and is sketched in Fig. 3.4-1. The onboard system supervisor of the Autonomy Testbed is able to execute TINA generated mission timelines which consider both time tags and key parameter values, the system state and resources for execution of OBCPs.

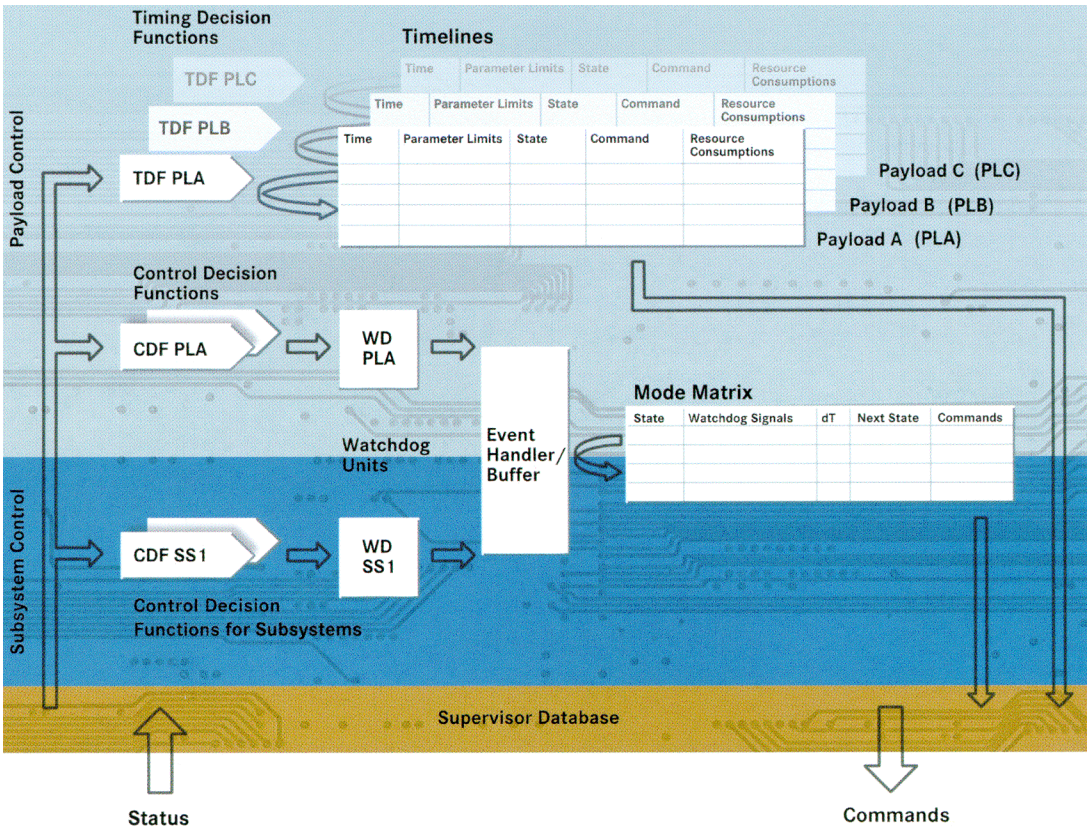

Fig. 3.4-1: Supervisor Functional Architecture

This concept has already been proposed to ESA for on-board SW of PROBA (Project for On-Board Autonomy) and in the “Autonomy Testing” Proposal.

For the LISA mission this advanced operations concept is not mandatory but according to the very complex mission scenario it would give extraordinary advantages for operations in view of flexibility, man power savings, and cost effectiveness. The optimum share between ground and onboard functionality of this supervisor concept for LISA should be elaborated in future phases.

3.4.3 Autonomy

For interplanetary missions the need for on-board autonomy is out of question. Signal transmission times between LISA spacecraft and ground in the order of 3 minutes in conjunction with complex spacecraft interactions, especially for Pointing Acquisition and Tracking, will become extremely difficult otherwise. Moreover, LISA is required to operate for a period of 72 hours without ground contact. Beyond these 72 hours each spacecraft is required to be able to survive autonomously in a Safe Mode for at least TBD days without the need for ground intervention.

In order to avoid misinterpretation of the term autonomy a short definition is given hereafter:

> ”Autonomy or autonomous operations are those on-board actions which are initiated on system level by the spacecraft itself following an on-board event (nominal or failure) in order to fulfil the goal/task of the actual phase or mode. Autonomy can concern nominal operations as well as

handling of contingency situations." All other operations are called predefined or automatic especially if they are handled on subsystem level only.

E.g.: The execution of a purely *time tagged* command timeline is considered an automatic functionality. The execution, however, of a timeline under *event driven* conditions considering alternatives depending on key parameter values is considered to be an autonomous functionality.

The envisaged autonomy concept can be characterised as follows:

All nominal and contingency operations necessary for the different mission phases are predefined and stored in On-Board Control Procedures (OBCPs).

The on-board system supervisor executes mission timelines which are conditional to time tags, key parameter values, the system state and the availability of resources. Event driven they initiate execution of the corresponding OBCPs. OBCPs are defined such that they cover a nominal case and failure cases.

If, in a failure case, the specified corrective action is able to cope successfully with the detected failure, then the mission timeline execution is continued autonomously.

If there is no success of the corrective actions or there is no predefined OBCP, as a last consequence for payload OBCPs the failing items of the payload, e.g. a particular laser link, will be deactivated and mission timeline execution will continue for all other payload items and subsystems. For non-recoverable spacecraft system failures Safe Mode is entered and autonomously maintained. All parameters used for autonomous operations, including fault management, orbit, drag-free and attitude control, etc., will be updateable by telecommand and related status information available in telemetry.

A demonstrator for such an advanced real-time onboard software controlling a simulated spacecraft by execution of event driven mission timelines has been realised in the System Autonomy Testbed at DSS.

3.4.4 Failure Detection Isolation and Recovery

The following conceptual definition is based on the ROSETTA defined levels of on-board autonomous FDIR. Consequently, the levels of autonomous FDIR for LISA are structured into four levels:

- Level 0 is the unit level
- Level 1 is the subsystem function level
- Level 2 is the high level DMS surveillance level
- Level 3 is the system alarm and Reconfiguration Module level.

The ground-rule to be observed for FDIR is that failures should be detected, isolated and corrected on the lowest possible level. Level 0 represents the lowest level. Only the levels 2 and 3 allow for a transition into Safe Mode.

The central item for autonomous FDIR on level 3 is the Reconfiguration Module. It has the highest level responsibility for the handling of unexpected system alarms.

3.4.5 Ground Control

The LISA operations follow the lines of a survey-type project that will be developed and operated as a Principal Investigator (PI) mission. Mission operations performed by the Mission Operation and Spacecraft Control Element, MSCE, after separation of the composite spacecraft from the launcher are composed of mission planning, spacecraft monitoring and control, and all orbit and attitude determination and control. The instrument operations will be under the responsibility of the PIs. The co-ordination of the instrument operations and the interface between the PIs and the MSCE will be under the responsibility of the Project Scientist supported by members of the PI teams in the LISA Science Data Centre LSDC. In support of the instrument operations, the MSCE will make available to the LSDC the extracted near real-time payload telemetry packages. It will also process the instrument telecommand and mission planning request from the LSDC, and it will distribute the raw instrument telemetry data augmented by auxiliary data on orbit, attitude, and spacecraft status.

All operations will be executed at the MSCE according to a Mission Timeline, Flight Control Procedure, and Contingency Recovery Procedures as defined in the Flight Operations Plan. The FOP will be prepared by the operations staff based on the LISA Users Manual, and on the LISA Database. The payload operation support is based on inputs from the experimenters and specified in the Payload Operations Plan.

During routine phase the nominal spacecraft control will be off-line. The period of contact with the spacecraft will be dedicated to collecting science and housekeeping data, for radio tracking measurements, and for up-link of the master schedule for pre-programming the autonomous operation functions of the three LISA spacecraft. As anomalies will normally be detected with a delay, the mission safety will be ensured by on-board autonomous systems.

3.5 Mission Phases

The mission is composed of the following operational phases:

- **Launch Phase**: This phase starts with the removal of the umbilical and ends with the separation from the launcher. Throughout the launch the power is provided by batteries.
- **Near Earth Commissioning Phase**: Triggered by the separation form the launcher, the spacecraft activation sequence is started to perform subsystem switch-on, RCS priming, rate damping and Sun acquisition. The spacecraft is 3-axis stabilised. This phase includes an initial spacecraft check-out and a first payload commissioning.
- **Cruise Phase**: During thrust phases one of the two ion-engines is working at full thrust and operations are reduced to S/M and P/M monitoring. Thrust vector orientation is controlled either through the hydrazine thrusters or by swivelling the gimbals of the ion engines. The P/M is commanded to keep the required thrust conditions. Attitude reference is given by means of the star trackers. Ground contact is restricted to LGA X-band communication.
  During thrustless coast phases HGA communication may be possible after appropriate attitude adjustments.
- **Commissioning and Verification Phase**: At the end of the Cruise Phase, each composite spacecraft is injected into its required orbit, put into the proper attitude (30˚off Sun pointing), and the S/M separated from the P/M. After P/M separation, the S/M AOCS performs the attitude and position control merely using the FEEPs. Commissioning and verification of all electrical and mechanical systems including the telescope pointing devices, lasers, discharge systems, electronics, clamping devices, and the Ultra Stable Oscillators.
  The attitude control for initial laser signal acquisition is preceded by calibration activities between star trackers and acquisition sensors. The laser acquisition will start with the S/Ms controlling their inertial attitudes based on knowledge on-board each S/M of the inertial positions of all 3 S/Ms in order to be able to point their laser beams towards their companion S/Ms. Star trackers supported by Inertial Reference Sensors will be used to ensure stable pointing in the desired direction towards the companion S/Ms. Further details of the Pointing Acquisition and Tracking (PAT) process are described in the section 'Laser Beam Acquisition Strategy'. After successful completion of this process all three optical links will have been established and drag-free control enabled. Now the final calibrations are performed. The S/M's FDIR functionality monitors the spacecraft subsystems and the payload and may take over control to enter a pre-established Safe Mode if it detects any failure that puts the mission in jeopardy.
  During this phase it will be possible to transmit not only the already compressed but in addition also the raw science data to ground. This gives the ground the means to check the validity of the on-board science-data compression.
- **Routine Phase**: Normal mode in this phase is Science Mode with all three optical links established and drag-free control active. Data will be stored on-board and transmitted to ground during the contact periods with the spacecraft of about 9 hrs every second day. For ground contact there will be a configurable master S/M collecting science and housekeeping data from its companions via the optical links, transmitting these data together with its own to the ground, receiving telecommands from ground and forwarding them via the optical links to its companion S/Ms. The ground will monitor and perform emergency recovery in case of failure or in the short

interruptions that may be required to correct external events causing disturbances to the S/M or its sensors (solar flares, interplanetary dust, micro-meteoroids, etc). Operation in the normal Science Mode is supposed to last for long periods of time with very few short interruptions.

A standard DSN X-band network will support the mission from launch until start of the interplanetary Cruise Phase. Afterwards, one single ground station is sufficient to support the mission. Radio tracking from two ground stations will be needed during campaigns to calibrate the orbit determination process.

All over the mission, each S/M will be under the control of its Centralised Processor System. The principal tasks of this system are

- Spacecraft control
- Payload control
- Spacecraft and payload data management

In case of failure, the Centralised Processor System will have the capability of predicting with the required accuracy the position of its own S/M as well as those of the other two spacecraft, the attitude to point to them, and the direction of the Earth, and shall autonomously try to re-establish the triangular spacecraft configuration and establish the optical links.

The Payload Controller will be in charge of accepting and responding to commands and reference values received from the Centralised Processor System. It will condition and forward these commands to the payload, acquire and condition payload signals and transmit them back to the Centralised Processor System.

3.6 Operating Modes and Mode Transitions

The basic system modes which are needed to fulfil the operational requirements of the LISA mission phases are defined below.

The **Prelaunch Mode** will be used during final preparation and checkout activities on the launch pad. It is automatically entered when the spacecraft is switched on. In this way it will be used during all ground testing, but in addition also for loading data for the separation sequence.

The spacecraft is in the **Launch Mode** from removal of umbilical until it has autonomously performed all operations after separation to achieve a safe Sun pointing 3-axis stabilised attitude including RCS priming and Sun acquisition (Sun incident on the Propulsion Module solar array). Communication via LGAs is established. These operations are controlled by a dedicated OBCP which is continued also in failure cases.

The **Activation Mode** follows the Launch Mode when control is taken over from ground. It is used for spacecraft check-out and first payload commissioning. The AOCS is in Star Sensor Mode. Minor trajectory correction manoeuvres using hydrazine propulsion are performed to compensate for launcher orbit insertion errors. Apart from these manoeuvres the spacecraft is leaving the Earth on a purely ballistic trajectory. The communication goes via LGAs.

The **Cruise Mode** follows on Activation Mode and is used during the interplanetary cruise phase. In this mode a sequence of thrust phases (using ion propulsion) separated by purely passive coast phases is used to transfer each spacecraft to its station. Only restricted communication will be possible, since most of the time the LGAs will have to be used. Due to their single-axis articulation the HGAs will normally never be Earth-pointing during cruise, especially, since the HGAs are mounted on the S/M which is oriented towards deep space during cruise. During coast phases, however, when the ion propulsion is off, it might well be possible to change the orientation of the spacecraft towards the Earth in a way that the HGAs can be made us of for extensive spacecraft monitoring and health checking. At the end of the Cruise Phase a precise orbit determination and orbit correction is mandatory to obtain good initial conditions for the mission orbit.

After end of cruise, **P/M Separation Mode** will be entered. In this mode the composite spacecraft will perform a180° attitude slew in order to have the S/M and no longer the P/M solar array Sun pointed. The Propulsion Module will be separated in two stages from the Science Module: first structurally by means of separation nuts and then regarding the electrical connectors smoothly by spindle devices. After end of P/M Separation Mode the P/M is drifting passively away from the S/M. The EPS of the S/M is now fully dependent on the power from the S/M solar array, since the batteries remain on the P/M. Attitude and position control authority is limited now to FEEPs. The FEEPs have to be used to compensate the separation rates and to reacquire the Sun pointing attitude.

Separation Mode is followed by **On Station Mode**. In this mode the S/M acquires its nominal attitude 30° off Sun and then permanently aligns its two telescope lines of sight towards its companion spacecraft. For communication with the ground the HGAs are used, since they can be permanently be Earth pointed now. Continuous on-board propagation of positions of S/M 1 to 3 and of Earth provides the knowledge necessary for pointing of telescope lines of sight and of HGAs. Further activities in this mode are related to payload activation: mechanical release of Optical Assemblies, test of Telescope Pointing Mechanisms, release and calibration of proof-masses, alignment calibration between Star Trackers and Acquisition Sensors, test of the laser assembly, of the front end electronics, etc.

PAT Mode is the mode in which the optical links between a S/M spacecraft and its two distant companions are established one by one. PAT Mode is necessary in both spacecraft trying to establish an optical link. In PAT Mode drag-free control will be enabled and the proof-masses used as additional inertial sensors to allow for a highly stable pointing towards the opposite spacecraft. The complex pointing acquisition scenario to be observed by both S/Ms in this mode needs only to be initiated from the ground and can then be followed autonomously by the two spacecraft, one being declared Master, the other Slave. For the establishment of a link between a Master S/C and a Slave S/C the steps to be taken in PAT Mode on the Master can briefly be summarised as follows:

M-1. The Master switches its laser on and slowly performs with the laser beam one full scan over the uncertainty cone surrounding the expected position of the Slave which is propagated over time accordingly. Then the laser is switched off.

M-2. Under nominal conditions the laser beam transmitted back from the Slave can be detected on the acquisition sensor of the Master immediately after switching off its own laser. The attitude of the Master, of its respective telescope and/or of its proof-mass are adjusted in order to orient the Master with an error smaller than the emitted beam width towards the Slave and to centre the incoming beam on the coherent detector of the Master. If the optical link between the Master and the third S/C has already been established then this attitude adjustment needs to be performed in a way that this link is safely maintained. Finally the laser on the Master is switched on again. After a predefined time the Slave should have accomplished its step S-2 so that the link is operational.

The following steps need to be taken on the Slave S/C:

S-1. The Slave points towards the expected position of the Master with its local laser off and waits for a beam from the Master (scanning with its laser the uncertainty cone) to be detected on its own acquisition sensor. This allows to determine the direction of the received beam and thus of the Master itself. The attitude of the Slave S/C and of its telescope are adjusted towards the Master with an error smaller than the emitted beam width and then the laser is switched on. Thus it is ensured that the Master will in step M-2 of its PAT sequence detect the beam. If the optical link between the Slave and the third S/C has already been established then this attitude adjustment needs to be performed in a way that this link is safely maintained.

S-2. After a predefined time the laser is shortly switched off and on again to check that the laser on the Master is on again. If this is the case, then the Slave can reacquire the incoming beam on the acquisition detector and subsequently centre it on the coherent detector by attitude adjustments of the overall Slave S/C, of the respective telescope and/or of its proof-mass. The local laser is now switched on and a frequency scan of the reference oscillator is performed. After detection of the beat signal on its coherent detector the Slave laser frequency is successfully adjusted to the Master frequency and the link is operational and can be used for data transfer between spacecraft.

Science Mode is the normal mode during Routine Phase. Normally, via both telescopes of a S/M optical links will be established when being in this mode. In a degraded Science Mode only one link could be operational. In Science Mode drag-free control will be enabled to compensate external disturbances such as solar pressure. Proof-mass discharging will be performed at regular intervals. The measurements obtained from the coherent detectors will be pre-processed and compressed on-board and downlinked

every second day via the HGAs. Science data quality should not be impaired by data transmission. Adjustment of the HGAs every second day, however, is likely to introduce mechanical disturbances that will corrupt science data for some tens of seconds.

Safe Mode is primarily designed to ensure a safe power situation (solar arrays Sun pointing) and accessibility from ground. For the different mission phases different safe modes will become necessary:

Safe Near Earth Mode
Safe Cruise Mode
Safe On Station Mode.

After an on-board anomaly, the spacecraft will always first attempt to recover from the failure and continue with the mission timeline. Only if this proves to be not feasible Safe Mode will be entered.

Survival Mode will be entered in case Safe Mode is unable to achieve a safe attitude due to a major on-board anomaly. In Survival Mode the spacecraft is capable of surviving on its own for a virtually unlimited time.

The transitions between these modes are visualised in Fig. 3.6-1.

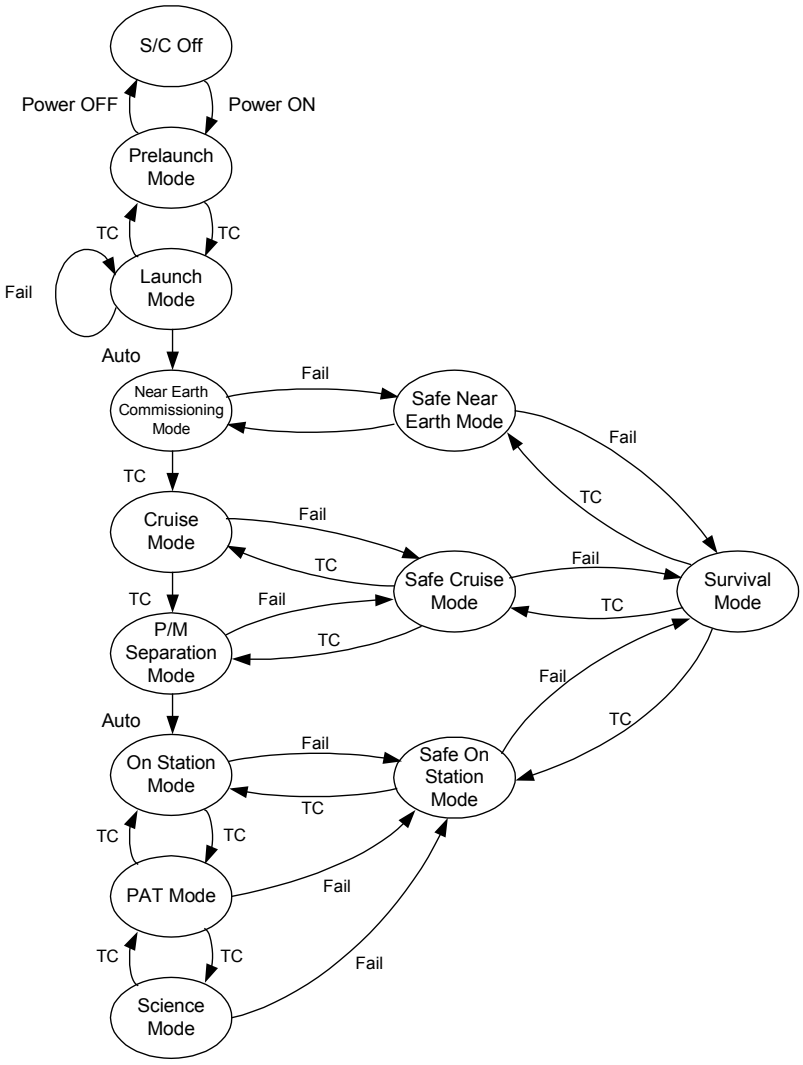

Fig. 3.6-1: System Mode Transition Diagram

3.7 Ground Segment

Within the ESA/NASA collaboration in the LISA mission, NASA will prepare a Ground Segment comprising all facilities (hardware, software, documentation, and trained staff) that are required to conduct the LISA operation under all expected conditions. The operations include planning and controlling the mission and the spacecraft operation. All ground facilities to be established for LISA support will be based on existing ground segment infrastructure tailored to support the specific requirements of LISA. In particular the following sub-systems will be available:

- The Mission Operations and Spacecraft Control Element, MSCE, to perform all mission operations, spacecraft planning, monitoring and control. It will operate the whole Ground Segment and monitor the facilities, resource and operations of the mission.
  The MSCE will generate the mission operations plan and the derived spacecraft and ground segment operation plan. The spacecraft operations plan shall results in an optimised distribution of functions between the space and the Ground Segment. The MSCE will interact with the LSDC for the generation of this plan, and it will report on the actual execution of the operations.
  Automatic analysis of essential spacecraft data will be performed to assess the status of the spacecraft and, if needed, to trigger automatically the reaction to planned contingencies.
  The MSCE will be able to start automatically sequences of pre-stored commands for routine operations or for planned contingencies.
  For contingency operations, the MSCE shall be able to handle other NASA or ESA ground stations that provide temporarily support.
  The MSCE will include facilities for:
  - Telemetry analysis
  - Telecommand generation
  - Flight Dynamics Facility to support the analysis, and execution of: orbit determination and orbit control; attitude determination and attitude control
  - The Spacecraft Software Simulator to be used for Flight Control system and operations procedures validation, and for staff training.
- The Command and Data Acquisition Element, CDAE, to perform all telemetry and command processing. It will be in charge of the Telemetry, Telecommand and Control, TT&C, links with the spacecraft and of the acquisition of the Scientific Payload Data. The CDAE will receive telecommands from the MSCE and will uplink them to the spacecraft as scheduled.
  All scientific and ancillary data will be processed as required, and temporarily stored for a period of at least one week.
  Data will be transmitted from the CDAE to any other element of the Ground Segment as required for mission operations.
- The Ground Stations and Communications Network will be shared with other users during the mission lifetime. Station support for nominal operations will be through stations of the DSN network, and the required sub-systems of the DSN Mission Ground Support Operations will be adapted to the specific requirements of the LISA mission. Daily use while supporting critical phases (LEOP, insertion into operational orbit, Laser beam acquisition, etc.), and in two days interval while on routine phases.

- The Processing and Archiving Element will provide the required processing of the data received to the level required for efficient archiving and delivery to the LSDC. The PAE will perform data quality control, archive the mission data, generate and maintain the data products catalogues, and provide access services to the user community.
- The external connections to the MSCE, LSDC, and the PIs will use commercial and/or public networks.

Before launch all dedicated LISA hardware and software will be developed or procured, installed, and verified. All documentation required for operations will be prepared and the operations staff will be trained. The general purpose facilities will be configured and scheduled for LISA followed by a sequence of Validation Tests and Rehearsals to verify the different elements, and the Ground Segment as a whole system.

For the full duration of the mission and up to ten years after launch the Ground Segment will provide to the LSDC and to the individual users the primary and the archived data. In routine operations data will be transmitted to the LSDC within one day from acquisition, and data from exceptional observations or events not later than 3 hours after acquisition at the ground station.

The Ground Segment will be prepared in accordance with a Mission Implementation Requirements Document issued in advance.

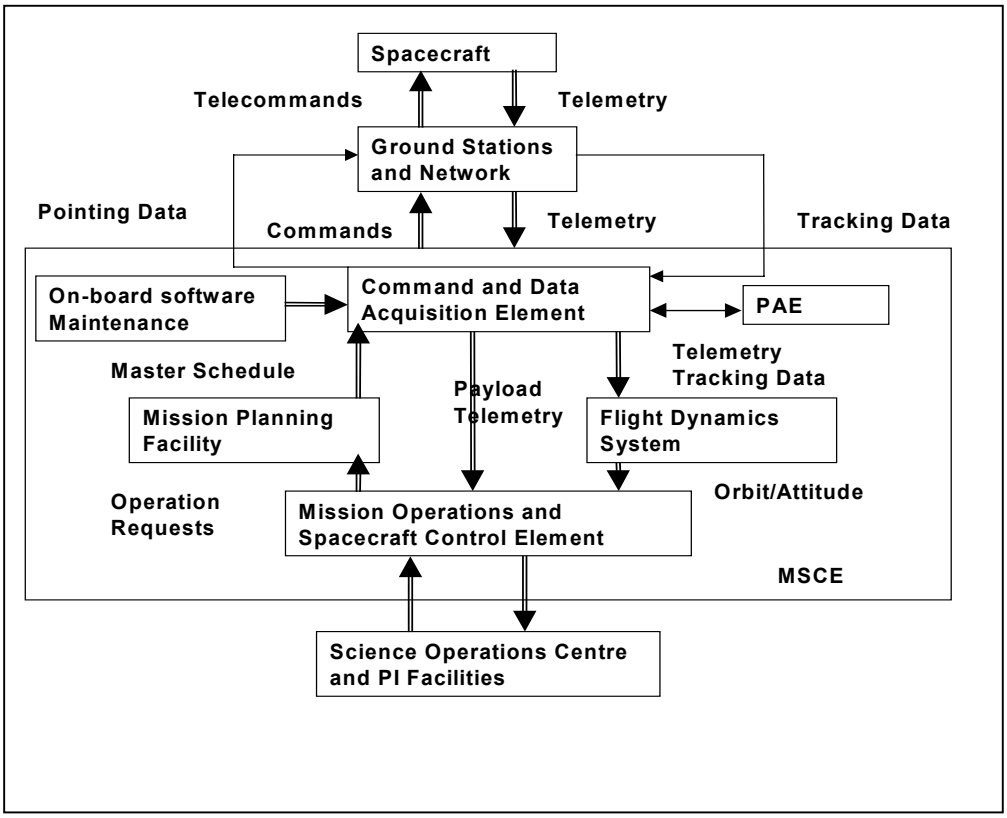

Fig. 3.7-1: LISA Mission Operations System

4 System Design Trade-offs

4.1 System Requirements

4.1.1 Overall System Analysis and Review

The general approach on LISA mission and system analysis is based on the heritage from previously investigated mission and payload concepts. These are documented in the applicable documents AD1, AD2, AD3, AD4. Hence, the mission and general system and payload requirements have been already defined there and the main goals of the system analysis within this study are:

- Validation of baseline payload concepts and specifications including optimisation and improvements
- Brief review of alternative payload concepts
- Spacecraft engineering and mission/spacecraft/ payload interface optimisation
- Identification of cost and development reduction potential

The LISA detection principle for low frequency gravitational waves is based on the observation of resulting minute laser phase changes in the Michelson interferometer arrangement, represented by the three satellite triangle constellation. The interferometer is spanned between freely floating proof masses inside the spacecraft, which are kept essentially inertial in a mission scale reference frame and inside the measurement bandwidth. The purpose of the rest of the spacecraft -besides housekeeping- is to provide the environment for this condition and to establish and maintain the laser interferometer links within the constellation.

The periodic or quasi-periodic gravity wave signals are embedded in an instrument generated noise manifold stemming from **laser shot noise** (masked by technical phase noise) in the medium frequency range and from residual **acceleration noise** on the proof masses for the low frequency part of the measurement band. The high frequency part in terms of instrument sensitivity is further limited by the **geometric antenna response**.

The geometry and therefore the spectral response of the instrument have been pre-selected according to scientific requirements. Hence, the measurement performance analysis, the conceptual design and the system, subsystem and assembly requirements are driven by the goal to minimise the phase noise budget and the acceleration budget in the relevant frequency ranges as mentioned above. However, design loads (cost drivers) of individual subsystems shall not be overburdened.

The gravity wave signals are not derived from a single phase change measurement, but are the result of a data reduction process involving a multitude of sensors on the three spacecraft. Hence, the top level system performance verification is based on a **LISA constellation measurement model**, which in turn establishes the requirements on the individual measurement process and the corresponding error budgets.

The shot noise limited theoretical sensitivity floor is determined by the **laser link budget**. The technical phase noise on top is determined by the laser power spectral density function, the USO noise power spectral density and the phase meter characteristics (filtering, aliasing), respectively. A phase noise cancellation technique utilising the round-trip time delay in the (unequal) interferometer arms is necessary and feasible to approach the shot noise limited sensitivity. An important trade within the

measurement model therefore is between the laser power spectral density performance, the (dynamic) arm length difference knowledge and the phase meter performance.

Accelerations of the probe masses within the measurement band can mimicry gravity wave signals. The support function to maintain the acceleration budget within acceptable limits is the **drag-free control (DFC)**. DFC assures that the probe masses stay essentially inertial within the measurement bandwidth by controlling the spacecraft *position* on the locations of the proof masses (and also the internal relative attitudes between spacecraft and proof masses). The spacecraft position is tracked relative to the inertial masses, which are kept essentially force free in band, by using capacitive internal sensors. The FEEP thrusters are used as positioning actuators and the electrostatic internal actuators for off-band relative positioning.

In order to properly shield external disturbance sources (solar pressure, etc.) spacecraft internal disturbance sources -leading to potentially unacceptable residual proof mass accelerations- need to be controlled accordingly. Sources are thermal gradients in the proof mass vicinity, EMC-effects (proof mass charging, magnetic moments) and control induced disturbance, e.g. by FEEP thrust noise. Main contributors are the **self gravity effects** at proof mass location, stemming from spacecraft mass distribution and thermally induced changes thereof. Thermal changes of the mass distribution function are mainly a result of electrical power dissipation changes and structural and units internal thermo-mechanical stability. A detailed **structural, thermal and gravity model** including all spacecraft-and payload components present in the operational mission phase is used to validate the drag-free control and to optimise parameters and performance. Further, the constraints on the inertial reference sensor proof mass attitude and position envelope are refined.

The second major support function for the coherent phase measurement process is the **pointing, acquisition and tracking(PAT)** of the laser links between the spacecraft. In the operational phase, the relative attitude of the spacecraft and the directions of the beam emission and reception are both tracked by payload optical sensors, providing the error signals for fine attitude control by monitoring relative wavefront tilts between received (beacon) and transmitted (local) laser beam. The attitude and line of sight control actuators are the FEEP thrusters, internal opto-mechanical actuators for adjusting the line of sight relative angle and the inertial sensor internal electrostatic actuators (variable point ahead angle compensation), respectively. For the acquisition phase a detailed strategy is employed to establish and lock the laser links for coherent tracking. Both functional modes are validated by link budget and pointing and attitude error budgets and control models.

The measurement performance model validation finally leads to refined design and optimised requirement specifications on subsystem, assembly and components level. Further, cost driving designs (e.g. power dissipation stabilisation in any component) are identified and can be avoided.

Figure 4.1-1shows a flow diagram for the LISA system analysis and performance validation methodology outlined above and as used in the course of the study. Activities within each block shown in the diagram are detailed in chapters 5, 6 and 7, respectively.

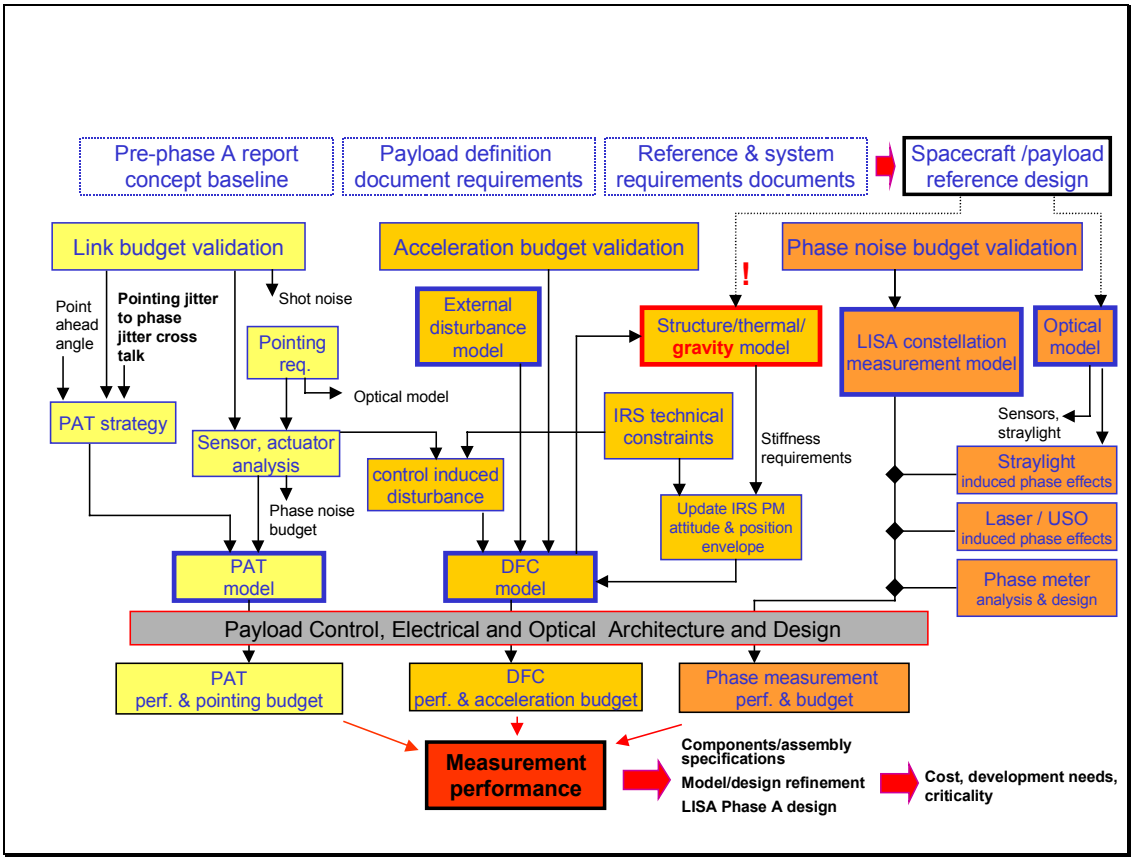

Figure 4.1-1 Flow diagram for the LISA system analysis and performance validation methodology followed in the study

4.1.2 System Requirements

The System Requirements for LISA are specified in the Applicable Documents, in [AD1],[AD2], [AD4]. Table 4.1-1 summarises key requirements relevant for the performance, including updates during the study. A detailed discussion of requirements related to subsystems is given in the corresponding sections. Operational requirements are not listed.

4.1.2.1 Summary of System Requirements

The following table gives an overview on the major system requirements.

Table 4.1-1 Summary of key system requirements (baseline configuration)

Main System Requirements		
Mission/Scientific Requirement	**Value**	**Comments**
Measurement error Δl	$4 \cdot 10^{-11} m$	Accuracy of measurement for the variation of distance between two S/C´s.
Strain sensitivity $\Delta l / l$	10^{-23}	To be achieved at one year observation with a signal to noise ratio of S/N=5
Frequency range of grav. waves	$0.1 - 100 mHz$	Selected spectral range of measurements. The spectral range determines the required distance between satellites and is a major design driver for S/C (thermally induced distortions)
Location of science objects Wave polarisation	< 1 amin (periodic) few degree (other)	Spatial resolution and wave polarisation are determined by analysing Doppler shift and differential amplitudes in the signals from three arms
Data acquisition		Observation data shall be acquired and processed on ground for not less than 90% of the mission time.
Mission duration	2 years at least	(10 years optional)
Orbit Requirements		
Heliocentric orbit		Three satellites form a equilateral triangle. Two arms form an interferometer.
Distance from the earth	$20\,\mathrm{deg}$	The centre of the triangular formation is in the ecliptic and 20 deg behind the Earth.
Plane of triangular S/C formation	$60\,\mathrm{deg}$	Selected inclination with respect to the ecliptic maintains S/C formation throughout a year. S/C´s rotate about the centre of the triangle once per year.
Distance between individual S/C´s	$5 \cdot 10^{9} m$	The arm lengths define both the sensitivity and the spectral response of LISA.
Difference of arm length Relative position	1% (AD1) 30 km (PDD)	Needs to be confirmed during the study. The allowed difference of arm length reflects a requirement for orbit maintenance, i.e. frequency of manoeuvres, thruster performance, propellant, etc.

		Correction of laser phase noise to achieve the required system sensitivity drives this requirement [AD1].
Max. relative velocity between S/C´s	$\leq 15 m/s$ (AD1) 0.03 m/s (PDD)	Needs to be confirmed during the study. The allowed relative velocity of satellites drives the requirement for orbit maintenance, i.e. frequency of manoeuvres, thruster performance, propellant, etc. Measurement of Doppler, heterodyne bandwith and reduction of USO noise to achieve the required system sensitivity drive this requirement [AD1].
Knowledge of arm lengths	$< 200m$ (AD1) 10 km (PDD)	Determines the quality of the noise reduction algorithm. Appears feasible e.g. by laser ranging
Payload Requirements - Laser		
Number of Lasers per S/C	2 + 2 spare	Nd:YAG monolithic non-planar ring laser. One laser plus one spare laser per optical bench.
Optical output power	$\geq 1W$	Drives the laser link budget together with space loss, receiver area and detection efficiency
Spectral density of frequency stability at 1mHz	$\leq 30Hz/\sqrt{Hz}$	One laser serves as master (commanded) which is locked to a reference cavity (Fabry Perot). All other lasers are phase locked (offset)to the master laser. Low frequency noise is reduced from the beat signal by a noise reduction algorithm [AD1]. The laser phase noise is to be traded against knowledge of arm lengths.
Spectral density of relative power stability at 1mHz	$\leq 2*10^{-4}/\sqrt{Hz}$	The variation of laser power contributes to acceleration noise of the inertial sensors (proof masses)
Payload Requirements - Optics		
Transmission of optics Optical isolation Depolarisation	≥ 0.3 TBD TBD	The achievable valuesin both the transmission and receiving path enter the laser link budget and affect straylight and crosstalk
Payload Requirements - Telescope		
Aperture	$0.3m$	The current design described in [AD1] assumes a primary mirror of

		0.3 m diameter. Low thermal expansion material for the mirrors or athermal design is to be used to minimise phase errors due to thermal effects.
Focal length	$f/1$	According to [AD1] a Cassegrain design of Richey-Chretien type is baseline.
Wavefront tolerance	$\lambda/10$	Besides pointing offset sensitivity, heterodyne efficiency and link budget are affected
Spectral density of temperature variations at 1mHz	$1 \cdot 10^{-5} K/\sqrt{Hz}$	The required thermal stability of the telescope takes into account low expansion material used for mirrors and the supporting structure. The requirement is driven by the allowed contribution to the distance measurement error.
Payload Requirement – Optical Bench		
Thermal expansion of bench	CTE ~ 10^{-8}/K	A trade off between Ultra Low Expansion (ULE) glass and Zerodur is performed during the study.
Spectral density of temperature variation	$\leq 1 \cdot 10^{-6} K/\sqrt{Hz}$	Spectral density of temperature variation at 1mHz caused by variation of the solar constant. (4min oscillation). Temperature variation by power dissipation of any electronics must comply with this requirement.
Payload Requirement – Inertial Sensor		
Resolution of inertial sensor	$1 \cdot 10^{-9} m/\sqrt{Hz}$	Required resolution of the sensors to limit disturbances induced by relative motions between proof mass and S/C.
Acceleration by disturbing forces per sensor at 0.1 mHz	$3 \cdot 10^{-15} m/s^2\sqrt{Hz}$	Various disturbances contribute to the acceleration noise. The corresponding distance (phase) error is proportional to $1/f^2$, i.e. acceleration noise limits the sensitivity of LISA towards low frequencies.
Payload Requirement - USO		
Allen Variance at 10^4 sec	$2 \cdot 10^{-13}$	This requirement is reported in [AD2]. The proposed algorithm for reduction of USO noise shows that after processing no USO noise remains. Consequently the required Allan variance possibly may be re-accessed.

Requirement - Drag Free Control		
Displacement between S/C and proof mass in sensitive direction	$< 2.5 \cdot 10^{-9} m / \sqrt{Hz}$	Requirement in measurement band width.
Displacement between S/C and proof mass in orthogonal directions	$< 2.5 \cdot 10^{-9} m / \sqrt{Hz}$	The cube positioning in the lateral beam direction must be similar to avoid excessive cross talk.
Relative attitude between S/C and proof mass	$< 1.5 \cdot 10^{-7} rad / \sqrt{Hz}$	Internal contribution to the beam pointing budget
Payload Requirement – Pointing		
Offset pointing error (DC)	$< 3 \cdot 10^{-8} rad$	This is a requirement on the allowed angular fluctuation of interfering beams. The distance (phase) error needs to be controlled by a dedicated pointing system that uses the phase information of the quad-diodes that are also used for detection of the beat signal. Since the product of DC pointing error and pointing stability defines the overall phase error a trade off of both requirements can be performed.
Spectral density of pointing stability	$8 \cdot 10^{-9} rad / \sqrt{Hz}$	See above. The values are affected by pointing jitter achieved and by astigmatism primarily
Point Ahead Angle	$3 \cdot 10^{-6} rad$	Nearly time independent angle between incoming and transmitted laser beam due to S/C motion, arm length and speed of light.
Measured Signals		
Number of signals to be acquired per SC	$4 + 2$	Based on the current design described in [AD1], six signals per S/C have to be acquired for elimination of laser and USO phase noise as well as for the determination of the Doppler. After down conversion and low pass filtering each signal is sampled at 1-2 Hz (TBD)

4.1.2.2 Magnetic field requirements

The magnetic field requirements had not been well defined at the begin of the study. As a potential design driving element, this issue has been specifically analysed in the following.

There are three main requirements on magnetic field environment. They all stem from the need to restrain forces on the test-mass.

The magnetic force on the test-mass is given by: $F_B = \frac{\chi}{2\mu_o} \int_S B^2 dS$ where the integral is extended to the surface of the mass assumed to have homogeneous susceptibility χ.

For the rest of this section a test mass cross sectional area of S=4×4 cm^2 and a magnetic susceptibility of $\chi=10^{-6}$. Is assumed.

The first request is that any dc magnetic force is well below other static dc forces. This requires that:

$$F_B \approx \frac{\chi S}{2\mu_o}\Delta B^2 \le 10^{-11}\,N \rightarrow \Delta B^2 \le 1.5\,10^{-8}\,T^2 \rightarrow \frac{\partial B^2}{\partial x} \le 4\,10^{-8}\,\frac{T^2}{m}$$

Notice that, with a belt and braces approach, $\Delta B^2 \approx B^2$, this can be translated to B< 1gauss.

Unfortunately this very last requirement is not safe for what relates to magnetic field fluctuations. Sun magnetic field fluctuations have approximately a 1/f spectrum with a value of ≈2 $10^{-7}T/\sqrt{Hz}$ at 0.1 mHz (Figure 4.1-2). As the rms fluctuation is around 2 nT the effect of this field can be calculated as

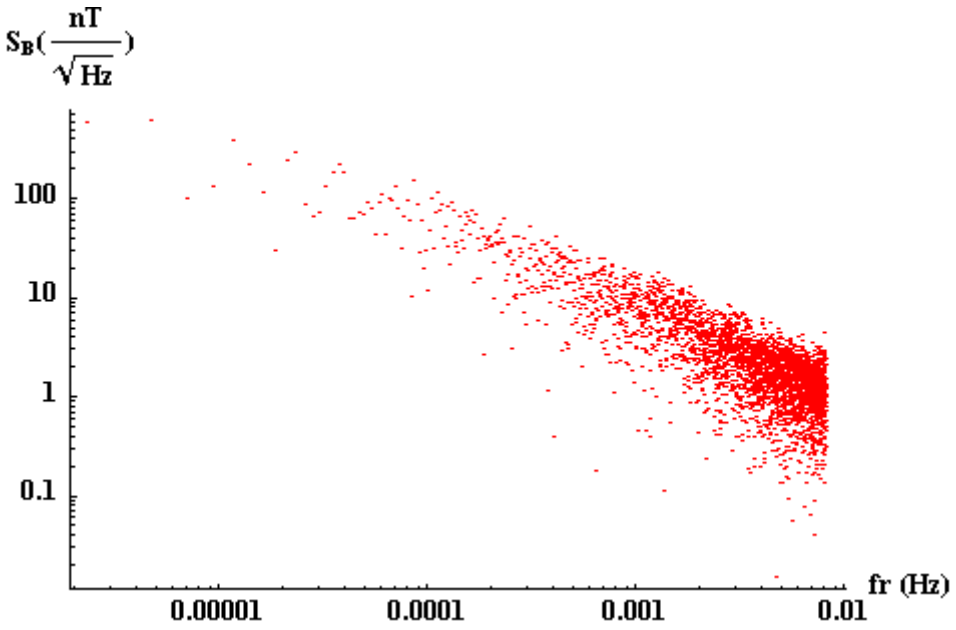

Figure 4.1-2 Sun magnetic field fluctuation as measured by Ulysses in 1990 with the s/c at ≈ 1 A.U. from the sun.

$F_B = \frac{\chi S}{\mu_o} \Delta B(dc) \delta B_{Sun}$, the gradient due to the magnetic field of the Sun being negligible.

The need to keep this random acceleration well below $10^{-15} ms^{-2}/\sqrt{Hz}$ at 0.1 mHz implies $\Delta B \leq 10^{-6}$T that is $\partial B/\partial x \leq 2.5\ 10^{-5}$ T/m. With this value the requirement on the absolute value of the dc field can be relaxed down to 10^{-2}T. In Figure 4.1-3 we report the average value of ΔB for a 1 Am^2 dipole oriented parallel to one of the faces of the test mass lying on a line orthogonal to the same face and located at distance d from the centre of the test mass. Notice that a $\Delta B \approx 10^{-6}$ T is achieved

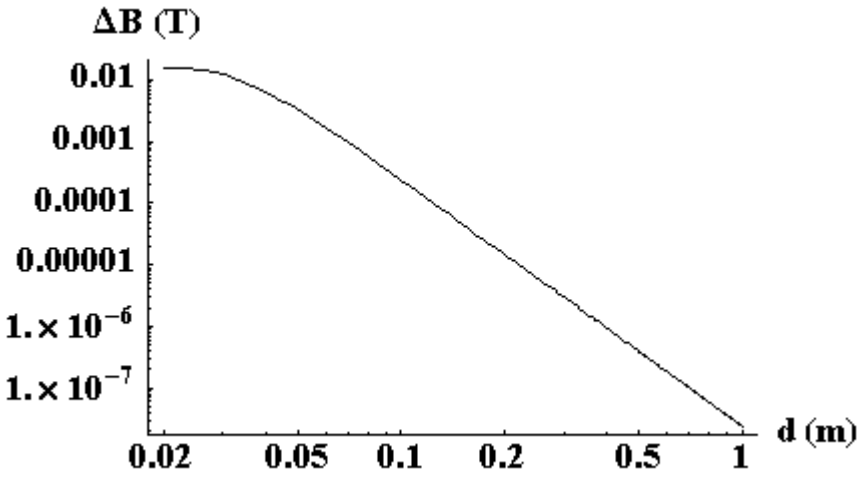

Figure 4.1-3 *The average value of ΔB for a 1 Am^2 dipole oriented parallel to one of the faces of the test mass lying on a line orthogonal to the same face and located at distance d from the centre of the test mass for d ≈ 40 cm. Closer dipoles have consequently to be less intense.*

For comparison in Figure 4.1-4 the same quantity for a 1 A linear current is reported. The safe figure is achieved at 10 cm.

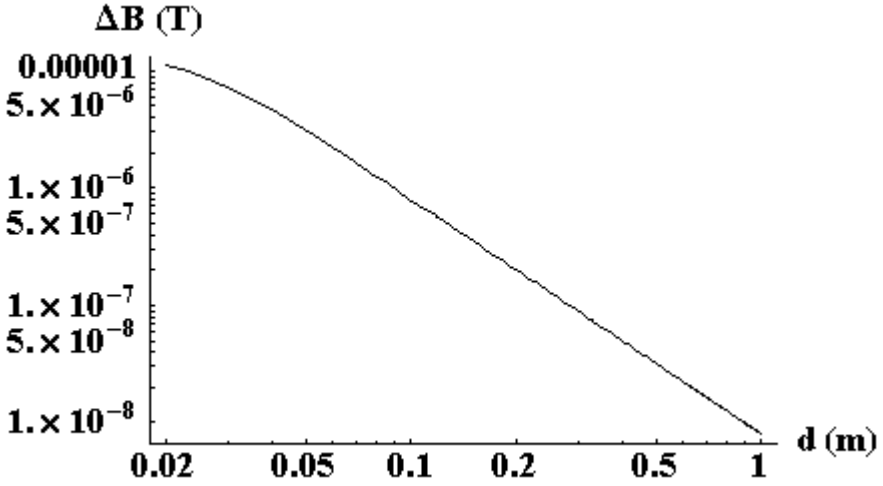

Figure 4.1-4 *The average value of ΔB for a 1 A linear current oriented parallel to one of the faces of the test mass and located at distance d from the centre of the test mass.*

Obviously the above figures remain safe provided that the level of magnetic fluctuations $\delta B_{s/c}$ due to sources located inside the s/c does not exceed that due to the magnetic field of the Sun. For comparison this means that a field with similar spectrum should have a rms value < 2 nT ≈ 20 μgauss.

For a dipole of 1 A m^2 like the one in Figure 4.1-3, located at 40 cm from the test-mass centre this would correspond to a relative fluctuation of ≈ 10% $Hz^{-1/2}$ at 0.1 mHz.

Parameter	Symbol	Value	Comments
Static field	B(dc)	< 10^{-4} T	Very cautious figure
Static magnetic field difference across test-mass	ΔB(dc)	< 10^{-6} T	
Magnetic field fluctuation	$\delta B_{s/c}$	< 3 10^{-7}T /√Hz @ 0.1 mHz	

The above considerations do not include any magnetic shield. If a shield with a shielding factor of 100 is assumed, figures can be relaxed accordingly, but the properties of the shield at very low frequency should be assessed.

As it can be seen from the discussion above, there is no specific request for the magnetic moment of the spacecraft.

4.1.3 System Architecture

A definition of system elements is illustrated in Figure 4.1-5. It is detailed on mission, configuration, spacecraft, science module, platform/payload, subsystem and partially on assembly level

The mission, deployment and operational aspects are addressed elsewhere in this report (chapter 3), hence the following sections deal primarily with the science module system options and trade-offs.

A functional block diagram of one of the three identical science module and the interface to its propulsion module is shown in Figure 4.1-6.

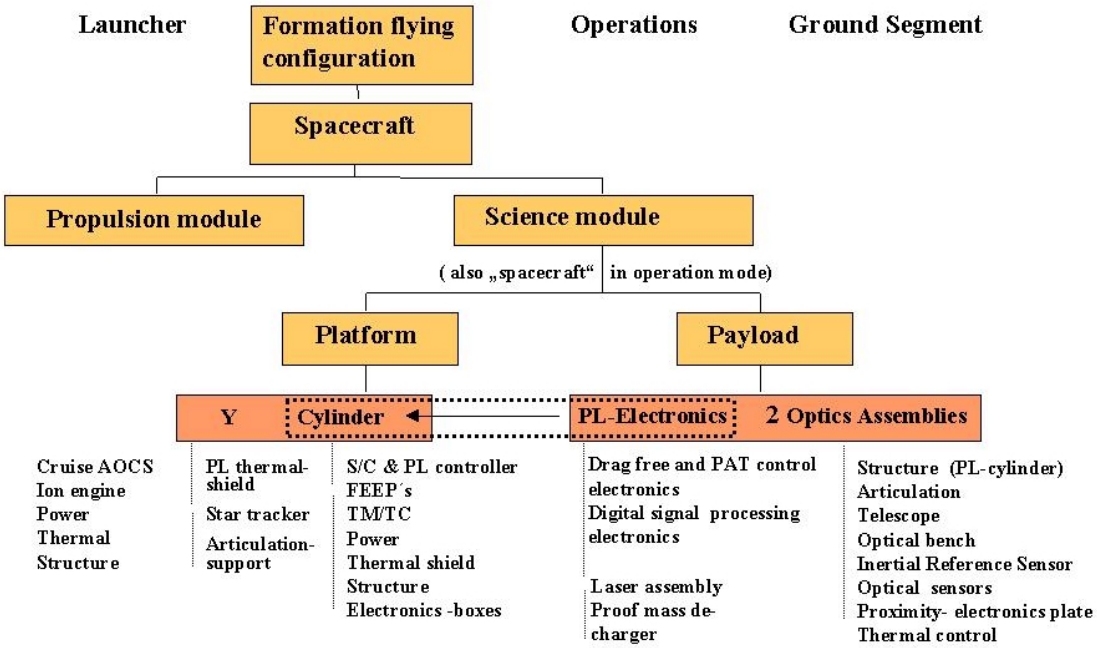

Figure 4.1-5: LISA baseline system elements

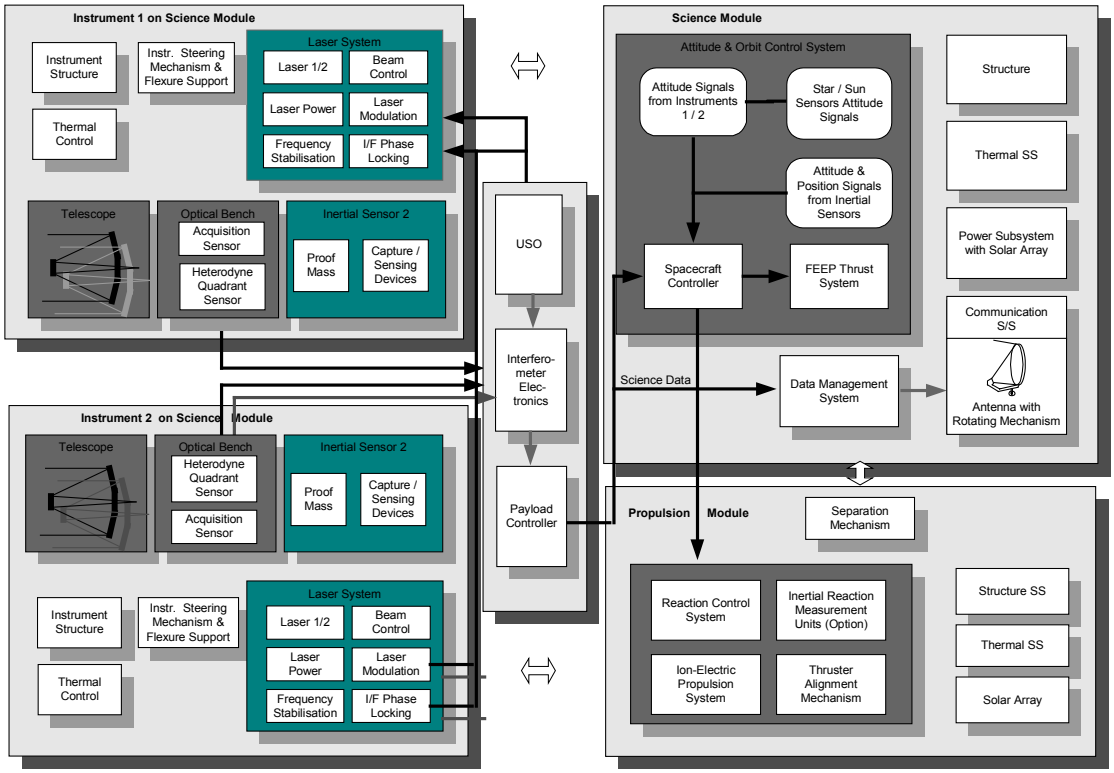

Figure 4.1-6: Functional architecture of a LISA science and propulsion module.
The payload, subsystems, assemblies and main links are shown in their baseline configuration

4.2 System Options and Trade-off

On mission and spacecraft level, several system options have been investigated in order to meet operational constraints (launcher, transfer orbit, cost cap). The mission scenario had been baselined (orbit, constellation, launcher). Major trade-offs therefore were focussing on the propulsion module / science module configuration, the communication link and the internal structural, electrical and thermal concept.

The LISA payload itself has been analysed in detail in previous investigations and has been defined as a baseline for this study by the LISA science group (AD2: Payload Definition Document). Nevertheless, at the begin of this study a brief qualitative review of alternative payload concepts on payload system level, subsystem, assembly and components level has been performed in order to identify concept and design options, which have the potential to:

- Solve encountered technical problems with the baseline approach
- Drastically reduce the technical complexity and hence the risk of failure
- Enhance mission reliability and redundancy
- Allow a better validation of performance in terms of AIVT procedures and costs
- Lead to less stringent tolerances in design parameters and to optimised share of design loads among subsystems
- Lead to significant reduction in cost and development effort

Of course within the scope of the study it was not possible to perform any detailed analysis of alternative payload concept options. Further, the baseline concept as described in the AD2:Payload Definition Document has been analysed so far in much more detail compared to the potential alternatives. Especially, for the CAESAR baseline inertial reference sensor, a long heritage of precursor developments exists. In an effort to identify less complex approaches, it may well turn out, that a promising alternative (e.g. featuring less control degrees of freedom) may be more complex at the end after detailed investigation. Hence, the alternatives have been identified as a pool of concept options to draw upon only in case principle difficulties would have been encountered with the baseline concept. However, as major result of this study, the baseline concept at the recent level of investigations turns out to be a valid approach indeed, with some modifications necessary on assembly level (e.g. point ahead angle compensation implementation).

4.2.1 LISA Alternative Payload Concepts

Single (spherical) proof mass. In a first approach, the payload concept alternatives identified have been focused on the desire to reduce complexity by replacing the two proof mass concept in each spacecraft by a single proof mass, serving as an inertial reference for both line of sight directions. A further reduction potential for the degrees of freedom to be controlled has been tentatively identified by replacing a (single) cubic proof mass by a sphere.

The number of degrees of freedom in the inertial reference system which need to be controlled would be reduced from 12 (2 proof masses) to 6 (1 cubic proof mass) or even to 3 (one spherical proof mass),

leading to a simplified control architecture. On the other hand, the two adjacent laser interferometer arms would be tightly coupled and in case of failure of the single proof mass, the mission would terminate. This is not the case for two independent optical assemblies in each spacecraft, because the Michelson interferometer could be still kept operational on two arms. A further complication is the requirement to continuously adjust the angle between the lines of sight by about +-1° over a period of 1 year. As a consequence either additional degrees of freedom have to be introduced in the interferometric optical path or the reference reflector, i.e. the proof mass mirror has to be shaped accordingly, e.g. as a spherical surface. A conceptual sketch is shown in Figure 4.2-1 for the case of a spherical proof mass and a tetrahedral geometry optical read out system for proof mass to cage position. In order to meet optical alignment requirements, the proof mass as part of the interferometer optics has tight position tolerances in all three DOF, which may be in the same order as already required from self-gravity effects minimisation (few nm) and which are well in the reach of optical read out systems. However, the necessary control stiffness needs to be assessed in a detailed analysis as well as the consequences for operation in the LISA desired low stiffness inertial mode (within the measurement band). The sensor is invariant to the attitude DOF for a perfect sphere only. Spheres presently can be manufactured to about 30 nm surface rms and bulk density variations of 10^{-6} (Silicon; Physikalisch Technische Bundesanstalt Braunschweig). Rotating the sphere at a rate larger than the measurement bandwidth would average out surface deformations. The rotation could e.g. be excited prior to the measurement phase by a rotating electro-magnetic field.

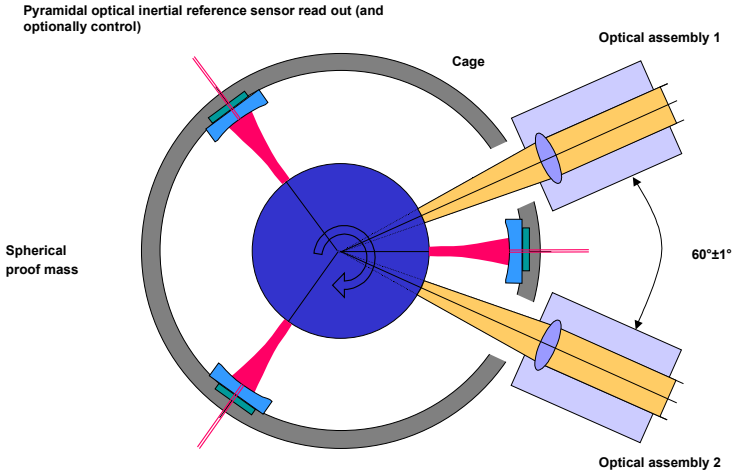

Figure 4.2-1 *Spherical proof mass inertial reference sensor concept, featuring an all optical read out, based on cavity gauge laser interferometers in a pyramidal geometry. Surface deformations can be averaged out by rotating the sphere at a sufficiently high rate.*

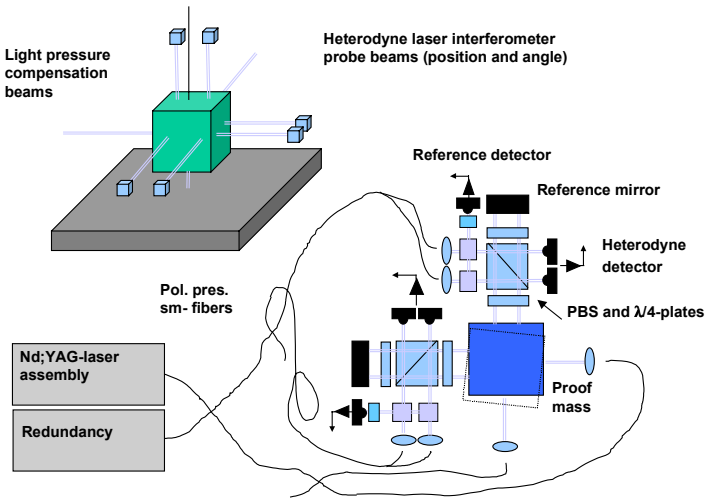

Figure 4.2-2 Inertial reference sensor all optical read out concept utilising pm-resolution polarisation /heterodyne laser metrology

IRS optical read out. Simplification potential has been identified in replacing the electrostatic capacitive internal sensors in the inertial reference by optical interferometric sensors, i.e. an overall optical readout assembly.

Laser interferometer measurement systems are already commercially available with nm resolution and – on laboratory or prototype level- with few pm resolution for relative distance change measurement. Two principles are prime candidates for this application: Heterodyne polarisation interferometers and resonant cavity gauge interferometers, both verified technologies. Principle layouts are shown in Figure 4.2-1 and Figure 4.2-3. (Small) attitude changes can be monitored in addition to position by using e.g. two adjacent probe beams or alternatively by quad-cell heterodyne detectors in the same way as already baselined for the LISA interferometer coherent tracking sensor. In the case of resonant cavities, the excitation of higher order cavity modes could also provide attitude information. The advantage of pm-optical read-out sensors over the baselined capacitive sensors would be a higher resolution, the possibility of a large gap between probe mass and cage (cm) and a large linear measurement range not affected by electrostatic stray fields between electrode arrangements. The laser source can be conveniently generated by splitting off a tiny fraction of the highly frequency stable LISA transmitter laser beam already on board. On the other hand, any probe beam light pressure accelerates the proof mass at a level, exceeding for the required power levels (μW) already the requirements. Hence a light pressure compensator beam is required and only differential effects (differential intensity fluctuations, straylight induced light pressure and thermal effects) need to be controlled.

IRS internal all optical control. An extension of the optical read out concept is the replacement of the electrostatic control of proof mass attitude and position relative to cage by a complete optical control (actuator), allowing an essentially electrostatically field free environment for the proof mass with large gaps to the cage. The accelerations to be controlled are in the order of 10^{-9} m/s^2, corresponding to power levels of 1 W. In principle, the power levels in the probe beams could be adjusted to operate as control actuator. However, at such optical power levels in the vicinity of the proof mass detrimental

effects from straylight, thermal deposit (mirror absorption) and unbalanced radiation fields need particular attention.

An interesting feature in this context is the inherent capability of cavity gauges of utilising the resonant stored power enhancement., The cavity Q-value strongly depends on internal absorption, alignment and laser mode matching, effects providing potential handles in order to perform the light pressure control action. This would allow to keep the laser light levels outside the resonator low; e.g. at a resonator input power of 1mW and for a resonator gain of 1000 an acceleration of 5 10^{-9} m/s^2 could be applied to re-centre the proof mass. In fact, when the laser is tuned to a slope of the resonator mode in a proper way, an optical self-centring action on the proof mass is possible in an arrangement where the proof mass is representing the floating mirror between two resonators, Figure 4.2-3. The set point and control stiffness can be selected by tuning the laser frequency. This principle of course requires precise alignment of the resonator / proof mass mirror arrangement, differential optical power stability below 10^{-4} as well as asymmetric stray light action on proof mass below 10^{-4} in order to keep residual accelerations below 10^{-16} m/s^2sqrt(Hz). Shot noise fluctuations are sufficiently low (10^{-7}) at the required power levels. No detailed analysis has been carried out so far for this conceptual idea and there are still many open issues to clarify with respect to feasibility, suitability and complexity. E.g. initial alignment and re-acquisition of the proof mass after loss of optical lock are critical items.

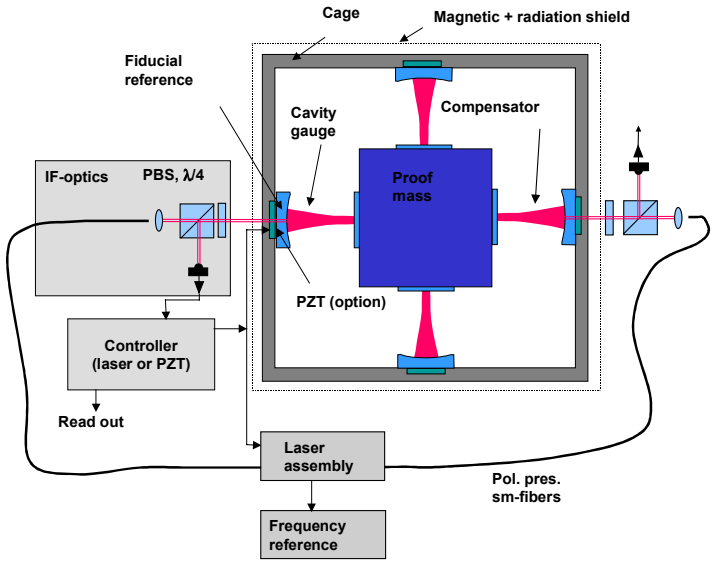

Figure 4.2-3 *Inertial reference sensor all optical read out concept utilising pm-resolution cavity gauge laser metrology*

Laser metrology harness. Once an optical read sensor for the inertial reference sensor has been developed which has pm-resolution capability, this subsystem could be extended to an optical assembly internal laser metrology harness (operating at a different wavelength, e.g. 1.5 µm), monitoring all critical internal optical paths with pm accuracy and ,hence, allowing a discrimination between laser phase changes generated by detrimental effects inside the spacecraft and those stemming from outside. However, despite of introducing a rather complex all optical active monitoring subsystem, it is not clear at the moment, whether this would detect all relevant internal optical path noise sources in a proper way. An advantage of such an approach would be, that the LISA laser interferometer could be optically separated from the inertial reference sensor, by having the reference mirrors on the optical bench rather

than on the proof masses, Figure 4.2-4. Any relative movements of proof mass and reference mirrors would be monitored and these signals could be integrated into the data reduction. Only one proof mass would be necessary. Also the annual angular variation of the line of sight directions could be implemented in a simple way.

Single proof mass as accelerometer. In combination with a sensitive optical monitoring system for all internal critical spatial degrees of freedom as sketched above, it could be interesting, to operate the inertial reference as an accelerometer. That means strong coupling to the spacecraft and precise monitoring of proof mass position by dedicated picometer-resolution laser metrology. Again, the LISA laser interferometer reference mirror could be located on the optical bench and the spacecraft motion, while freely floating, is affecting the heterodyne beat. Its influence, however, could be separated by employing the accelerometer read out for data reduction.

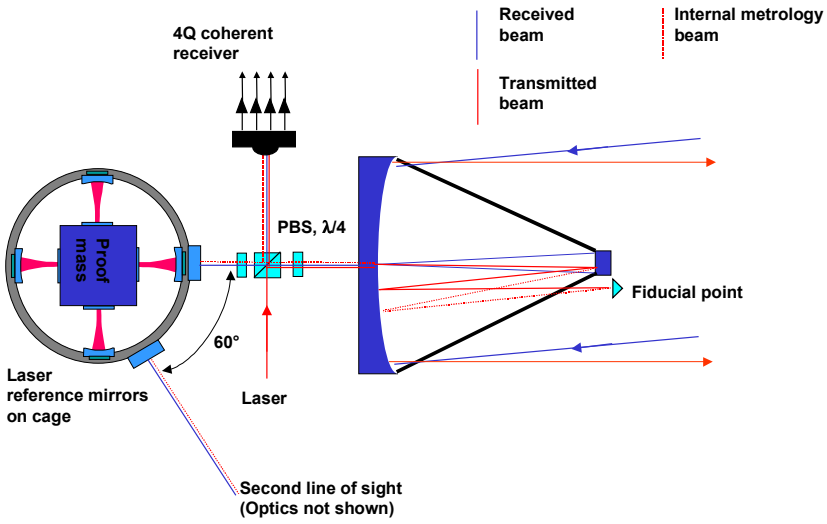

Figure 4.2-4 *Internal laser metrology harness to monitor all relevant distance changes at pm resolution. One single proof mass (all optical read out to provide the necessary pm accuracy) is the inertial reference. The LISA laser interferometer reference mirrors are rigidly mounted on the optical bench. They can be shaped to allow the annular angular variation of line of sight without introducing additional degrees of freedom in the interferometer path.*

4.2.2 LISA Spacecraft System Options and Trade-off

4.2.2.1 Configuration Concept Options and Trade-off

The configuration of the LISA spacecraft is dictated by two factors. The first is the large instrument assembly for the two laser telescopes, and the second is the restriction from use of the Delta II launcher.

The possible concepts for carriage of 3 identical spacecraft have then to be of a short cylindrical form. Within this form 2 basic arrangements are possible.

- Integrated science module (instrument, bus) and propulsion module.
- Autonomous science module as one element, and a separable propulsion module

The propulsion elements are to provide the energy for transfer from near-Earth to the operational orbit.

It was decided early in the study to choose the separable version, due to the potential disturbances to the science operation by the propulsion elements that may deteriorate measurement accuracy. Only the separable version has thus been considered in detail and represents the baseline concept.

It had been briefly discussed early in the study to use one or all of the separated propulsion modules during the operational mission phase as data relay stations to earth, a concept, having some advantages for the communication link. However, due to the then increased complexity of the whole mission operation and the availability of alternative solutions for communication this option has not been carried on.

Further trade-offs to be considered for the instrument and bus (science module) configuration are as follows:

- Optimisation of diameter to height
- Location of star trackers
- Structure concept for the carry-through structure of the stack of 3 spacecraft combinations
- Optimisation of unit accommodation within the allowed volume
- Thermal measures to allow for the inclined flight attitude of the satellite to the sun-satellite line
- Accommodation of the link antenna
- Accommodation of the FEEP thrusters
- Arrangement of the propulsion motors to allow for centre of gravity movement during transfer orbit

These factors do not allow a clean and simple classical trade-off, since almost all the items are related to each other. In consequence the derivation of the optimised configuration is discussed further in Chapter 5.2 and 5.4 and forms part of the description of the final concept.

Integrated module concept. Driven by the requirement to minimise the stack height of the three spacecraft configuration, as dictated by the launcher selection, the propulsion module comes out as a very flat cylinder, surrounding the science module (see chapter 5). This has negative consequences for the structural concept and solar array arrangement, increasing e.g. the mass budget. Hence, re-

consideration of the integrated module configuration, taking into account these constraints may be of interest in further studies. Of course, the concerns related to the instrument operation remain valid:

More components need to be included into the detailed thermal and gravity model to model gravity effects at the proof mass locations. Especially critical are uncertainties in remaining propellant distribution from the coarse AOCS subsystem. A nearly reaction-free venturing prior to science operation appears necessary. Similarly, the mass distribution of the ion engine Xenon propellant would need careful balancing.

The spacecraft mass to be handled by the fine AOCS system (FEEP´s) is increased.

EMC aspects: The sensitivity of the proof masses to magnetic stray fields, leading to torque and accelerations due to interacting magnetic moments from the interplanetary field, the spacecraft internal fields and the induced proof mass field requires a compensation of potential internal sources. In the propulsion module main candidates are the ion engines and propellant valves. Dornier Satellitensysteme has gained experience from careful compensation of magnetic stray fields from valves and other sources (e.g. electrical harness) in the CLUSTER spacecraft design, aiming at minimisation of disturbance for the magnetometer measurements. This gives confidence, that the problem can be handled in a similar way for LISA; exact requirements are however still lacking, as the magnetic susceptibility of the proof mass alloy is presently not specified (see section 4.2). The RITA ion engines developed at Dornier Satellitensysteme do not employ any permanent magnets and hence are essentially stray-field free when shut-off.

On the other hand, the availability of the ion engines during the whole mission would maintain coarse delta V capability. This could be of interest for an extended mission duration, in order to keep the triangle configuration within constraints in terms of relative spacecraft velocities and arm lengths.

Mechanisms: An integrated module would of course require no internal separation mechanisms, thus increasing the mission reliability and reducing complexity. Possible detrimental gravity effects from mechanically moving parts as engine pointing mechanisms and loose valve components, caused by unknown mass distributions at the end, need to be investigated in detailed modelling.

4.2.2.2 Structural concept options and trade-off

The overall configuration is driven by the available fairing size. The potential structural concepts are further constraint by thermal needs. Thus only a very limited number of options are available.

- The solar array either needs to be stiff in itself or needs a large number of fixation points. The number of fixation points has to be minimised in order to maintain sufficient thermal decoupling, therefore a sandwich design is needed. For reasons of thermal decoupling a 20mm Polyimide foam shall be used in the sandwich core. The mechanical properties of that material do not allow to rely on that foam core also for panel stiffness. An additional sandwich layer with an aluminium honeycomb core has to be introduced. As an alternative also a Nomex or Kevlar honeycomb could be used, which could save mass and provide additional thermal insulation. The solar array of the Mars Pathfinder e.g. made use of a Nomex honeycomb. The solar array is a driver for the thermal stability performance and also significantly adds to overall mass. Full use of Nomes properties could be made if the honeycomb cells could be filled with foam. This is considered to be a technology problem to be covered separately. As baseline the aluminium honeycomb was used. In case a foam filled Nomex honeycomb could be made available, the thermal performance could be improved and

some mass savings achieved. The stiffness is driven by the panel thickness and the material selection for the face sheets. CFRP face sheets are selected and the panel thickness is adapted for the required stiffness.

- The transfer of loads through the modules requires 3 tubes which are connected by shear walls. Plane walls are used as well for structural as for unit accommodation reasons. Cylindrical walls neither provide better mechanical behaviour nor allow for more space for unit accommodation.
- For the accommodation of units a top and a bottom plate are needed. They have to provide sufficient stiffness to carry the mass of all units. Since the shear walls cannot support the outer parts of the plates, additional webs are needed. Radial webs cannot be used for accommodation and thermal reasons. Since the circumference would have to be closed anyhow, a conical wall connecting top and bottom plate is used. This gives a closed casing with sufficient stiffness.
- The material selection is not driven by stiffness considerations since all facesheets of the sandwich panel are at the minimum acceptable value from manufacturing and handling point of view. However, CFRP could provide for mass savings because of its lower density.

4.2.2.3 Thermal concept options and trade-off

Since space for unit accommodation is very limited, there is little freedom in the thermal design. Ideally, all dissipating units would have been placed on one plate on the shadow side of the science module thermally insulated from the rest of the module. For unit accommodation reasons however, top and bottom plate had to be used. This only leaves the conical sidewall as radiating surface for heat rejection. For payload units relying on very stable temperatures, also a dedicated insulated radiator on the anti-sun side can be provided.

Normally MLI would be used as thermal insulation material. The insulation properties of MLI can only be predicted with a limited accuracy. Furthermore the properties undergo changes due to handling on ground and due to deformation of the foils because of moisture release and other effects in orbit. Therefore gold coatings will be used as insulation.

In case of the solar array, also heat capacity is needed to reduce the transfer of solar constant induced temperature fluctuations from the front to the rear side of the solar array. In this case a polyimide foam is used, which gives a very uniform insulation over the whole solar array area.

The thermal coupling of the rear of the solar array to the rest of the science module is driven by radiation and thus increases with T^4. Therefore the solar array temperature has to be minimised. This is achieved by covering all solar array areas which is not needed for solar cells with OSR.

All electronic units will show some variation in their dissipation. In order to reduce resulting temperature disturbances of the payload, the heat has to be rejected as directly as possible to space. This is achieved by mounting the units on insulating feet and by providing a gold coating on the faces of the units with view to the payload. A limited number of units could be mounted on the anti-sun side with a dedicated radiator insulated from the rest of the science module. This has to be done for all units showing a fluctuation of dissipation of more than 0.1W. However, due to limited space, this is only an alternative for a very limited number of units.

4.2.2.4 Electrical Architecture Concepts and Trade-off

Centralised Processing System Concept. For Phase A2 an early decision has been made to aim for a centralised processor system (CPS) for the adoption of the S/W tasks for C&DH, AOCS, and Instruments because of the necessity for complex integrated control during the science phase, i.e. mainly telescope pointing, fibre positioning, proof mass control with drag-free control. The envisioned processor module is based on an ERC-32 single chip microprocessor which implements SPARC V7 architecture. The performance provides 17 Mips / 3.4 Mflops @ 24MHz which is manifold (factor of ca 15) the performance of the 31750 processor of ROSETTA.

As it would be a major design driver to implement also the electrical physical layer interface into a centralised unit this CPS must be supported on this physical layer by a dedicated LISA Instrument Controller (controller in this sense is a very simple micro-controller which cannot run complex control software but adopts the electrical interface to the instrument sensors, actuators and data front-ends.

LISA Telemetry Ka- Band versus X-Band Trade-off. Ka-Band would seem to offer the advantage of a possible higher data rate compared with X-band.

KA-band pros:

- increased gain with respect to that provided by an X-Band antenna at same diameter

Ka-band cons:

- G/T for the DSN Ground Stations is lower for Ka-Band than for X-Band
- free space losses are higher
- limited data transfer times because of atmospheric losses at low elevation angles of GS antenna
- for tracking of the Earth the antenna drive mechanism would have to provide a second degree of freedom for the antenna elevation pointing (LISA specific)
- disturbance torques will have a greater effect owing to the necessity to change the boresight pointing of the antenna more frequently

In fact a link budget shows that the X-Band solution offers the most favourable margin.

The X-Band solution appears to be the best, both electrically and mechanically.

Power Concept:. The requirements on thermal stability and magnetic cleanliness (initially, but potentially relaxed at the end of the study) can either by fulfilled by a linear control of the power subsystem (realised on CLUSTER) or a Maximum Power Point Tracker (MPPT).

The linear shunt concept has been rejected because of the high power dissipation behind the thermal shield or even inside the S/C via power dumpers. The MPPT concept has been selected for the Science Module as well as for the Propulsion Module. Each PCDU can be mounted with recurring modules in a common procurement.

There is no explicit need for energy storage on the Science Module yet, a potential loss of attitude which would totally de-point the SA from the sun has not yet been expected to be a credible failure which the

S/C should cope with. Therefore the battery has been allocated to the propulsion Module. This gives several benefits for the Science Module design.

Recent an analysis for reorientation with stored energy for the FEEPs instead indicate that such a disorientation failure could be corrected with a battery of some 100 Wh of energy.

Thermal stability is maintained at quasi-constant load within the measurement frequency band, e.g. the power consumers like the RF transmitter will be active during the whole science phase.

4.3 Baseline Payload Design Options and Trade-off

4.3.1 Payload Electro-optical Design

Each of the three LISA spacecraft hosts a payload constituted in the baseline design by the following electro-optical components (see Figure 4.3-1)

- two laser subsystems composed by four **laser sources** (a), 2 nominal sources (each feeding one optical bench) + 2 spare sources, and their **drive and control electronics** (b);
- two **optical benches** (c), each supporting an **inertial sensor head** (d), the optical elements and the detectors of the laser interferometers;
- two **inertial sensor electronics** (e) for detecting and controlling the proof mass movement;
- two **telescopes** (f) for transmitting and receiving the laser beams between the S/Cs;
- two **ultra stable oscillators** (g) providing the on-board frequency reference;
- the **optical fibre** (h) for the laser beam delivery to the OBs and to link the OBs;
- two **interferometer electronics** (i) containing the components for the measurement of the beat signal phase between the laser beams interfering on the OBs;
- a **UV discharge system** (j) for removing the electric charges accumulated on the proof masses of the inertial sensors.

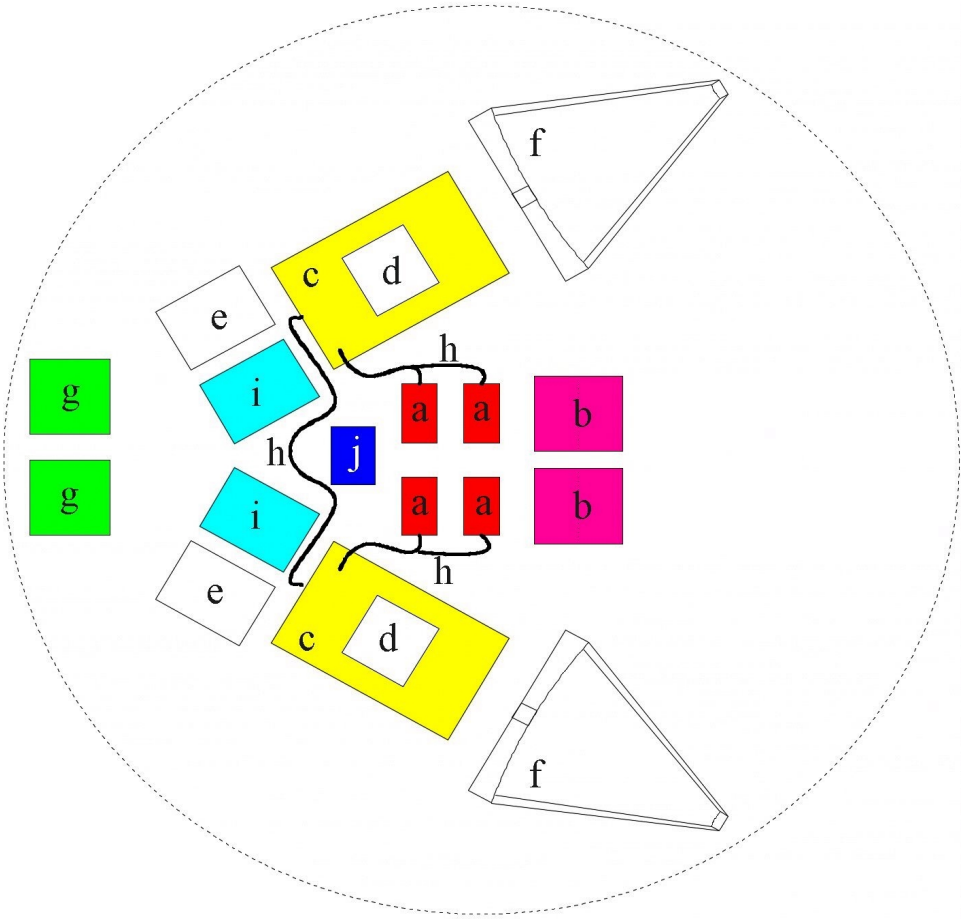

Figure 4.3-1- *LISA payload electro-optical system contained in each spacecraft*

The two laser beams generated on each spacecraft are exchanged between the two OBs of the same S/C through the optical fibre and through the OBs of the other two S/C through the telescopes, as shown in Figure 4.3-2. Among all the laser sources one acts as master laser (e.g. the laser A1 injected on the OB A1 of the S/C A). Its frequency is locked to a resonance peak of a reference optical cavity located on the bench A1, while the laser A2 is phase locked to laser A1 with a frequency offset of about 10 kHz. The laser A1 is transmitted through the telescope to the spacecraft C where it is beaten with a fraction of the local laser C2 on the bench C2, after a reflection on the proof mass contained in the inertial sensor hosted by the bench C2. The laser C2 is phase locked to the incoming laser A1 with a frequency offset of about 10 kHz and transmitted back to the spacecraft A. This schemes implements a sort of laser transponder: the effect is the same of an amplification with phase maintenance of laser A1 received by S/C C, and its back transmitted. The laser C2 received on the spacecraft A bounces off the proof mass and is beaten with a fraction of the local laser A1 on the bench A1. This optical link between the benches A1 and C2 defines one of the three arms (Arm 1) of the LISA laser interferometer, with end mirrors (the reference points for the measurement of the distance variation) defined by the proof masses contained in the inertial sensors hosted by OB A1 and C2. The same link is repeated between the OBs A2, B1 (Arm 2) and B2, C1 (Arm 3).

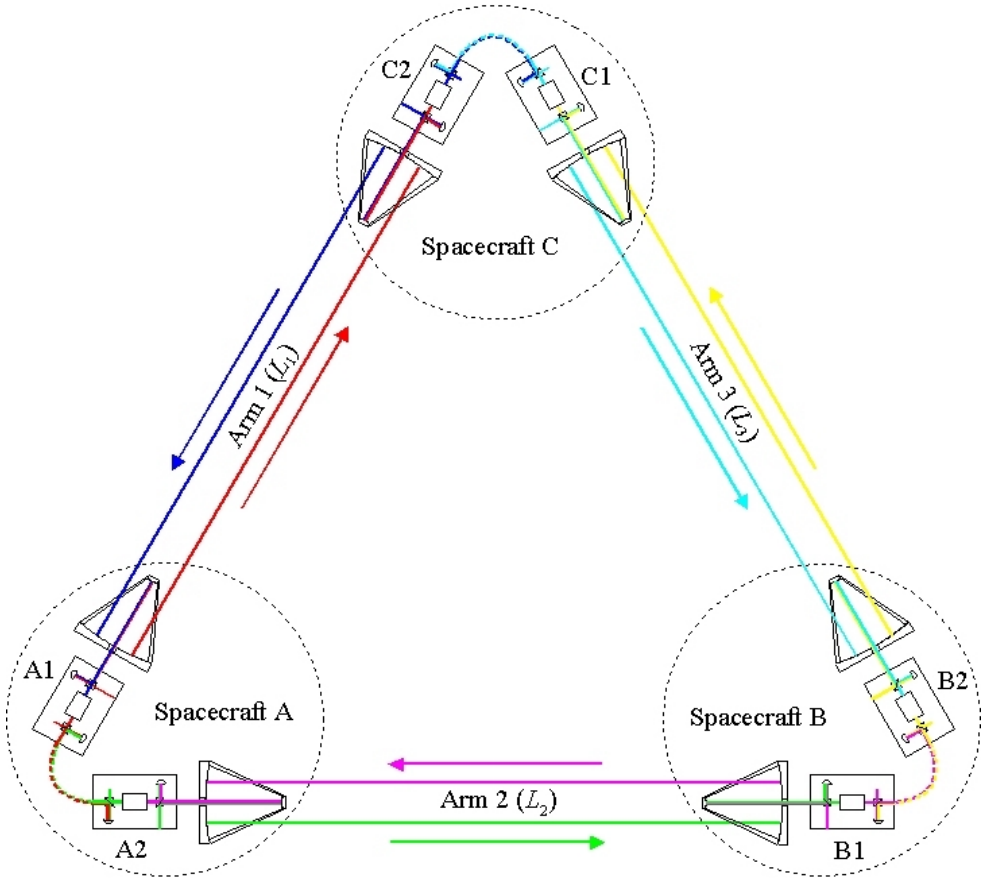

Figure 4.3-2 - Lasers beam exchanges between the 3 pairs of OBs hosted by the 3 LISA S/C

The following sub-sections describe the Pre-Phase A design of the payload components (from [1] and [2]), the alternative options defined and investigated during the Phase A study and the trade-off outcomes. The baseline design solutions of the various payload elements selected from these trade-offs are described in details in Chapter 7.

4.3.1.1 Telescope

The **Pre-Phase A configuration** of the telescope is shown in Figure 4.1-1. It has a Ritchey-Chretien optical configuration (hyperbolic primary and secondary mirror), with aspheric surfaces to obtain a compact configuration with minimum optical aberrations. The $f/1$ primary mirror has a diameter D = 30 cm and is made in Ultra-Low Expansion (ULE™) material with a light-weighted, double-arch shaped structure. The secondary mirror has a diameter of 3.2 cm and a focal length of 2.6 cm. It is supported by a three-leg CFRP spider at a distance of 27.62 cm from the primary mirror.

The two-mirror telescope is an a-focal system with magnification ratio = 10. A negative lens located in the central opening of the secondary mirror expands the collimated beam coming from the optical bench to a diameter of 3 cm at the secondary mirror.

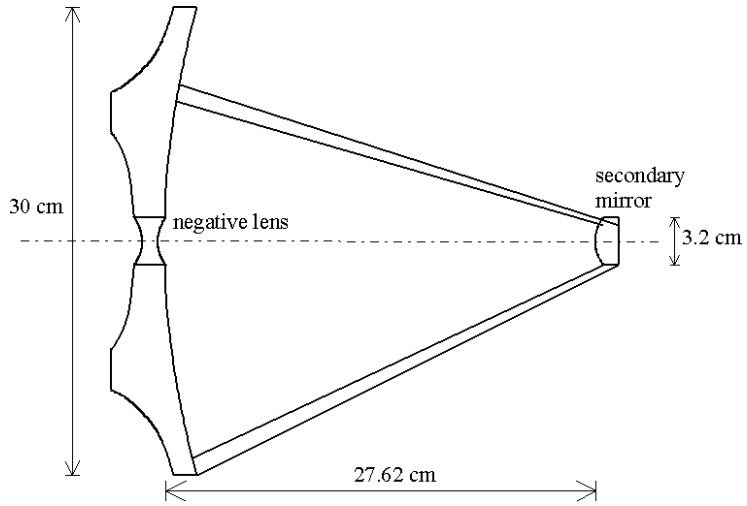

Figure 4.3-3- Scheme of the telescope configuration: Pre-Phase A design

In this study it was decided to remove the beam expansion lens from the centre of the primary mirror (primarily, in order to remove the back-reflection from this element towards the OB) and the following main alternative options were considered for the two-mirror telescope w.r.t. the Pre-Phase A design:

- Optical configuration: Dall-Kirkham (elliptic primary mirror and spherical secondary mirror)
- Telescope magnification: 60x and 30x (the magnification increase w.r.t. Pre-phase A is a direct consequence of the removal of the beam expansion lens from the primary mirror centre)
- Telescope material alternative: all SiC for mirrors & mirror support structure

For the **optical configuration** the Dall-Kirkham solution was preferred for its greater simplicity (due to the spherical secondary mirror) implying a cost saving. In fact, although the Dall-Kirkham configuration is not aplanatic, like the Ritchey-Chretien, the resulting aberrations in the very narrow FOV (± 2 arcsec) in which it has to operate are still very small (see chapter 7.1.2), and compatible with a global WFE of $\lambda/20$ for the transmitted beam (better than the $\lambda/10$ original requirement).

For the **telescope magnification** the 60x ratio was finally selected as baseline. In fact, although the 30x ratio lead to a larger secondary mirror with a larger curvature radius (and thus easier to

manufacture), the resulting beam diameter at the telescope output (1 cm) would require a beam compressor at the OB input to reduce the beam to a size compatible with optical elements easily to be accommodated on the OB. In particular a 20x beam compressor would be required in order to match directly the telescope output beam with the active area (∅ = 0.5 mm) of the heterodyne detector of the laser interferometer.

The consequences of the addition of this beam expander would have been a large back-reflection of the outgoing beam towards the OB detectors and an increase of a factor 10, w.r.t. to the 60x telescope without beam compressor, of the incoming laser beam tilt on the OB due to the Point Ahead Angle (PAA) effect.

Telescope material: The selection of the telescope material turned out to be a critical trade-off. The all-SiC solution was preferred initially because of its lower cost and proven homothetic athermal behaviour, meeting requirements on the optical quality as a transit/receive antenna. The ULE+CFRP (or Zerodur+CFRP) alternative is more costly to manufacture, ageing effects need attention, but it represents also a well established suitable technology. However, a peculiarity of the LISA mission is the requirement on the interferometer optical path length stability within the measurement band, allocating only around 10 pm to any path length changes inside the telescope, due to inter-mirror distance changes. So although SiC maintains optical quality under thermal changes and (on- ground to in-space thermal changes) it exhibits a rather large inter-mirror distance change due to its large thermal expansion coefficient, compared to optimised CFRP. For a telescope thermal fluctuation of 10^{-4} K within the measurement band, this leads to unacceptable optical path length changes (170 pm). Hence, SiC is marginally a valid material choice only in case the relevant thermal stability in the telescope environment is better than 10-5 K, a figure, which still needs validation from more detailed thermal analysis. Both options are maintained at this level of investigations.

4.3.1.2 Optical Bench

The Pre-Phase A layout of the OB is shown in Figure 4.3-4.(it refers to the bench A1 according to the nomenclature of Figure 4.3-1). The OB is composed by a ULE baseplate supporting the inertial sensor and the optical and opto-electronic elements that constitute the LISA laser interferometers.

The laser beam is sent to the bench through a polarisation-maintenance fibre that ends in a mechanical positioner for the in-flight fine adjustment of alignment and focus. Then the beam passes through a phase modulator and is split in two components: a small fraction arrives at the quadrant photodiode qp1 (providing the local reference for the phase measurement) while the largest amount is sent towards the telescope for its transmission to the remote spacecraft.

Before leaving the OB another small fraction of the beam is split by s1, which sends it towards a reference optical cavity (utilised for the laser frequency stabilisation) and to the backside of the proof mass before being sent to the bench A2 via a polarisation-maintenance optical fibre. No more than 100 μW shall bounce on the back of the proof mass for an acceptable radiation pressure induced acceleration noise). A small fraction of the beam reaches the photodiode p1, which is used for the offset locking of the laser A2 (routed to the bench A1 through the same back fibre) and for removing at first order from the interferometric measurement the effect of the proof mass movement relative to the OB.

The laser beam received from the remote spacecraft C bounces off the front side of the proof mass and is routed by a polarising beamsplitter cube towards qp1 to beat against the local reference. On the

reception path, part of the incoming beam is split by s1 towards the quadrant photodiode qp2 utilised for the initial acquisition and tracking of the remote laser.

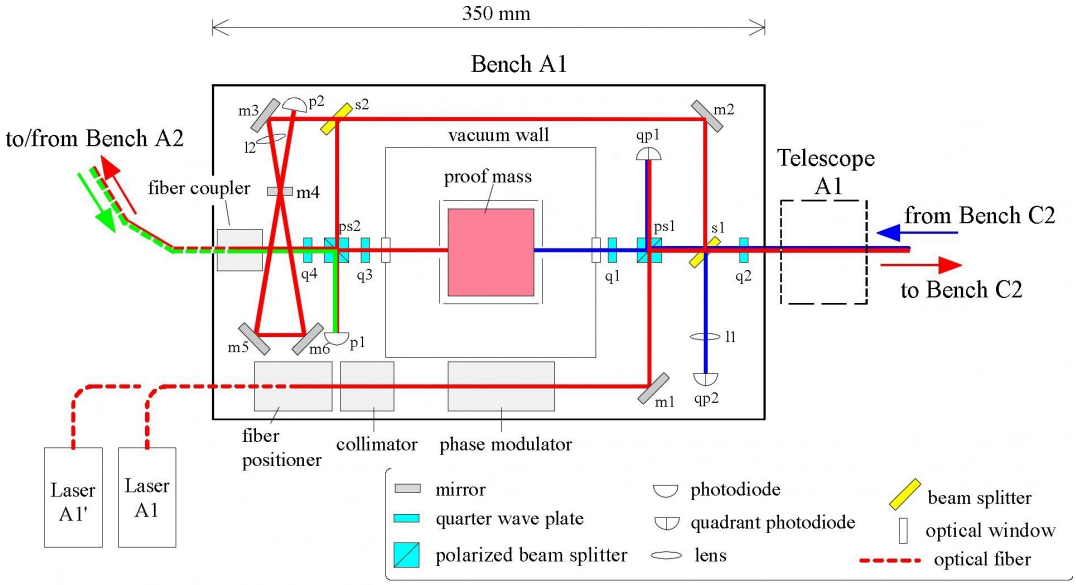

Figure 4.3-4- OB layout: Pre-Phase A design

The main alternative options for the optical bench w.r.t. the Pre-Phase A design considered during the Phase A study are summarised in Table 4.3-1

Table 4.3-1 List of the main OB alternative options w.r.t. Pre-Phase A design

Element	Option	Rationale
Optical cavity	Removal of the optical cavity from the OB and accommodation in a separate enclosure inside the P/L cylinder.	Possibility of improving the dimensional stability thanks to a dedicated thermal insulation.
Phase modulator	Removal of the phase modulator from the OB and accommodation before the optical fiber.	Reduction of the power dissipated on OB and of the radio-frequency interference with the photodiodes. Elimination of beam wandering at the modulator output by the fiber.
Quarter waveplate q2	a) Placement of the quarter waveplate q2 before the polarising cube ps1.	Removal of a major straylight source towards the acquisition sensor qp2.
	b) Removal of q2 and OB tilt by 45° along the optical axis to rotate the polarisation between the remote OBs.	Removal of an optical element from the OB and of a major straylight source on qp1 and qp2.
Quarter waveplate q4	Removal of the q4 and twist of the back fibre by 90° to rotate the polarisation between the near OBs.	Removal of an optical element from the OB and laser coupled to the fiber with linear polarisation.
Beam expander/ compressor	a) Addition of 20x beam expander/ compressor at the output/input of the OB	Matching of the incoming beam diameter received by a 30x telescope to the 0.5 mm diameter of qp1.
	b) Addition of 10x beam compressor before the photodiode qp1	Matching of the incoming beam diameter received by a 60x telescope to the 0.5 mm diameter of qp1.
Detectors	a) Addition of a photodiode (p3) for the stabilisation of the laser power.	Obtain the signal for the laser power stabilisation directly on the OB.
	b) Replacement of the quadrant photodiode qp2 with a CCD	Greater sensitivity (critical, because of the tiny power to be detected)
	c) Use p3 as a 4Q-diode for transmitter boresight calibration	Calibration and monitoring sensor for fiber positioner

The proposal of removing the optical cavity from the bench was put aside for the time being, since the required laser frequency stability ($\delta\nu \leq 30$ Hz $/\sqrt{\text{Hz}}$) can be achieved also with the cavity on the OB if its temperature remains stable within 10^{-5} K/$\sqrt{\text{Hz}}$, a target that seems achievable. This option could be re-considered in the future if the thermal analyses results will indicate that it is critical to maintain such a level of thermal stability for the whole OB, or if more stringent requirements will be placed on the laser frequency stability.

The removal of the phase modulator from the OB has been retained as baseline solution. Consequently, two alternatives were investigated for the phase modulator type and location:

- Phase modulator integrated in the optical fibre connecting the laser source to the OB

- Bulk phase modulator integrated in the laser head, before the fibre coupling.

With the first solution, the laser head can maintain the very compact and lightweight design defined in the phase A study (see section 4.3.1.3). The main drawback is that, among all the existing in-fibre phase modulators, very few of them are designed to operated at the 1064 nm wavelength of the LISA laser and all are characterised by small transmission efficiency (less than 40%, because of the modulator-to-fibre coupling) and cannot accept a large input optical power (Table 4.3-2). Because of the limitations of the present devices, that would impose the development of a new, dedicated in-fibre modulator for LISA, the utilisation of a bulk modulator is considered the baseline solution. Among the available bulk modulator with features close to the LISA needs, the New Focus resonant modulator model 4003 was considered the most suitable, due to its smaller dimensions and power Table 4.3-3). This device will have to be submitted to space qualification tests to certify its applicability to the LISA mission.

Table 4.3-2 Relevant features of some off-the-shelf in-fibre phase modulators

Manufacturer	Ramar Corporation	SDL	Institute of Applied Physics (University of Jena)
Laser wavelength (nm)	1064	1310 or 1550	1064
Insertion loss (-dB)	4.5	3.8	4
Optical power (W)	0.1	NA	0.5

Table 4.3-3 Features of the New Focus resonant modulator model 4003

Crystal	$MgO:LiNbO_3$
Operating Frequency (MHz)	0.01 to 190
RF Bandwidth	2-4%
Impedance (Ω)	50
V_π (V_{p-p})	31
Aperture (mm)	2
Maximum optical intensity (W/mm^2)	4
Optical insertion loss (dB)	-0.18
RF drive power (W)	0.3 (to get a modulation index = 0.6)
Mass (kg)	0.08
Dimensions (mm)	55.5x30.1x38.1 (40×4×2 crystal only)
Space qualification	NO (*)

(*) A similar device was only tested - and worked properly afterward - by NASA under the conditions: random vibration in all three axes up to 19 g and shock test up to 50 g.

The removal of the quarter waveplate q2 from the OB, with the consequent rotation by 45° of the bench to correctly rotate the linear polarisation between the remote bench pair A1-C2 etc.., was rejected after a mechanical analysis of the OB mounted with such a tilt angle (see Annex 11 – Optical Bench

Mechanical Analysis) that highlighted an higher (and critical) stress in the material w.r.t. the horizontal mounting.

The positioning of the quarter waveplate q2 before the beam splitter s1 was instead retained as baseline solution. Consequently a different path of the local laser towards the back of the OB (i.e. towards the reference cavity and the back fibre) was defined, with the addition of another splitter, in order to preserve the linear polarisation of the light following this path and to avoid any possible back-reflection on the acquisition sensor from the optical elements placed on the back of the OB.

The removal of the quarter waveplate q4, with the consequent back fibre twist by 90° to correctly rotate the linear polarisation between the close bench pair A1-A2 etc.., was retained as baseline solution.

The two OB layouts with the 20x beam expander (coupled with a 30x telescope) and the 10x beam compressor before qp1 (coupled with a 60x telescope) are shown in Figure 4.3-5. With a 30x telescope the geometric diameter of the incoming beam on the OB is 1 cm, and the beam outgoing from the bench must have the same gaussian diameter (truncated at $1/e^2$ intensity) to match the primary mirror diameter. With a beam of such a size on the OB, the utilisation of large optical elements would be required, with serious accommodation problems. Thus this telescope magnification forces the introduction of a beam expander/compressor at the output/input of the OB (with a 20x magnification a direct matching of the incoming beam to the qp1 size is achieved). The consequences of this optical elements have already been mentioned in chapter 4.3.1.1: large back-reflection towards the OB detectors magnification by a factor 600 of the incoming beam tilt on the OB due to the PAA effect. For these reasons this option was dropped in favour of the 60x telescope. In this case, in fact the beam diameter on the OB is 0.5 cm and can still be “handled” with an optical element size that can be accommodated on the bench. Thus no beam expander/compressor is needed at the OB output/input, but only a 10x beam compressor just before qp1 (a second compressor is added in the path towards the back of the OB to reduce the size of the successive optical elements). Here the PAA is amplified by only 60 times on the OB, thus its compensation is simplified. About the PAA compensation the preferred solution is to receive off-axis the incoming beam and to tilt the proof mass to maintain it parallel to the local beam at qp1. The alternative option of transmitting off-axis the outgoing beam, using the fiber positioner to change its orientation, was discarded because of the large beam shifts and tilts induced in the rest of the OB.

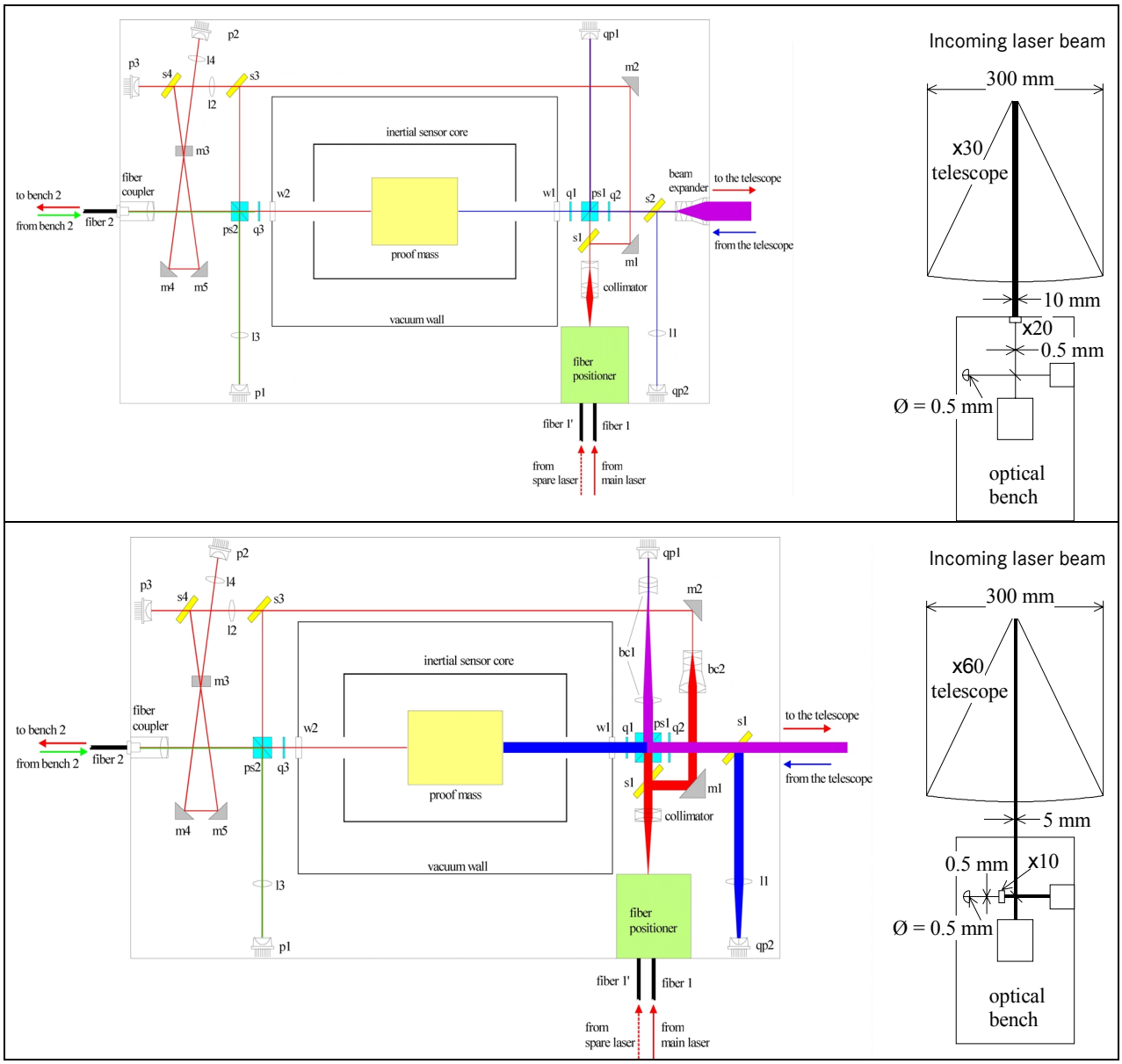

Figure 4.3-5: OB layout for the 30x telescope (above) and for the 60x telescope (below)

About the detector options, the addition of the photodiode p3, to be used for the laser power stabilisation, was included in the baseline OB design, as well as the replacement of qp2 with a CCD as initial acquisition sensor. In fact, this device enables to achieve a much better SNR figures w.r.t. silicon avalanche photodiodes or InGaAs photodiodes in presence of the tiny amount of power (few pW) to be detected. Among the existing devices, the CCD02-06 deep depletion CCD manufactured by EEV is the one that better meets the LISA needs and has been therefore assumed as reference sensor.

4.3.1.3 Inertial Reference Sensor Concepts

Each spacecraft contains two inertial sensors, at the end of each laser link from/to the two other LISA spacecrafts. The proof-masses of the inertial reference sensors reflect the light coming from the YAG laser and define the reference mirrors of the interferometer arms. These reference mirrors, due to their full attitude alignment capability also are active elements in laser beam pointing control. The same proof-masses are also used as inertial references for the drag-free control of the spacecraft which constitutes a shield to external forces. For LISA, in the operational mode of drag-free control, it is operated as freely floating inertial mass with low coupling to the surroundings (within the measurement band) in terms of self-gravity effects, electromagnetic and non-equilibrium thermal interactions and sensor and control back-action and stiffness, respectively.

The technical baseline for the inertial reference sensor is the well developed capacitive and electrostatic sensitive accelerometer reference (CAESAR) with a well established heritage in precursor missions. Some modifications, identified in this study and earlier investigations to adopt the design to LISA requirements have been incorporated.

Six capacitive sensors for position and attitude of the proof mass are employed. The control loop acts on the corresponding electrostatic electrodes. The digital implementation of the control law enables the sensor to operate in different modes according to the stiffness and bandwidth requirements in acquisition, initialisation and operation.

Alternative design concepts and modifications have been briefly investigated to explore their potential to reduce IRS complexity, to support the “low interaction” drag-free operation mode, and to adopt to the updated requirements stemming from engineering activities within this study.

Main alternatives identified are:

- Low back action all optical read out system
- Actuation with light pressure
- Enlarge gapes between proof mass and cage (electrodes; to reduce stiffness)
- Optimised or symmetric control law for the line-of-sight and lateral axes (reduce cross-coupling; adopt to DFC law)
- Sliding electrodes or gap varying electrodes for capacitive sensing
- Implementation of proof mass attitude biasing to compensate variable point ahead angles.
- Re-consideration of proof mass materials choice in terms of magnetic susceptibility
- Electrodes metallic or non-metallic materials with respect to geometric and thermal stability
- Reduction of housing volume and mass to accommodation constraints on optical bench.
- Proof mass clamping and caging during launch and initialisation of in-orbit operation; associated AIVT problems and optical alignment issues.

All optical read-out and control. Concerning the actuation with light pressure, the induced complexity of the device increases its risk. Moreover the initialisation of the sensor needs forces far beyond the possibility of the pressure induced by the envisaged laser light (roughly a dc value of a few $10^{-8}ms^{-2}$ has to be applied on the Proof-Mass before DFAC operation), unless a rather complex resonant enhancement of light pressure, as described above in section 4.2, is employed.

Now, concerning the all or partial optical read-out, the absolute position of the proof-mass, at least at the initialisation, must still be measured by an external device like a capacitive position read-out. Also, the position resolution is quite a challenge at very low frequency (typically 10^{-4}Hz) for the classic interferometric devices where a nanometer/√Hz is needed. Another difficulty appears with the ground calibration or the test of such a sensor. Because the proof-mass cannot be levitated and is then a few tens of micrometer far from its centred flight position, the reflecting proof-mass cannot be used for the adjustment of the interferometers elements and mirrors. At last, the optical read-out needs additional electronics and then additional power, mass and volume.

As a baseline the capacitive read-out must be considered for the normal operation and a measurement mean of acceleration for the Drag-Free and Attitude Controller (DFAC). However the possibility of a complementary Proof-Mass position readout in the main direction of the Laser light might be analysed in future studies by using the available data output from the existing Laser beam in the optical bench.

The other listed design options and possible modifications of the selected baseline (i.e. the CAESAR concept) are further described in chapter 7.

4.3.1.4 Laser Assembly Concepts

Laser requirements. The following requirements in table 4.1-1 apply for the laser assembly:

- Output power and output power noise

The nominal output power available on the optical bench shall be at least 1 W.

The required laser power stability of the actively stabilised system between 10^{-4} Hz and 10^{1} Hz is:

$$\frac{\Delta P}{P} \leq 4\times10^{-4} \; 1/\sqrt{Hz}$$

- Beam quality and Polarisation

The laser beam quality shall be single transverse TEM_{00} mode. Polarisation shall be linear.

- Laser frequency noise

The laser frequency noise between 10^{-3} Hz and 1 Hz shall be less than

$$\Delta f \leq 30 \, \mathrm{Hz}/\sqrt{\mathrm{Hz}}$$

- Mass and power budget

Due to the limited capacity of the LISA spacecraft, the laser systems dimensions, mass and power requirement shall not exceed the following limitations

Dimensions	10cm x 10cm x 10cm
Mass	1.5 kg
Power input total	15 Watt

Laser System Concept Trades. The LISA mission requires a 1 W laser system with single-frequency operation and very high frequency and amplitude stability. In what follows the possible options for a single frequency laser will be discussed and the most suitable options for the LISA mission proposed.

The above mass and power constraints can only be met by a solid state laser system.

Single frequency solid state laser alternatives. In general four mechanisms are possible to achieve the single-frequency emission of solid state lasers:

1) In the case of a homogeneously broadened laser material, the unidirectional operation of ring laser
2) Utilisation of filter elements (e.g. etalons) in the resonator or frequency selective endmirrors
3) Micro chip laser arrangement, i.e. utilisation of a small laser crystal length with a free spectral range larger than the gain width of the laser material
4) Injection locking with a single frequency seed laser (not appropriate here).

In what follows, the most suitable design concepts using the techniques 1) – 3) are reviewed in more detail.

Monolithic, nonplanar ringlaser (NPRO). In the case of the NPRO (Non Planar Ring Oscillator) TEM_{00} mode, hence single transverse mode, operation is achieved by focussing the diode laser-beam into the crystal. When the beamwidth of the diode laser radiation in the crystal is smaller than the diameter of the TEM_{00} mode over the absorption length of the pump radiation, the laser is forced to operate in a single transverse mode.

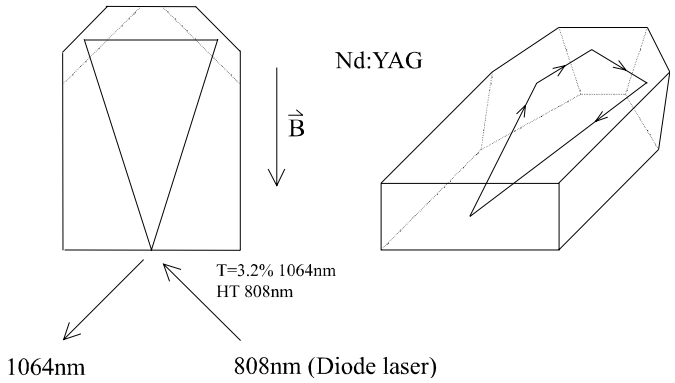

Figure 4.3-6 Arrangement of the monolithic non-palanar Nd:YAG ring laser

Nevertheless, homogeneously broadened solid-state lasers oscillate on several longitudinal modes even at low output power because of the spatial hole burning effect. To enforce single-frequency operation, resonator internal elements can be applied. However, these additional intracavity elements strongly reduce the efficiency and stability of the laser system. The monolithic Nd:YAG ring laser enables single-frequency operation at high output power without intracavity elements. Unidirectional and hence single-frequency oscillation is enforced by an intrinsic optical diode. This diode is formed by the laser material with a non-zero Verdet-constant in a magnetic field in combination with a polarising output coupler.

The optical beam path in the crystal is determined by three total reflections and one reflection at the negatively curved front surface. This front surface is dielectrically coated, reflecting about 97% of the 1064nm laser radiation and highly transmitting the pump radiation at 808nm (Figure 4.3-6). A very high intrinsic frequency stability results from the monolithic and compact design of the resonator and from the excellent thermal properties of the host material.

Microchip laser. Microchip lasers are miniature solid-state lasers commonly emitting radiation in the near infrared frequency range (NIR) and pumped by a diode laser. A small crystal-chip (feasible length is about 1 mm) constitutes both the active medium and the resonator of the microchip laser i.e. the resonator mirrors are directly coated onto the surfaces of the chip. The setup is quite simple: The significant elements required are a lens focusing the pump beam on the crystal front face and a heat sink cooling the chip. Figure 4.3-7shows the arrangement of a microchip laser longitudinally pumped with a diode-laser pump module.

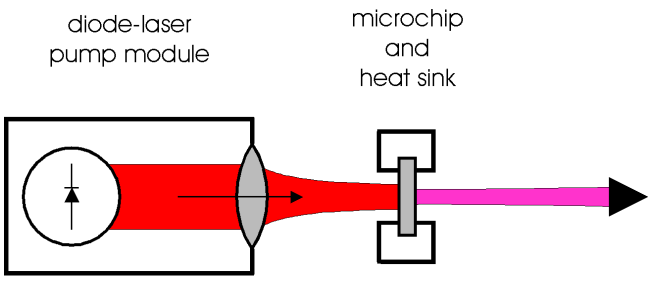

Figure 4.3-7 Experimental setup of a diode-pumped microchip laser

Single-frequency operation of microchip lasers is based on the realisation of a small resonator length, which results in a mode spacing larger than the gain bandwidth of the laser medium. One example is a monolithic Nd:YAG chip pumped by a diode laser. Measured short-term linewidths of the free-running laser are below 1 kHz. However, the Nd:YAG chip shows an induced birefringence, which is not easy to control. Further disadvantages of microchip lasers are the high sensitivity on back-reflections, beam walking problems and low efficiency.

High output powers can be obtained but a quite high pumping power is required, because the optical to optical efficiency is below 10%. Extra thermal contacts are necessary to ensure proper cooling of the crystal's surfaces, e.g. clamping the chip between sapphire plates.

Furthermore, whatever the operating output power is, the small laser crystal exhibits a high sensitivity to environmental temperature changes. This leads to frequency fluctuations which can only be suppressed by a very accurate temperature stabilisation of the laser crystal and its environment.

External-cavity diode lasers. Diode lasers are compact, reliable, efficient and cost effective light sources in combination with a simple handling. In addition, the wide variety of visible and near-infrared frequencies (600-1600 nm), tuneability and output power practicable up to several ten watts make diode lasers suitable for many applications.

The use of diode lasers for the LISA laser system demands frequency narrowing due to the big linewidth of a common laser-diode (10-100 MHz). This can be realised with frequency selective component inside the laser resonator. DFB and DBR lasers (as described below) and external-cavity lasers are well established using internal frequency selection.

An External-cavity diode laser usually uses an external diffraction grating for frequency selection. The resonator is composed of a laser-diode with one AR coated surface and the external grating (Littrow configuration) or an additional mirror reflecting the light of the first order of diffraction (Littman configuration). In both configurations order 0 of diffraction is used as light output. Figure 4.3-8 demonstrates a setup with Littman configuration.

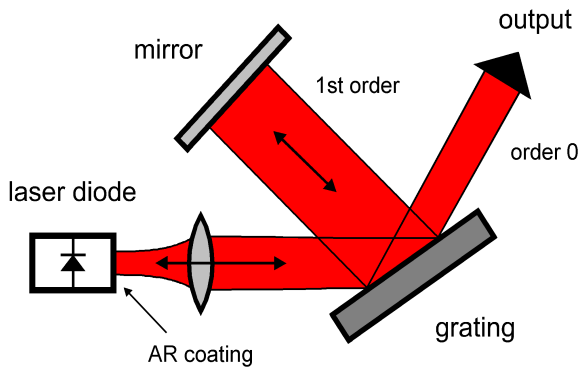

Figure 4.3-8 External-cavity diode laser in Littman configuration

Diode lasers with external cavity provide stable single mode operation with achieved linewidths of less then 100 kHz in the visible or infrared range. Tuneability of 20 nm and more is possible with precise rotating of the grating (and additional movement of the mirror in Littman configuration). The main disadvantage seems to be the great sensitivity to mechanical instabilities which prevents long term reliable operation that is necessary for space applications. A horizontal misalignment in the dispersion plane of the grating corresponds to a wavelength detuning. But a vertical one in the sagittal plane is critical because only a few µm shift is enough for total misalignment of the external cavity. For that reason maintenance of alignment requires the possibility of adjusting the components during the use of the laser. Self aligning techniques could solve this problem so a reliable operation using these techniques may make this type of lasers available for satellite flights.

Also the output power of state-of-the art external cavity diode lasers are to low (20 mW) for an application as the LISA laser system.

DFB/DBR laser diodes. Another possibility for frequency narrowing is to connect the active semiconductor medium directly to Bragg gratings used as frequency selective components: DFB and DBR diode lasers (DFB: distributed feedback, DBR: distributed Bragg reflection) are laser diodes which compose small quasi-monolithic external cavities together with integrated Bragg gratings. They combine the small dimension, reliability and stable operation of a laser diode with a comparable narrow linewidth.

A DBR laser resonator contains the active region and one or more Bragg gratings used as reflectors instead of the high-reflection coatings of a common laser diode. The DFB laser integrates a Bragg grating directly into the active layer, so the regions of gain and reflection are not separated. That means an optical wave travelling in one direction is continuously scattered into the optical wave in the reverse direction. This concept represents a combination of continuous feedback and gain.

However, frequency tuning is very difficult since several modulation currents are to be controlled . Typical frequency modulation coefficients of 5 MHz/µA imply that an electronic power supply with very low current noise is necessary. Therefore, a stability and tuneability corresponding to the LISA requirements seems difficult to achieve. Additionally, neighbouring mode suppression is problematically, so these devices tend to multi-frequency operation, which would be catastrophic for the signal detection process. Furthermore, DFB/DBR laser diodes have the disadvantage of a very high sensitivity to back-reflections.

The output power of a typical DFB/DBR laser is very low, so as LISA laser system they will require an additional power amplifier. For this purpose monolithic master oscillator power amplifiers (M-MOPA) are

well established. These are monolithic assemblies of a DFB/DBR laser as master oscillator and a connected gain region as power amplifier. Figure 4.3-9 shows a M-MOPA with single mode waveguide, edge emission and an integrated DBR semiconductor laser as master oscillator.

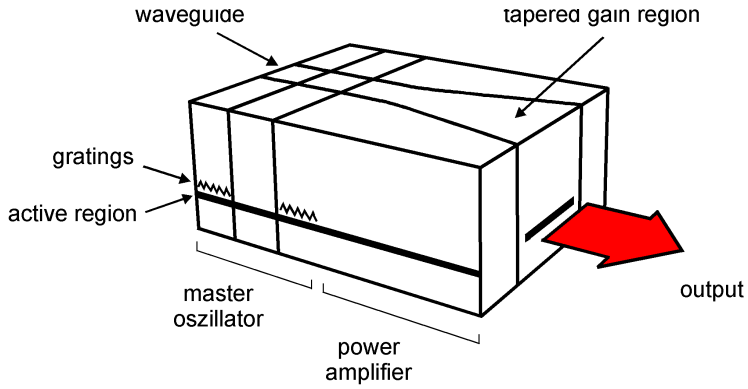

Figure 4.3-9 M-MOPA with DFB semiconductor master oszillator

A variety of DFB/DBR diode lasers with appropriate performance characteristics is available at the telecommunication wavelengths 1310 nm and 1550 nm because of the huge demand. However, 1064nm is a critical wavelength for diode laser and only so-called *strained InGaAs material* can be used. Output power in the order of 100mW is available from commercial strained InGaAs DFB or DBR laser diodes, but these devices are usually quoted preliminary products and SDL, the largest diode manufacturer, even ceased the production because of too small customer interest. Also a laser linewidth of less than 5 MHz is a major problem because of the huge free spectral range of laser diodes as such.

Fibre laser. Development of diode-pumped fibre lasers is a fast growing field of research. Fibre lasers are very suitable and easy scaleable in laser power. However, the emission bandwidth is very high (several nm) and the fibre resonator is sensitive on temperature, stress etc. By the implementation of fibre Bragg gratings single-frequency operation was already demonstrated. However, the linewidths are around several MHz and not suitable for the LISA laser system. Also radiation hardening of doped fibres has only been investigated very barely and seems to be a major problem.

Master oscillator fibre power fibre amplifier (MOPFA). The non-resonant amplification of a low noise, low power master oscillator (e.g. NPRO or external cavity diode laser) is another approach to fulfil the LISA laser requirements. For this type of laser the radiation from the stable master oscillator is mode matched into the approximately 10 µm wide inner core of a double clad fibre (see Figure 4.3-10). This inner core consists of (e.g. Nd) doped glass.

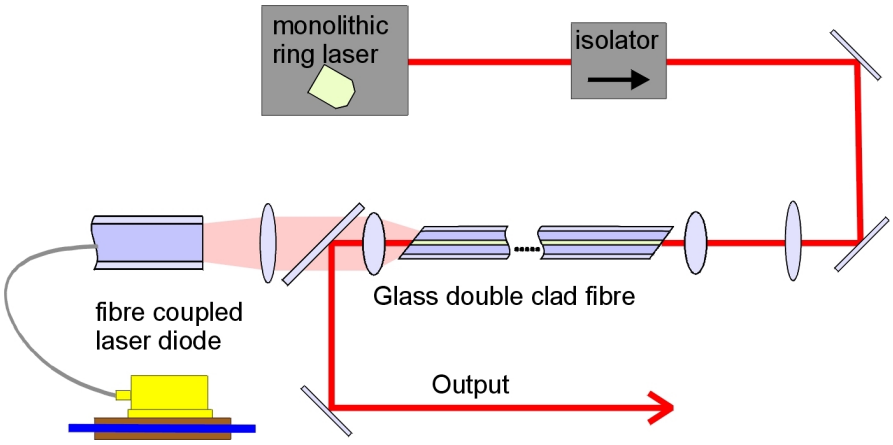

Figure 4.3-10 Arrangement of master oscillator fibre power amplifier (MOPFA)

The inner undoped cladding of the fibre, which serves as the pump core, has a diameter of several hundred µm. A silicone outer cladding protects the glass fibre and leads to a NA of approximately 0.4 for the pumplight. The fibre amplifier is pumped with one laser diode bar, which is available with output up to 30 W at 809 nm. The light is matched into the outer core of the fibre.

The phase noise characteristics of the master laser are usually maintained through the amplification process, whereas the low frequency power fluctuations are significantly increased due to the noisy high power diodes. More than 5 W amplified emission at 1064 nm have been demonstrated using a 500 mW NPRO as the master oscillator and 25 W of 809 nm radiation. This corresponds to 20 % optical-to-optical efficiency. For the LISA mission the master laser power would be reduced to approximately 50 mW, suitable for high frequency phase modulation, which could be amplified to more than 4 W. The main drawback of the MOPFA system are its low efficiency and the large number of optical components that are fragile and costly to qualify. Also the high radiation sensitivity of the doped fibre is an unsolved problem.

Concept selection. Table 4.3-4 summarises the system properties of the different laser alternatives

Table 4.3-4 Laser Concept Trades

	NPRO	Micro Chip Laser	External Cavity Laser	DFB/DBR MMOPA	Fibre Laser	MOPFA
Power	+	0	-	+	++	++
Beam Quality	+	+	+	+	+	+
Power Stability	+	-	-	-	-	0
Frequency Stability	+	-	-	-	-	+
Efficiency	+	0	+	++	+	0
Physical Dimensions	+	++	+	++	++	0
Technology Status	+	0	-	0	-	+

++ meets the requirements with large margin, standard space component

+ meets the requirements, commercial product with potential for qualification

0 meets the requirements only with additional development, requires development

- does not meet requirement, requires basic technology development

Based on the advantages and drawbacks as shown in table Table 4.3-4 the NPRO laser concept is clearly identifiable as superior to the other alternatives and it is therefore selected as the baseline. However, the MOPFA concept shall be regarded as the second option, as no major obstacles are identified and the possibility of scaling the output to higher power is very attractive.

Laser components identification and trades. Based on the laser concept selection as shown in the preceding section, trades for specific laser components have been performed. The following parts and components have been identified that are required for the utilisation of a laser diode pumped non-planar ringlaser (NPRO) for the LISA laser system:

- Laser crystal
- Laser diode pump source
- Pump light optics
- Electro-optic modulator (EOM)
- Faraday isolator
- Fibre coupler

Laser crystal. The only laser crystal material that has been taken into account is Nd:YAG, which stands for neodymium doped yttrium aluminium garnet. The reason for this are the unique laser specific properties of Nd:YAG, such as excellent thermo-optical properties and good quantum efficiency, combined with extensive space heritage.

Two different mechanical designs of the non-planar ring oscillator (NPRO) have been experimentally investigated regarding their suitability for the LISA laser system, the so-called “standard” design and the “ETR” design. The main difference is the overall dimension of the crystal and therefore the overall optical path length inside the laser resonator. The crystal dimensions are 3x8x12 mm^3 for the standard geometry and 2x4x7 mm^3 for the ETR geometry. The main advantage of the ETR is an increased mode-hop free tuning range of approximately 30 GHz. Also the optical to optical efficiency is slightly higher. The main drawback of the ETR geometry is the decreased size of the required pump radiation focus.

Due to the small laser focus that puts demanding constraints on the pump source beam quality, the baseline for the LISA laser system is the standard crystal geometry. However, an intermediate crystal design should be investigated.

Laser diode pump source. The two main options for the laser diode pump source are direct imaging of the radiation from the semiconductor chip into the laser crystal or application of fibre coupled laser diodes and imaging the radiation from the fibre end. The advantages of fibre coupled diodes are a separate thermal management of the laser system and the pump unit, the availability of higher pump power levels and the possibility of switching between more than two redundant devices. The advantages of direct pumping are infinitely small pump power losses and therefore high optical to optical efficiency and a rigid connection of the laser crystal and the pump that is insensitive to misalignment and introduces no additional optical components such as fibres and fibre couplers and no additional pump units.

As direct pumping can be done with two polarisation coupled laser diodes, sufficient pump power and redundancy are guaranteed. Therefore direct pumping is selected as the baseline for the LISA laser system.

A number of specific laser diodes have been experimentally investigated regarding their suitability for the LISA laser system. Firstly direct diode parameters have been measured and then the devices have been used to pump a NPRO laser crystal to determine laser threshold and optical-to-optical efficiency.

Table 4.3-5 Experimental results on laser diode properties

Laser Diode	Coherent S-81-3000C-200-H	Opto-Power D003-808-HB100	Siemens SFH 487401
Power [W]	3	3	1
Emitter Size [µm]	200	100	100
(Half) divergence angle [°]	8	13	16
Treshold [mA]	611	4000	400
Electrical-optical Efficiency [W/A]	1.0	0.5	0.6
FWHM Linewidth [nm]	1	1	1.5
NPRO threshold [mW]	130	196	235
Optical-optical Efficiency [%]	66	50	42
Qualificatio aspects investigated	No	No	YES

The laser Coherent laser diode is selected as the baseline for the LISA laser system, because the physical laser related properties are clearly superior to the other devices. Also, Coherent is the only manufacturer that uses aluminium free semiconductors for the diodes, which improve lifetime properties.

Pump light optics. The collimation and of the pump radiation is done with a aspherical, plano-convex fused silica lenses per diode. The two collimated beams are combined on a polarising beam splitter and focused into the laser crystal with a single aspherical, plano-convex fused silica lens.

No alternatives to this pumping scheme have been identified. The redundancy concept appears sufficient with respect to the expected lifetime and reliability figures of then available pump laser diodes. It could be further improved, if necessary, by using fibre coupled pump units and fiber switches for example.

Electro-optic modulator (EOM). In the Pre-Phase A design, the phase modulator was placed on the optical bench. Another option is to have the phase modulator placed inside the laser head. Figure 4.3-11 shows the two options. Table 4.3-6 summarises the advantages and the drawbacks for the two options.

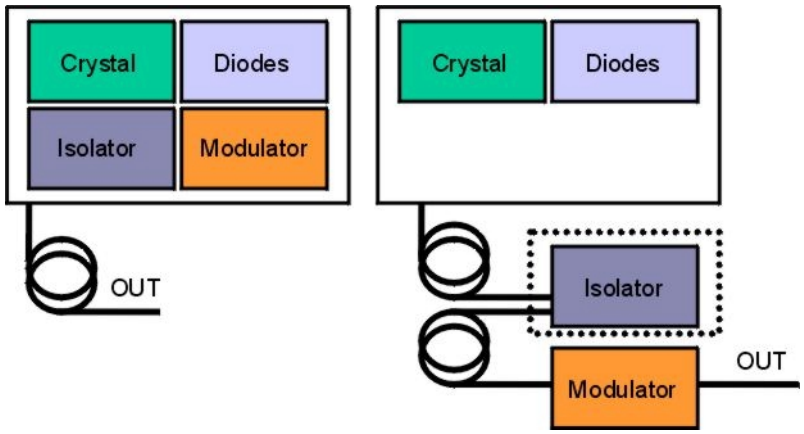

Figure 4.3-11: Options for the laser head

(left: baseline; right: Pre-Phase A, dotted border: option)

Table 4.3-6 Advantages and drawbacks for the phase modulator placement options

Option	Advantages	Drawbacks
PM on optical bench	Reduced mass and size Mechanical stability Simple design	Modulator development High coupling losses
PM inside laser head	Standard modulator use Low coupling losses	Complex design Increased mass and size

Based on these advantages and drawbacks the second option, phase modulator inside the laser head, has been identified as superior and selected as the baseline for LISA laser system.

Faraday isolator. A faraday isolator is required to suppress back reflection into the laser crystal. Any light that is redirected to the crystal must be attenuated by at least 26 dB or it will lead to self injection locking phenomena and disturb the single frequency operation. Two options for the Faraday isolator have been identified:

- A fibre-optic isolator
- Free space beam isolator.

As the baseline for the EOM foresees the location of the phase modulator inside the laser head, the baseline for the faraday isolator must be a free space beam isolator inside the laser head.

Fibre coupler. Two options have been evaluated for the fibre coupler: A standard fibre coupler with a movable lens in combination with a rigidly fixed fibre end and secondly a movable fibre end with a lens permanently glued to the fibre. The advantage of the former is a high maximum coupling efficiency (~ 100 %). The latter has the advantage of low sensitivity to misalignment, a coupling efficiency of more than 80 % is possible.

A fibre coupler with a movable fibre end with a lens permanently glued to the fibre is selected as the baseline.

Photodiodes. Table 4.3-7lists the photodiodes which have been identified for use in the laser subsystem. Those devices are not space qualified; nonetheless, the manufacturer has qualified similar devices for particular programs.

Table 4.3-7 Photodiodes for use in the laser subsystem

Diode	Type	Model	Purpose
p1	InGaAs PIN	EG&G C30619G	Laser phase locking
p2	InGaAs PIN	EG&G C30619G	Laser frequency stabilisation
p3	InGaAs PIN	EG&G C30665G	Laser power stabilisation

Table 4.3-8 - EG&G photodiodes characteristics

Part #	$\varnothing_{active}$ (mm)	Responsivity (A/W)		I_d (nA)	NEP (pW/√Hz)	C_d (pF)	BW (MHz)	P_{MAX} (dBm)	Bias voltage for these specs (V)
		(a)	(b)		(c)	(d)	(e)		(b)
C30619G	0.5	0.2	0.86	5	8	350	>+13	5	< 0.1
C30665G	3.0	0.2	0.86	25	1000	3.0	+11	0	0.2

(a): @ 850 nm; (b): @ 1300 nm; (c): @ 100 kHz; (d): into 50 Ω; (e): for 0.15 dB linearity

4.3.1.5 Phase Measurement Assembly Concepts and Trades

The phase measurement assembly consists of:

- An Ultra Stable Oscillator (USO), providing the frequency reference;
- The phase measurement electronics. The subunits are the sensor proximity electronics, the analog electronics plate, the digital signal processing electronics, respectively.

The **USO** is a key element in the phase measurement chain. Its main and most critical requirement concerns the frequency stability: $\sigma_y(\tau) = 2 \cdot 10^{-13}\ \tau^0$ for an integration time τ 1 s < τ < 10^4 s [2] in order to keep, after phase noise measurement and correction, the contribution to the optical path noise below 10 pm/√Hz.

The Mars Observer oscillator, manufactured by Syntonics LLC, was assumed as reference USO in the LISA Pre-Phase A study. A review of the USO's currently available has been carried out during the present study, but, no space qualified oscillator of the same type (quartz oscillator) with better performances was identified. The only system that is able to provide a more stable frequency reference in the whole range of integration times seems to be the hydrogen maser, which however cannot be considered a viable alternative to the Mars Observer oscillator, because of its much larger mass, power consumption and cost.

The **phase measurement electronics** employs a phase difference measurement method in order to determine the path-lengths changes of the interferometer arms. Corrections are needed for:

- the laser phase noise;
- the clock noise;
- the motion of the proof masses w.r.t. their housing.

The beat signal between the local and the remote laser is detected at the main photodiode (baseline is a quadrant InGaAs PIN photodiode). After conditioning, the signals from the four quadrants is sent to the interferometer electronics, which has the following functions:

- provides the signal for phase locking the local and remote laser;
- provides information on the angle jitter and DC pointing of the test mass
- monitors the long term variations in the laser locking on the remote S/C
- removes the Doppler shift in the beat signal;
  - this function is accomplished by beating the main signal with a suitable comb of reference frequencies (in the range from 0.1 MHz to 15 MHz) in order to have a final beat frequency of the order 10 – 100 kHz;
- measures the phase difference between the local and remote laser in order to measure the differences in round trip path length between the two interferometer arms (GW detection);
  - this function is accomplished by shaping the final beat signal in order to get zero-crossing pulses. The number of the USO clock pulses between successive zero-crossings is then counted in order to measure the arm path length variation.

Figure 4.3-12 shows the measurement schematics from the photodetector (only one quadrant channel is shown) to the phase meter. The USO frequency reference is used to count the time period of the final beat signal.

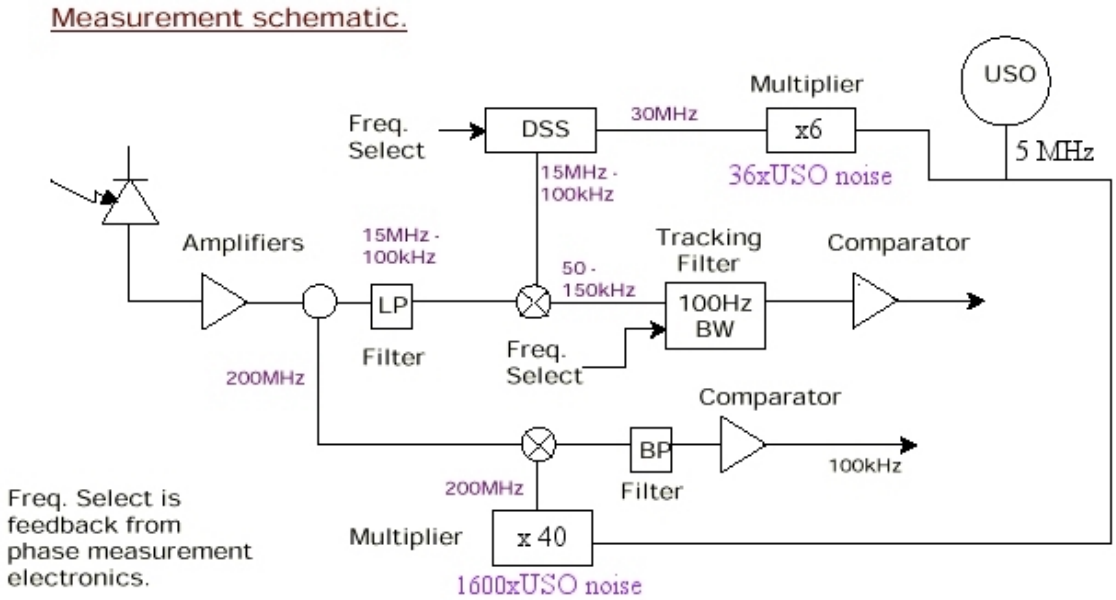

Figure 4.3-12: ***Measurement schematics***

Two measurement principles have been considered:

- counter method (such as MAM/JPL phase meter);
  - the input frequency should be sufficiently high (of the order of 1 MHz) to prevent aliasing of the laser phase noise into the measurement bandwidth. An increase of the counter clock frequency may be needed;
  - the accumulation scheme must be replaced by an elaborated digital decimation filter;
  - analogue pre-processing must be analysed w.r.t. SNR preservation and freedom from in-band artefacts. Instabilities in the electronics, producing phase changes at the level of 10-5 rad, were considered during the study – in particular the voltage stability w.r.t temperature was studied;
- PLL method, either totally digital or a combination of digital and analogue electronics;
  - digitalisation is straight forward at sampling frequency above 2×"edge frequency";
  - control loop must be dimensioned to render residual error in measurement band insignificant;
  - digital decimation filtering must be applied to the NCO phase signal. There is a major problem with the digital version of the PLL, as the microprocessor clock would have to run at GHz to perform the measurement at the high frequencies discussed.

The phasemeter electronics is baselined to consist of a period counter providing frequency information at the kHz rate.

Radiation hardness is a worry for most components as in the LISA mission non-standard components, as far as the S/C electronics is concerned, will be used. A critical point is that of the radiation hardness of the first detection stages, because of possible bandwidth reduction and SNR degradation. No suitable rad-hard components have been found on the market; specific radiation tests must be performed on the device selected as the baseline.

As a final point, no quadrant photodiode with the performances required for LISA is available today; this device needs to be specifically developed.

4.3.2 Payload Control Design Options and Trade-off

4.3.2.1 Laser Pointing Acquisition and Tracking Strategies

The acquisition cone corresponds to the angular sector to be covered by the emitting spacecraft to illuminate the receiving one during the acquisition phase. The acquisition cone being larger than the emitted beam FWHM, the acquisition can not be direct. Two possibilities have been considered to perform the acquisition, defocus of the emission beam or scan of the uncertainty cone

Defocus of the emitted beam. This solution consists in defocusing the emission beam so that its FWHM covers the acquisition cone. The emitted beam FWHM has in that case to be increased from 2.6 µrad to 18 µrad, using for example the defocusing capability of the fibre positioner. The acquisition is then direct, but the flux received on the opposite spacecraft is degraded by a factor 100 wrt the current link budget peak value, which means a 0.03 pW flux.

This solution is discarded as the detection of the defocused beam is critical.

Scan of the acquisition cone. The principle is to have the emitting spacecraft scan the acquisition cone until the beam is detected by the acquisition sensor of the receiving instrument. Once the signal is detected, the direction of the incoming beam is derived from the spot position on the acquisition sensor and the receiving instrument is pointed towards the emitter. This strategy requires an emitted beam pointing capability which can either be implemented at the fibre positioner level or requires to re-orient the whole optical.

With the baseline Optical Assembly design, the ± 9 µrad scan can be achieved by a ± 2 µm displacement of the fibre positioner, which is within its stroke whatever the selected fibre positioner design.

The straylight generated by the emitted beam on the acquisition sensor is estimated to 60 pW / pixel, with a peak to 650 pW for the detector four central pixels. The signal of the opposite spacecraft (3 pW max) is to be detected in this straylight environment. Two solutions have been considered to overcome this difficulty :

- to modulate the emitted beam and the received beam at different frequencies, in order to retrieve the acquisition signal on the CCD by heterodyne detection. This solution, which has not been further investigated, would however have to cope with the problem of the CCD central pixels strong illumination by the secondary mirror apex reflection. The constant point ahead angle between emitted and received beam of 3.3 µrad in plane is not sufficient to separate the receiving sensitive pixel area from the transmitter straylight saturated pixel area. However, estimations show that for the calculated straylight intensity (633 pW/4pixels) a read-out rate of the CCD of a few kHz should be sufficient. This would yet avoid saturation and allow detection of the modulated received beam against the straylight background of the transmitted beam using frequency and phase sensitive techniques. The transmitted beam is modulated at a frequency different from the received one (both modulation frequencies are small compared to the CCD sampling frequency). This solution needs more detailed study.
- to shut down the emitted beam when the acquisition detector is used. This solution is presently the proposed baseline, and the studied acquisition strategy takes this constraint into account.

Remark 1: Shutting off the emitter laser itself could jeopardise the spacecraft thermal balance, so a preferable solution is to fold the emitted beam out of the optical bench and send it towards space before it is mixed with the received beam and generates straylight toward the acquisition sensor. This task can be performed by the fibre positioner (long lateral stroke option only) or by an optical switch located between the laser and the optical bench.

Control aspects. In addition to the pointing accuracy achievable by the STR, the realisation of the scan must be carefully studied.

Two control strategies are possible :

- Have the S/C in a steady attitude, and perform the scan through the fibre positioner.
- Point the beam by re-orienting the entire spacecraft.

The drawback of the first solution is the necessity to design a quite complex, and bulky fibre positioner. Then it is proposed here to show the feasibility of the second solution.

The proposed approach consist in scanning several discrete position, overlapping to cover the entire uncertainty cone.

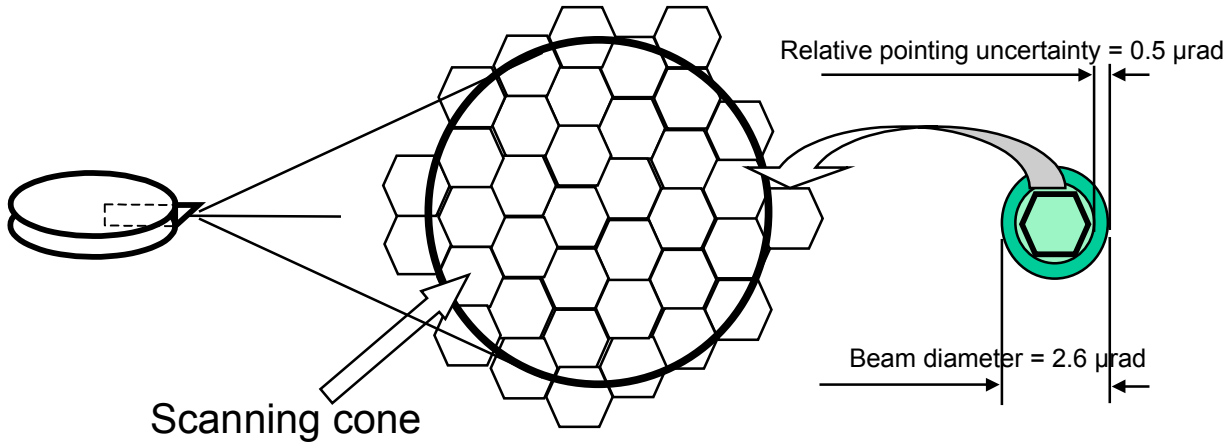

Figure 4.3-13: Uncertainty cone scanning with discrete positions

The number of discrete position is function of the cone width (9µrad), of the emitted beam FWHM (2.6µrad), and of the relative pointing uncertainty (0.5µrad). With the given values, it is equal to 125.

With this strategy, a step is applied to the reference of the attitude controller each time the S/C has to go from one spot to the other. This step will be commanded to the FEEP thruster to orient the S/C on the one side, and of the telescope tilt angle mechanism on the other side (this is at least required for the laser acquisition of the second optical link).

The full convergence (cancellation of the bias through the long-term integral effect) takes quite a long time (>1000 sec), but a pointing accuracy of 10 % of the step, sufficient for the scan is achieved after 30 sec. If we take into account another 10 sec for the receiving sensor integration, the scanning sequence can be achieved in less of 6,000 sec, which is not critical as far as this sequence occurs only a few times over the mission (ideally once).

Another strategy with a continuous scan has not been investigated, but is expected to give equivalent results.

Remark : according to the acquisition detector performances budgets, a solution associating both scan and defocusing could allow to achieve a quicker acquisition by increasing the emitted beam FWHM and therefore reducing the number of scan steps. This is an optimisation to be considered in subsequent phases.

4.3.2.2 Variable Point Ahead Angle Compensation Options

The orbit dynamic analysis by DSS has uncovered an additional difficulty not yet discussed in previous studies, viz. the variation of the point ahead angle between the transmitted and received beams with the orbital period. This angle is caused by the fact that the triangle formed by the spacecraft is both rotating around its normal axis and, simultaneously, its plane is nutating with the orbital period. Thus, each spacecraft as seen from the other spacecraft has an apparent lateral motion, which leads to a varying

offset angle between the emitted and received beams. Although this effect does not imply a critical issue, it causes some technical implications on the system design and on assembly level.

The dynamic analysis generated following results (Section 3.3):

- In plane bias 3.3 µrad - variation +- 55 nrad;
- Out of plane bias 85 nrad - variation +- 5.7 µrad

These values are defined in free space (telescope entrance) and vary approximately sinusoidally with the orbital period of 1 year.

The constant in-plane bias can be compensated for by proper parts alignment, e.g.by tilting the polarisation cube (PBS), as proposed in previous studies.

The in-plane 55 nrad variation is marginally critical only for the transmitter bias relative to the nominal position (specification is < 30 nrad), because the S/C attitude reference is the received beam wavefront tilt, which is tracked with better than 8 nrad/√Hz on the heterodyne detector.

While the out-plane bias of only 85 nrad does not present a problem, the out-plane variation of 5.7 µrad is the most critical factor. It translates for the relevant beam size on the optical bench (baseline selected 5 mm diameter @ telescope mag. 60x) into +- 342 µrad variation perpendicular to plane for the required offset angle between TX and RX beam at bench level.

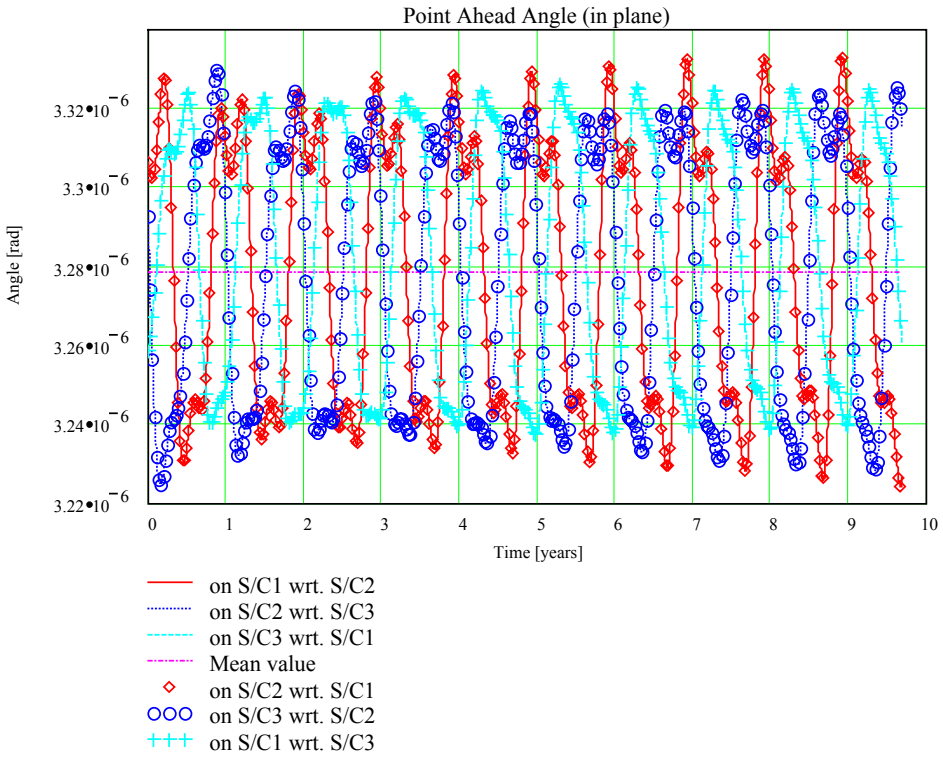

Figure 4.3-2: In-plane point ahead angle variation over orbital periods

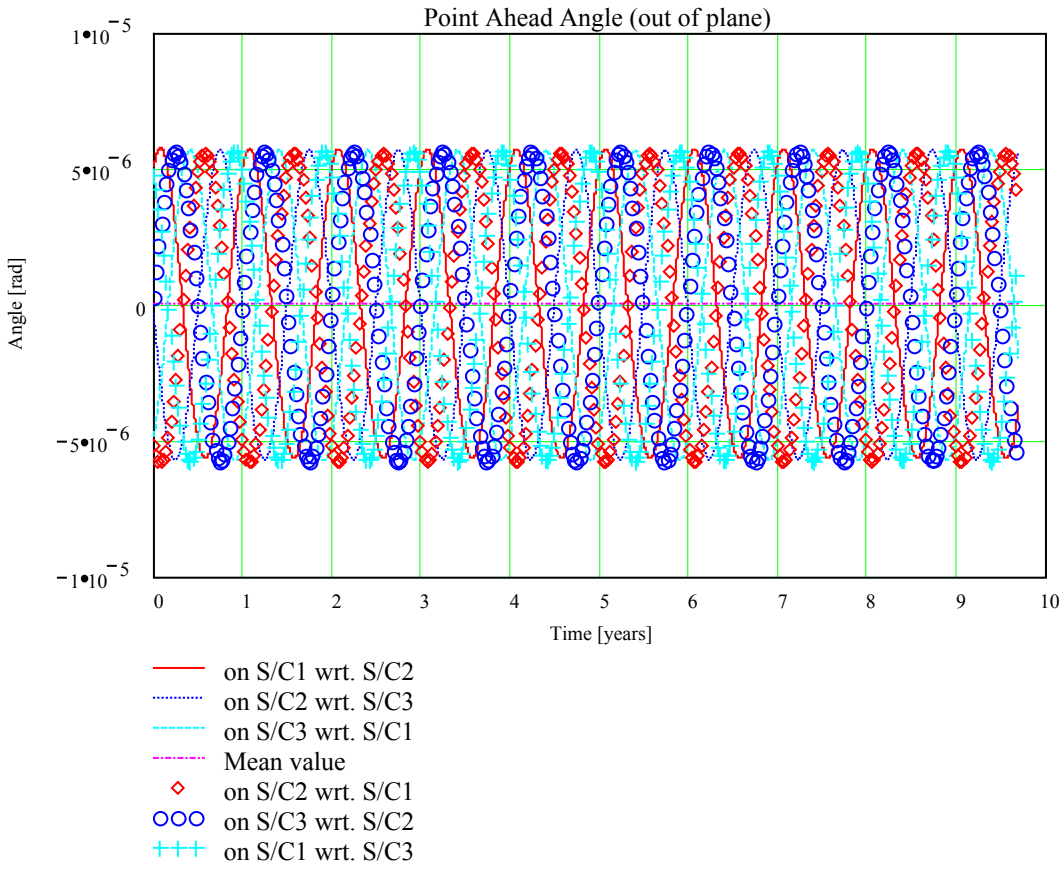

Figure 4.3-3: Point ahead angle variation out-of-plane over orbital periods

Due to the limited study resources, several options to cope with this situation could only briefly be addressed:

1) Do nothing:
   the S/C keeps tracking the received beam, but the transmitted beam would be mispointed in the order of the central lobe divergence not acceptable

2) Use the fibre positioner to adjust the offset angle (periodically or continuously) and the transmitter beam axis:
   This was the first idea, but will misalign the complete optical bench, especially the local oscillator beam and the beam to the rear interferometer and reference cavity. Of course additional pupil shifting optics or/and additional DOF in the fibre positioner assembly could possibly mitigate the impact, but it complicates the situation significantly. In addition, the transmitter beam is tilted towards the optical axis and may lead to a degradation of the far field wavefront (however, should be ok for 5.7 µrad).

3) Use an additional active element in the dedicated transmitter or alternatively receiver beam; e.g. move lens groups or tilt the PBS by PZT:
   Implies complication by additional noise sources, control elements and thermal sources, but is otherwise a clean solution.

4) Use the inertial mass as an already existing active mirror to tilt the received beam (open loop or by using tracking information from the het. detector as error signal for the IRS-control:
This is the proposed baseline, provided, the associated problems in IRS design can be solved. But this function is required anyway to initialise and calibrate the proof mass mirror as an optical element after launch.

The problems that are introduced when considering the latter solution are:

- The tilt angle of +- 171 µrad for the proof mass attitude is too large for the present ONERA design. A budget has already to be allocated for the initialisation, which must be added to this requirement. ONERA quotes presently that about 50 to 70 µrad may be acceptable after all, which is not yet sufficient. Unfortunately, this became apparent only at the end of the study and is only a crude estimate. The physical effects are: the performance of the capacitive sensors, non-linearities and internal DOF cross-talk to be analysed in more detail.
- The rear interferometer will be misaligned during the process. An additional lens introduced to translate the angular tilt into a slight parallel displacement has no direct impact. A transfer function between proof mass attitude noise and rear interferometer phase noise is also introduced, which is assessed to be acceptable (TBC).

The tilt angle at proof mass level can be reduced by selecting a larger beam diameter on the optical bench (or at least at proof mass level by introducing a beam expander in front of the mirror surface). E.g. a factor of 4 brings the tilt angle down to 43 µrad. In addition, also a slight but defined wavefront tilt at the heterodyne detector may be acceptable.

The IRS is already a critical assembly in the payload and the design should not be driven too much by the point ahead angle requirement. Hence, albeit it is cautiously maintained as present study baseline, alternatives shall still be considered.

4.3.2.3 Drag-Free Control Strategy Options and Trade-off

The goal of the drag-free control is to make inertial the two proofmasses, which mirrored sides are used to reflect the laser beams, defining the interferometer armlength. This is obtained by the following complementary actions:

1. reducing as far as possible the linear/angular acceleration experienced by the S/C (role of the DFACS)
2. providing best possible isolation of the P/Ms relative to the S/C (optimisation of the inertial sensor servo loops in close relation with DFACS "outer loops")
3. making sure the P/M are "quiet" in the MBW (acceleration< 2.5 10^{-15} $m/s^2/Hz^{1/2}$).

Point 3. is independent of any control strategy, whereas the first two points are really the core of MMS's task in this project.

Various drag-free missions in which MMS has been involved in the past (Gravity Probe-B, STEP, GOCE) relied on the concept of "drag-free reference point". This point is the point chosen on the S/C to ideally follow a purely gravitational motion.

This concept could be applied to LISA, but the selection of this point is not trivial at all, since we would ideally like to have two drag-free points on the S/C (at each mirror location), which is not physically

possible. A trade-off is then necessary to select the best DFRP. This trade-off is presented in Appendix 1. Two candidates are retained for the discussion here : the intersection of the LOS, and one of the P/M location.

But this concept of drag-free reference point can be bypassed in the case of LISA. Indeed, for each proof mass, only one axis must be inertial, while there are only requirements on the P/M-cage relative position on the other two axes.

Therefore another family of strategies consists in performing the drag-free control using only the "sensitive" axis of each P/M (i.e. in the telescope LOS direction), while the other axes of the P/M are only suspended, through the electrostatic suspension loops

Thus, four strategies can be preliminarily selected for a detailed trade-off :

- **Strategy 1** : DFRP located at one of the proof masses. In other words, one P/M is the only reference for the DFC (master P/M), the other one has no role in DFC (slave P/M).
- **Strategy 2** : DFRP located at the intersection of the LOS. DFC measurement is reconstructed from measurements of both P/M to be fed into the DFC controllers.
- **Strategy 3** : Strategy without any defined DFRP : The DFC is performed with the raw measure of each sensitive axis.
- **Strategy 4** : Same strategy as 3, but no suspension is implemented along the sensitive axis. The cancellation of instability effects, constant forces (self-gravity), etc, is handled by the DFC loop.

From a detailed analysis presented in chapters 5 and 7, the following conclusion has been obtained:

Strategies 3 & 4, without DFRP, allow to meet requirements with margins (this is also the case for other requirements, such as P/M position, not detailed here).

Strategy 3 is recommended by MMS to be the baseline for this phase A, with the possibility of preferring strategy 4 in subsequent phases, provided that constant force cancellation does not rise the complexity of the control scheme, which still needs to be demonstrated for strategy 4.

5 System Baseline

5.1 System Conceptual Design and Performance

5.1.1 System Control Architecture

LISA is an interplanetary constellation mission consisting of three identical spacecraft. Due to their strong mutual interaction in routine phase via optical inter-satellite links, system control is not restricted to spacecraft level but has to encompass the whole spacecraft constellation.

5.1.1.1 System Control Architecture on Constellation Level

The establishment and maintenance of highly stable, bi-directional laser links within the routine phase constellation of the three LISA science modules which are then located at the vertices of a quasi-equilateral, slowly rotating triangle, represents a challenging control task. The narrow width of the laser beams (2.6 μrad FWHM) in conjunction with the huge inter-spacecraft distance of 5 million km requires a rather stable beam pointing all over the Pointing Acquisition and Tracking (PAT) process. Details of this process are described in section 5.4 of this report.

An important feature of the proposed PAT scenario is that it does not necessarily rely on direct ground intervention and control of the science modules that are supposed to establish a laser link between each other. For the ground it is sufficient to send a time-tagged command to the two spacecraft (both assumed already in PAT Mode) that defines their mutual role as master or slave in this process. The execution of this command on-board each spacecraft is a fully autonomous process that normally requires no further ground interaction. After completion of the pointing acquisition the optical link allows both spacecraft to directly exchange information necessary for subsequent payload commissioning and routine operation.

The control architecture on constellation level is hence anticipated to be highly autonomous and decentralised and to avoid slow indirect inter-spacecraft communication via ground.

After proper orbit insertion no control of the orbits of the constellation satellites is presently foreseen.

5.1.1.2 System Control Architecture on Spacecraft Level

The challenging nature of the LISA requirements necessitates a control architecture which closely integrates payload and spacecraft functions. The principal control functions to be considered are

- S/C Attitude, Drag-Free and Orbit Control
- Proof-Mass Attitude and Position Control
- Telescope Articulation Control
- Fibre Positioning Control
- Laser Phase Locking
- HGA Pointing Control

In the sequel the most important of these control functions shall be briefly addressed. For details the gentle reader is referred to section 5.4.

A schematic of the system control architecture in routine phase after completion of the optical acquisition with both telescopes is given in Figure 5.1-1.

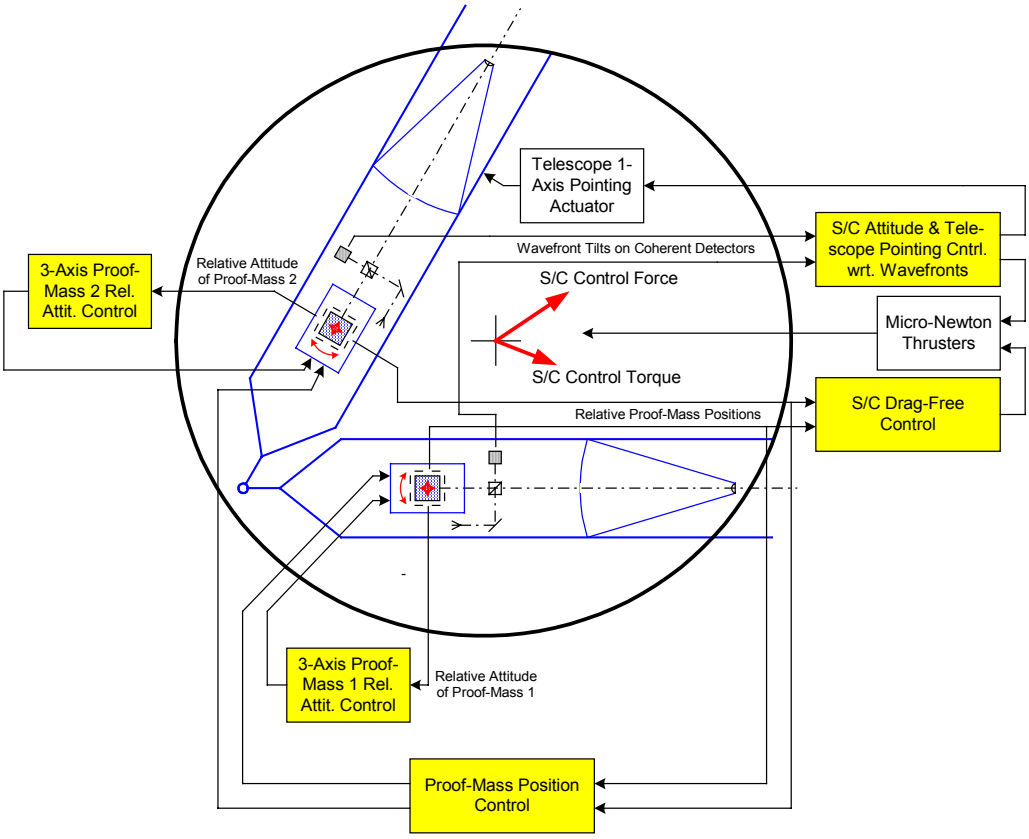

Figure 5.1-1: Simplified system control architecture after completion of optical acquisition

Spacecraft drag-free and attitude control . The objective of the LISA Drag-Free and Attitude Control System (DFACS) is to point the telescope lines-of-sight with pointing errors not exceeding 30 nrad towards the incoming wavefront and to adjust the spacecraft position in a way so that the proof-masses remain centred within their cages, at least along the respective optical axis, with a position error of not more than 2.5 nm/√Hz within the measurement bandwidth. The DFACS uses the inertial proof-mass sensors and the coherent quadrant detectors of the two optical assemblies as sensor information and controls the spacecraft attitude and position by means of FEEP thrusters. The number of degrees of freedom to be controlled implies a close interaction of DFACS with telescope articulation control and proof-mass control.

Telescope articulation control. The adjustment of the optical axes of the two telescopes towards the incoming wavefronts requires 2x2=4 rotational degrees of freedom. Therefore the three basic rotational degrees of freedom of the spacecraft have to be complemented by an additional one allowing to adjust the angle between the two telescope lines of sight. This angle is anyway subject to a variation of ±0.6° over the year. The a.m. stringent pointing bias requirement of 30 nrad w.r.t. the incoming wavefront necessitates a permanent control of the telescope articulation using a dedicated single-axis telescope pointing mechanism. For redundancy purposes both telescopes will be articulated in this way.

In case the attitude control using FEEP thrusters should in future phases prove too noisy there is still an option to implement two-axis telescope articulation each. This, e.g. in view of redundancies, considerably more complex control concept is presently not considered baseline.

Proof-Mass Control. The completion of the optical acquisition phase implies that the proof-mass inside the inertial sensor of each telescope assembly has been mechanically released and correctly positioned so that light coming from the distant spacecraft is properly reflected off the proof-mass and can be correctly superimposed at the beam splitter with the light coming from the local laser. During Pointing Acquisition and Tracking it is mandatory to have the proof-mass electro-statically caged, since it needs to be used as an accelerometer and its attitude has to be properly adjusted so that the received laser beam is reflected off the proof-mass and hits the coherent detector.
In science mode, however, drag-free control will be enabled and the proof-masses should ideally be floating around free of external forces and the spacecraft should control its own position such as to maintain the proof-masses centred in their housings. Obviously, a rigid spacecraft is necessarily unable to control its position in a way to have two diverging proof-masses centred. Therefore a control law needs to be applied to the proof-masses that acts as a very soft spring and does not introduce control action within the measurement bandwidth.

In order to reduce the control action on the proof-masses to the absolute minimum, the proof-mass control can be restricted to those errors that can definitely not be compensated by spacecraft common-mode position control. This is equivalent to a drag-free control concept without a body-fixed drag-free reference point. This drag-free control concept has been analysed and found to meet the requirements.

A point that is still open is the number of sensitive axes to be foreseen for the proof-mass sensor. From a control point of view both the single-axis and the two-axis option appear equally apt to meet the requirements.

5.1.2 System Optical Architecture

The mission redundancy scheme is such that the three satellites are equivalent. Within one satellite the optical payload is made of two identical opto-mechanical arrangements, each communicating with one opposite spacecraft. The operational difference between the two parts is only that one operates the master laser while the other has its laser enslaved. However for redundancy reasons the master function can be performed by any of the two parts if needed so their designs are identical.

The optical payload emits a monochromatic (1064 nm) beam to the opposite satellite and receives its retro-emitted beam. The size of the beam maximises the energy transfer efficiency while staying within payload reasonable size and mass budgets. The transmission and the reception directions shall be the same to also maximise the transfer efficiency and to reduce the sensitivity to pointing jitters. On the slave optical assembly the received beam bounces on the proof mass mirror and is amplified while keeping its phase reference to be resent to the master optical assembly on the opposite spacecraft. In the master optical assembly, the received beam is, after reflection on the proof mass mirror, mixed with a fraction of the emitted laser beam to produce the scientific measurement.

The beam is emitted by a 1W YAG laser source. To avoid introducing thermal stresses on the optical bench which has to remain very stable this laser is coupled into a fibre sent to the optical bench. This fibre is monomode and maintains the polarisation state of the laser beam as the beam dispatching on the optical bench is made by polarisation sensitive components. The laser fine stabilisation is performed using an external optical cavity located on the optical bench.

The beams are collimated on the optical bench to avoid using relay optics. The emission and reception are ensured by an a-focal telescope. The link budget between the satellites increases with the diameter of the telescope. A pupil diameter of 30 cm features a good compromise between the payload size and mass and the link budget required to ensure the scientific measurement performance. The telescope Dall-Kirkham optical design enables to meet the required imaging quality for both the emitted and received beams over the mission field of view.

The resulting emitted beam divergence is smaller than the acquisition uncertainty cone so that a scan of the acquisition cone is necessary to establish the link between the spacecraft. This can be made by orientating the optical payload, or thanks to the fibre positioning mechanism. This three translations mechanism also enables the emitted beam collimation optimisation, and translates the fibre in a plane perpendicular to the optical axis to co-align the emission and the reception (taking into account the point ahead angle). Its use to switch to the redundant laser has however been discarded for bulkiness reasons, this function being devoted to a dedicated switch mechanism away from the optical bench.

The x60 telescope magnification ratio is a compromise between manufacturing limitations and the beam diameter on the optical bench. The advantage of a large lateral magnification ratio is that small angles at telescope output correspond to larger ones inside. This reduces the constraints on the angular stability or sensitivity of the internal components as well as on the fibre positioning mechanism resolution.

During measurements the optical assembly must remain stable within its thermal environment to avoid spurious phase delays and must feature an excellent emitted beam imaging quality ($\lambda/20$ rms wavefront error @ 1.06 µm) to meet the required link budget. The stability is ensured using a low expansion material for the optical bench (ULE), and by radiative and conductive discoupling of the telescope from its thermal environment. This is especially important for the all silicon carbide telescope solution. The imaging quality is reached thanks to high quality polishing of both telescope and optical bench optics. The emitted beam refocusing is ensured by the fibre positioner.

The mirrors of the interferometer are the proof-masses themselves. They are circumscribed by the optical bench which supports all the beam dispatching optics and the various detectors used for received beam acquisition, emitted beam monitoring and interferometric measurement. The relative position of these components must be extremely stable (a few $10^{-12}\ m/\sqrt{\text{Hz}}$), otherwise their movements generate spurious optical path differences or change the mass arrangement and thus the gravitational field around the proof-mass. The external laser cavity also needs this dimensional stability for frequency stabilisation. The required stability is achieved by a low expansion ULE bench where the optical components are bonded in a stable manner (hydroxyl catalysis).

The interferometric mixing of the emitted beam with the return beam after its reflection on the proof-mass mirror is achieved with a maximum efficiency using quarter wave plates and a polarisation beam splitter. To ensure the fine pointing specification in the order of a few $\text{nrad}/\sqrt{\text{Hz}}$, the detector is a quadrant detector. The tilt difference between the received and emitted beams generates a different phase shift on the quadrants thus enabling to detect mispointings.

The internal transmission of the laser beam from the master assembly to the slave one is performed via a fibre link similar to the one used for the transmission from the laser to the optical bench. This enables to be insensitive to the relative pointing movements of the two internal assemblies.

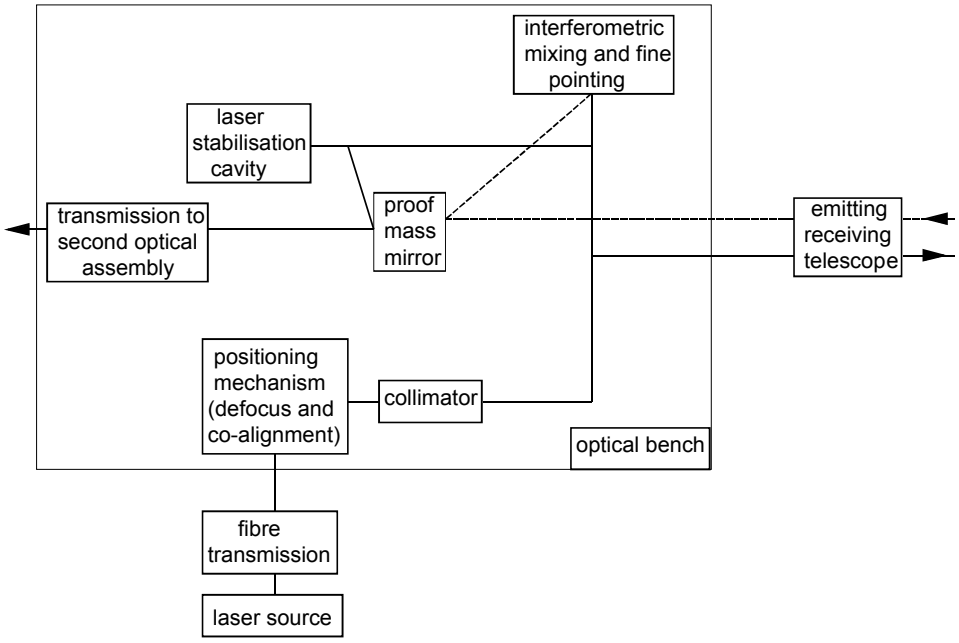

Figure 5.1-2: *The opto-mechanical architecture is driven by the functional needs of the payload. It is based on the use of a telescope for emission reception of the laser beam. This telescope is coupled to a stable optical bench where the other functions are implemented. The source is decoupled from this stable part thanks to the use of a fibre link.*

5.1.3 System Performance

5.1.3.1 Performance Overview

The purpose of the LISA system is the measurement of gravitational waves characterised by the dimensionless amplitude h which can be viewed as cause of proportional change of the distance between two proof masses induced by the gravitational wave.

Following [Ref. 1] the average sensitivity of a measurement system based on a Michelson-Interferometer can be expressed as

$$\Delta h(f) = \frac{\delta L(f)}{L} \cdot Sinc\left(\frac{\pi L f}{c}\right) \cdot Sin(\alpha_{arm}) \cdot \frac{SNR_{desired}}{T_{observation}} \cdot \beta_{averaging} \qquad \text{(EQ 5.1-1)}$$

where

$\Delta h(f)$	Spectral sensitivity in terms of h [$1/\sqrt{Hz}$]
L	Armlength of Interferometer [m]
f	Frequency (Hz)
δL	Spectral amplitude of error in measurement armlength difference [$m/\sqrt{Hz}$]
α_{arm}	Angle between interferometer arms
$SNR_{desired}$	Desired SNR (in terms of amplitude) after specified observation time
$T_{observation}$	Observation time [s]
$\beta_{averaging}$	averaging factor resulting from averaging over various directions of incidence (assumed to be about 5)
c	Velocity of light [m/s]
Sinc(x)	Sin(x)/x

The angle between the interferometer arms is 60° resulting from the configuration of the three spacecraft in form of an equilateral triangle. The arm length is determined by the separation of the spacecraft (5 10^9 m). The characteristic performance parameter of the LISA measurement is the uncertainty in the determination of the armlength difference (δL). This parameter is only of concern within the LISA measurement bandwidth (10^{-4} Hz to 10^{-1} Hz). Hence absolute knowledge of the arm length difference is not required.

In the triangular configuration two independent difference measurements can be carried out yielding information on direction and polarisation of the incident gravitational wave.

As δL is defined with respect to the undisturbed proof mass positions it includes not only distance measurement errors but also arm length variations resulting from (unknown) acceleration acting on the proof-masses. This results in a performance model as shown in Figure 5.1-1.

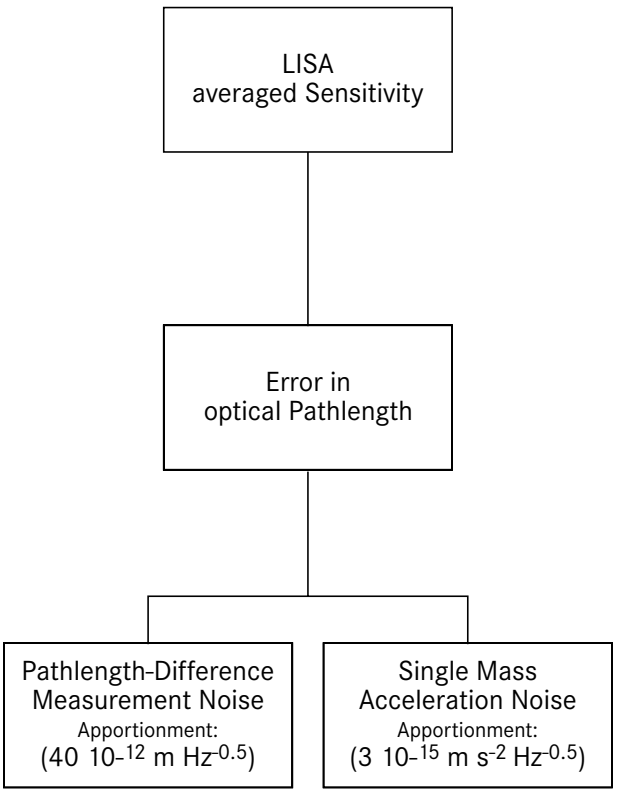

Figure 5.1-1: Performance Model Structure

In the pre-phase A study an apportionment of the two main error contributors has been performed. LISA has to show a performance equal or better than the measurement sensitivity that would result from an optical pathlength measurement error of 40 pm/√Hz and an acceleration noise of 3 1015 m s^{-2}/√Hz. Both contributions to be assumed as white processes in the measurement spectral range. Following these apportionment, effective error in the optical pathlength difference and resulting averaged sensitivity over one year of observation are shown in Figure 5.1-2 and Figure 5.1-3

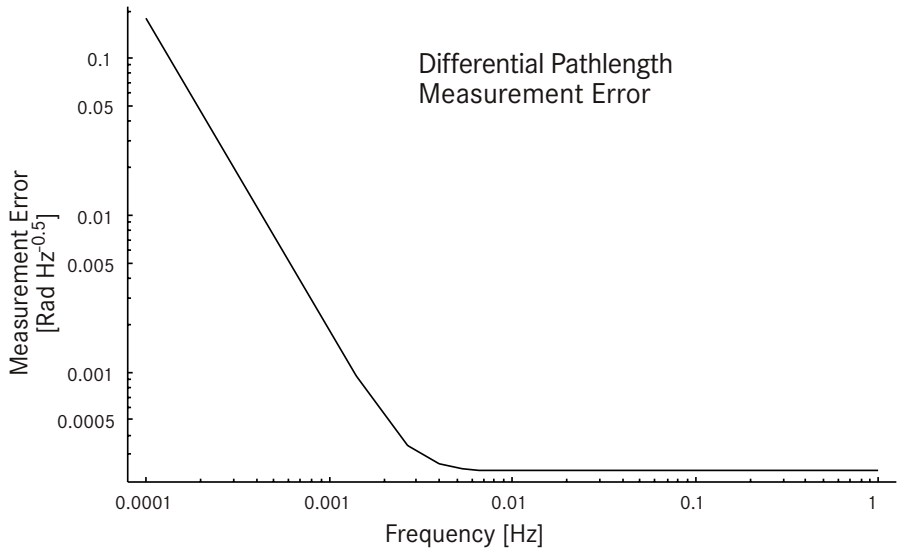

Figure 5.1-2: Specified error bound for optical path-length (as phase error)

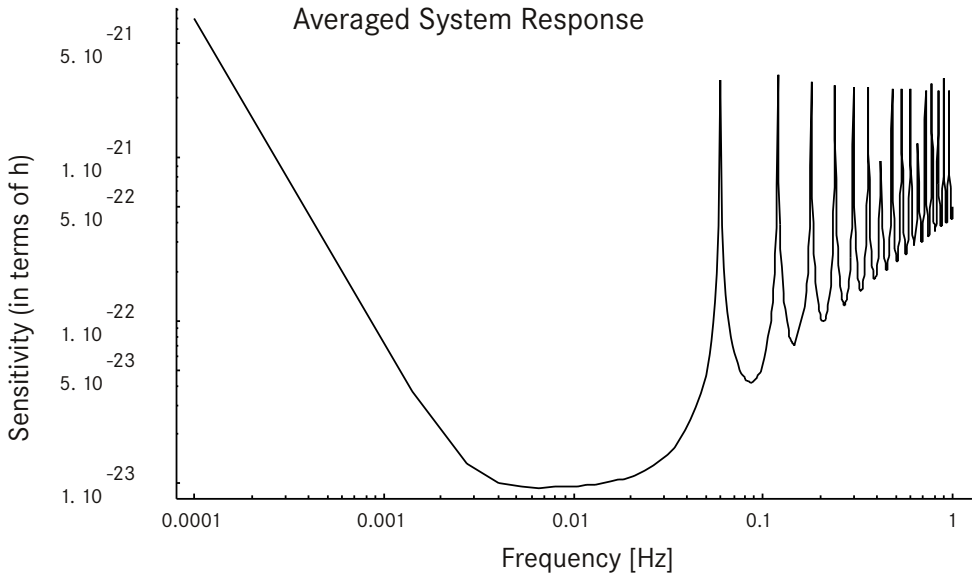

Figure 5.1-3: Required system sensitivity for one year of observation

In a practical implementation both error contributions are not likely white processes over the measurement frequency band. It is expectable that acceleration resulting from the drag free control loop residual error will rise at the upper edge of the frequency band while measurement noise resulting from uncompensated laser phase noise will rise at the lower band edge. Since however the system sensitivity is dominated by length measurement noise at he high frequencies and by acceleration noise at the low frequencies these effects will not necessarily compromise the overall sensitivity.

The length measurement noise has several causes:

- Shot noise due to the limited number of received photons
- Laser Phase Noise
- Measurement Clock Phase Noise
- Variation of measured phase due to motion of optical components inside the instrument
- Variation of phase due to wavefront curvature and pointing interaction

The unavoidable factor is the shot noise on the received signal. It is ideally the dominating noise source for the length measurement, determined by telescope diameter and transmitter power. Optical losses, wavefront mismatch at the detector and detector quantum efficiency contribute to the shot noise level. However state of the art optical design is so close to the theoretical limit that practical improvement of shot noise is only expectable via higher transmitter power or larger telescopes. For the required measurement accuracy a transmitter power of 1W and a telescope diameter of 0.3 m is sufficient with some margin to accommodate the above mentioned losses.

Although not limited by first principles it is technologically demanding to reduce the other measurement error contributions to a magnitude comparable with the shot noise as determined above.

The approach to deal with laser phase noise and measurement clock noise is the use of noise cancellation techniques. This eliminates the first order effect of these noise sources to the system measurement sensitivity. However the actual magnitude of the phase noises determines the accuracy required for the cancellation process and hence poses requirements to equipment and accuracy of ancillary data. E.g. phase meter

dynamic range and aliasing behaviour.

An ancillary interferometer measurement is used to determine the relative motion of proof-mass versus spacecraft to eliminate the dominating internal pathlength variation.

Residual pathlengths variations have to be addressed by technological means, i.e. mechanical/thermal stable design of the optical bench, control of straylight intensity and mechanical stability of straylight paths. Tight control of transmitter pointing in combination with good optical quality of the telescope (to reduce errors in phasefront curvature) is required to achieve a small pointing induced measurement error.

The acceleration noise is also resulting from several causes:

- External forces directly acting upon the proof masses coupled by interplanetary magnetic fields (e.g. Lorentz force)
- Forces induced by time varying local fields (gravity, magnetic (gradient))
- Forces directly resulting from the electrostatic actuators of the drag free control loop
- Forces resulting from gradients of magnetic and gravity fields bound to the spacecraft and relative motion between spacecraft and proof mass

The key element governing the acceleration noise budget is the drag free control loop. It shields the proof masses from most external forces acting upon the spacecraft, specifically from time varying radiation pressure originating from the sun. The control loop uses the FEP thrusters to control spacecraft position and attitude such that the proof masses remain centred in their cages and the telescopes remain pointed to the two other spacecraft of the formation. Since the 6 degrees of freedom of spacecraft position and orientation are not sufficient to achieve the control objective for two proof-masses and two telescopes other actuators additional actuators are employed. Specifically the pointing angle between the telescopes can be controlled and electro-static actuators are employed to impose forces and torque to the proof masses. The design of the control loop is constrained by stability considerations arising from static forces and "spring constants" acting on the proof masses (resulting from field-strength and field-strength gradient of magnetic and gravitational fields). Aim of the control loop optimisation is the minimisation of forces in the measurement bandwidth arising from electrostatic actuator action or resulting from relative motion of the proof-masses with respect to the field gradients coupled to the spacecraft.

The two aspects of LISA performance (path length measurement error and acceleration noise) are discussed and budgeted in the following two chapters. Compensation of phase and clock noise as well as accounting for relative motion of spacecraft versus proof masses is essential to measurement performance. The section on the path length measurement error includes therefore also the description of the measurement setup and processing strategy addressing these aspects.

5.1.3.2 Pathlength Difference Measurement

The basic measurement configuration of the LISA system is specified in [Ref. 1] and [Ref. 2]. One Michelson Interferometer is implemented using the payload of 3 spacecraft. The interferometer setup using spacecraft 2 as centre node and spacecraft 1 and tree as edges of the two arms is shown in Figure 5.1-4.

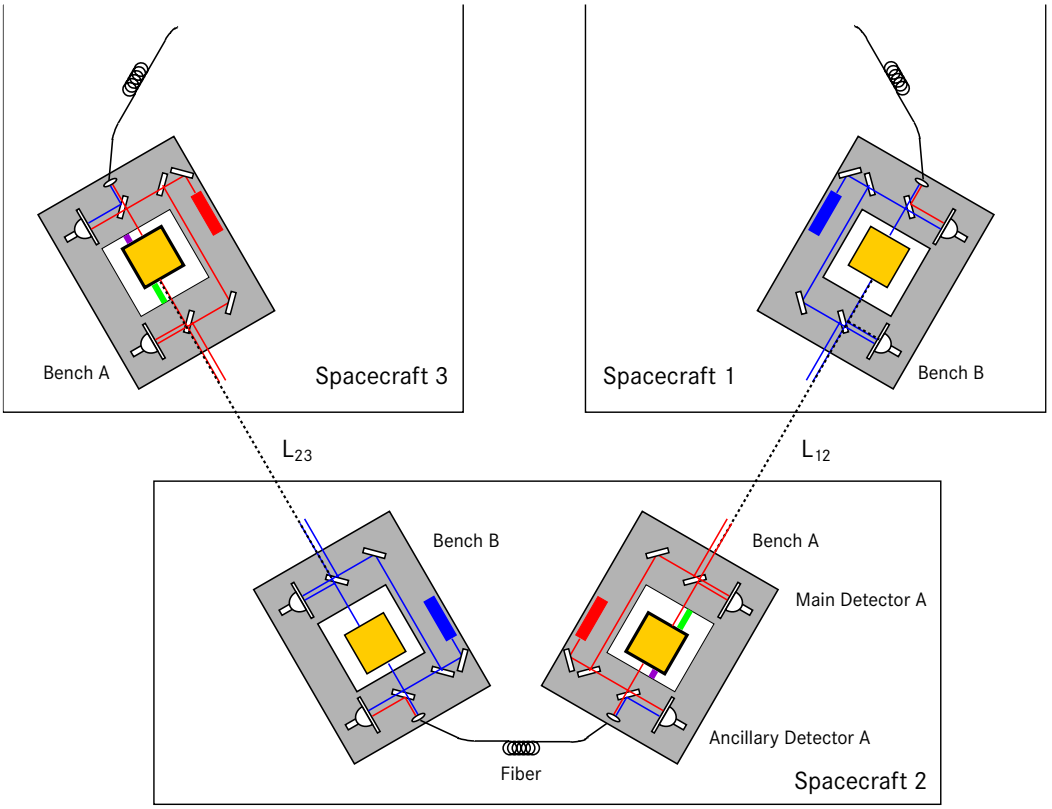

Figure 5.1-4: Lisa Measurement Setup

Since the formation is an equilateral triangle and all spacecraft are identical 2 equivalent setups can be formed by cyclical permutation. However only 2 simultaneously derived results provide independent information on the gravitational wave.

TX/RX units assembled on individual optical benches are used on the ends of the interferometer arms. Each spacecraft house two of such units. Each unit contains:

- an individual transmitter laser
- a phase modulator to create sidebands on the transmitted laser beam used to convey information on the local clock (and for data exchange between the spacecraft)
- an individual proof-mass (with electrostatic sensors and actuators, used by the drag-free control),

- a main detector where the interference signal of the received light and a fraction of the light from the local transmission laser is converted to an electrical signal containing the beat note of the carriers and the modulation sidebands
  (actually the main detector signal is the sum of four quadrant signals of a segmented detector)
- a secondary detector where a heterodyne signal between the two transmitter lasers on board the same spacecraft is generated
- ancillary functions supporting pointing and beam alignment; including quadrant channels of main detector for measurement of wavefront tilt
- a reference cavity which may be used for stabilising the transmitter laser

The optical signal path is selected such that changes in the distance between the proof masses of an interferometer arm is represented as phase change on the main detectors. Due to the long roundtrip time of about 32s relative motion of the optical bench versus the floating proof mass is visible in the main detector signals. Therefore the light path associated with the secondary detector contains a reflection on the backward surface of the proof mass such that an interferometer is formed measuring the motion of the optical bench relative to the proof mass. This information can be used for correcting the spacecraft relative motion effect on the main interferometer. On all detectors light from different laser sources is superimposed. Hence all interferometer signals are heterodyne signals with beat frequencies not necessarily close to zero, even when no significant Doppler shift is involved in the respective light path. The strategy to obtain reasonable frequencies of the detector signals is to use one laser in the configuration as reference and lock the other lasers directly or indirectly to this master laser. The master laser itself is stabilised by a control loop using the above mentioned cavity. The ancillary detectors serve aside from their function in the backside interferometers as means to establish a phase relation between the two lasers in the same spacecraft. By using offset locking between the different lasers the frequency of the beat signals can be conveniently controlled. However at some detectors a beat frequency as high as the maximum one way Doppler shift between any two spacecraft is unavoidable (about a1 MHz per 1 m/s relative velocity). Handling high frequencies at the input of the phase measurement devices requires appropriately accurate reference clocks.

The desired data product from the described configuration is the armlength difference L_{23}-L_{12} which should be representative in the measurement bandwidth 10^{-4} Hz to 10^{-1} Hz. It is needed from two of the three possible interferometer configurations in the triangular formation. The main problem in determining this quantities from the measured detector signals is the large phase noise on the laser signals and on the local clock signals which dominate the wanted measurement signal by orders of magnitude.

The pre-phase A design has adopted cancellation techniques for both noise types.

The phase noise cancellation technique follows G. Giamperi [Ref. 18]. It operates in the frequency domain (Fourier transform of the time series from the detector). Essentially instead of $L_{23}(f) - L_{12}(f)$ the system is solved for $L_{23}(f) - \gamma(f)L_{12}(f)$ where $\gamma(f)$ is a known complex valued function depending on system geometry with an absolute value close to 1. This particular linear combination can be shown to be independent of the laser noise with perfectly known system geometry. When the absolute values of the interferometer arm length difference is only approximately known the residual amplitude error is proportional to the laser phase noise amplitude and (at least at sufficiently low frequencies) proportional to the error in knowledge of the absolute armlength difference. At low frequencies the residual error follows a 1/f characteristic.

The clock noise compensation is a derivative of the method described in [Ref. 19] by Hellings and Giamperi. (It differs in the method of generation of the clock synchronisation signal.) Basically a high frequency signal (200 MHz) synchronised to the local reference clock is modulated on each transmitted laser beam and demodulated at each main detector. The demodulated signals allow referencing of the local clocks (one per spacecraft) to exactly monitored delay lines established by the precisely measured path delay on the interferometer arms. The achievable clock noise (at modulation frequency level) after correction is proportional to

the shot noise on the ancillary carrier. As the fraction of this noise relevant to the LISA measurement is determined by he ratio of the beat signal frequencies to the ancillary modulation frequency, a sufficient low corrected clock noise can be achieved for nominal detector signals with frequencies small compared to the modulation frequencies. Generally the residual effect of the clock noise should be negligible when the frequency ratio can be made large compared to the power ratio of laser carrier and used modulation side-band.

Formal description of the measurement setup.

The setup given in Figure 5.1-4 can be reduced to a formal diagram identifying the relevant optical paths and phase relationships as shown in Figure 5.1-5 for spacecraft number 2.

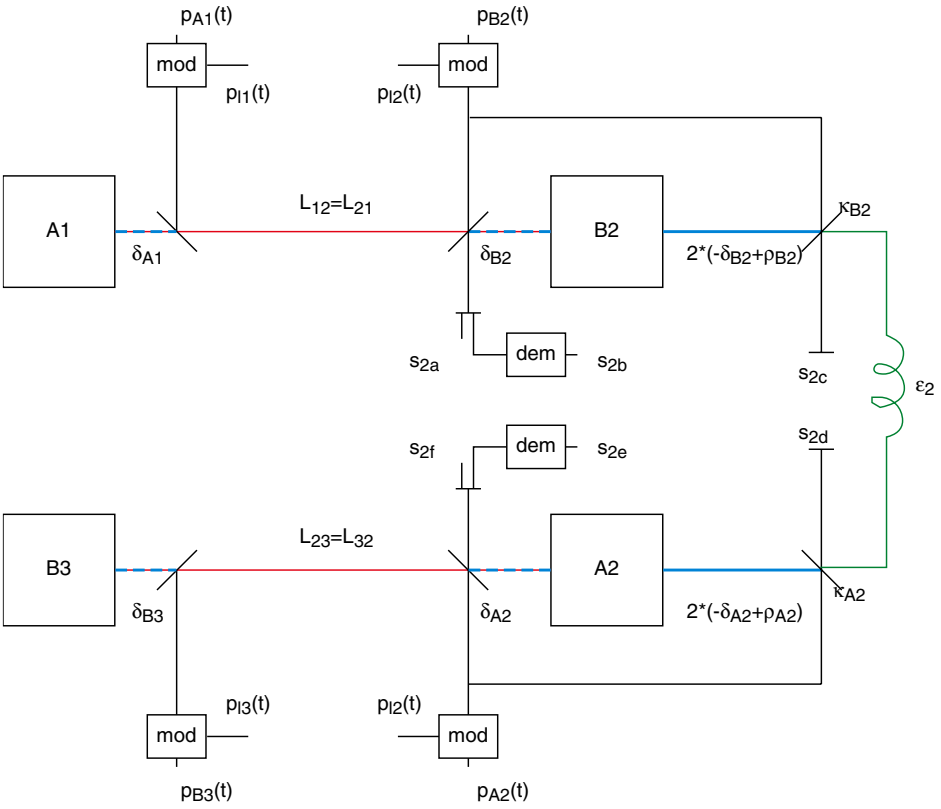

Figure 5.1-5: Lisa Measurement Setup Parameter Diagram

The optical components needed for changing polarisation as needed for the TX/RX beam splitting are not shown. Their effect is included in the relevant optical pathlengths; pathlengths variations are assumed negligible in the measurement bandwidth.

Figure: 5.1.3-2 identifies the 6 possible phase measurements per space craft

s_{2a}	beat note of optical carriers in spacecraft 2 for link S/C 1 to S/C 2
s_{2b}	beat note of optical carrier in spacecraft 2 with upper modulation sideband of received signal for link S/C 1 to S/C 2
s_{2c}	beat note of backside interferometer with measurement path via proof mass A2
s_{2d}	beat note of backside interferometer with measurement path via proof mass B2
s_{2e}	beat note of optical carrier in spacecraft 2 with upper modulation sideband of received signal for link S/C 3 to S/C 2

s2f beat note of optical carriers in spacecraft 2 for link S/C 3 to S/C 2

The unknown quantities are:

Laser and Clock phase functions
(referenced to the nominal master signals optical respectively USO)

p_{B2} phase function of laser associated with proof-mass B2 (reference point is polarising beam splitter in front of proof-mass B2)

p_{I2} clock phase function (S/C 2) as modulated onto optical carrier, i.e. as represented by difference of carrier and sub-carrier phase (reference point is polarising beam splitter in front of proof-mass B2, however differences other than a constant phase are not assumed when the modulation is observed at polarising beam splitter in front of proof-mass A2)

p_{B2} phase function of laser associated with proof-mass A2 (reference point is polarising beam splitter in front of proof-mass A2)

Optical Path-lengths

L_{12} distance between the proof-masses A1 and B2 which is the interferometer arm lengths S/C 1 to S/C 2,

δ_{B2} distance between polarising beam splitter in front of proof-mass B2 and proof-mass B2 (part of optical path from S/C 1 to S/C 2)

δ_{A1} distance between polarising beam splitter in front of proof-mass A1 and proof-mass A1 (part of optical path from S/C 2 to S/C 1)

ρ_{B2} difference in distance from the front surface of the proof mass B2 to the main beam splitter and the distance from the backside of the proof-mass to the ancillary beam splitter; this quantity is assumed to be constant as depends only on mechanical dimensions of proof-mass and optical bench

κ_{B2} phase difference between p_{B2} and the optical phase of the B2 transmitter laser observed at the ancillary beam splitter; this quantity is assumed to be constant as it depends only on mechanical dimensions of the optical bench

ε_2 optical path-length of the fibre path between the two ancillary beam splitters; both directions are assumed to exhibit identical optical pathlength (neglected dispersion and polarisation dependency effects)

L_{23} distance between the proof-masses B3 and A2 which is the interferometer arm lengths S/C 3 to S/C 2,

δ_{A2} distance between polarising beam splitter in front of proof-mass A2 and proof-mass A2 (part of optical path from S/C 3 to S/C 2)

δ_{B3} distance between polarising beam splitter in front of proof-mass B3 and proof-mass B3 (part of optical path from S/C 2 to S/C 3)

ρ_{A2} difference in distance from the front surface of the proof mass A2 to the main beam splitter and the distance from the backside of the proof-mass to the ancillary beam splitter; this quantity is assumed to be constant as depends only on mechanical dimensions of proof-mass and optical bench

κ_{A2} phase difference between p_{A2} and the optical phase of the A2 transmitter laser observed at the ancillary beam splitter; this quantity is assumed to be constant as it depends only on mechanical dimensions of the optical bench

For the purpose of the LISA measurement changes in the quantities describing optical pathlengths are relevant in the picometer scale while the effect of the same quantities in terms of delay as relevant for the measurement of the phase noises is only noticeable in the meter scale. Therefore the equations describing the

measurement setup will be formulated in terms of difference quantities ΔL_{12}, ΔL_{23}, $\Delta\delta_{B2}$, $\Delta\delta_{A1}$, $\Delta\delta_{A2}$, $\Delta\delta_{B3}$, de2, referring to some arbitrary starting value and of estimates of the absolute quantities as needed for the phase noise cancellation. I.e. ΔL_{12} shall be the unknown variation of the interferometer arm length S/C 1 to S/C 2 (relevant in picometer scale) while L_{12} is the estimate of the absolute value (relevant in meter scale).

The resulting LISA equations for S/C 2 are given below (Eq.). The equivalent equations for the measurements on the spacecraft 1 and 3 can be derived by cyclic permutation of the indices and assuming identity of L_{23}/L_{32} and L_{12}/L_{21}.

Equations for S/C 2 Measurements in time domain

$$2a: \quad s_{2a}(t) = n_{2a}(t) + \alpha_{2a}\cdot p_{l2}(t) + \frac{2\pi}{\lambda}\cdot\left(\Delta L_{12}(t) + \Delta\delta_{B2}(t) - \Delta\delta_{A1}\left(t - \frac{L_{12}(t)}{c}\right)\right) - p_{A1}\left(t - \frac{L_{12}(t)}{c}\right) + p_{B2}(t)$$

$$2b: \quad s_{2b}(t) = n_{2b}(t) + \frac{2\pi}{\lambda}\cdot\left(\Delta L_{12}(t) + \Delta\delta_{B2}(t) - \Delta\delta_{A1}\left(t - \frac{L_{12}(t)}{c}\right)\right) - p_{A1}\left(t - \frac{L_{12}(t)}{c}\right) + p_{B2}(t) + (1+\alpha_{2a})\cdot p_{l2}(t) - p_{l1}\left(t - \frac{L_{12}(t)}{c}\right)$$

$$2c: \quad s_{2c}(t) = n_{2c}(t) + \alpha_{2c}\cdot p_{l2}(t) + \frac{2\pi}{\lambda}\cdot\left(\Delta\varepsilon_2(t) - 2\Delta\delta_{B2}(t) + 2\rho_{B2}(t)\right) - \left(p_{A2}\left(t - \frac{\varepsilon_2(t)}{c}\right) + \kappa_{A2}\right) + \left(p_{B2}(t) + \kappa_{B2}\right)$$

$$2d: \quad s_{2d}(t) = n_{2d}(t) + \alpha_{2d}\cdot p_{l2}(t) + \frac{2\pi}{\lambda}\cdot\left(\Delta\varepsilon_2(t) - 2\Delta\delta_{A2}(t) + 2\rho_{A2}(t)\right) - \left(p_{B2}\left(t - \frac{\varepsilon_2(t)}{c}\right) + \kappa_{B2}\right) + \left(p_{A2}(t) + \kappa_{A2}\right)$$

$$2e: \quad s_{2e}(t) = n_{2e}(t) + \frac{2\pi}{\lambda}\cdot\left(\Delta L_{23}(t) + \Delta\delta_{A2}(t) - \Delta\delta_{B3}\left(t - \frac{L_{32}(t)}{c}\right)\right) - p_{B3}\left(t - \frac{L_{32}(t)}{c}\right) + p_{A2}(t) + (1+\alpha_{2f})\cdot p_{l2}(t) - p_{l3}\left(t - \frac{L_{23}(t)}{c}\right)$$

$$2f: \quad s_{2f}(t) = n_{2f}(t) + \alpha_{2f}\cdot p_{l2}(t) + \frac{2\pi}{\lambda}\cdot\left(\Delta L_{23}(t) + \Delta\delta_{A2}(t) - \Delta\delta_{B3}\left(t - \frac{L_{23}(t)}{c}\right)\right) - p_{B3}\left(t - \frac{L_{23}(t)}{c}\right) + p_{A2}(t)$$

In (Eq.) n_{2a} to n_{2f} is the shot noise associated with the respective measurements. These noise can assumed to be white in the frequency range of interest. The factors a_{2a} to a_{2f} are the fraction of the USO phase noise at modulation frequency to be applicable for the respective phase measurement. This factor is given by the frequency ratio of the beat note at the detector compared to the modulation frequency of the ancillary modulation. The sign depends on which of the two mixed laser frequencies is larger. These factors are treated like the estimate of the absolute am lengths.

The Fourier transform of equations (Eq.) is given in (Eq. 5.1-2) under the simplifying assumption that the time dependency of $L_{12}(t)$, $L_{23}(t)$, $L_{13}(t)$ can be neglected. This simplification is equivalent to assuming that the variations of arm lengths and Doppler frequency although significant for the phase of the beat signal are sufficiently small to be ignored in the domain of the phase variations considered as a modulation on the light signal (laser phase noise, phase modulation due to relative proof mass motion). This slow phase variations can be considered as processed representing a wAvelength very large compared to the arm length variations in question. Similarly the α_l are considered constant which assumes negligible Doppler variations. The resulting set of equations is for each given frequency linear with respect to the unknowns.

Equations for S/C 2 Measurements in frequency domain
(transforms of constant values omitted

$$2a: \quad s_{2a}(f) = n_{2a}(f) + \alpha_{2a} \cdot p_{l2}(f) + \frac{2\pi}{\lambda} \cdot \left(\Delta L_{12}(f) + \Delta\delta_{B2}(f) - \Delta\delta_{A1}(f) \cdot e^{-j2\pi f \frac{L_{12}}{c}} \right) - p_{A1}(f) \cdot e^{-j2\pi f \frac{L_{12}}{c}} + p_{B2}(f)$$

$$2b: \quad s_{2b}(f) = n_{2b}(f) + \frac{2\pi}{\lambda} \cdot \left(\Delta L_{12}(f) + \Delta\delta_{B2}(f) - \Delta\delta_{A1}(f) \cdot e^{-j2\pi f \frac{L_{12}}{c}} \right) - p_{A1}(f) \cdot e^{-j2\pi f \frac{L_{12}}{c}} + p_{B2}(f) + (1 + \alpha_{2a}) \cdot p_{l2}(f) - p_{l1}(f) \cdot e^{-j2\pi f \frac{L_{12}}{c}}$$

$$2c: \quad s_{2c}(f) = n_{2c}(f) + \alpha_{2c} \cdot p_{l2}(f) + \frac{2\pi}{\lambda} \cdot \left(\Delta\varepsilon_2(f) - 2\Delta\delta_{B2}(f) \right) - p_{A2}(f) \cdot e^{-j2\pi f \frac{\varepsilon_2}{c}} + p_{B2}(f)$$

$$2d: \quad s_{2d}(f) = n_{2d}(f) + \alpha_{2d} \cdot p_{l2}(f) + \frac{2\pi}{\lambda} \cdot \left(\Delta\varepsilon_2(f) - 2\Delta\delta_{A2}(f) \right) - p_{B2}(f) \cdot e^{-j2\pi f \frac{\varepsilon_2}{c}} + p_{A2}(f)$$

$$2e: \quad s_{2e}(f) = n_{2e}(f) + \frac{2\pi}{\lambda} \cdot \left(\Delta L_{23}(f) + \Delta\delta_{A2}(f) - \Delta\delta_{B3}(f) \cdot e^{-j2\pi f \frac{L_{23}}{c}} \right) - p_{B3}(f) \cdot e^{-j2\pi f \frac{L_{23}}{c}} + p_{A2}(f) + (1 + \alpha_{2f}) \cdot p_{l2}(f) - p_{l3}(f) \cdot e^{-j2\pi f \frac{L_{23}}{c}}$$

$$2f: \quad s_{2f}(f) = n_{2f}(f) + \alpha_{2f} \cdot p_{l2}(f) + \frac{2\pi}{\lambda} \cdot \left(\Delta L_{23}(f) + \Delta\delta_{A2}(f) - \Delta\delta_{B3}(f) \cdot e^{-j2\pi f \frac{L_{23}}{c}} \right) - p_{B3}(f) \cdot e^{-j2\pi f \frac{L_{23}}{c}} + p_{A2}(f)$$

(EQ 5.1-2)

The measurement equations in Fourier representation from all 3 spacecraft of the Lisa configuration can be combined in several ways to form linear equation systems that can be solved for armlength differences representing the desired measurement result. Solution is performed separately and independently for every frequency bin in the interesting frequency range.

Equation systems describing the measurement setups

With the three spacecraft two measurement setups can be formed:

- a closed ring configuration in which all links are supposed to be operational
- a fall-back configuration in which one arm can not be used due to failure of a laser link.

In the closed ring configuration the desired measurement result is set of two armlength differences, i.e. (ΔL_{12} - ΔL_{23}) and (ΔL_{23} - ΔL_{13}) while in the fall-back configuration only one armlength difference is determined (three possible variations depending on the arm with the unused or defective link).

The phase noise compensation technique as described in [Ref. 18] and the clock noise compensation as described in [Ref. 19] operate in Fourier space. The equations for the (transformed) phase measurements (Eq. 5.1-2) form a linear equation system with complex frequency depending coefficients which has to be solved for the desired armlength differences.

Fall-back configuration equation system

In the fall-back system only measurements not depending on the light of one of the two lasers operating on the arm with the failed link can be used. In case of a defective arm from S/C 1 to S/C 3 the usable detector equations are: 1e, 1f, 2a, 2b, 2c, 2d, 2e, 2f, 3a, 3b

The set of unknowns consists of $\Delta\Delta L_{123}$, ΔL_{12}, Δ_{L23}, p_{i1}, p_{i2}, p_{i3}, $\Delta\delta_{A1}$, $\Delta\delta_{A2}$, $\Delta\delta_{B2}$, $\Delta\delta_{B3}$, $\Delta\varepsilon_2$, p_{A1}, p_{A2}, p_{B2}, p_{B3}. It is clear that on the two side spacecraft the backside interferometer is not operational, hence no information on the relative movement of the proof-masses can be retrieved (i.e. on $\Delta\delta_{A1}$, $\Delta\delta_{B3}$). However as it will be demonstrated formally below by examination of the Null space of the equation system this does not affect the ability to solve for the arm length difference. Relative motion of spacecraft versus proof mass affects the armlength measurement due to the round trip delay time: The position of the polarising beam splitter (relative to the proof mass) is the reference point for the phase measurement, it may change during the roundtrip time causing an measurement error. On the side spacecraft however, phase measurement serves only for relating the instantaneous phase of the outgoing beam to that of the incoming beam. Here any change of the beam

splitter position is compensated because length changes on the reception path correspond to the same length changes on the transmission path but with opposite sign. This is different for the centre spacecraft as the distance of beam splitter versus proof mass on the transmit path corresponds do the same distance on the receive path at a different instance in time.

From the 10 equations describing possible phase measurements in the fall-back configuration (i.e. disregarding all measurements involving the unused link) only 9 are linear independent. The USO noise is over-determined by 1e, 2b, 2e, 3b. Dropping any one of this four measurements results in a non contradicting set.

An additional equation has to be added to define the desired result $\Delta\Delta L_{123}$ which is the armlength difference. This results in 10 linear independent equations for 15 unknown quantities. This can be written in the form (one equation system per each frequency bin)

$$M \cdot \vec{\xi} = \vec{s} \qquad \text{(EQ 5.1-3)}$$

where

M	is the matrix (15*10 for fall-back solution) of complex coefficients applicable at the actual frequency bin
ξ	is the vector of unknowns (length = 15 for fall-back solution)
s	is the vector of Fourier transformed phase measurements at the actual frequency

A unique solution for all unknowns does not exists. An infinite set of solution vectors is compatible with the same measurement input. The structure of the space of solutions is described by the Null space of matrix M.

The general form of the solution is:

$$\vec{\xi} = \vec{\xi}_0 + \sum_{j=1}^{n} \beta_j \cdot \vec{\xi}_j \qquad \text{(EQ 5.1-4)}$$

where

ξ_0	an arbitrary solution of the inhomogeneous system (Eq. 5.1-3) In the practical measurement problem this can easily be determined by standard numerical algorithms to solve linear equations, such as Gauss elimination. The undetermined variables are simply set to zero.
ξ_j	vectors of the Null space of matrix M
β_j	arbitrary complex numbers
n	number of vectors in the Null space (5 for fall back solution)

In useful measurement setup the solution for $\Delta\Delta L_{123}$ must not depend on the arbitrarily selectable β_j which is equivalent to requiring that in all ξ_j the element corresponding to $\Delta\Delta L_{123}$ is zero. In this case desired measurement result is uniquely defined by the measured phase values. However some or all of the other unknowns can not be determined unambiguously. For the most obvious definition of $\Delta\Delta L_{123}$, i.e. $\Delta\Delta L_{123}=(\Delta L_{12} - \Delta L_{23})$ the resulting equation system lacks the above mentioned property, i.e. a solution is not unambiguously determined by the vector of measurements.

Essentially the laser phase noise cancellation scheme introduced in [Ref. 18] solves this problem by determining $\Delta\Delta L_{123}=(\Delta L_{12} - \gamma^*\Delta L_{23})$ where g is a factor depending on frequency and known system geometry determined such that a unique solution for $\Delta\Delta L_{123}$. For low frequencies and LISA system geometry γ is a complex number close to (1.+0j). The definition which yields the uniqueness requirement with the equation system used here is:

$$\Delta\Delta L_{123} = \Delta L_{12} - \frac{e^{\frac{2\pi i f\cdot(L_{23}-L_{12})}{c}}\cdot\left(e^{\frac{2\pi i f\cdot L_{12}}{c}}-1\right)}{\left(e^{\frac{2\pi i f\cdot L_{23}}{c}}-1\right)}\cdot\Delta L_{23} \qquad \text{(EQ 5.1-5)}$$

The resulting equation system have been analysed using a formula manipulation program. The Null space has been determined as:

Table 5.1-1: Null Space of Fall back Configuration Equation System

ξ_1	ξ_2	ξ_3	ξ_4	ξ_5	Unknown
1	0	0	0	0	p_{B3}
0	1	0	0	0	p_{B2}
0	0	1	0	0	p_{A2}
0	0	0	1	0	p_{A1}
0	0	0	0	1	$\Delta\delta_{B3}{}^* 2\pi/\lambda$
1	0	0	-1	1	$\Delta\delta_{A1}{}^* 2\pi/\lambda$
2	-1	-1	0	2	$\Delta e_2{}^* 2\pi/\lambda$
1	-1	0	0	1	$\Delta\delta_{B2}{}^* 2\pi/\lambda$
1	0	-1	0	1	$\Delta\delta_{A2}{}^* 2\pi/\lambda$
0	0	0	0	0	pi_3
0	0	0	0	0	pi_2
0	0	0	0	0	pi_1
$e^{\frac{-2\pi i f\cdot L_{23}}{c}}$	0	0	0	$e^{\frac{-2\pi i f\cdot L_{12}}{c}}$	$\Delta L_{23}{}^* 2\pi/\lambda$
$e^{\frac{-2\pi i f\cdot L_{12}}{c}}$	0	0	0	$e^{\frac{-2\pi i f\cdot L_{12}}{c}}$	$\Delta L_{12}{}^* 2\pi/\lambda$
0	0	0	0	0	$\Delta\Delta L_{123}{}^* 2\pi/\lambda$

This demonstrates that $\Delta\Delta L_{123}$ is indeed uniquely determined while ambiguous solutions exist for ΔL_{12} and ΔL_{23}. When examining the vectors of the Null space it becomes apparent that the main source of ambiguity is that laser phase-noise (p_{xx}), proof-mass relative motion ($\Delta\delta_{xx}$) and effective length of the coupling fibre ($\Delta\varepsilon_2$) have indistinguishable effects. This is a specific feature of the layout of the backside interferometer following [Ref. 8]. It is characterised by routing the light from the laser associated with a proof-mass via the backside of that proof-mass and then interfere with the light of the other laser on the same spacecraft which has not been reflected at any proof mass. Using the proof-masses over cross would for example not lead to an equation system with unique solution for $\Delta\Delta L_{123}$.

The above given results have been obtained assuming that the absolute optical length ε_2 of the fibre is insignificant to the phase noise of the lasers as observed by the detectors at either end. I.e. $e^{\frac{-2\pi i f \cdot \varepsilon_2}{c}}$ is assumed to be exactly 1. This is only then an acceptable assumption when the difference between the correct number and "1" is small compared to the ratio of shot noise induced phase measurement error and laser phase noise. With an arbitrary length fibre a unique solution for $\Delta\Delta L_{123}$ or a similar linear combination has not been identified.

Nominal configuration equation system

Similar to the fall back solution equation system an equation system for the complete configuration can be established. The equations for the 18 detector signals contain 4 linear dependent left sides. This is due to the over determination of USO noise by equation 1b, 1e, 2b, 2e, 3b, 3e only 3 of which are needed for an unambiguous determination of the USO noises. Dropping for example the "b" equations leads to a valid set. In a practical implementation the remaining three measurement values can be utilised to improve the USO phase estimate in the presence of measurement noise. Aside from selecting only 3 of the 6 USO equations it is also necessary to drop one of the 6 backside interferometer equations 1c, 1d, 2c, 2d, 3c, 3d. The unused measurement has to be on the spacecraft not used as vertex of one of the two armlength differences, i.e. with $\Delta\Delta L_{123}$ and $\Delta\Delta L_{231}$ as differences to be determined 1c or 1d must be selected. The remaining backside interferometer measurement on that spacecraft does not lead to a contradiction in the equation system, but it is also not required to determine the armlength differences and therefore it can also be omitted. (Using all 6 equations is equivalent to try to synchronise all lasers to each other in a ring structure. Dropping one equation cuts the ring to a chain synchronised to the master. The information coming from the backside interferometer is not required on the wing spacecraft for the same reason as in the fall back configuration, allowing to drop the mentioned fifth equation as well. The fibre connection associated with the two unused detectors is then also not needed allowing to remove the change of fibre optical pathlength $\Delta\varepsilon_1$ from the list of unknowns.)

Together with the defining equations for $\Delta\Delta L_{123}$ and $\Delta\Delta L_{231}$ this considerations lead to a system of 15 equations with 22 unknowns ($\Delta\Delta L_{123}$, $\Delta\Delta L_{231}$, ΔL_{12}, Δ_{L23}, ΔL_{13}, p_{i1}, p_{i2}, p_{i3}, $\Delta\delta_{A1}$, $\Delta\delta_{B1}$, $\Delta\delta_{A2}$, $\Delta\delta_{B2}$, $\Delta\varepsilon_2$, $\Delta\delta_{A3}$, $\Delta\delta_{B3}$, $\Delta\varepsilon_3$, p_{A1}, p_{B1}, p_{A2}, p_{B2}, p_{A3}, p_{B3}). The defining equations for $\Delta\Delta L_{123}$, $\Delta\Delta L_{231}$ are

$$\Delta\Delta L_{123} = \Delta L_{12} - \frac{e^{\frac{2\pi i f \cdot (L_{23}-L_{12})}{c}} \cdot \left(e^{\frac{2\pi i f \cdot L_{12}}{c}} - 1 \right)}{\left(e^{\frac{2\pi i f \cdot L_{23}}{c}} - 1 \right)} \cdot \Delta L_{23} \qquad \text{(EQ 5.1-6)}$$

$$\Delta\Delta L_{231} = \Delta L_{23} - \frac{e^{\frac{2\pi i f \cdot (L_{13}-L_{23})}{c}} \cdot \left(e^{\frac{2\pi i f \cdot L_{23}}{c}} - 1 \right)}{\left(e^{\frac{2\pi i f \cdot L_{13}}{c}} - 1 \right)} \cdot \Delta L_{13}$$

Again the Null space has been determined, this time however using numerical methods instead of symbolical calculations because of the complexity of the involved expressions. For representative geometry at frequency 1mHz the vectors of the Null space are given below.

Table 5.1-2: Null Space of Nominal Configuration Equation System (absolute values of numerical solution at 1mHz)

$\|\xi_1\|$	$\|\xi_2\|$	$\|\xi_3\|$	$\|\xi_4\|$	$\|\xi_5\|$	$\|\xi_6\|$	$\|\xi_7\|$	Unknown
1	0	0	0	0	0	0	p_{B3}
0	1	0	0	0	0	0	p_{A3}
0	0	1	0	0	0	0	p_{B2}
0	0	0	1	0	0	0	p_{A2}
0	0	0	0	1	0	0	p_{B1}
0	0	0	0	0	1	0	p_{A1}
0	0	0	0	0	0	1	Δe_3
0.5	0.5	3.93E-17	0	0	2.64E-19	0.5	$\Delta\delta_{B3}$
0.5	0.5	1.39E-17	0	0	2.64E-19	0.5	$\Delta\delta_{A3}$
1	1	1	1	0	3.93E-18	1	Δe_2
0.5	0.5	1	0	0	1.88E-18	0.5	$\Delta\delta_{B2}$
0.5	0.5	1.12E-16	1	0	1.88E-18	0.5	$\Delta\delta_{A2}$
0.5	0.5	2.78E-17	0	1	3.72E-19	0.5	$\Delta\delta_{B1}$
1.11E-16	1	0	0	0	1	0	$\Delta\delta_{A1}$
2.22E-16	2.18E-16	0	0	0	1.45E-17	2.22E-16	pi_3
2.22E-16	9.27E-16	8.88E-16	0	0	1.45E-17	2.22E-16	pi_2
4.44E-16	1.00E-15	8.88E-16	0	0	1.45E-17	4.44E-16	pi_1
0.056	0.056	5.72E-17	0	0	7.41E-19	0.056	ΔL_{13}
0.054	0.054	1.24E-16	0	0	7.74E-19	0.054	ΔL_{23}
0.053	0.053	1.73E-18	0	0	2.82E-20	0.053	ΔL_{12}
4.20E-17	3.85E-17	1.79E-17	0	0	2.02E-19	4.51E-17	$\Delta\Delta L_{231}$
6.19E-19	5.04E-17	0	0	0	7.61E-19	0	$\Delta\Delta L_{123}$

The vectors are normalised to their largest element. Hence the absolute values below 10^{-14} effectively represent zero. The null space has essentially a similar structure to that of the fall back configuration.

- unambiguous solutions for $\Delta\Delta L_{123}$, $\Delta\Delta L_{231}$ exist
- ambiguities exist between laser phase noises and various variables describing relative position between S/C and proof masses or fibre delays
- USO phases are unambiguously defined

Again the restriction applies that the effective path-delay in the optical fibres must be negligible in the sense described above for the fall back configuration.

If the only relevant cause of armlength changes in the interesting frequency range where gravitational waves a relation between the three armlengths variations could be established. Introduction of such a condition e.g. $\Delta L_{12} + \Delta L_{23} + \Delta L_{13} = 0$ for a setup in form of an equilateral triangle reduces the Null space from seven to 6 vectors and allows unambiguous solution for ΔL_{12}, ΔL_{23}, ΔL_{13}. It is not longer necessary to solve for the linear combinations $\Delta\Delta L_{123}$, $\Delta\Delta L_{231}$ to get an unambiguous solution, i.e. to cancel the phase noise. However length variations due to spacecraft relative motion do not obey the relations between the arm-lengths as derived from gravitational wave properties. Introduction of properties of gravitational waves into the equation

system is therefore only permissible for frequency intervals in which the motion introduced spectral components of the armlength variation are negligible. However assimilation of the data to gravitational wave amplitudes is probably better left to a post-processing step where more observations can be combined and interfering effects can be calibrated out than it is possible on basis of a single observation.

Numerical condition of the equation system

The numerical condition of the equation systems has been analysed using singular decomposition. The ratio of the largest to the smallest singular value sometimes referred to as condition number is about 10. for both configurations. This indicates that very little problems with the accuracy of numerical solutions are to be expected.

Sensitivity to phase measurement noise

The determination of one solution of the equation system as it may be obtained by a variety of numerical methods may also be expressed as matrix operation.

$$\vec{\xi_0} = R \cdot \vec{s} \qquad \text{(EQ 5.1-7)}$$

As described above ξ_0 is only one arbitrary selected solution off the equation system but the vector component representing the result variable(s) are unambiguous.

If the desired result variable is the ith component of ξ_0 the standard deviation σ_i resulting from the standard deviations of the phase measurements s_j can be calculated as

$$\sigma_i = \sqrt{\sum_j (R_{ij} \cdot \mathrm{stdev}(s_j))^2} \qquad \text{(EQ 5.1-8)}$$

Phase measurements in the LISA measurement setup are performed on heterodyne signals resulting from beating of two laser beams on a photodiode. Shot noise limited heterodyne detection is approximated when receiving the weak signals on the inter satellite links. In this detection mode the local oscillator (LO) intensity is increased until the shot-noise of the LO signal renders technical noise from the electrical pre-amplifiers insignificant. As the amplitude of the beat signal in terms of detector current increases proportional to the electric field amplitude of both received signal and LO and the shot noise in the detector signal (in terms of current rms fluctuation) increases also proportional to the electric field amplitude an operating point can be reached where noise sources other than the quantisation of the received signal (i.e. the weaker of the two heterodyned light signals) can be neglected. The electrical signal exhibits in this case a carrier to noise density C/N_o ideally identical to the photon rate (in terms of photons per second) of the received signal incident at the detector. Practically however this figure is reduced by imperfect matching of LO and received signal wavefront (accounted for in terms of modulation efficiency η_h; typical value in the order of 0.9) and by a detector quantum efficiency η_q smaller than 1 (typical value in the range 0.7 to 0.8). An ideal phase measurement on a sinusoidal signal with a given carrier to noise density results in a (phase) measurement noise of $N_o/C = N\varphi$ [in terms of rad^2/Hz]. Hence the phase noise is inverse proportional to the power of the received light signal

In the LISA setup three different types of beat signals are measured:

- main link detector signals (s_{1a},s_{1f},s_{2a},s_{2f},s_{3a},s_{3f})
  resulting from beating the carrier of the received signal with a fraction of the transmitter signal used as LO. The phase noise N_{main} determined by the power of the received carrier signal on the inter satellite should ideally constitute the largest part of the random measurement error.
- ancillary carrier detector signals (s_{1e},s_{2e},s_{3e})

resulting from beating an USO synchronized subcarrier carrier of the received signal with a fraction of the transmitter signal used as LO.
The power of the subcarrier is a comparatively small fraction of the main carrier power. Nominally a fraction of 10% is foreseen. Consequently a factor of $\sqrt{10}$ increased rms phase noise must be expected.

- backside interferometer signals (s_{2c},s_{2d},s_{3c},s_{3d})
  resulting from beating fractions of the two transmitter signals on a spacecraft on the detectors of the backside interferometer setup.
  The backside interferometers have not the typical setup of an shotnoise limited heterodyne detector with a dominating LO signal and a received signal of considerably lower power. Instead two beams of about the same power (order of 100μW) are used. This will not necessarily lead to a shot noise limited operation but this is by far not necessary in view of the high photon count available. However considering the high phase noise of the laser signals, the dynamic range of the phase detectors will not allow to utilize a very largely improved analog input signal to its full extent without adaptation in the phase meter electronic. In the following discussion on noise sensitivity therefore a moderate improvement of only 20dB lower phase noise for this signals as compared to the main link signals has been assumed.

Table 5.1-3: Sensitivity of measured arm length differences from measurement phase noise (arm length differences expressed in units of $\lambda/2\pi$)

	0.1mHz		1mHz		5mHz		10mHz		
Signal	$\frac{2\pi}{\lambda}\cdot\Delta\Delta L_{123}$	$\frac{2\pi}{\lambda}\cdot\Delta\Delta L_{231}$	$\frac{2\pi}{\lambda}\cdot\Delta\Delta L_{123}$	$\frac{2\pi}{\lambda}\cdot\Delta\Delta L_{231}$	$\frac{2\pi}{\lambda}\cdot\Delta\Delta L_{123}$	$\frac{2\pi}{\lambda}\cdot\Delta\Delta L_{231}$	$\frac{2\pi}{\lambda}\cdot\Delta\Delta L_{123}$	$\frac{2\pi}{\lambda}\cdot\Delta\Delta L_{231}$	Incident Noise Power
s_{1a}	0.	0.491	0	0.491	0.	0.510	0.	0.578	N_{main}
s_{1e}	0.014	0.027	0.014	0.028	0.023	0.038	0.336	0.341	$10*N_{main}$
s_{1f}	0.486	0.027	0.486	0.028	0.495	0.038	0.912	0.341	N_{main}
s_{2a}	0.500	0.	0.501	0	0.518	0.	0.581	0.	N_{main}
s_{2c}	0.005	0.	0.053	0	0.264	0.	0.509	0.	$0.01*N_{main}$
s_{2d}	0.005	0.	0.053	0	0.264	0.	0.509	0.	$0.01*N_{main}$
s_{2e}	0.011	0.015	0.012	0.016	0.025	0.025	0.326	0.355	$10*N_{main}$
s_{2f}	0.502	0.485	0.503	0.485	0.524	0.494	0.577	0.931	N_{main}
s_{3a}	0.490	0.500	0.491	0.501	0.509	0.519	0.575	0.585	N_{main}
s_{3c}	0.	0.005	0	0.054	0.	0.269	0.	0.518	$0.01*N_{main}$
s_{3d}	0.	0.005	0	0.054	0.	0.269	0.	0.518	$0.01*N_{main}$
s_{3e}	0.026	0.015	0.026	0.015	0.036	0.028	0.322	0.345	$10*N_{main}$
s_{3f}	0.026	0.506	0.027	0.506	0.036	0.529	0.322	0.595	N_{main}
Total (rms):	0.99	1.00	1.00	1.00	1.04	1.04	2.27	2.37	N_{main}

Table 5.1-3 shows the sensitivity of the estimate of the armlengths differences to measurement phase noise. The column "Signal" identifies the measured signal following the convention of Figure 5.1-5. The column "Incident Noise Power" specifies the applicable measurement noise in terms multiples of the main link phase noise [rad^2/Hz]. The other columns show the factors R_{ij} as for (Eq. 5.1-8) for both result variables $\Delta\Delta L_{12}$ and $\Delta\Delta L_{23}$ at different frequencies (0.1mHz, 1mHz, 5mHz and 10mHz).

Relative large differences between armlengths (order 10%) have been assumed for the calculation to demonstrate the range of variability of sensitivity factors due to geometry. In a perfect symmetrical configuration the factors associated with measurements on the two contributing arms are identical.

The following can be observed

- The factors associated with the main link detector signals (orange shading) are for frequencies below 5mHz approximately independent of frequency and are close to the expectable value of 0.5. Deviations result from armlength differences in combination with the phase noise compensation scheme.
- The factors associated with the backside interferometer signals are approximately linearly increasing with frequency. However the magnitude of the factors seen in combination with the applicable measurement noise shows that the contribution to the total measurement error is always negligible in the measurement frequency range.
- The factors associated with ancillary carrier detector signals are only weekly frequency dependent (factor 2 over the interval 0.1mHz to 5 mHz). The are well below the factors associated with the main link detector signals (<1/20) which is needed to allow for the higher phase noise associated with the ancillary phase measurement. These factors depend linearly from the ratio of main detector signal beat frequency versus ancillary modulation frequency. The values in the table have been calculated assuming ratios in the order of 1/40 which is compatible with a modulation frequency of 200MHz and beat signals in the 5MHz range. Due to the use of the transmitter lasers as local oscillators on the receive channels the control of beat frequencies is restricted by the Doppler shift. In particular it is impossible to generate beat notes on both detectors of an interferometer arm with frequencies below the 1 way Doppler shift. At 1μm wavelength an assumption of 5MHz main carrier beat frequency corresponds therefore to relative velocities of the two related spacecraft below or equal 5m/s. The sensitivity factors shown in Table 5.1-3 lead to negligible contribution to the total measurement error in the frequency range below 5mHz when considering the assumed phase measurement noise on the ancillary signals. However considering the dependency on spacecraft relative motion maintaining of some margin is reasonable.
- Generally the calculated sensitivities are such that below 5mHz the expected simplified behaviour of the LISA setup is closely met: In a simple interferometer system with active transponders at the edge spacecraft without any ancillary measurements for phase noise compensation etc., the expectable rms error in for the armlength difference should be 0.5 $(\lambda/2\pi)^* \sqrt{4}\sqrt{N_{main}}$ (where the factor 0.5 results from armlength difference being half as large as the optical pathlengths difference and the factor $\sqrt{4}$ results from the four measurements entering with equal weight). The calculated values are within 4% of this simple model in the frequency range below 5mHz.
- A frequencies of 10 mHz and above the sensitivity factors are dominated by the extrema/poles resulting from the phase noise compensation scheme. With all interferometer arms at equal length of 5 10^6 km a pole would be expected at about 30 mHz. The calculated values show that the increase in sensitivity to phase measurement noise is already significant at 10mHz (factor 2.3). I.e. one of the consequences of implementing the phase noise cancellation scheme is a an increase of noise in the measured quantity (arm length difference) in the vicinity of frequencies determined by 1/(round-trip-delay) and multiples thereof. For the use of the frequency band 10mHz to 100mHz a degeneration of the measurement due to the combined effects of

  -System response (Eq. 5.1-1)
  (the frequencies of the error maxima are multiples of the 1-way propagation delay)

  -Measurement error due laser phase noise (Eq. 5.1-11)
  (the frequencies of the error maxima are multiples of the roundtrip delay)

  -Measurement error due to shot noise (described above)

(the frequencies of the error maxima are multiples of the roundtrip delay)

has to be accounted for.

Sensitivity of solutions to uncertainty of knowledge of absolute armlength

If the coefficients of the Matrix M in (Eq. 5.1-7) are only approximately known, such that instead of the correct matrix M an approximation M + ΔM is used, an error $\Delta\vec{\xi}$ follows for the result vector $\vec{\xi}$. The matrix ΔM is the matrix of the errors in components of M.

$$(M + \Delta M) \cdot (\vec{\xi} + \Delta\vec{\xi}) = \vec{s} \qquad \text{(EQ 5.1-9)}$$
$$M \cdot \vec{\xi} + M \cdot \Delta\vec{\xi} + \Delta M \cdot \vec{\xi} + \Delta M \cdot \Delta\vec{\xi} = \vec{s}$$
$$M \cdot \Delta\vec{\xi} \approx -\Delta M \cdot \vec{\xi}$$
$$\Delta\vec{\xi}_0 \approx -R \cdot \Delta M \cdot \vec{\xi}$$

For the unambiguous components of ξ the appropriate component of ξ_0 can be interpreted as the error in the calculated measurement result originating from assuming a matrix which is wrong by ΔM.

The matrix $M_{i,j}$ depends on only approximately known properties xi of the system such as the absolute armlengths L_{12}, L_{23}, L_{13}, and the input frequency to modulation frequency ratios $\alpha_{1a}...\alpha_{3f}$. Using the result from (Eq. 5.1-9) the standard deviation of the armlength difference can be calculated from the magnitude of the unknowns and the standard deviation of the parameters used for the establishment of the Matrix coefficients. Note that the actual values of the unknowns are here treated as un-correlated random variables.

$$-R\left(\frac{\partial M}{\partial x_j} \cdot \mathrm{stdev}(x_j)\right) = N_j \qquad \text{(EQ 5.1-10)}$$

$$\Delta\Delta L_{123} = \xi_1$$

$$\mathrm{stdev}(\Delta\Delta L_{123}) \approx \sum_j \sum_i \left|N_{1,i}\right|_j^2 \cdot \left|\xi_i\right|^2$$

This approach has been used to assess the sensitivity of the measurement results to uncertainties in the above mentioned parameters. To test the credibility of the approach the numerical results have been compared to the analytical results obtained by Giamperi [Ref. 18] for a simplified configuration. The analytical expression for the sensitivity follows from equation 14a of the reference.

$$\mathrm{stdev}\left(\frac{2\pi}{\lambda}\Delta L_{123}\right) = 0.5 \cdot \frac{4\pi f \cdot p_{laser} \cdot stdev(L)}{c} \sqrt{\left|e^{\frac{4\pi i f \cdot L_{23}}{c}}\right|^2 + \left|e^{\frac{4\pi i f \cdot L_{12}}{c}} \cdot \frac{e^{\frac{4\pi i f \cdot L_{23}}{c}} - 1}{e^{\frac{4\pi i f \cdot L_{12}}{c}} - 1}\right|^2} \qquad \text{(EQ 5.1-11)}$$

The factor 0.5 results from the fact that the Giamperi equation is expressed in terms of path length while here the difference of arm lengths is used as result parameter.

With the nominal system geometry at 1mHz the following results where obtained:

stdev(ΔL_{123} $2\pi/\lambda$) = 2.079 10^{-11} [m^{-1}] p_{laser} stdev(L) following (Eq. 5.1-10)

stdev(ΔL_{123} $2\pi/\lambda$) = 2.993 10^{-11} [m^{-1}] p_{laser} stdev(L) following (Eq. 5.1-11)

where stdev(L) stands for the uncertainty in armlength in a standard deviation sense and p_{laser} for the phase noise magnitude in rad/√Hz. The approximate factor of √2 between the analytical prediction an the numerical result is probably due to using only a single arm for phase noise estimation in the original Giamperi paper, therefore a slight improvement when using both arms is not unreasonable. Typical laser phase noise at 1mHz is about 10^6 rad/√Hz and the desired noise floor for stdev(ΔL_{123} $2\pi/\lambda$) is about 8 10^{-5} rad/√Hz. To achieve this highly accurate determination of armlength (or differential armlength) is required (in the low meter range).

Impact of laser phase noise

To achieve reasonable suppression of laser phase noise joint optimisation of the system elements is needed.

- the laser transmitter (phase noise properties)
- the main detector phase meter
- the arm length estimation procedure

Laser frequency noise is typically close to 1/f characteristics in the measurement frequency range. At frequencies above 1Hz the noise characteristics depends on the employed control concept. With additional effort, e.g. involving the use of an electro-optical modulator, the 1/f characteristics can be maintained until the resulting phase noise falls below the main link shot noise threshold. With more conventional concepts a flat plateau in therms of frequency noise exists above 1Hz until at several KHz the system behaves like a free running laser again exhibiting an approximate 1/f characteristics. In Figure 5.1-6 resulting phase noise intensity is shown for a transmitter laser system conforming to the assumptions given in LISA pre phase a report [Ref. 1] and (based on LZH experience) for predicted laser performance with and without enhanced regulation at frequencies above 1 Hz. At the frequencies in the measurement bandwidth the LZH figures are somewhat above the pre phase A assumptions (10^6 rad/√Hz versus 3 10^4 rad/√Hz both at 1mHz).

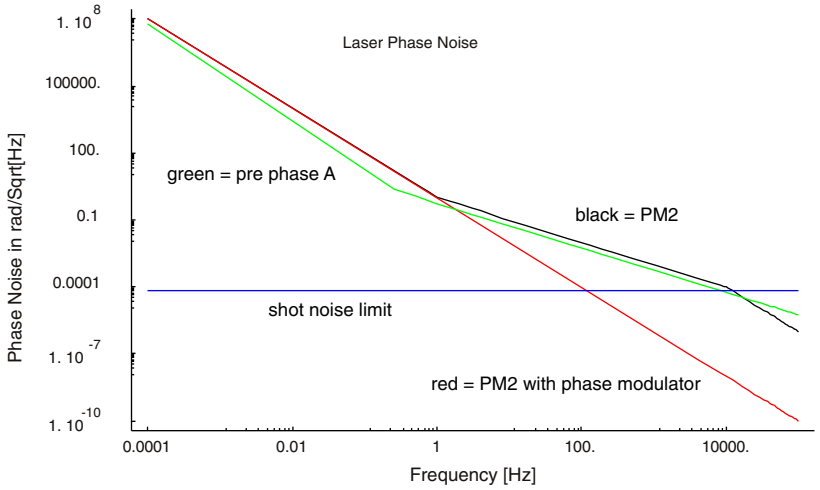

Figure 5.1-6: Typical laser phase noise

As described in Chapter 5.1.3.1, the total measurement error of the LISA system is composed of a contribution resulting from unknown parasitic acceleration acting on the proof-masses and the measurement error of the interferometer system. The measurement error itself results from phase measurement noise as discussed in the previous section "Sensitivity to phase measurement noise", the residual error of the phase noise cancellation as discussed in the previous section and additional contributions resulting from pointing errors and thermoelastic deformation of the optical setup. If the latter contributions are negligible the total error of the

pathlength difference measurement has a typical behaviour as shown in Figure 5.1-7 (red curve). The error is given in terms of effective phase measurement error. At low frequencies (below 2mHz) the total error is dominated by acceleration effects (blue curve). Likewise at high frequencies the phase measurement noise (mostly resulting from shot noise) dominates (horizontal plateau of the red curve). Depending on the accuracy of the absolute pathlengths estimation the laser phase noise residual error may affect the total measurement error in the transition region between acceleration error dominated frequency region and shot noise error dominated frequency region. In Figure 5.1-7 the green curve for the residual error from laser phase noise has been calculated for 20m rms estimation error of armlength and LZH laser phase noise characteristic.

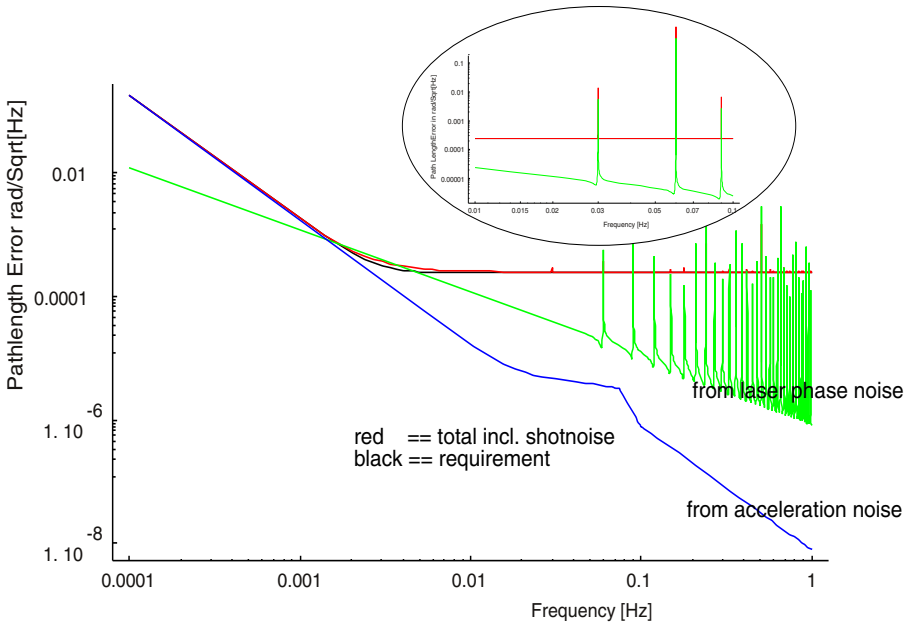

Figure 5.1-7: Effect of Laser Phase Noise to System Measurement Error
(large scale plot does not show all poles due do to plot resolution limits, see inserted image for details)

This error contribution scales proportionally with the rms estimation error of the armlengths. With 20m estimation accuracy there is just a small impact in the transition frequency region. The laser phase noise residual error is entirely negligible for better armlength estimation accuracies and for inferior estimation accuracies it becomes significant in the 1mHz to 10mHz frequency interval. However the armlengths can be determined from the nominal measurements itself. One method would be to minimise the effective noise power in the corrected difference estimates by variation of the assumed armlengths. The most appropriate frequency range for this operation would be above the transition region as there are more frequency bins available and the noise floor from the shot noise can be assumed to be more stable than that from the acceleration as it is created by a comparatively simple process. Within the frequency interval where the pathlength estimation is performed a suppression of the residual phase noise level well below the shot noise level is reasonable, because many frequency bins can be averaged (in terms of noise power) for this operation thus allowing improved accuracy for the determination of noise power levels. In principle the accuracy of the mentioned armlengths estimation procedure can be improved just by artificially adding a phase modulation on the laser signal at some frequency above the scientifically relevant frequency range. The armlength estimation procedure would than use this "artificially introduced laser phase noise".

The laser phase error is not perfectly compensated and therefore leads to an residual error that may affect a particular frequency interval in the final measurement result. As shown above this leads however not to a

direct requirement on laser phase noise because the quality of compensation depends first order on the accuracy of the arm length estimation which has no obvious limit in the range of the required accuracies. With the proposed technique the arm length estimation accuracy is even linked to the laser phase noise compensation technique such that it provides sufficient accuracy for any laser phase noise. The requirements to the transmitter laser phase noise characteristics are therefore not determined by first order effects (as they are compensated by the phase noise cancellation) nor by first order effects of the cancellation procedure itself (because its first order efficiency can be arbitrarily improved by the mentioned improving of arm length estimation accuracy).

The next order effects that can limit the correction capability for large laser phase noises are

- Limited accuracy of the assumptions underlying the measurement equation system (Eq. 5.1-2)
- Limitation of phase meter measurement accuracy when subjected to phase noise many orders of magnitude above the white shot noise

The most important simplification in the equation system in Fourier domain is the summation of a negligible effect of arm length variations with respect to the calculation of the Fourier transform of a phase spectrum after a round trip. When considering required armlength accuracies in the order of 20m rms relative velocities between spacecraft of 5m/s and a time interval for a discrete Fourier transform of >10000s (to resolve to 0.1mHz) this is likely not sufficiently accurate. In the Fourier representation a time variation of the arm lengths adds considerable complexity. In particular the transform of (Eq.) will in general no longer result in a linear equation system when L_{12}, L_{23}, L_{13}, are considered to be time depending.

The following refinements could be considered

- implementing the special case of constant spacecraft relative motion (e.g. L_{12}=at+b)
  (this leads to a still linear equation system in the Fourier domain, however different frequency bins are now coupled)
- solve for the armlength difference in time domain
  (the solution (Eq. 5.1-7) has a time domain representation which can be obtained by inverse Fourier transform; the $\Delta\Delta L_{123}(t)$ can be represented as a sum of measured phase values $s_i(t)$ each convolved with a function obtained by inverse Fourier transform of the frequency depending matrix coefficients $R_{ij}(f)$ (assuming that $\Delta\Delta L_{123}(f)$ is the i-th component of the solution vector $\xi_0(f)$; under the simplifying assumptions of constant armlengths this represents a linear time invariant system linking the measured time series of phase values with the desired output variable; this could be generalised by considering time depending armlengths, which would lead to a linear time variant system)

Within this study no further investigations about refinement of the LISA equations in the above mentioned sense have been performed. However it is likely that any desirable degree of accuracy in description of the delay effects is obtainable but the required effort for solving the equations will increase when higher precision is needed. With the relative low data rate of the LISA experiment this may not constitute a problem if the data evaluation including low level processing is performed on earth but it would be difficult to perform the part of the processing that compensates for phase noise on board (which might be useful to save data volume on the space to earth link). Nevertheless it is not assumed that the complications to data evaluation which are caused by high laser phase noise establish a firm requirement for the tolerable laser phase noise.

The relation of the transmitter laser properties to the phase detector properties results from the necessity to represent the phase of the received signal in the measurement bandwidth with an accuracy not inferior to the shot noise limit. Neither intermodulation or clipping effects due to the large signal dynamic nor aliasing effects resulting from representation in a discrete time series must introduce errors larger than the shot noise. The normalisation to the shot noise results from the fact that the LISA link is dimensioned such that length measurement error due to shot noise consumes most of the allowance in the measurement error budget.

When considering the transmitter laser performance using only thermal control (black curve in Figure 5.1-6), the phase noise resulting from laser frequency noise in the measurement bandwidth (0.1mHz to 1Hz) is 198dB above the shot noise, which would require about 33 bit representation for a discretisation noise comparable with the shot noise. However this large dynamic is largely due to slow drifting of frequency, i.e. the dynamic range increases with about 30dB for extending the measurement frequency range for a decade towards lower frequencies. The 33bit dynamic in the measurement bandwidth is however not necessarily the driver for data rate on the links or length of registers in the phase measurement devices. Simple encoding techniques such as BAQ can be used to reduce data rate on links and software unwrapping of a phase meter which uses a modulo n representation of its measured value can be used to reduce the required register size in the phase meter. A representation comparable to 24bits per sampled value on links and phase registers is likely sufficient as it represents approximately the dynamic range in a 0.01Hz to 1Hz intervals of the order 100s for unwrapping of modulo counters and block coding.

Therefore the dynamic range in the phase measurements resulting from laser phase noise as it is represented in data rate and detector numerical resolution is also not a design driver.

More difficult is the avoidance of errors introduced by filtering and aliasing. The laser phase noise spectrum exceeds the phase noise induced by shot noise on the main links over a frequency range much exceeding the measurement frequency band. Referring to Figure 5.1-6 the phase noise of the envisaged laser (LZH) reaches the shot noise limit on the main link at about 12 KHz (break even point). When an optical phase modulator is included in the control loop the laser can achieve a break even point of about 200Hz. For the thermal controlled laser the power of the laser phase noise in the frequency interval from the upper edge of the measurement bandwidth (1Hz) to the break even point is about 83 dB above the main link shot noise level in the measurement interval. It is not significantly lower (78dB) for the alternative laser with additional phase modulator as the higher frequencies do not significantly contribute to the total noise power.

The importance to the phase detector design rises from the fact that a digital representation of the measured phase at a low sampling rate is needed to maintain low data rates. Representation with 2 Hz sampling frequency requires filtering of the out of band phase noise at the detector input such that aliasing products within the measurement bandwidth are negligible compared to the in band shot noise level. A suppression of about 90dB for frequencies above 1 Hz (with relaxing requirements at higher frequencies) is required. On the other hand a precise control of the pass-band attenuation is needed: the relative amplitude error due to uncertainty in pass band attenuation must be comparable to the ratio of in band laser phase noise to shot noise induced phase noise. These demanding requirements are probably only feasible if numerical filtering is applied. The primary digitalisation process is therefore to be performed at a considerably higher sampling rate. Depending on the type of phase detector the digitalisation is either performed explicitly by an ADC sampling the down converted detector signal (the phase detection is than numerically performed by various techniques) or the digitalisation is implicit in the phase measurement principle such as for counter based detectors evaluating the zero crossings of the detector signal in comparison to a reference signal. In any case the effective sampling frequency should be selected (slightly) above the break even frequency to avoid aliasing in the first processing step without relying on (high performance) analog pre-filtering for the purpose of laser phase noise rejection (some pre-filtering will nevertheless be required to avoid aliasing fro the shotnoise itself).

Phase estimates are then generated at a comparatively large sampling rate (12 KHz or 200Hz for the modulator controlled laser) and must be digitally filtered with an decimation filter meeting the filtering requirements driven by the laser phase noise.

Laser development and detector development have to be seen as a joint effort where properties of both equipment can be traded:

- effort on the laser to suppress out of band noise (above 1Hz) e.g. by employing an optical modulator trades against internal sampling frequency in the detector equipment related to internal timing require-

ments and numerical work load in the decimation filtering

- effort in the laser to suppress in band phase noise are related to the stability retirement of the in band filter characteristics (in addition to the already mentioned impacts to dynamic range of the data representation and the accuracy required for the interferometer arm length estimate

Laser Synchronisation

The properties of the LISA measurement equation system in nominal or fall-back configuration do not depend on any assumption about the locking of the laser frequencies or USOs to each other. The only requirement is to maintain the beat frequencies of the signals heterodyned at the various detectors within an acceptable frequency range. The allowable frequency range is determined by the capability of the USO phase noise compensation scheme which is reflected in the sensitivity of the measurement result to the noise on the s_{1e}, s_{2e}, s_{3e} signals (see discussion of Table 5.1-3). With the baseline design the beat signal frequencies should be below 10 MHz (except for the modulation signal). This condition is not achievable with lasers individually locked to their reference cavities. Hence some form of (offset) locking of all employed lasers to a single reference is required while no explicit locking of USOs is needed.

If the lasers are named according to their optical bench (see Figure 5.1-4) a typical chain of synchronisation is:

A_2->B_3->A_3; A_2->B_2->A_1->B_1;

where A_2 is the master laser synchronised to its cavity and "x->y" means laser y is offset locked to laser x. Whenever the lasers locked to each other are not on the same spacecraft an inter satellite link is used. Therefore the frequency of both lasers differ not only due to the deliberately introduced offset but also due to the Doppler shift. In general the frequency offsets are selected such that beat frequencies close to zero are avoided and that the maximum beat frequency does not exceed the maximum allowable one-way Doppler shift.

Introduction of frequency locking does not change the structure of the lisa equation system nor the magnitude of the phase noises of the laser. The laser phase noises become however correlated. The characteristic of the phase signal derived from the detector signals differs from the free running case. While in the free running case all signals show the large phase noise which results from the independent phase noise of the two heterodyning laser sources this is different for synchronised lasers as the phase noises are now correlated. The shot noise is the same in both cases it depends only on the light intensity on the respective detectors (see Table 5.1-3). In measurement setup with synchronised lasers three different types of phase characteristics can be observed:

- for the detectors used for the frequency control of a laser the phase is entirely predictable, it depends only on the used offset frequency; if the synchronisation is not perfect the measurable phase deviates from the prediction value in the sense of a control loop error
- for detector signals of the backside interferometers that are not used for synchronisation and for modulation signals on detectors that are used for laser synchronisation the phase varies with low dynamic relative to the predictable mean resulting from the offset locking of the two involved lasers. These small phase variations carry information on relative proof-mass movement or USO phase noise
- for the remaining signals a phase noise resulting from main laser phase-noise superimposed to itself after a round-trip delay is present; the phase noise spectrum is comparable to that of the main laser itself except for an attenuation at frequencies below 1/Roundtrip_delay.

For the above proposed hierarchy of laser synchronisation the different characteristics are distributed among the 18 phase signals as shown in Table 5.1-4. The signal names refer to Figure 5.1-5 and a full LISA configuration (two differences measured) is assumed. There are 5 signals with high phase dynamic, 8 signals with low phase dynamic and 5 signals that are either entirely predictable or exhibit a low phase dynamic (depending on

properties of the phase locked loops).

Table 5.1-4: Properties of the detector signal in a LISA setup with laser phase locking

Spacecraft	Detector signals to which a laser is locked (ideally entirely predictable)	Detector signals with low phase dynamic	Detector signals with high phase dynamic
1	s_{1f}, s_{1d}	s_{1c}, s_{1e}	s_{1a}, s_{1b}
2	s_{2d}	s_{2c}	s_{2a}, s_{2b}, s_{2e}, s_{2f}
3	s_{3a}, s_{3c}	s_{3b}, s_{3d}	s_{3e}, s_{3f}

As phase locking does not change the shot noise level and the master laser phase noise characteristics the measurement accuracy is not affected. The essential properties phase detectors in a synchronised system also do not differ significantly from the un-synchronised case as the characteristics of the signal with high phase dynamic differs from the case with not synchronized lasers only with respect to the low frequency dynamic range which is of little impact to the detector design and the data rate.

The impact of using a synchronised measurement setup is therefore apart from the purpose to maintain a desirable frequency separation of the individual lasers mainly a reduction in raw data rate however for less than a factor of 2. Instead of avoiding the 5 measurements on the signals used for locking entirely by appropriate design of the control loops it is probably more efficient to perform this measurements and relax on the control loop requirements.

To relax the requirements to the accuracy of the phase noise cancellation as reflected in the need to determine absolute armlength and the required precision in the representation of the measurement equation system and to the in-band transfer characteristic of the phase meters, a reduction of low frequency phase noise is highly desirable. In the synchronised setup this affects only the master laser which in the baseline design is stabilised by coupling to its reference cavity. It has not been investigated in this study whether a potential exists to reduce the in-band phase noise by synchronising the master laser to the delay line provided by the round trip on one interferometer arm. A combined use of detector signals fro the reference cavity and from the main link phase detector signal associated with the reference laser (s_{2f} if the master laser is A2) could be used to reduce in-band phase noise.

Summary on Pathlength Difference Measurement

The pathlength difference measurement including all necessary corrections can be performed with the baseline measurement setup.

The achievable accuracy is (almost) entirely determined by the main link phase noise in the way it would be expected in a simple setup that would not need any of the corrections foreseen for the LISA setup) laser phase noise, clock phase noise and proof-mass relative motion.

With the conditions described in the sections above (sufficient low Doppler shift, phase detector quality matched to laser phase noise, accuracy of representation of the measurement equation system) the residual impact of the error sources for which compensation is implemented can be neglected, except for a small impact of laser phase noise close to the frequency where acceleration noise dominates the system sensitivity. This residual error is mostly depending on the principle of arm length estimation and not so much on the magnitude of the phase noise itself.

The most critical problem is the matching of the capabilities of the phase detector to the laser phase noise properties. Due to the large magnitude of the laser phase noise compared the main link shot noise small parasitic errors in the phase detection process (aliasing, non-linearity) may severely affect the measurement accuracy.

5.1.3.3 Residual Proof Mass Acceleration

The budgeting of parasitic acceleration effects acting on the proof masses follows the Pre-Phase A Study [Ref. 1]. In Table 5.1-5 the respective budget is repeated. The effects have been grouped according to error mechanism into following groups:

- Acceleration resulting from of external magnetic fields to the proof-mass.
  Magnetic effects of fluctuating interplanetary magnetic fields (coupling with static local fields) and Lorentz forces acting on the charged proof-mass have been considered. No
- Acceleration resulting from CESAR internal effects
- Acceleration resulting from displacement of masses on board the spacecraft due to thermo-elaststic distortion and due to antenna motion
- Acceleration resulting from relative motion of spacecraft versus proof mass as result of residual DFC control lop error in reaction to external forces acting on the spacecraft
- Other effects not specified in detail

Work within this study has concentrated on

- Analysis of local gravitational field (see §6.3)

  -DC acceleration at center of test mass

  -Gradient at center of test mass

  -Dynamic-parasitic acceleration over measurement band (driven by thermoelastic distortion)

  From these analyses only the last item "Dynamic-parasitic acceleration" enters directly in the performance budget while the other two aspects constitute boundary conditions for the analysis of the drag free control loop.
- Analysis of the drag free control loop (covering item "Gravity noise due to spacecraft displacement" and some of the unspecified effects)
  The analysis (§7.2.4) covers properties of CESAR including inter axis cross coupling, modelling of external disturbing forces and impact of FEEP noise. The mayor input into the analysis except for CESAR properties and FEEP characteristics is the assumption on the magnitude of the "negative spring stiffness" resulting from gravitational field gradients and magnetic field gradients where control loop properties critically depend on. The latter issue enters in terms of requirements into "Analysis of static gravitational field gradients"and "Derivation of requirements to internal magnetic field generation". As the gravitational analysis has been performed in parallel to the analysis of the drag free control an assumption on negative spring stiffness has been used in the latter analysis. The gravitational calculations now available justify the assumptions although some mass balancing is needed to meet the DC acceleration assumptions. The gradient assumptions are already close to the required values without compensation measures.
- Derivation of requirements to internal magnetic field generation for compatibility with "Magnetic force on proof mass from fluctuating interplanetary field" assumption and negative spring stiffness requirement (see §4.1.22)

Table 5.1-5: Acceleration Budget following [Ref. 1]

Error Source	Acceleration @10^{-4} Hz [$10^{-15}ms^{-2}/\sqrt{Hz}$]	Number of effects per proof-mass	Sum of group (rms) [$10^{-15}ms^{-2}/\sqrt{Hz}$]	Description of Group
Magnetic force on proof mass from fluctuating interplanetary field	0.50	1	1.12	External effects directly acting on proof mass
Lorentz force on charged proof mass from fluctuating interplanetary field	1.00	1		
Noise due to dielectric losses	1.00	1	2.00	CESAR internally generated Acceleration
Electrical force on charged proof mass	1.00	1		
Temperature difference variations across cavity	1.00	1		
Residual gas impacts on proof mass	1.00	1		
Thermal distortion of spacecraft	1.00	1	1.22	Gravitational effect due to thermally induced mass displacement
Thermal distortion of payload	0.50	1		
Telescope thermal expansion	0.50	1		
Gravity noise due to spacecraft displacement	0.50	1	0.50	Contributor to residual acceleration resulting from control loop action
Other substantial effects	0.50	4	1.56	Other Effects
Other smaller effects	0.30	16		
Total effect of acceleration			3.1	

The updated acceleration noise budget per proof-mass assumes a constant acceleration spectrum except for the residual acceleration resulting from the DFC. The constant part is budgeted in Table 5.1-6, the total acceleration spectrum acting on a single proof-mass is shown in Figure 5.1-8. Note that the increase of parasitic acceleration towards higher frequencies is uncritical because the effects will be masked by the white noise component of the interferometric measurement.

Table 5.1-6: Acceleration Budget resulting from this study (white noise part)

Error Source	Acceleration @10^{-4} Hz [$10^{-15}ms^{-2}/\sqrt{Hz}$]	Comment
External effects directly acting on proof mass	1.12	Taken from pre-phase A
CESAR internally generated Acceleration	2.00	Taken from pre-phase A
Gravitational effect due to thermally induced mass displacement	0.13	Refer to §6.3.6
Gravity noise due to space-craft displacement	no flat spectrum	Analysis result shows essentially non-white behaviour; the effect is therefore handled separately, refer to Figure 5.1-8
Other Effects	1.56	Taken from pre-phase A; this is slightly pessimistic as some of the effects enter into "Gravity noise due to spacecraft dis-placement"
Total effect of acceleration (white noise)	2.8	

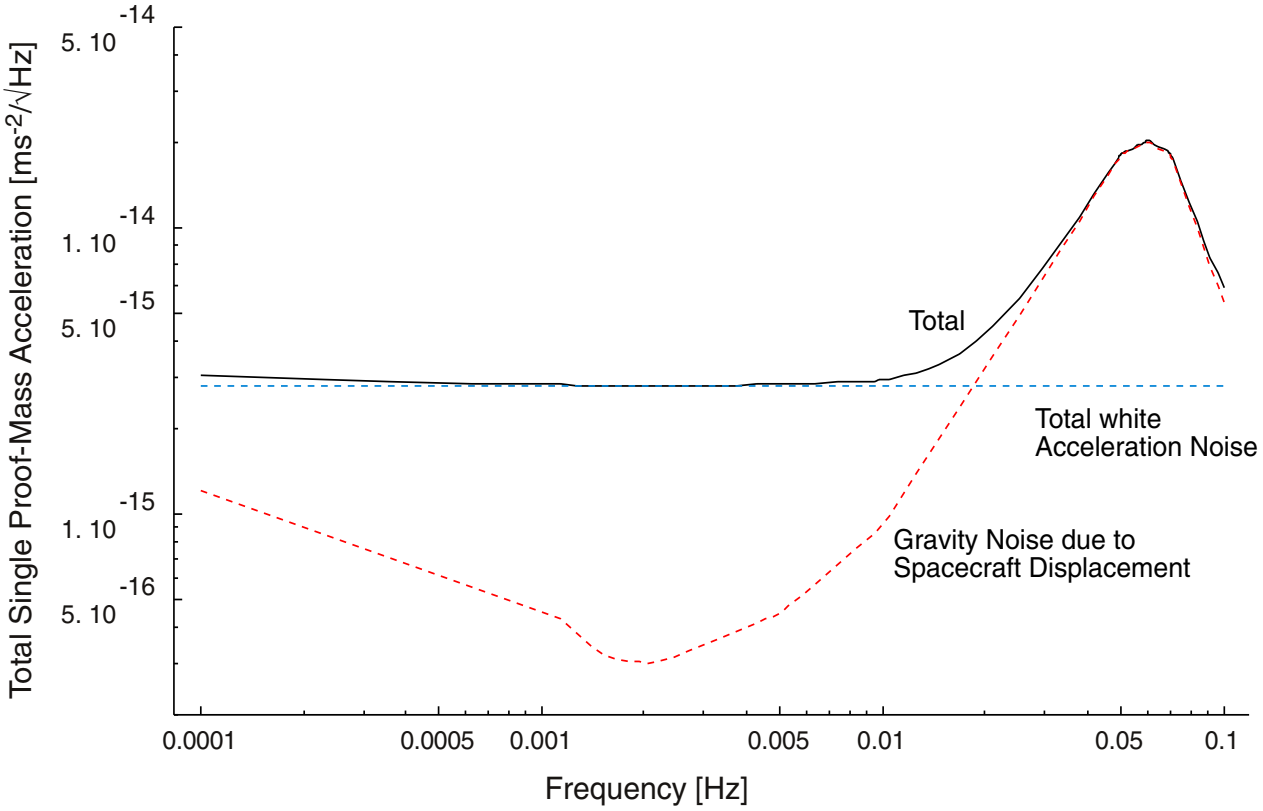

Figure 5.1-8: Single.Proof-Mass-Acceleration Spectrum

5.1.3.4 Optical Path-Noise Budget

The measurement errors not resulting from acceleration acting on the proof-masses are summarized in the optical path-noise budget. The main component is the error of the interferometric measurement itself as described in Chapter 5.1.3.2. It is composed from shotnoise error and residual effects from compensated laser phase noise. However the optical path-noise budget also contains thermo-elastic pathlength variations in optical bench and telescope straylight effects and interaction of pointing jitter on the transmitted beam with wavefront curvature. The optical path-noise budget as assesses in the LISA Pre-Phase A study is given in Table 5.1-7 for reference. It is expressed in terms of length variation of the total optical path (4 space links).

Table 5.1-7: Pre Phase A Optical Path-Noise Budget [Ref. 1]

Error Source	Magnitude 1 way [pm/√Hz]	Number in Path
Main detector Shot Noise	11	4
Master Clock Noise	10	1
Residual laser phase noise after correction	10	1
Laser phase measurement and offset lock	5	4
Laser beam pointing instability	10	4
Scattered-light effects	5	4
Other substantial effects	3	32
Total	40	

The shot noise dependent measurement error is budgeted in Table 5.1-8.

- The detailed optical power budget (as presented in Table 7.1-8) is used as input.
- Energy loss on the main carrier resulting from modulation is taken into account
- Numerically calculated modulation efficiency of the heterodyning at the main detector is used
- Electrical and phase measurement noise is accounted for (following Table 7.1-22)

The resulting effective phase noise (8,5 10^{-5} Rad/√Hz) and the corresponding optical pathlength error is slightly larger than predicted in the previous project phase. In the last row of Table 5.1-8 another degradation of about 4% has been introduced to account for the effect of noise on the ancillary detectors as described in Chapter 5.1.3.2.

Table 5.1-8: Shot Noise Budge on Main Link (phase standard deviation)

Parameter	Value	Remark
Received signal power on main detector (P_{in})	65 pW	see Table 7.1-8
Fraction thereof attributable to main carrier (η_{mc})	0.8	10% for subcarrier
Modulation Efficiency (η_{mod})	0.9	numerical simulation
Detector Quantum Efficiency (η_{qe})	0.56	resulting from 0.65A/W sensitivity
Resulting electrical carrier to noise density	81.4 dBHz	$PND = \frac{\eta_{mc} \cdot \eta_{mod} \cdot \eta_{qe} \cdot P_{in}}{h\nu}$
Resulting phase standard deviation not accounting for electronics/ phase meter errors	8,5 10^{-5} rad/$\sqrt{}$Hz	$stdev_{\varphi} = \frac{1}{\sqrt{PND}}$
Analog electronics error contribution	3 10^{-6} rad/$\sqrt{}$Hz	from Table 7.1-22 converted to rad/$\sqrt{}$Hz
Phase meter error contribution	6 10^{-6} rad/$\sqrt{}$Hz	from Table 7.1-22 converted to rad/$\sqrt{}$Hz
Resulting phase standard deviation	8,5 10^{-5} rad/$\sqrt{}$Hz	(phase meter and electrical noise is about negligible)
Equivalent error in optical path-length measurement	28.5 pm/$\sqrt{}$Hz	
Accounting for noise on ancillary detectors	29.6 pm/$\sqrt{}$Hz	estimated using the results from Table 5.1-3

The effect of transmitter pointing jitter on optical path-length is budgeted in Table 5.1-9. As the pointing performance of the DFC and the optical quality of the telescope are both predicted to be better than the respective values used in the pre-phase A study the resulting effect is now smaller than previously assumed.

Table 5.1-9: Effect of beam pointing instability

Parameter	Value	Remark
Wavelength	1.06µm	
Transmitted beam pointing offset error	30 nrad	requirement to pointing acquisition procedure
Transmitted beam pointing yitter	6 nrad	see analysis 4.6.3
Telescope diameter	0.3 m	design parameter
Telescope wavefront error (as fraction of wavelength)	1/30	telescope manufacturing quality
Resulting phase error due to pointing yitter	3.73 µrad/$\sqrt{}$Hz	using relation 3.6 of [Ref. 1]
Equivalent 1 way pathlength error	3.95 pm/$\sqrt{}$Hz	

The path-noise budged is summarized in Table 5.1-10. The evolution from pre-phase A can be observed by comparison with Table 5.1-7.

- The shot noise dependent contribution has increased. This is partly due to some loss factors not previously accounted for. However electrical noise and phase measurement noise are now included in this budget point.
- A residual effect of USO noise could not be demonstrated
- The residual impact of laser phase noise is separately accounted for because of its frequency dependency (see also discussion in Chapter 5.1.3.2)
- With the proposed data evaluation technique the error in the locking process of the lasers does not create an measurement error (it just serves to reduce phase noise on some measured signals)
- Scattered light effects have been analysed in this study. However the dominant straylight paths mainly involving the sub and main reflector enter directly in the pathlength budget, hence the path-length effect of the stray light is negligible (small compared to the direct effect). Since it was not clear which other stray paths have been accounted for in pre phase A the old values have been taken over as margin. The same has ben applied to the unspecified effects.
- Two types of thermo-elastic path lengths changes have been accounted for

  -variation of the optical path-length on the optical bench (mainly resulting from thermal effects on components)

  -variation of the optical pathlength in the telescope

Two types of telescope design have been analysed. Very good stability could be reached with a design using CFRP struts. This has been selected as baseline and the respective performance has been used in the budget. However an all-SIC design can reach path length effects in the order of 17pm/$\sqrt{\text{Hz}}$ which also comes close to useful performance.

Table 5.1-10: Optical Path Noise Budget

Error Source	Magnitude 1 way [pm/√Hz]	Number in Path	
Pathlength error due to phase measurement noise	29.6	1	See Table 5.1-8 The value Includes • shot noise on all detectors (incl. ancillary) • electrical and phase meter noise
Master Clock Noise	negligible	-	
Residual laser phase noise after correction	see Figure 5.1-9	1	separately accounted because of frequency dependence
Laser phase measurement and offset lock	-	-	phase measurement noise included in point 1; offset lock error is transparent for selected processing principle
Laser beam pointing instability	4.0	4	See Table 5.1-9
Scattered-light effects	5	4	from pre-phase A
Other substantial effects	3	32	from pre-phase A
Optical Pathlength Variation on bench	5.8	4	see Table 7.1-5 rms sum of 3.9pm/√Hz and 4.3pm/√Hz
Optical Pathlength Variation within telescope (1 way)	0.6	4	Composite telescope with CFRP struts SIC telescope design would contribute 17pm/√Hz
Total	38.3		Use of SIC telescope would result in 51.2 pm/√Hz optical path error

A graph of the optical path-noise budget including the frequency depending residual error from laser-phase noise is shown in Figure 5.1-9. An accuracy of 20m (rms) for absolute arm-length determination and LZH laser phase noise characteristic has been assumed in accordance with the argumentation presented in Chapter 5.1.3.2.

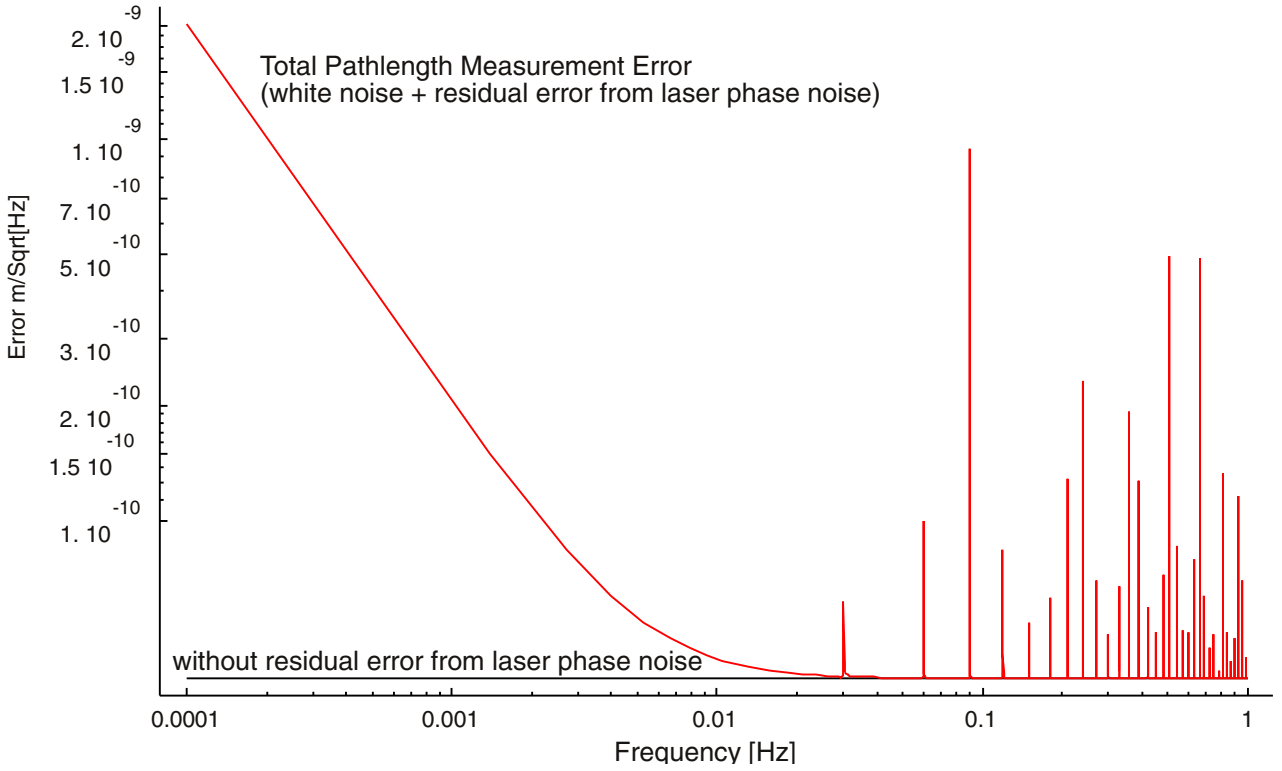

Figure 5.1-9: Total Path-Length Measurement Error

5.1.3.5 Performance Synthesis

The combined effect of proof-mass acceleration and measurement errors budgeted in the previous chapter is shown in Figure 5.1-10. All effects are presented in terms of optical pathlength error.

It can be seen that the assumed white components of the acceleration budget and the path-noise budget dominate over most of the measurement frequency range. The white acceleration errors dominate below about 3mHz the white path-length errors above 5mHz. In the transition region residual effects from laser phase noise play a role. How large this effect is and whether it is possible to suppress it entirely depends on the strategy of arm length determination as described in Chapter 5.1.3.2. It is not directly linked to the magnitude of the laser phase noise except when an independent technique not depending on the laser phase noise is used for the arm length determination.

The residual acceleration resulting from the DFC action does at no frequency significantly influence the total error budgets. At the high frequencies where the DFC residual acceleration exceeds the white acceleration noise the total error is dominated by the white path-length noise by more than an order of magnitude.

From the total measurement error the system sensitivity for gravitational waves can be predicted. The resulting sensitivity for 1 year averaging and gravitational SNR=5 is shown in Figure 5.1-11. As reference the sensitivity that would result from the pre-phase A report budget values for acceleration noise ($3\ 10^{-15}$ $ms^{-2}/\sqrt{Hz}$) and path-length noise (40 $pm/\sqrt{Hz}$) is printed as requirement curve. The deviation is mainly resulting from the residual effect of laser phase noise.

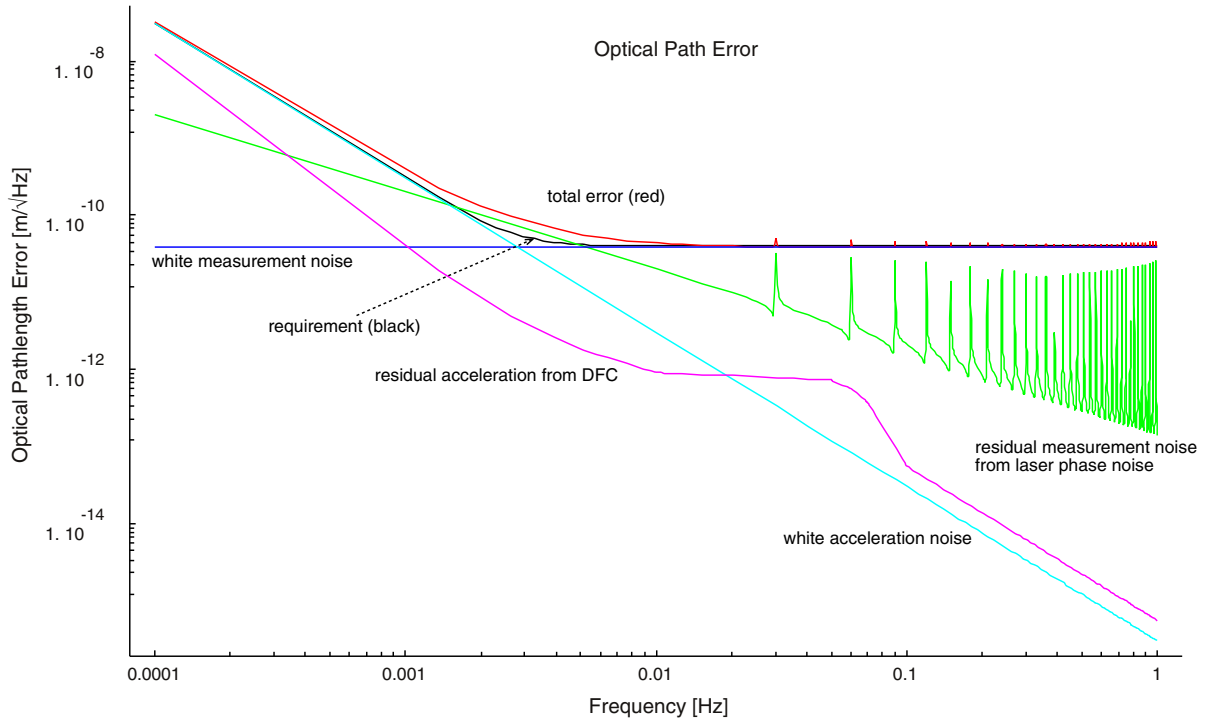

Figure 5.1-10: Synthesis of all error components (in terms of path-length error)

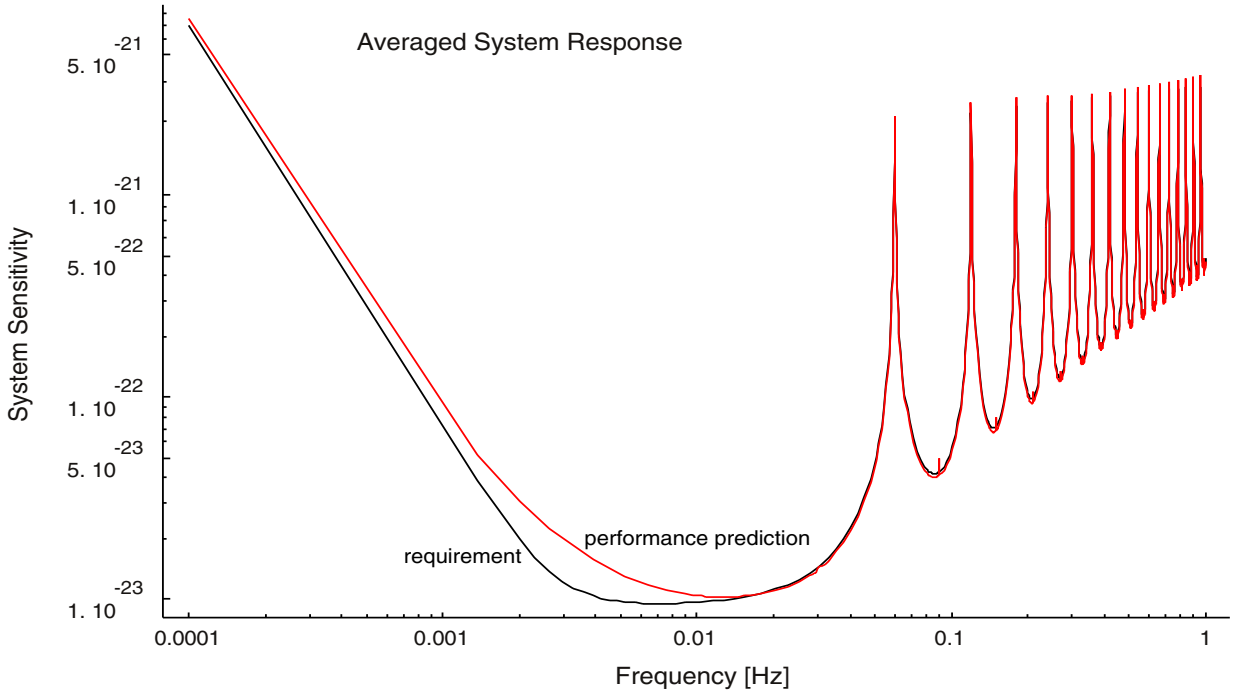

Figure 5.1-11: Total System Sensitivity (1 year averaged gravitational wave amplitude)

5.2 System Mechanical and Thermal Design

5.2.1 System configuration

5.2.1.1 Background

Prior to, and at the beginning of the present study, a number of decisions were made and a number of constraints recognised that dictated in large measure how the satellite element of the LISA mission would be configured.

The first involves the method of transfer from a point near the Earth at escape velocity, to the operational orbit and location of each of the 3 identical spacecraft that form the mission constellation. It was concluded that each of the 3 vehicles shall be delivered by its own propulsion system, rather than having one large propulsion system to deliver each one after the other to the 3 different operational orbits.

The second factor was the decision to have for each satellite a separate and separable propulsion module. This choice removes all the potential disturbances on the operational satellite that could be caused by the remainder of the transfer fuel and the large solar array required for the ion motors in the transfer phase.

The third factor driving the configuration is the LISA instrument. This is a large Y shaped fork of whose dimensions are such as to dictate that the satellite configuration is formed around the instrument.

The fourth factor is the launcher selected as baseline for the study. The available volume under the fairing compared to the dimensions of the instrument forced the 3 satellites and their propulsion modules to be a vertical stack with each instrument fork laid across the stack. The resulting height of this stack limited the overall diameter of both the science and the propulsion modules, because the stack, including a launch adapter, intruded into the conical portion of the 9.5ft fairing.

These factors and decisions had already been recognised in a previous study [1], and resulted in the configuration shown in Figure 5.2-1 and Figure 5.2-2. Here a stack of 3 satellites (named science modules) and their associated propulsion modules are seen in the original baseline Delta II 7925H launcher with the 9.5ft diameter metal fairing. The launcher performance then placed a limit on the maximum mass each satellite could be, and this allowed a total launch mass of 1407Kg.

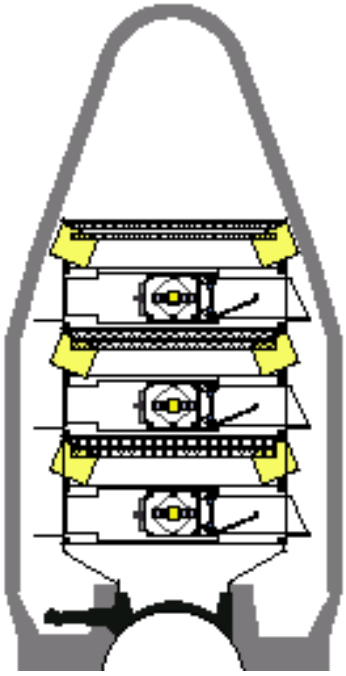

Figure 5.2-1: ***Original stack of science and propulsion modules in launcher***

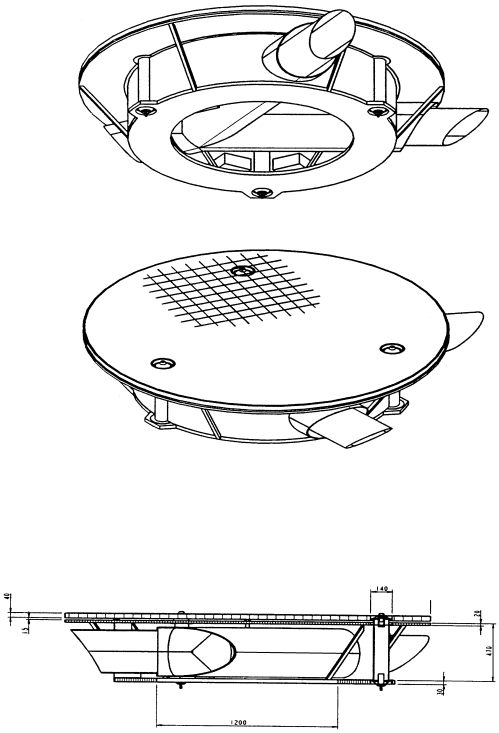

Figure 5.2-2: ***Science module configuration at start of Study***

The direction of illumination of the sun in operational orbit also played a part in the overall configuration.

The two arms of the instrument fork are aligned along the optical axes of the laser telescopes contained in these arms, which are at 60deg to each other. The plane containing the optical axes is itself at 60deg to the sun-satellite line. This means that the sidewalls of the science module must then be conical to avoid sun illumination, making the anti-sun surface smaller in diameter than the sun face with its solar array.

Two basic assumptions regarding the configuration were also made for the earlier study. The first was that the basic structure was a cylinder, carried through each science and propulsion module, with appropriate separation mechanisms. The second was that all the electronic and mechanical units could be accommodated within the volume between the instrument fork and the cylindrical walls, plus the small volume available outside the cylinder, allowing for the restriction caused by the conical outer side walls.

5.2.1.2 Review of the science module configuration concept approach

To ascertain if the configuration concept of the earlier study could be confirmed, or whether any changes or alternative concepts were necessary, it was first necessary to establish the subsystem elements definition, for mass, thermal dissipation, power consumption and size. This also applied to all the units associated with the payload experiment. The result can be seen in the Mass Budgets of Section 5.5 but in particular the extent to which the payload in particular has demanded more volume than originally foreseen can be seen in Table 5.2-1 (the original list is in Table 5.2-2), partly due to a reassessment of what units can remain in the fork tubes while maintaining the stable thermal conditions in these tubes.

It then became clear that the originally conceived volume was inadequate, and that the baseline science module constraints must be reassessed.

It was initially thought that all the units must be mounted directly to the radiator on the anti-sun side of the spacecraft, to assist in the thermal stability of the satellite interior. Further, since the side walls of the satellite "cylinder" should also not be illuminated by the sun, this anti-sun area is more limited than the surface under the solar array panels. The consequences are seen in Figure 5.2-3, where it is clear that such a simple approach cannot be used. It should be noted that the units shown in this drawing are not the full complement eventually established, but an interim status defined during the process of establishing the full complement, and do not include some previously internal telescope units are now outside the telescope tubes.

Table 5.2-1: ***Payload and platform unit definitions***

Unit	No.	Tot. Mass
Laser head (incl. phase mod)	4	8
Laser head electronics	2	4
USO	2	0.8
Inertial sensor	2	13
IRS Electronics	2	4
UV box	2	1
Interfer. analogue elec.	2	3
Interfer. digital elec.	2	7
Instrument control elec.	1	4.5
Optical bench	2	11.2
Fibre Positioner	2	0.6
Telescope	2	13
Optical assy. structure	2	10
Optical assy. mechanisms	2	4
Optical assy. thermal	2	2
Str/Therm shield	1	13
Total		99.1

Table 5.2-2: ***Original payload definition at start of study***

Unit/Element	No of Units
Fork assembly	1
Payload shield	2
Laser Electronics	3
Laser	4
UV Unit	1
Radiator plate	1
Total Mass Kg	**84.2**

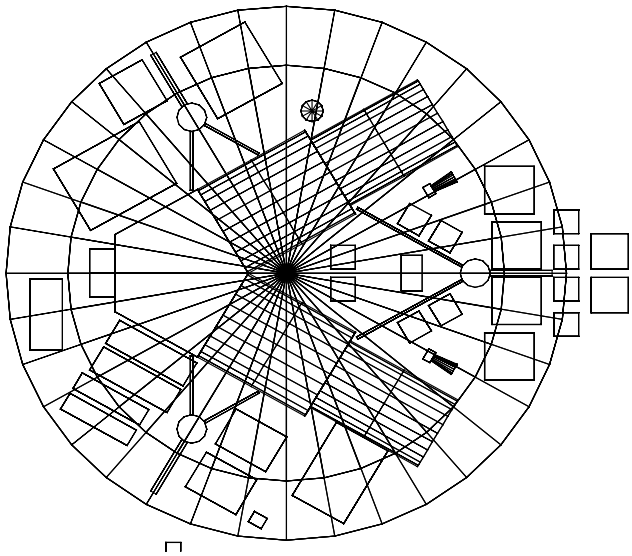

Figure 5.2-3: ***Initial assessment of unit accommodation in the science module***

5.2.1.3 Amendment to Launcher Baseline

The first relaxation in this situation was to allow the use of the newer 10ft composite fairing for the Delta II, which replaced a heavier metal one. In consequence the launcher performance was not significantly reduced (1380Kg down from 1407Kg), while gaining significantly in volume. The full 10ft diameter could be used since the cylindrical portion of this fairing is longer than that of the 9.5ft fairing.

5.2.1.4 Assessment of structural/mechanical concept

The use of the triangular rather than the circular structural wall concept is mainly a consequence of a review of the separation joint concept for the stack of modules. It also has the fortunate advantage of being more efficient for unit accommodation than the circular concept as originally conceived, as Fig 5.2-5 shows.

The use of cylindrical walls also implies the use of circular adapter attachments e.g. marmon clamps to meet the load transfer concept. Two factors militate against the use of such devices.

One is that a stay out volume, that intrudes into the volume needed by the science module, must be created to allow for the release dynamics of the clamp. Alternatively the stack could be made significantly taller, but this is limited by the eigenfrequency of the stack with 6 clamp interfaces in it, and height limits driven by the fairing and the stack centre of gravity height.

The second is that, since all clamps must be retained by the propulsion module, there is a loose clamp attached to the propulsion module for the duration of the transfer phase to operational orbit. (This is the clamp between two adjacent science/propulsion combinations).

The third is that the separation velocities are not easily controlled and small between the science module and propulsion module on separation in the operational orbit.

The change to a triangle formed around 3 strong columns is also a consequence of reviewing the instrument fork structure and its mounting. It is necessary to retain the outer fork of two tubes and the "root" as a stand-alone structure containing the instrument telescope elements and front end electronics.

To avoid any undesired distortion and thermal effects from the main structure feeding into the fork, and thus its internal elements, the attachments for the fork must be so designed to carry the expected loads but be so arranged to minimise carry-over of distortions. This means the walls themselves should not be the main load carriers throughout the entire satellite stack as were the cylindrical walls. The introduction of the columns is then necessary for the transfer of loads between stacked satellites.

The ends of these columns are used as the load transfer points between modules and are fitted with hold-down and release mechanisms. These mechanisms form 2 groups. The first group connects each science module to its partner propulsion module forming a combination, and the second group connects each module combination to each other, and the lowest to the launcher adapter.

These mechanisms carry the high launch loads, and after launch each science/propulsion module combination is released to enter its own unique transfer orbit. The separation shock caused by these mechanisms are not significant for this operation. However, for the separation of science and propulsion module at the operational orbit they become important. The science module is only equipped with FEEP thrusters, and these cannot deal with high tip-off rates at separation. The separation must thus have a very low tip-off rate and a low separation velocity. To achieve this a fourth separation mechanism is incorporated at the centre of the circular anti-sun face of the science module and the adjacent propulsion module face, and does not carry the main launch loads. First the 3 main mechanisms are released, but the combination remains together using the central attachment. This, with its small separation forces, is then actuated to perform the delicate separation of the propulsion module in the operational orbit.

The consequence of the adoption of the 3 column approach is that a dedicated adapter must be developed for the Delta II to interface with the 3 load carrying columns of the payload.

To ensure that the structure modal response remains comfortably within the requirements of the launcher, the upper and lower circular plates of the science module are joined around the rim by a conical wall, broken where necessary for telescope apertures and the rear fork radiator.

Holes or cut-outs in the solar array caused by interfaces between modules are minimised by using the 3 column approach. This eases the accommodation of solar arrays, especially for the propulsion module, which requires a large area and further avoids the implementation of deployable panels for the propulsion module.

5.2.1.5 Other unit accommodation aspects

Using the revised structural concept, a review of all the units and elements to be accommodated in the science module was undertaken. Allowing for the small but significant growth in the assumed telescope outer tube diameter, driven by mirror mounting constraints, it was possible to mount some of the units on the backside of the sun illuminated wall. The volume and surface areas then proved adequate, as is seen in the internal layout shown in Figure 5.2-4.

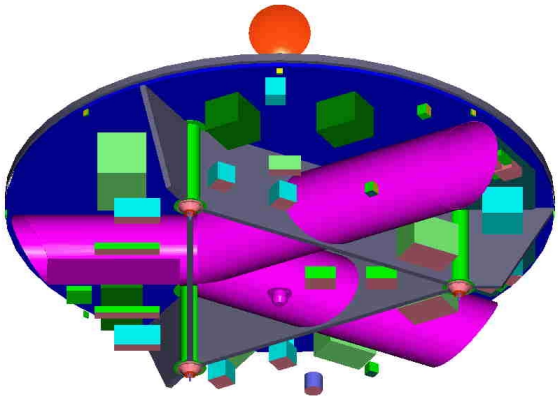

*Figure 5.2-4: **Internal layout of the science module***

The star trackers are collocated alongside the two telescope apertures and aimed in the same directions, so that each telescope has one coaligned ST. The telescope baffles themselves have ejectable doors, necessary to prevent sun radiation damage during the LEOP and transfer phase when the satellite combination may assume any attitude.

The thrusters are required to be arranged as in Figure 5.2-5.

This means that they may be conveniently be attached to the supporting triangular substructures on the periphery of the larger science module upper structural plate. They are also thus located away from the telescope apertures, avoiding contamination of the optics.

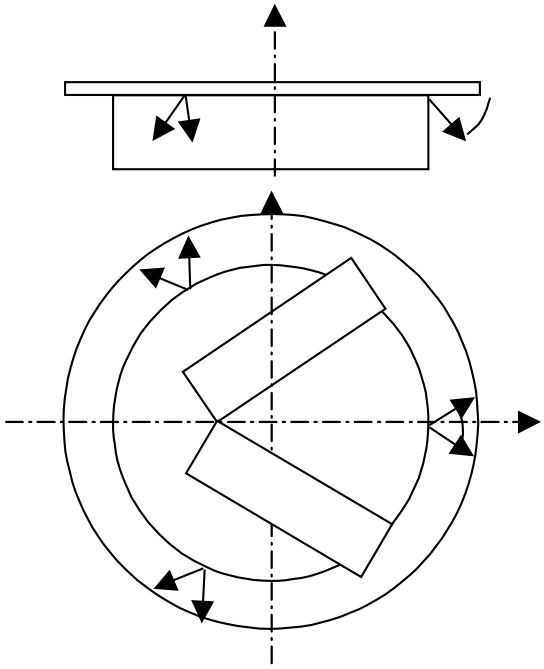

It is essential that the main internal volume of the science module has stable and moderate thermal conditions. To achieve this there is an additional thermal shield plate attached to the sun facing circular surface by thermally isolating mountings with a small gap between the thermal and structural plate. This thermal shield can then carry the relatively small solar array on its front face and thus also protects the structure from thermal heating effects of the solar array itself.

It should be noted that the science module carries no battery, since no failure case is envisaged where solar power is not available. Power for heating during the transfer phase must then come from the propulsion module, with the corresponding electrical connecting interfaces between science and propulsion module.

*Figure 5.2-5: FEEP **Thruster arrangement***

5.2.1.6 Communications antenna mounting

External to the science module satellite body are the communication antennas. There are 4 basic configurations for the antenna, which consists of a 30cm diameter dish and feed pointing at Earth about 10deg away from the plane of the front face of the science module towards the sun. A 360deg rotational scan of the antenna around an axis perpendicular to the module front face plane is also required during 1 year. The alternatives are shown in Figure 5.2-6.

Option 1 of a central antenna on the sun face is the obvious candidate if the science module was on its own. However the limited stack height drives the option to need either a large hole in the modules above it, or a stowage mechanism that would still be too thick for the total allowable stack height.

Option 2 of a single antenna at the anti-sun side has the additional disadvantage of requiring a long post to allow the antenna to look past the satellite rim with the required 10deg angle, as well as a stowage mechanism with the disadvantages of option 1. Also the post and its joints must be very stiff to avoid disturbances to the science measurements.

Option 3 of 2 antennas, each with 180deg motion on opposite sides of the science module seems attractive, as it saves on stack height. However, too much of the module body must be cut away to allow a satisfactory field of view at the limits of the 180deg arc.

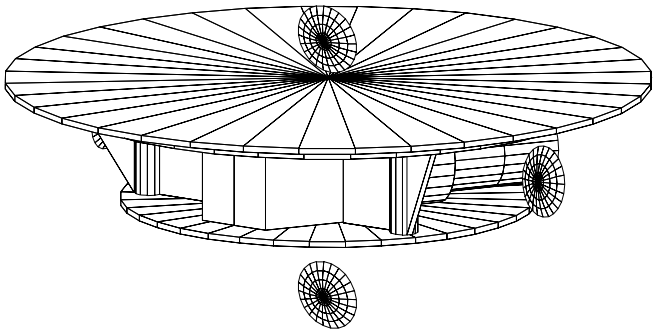

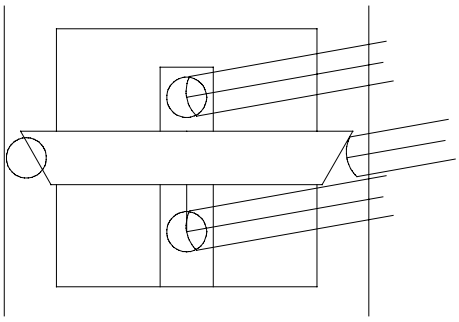

Figure 5.2-6: Antenna options Illustrations

Option 4 utilises the concept of option 3, but with the advantages of option 1 in being mounted on the front face of the satellite. There is enough volume available at the rim of the science module due to the conical shape of the body to allow the antennas from one module to intrude into the vacant space of the module above. 2 antennas are needed since both must be moved in unison to minimise the disturbances to the science measurements.

This Option 4 is the option that has been selected for all the above stated reasons.

5.2.7 Factors influencing the science module depth

In minimising the depth or "thickness" of the cylindrical height of the science module, some factors need to be taken into account.

To accommodate the nominal 300mm diameter instrument telescope mirror, mountings and alignment equipment, the outer diameter of the instrument fork structure tube is around 400mm.

Additionally the solar array is mounted directly on the thermal shield with a gap between the shield and the of the main module. When the science module structure, thermal shield and separation mechanisms are taken into account, then the total "thickness" of the science module is 592mm, for an overall diameter of 2700mm, matching the 2743mm available from the 10ft fairing. This is seen in Figure 5.2-7 below.

The resulting overall configuration of the Science and Propulsion module combination is shown in Figure 5.2-8 and Figure 5.2-9.

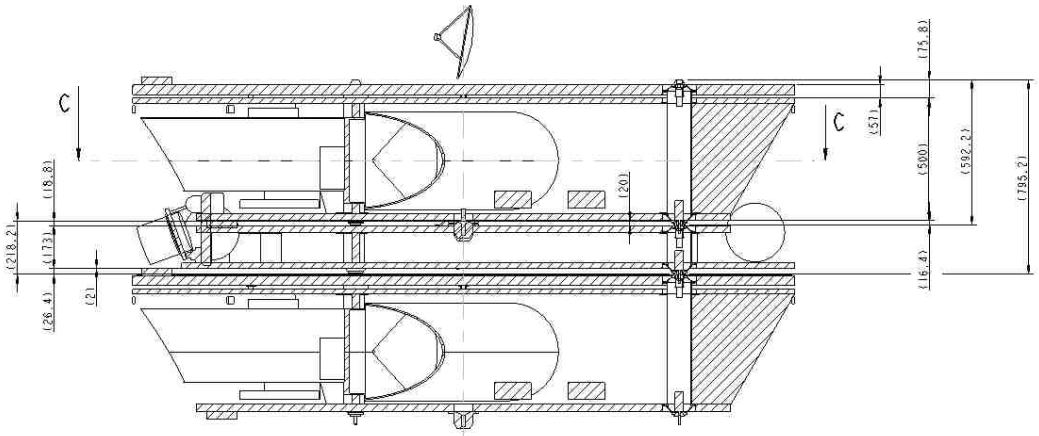

Figure 5.2-7: ***Cross section of Science and Propulsion modules***

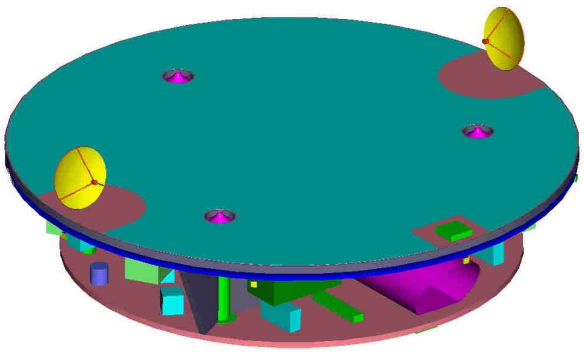

Figure 5.2-8: ***Overall Configuration of Science Module***

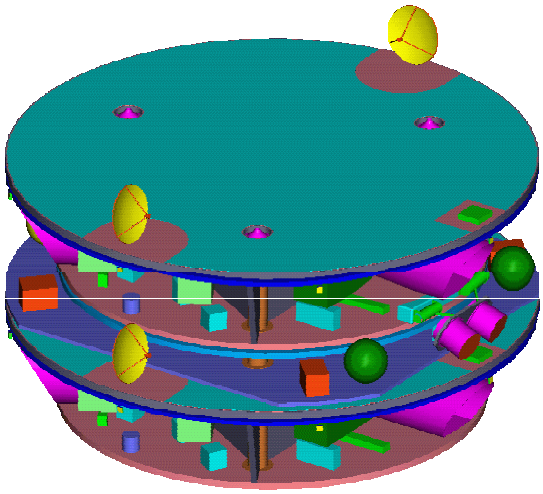

Figure 5.2-9: ***Overall Configuration of Science and Propulsion Modules***

5.2.2 Science Module Gravitational Design

This section summarises the requirements related to self-gravity and addresses the basic principles used for gravitational design. For detailed gravitational analyses and design considerations the reader is referred to sections 6 and 7 of this report.

5.2.2.1 Requirements for Gravitational Design

The LISA requirements related to self-gravity at proof-mass locations can be summarised as follows:

- Constant (or nearly constant) self-gravity effects below the Measurement Band Width (MBW), i.e. below 0.1 mHz
    - Constant self-gravity induced accelerations at proof-mass locations along sensitive axis: <1. E-10 m/s^2 (Payload Definition Document, sect. 5.6)
    - Constant self-gravity induced gradients of the acceleration field at proof-mass locations along sensitive axis: < 5.E-8 1/s^2 (requirement slightly more constraining than the value given in sect. 5.6 of the Payload Definition Document but necessary to limit the proof-mass total negative stiffness for control reasons to 1.E-7 N/m)
- Fluctuations of self-gravity induced accelerations within the MBW (0.1 – 100 mHz)
    - Fluctuations of self-gravity induced accelerations at proof-mass locations along sensitive axis due to thermal distortion: < 3.E-16 m/s^2 (rms) (Payload Definition Document, sect. 5.3)
- Variations of self-gravity induced accelerations above the MBW (> 100 mHz)
    - No requirement

5.2.2.2 Basic Concepts for Gravitational Design

The concepts to be applied depend on the frequency ranges at which gravitational disturbances need to be avoided or restrained.

5.2.2.2.1 Constant Self-Gravity

The gravitationally ideal shape for LISA would be that one of a homogeneous hollow sphere, since there would be no gravitational forces exerted by this sphere on bodies (such as the proof-masses) contained inside of it.

A more realistic concept for a gravitational design is to minimise constant self-gravity at proof-mass locations by shifting heavy structural parts and boxes as far as possible away from the proof-masses, since the gravitational attraction is inversely proportional to the distance squared between the attracting masses. Unfortunately, this proves to be unfeasible in view of the considerable number of boxes and of the constrained dimensions under the Delta II fairing. The configuration selected for LISA could therefore not be tailored to meet the requirements for constant self-gravity. As a consequence, the constant self-gravity at proof-mass locations will have to be compensated by dedicated balance masses.

These balance masses should be mounted preferably in the vicinity of the proof-masses in order to avoid them getting too bulky. The subject of gravitational balancing on payload level is covered in section 7.3.3. It is evident that the proposed method of balancing will be based on math model predictions and therefore depend on the fidelity of the underlying models.

An question to be analysed in a future phases is whether there is a need to compensate for the gravitational repercussions of the launch distortion.

5.2.2.2.2 Quasi-Static Self-Gravity Variations

For very slow, quasi-static variations of self-gravity the same requirements apply as for constant self-gravity. The compensation of these variations would require mechanisms slowly moving balance masses around. In order to avoid such mechanisms, moving masses have to be avoided or minimised. The only macroscopically moving masses on-board the LISA Science Module are the HGA and the Optical Assembly. It is shown in section 6 that the variation of gravity due to HGA rotation and Optical Assembly swivelling is sufficiently small and needs not to be compensated.

5.2.2.2.3 Self-Gravity Fluctuations within the MBW

Temperature fluctuations within the MBW result in thermo-elastic distortion which itself leads to self-gravity fluctuations. Main reasons for temperature fluctuations are fluctuations of the solar radiation and variations in the power dissipation of on-board units. There are consequently several design measures necessary in order to minimise these self-gravity fluctuations:

1. Shielding against solar radiation
2. Variations in dissipation of electrical units to be minimised, e.g. by constant operation
3. Thermal decoupling of electrical units with fluctuating dissipation
4. Selection of materials with low CTE

These design measures are discussed in more detail in sections 5.2.3 and 5.3.2.

Another cause for low-frequency self-gravity fluctuations could be sloshing propellant masses. For this reason, a separable Propulsion Module has been baselined which contains tanks and pipework of the hydrazine RCS system and the ion propulsion.

5.2.3 Structure & Mechanisms

5.2.3.1 Requirements

5.2.3.1.1 Compatibility with the Delta II launch

The LISA spacecraft design shall ensure compatibility with a Delta II launch. Although this launch vehicle will be most probably no more available at the envisaged launch date, it shall be shown that a spacecraft design with the limited mass and volume capacity of a Delta II class launcher is possible.

- The resulting limitations on spacecraft size and mass have been discussed in chapter 5.2.1.
- The required minimum fundamental frequencies are 15Hz for the lateral modes and 35Hz for axial modes, which are value typically found for several launchers
- The Delta II only allows for a limited distance of the spacecraft CoG from the separation plane resulting in severe limitations on spacecraft height
- A clamp band fixation shall be avoided for mass saving reasons, thus loads have to be transferred via individual separation devices. Although the 3-stage Delta II only provides clamp band interfaces, the 2-stage 6915 PAF adapter was considered assuming that it would be possible to adapt it to the 3-stage launcher.

5.2.3.1.2 Launch in a stack

The launch has to be performed in a stack of 3 science modules (S/M) and 3 propulsion modules (P/M). Separation into 3 pairs of S/M and P/M occurs immediately after separation from the launch vehicle, the separation of S/M and P/M occurs only after achievement a final operational orbit. Thus:

- 6 separation planes with the associated separation mechanism, interface fittings and connectors are needed.
- The individual modules, especially the P/M's have a very small height to diameter ratio. The structure has to accommodate the units under these conditions
- The separation devices have to be compatible with
  - the loads to be transferred
  - the transfer phase duration of one year
  - a final orbit achievement accuracy of 0.3cm/s
  - electrical connectors between S/M and P/M
- the antenna has to be accommodated in a way that does not interfere with the stacking

5.2.3.1.3 Payload performance related

In order to limit the disturbances on the payload specific constraints result:

- The solar array has to be thermally decoupled from the spacecraft. The solar array it self has to provide shielding of temperature fluctuation for which a core layer of 20mm Polyimide foam is needed. The equipment accommodated on the top of the solar array (e.g. sun sensor, antenna) shall preferably be mounted on the outer face sheet. If this is not possible, the mounting has to provide a very efficient thermal decoupling.
- The fixation of the payload Y-shaped tube has to account for differential thermal deformation. Due to the required stability of the gravitational field deformations occurring on the spacecraft side may not be transferred into the payload tube. A thermal decoupling is also needed, however less stringent than in the case of the solar array because the radiative coupling is dominating . This is not a design driver because it will be automatically provided due to the required mechanical decoupling.
- For thermal and configuration reasons, the heat rejection of the units can occur to the conical rim of the spacecraft. In this direction only one wall between any dissipating unit and space is acceptable.

5.2.3.2 Structure Design

In Figure 5.2-11 the Delta II adapter, based on which the design has been established, is shown. The structure makes use of the 3 attachment points available on the Delta II adapter. In order to directly transfer the loads from the upper modules to the launcher interface, tubes have been used connecting all modules

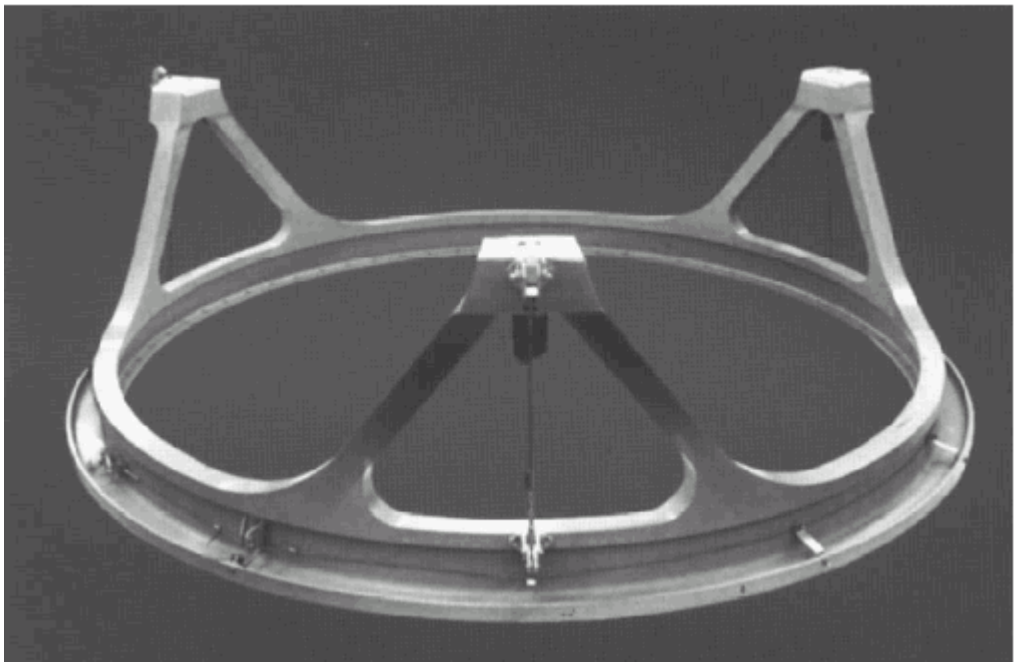

Figure 5.2-10: Delta II Adapter 6915 PAF
(taken from Delta II Payload Planner's Guide, APRIL 1996 MDC H3224D)

5.2.3.2.1 Science Module

The principle design of the science module structure is shown in Figure 5.2-11.

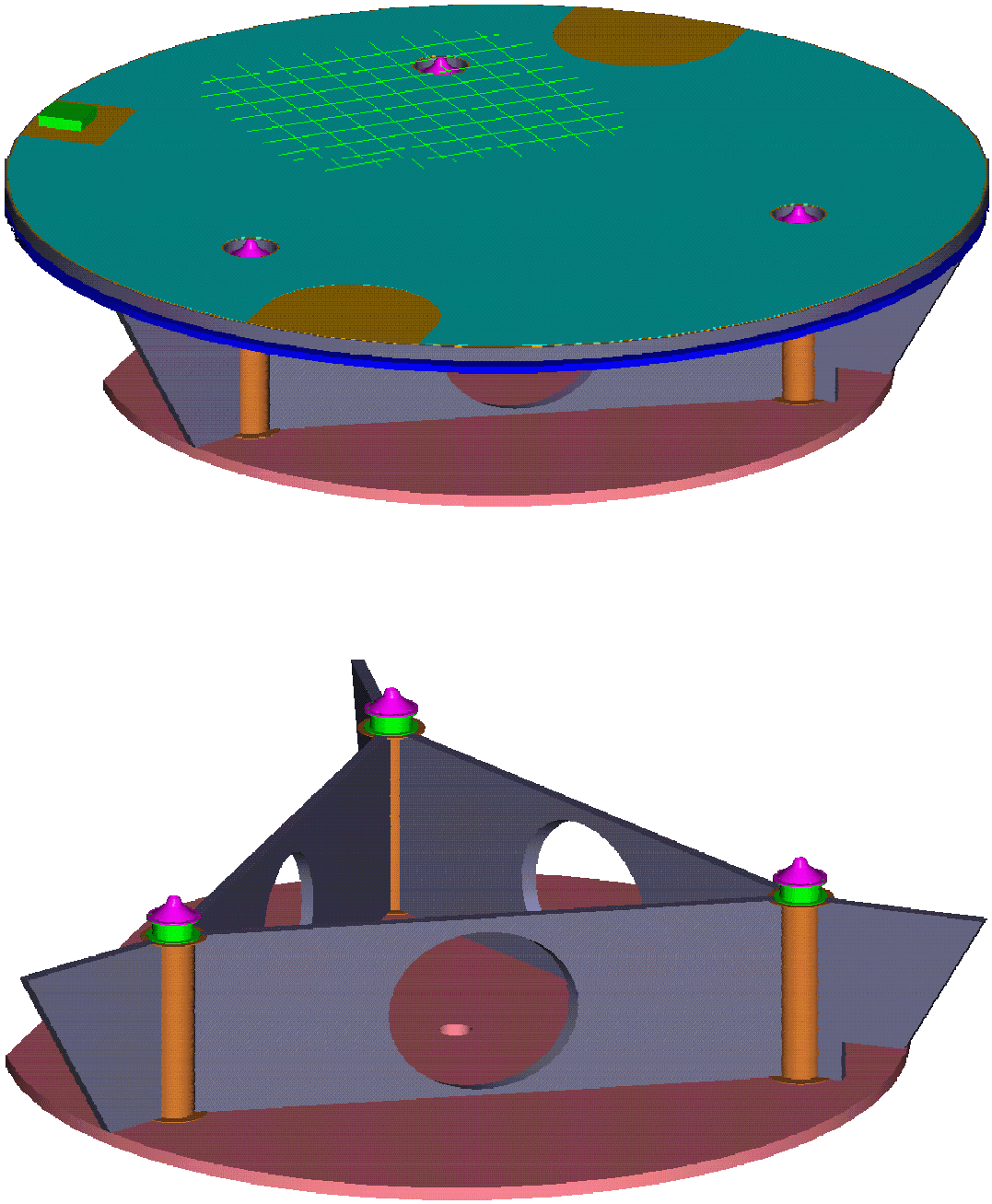

Figure 5.2-11: Science module structural design

In the Science module the 3 tubes are connected by shear wall. These tubes provide for

- Overall lateral bending stiffness of the stack
- Mounting provision for the payload Y-shaped tube
- Transfer of loads from the top and bottom plate into the tubes
- Stiffening of top and bottom plate

All equipment outside the payload Y-shaped tube is accommodated on the top and bottom plate. From thermal stability point of view it is required to place all dissipating units on the bottom plate. This was not possible because of lack of available space. A less favourable, but still acceptable place are the areas on top and bottom plate close to the rim. This now leads to a mechanical unfavourable mass distribution. Besides the stiffening provided by the shear walls, also the conical rim of the module has to be closed by a conical panel.

Considering the stiffness and thermo-elastic behaviour, an all aluminium structure could be used. However, for mass reasons, CFRP panels with aluminium honeycomb are needed. The solar array panel serves as a thermal shield. Initially a sandwich with pure foam core was selected. However, this did not provide sufficient stiffness. Thus a double sandwich with a foam core for thermal isolation and a aluminium honeycomb core for stiffness is used. The solar array is mounted on 13 thermally insulating attachment provisions.

Main plates: 30mm sandwich consisting of 0.5mm CFRP face sheets and an aluminium honeycomb core with a density of 50Kg/m³

Stiffening Webs: 20mm sandwich consisting of 0.5mm CFRP face sheets and an aluminium honeycomb core with a density of 50Kg/m³

Connecting tubes: Aluminium tubes with outer diameter 100m and 2.5mm wall thickness

Solar array: sandwich consisting of: (starting from solar cell side)

- 0.6mm CFRP facesheet
- 20mm polyimide foam
- 0.6mm CFRP facesheet
- 20mm aluminium honeycomb core
- 0.6mm CFRP facesheet

5.2.3.2.2 Propulsion Module

The structural design of the propulsion module is shown in Figure 5.2-12. The main driver is the very small available height. For thermal reasons, the solar array panel cannot be used for unit accommodation. Therefore, all the propulsion module units have to be accommodated on the module rim.

Instead of the triangular shear walls, a cylinder is used in order to also provide for a stiffening of the panel at the outer rim. This is still not sufficient, additional webs have to be used locally at unit mounting positions. The top plate is needed for the solar cell fixation. Some mass savings could be cut-outs in the bottom plate

In any case the very stringent limitation in height does not allow to apply lightweight design principles. Essential mass savings can only be achieved by material selection, e.g. by using CFRP facesheets composed of strands with some spacing between each other.

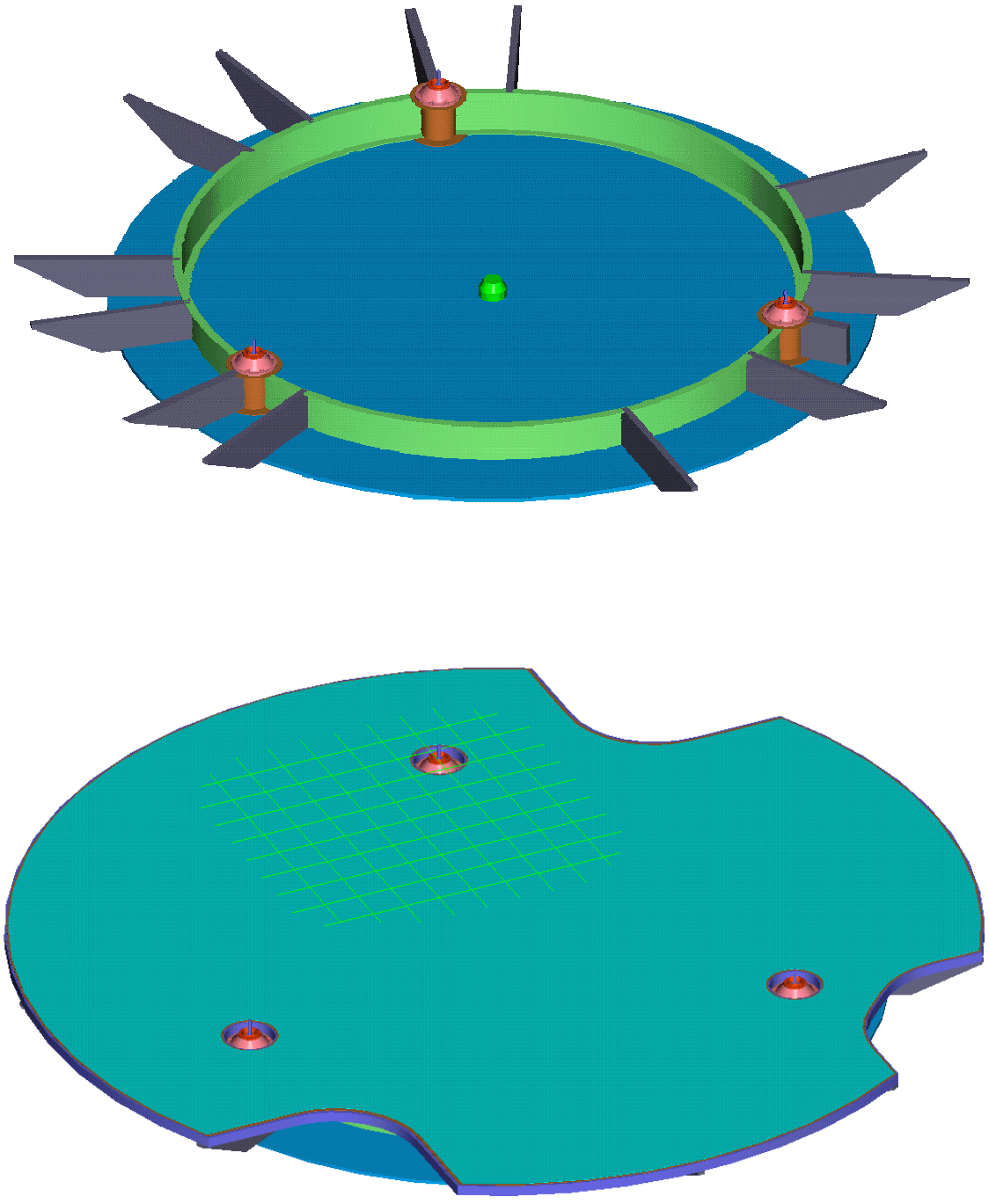

Figure 5.2-12: Propulsion Module structural design

5.2.3.3 Structure Performance

5.2.3.3.1 Stiffness

The stiffness of the overall spacecraft is defined by the minimum fundamental frequencies which have been determined in a FEM analysis which is described in section 6.1. The achieved frequencies are:

	Achieved Frequency	Delta II Required Frequency
Lateral modes	15.9Hz	15Hz
Axial modes	46.6Hz	35Hz

5.2.3.3.2 Stability

Inputs to be provided by RAL

Generally an aluminium structure should be preferred because of the better stability from ambient to vacuum due to moisture release. The advantage of the smaller coefficient of thermal expansion can hardly be used because the electronic units present most of the mass and show the largest temperature fluctuations. Using a different material than aluminium for housing of the electronics seems not to feasible. Thus the fluctuations of the gravity field would be determined by the thermal deformation of the units themselves. Except for the very high modulus carbon fibres, the thermal conduction of aluminium is higher than that of CFRP.

Use of an all aluminium structure avoids the problems of moisture release. The created thermal deformations have a magnitudes that can not be avoided anyhow as long as aluminium housings are used. Aluminium allows for a more uniform temperature distribution which can even reduce the thermal deformation effects.

5.2.3.4 Mechanism Design

5.2.3.4.1 Spacecraft separation mechanism (SSM)

The SSM separates the 3 spacecraft's from the launcher. After separation from the launcher the spacecraft are separated from each other. In all cases the same mechanism will be used. The mechanism has to separate at the 3 interface points provided by the launcher. Between each spacecraft, the same arrangement of interface points is given due to the tubes used for load transfer through all spacecraft's. A cup-and-cone connection will be used, the fixation is provided by a preloaded bolt which is separated by a Pyronut. Such a mechanism has already been defined in the DSS phase A study for Mars Express.

5.2.3.4.2 Module separation mechanism (MSM)

The separation into modules is done at the final orbit position. The orbit position has to be achieved with a very high accuracy, the allowable uncertainty must be less than 3mm/s. Since the science module

attitude control relies on the FEEPs which only provide very low thrust levels, also the rotation rates after separation have to be limited to less than 1 mrad/s. Electrical connection between the 2 modules is needed during transfer phase. Thus also an electrical connector has to be separated.

Separation will be performed in 2 steps:

- Immediately after injection into the transfer orbit, a separation of the load carrying parts will be done. This is a mechanism identical to the one used for SSM. This avoids cold welding effects during transfer. During transfer a spindle will maintain both spacecraft's connected to each other. The interface forces only results from the ion thrusters which is less than 0.1N.
- After injection into the final orbit the spindle drives will be operated to separate the 2 modules. The separation direction has to be fixed by the propulsion module AOCS, the spindles will than produce an exactly defined separation velocity, high enough to bring them at a safe distance in an acceptable time. The solar radiation pressure will ensure steadily increase of this separation.

- The principle arrangement is shown in Figure 5.2-13. For redundancy reasons, 2 separation drives and a harness separation mechanism are needed. Each separation drive includes an override which would disconnect the spindle. The harness separation mechanism is operated first. Once the connector is retracted, the spindle drive will separate the 2 modules. In case of failure of the harness separation mechanism failure, the separation drives would press the connector out of its interface. Thus the following operation modes are possible:

	Spindle Drive 1	Spindle Drive 2	Harness separation mechanism
Nominal	Operational	Operational	Operational
Spindle drive failure	Spindle separated	Operational	Operational
Harness separation mechanism failure	Operational	Operational	Separated by spindle drives

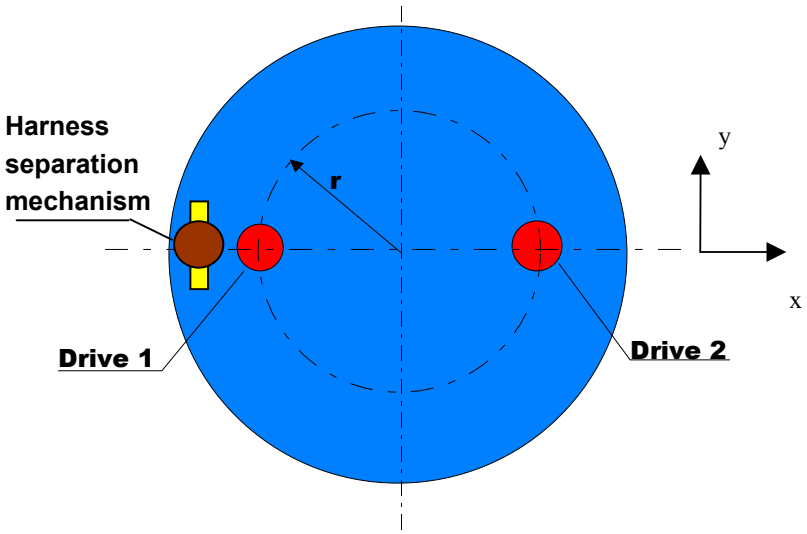

Figure 5.2-13: Arrangement of separation mechanism spindle drives and electrical connector

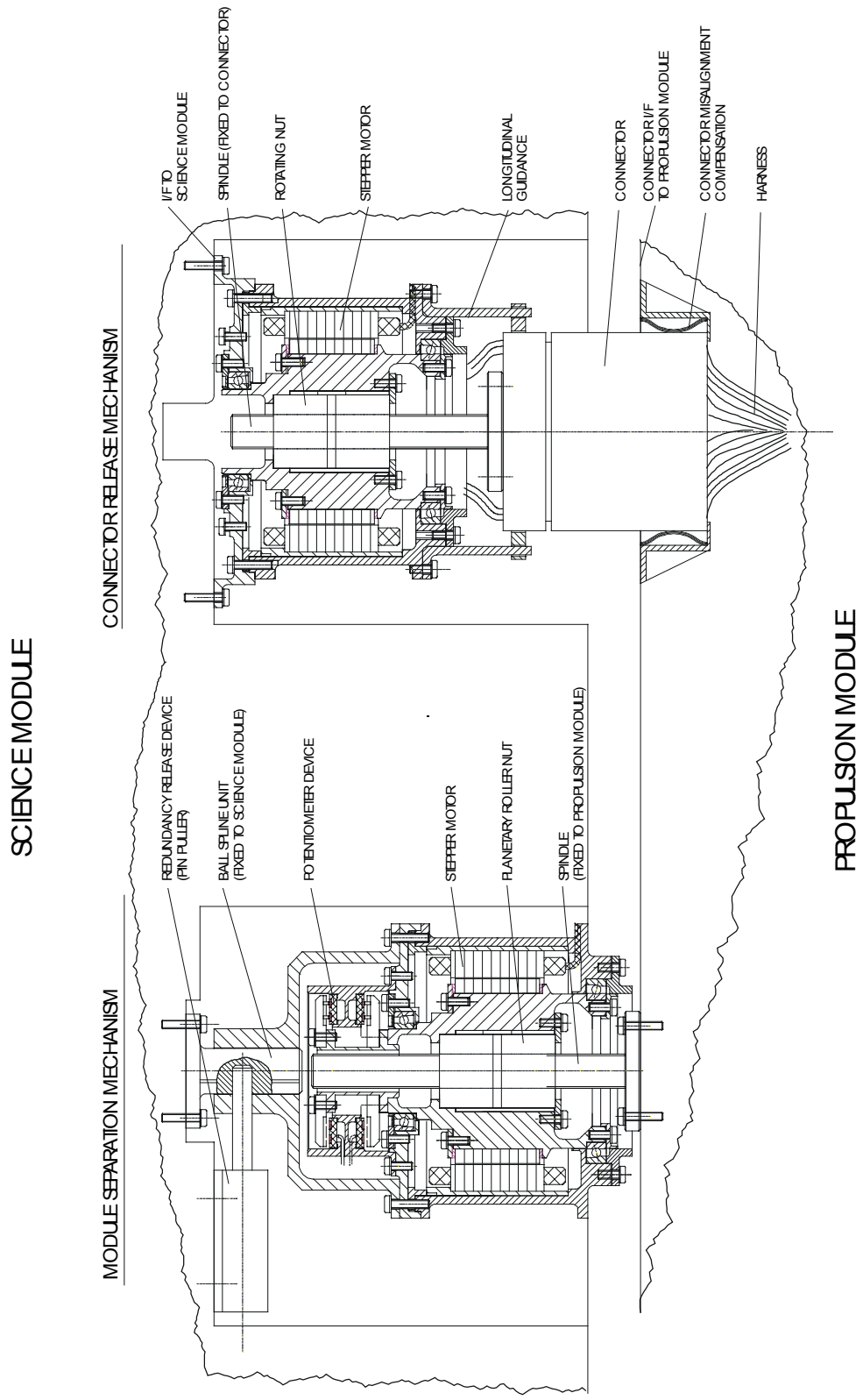

Figure 5.2-14: Science Module/Propulsion Module Separation Device

Figure 5.2-14 shows and detailed drawing of the separation mechanism design. The module separation mechanism (MSM) basically consists of a spindle which is fixed to the propulsion module and a nut driven by a stepper motor which is fixed to the science module. For the nut 2 planetary roller nuts are used with springs in between to eliminate backslash by providing a pre-load on the threads. The stepper motor rotor directly drives the nuts. The stator is fixed inside the housing which also houses the bearings of the nuts and a potentiometer used for the spindle motor speed control. The fixation of the nut drive housing to the science modules is via a pin/bush connection which is maintained in place by the pin of a pin puller device. This allows a disconnection of the nut housing from the science module by operation of the pin puller device in case the nut drive fails.

The set-up of the connector release mechanism (CRM) is very similar. In this case the spindle is attached to the connector and prevented from rotation by a longitudinal guidance. On the science module side an override for disconnection is not needed in this case, the housing is mounted on a flange.

5.2.3.4.3 Telescope launch lock

In the investigation on the payload telescope pointing mechanism it is shown that a launch lock for the telescope can be avoided. For more details refer to section 7.

5.2.3.4.4 Telescope pointing mechanism

This mechanism is covered in section 7

5.2.3.4.5 Antenna pointing mechanism

The design of the antenna pointing mechanism is driven by

- Antenna pointing requirements
- Allowable disturbance torque's
- Allowable changes in the self-gravitation field

The pointing requirements are not very stringent. In principle this can be fulfilled by a stepper motor without gear reduction. The torque disturbance resulting from the movement by 1 step is compensated in case 2 antennas are used and if the rotation axis is parallel to the principal axis of rotational inertia. If this is not achievable, a micro-step drive can be used for the motor which could reduce the reaction torque below the FEEP thrust capability and could thus allow operation during antenna pointing activity.

In any case the antenna pointing mechanism will not present any technology difficulties.

5.2.3.5 Mechanism Performance

5.2.3.5.1 Spacecraft separation mechanism (SSM)

The SSM will be based on a cup-and-cone connection employing a pyronut which is available from Pyrospace, F. These nuts are available for pre-loads of up to 50KN which is fully in-line with the launch loads.

The pyronuts can be operated in a re-settable manner on ground by pressurised air to allow testing and have only to be charged immediately before launch. Such a device has already been developed by DSS. The pyronuts include internal redundancy and have a proven reliability.

5.2.3.5.2 Module separation mechanism (MSM)

The parameters of the MSM design are selected to provide:

- An acceleration of 0.01m/s² to limit the reaction force to 0.8N
- An acceleration time of 3s to achieve a separation velocity of 0.03m/s
- A spindle length of 100mm for sufficient time to damp any created spacecraft vibration resulting in inaccuracies in separation velocity

The separation profile is shown in Figure 5.2-10. The spindle length has been selected to 100mm. The 2 changes in acceleration at t=0s and at t=3s induced a vibration of the spacecraft. In Figure 5.2-16 the oscillation of the spacecraft during separation is shown starting at t=3s. The end of the spindle is reached at t=3s+2s. Then the amplitude in acceleration has dropped to $7*10^{-5}$m/s². The load on the spindle due to this oscillation is 0.014N. This is the minimum pre-load on the nut to be used in order to prevent backslash. For adjustment reasons a pre-load of 0.1N is selected. The tolerances which determine the separation speed will be in the order of 1% resulting in an inaccuracy of the separation speed of less than 1mm/s

The rotation rate at separation in the nominal case results from the elastic energy stored in the pre-loaded nut. In the worst case, this can induced a rotation rate of $4.5*10^{-5}s^{-1}$. In case of a failure of 1 spindle the rotation rate depends on the bending stiffness of the spindle. In case of a steel spindle with ∅8mm the worst case rotation rate is $2.4*10^{-4}s^{-1}$, for ∅12mm the worst case rotation rate is $4.7*10^{-5}s^{-1}$.

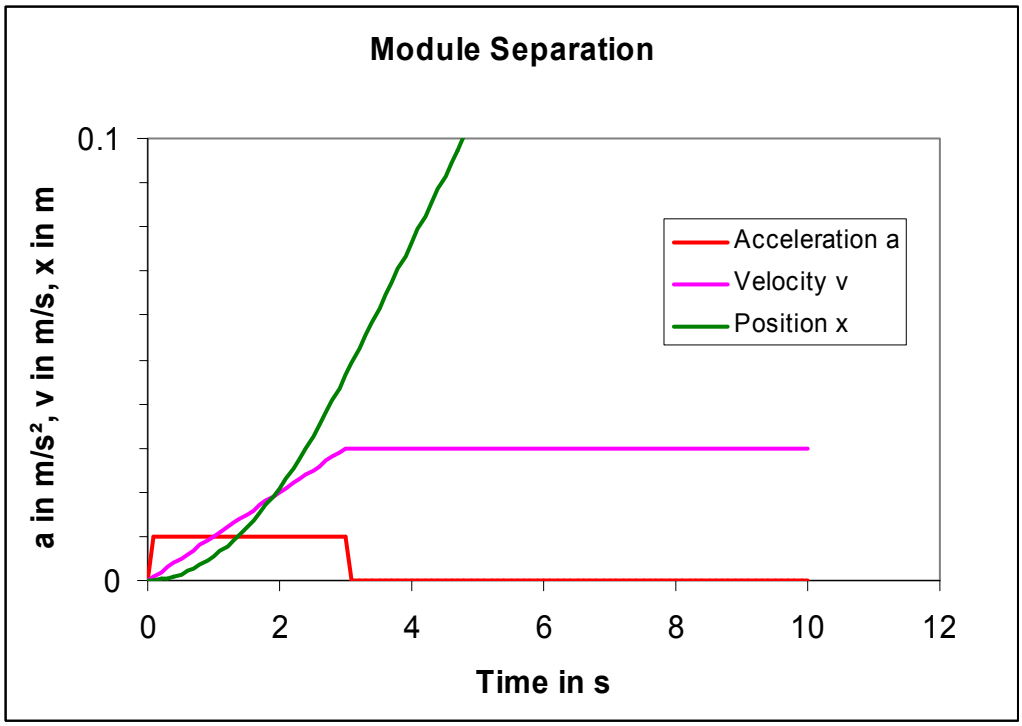

Figure 5.2-15: Separation acceleration, velocity and spacing

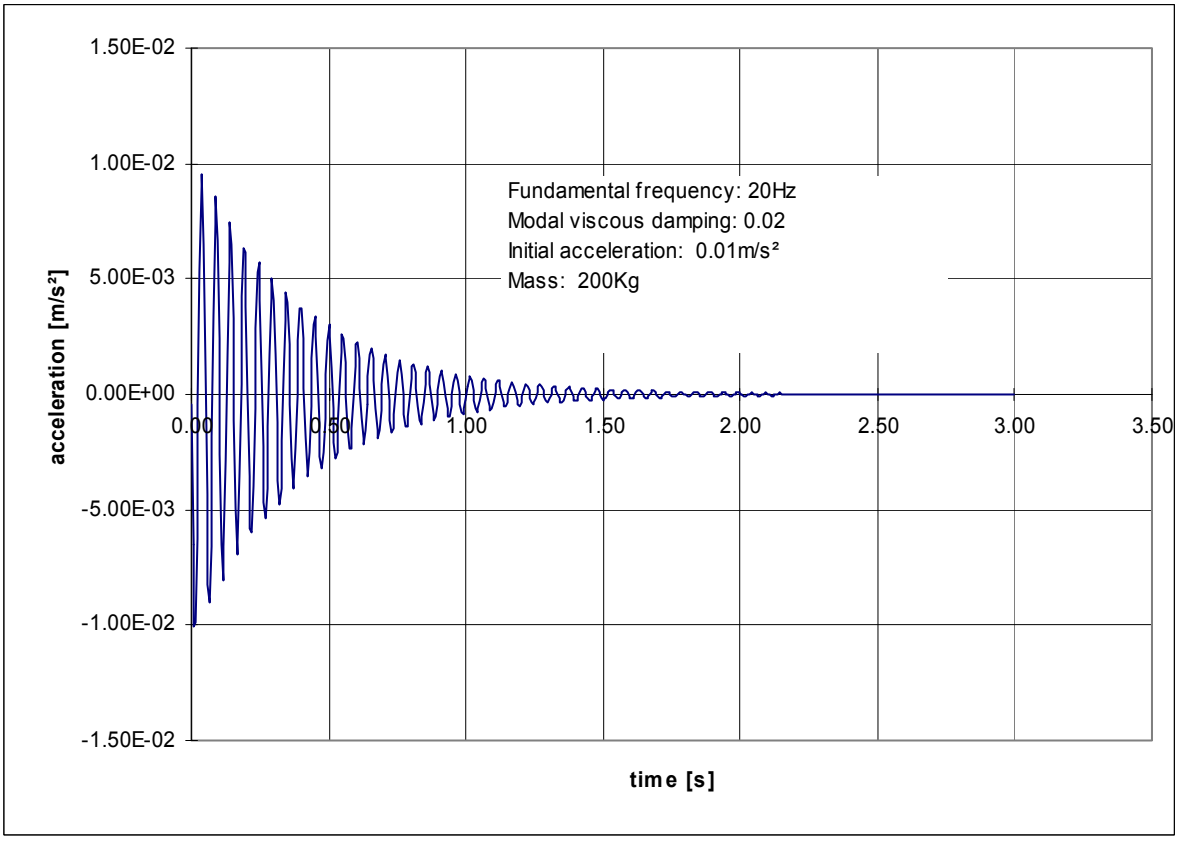

Figure 5.2-16: Spacecraft oscillation in fundamental mode during separation

5.2.4 Thermal Control

5.2.4.1 Requirements

5.2.4.1.1 Temperature requirements

The standard requirement is as always to maintain the temperatures within their acceptance temperature range. Besides that that are 2 important requirements on temperature stability and on stability of a temperature gradient within the measurement frequency range:

- Minimise temperature fluctuations on the optical bench with a goal of $\Delta T \leq 10^{-6} \frac{K}{\sqrt{Hz}}$. The requirement actually results from optical path length variations within the laser cavity and thus potentially only applies locally. The required value rather represents the value found to be achievable in pre-phase A and is considered as a design goal
- Maintain the fluctuation of the temperature difference across the proof mass cavity below $\Delta(\Delta T) \leq 2 \cdot 10^{-5} \frac{K}{\sqrt{Hz}}$

5.2.4.1.2 Implicit Thermal Requirements

Implicit requirements result from requirement on the gravitational field. They concern both, the long term drift and the stability within the measurement frequency range.

- Long term drifts in the temperature field shall be limited such that changes in the self-gravitation field are $\Delta a \leq 10^{-9} \frac{m}{s^2}$
- the temperature stability of the spacecraft shall provide a stability of the self-gravitational field of $\Delta a \leq 10^{-15} \frac{m/s^2}{\sqrt{Hz}}$

The effect on the gravitational field strongly depends on the distance from the proof mass location. In order to provide a guideline for the thermal design a temperature fluctuation budget can be established. If it is assumed that all items contribute statistically to the overall disturbance and if the mass of all individual items is in the same order of magnitude, a budget only depending on the distance from the proof mass can be established. The acceptable values under these assumptions are shown in Figure 5.2-17. These can be used for preliminary justment on the acceptability of unit temperature fluctuations without the need to perform an overall thermo-elastic and gravitational analysis.

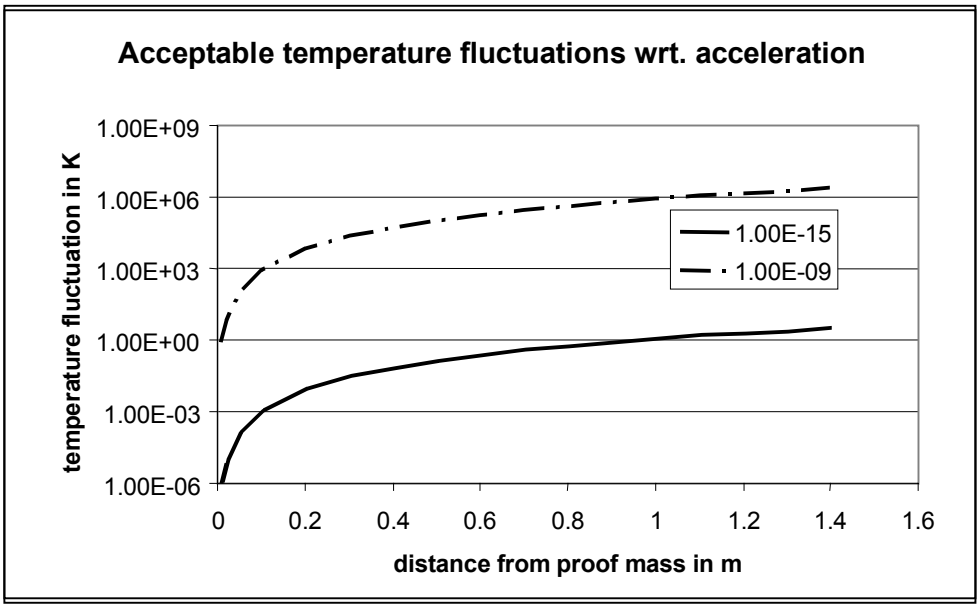

Figure 5.2-17: Temperature fluctuation budget for short term (1.00E-15) and long term (1.00E-09)

5.2.4.2 Thermal Design

5.2.4.2.1 Science Module

The thermal design principle is shown in

Figure 5.2-18. As a general design principle no MLI has been used in order to prevent any effects from changing properties due to crinkling by thermal or ageing effects.

The solar array is used as sun shield in order to isolate the science module from the disturbances created by the solar constant fluctuations right at the source. All areas not needed for solar cells will be covered with SSM to minimise the absorbed solar flux and to reduce the solar array temperature. The reduction in temperature reduces the radiative couplings and thus improves the isolation. No illumination of any other science module surface shall occur. The size of the solar array is limited by the launcher fairing diameter. Thus all other external surfaces have to be within a 30° cone behind the solar array. By this approach only the solar array experiences temperature fluctuations due to the solar constant variation.

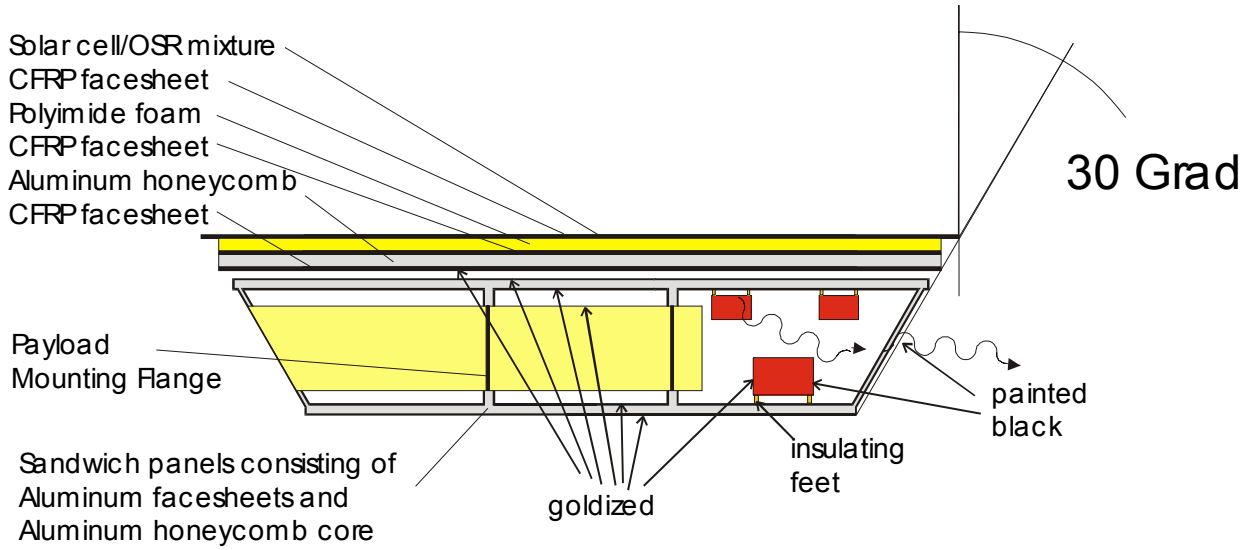

Figure 5.2-18: Thermal design principle

The transfer of these temperature fluctuations into the science module needs to be minimised by an effective thermal decoupling. The solar array panel is built-up by CFRP face sheets with a polyimide foam core. This reduces the transfer of temperature fluctuations to the solar array rear side by both, insulation and thermal capacitance. On the rear side insulating fixation elements are used for mounting the solar array to the structure. A main contributor is the thermal radiation from the rear side because of the large area and the direct transfer to the payload tube. This is limited by a gold coating on all surfaces in the view of the solar array rear side and the solar array rear itself.

The sensitive payload parts are accommodated within the Y-shaped tube , therefore the tube surface is goldized to provide radiative decoupling also on the inside. The mounting of the tube is via a thin walled flange to accommodate differences in coefficient of thermal expansion, further decoupling is not needed because of dominating radiative coupling

Difficulties arise from the disturbances in dissipating of the electronic units. Ideally they would all be mounted on the rear side of the science module, insulated from the structure as good as possible and directly reject their heat to space. This is not possible for accommodation reasons. Both, bottom and top plate of the structure have to be used for the mounting of the units. In order to limit the transfer of temperature fluctuations from these units to the structure, they are mounted on insulating feet. Heat rejection is done by radiation the science module side wall which acts as a screen radiator. The radiative coupling from these units to the payload tube is reduced by covering the areas with direct view to the payload tube with gold. For smaller boxes eventually doubler plates have to be used or such units have to be mounted on the bottom plate for direct heat rejection. Due to the current status of design this is not yet investigated in detail

The payload tube is very well decoupled from the rest of the science module, this efficiently filters temperature disturbances and allows a very stable optical bench. The telescope will be provided with low emissivity coatings as far as possible to thermally de-couple from the tube. The temperature level inside the optical bench is only determined by the dissipation inside the tube and the remaining small radiative exchange through the telescope aperture. A calculation of actual temperature level will contain high uncertainties and the system will react very sensitive to parameter changes.

5.2.4.3 Thermal Performance

5.2.4.3.1 Temperature Level

The temperatures of electronic unit can be adjusted by the size of the conical radiator. A trimming of this radiator was performed in order to achieve an overall temperature level of about 20°C. The actual temperatures of the units are shown in Table 5.2-3.

All units a have to reject their heat by radiation from their housings. Due to the varying ratio of unit size to unit dissipation, the actual temperatures cover a rather wide range which gives in some cases values outside the acceptable temperatures. Therefore, this range needs to be reduced by an individual trimming of the units. For hot units this can be achieved by placing a doubler plate under the unit, cold units can be covered with low emissivity coating. This also needs to be addressed in conjunction with the transfer of temperature disturbances to the payload, this needs a low emissivity on the unit areas facing the Y-shaped tube. This type of design activity needs to know the exact shape and dissipation of each unit. Since major changes are expected towards the real start of LISA phase B activities, the detailed thermal design was not covered in detail. The overall solution is compatible with the system needs, for the trimming of individual units sufficient trimming capability is available and this also allows for sufficient growth potential of the system.

Table 5.2-3: Steady State Temperatures

	Cold Case Temperature in °C	Hot Case Temperature in °C
Solar Array	81.8	96.4
PCDU	32.9	34.7
CentEl CPS	31.9	33.7
Transpond 1	20.3	22.8
Transpond 2	8.6	11.3
FEEP El. 1	18.8	21.2
FEEP El. 2	4.3	7.0
StarTrack 1	13.1	16.3
StarTrack 2	8.5	11.8
HGA Drive 1	11.0	13.9
HGA Drive 2	7.2	10.1
RFDU	13.3	15.7
Gyro Pack	5.6	8.1
EPC 1	51.3	52.9
EPC 2	23.9	25.8
TWT 1	21.5	23.5
TWT 2	19.0	21.0
ST Elec. 1	16.5	18.9
ST Elec. 2	10.9	13.5
ST Elec. 3	6.4	9.0
ST Elec. 4	7.3	9.9
StarTrack 3	10.6	13.1
StarTrack 4	5.5	8.0
UV Box 1	17.0	19.4
UV Box 2	17.2	19.6
InstConEl 1	28.9	31.2
InstConEl 2	8.0	10.7
Laser Head 1	43.7	46.3
Laser Head 2	31.0	33.7
Laser El. 1	22.8	25.5
Interfer El. 1	31.4	33.8
Laser Head 3	34.0	36.8
Laser Head 4	21.3	24.2
Laser El. 2	13.2	16.0
Interfer El. 2	7.7	10.6
Optical bench	9.1	11.2
Proof mass	8.4	10.6
Sensor	8.4	10.6
Titanium housing	8.4	10.6
Primary mirror	-14.0	-12.0
Baseplate	-13.2	-11.1
Secondary mirror	-13.6	-11.6
Mast	-13.6	-11.5
Telescope thermal shield	-0.3	1.9
Electronics plate	24.2	26.3
Analogue electronics box on plate	25.6	27.8
Digital electronics box on plate	26.0	28.1
USO box plate	-3.4	-1.3
USO box A	-5.6	-3.7
USO box B	-7.4	-5.5

5.2.4.3.2 Temperature Stability

With respect to temperature stability the following cases have to be considered:

5.2.4.3.2.1 Temperature fluctuations due to solar constant fluctuation.

The fluctuation of the solar constant is given as a spectral density, thus it is only required to determine the frequency dependant transfer function. This was done by performing a transient thermal analysis at 3 different frequencies. As shown in Annex B - Temperature Stability Analysis Method the temperature response is always decreasing with the frequency, thus 3 cases are sufficient. The solar constant fluctuation is given as $1.75 \cdot \left(\frac{f}{1mHz} \right)^{-1/3} \frac{W}{m^2 \cdot \sqrt{Hz}}$ in the pre-phase A report. The thermal analysis made use of rounded values.

Table 5.2-4: Temperature fluctuations due to solar constant fluctuation

	Solar Constant Fluctuation in W/m²√Hz			Transfer Function in K/W			Temperature response in K/√Hz		
	10^{-1}Hz	10^{-3}Hz	10^{-4}Hz	10^{-1}Hz	10^{-3}Hz	10^{-4}Hz	10^{-1}Hz	10^{-3}Hz	10^{-4}Hz
Optical Bench	0.377	1.75	3.77	n/a	2.2E-11	2.9E-7	<1E-12	3.8E-11	1.1E-06
Primary Mirror	0.377	1.75	3.77	n/a	2.0E-11	2.6E-7	<1E-12	3.5E-11	9.9E-07
Payload E-Boxes	0.377	1.75	3.77	n/a	2.0E-11	5.8E-5	<1E-12	3.5E-11	2.2E-05

The Issue for the performance is the temperature difference across the proof mass cavity. This temperature difference is not represented in the model because it depends too much on the actual configuration which is not known in full detail today. However, the fluctuation in temperature difference will be similar to the fluctuation in temperature level on the optical bench. The actual fluctuation of the temperature difference will be at about 1.1E-06 and will thus be a factor of 20 better than the requirement.

5.2.4.3.2.2 Temperature fluctuation due to a correlated fluctuation of unit dissipations

Such a correlated fluctuation could occur due to fluctuation in the voltage of the power supply or due to operation profile characteristics with effect on the dissipation of many units. Only the lowest frequencies are of concern in this case. The resulting temperature amplitude can be taken to determine the maximum acceptable dissipation fluctuation. Once a transfer function from voltage to dissipation fluctuation is known, a requirement for the voltage stability can be derived. The dissipation stability's can be specified in terms of spectral densities, respectively in terms of upper limits to the response to voltage fluctuations. Therefore it was sufficient to consider only the lowest frequency which is the worst case A . In Table 5.2-5 the resulting temperature fluctuations and transfer functions are summarised.

As for solar constant fluctuation, the temperature difference across the proof mass cavity is important. The required 2E-5K/√Hz are exceeded. The correlated fluctuation of dissipations should be less than 0.2%.

Table 5.2-5: Temperature fluctuations due to 1% electronic units dissipation variation at 10^{-4}Hz

	Temperature Response in K	Transfer Function in K/ppm
Optical Bench	6.5E-05	6.5E-09
Titanium Housing	2.0E-05	2.0E-09
Primary Mirror	3.0E-05	3.0E-09
Secondary Mirror	5.0E-05	5.0E-09
Payload Analogue E-box	1.0E-03	1.0E-07
Payload Digital E-box	1.0E-03	1.0E-07
USO box A	8.5E-03	8.5E-07
USO box B	8.5E-03	8.5E-07

5.2.4.3.2.3 Temperature fluctuations due to single events

Such single events are e.g. switch on and off of the down-link assembly. Although it is foreseen to keep all components permanently switched on, this case was used to establish an upper limit for any single event dissipation change. For the resulting temperature disturbance a spectral analysis has to be performed in order to achieve the resulting spectral densities in temperature fluctuation. However, the result also depends on the bandwidth which is used to derive spectral density from the amplitude at discrete frequencies. For this case a more specific definition of the requirement is needed.

In the analysis a down-link event leading to an additional dissipation of 36W over 3 hours was considered. The resulting temperatures of optical bench, titanium housing and the temperature difference between both is shown in Figure 5.2-19.

In order to check against the temperature fluctuation requirements, a Fourier analysis has been performed. From the Fourier coefficients the spectral densities were then derived using 1 octave intervals. These results are shown in Figure 5.2-21. The same spectral analysis was also performed for the temperature difference. The result is shown in Figure 5.2-20. The temperature response is included in the same diagram. It can be seen that in the interesting frequency range the spectral densities of both are almost the same.

The response is about a factor of 100 above the requirement. Thus any switch-over in electronic units needs to be limited to less than 0.36W.

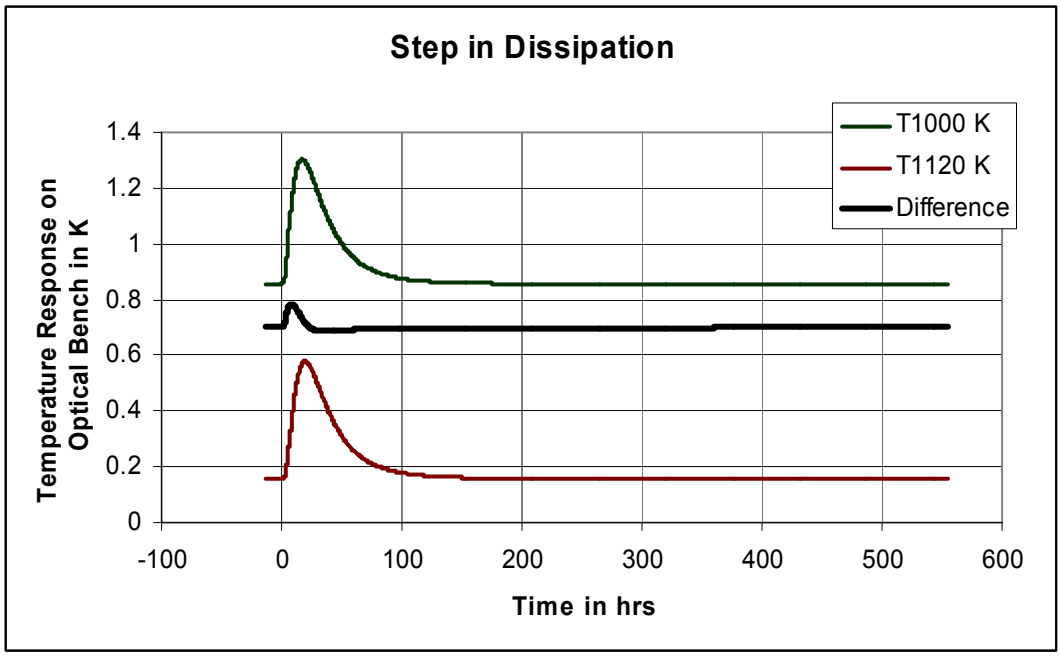

Figure 5.2-19: Temperature response to a down-link event (Temperature scale shifted)

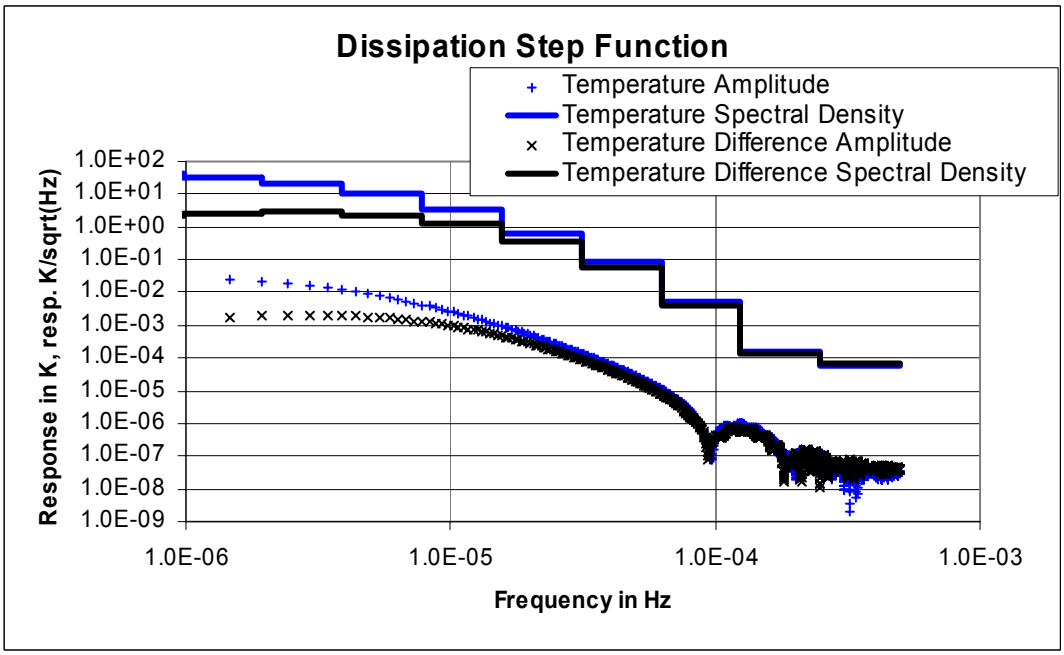

Figure 5.2-20 Spectral analysis of temperature difference response

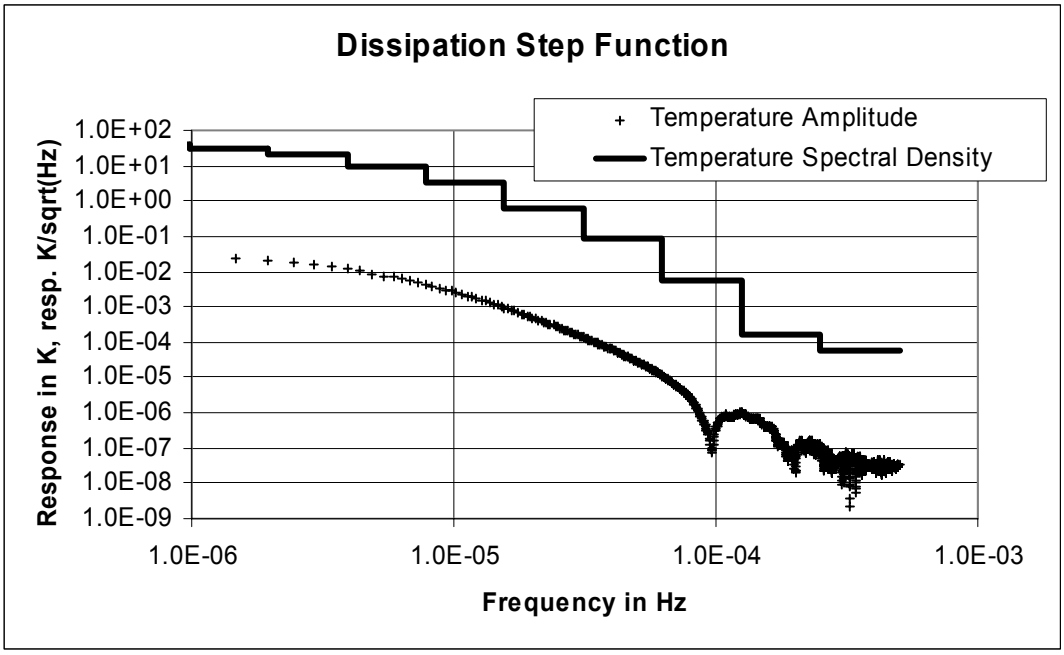

Figure 5.2-21 Spectral analysis of the temperature response of the optical bench

5.2.4.3.3 Verification of thermal performance

Because of the specific thermal design of the science module, the verification of the system will be difficult and has to be investigated in detail at an early stage. For the verification of "standard" thermal requirements the simple environment will allows end-to-end verification by test. However, the extreme thermal decoupling will result in very long stabilisation periods

For the verification of temperature stability requirements test chamber environment will not be sufficiently stable. Also the long stabilisation period will only allow for few parameters to be tested. Therefore the verification has to be performed in terms of transfer functions

Verification of the acceleration noise requirements has at least to be supported by analysis. The acceleration noise calculation needs knowledge of displacements of science module. Anyhow, the structure can only reduce acceleration noise by material selection. TCS has to reduce disturbances from solar constant and unit dissipation fluctuations. From achievable TCS filtering, the upper limit of unit dissipation fluctuations can then be established in terms of dissipation fluctuation spectral density and worst case dissipation profile in time domain. This are then the parameters which can be tested, for all the rest one has to rely on analysis.

5.3 Spacecraft Electrical Subsystems

The LISA electrical configuration concept is primarily composed of the electrical subsystems on the Science Module and necessary add-ons on the Propulsion Module according to the sketch of Figure 5.3-1:

- the Avionics subsystem which includes the classical Command & Data Handling (C&DH) and the AOCS/RCS; today's Avionics applies an integrated processing system with the C&DH and AOCS software task running quasi in parallel in the so called Control & Data Management System (CDMS, nomenclature of ROSETTA and Mars Express)
- the Ion Propulsion subsystem on the Propulsion Module
- the Power subsystem and the Solar Array with some dedicated parts on the Propulsion Module
- the RF Communication subsystem
- thermal control (T/C) equipment
- and dedicated external and internal functional/electrical interface.

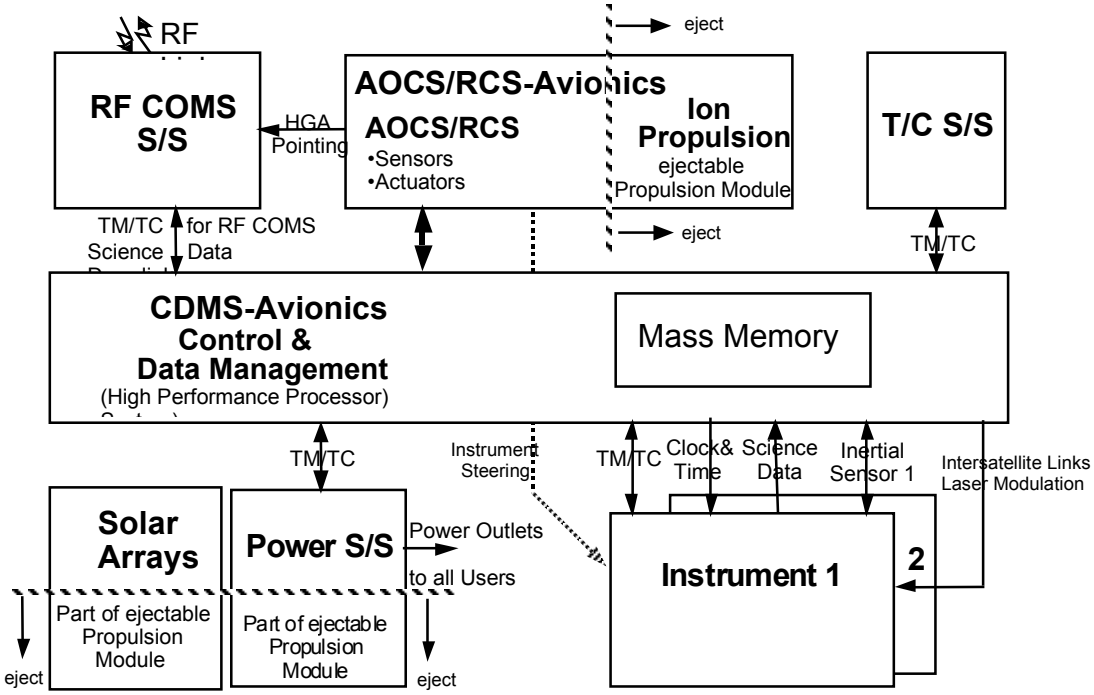

Figure 5.3-1: Survey of Electrical Subsystems

The aim within this study was to define and design a system fulfilling all mission and payload requirements in a reliable, effective way with the heritage of European state off the art subsystems and units, in order to meet the mass, schedule, and cost constraints.

The pre-Phase A Avionics system instead had been designed with US heritage based on the recent Mars missions recurring units with the VME backplane Bus (in the Processing Unit) and high performance RAD 6000 processors.

5.3.1 System Electrical Architecture

LISA specific Functions and Requirements

The electrical spacecraft functions for the LISA mission involve classical subsystem services as well as some interdisciplinary features with the integrated satellite .

Before starting the design of the electrical architecture in a block-diagram, the major LISA functions and features have to be identified. These are gathered in a graphical form in Figure 5.3-2. This figure depicts the main configuration items, major internal and external interface, and the major processor control tasks, indicated in the respective colours which are applied for the subsystem discipline (green for C&DH, reddish/brown for AOCS/RCS, and yellow for the Instrument). For Phase A2 an early decision has been made to aim for a centralised processor system (CPS) for the accommodation of the S/W tasks for C&DH, AOCS, and Instruments because of the necessity for complex integrated control.

The LISA specific functions are:

- Attitude and orbit control with chemical propulsion and ion propulsion for LEOP and cruise phase; both propulsion systems will be installed on the propulsion module; if ion thrusters are mounted on optional gimbals the chemical propulsion could be deleted
- FEEPs for coarse acquisition after separation of the propulsion module, and for fine pointing during nominal operations phase;
- In this nominal operations phase the Instrument Inertial Sensor (Proof Mass) and the additional elements for instrument control (telescope pointing, fibre positioning) and spacecraft control are to be combined in close control loops to serve for drag free attitude control and undisturbed science data measurement.
- telemetry (HK and science data), tracking, and commanding in X-band with DSN 34 m antenna
- accommodation of two high or medium gain antennas with 1 DOF to rotate +/- 180°
- providing external and internal umbilical/harness for the stacked composites on the Launcher which shall allow for soft separation of the propulsion modules from the Science Modules
- the power and energy concept only needs stored energy (from battery) during LEOP, the cruise phase, and the turning of the stack before separation of the propulsion stage; thus the battery is only proposed to be accommodated on the Propulsion module (Safe Mode of the Science Module later is sun pointing of the SA, beyond that the Power subsystem will always safely start-up when the solar generator will be illuminated by the sun)
- the functional interface between the Central Processing System and the instruments, as there are sensor raw data acquisition, instrument sensor & actuator control, synch. interface, and inter-satellite communications data.

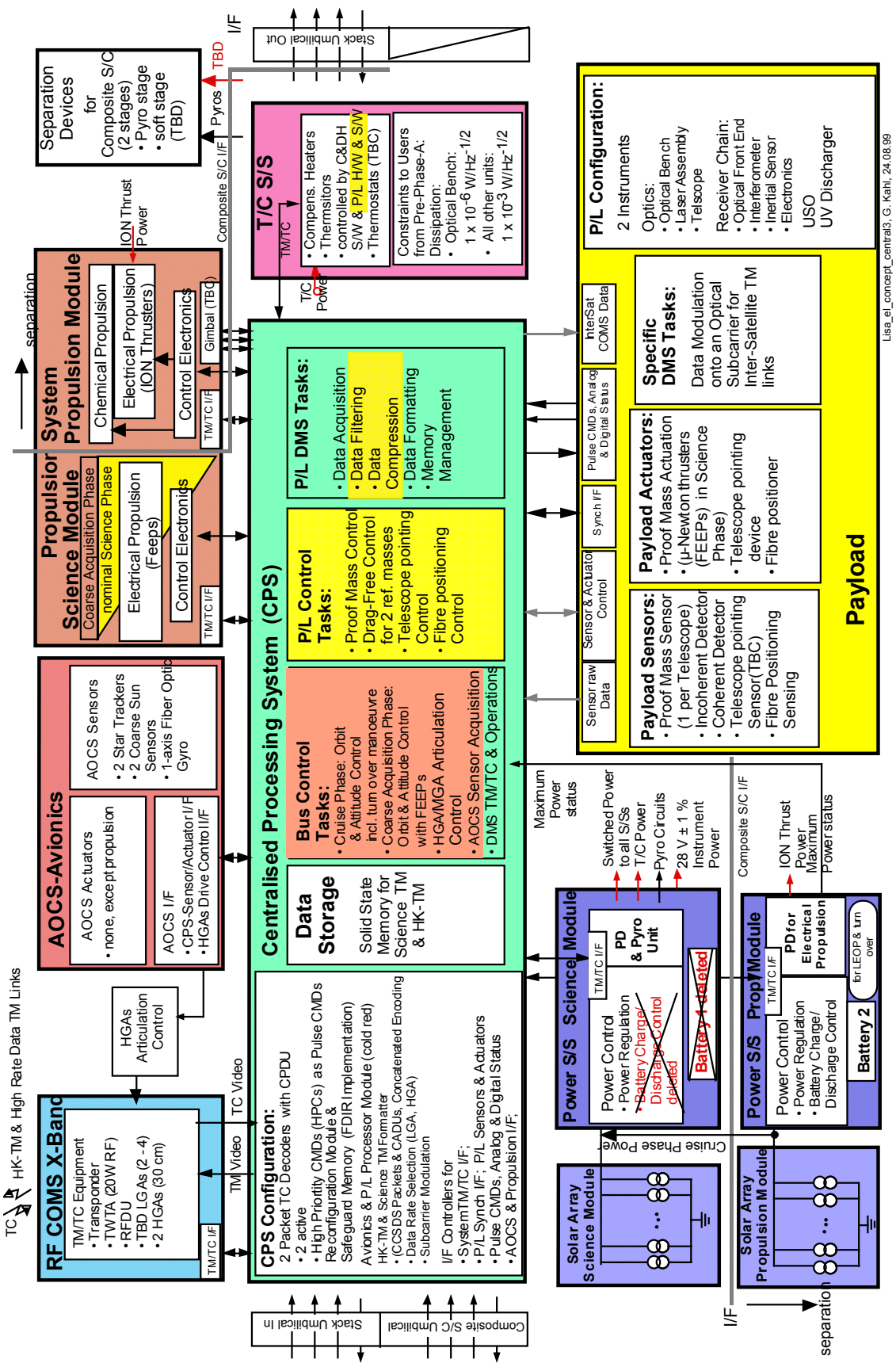

Figure 5.3-2: Functional/Electrical Concept with Centralised Processor System

Conceptual Design

The electrical service functions have to be allocated to units with a minimum of overhead to serve the stack of Science and Propulsion Modules as well as the separated Science Modules during the Nominal Mission Phase.

Figure 5.3-3 gives the proposed allocation of units to the electrical subsystems and the interconnecting interface. This concept is closely oriented to state-of-the-art ESA electrical design concepts of today's scientific satellites, but also respects the specific functions of the previous section. The centralised processor system runs the DMS tasks, AOCS tasks, and Instrument tasks with the estimated processor loads as indicated in the figure, instrument tasks run only on the Application Layer.

The applied background colours correspond with the allocation of responsibilities and competence (H/W tree), design, for cost estimates in the early phases , and later-on for procurement.

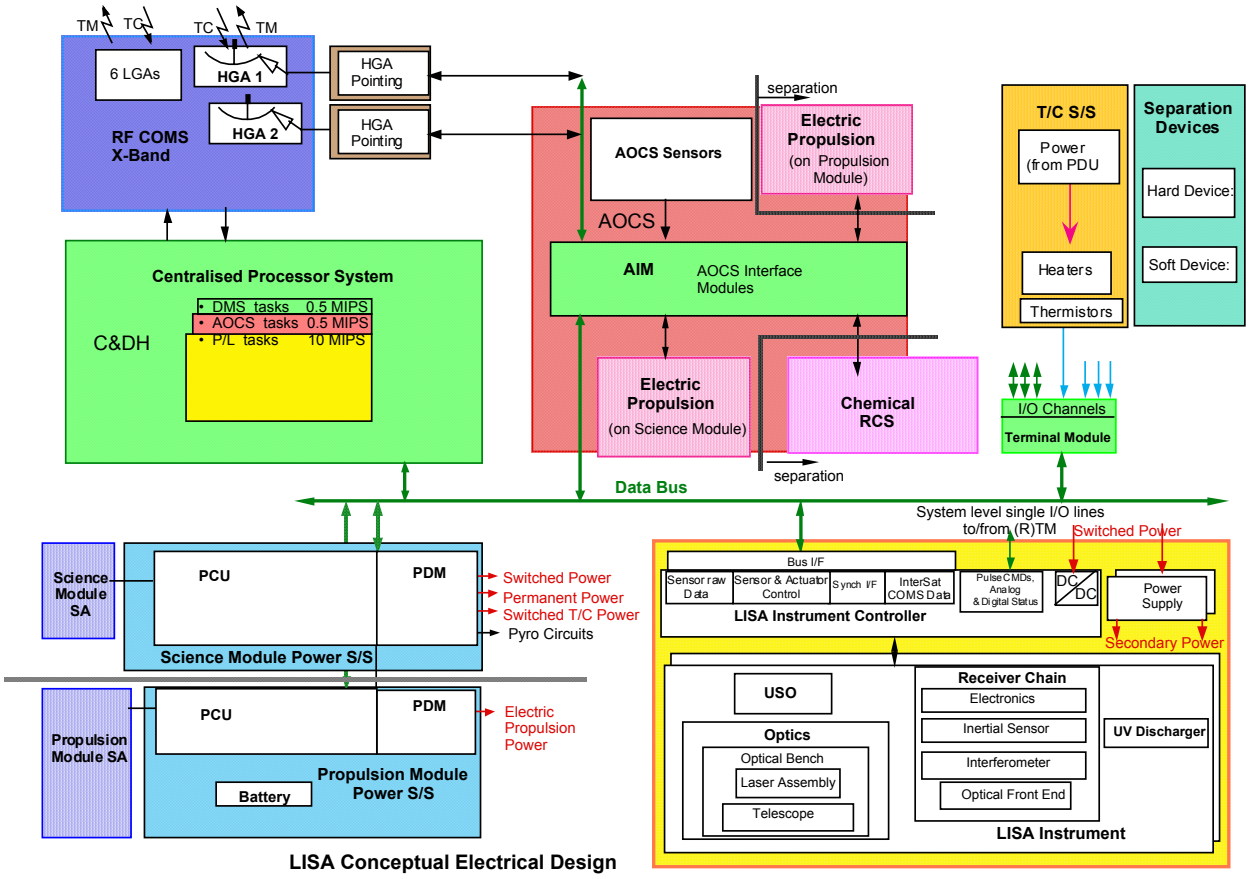

Figure 5.3-3: Conceptual Electrical Design

The baseline design is the implementation of the functional breakdown into an architecture. This is depicted in Figure 5.3-4. It is composed of state of the art subsystem designs for ESA spacecraft and comprises the following functions:

- The avionics system comprises the classical Command & Data Handling System (C&DH) and the AOCS sensors and actuators electrical interface. The avionics system is applying an integrated avionics processor system sharing the processor for the C&DH, the AOCS/RCS, and the Instrument tasks. To ease the graphical lay-out the green AOCS interface module and the (Remote) Terminal Module are drawn separately from the CPS but in the baseline design they are embedded

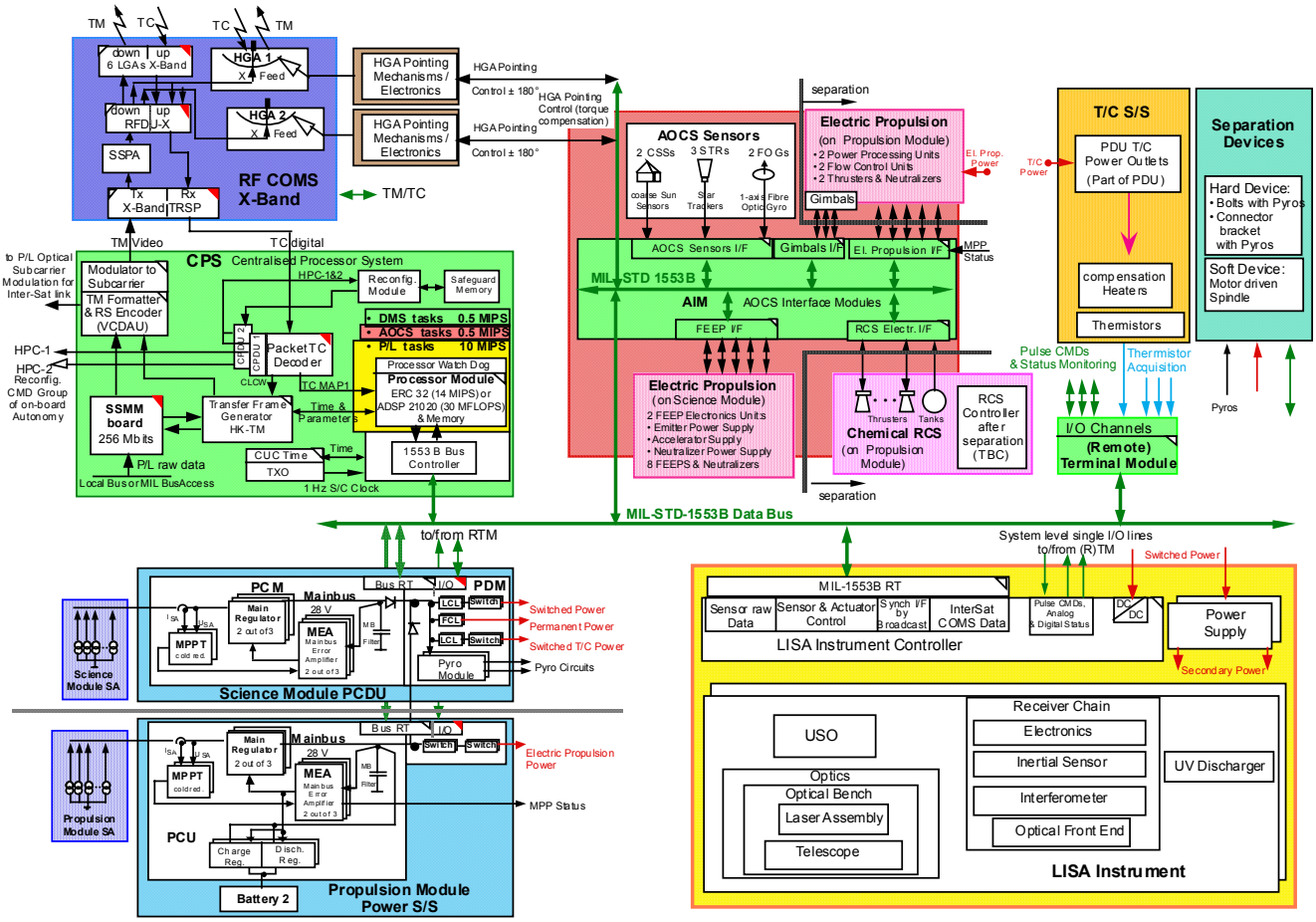

Figure 5.3-4: Functional/Electrical Architecture

- The power discipline is realised by two sets of Power Conditioning and Distribution Unit (PCDU) and solar array, one set for each of the two modules. The battery is accommodated only on the propulsion module. The PCDU and the solar arrays are designed for the selected power control concept (PPT).
- The RF communication system is an X-band system with two transponders at 5 W RF power outlet. Six low gain patch antennas provide a quasi-omnidirectional coverage in LEOP, Cruise and Safe Modes. 2 HGAs (1 DOF) compensate the torque disturbances when rotated. Only one HGA will be active at a time in nominal science phase. A Radio Frequency Distribution Unit (RFDU) performs the selection of the transmitting antenna.
- Thermal control electrical items are the heater mats, thermistors, thermal control power outlets in the PCDU for survival heater power switching; nominally the temperature control is performed via software controlled circuits.
- The interconnecting medium is the serial MIL-STD-1553B data bus.
- The satellite operations interfaces will be applied via the Command and Data Handling System (C&DH) of the avionics system and will be based on the ESOC SOIRD (S/C Operations Interface Requirements Document).

5.3.2 Electrical Power Subsystem

Major Requirements:

- According to the strong requirements on AOCS control stability, very low electromagnetic* and thermal disturbances shall be generated by the Power subsystem.
- The solar panel shall not generate temperature gradients during the measurement phase, which requires a SA power control scheme, that exploits the SA power homogeneously but not in switched strings or sections.
- The battery shall generate low magnetic momentum*, magnetic materials shall be omitted as far as possible.

*the initial stringent requirement for low magnetic momentum was the design driver but has been 'provisionally' relaxed, refer also to the EMC section.

The Power subsystem and the solar arrays shall comply with the calculated total power demand of Table 5.3-4.

Power Design:

Based on the discussion of the power concept of section 4.2 the Electrical Power Subsystem (EPS) architecture is selected as given in Figure 5.3-5.

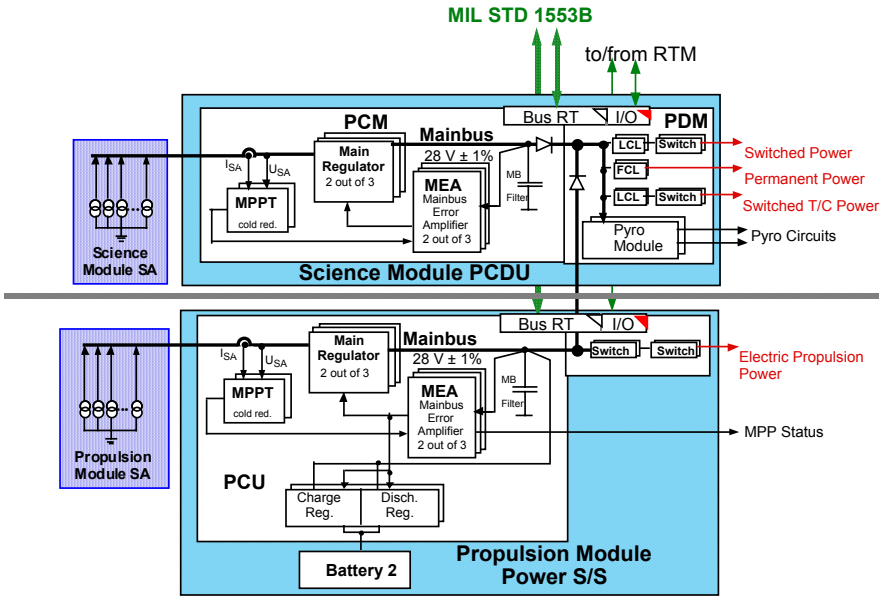

Figure 5.3-5: Power Subsystem Block Diagram, baseline

EPS Units:

- Science Module Solar Array
- Propulsion Module Solar Array
- Power Control and Distribution Unit (PDCU) with Maximum Power Point Tracker (MPPT), Main Regulator and Main Error Amplifier (MEA), one of these on each of the modules
- Power Distribution of the Science Module with a Pyro Module

- Battery of Li-ION type; charge and discharge regulators are located in the PCDU of the Propulsion Module.
- The MPPT builds a closed control loop with power regulators of the buck converter type, which transfer the SA power into a 28V regulated main bus voltage. During LEOP and the cruise phase the SA and/or battery power of the Propulsion Module is transferred to the main bus of the Science Module. For separation of the composites after cruising this power path shall be disconnected at zero current flow to avoid potential connector welding by arcing.
- Main bus voltage regulation, performed by a 2 out of 3 hot redundant voltage controller, including the main error amplifier (MEA), which delivers the control signal of the primary power control loop, built by SA power regulators - only on the Propulsion Module together with the battery charge and discharge regulators (BCR and BDR).
- The primary power distribution interface to the users must be designed that no single failure at a distributed power line can lead to a permanent shutdown of the main bus. The PCU power bus (on both modules) recovers automatically from any shutdown transition if the cause of it is disappeared.
- The PCDU will be designed such that it safely starts up when it receives power from the SA. Battery charging and survival heating shall not prevent the PCDU from start up capability, even when the battery is fully discharged.
- The EPS is monitored and controlled by the Data Management System (DMS) via a serial data bus and discrete command lines from the (Remote) Terminal Module (RTM).

The following table give the detailed figures for mass and dimensions of the PCDUs on the Science Module and the Propulsion Module.

Table 5.3-1: Science Module PCDU Mechanical Characteristics

Module	Mass / g	No	Total Mass / g	Module Width / mm	Length / mm	
Input Module	1250	1	1250	50	50	MB-Filter 800u, 2 Batt-relay, 2 Curr. Sensors, 2 D*M 25 pins
SAR Module PPT-400W	900	2	1800	50	100	2 Power Regulators 400W, 1 of 2 redundant
LCL Module	530	2	1060	25	50	2*8 Instrument outputs
Heater - LCL Module	560	3	1680	25	75	3* 8 Heater outputs LCL + Switch
FCL Module	500	1	500	25	25	8 Current Limiter outputs
Pyro Module	680	2	1360	25	50	2 * 8 Pyro Outputs (2 * Arming-Relay, Fire)
Auxiliary Supply	650	1	650	25	25	Dual-Supply 2*6W, 2*DxM
I/F Module	440	2	880	25	50	MIL STD 1553 I/F
HK-stage MEA, PPT	540	1	540	25	25	MEA, PPT , HK-acquisition (M+R) 2*DxM25
Housing	2700	1				
Total Mass			**12.42 kg**			
Dimensions:			**H x W x L (mm x mm x mm) 203 x 204 x 450**			

Power Design Option:

The Electrical Power Subsystem (EPS) architecture of Figure 5.3-6 is given as a compromise with some advantages for the power discipline (mass and cost reduction) but also disadvantage on system level for thermal aspects.

The initial reason for a separate SA on the propulsion module has been the initially smaller area of the Science Module SA because of its location in the cone of the fairing. The constraints of the Launcher CoG reduced the height of the Propulsion Module and caused the upside down orientation of the composite stack on the Launcher, thus the area of the Science Module SA increased to 5.7m².

Deleting the SA on the Propulsion Module would demand for a complete lay-out of the Science Module upper plate with solar cells which does no longer allow to optimise its thermal control with second surface mirrors.

Table 5.3-2: Science Module PCDU Mechanical Characteristics, minimised option

Total Mass	**15.07 kg**
Dimensions:	**H x W x L (mm x mm x mm) 203 x 204 x 550**

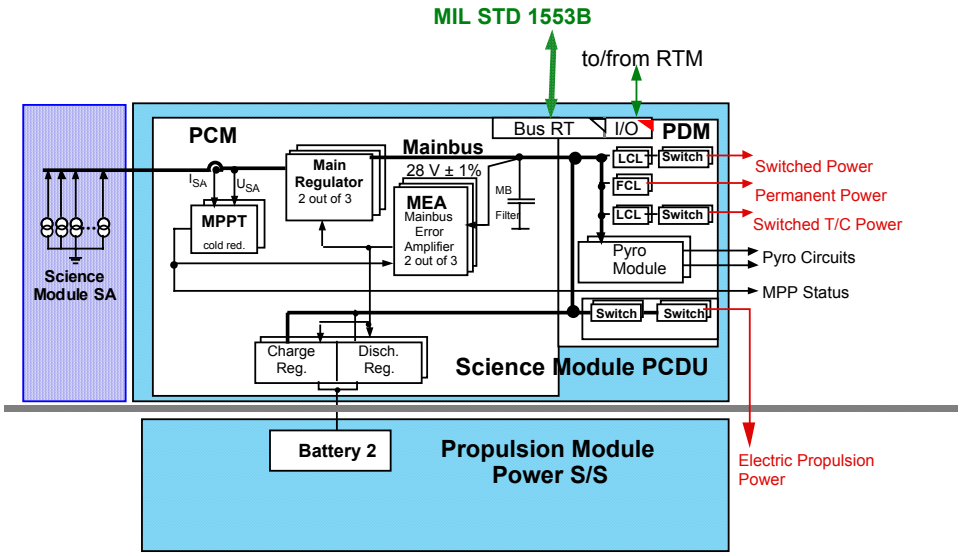

Figure 5.3-6: Power Subsystem, minimised option

Solar Array:

The solar array of the Science Module under normal operating conditions is orientated to the sun under an aspect angle of 60°. In order to cover the maximum bus power demand of 315W any type of solar cells could be applied for this Module. Table 5.3-3 is listing the major parameters for standard GaAs and triple junction GaAs cell designs. In a common procurement with the solar array of the Propulsion Module the triple junction GaAs cells are baseline.

There remain large areas for the application of Second Surface Mirrors for thermal design on the Science Module SA and to add SA strings from redundancy reasons (one failure tolerance at minimum). The minimum cell area must be 1.9 m² (without string redundancy).

Each of the SA string is terminated with a protective diode to avoid propagation of short-circuit failures into the power system.

Table 5.3-3: Potentially Available SA Power at EOL

Parameters	Science Module	Science Module
Available Area / m²	5.7	5.7
Applied GaAs cells	standard	triple junction
Efficiency of cells at 28°C	18.3%	24.5%
Temperature Coefficient	0.19%/K	0.25%/K
Array Temperature /°C	70	70
Efficiency at ops temperature	16,84%	21.93%
Solar Aspect Angle	30°	30°
EOL	10 years	10 years
Required Power (SA area)	315 W	315 W (1.9 m²)
Available SA Power at EOL	**837 W**	**950 W**

Power Degradation: 2.75% per year, as for GEO application assumed for both types of cells

Table 5.3-4: Detailed Power Budget with Power Demand of the Solar Arrays

Sub-System	NO.	Unit Name	Ops Power / unit	No. of operating units	Average	Contin-gency factor	Gross Total Science Module	Gross Total Propulsion Module
			[W]		[W]		[W]	[W]
AOCS	1	Star Camera Assembly	7,6	1,0	7,6			
	4	Coarse Sun Sensor	0,2	0,0	0,0			
	1	Fibre Optical Gyro Unit	12,0	1,0	12,0			
	2	HGA Drive	2,5	2,0	5,0			0
		AOCS				0,10	**27,1**	21,6
Instrument	2	Laser Assembly	5,0	2,0	10,0			
	2	Laser Phase Modulator	6,0	2,0	12,0			
	2	USO	0,6	1,0	0,6			
	2	UV Discharger	3,0	2,0	6,0			
	2	Interferometer:						
	2	optical bench	4,5	2,0	9,0			
	2	electronics box	11,9	2,0	23,8			
	2	DHU	10,0	2,0	20,0			
	2	Inertial reference EL.	5,0	2,0	10,0			
	2	LISA Instrument Controller	8,0	1,0	8,0			
	2	***Instruments total***				0,25	**124,3**	0
Power	1	PCDU Basic Power	6,0	1,0	6,0			
		Battery trickle charge						5
		Power Subtotal				0,10	**6,6**	6,6
CDMS	1	Centralised Processor	23,0	1,0	23,0			
	2	Solid State Mass Memory	2,0	1,0	2,0			
		OBDH Subtotal				0,10	**27,5**	27,5
RF COMS	4	LGA X-band						
	1	RFDU	1,0	1,0	1,0			
	2	Transponder X-band	5,0	2,0	10,0			
	2	HGA X- band		1,0	0,0			
	2	modulator in TRSP	2,0	1,0	2,0			
	2	SSPA (5W RF power)	30,0	1,0	30,0			
	1	WG, Switch,Cabling		1,0	0,0			
		RF COMS Subtotal				0,10	**47,3**	47,3
FEEPs	2	FEEP Electronics	8,0	2,0	16,0			
	3	FEEP Clusters	2,8	3,0	8,4			
		RCS Subtotal				0,25	**30,5**	
Propulsion	1	Electric Propulsion						
		Propulsion Subtotal	***588,00***			0,15		676,2
Thermal		S/S thermal stabilisation						
		Instrument						
Total Power required							**263**	**784**
PCDU load depend. losses & harness : 8%							23	68
Module power							**286**	**852**
		System Margin				0,10		
SA Power demand							**315**	**938**

5.3.3 Command and Data Handling/Avionics

As depicted in Figure 5.3-7 state-of-the-art Control and Data Handling systems also serve the interfaces to the AOCS/RCS sensors and actuators and run the C&DH and the AOCS software in their common processor system. For these systems the expression 'AVIONICS' is well established.

For LISA the Avionics System also has been envisaged to run the instrument specific S/W to ease the integrated scientific control applications. Thus a 'Centralised Processor System' is a LISA specific item.

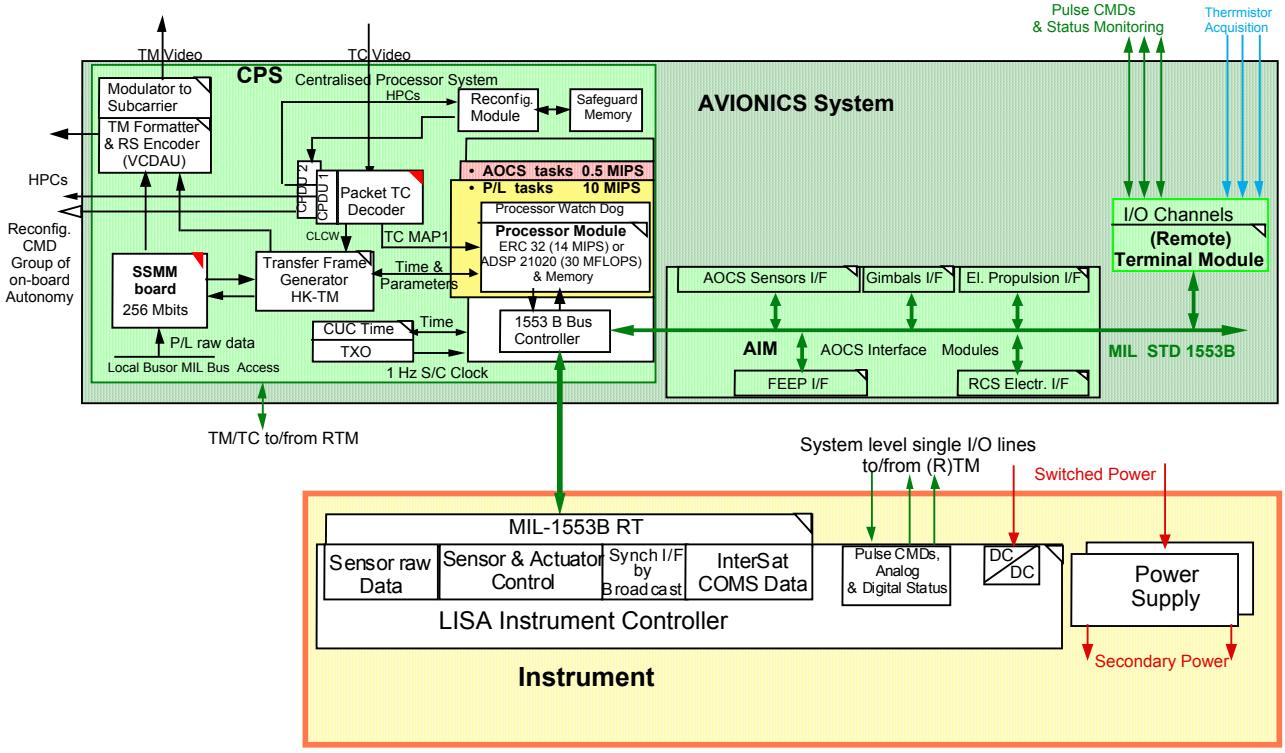

Figure 5.3-7: Avionics System with Interface to Instrument

The functional interface with the instruments which will serve for

- Sensor raw data acquisition
- Sensor and Actuator Control
- Synchronisation
- and Inter-Satellite Communication Data transfer.

will be implemented via the MIL-STD 1553B data bus and a specific simple LISA Instrument Controller.

LISA Instrument Controller:

Proposed definition of general tasks and implementations:

- Acquisition of instrument raw data and formatting into CCSDS Source Packets
- Monitoring and reporting of all instrument modules/units (HK-TM acquisition, formatting to CCSDS Source Packets and distribution to system DMS, i.e. the CPS)
- Serving all instrument sensors and actuators on their lower OSI layers - as Data Link and Physical Layer (ISO/OSI 7 layer structure as reference); the Application Layer (e.g. complex control algorithms for drag-free control) are processes in the CPS

- Timing Synchronisation, e.g.1 Hz clock via MIL-Bus Broadcast correlated to S/C elapsed time (in CCSDS Unsegmented Time Code (CUC)), if necessary a dedicated TBD MHz clock for sub-seconds counts at high resolution could be amended.
- Inter-Satellite Communication data will simple be identified according to their Application Process ID.

The LISA Instrument Controller is proposed to be designed of one single cold redundant unit. It shall incorporate for each redundant path:

- 1 Processor board with a rather simple controller, baseline could be 80C32 (radiation tolerant design, Temic), ROM, EEPROM, and RAM on board
- 1 interface board with ADC for analog status and thermistor acquisition, a set of pulse command outlets, detector telemetry I/F: 1 serial IEEE 1355 link (link performance ca. 100Mbps) or optionally RS 422 I/F with UART (link performance ca. 10 Mbps for 10 m cable length) to the dedicated data electronics, a set of digital status acquisition lines and the System interfaces MIL-STD 1553B RT, Clock and Time synch. I/F
- 1 DC/DC converter.

5.3.3.1 AVIONICS System Design

The proposed avionics design for the Centralised Processor System (CPS) is based on an Integrated Platform Computer (IPC) named LEONARDO.

LEONARDO (LEo On-board Novel ARchitecture for Data handling) is a novel Integrated System especially suited for small and medium size satellite.

The CPS gathers, in a unique mechanical box, Command, Data Handling, Attitude and Orbit Determination/Control and Housekeeping capabilities, with great advantages in terms of compactness. A local Solid State Mass Memory module can also be included In the same housing.

The CPS is based on an internal modular fault tolerant architecture employing fast internal serial lines (IEEE- 1355 DS-link/"Spacewire") for communication among the various modules. A MIL-STD 1553B bus is adopted as a main avionics system bus and also internally to transfer data between the Processor and the peripheral I/O modules.

CPS Description:

The CPS is the core of the Satellite avionics and includes in the same box the typical Data Handling (DH) and Attitude/Orbit Determination and Control (AOC) functions.

For this purpose it interfaces:

- The S/C subsystems via MIL-STD-1553 bus and discrete TM/TC channels
- The AOCS sensors and actuators via either MIL-STD-1553 bus or dedicated specific interfaces
- The Payload via MIL-STD-1553 bus and discrete TM/TC channels
- The TT&C and RX Payload for Ground Telecommands processing and execution and for sending Telemetry to Ground.

LEONARDO hosts a dual redundant electronics.

Normally the main modules are switched on (except the TC decoders that are both powered on). In case of failure the redundant module can be switched over independently from the other modules: a full cross-strap is in fact implemented within the unit to allow any module to exchange data with all of the others. Moreover the unit is conceived in such a way to allow switching on both redundancies at the same time (for emergency or diagnostics reasons).

Figure 5.3-8 shows the block diagram of the proposed Integrated Platform Computer.

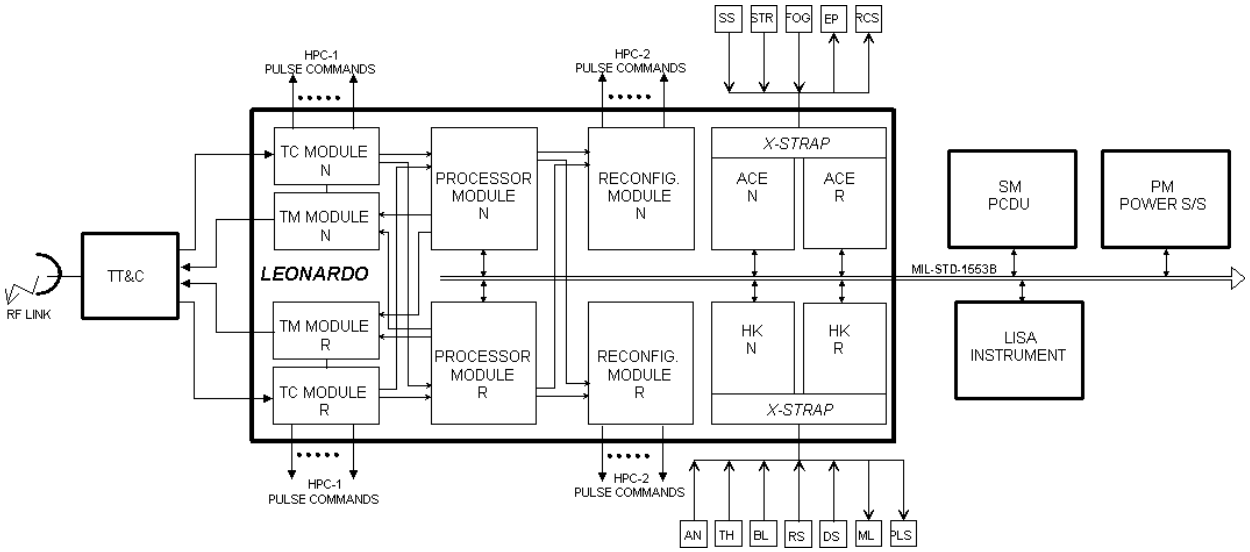

Figure 5.3-8:Centralised Processor System(LEONARDO) Block Diagram

The CPS basic modules are:

- *TC Module* implementing a fully compliant ESA PSS-04-107 Packet Telecommand Decoder : Video BPSK or digital input interfaces towards TT&C Receivers and EGSE, telecommand video BPSK stream digital demodulation, single ASIC Telecommand Decoder Core functions including internal standard Authentication Unit and Command Pulse Distribution Unit logic. Moreover, High Priority command pulse drivers, MAP demultiplexing and distribution interfaces are housed in the same module.
- *TM Module* implementing a fully compliant ESA PSS-04-106 Telemetry Generator providing on the same module up to 4 Virtual Channels, Virtual Channels multiplexing, Telemetry formatter and Telemetry Interfaces towards TT&C Transmitter and EGSE. Essential telemetry generation HW is also provided.
  The Reconfiguration Module is connected to the nominal and redundant Processor Modules through DS-Links IEEE-1355 ("Spacewire")
- *Processor Module.* The Processor Module is based on an ERC-32 single chip microprocessor (TEMIC TSC695E), which implements SPARC V7 architecture. The Processor Module features 17 Mips / 3.4 Mflops @ 24MHz. Thanks to this performance it is possible to execute on the same Processor Module the classic Data Handling tasks, Attitude/Orbit Control tasks as well as Payload specific tasks with great advantage at system level in terms of mass and power consumption. The Processor Module comes with Start-up/Boot PROM, Application SW EEPROM and SW Working SRAM (the

latter two SED/DED EDAC protected).
The following Interfaces are foreseen: serial MAP I/F's toward TC module; 6 IEEE-1355 DS-Links towards TM / RM modules. Figure 5.3-9 shows a block diagram of the Processor Module.

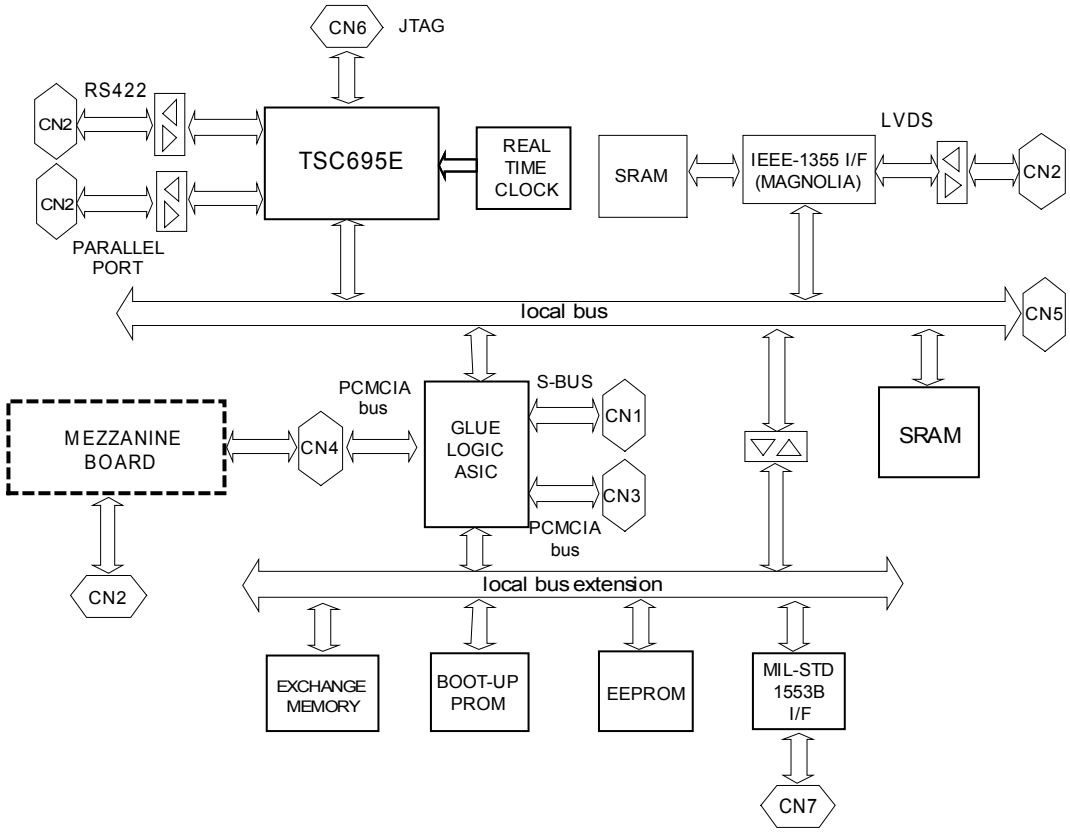

Figure 5.3-9: Processor Module Block Diagram

- Reconfiguration Module. The Reconfiguration module gathers all of the functions pertaining to Failure Detection Isolation and Recovery (FDIR). In details, it provides: the Reconfiguration Function, the Protected Resources, the On Board Time counter, the Reconfiguration Commands logic and drivers. The Reconfiguration Module is connected to the Nominal and redundant Processor Modules through IEEE-1355 DS-Links.
- Attitude Control Electronics (ACE) Module. The ACE module is in charge of interfacing the AOCS actuators and sensors. It provides functions for AOCS command distribution/actuation and data acquisition. The ACE module can support the LISA AOCS Sensors: Sun Sensors, Star Trackers and Fibre Optic Gyros (in case they request particular interfaces different from MIL-STD-15553B). The Propulsion Actuators (FEEP as well as Chemical propulsion systems) are also supported. This module interfaces the Processor Module via MIL-STD-1553B data bus.
- Housekeeping Module. The PF-HK module interfaces the MIL-STD-1553B data bus and collects standard acquisitions and distributes standard commands from/to external users, implementing the classical OBDH Remote Terminal Unit (RTU). Acquisition interfaces include: Analogue, Digital Bi-

level, Relay status, Digital Serial and Thermistor channels; commands interfaces are for Digital Memory Load and for discrete Pulse Command. I/O Interfaces are ESA TTC-B-01 compliant.

LEONARDO heritage and future improvements:

LEONARDO has been developed for the Italian standard satellite platform PRIMA, intended to be mainly exploited for small/medium class satellites (<1000 kg) carrying either Scientific or Earth Observation Payloads.

Every module is implemented on the basis of the LABEN experience in designing On Board Electronic equipment: most of the proposed electronics is inherited from existing hardware already flown or installed on current space programmes.

The Processor Module is an evolution of the one developed for the Italian Star Tracker which will fly on board the SAC-C satellite. TM, TC and Reconfiguration modules largely take into account the experience gained on Cluster/XMM/Integral CDMU's. The Housekeeping I/O Standard (Analogue, bi-level and digital channels, discrete Pulse commands) are based on the above programmes Remote Terminal Units (RTU's), while interfaces towards actuators and sensors are based on ARTEMIS Remote Unit A (RUA) which has been designed to support command and control of Propulsion System, Reaction and Momentum Wheels, Gyros, Earth and Sun sensors.

Although the present LEONARDO design is based on state-of-art technology with large use of VLSI's (ASIC) and hybrid modules, it can be argued that, considering the schedule of LISA development, new technologies will become available to the space market. This will allow further improvements in terms of compactness, mass, power consumption, capability and processing performances. Some already foreseen expected improvements are for instance:

- 3.3V digital families, improving power consumption of the logic electronics
- Memory density, allowing to host the requested Mass Memory capacity (256 Mbits) by expanding the one already present on the Reconfiguration Module (currently 64 Mbits)
- Increased adoption of MCM (including 3D) and "system on chip" technology
- Increase of the processing power adopting the forthcoming SPARC V8 which is being developed by ESA

H/W Budgets:

The following budgets have been estimated for the LISA CPS:

- Mass: 15.9 kg
- Dimensions: 410x243x185 mm (LxWxH) (410x275x190 including mounting feet and connectors)
- Power consumption: 25 W (average)
-

5.3.3.2 Software Design

A reference software layout of the Command & Data handling and AOCS/RCS systems is proposed to be composed out of three layers:

1. Basic Software
2. Standard Application Software
3. Mission Specific Software

The general functions and their implementation are described in Table 5.3-5. The standard application software will basically comprise the following functions:

- TC Handler, TM Handler, Time Tag Buffer Handler, HK Monitor, History Monitor, TM Transfer Frame Generator, Instrument data formatter (VCDAU) Handler, S/W Reporter, DMS serial links Handler (IEEE 1355), Data Bus Control Handler (MIL 1553B), CDMS/Avionics Processor Unit Control, SSMM File Handler, SSMM Patch/Dump Handler (back-up for failure analyses), PT to PT Communication Handler via MIL-1553B Data Bus), Time Synchronisation Service

The mission specific software is decomposed into its major constituents servicing the instrument and the individual subsystems (services in this sense are functions not provided by the Standard Application S/W package). It contains the mission specific criteria and nominal operational cases for which OBCPs are selected and initiated. In addition, it comprises

- System Nominal Autonomous Control (allowing an unattended operation of TBD hours)
- High level Anomaly Control, Anomaly Procedures Execution
- Macro Procedures Execution
- Power S/S Control Service
- Thermal Control Service
- C&DH Control Service
- Instrument Service
- RF communication service for TT&C and Science Data downlink
- Inter-Satellite Laser link communication

Including AOCS/RCS mode management, attitude & orbit control and orbit maintenance during LEOP and Cruise, and drag-free control during the science phase..

Table 5.3-5: LISA Software Layers:

Layer	Functions	Implementation
Basic S/W	1. Processor dependent basic operating system functions 2. Real time execution environment 3. Services for the non-basic software 4. Interface Drivers	5. is VxWorks (for the ERC 32 processor) which is a commercial operating system offering all necessary software development tools available
Standard Application S/W	6. Implementation of mission operational interface requirements based on ESOC's SOIRD (handler software) 7. AOCS and RCS equipment handlers	8. Proposed by On-Board Control Procedure language (OBCP)
Mission Specific Service S/W	9. Implementation of services not provided by standard application S/W e.g.: 10. System nominal autonomous control (tbd h autonomy) 11. CPS applied instrument service functions and 12. Laser inter-communication service 13. AOCS / RCS software for mode management, navigation, drag-free control etc.	14. To reduce S/W development costs, goal is to implement majority of functions by already existing modules in lower layer software

5.3.3.3 Data Budget

Data Acquisition (from Master S/C instruments and also via Laser Inter-Satellite Links), storage, and transmission by LISA Master S/C:

Science data: 14 Variables x 24 bit x 2 Hz = 672 bps (desired from instrument experts)

Auxiliary data TBD, assumed: 3 S/C x 100 bps = 300 bps (minimum)

S/C HK data TBD, assumed: 3 S/C x 100 bps = 300 bps (minimum)

Data Formatting into CCSDS Packets: 5% overhead

Formatting into Transfer frames for play-back: and RS encoding: 15% overhead

Table 5.3-6: LISA on-board Data Rates and Volumes:

Parameter		**Data Rates/ bps Status: Start Ph. 2**	**updated**
Science Data	- raw	1000	**672 (3 S/C)**
	- compressed	200	
Instrument Data (Auxiliary data)		100	**3 x 100**
S/C HK Data		100	**3 x 100**
Total for Master S/C		400	**1272**
CCSDS Packets	into SSMM		**1336**
Transfer Frames factor with RS encoding	during play-back		**(1.15)**
Data Volume	per 48 h	69 Mb	**231 Mb**
Downlink duration at 7 kbps data rate	per 48 h	2,74 h	**9.17 h**

As identified in the table above the required data volume of ca 231 Mb for the 'Mass Memory' is far below 1 Gbits. Its implementation can be easily done with the expansion of the processor memory or the Safeguard Memory. From 2002 the available SSMM boards instead provide a memory capacity of 132 Gbits on a single double-eurobord.

5.3.4 RF Communications

The configuration of the RF Communications Sub-system is shown in

Figure 5.3-10. It comprises two high gain antennas and six low gain antennas connected to a redundant X-Band Transponder by an RF Distribution Unit.

The two high gain antennas are steerable dish antennas of 30 cm diameter, each providing 180° coverage in azimuth. They are mounted on the science module to provide a complete 360° of coverage (refer also to the configuration drawings).

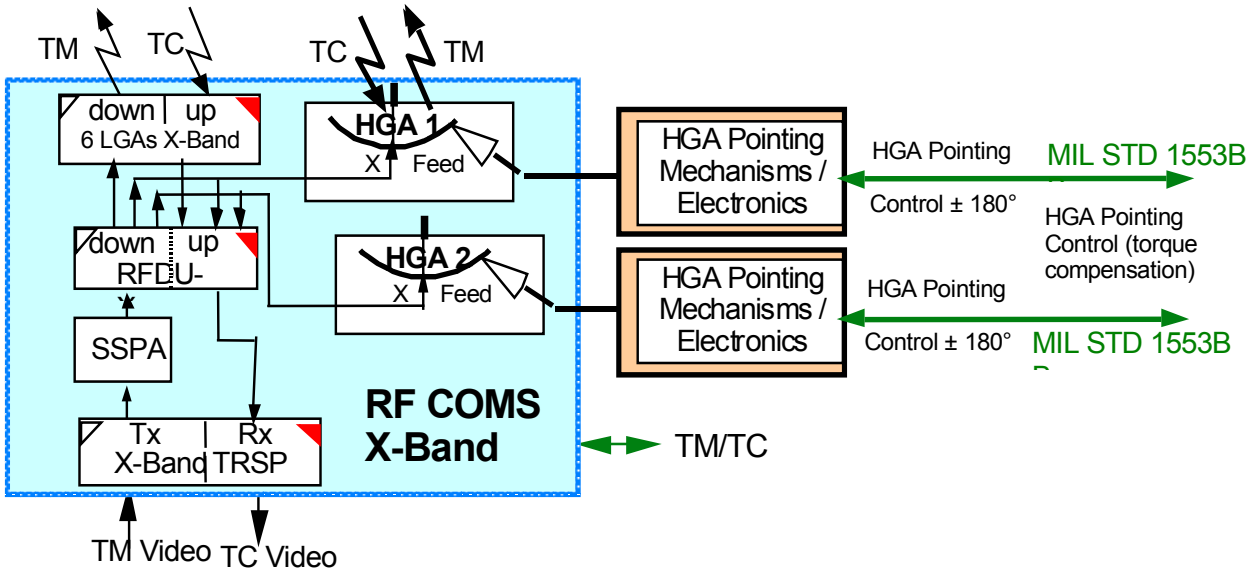

Figure 5.3-10: RF Telecommunications Sub-system Block Diagram

During the operational phase the science module makes a stable 360 degree rotation around its symmetrical body axis once per year. In order to minimise the torque of the antenna to the science module, the antenna drives will be actuated 2 degrees every second day (two minutes motion time assumed). The antenna actuation will be controlled by the AOCS, the disturbance torque is further minimised by moving the antennas simultaneously in opposite directions. The driving motor could be a piezoelectric drive, if the magnetic momentum has to be minimised (refer also to the EMC chapter).

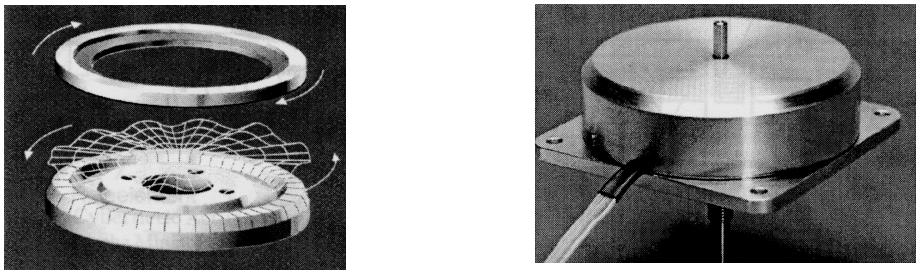

Figure 5.3-11: Piezoelectric Rotary Drive; Concept of Travelling Wave and Example of Design

Each 30 cm diameter dish antenna will have an antenna boresight gain of about 26 dBi and a 3 dB beamwidth of ca. 7 degrees.

The antenna movement is done only in azimuth. The boresight in elevation varies by ±0.5° as shown in the orbit analysis. This gives a pointing loss of 0.13 dB. This loss is respected in the link-budget.

An X-Band Standard Deep Space Transponder (recurring from SMART 1, but without Ka-Tx) with a transmission output power of 5 W is baseline (further enhancement by a 20 W SSPA is an option which would allow to increase the data rate up to 28 kbps and thus reduce the actual downlink transmission time from 9.17 h per two days time intervals below 2.3 h).

Six low gain patch antennas, mounted equidistantly on the spacecraft rim, will provide an quasi-omnidirectional coverage (actually a torroidal pattern around the x axis). If more detailed analysis reveal the necessity for full omnidirectional coverage two additional patches may be adopted into the directions of the main rotational axis.

The RF Telecommunications has two downlink modes, one with high rate to transmit science and HK data in the normal operations mode, another with a 1 bps (at 5 W RF power (or 5 bps at 20 W RF power) low rate for the final transfer phase and for spacecraft health and emergencies. At lower distances for the early mission phases this rate should be increased reverse proportionally to the smaller path losses The DSN 34-m beam waveguide (BWG) station will receive the X-band downlink in both modes and will also uplink X-band commands at a rate of 2000 bps via the HGA.

The high rate X-band link budget is based on the following parameters:

The 7 kbps downlink uses a modulation index of 1.4 radians peak, directly modulating the carrier. The system will employ rate 1/6, constraint length 15, convolutional code, concatenated with the JPL standard Reed Solomon code. The assumed bit error rate (BER) of 10^{-6} requires an S/N of about 0.81 dB. The antenna will have a 3 dB beamwidth of about 6.97°, and a pointing loss of 0.13 dB.(for the boresigth elevation variation of ±0.5). It is assumed the DSN receiver will have a bandwidth of about 5 Hz. With this assumption, the data margin will be > 3 dB and carrier margin will be at least 6 dB. Table 5.3-7 shows these link budget results. Positive link margins (at least the add-on relative to 3 dB) indicate that the BER will be better than assumed for the link budget calculations. As there are presently no dedicated data available for the DSN concatenated encoding scheme from above (rate 1/6, constraint length 15) Table 5.3-1 gives the required S/N ratios for achievable BERs. As indicated an additional 0.1 dB reduces the BER from the assumed 10^{-6} to at least 10^{-7}.

The low-rate (1 bps) TM mode will use six fixed 3 cm low-gain patch antennas (LGAs), each with a 3 dB beam-width of about 67.2°. This link will also use the same coding scheme used by the high-rate downlink. Under these conditions the link will provide a reasonable data margin of 3 dB and a carrier margin of about 6 dB. Table 5.3-7 also shows the link budget results for this case.

For emergency mode and cruise phase communications, that will use the low-rate mode, the spacecraft will be pointed towards the sun and the one LGA facing the earth will be switched active. It will receive TC and transmit the spacecraft HK data to the ground. In the case of total failure of the attitude control system the CPS computer will sequentially switch the antennas in a predetermined way and identify the respective antenna active which will cause a receiver locked signal. Emergency commanding will be done using the 34-m BWG antenna to transmit X-band at 20 kW. In both cases the link is a viable link with reasonable margins.

Table 5.3-7: TM Link Budgets Results:

Antenna	*Band*	*Amplifier*	*Gain*	*Beam*	*EIRP*	*eff. Rate*	*Margin [db]*	
		W	dBi	deg	dBWi	kbps	Carrier	Data
HGA-0.3m	X	5.0	26	7	63	7	8.12	3.12
	X	20.0	26	7	69	28	14.12	3.10
LGA	X	5.0	0	67.2	37	0.001	3.27	3.21
	X	20.0	0	67.2	43	0.005	8.11	3.69

Table 5.3-8: Required E_b/N_0 for different Bit Error Rates (BER) (for ESA compatible links):

Encoding Scheme	**E_b/N_0 at required Bit Error Rates (BER)**				
	10^{-5}	10^{-6}	10^{-7}	10^{-8}	10^{-9}
uncoded	9,6	10,5	11,3	12	12,5
R_S	6,1	6,4	6,6	6,8	7
convol (1/2)	4,3	4,9	5,4	5,9	6,3
concat (1/2)	2,4	2,5	2,55	2,65	2,7

5.3.5 EMC

For LISA a spacecraft design resulting in a moderate to low EMI level is proposed. Areas of particular EMC-concern will be

- Grounding and shielding concept of Science Module and Propulsion Module
- EMI Propulsion module to Science Module
- EMI S/C bus to payload
- RF compatibility (RFC)
- Electrostatic charging / ESD.

The grounding concept shall be Distributed Starpoint Grounding (DSPG) for the entire system with the primary starpoint inside the Science Module PCDU. DSPG requires primary isolation within any unit on both Modules as well as signal interface isolation (basically on the receiver end). To achieve a low EMI environment the shielding concept will include requirements for harness-, box, and panel shielding.

For EMI between Propulsion Module and Science Module no major interference is expected due to the fact that the two modules are not going to work simultaneously during the nominal science phase, ie. the EMI driving science instrument will not work during the transfer phase.

EMI to/from the payload is mainly dependent on the satellite design. No particular EMI precautions shall be foreseen according to the actual design. Nevertheless the special voltage stability which is required in the range of 2.8 to 4 x$\cdot 10^{-6}$ V/$\sqrt{}$Hz for some instrument electronic units (Phasemeter electronic, Front-end electronic, ...), which is required by the thermal analysis, shall not be part of the EMI requirements due to the fact that the voltage stability shall be realised inside each critical unit on secondary voltage level. The required voltage stability shall not be part of the EMI requirements on the power bus. The FEEP thruster system is working at high voltages. The design of the FEEPs and their control electronics shall prevent any radiated emissions EMI.

For Magnetic Cleanliness some analyses were performed. The initial requirement for magnetic momentum of < 3mAm^2 is now provisionally relaxed (Memo form S. Vitale, 25.11.1999: '... there is no specific request for the magnetic momentum of the spacecraft'; i.e. no particular design needs to be established on LISA according to the referenced document. This information is presently to be consolidated from further experts. If this statement will be revised to a strong requirement on magnetic cleanliness again there will be some possible applications with piezo-electrical drives. Presently there are some activities at the ESTEC mechanisms division for the TRP-Plan (2000-2002) for linear and rotary drives and also for piezo-electrical valves.

RF Compatibility (RFC) will be a minor issue because of the two TT&C high gain antennas (X-band Rx and X-band Tx) on every satellite. The antennas will be mounted on top of the science module with the main beam of each antenna in opposite directions. One antenna only is actively used during each mission phase on every satellite. The coupling between the antennas is therefore reduced by the accommodation and orientation of the antennas. Nevertheless the influence of unwanted coupled signals shall be reduced by the design of the RF communication units and an RFC analysis in future design phases.

The electrostatic charging and ESD respectively depend mainly on the satellite design. The S/C will usually charge up negatively due to the space plasma. Space exposed surfaces must avoid high voltage gradients caused by dielectric materials to prevent ESD (S/C body and S/A). The influence of the Ion-Emitter propulsion system on the S/C charging must be investigated. The FEEP thruster system is expected to have no negative influence on S/C charging according to the analysis of ARCS: 'Parameters of the ARCS In FEEP Thruster System', 24./25.10.1999).

5.4 Attitude and Orbit Control

5.4.1 Introduction

The LISA Attitude & Orbit Control System (AOCS) requires a particular attention, since the mission combines a transfer to a deep space orbit (heliocentric orbit 30° behind the Earth), the acquisition of inter-satellite links between very distant spacecraft and finally pointing & translation control with an extreme accuracy during the operation phase. Both, the acquisition of the optical link between the S/C and the Drag-Free and Attitude Control are the major challenges of this mission. But other modes must also be carefully studied, LISA being a deep-space mission with unique features.

All modes up to the Laser beam acquisition will be described in this section. before a detailed study of the most critical ones in the next sections. As the Drag-Free and Attitude Control System (DFACS) is one of the key issue with a direct impact on the scientific performance. This mode alone requires large efforts to be developed, since the targeted acceleration level is smaller than for any other mission, flown or under development.

5.4.2 AOCS Modes

5.4.2.1 Overview

The LISA AOCS modes are presented in the following diagram, with a clear distinction between the "coarse" pointing modes of the transfer phase to the operational orbit and the acquisition & fine pointing drag-free modes after the separation from the Propulsion Module. In the frame of this Phase A, we will focus on the most critical & innovative modes, only a brief description of the more conventional modes is given in the following, with as main objective to identify requirements on sensors and actuators.

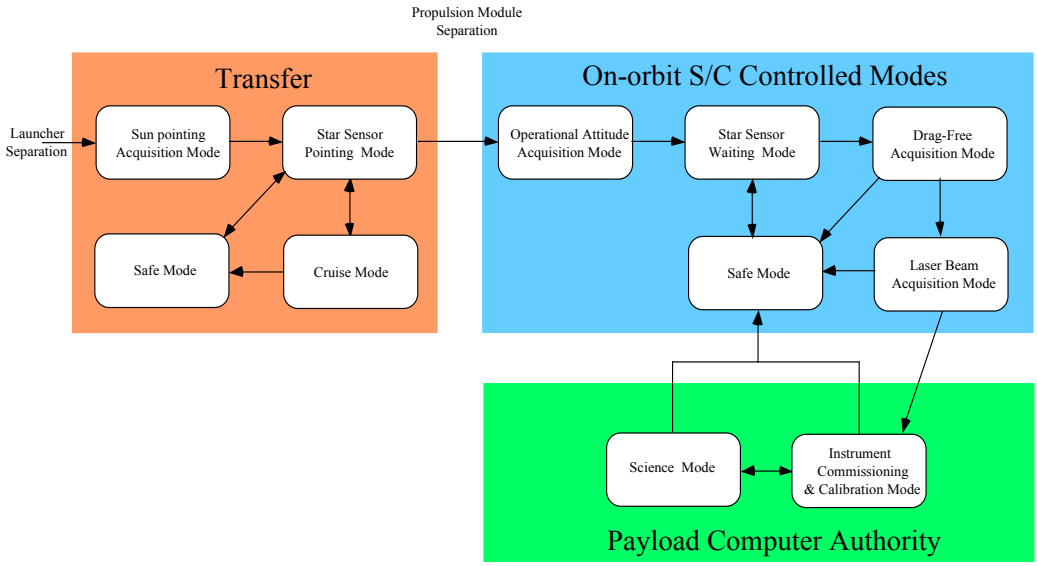

Figure 5.4-1: Diagrams of the AOCS modes

5.4.2.2 Modes during transfer

Sun Pointing Acquisition Mode & Safe Mode (S/M + P/M)

The Sun Pointing Acquisition mode is the first mode to take place right after the launcher separation. Its role is to damp initial angular velocities (due to the separation itself), and then to point the spacecraft Solar Arrays (SA) toward the Sun to provide power and safe thermal conditions. A secondary objective is to allow communication with the ground through correct orientation of the TM/TC. These are also the objectives of the safe mode.

The attitude control is performed in two steps :

- First, through the application of a control torque proportional to the cross-product of measured and wanted Sun vector, to reorient the S/C toward the Sun.
- Then reduce the rate about the stabilised Sun direction to zero.

To perform these sequences, 1-N hydrazine thrusters will be used with full torque authority. For attitude determination, the use of star trackers cannot be baselined for the Acquisition Mode because of the possible high angular rate (0.5°/s typically, and up to 2°/sec for some launchers), and for the Safe Mode for failure isolation considerations. Therefore it is recommended to use two coarse/wide Field Of View (FOV) Sun sensors (one on the Science Module, one on the Propulsion Module) for nearly full sky coverage. This provides in formation around two axes. For sensing the rotation about the Sun line, the baseline is to use a magnetometer. This is adequate for the initial Sun Pointing Acquisition that takes place in the neighbourhood of the Earth, but not for the safe mode which may occur in deep space, where no valuable magnetic information is available. For this mode, where the angular rates will be small enough, it is proposed to use the star sensor, possibly in relative mode for initial rate damping.

Cruise Mode & RCS configuration

The objective of this mode is to perform the transfer from the Earth toward the nominal orbit around the Sun. To reach the operational location (30° behind the Earth ojn its orbit around the Sun), an ion thruster will be constantly fired, S/C attitude being continuously varied to orient the thrust vector according to the navigation profile . The role of the AOCS in this mode is therefore to perform 3-axis attitude stabilisation around the (slow) guidance profile, while ensuring maximum illumination of the solar array.

During this mode, the attitude reference is given by the star trackers (STR). The STR LOS are always at least 70° away from the Sun, and at least one of them is not blinded by the Earth, Thus no star hole is expected provided that the sensor FOV is sufficient (this is actually the case with the baselined wide FOV autonomous star sensors.

The main difficulty in this mode is to cope with the high disturbing torques created by the IPS (Ion ropulsion System) (misalignments of the thrust vector and uncertainty on the centre of mass location). The hydrazine thruster will be used to cancel out these disturbing torques, with possibly the use of tilt mechanism for the IPS. Such a mechanism would reduce the torques, and consequently the hydrazine consumption.

Two cases are then studied to assess the need for a tilt mechanism. In the first case, the IPS is used without mechanism, whereas in the second case, the IPS is mounted on two-axis gimbals.

The hypotheses to calculate the disturbing torques are an IPS thrust level of 18 mN, a bias on thrust direction of 1° (typical of IPS systems like the RIT10), and a centre of mass uncertainy of 15 mm in the X direction (the considered configuration is described in section 2.3).

Without gimbals, the hydrazine budget is **10 kg** for a 450-day transfer (no margin), whereas it would be reduced to less than 2 kg with a 2-axis mechanism (i.e. to compensate for the solar torque only).

Therefore, since the propellant mass saving (typically 5 kg when accounting for the mass of the two gimbals) is small, it is not recommended to implement gimbals, which would add complexity and cost. This point may need to be reconsidered in further stages if the S/C mass budget happen to be critical.

5.4.2.3 Modes after the Propulsion module separation

Sun Pointing Acquisition Mode & Safe Mode

After the separation of the Propulsion module, the pointing of the S/C towards the Sun has to be re-acquired. Quite hopefully, the initial dynamic conditions are much more benign compared to the separation from the launch : the angular rates have been evaluated to 0.03°/sec by DSS. Indeed, the actuators available on the S/M (Sience Module) FEEP thruster, have a very low force authority (20 µN).

The convergence duration is evaluated to 15 min, with a maximum pointing error wrt the Sun limited to less than 5°. Therefore, there is no need for full sky coverage. The single Sun sensor implemented on the S/M (the other is on the P/M) is therefore sufficient . An attractive solution is however to rely on the star sensors, so that the acquisition sequence is greatly simplified (the separation is only a transient within a single stellar mode.

For the safe mode , the same concept could be utilised, with automatic reconfiguration to redundant thrusters and star sensor. The Sun sensor is then used as an attitude anomaly detector, providing separate failure detection & failure recovery means. Using a single mode for Attitude Acquisition and Safe Mode also contributes to high robustness and autonomy with a reduced development effort.

Drag-Free Acquisition Mode

The detailed study of this mode has been left to further studies, since the priority was given to the Science Mode and the Laser Beam Acquisition Mode. However, this mode deserves a specific attention since it is likely to be quite challenging from control point of view. Indeed the rejection ratios required in Science Mode are quite high (100 dB typically), which represent a dramatic reduction of the natural acceleration errors. Progressive reduction of these errors will be necessary to avoid excessive transients (e.g. the Proof Mass (PM) may hit the cage). This is however an issue common to all missions requiring high accuracy drag-free performances, that is generally solved by implementing gain scheduling and transition smoothing filters. A point to be assessed in future phases is the required dynamic range of the sensors involved in the drag-free acquisition process.

The current approach is to perform the drag-free acquisition prior to laser beam acquisition (see the bloc-diagram of Figure 5.4-1). This is however not frozen, since only detailed analysis and design of these transition modes will allow to select the best sequencing of events.

The Laser Beam Acquisition Mode and the Science Mode are studied in details in dedicated sections.

5.4.3 AOCS Electrical Architecture

The block diagram of the AOCS subsystem is presented in the following figure. The majority of the AOCS hardware is part of the S/M, only the actuators specific to the transfer phases (hydrazine thrusters and IPS) are implemented on the P/M. Consistently with the overall avionics layout proposed by DSS, the AOCS is organised in a centralised architecture, an unique data bus (1553 bus assumed) connecting the different sensors & actuators to the centralised computer where AOCS/DFACS software modules for all modes are executed.

The AOCS sensors & actuators are interfaced with the data bus through dedicated interface electronics, with the exception of the star sensors, which generally have direct connections. A single electronics box houses the interfaces with the standard analogue sensors, while FEEP thrusters are interfaced through their specific electronics, to be provided by the manufacturer.

The DFACS also interfaces with the payload, for the acquisition of the telescope pointing sensors (acquisition & heterodyne photodiode detectors), the Inertial Reference Sensor and to drive the telescope steering mechanisms.

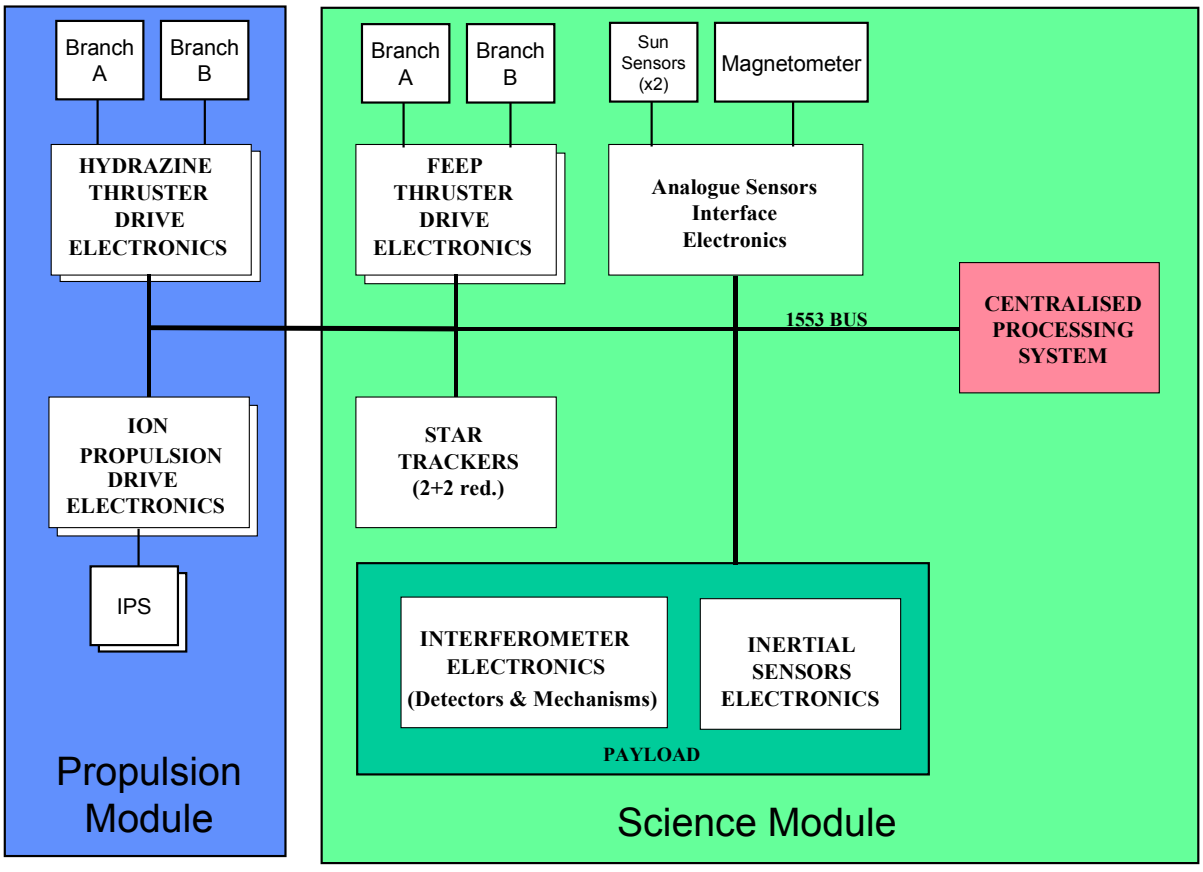

Figure 5.4-2 AOCS/DFACS Electrical Architecture

5.4.4 Reaction Control

5.4.4.1 Propulsion Needs

Three very different propulsion needs are identified for the LISA mission:

- To generate the large velocity increment (up to 1100 m/s) required for the long transfer to the operational orbit, continuously thrusting ion propulsion has been preferred to conventional bipropellant chemical propulsion since it allows to significantly reduce the mass of the propulsion module. Two 20 mN class ion thrusters will be implemented on the P/M, one being in cold redundancy. There are a number of potential suppliers in Europe, such as DASA (RITA) or MMS-UK (UK10)
- For coarse attitude control (1° typically) during the transfer phase, conventional impulsive chemical thrusters are more adequate than reaction wheels, which would be heavier and would anyway require additional actuators for momentum off-loading. Off-the-shelf 1 N hydrazine thrusters (e.g. from DCA, or PRIMEX in the USA) are recommended for LISA;
- For high accuracy DFACS on the operational orbit, FEEP microthrusters (maximum thrust set to 20 μN, see section 2.4.5) are the only actuators able to deliver continuous thrust with the required accuracy. Two FEEP thruster technologies are candidate for application to LISA, caesium-propellant / slit-shape thruster developed for years by Centrospazio and more recent alternative of indium-propellant ion emitters derived from spacecraft potential control devices from the Austrian Research Centre Seibersdorf (ARCS), as further described in the following section.

The first two reaction control assemblies used during the transfer phase are implemented into the propulsion module and therefore described in section 5.5.

5.4.4.2 Centrospazio FEEP thruster technology

Field Emission Electric Propulsion (FEEP) is an electrostatic propulsion concept originated at ESTEC in the 70's. Unlike other ion engines, FEEP does not require propellant vaporisation in order to obtain ionisation; on the contrary, ions are directly extracted from the liquid phase. The thruster can accelerate a large number of different liquid metal or alloys; caesium proved to be the best choice, due to its high molecular weight and its low ionisation potential. As caesium liquefies at 28.4°C, the thruster thermal power requirement is much lower than in conventional ion thrusters, and the emitter thermal control is quite simple. The efficiency of conversion of electric power to propulsive power reaches values as high as 98% as opposed to maximum values of about 80% met in other ion engines. Specific impulse is in the range of 6000 to 10000 s, and may be easily adjusted to meet specific mission requirements. Thrust level is finely tuneable, and instantaneous switching capability allows pulsed mode operation. Clusters of emitters have been successfully tested.

Thrust is obtained by exhausting a beam, mainly composed of singly-ionised caesium atoms, produced by field emission. The emitter module consists of two plates in Inconel (a Ni alloy with 14 to 17 % Cr), with a small propellant reservoir. A sharp blade is accurately machined on one side of each plate. A thin layer of Ni is sputter-deposited on the other three sides; when the two emitter halves are tightly clamped together, a 1 μm slit is left between the blades. Caesium flows through this tiny channel, forming a cylindrical free surface at the exit of the slit, with a radius of curvature of about 1 μN. Under a strong

electric field, generated by the application of a voltage difference of about 10 kV between the emitter and an accelerator electrode located in front of it, the free surface of the liquid metal approaches a situation of local instability, due to the combined effects of the electrostatic force and the surface tension, and creates a series of protruding cusps (Taylor cones) ; the local electric field at the tip increases as the radius of curvature of the cusps decreases. When the electric field reaches a value of about 10^9 V/m the atoms at the tip spontaneously ionise and an ion jet is extracted by the same electric field, while the electrons are rejected in the bulk of the liquid. Mass flow rate is extremely small and requires no control, as the particles extracted are replaced by the capillary actions from the propellant reservoir in the amount necessary to maintain dynamic equilibrium at the emitter tip. When voltage is removed, the capillary force prevents the propellant from pouring out of the slit. The emitter/accelerator arrangement is shown in Figure 5.4-3.

The main parameters in the design of a FEEP thruster are the height of the slit and the width of the blades ; the latter is limited only by machining problems, since the inner surfaces and the slit tips require very precise surface finishing. The value of the gap between the emitter and the accelerator electrode (in the order of 1 mm), as well as the details of the shape of the accelerator window, have only a second-order effect upon the thruster performance. At a total applied voltage of 10 kV, specific impulse is better than 6000 s. Specific power is in the range of 60 W/mN ; although this figure is quite high as compared to conventional ion thrusters, it poses no practical restriction on the use of these thrusters when the thrust level involved is in the order of several tens of μN. Emission rise time ranges from 10 to 30 ms, depending upon the ion current; the minimum impulse bit is a small as 10^{-8} Ns.

The most likely cause of malfunctioning in the operation of FEEP thrusters is the emitter contamination during the early wetting of the emitter inner surfaces by the liquid propellant. The emitter performance is very sensitive to the presence of water vapour or other impurities on the channel and slit surfaces, as caesium reacts with water forming a solid hydroxide, that can obstruct the propellant duct and severely reduce the effective emitting length. This problem can be overcome by adopting a correct pre-flight procedure, i.e. performing a careful outgassing of the emitter in ultra-high vacuum before the introduction of the propellant. If started correctly, the ion emission characteristics become stable and can be reproduced precisely. No other failure mode has been reported.

While thruster performance has been thoroughly assessed (see ref. [3]) and found consistent with the LISA requirements, several aspects of the thruster/spacecraft interaction are to be investigated, including the possible back flow of propellant to the spacecraft surfaces, electrostatic interactions, etc. Moreover, the propulsion system configuration has not been frozen: such aspects as the thruster cluster configuration (including the number and location of neutralisers), the number and location of clusters on the spacecraft (redundancy philosophy), and the power and data interfaces specifications, are still to be defined. The low power oxide cathode neutraliser developed at Centrospazio has shown satisfactory performance in terms of current emission, but some further development is needed to minimise the power consumption.

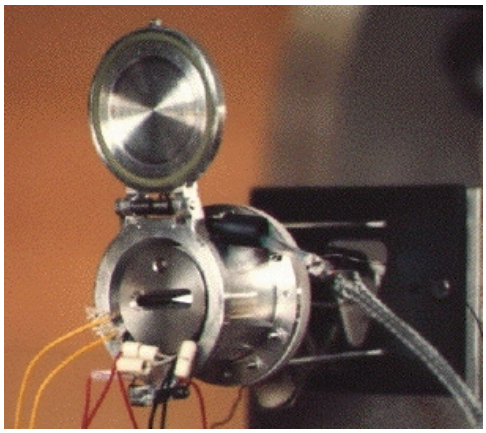

Figure 5.4-3 Centrospazio prototype μN FEEP thruster assembly

The FEEP system will be flight tested on a Get Away Special canister onboard the Space Shuttle in mid 2000 (EMITS experiment, GAS payload G-752). A 2000 hours endurance test is under preparation in the ESTEC Electric Propulsion Laboratory under the responsibility of Centrospazio. This test will exploit a set of diagnostics (ion beam probes, quartz crystal microbalances, etc.) to fully characterise the thruster performance and the plume effects on nearby surfaces. Realisation of a thrust balance aimed at measuring 100 μN maximum thrust with a resolution of 0.1 μN is underway. A joint test of the thruster and the ONERA accelerometer is planned to investigate the drag-free system closed-loop performance. A 3D computational model of the ion beam has been realised and is used to evaluate the plume characteristics and to study propellant backflow, electrode erosion (to estimate thruster lifetime), and neutraliser effectiveness. Advanced thermionic neutraliser and microtip field emission electron sources development is underway. Investigation of alternative propellants (indium) is funded by ESA.

5.4.4.3 ARCS FEEP thruster technology

The ion thrusters developed by the ARCS are based on field emission ion emitters with indium as charge material. A sharp needle made of tungsten is mounted in the centre of the charge reservoir and covered by a thin film of indium. For operation a voltage of about 6–7 kV is applied between the needle and an accelerator electrode. Under the counteractive forces of the resulting electric field stress that moves the liquefied indium film towards the electrode and the surface tension that pulls it back a cone like protrusion is formed on top of the needle tip. The field at the apex of that cone is high enough to remove surface atoms in an ionised state by the process of field evaporation. These ions are replenished by hydrodynamic flow from the reservoir so that a stable and continuous current emission is maintained. A prototype of a thruster module is shown in Figure

The thruster system proposed for application to LISA fine attitude & drag-free control here is based on the sound concept of the space proven ARCS S/C potential control instrument. Extensive databases exist both from operations in space and in the laboratory. The indium emitter itself is well understood and characterised, electronics and especially neutraliser hardware developments are carried out under different programs. From this ongoing work neutraliser evaluation, LISA thruster design and a fuel supply concept will be derived. An assessment of miniaturised electronics and a trade off of mass savings vs. reliability will also be done based on these hardware developments.

The principal arrangement of the ARCS thruster system is shown schematically Figure 5.4-5 below. The indirectly heated ion thruster emitter needs the accelerator (< 12.5 kV) power supply only for beam forming and one small heater supply (near ground potential). The electron neutraliser is of the directly heated thermionic type and needs a heater supply floating at emitter potential and an accelerator supply (2000 V).

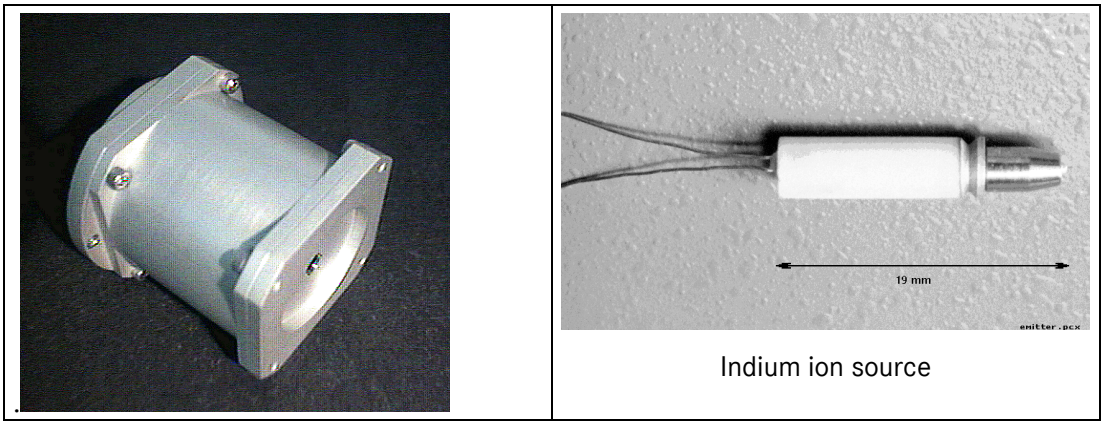

Figure 5.4-4 Prototype ARCS thruster module (80 grams, diameter 45 mm).

The accelerator supplies for thruster and neutraliser are off – the shelf US – made high voltage converters. They must be controlled and supplied by variable voltage DC/DC converters (VVDC) and regulated in a control loop (see Figure 5.4-6). In actual measurements, it was shown that regulation of emission current gives better noise figures than regulation of emission voltage. Still better however is thrust regulation which however needs more circuitry, mass and power.

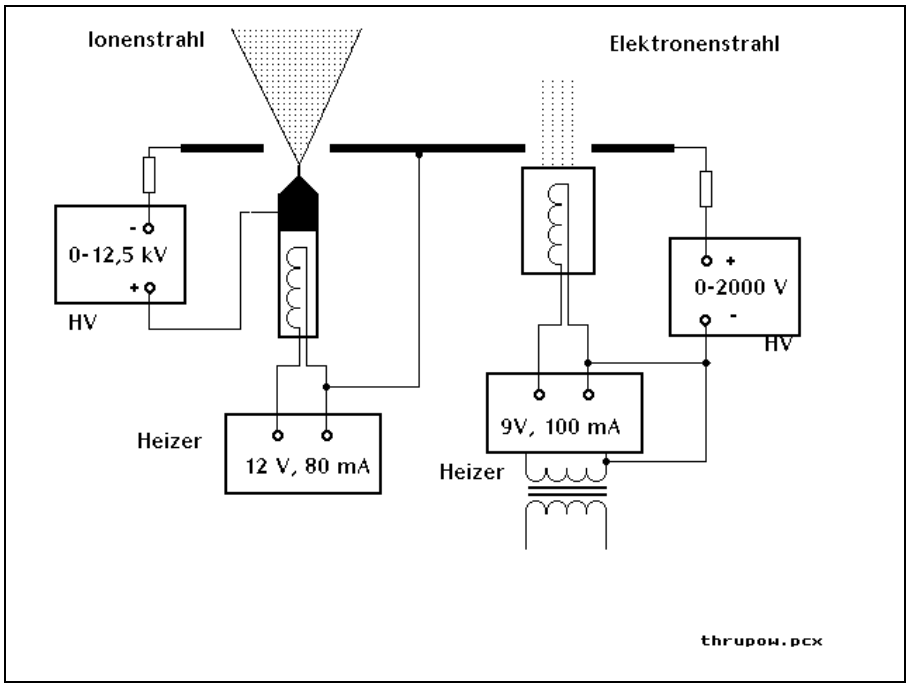

Figure 5.4-5 Thruster and neutraliser alimentation of ARCS FEEP system, schematic

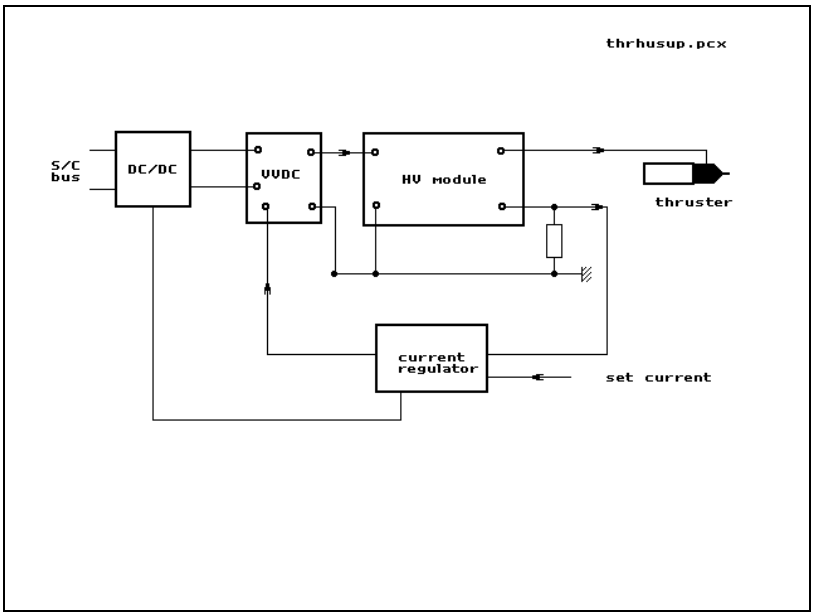

Figure 5.4-6 ARCS Thruster supply and regulation, schematic

5.4.4.4 FEEP thruster Configuration

The proposed FEEP thruster configuration is similar to the one selected for GAIA, as shown below. The 3 clusters of 4 FEEP thruster (2+2 redundant) feature a 6 DOF authority. This configuration does not allow the S/C to provide negative control forces along Z_axis. This is not a problem since the major disturbance on the operational orbit, the solar pressure force, has always a negative component along Z direction (in other words, the Z-control force will be always positive)..

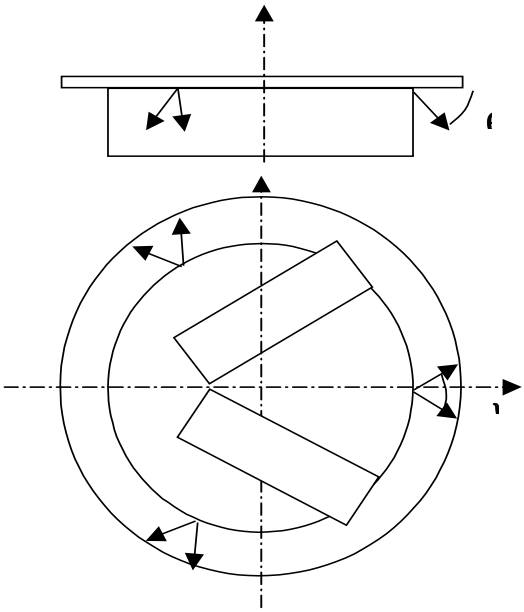

Figure 5.4-7 : FEEP Thruster configuration

Thrust direction optimization

As for hydrazine thrusters, the optimisation parameter is the thrust direction, defined by two angles, θ the angle between thrust vector and the X-Y-plane and ψ the angle between the projections on the X-Y-plane of the directions of the nozzles of a same cluster.

The optimization of these angles has been performed in order to minimise the maximum thrust required for the FEEP thrusters, calculated over one year. Indeed, there are very stringent requirements on the FEEP thrusters noise, so minimising the max thrust level allows to reduce the required dynamic range.

The optimisation accounts for constant and slowly varying solar perturbations (1-year period), bud does not take consider the needs for DFC and attitude control in the MBW, small compared to the others. The forces and torques are evaluated using a simple geometrical model of the S/M:

Fxmax = 4.6 E-6 N	Fxmin = -4.6 E-6 N
Fymax = 4.5 E-6 N	Fymin = -4.5 E-6 N
Fzmax = -3.24 E-5 N	Fzmin = -3.24 E-5 N
Txmax = 1.0 E-6 Nm	Txmin = -1.0 E-6 Nm
Tymax= 4.2 E-6 Nm	Tymin = 2.2 E-6 Nm
Tzmax= 4.5 E-7 Nm	Tzmin = -4.5 E-7 Nm

Figure 5.4-8 shows the maximum thrust required from the thrusters versus the configuration angles. We can notice that as far as we keep away from $\theta = 0$, and from $\Psi = 0$, the required thrust is little sensitive to these angles.

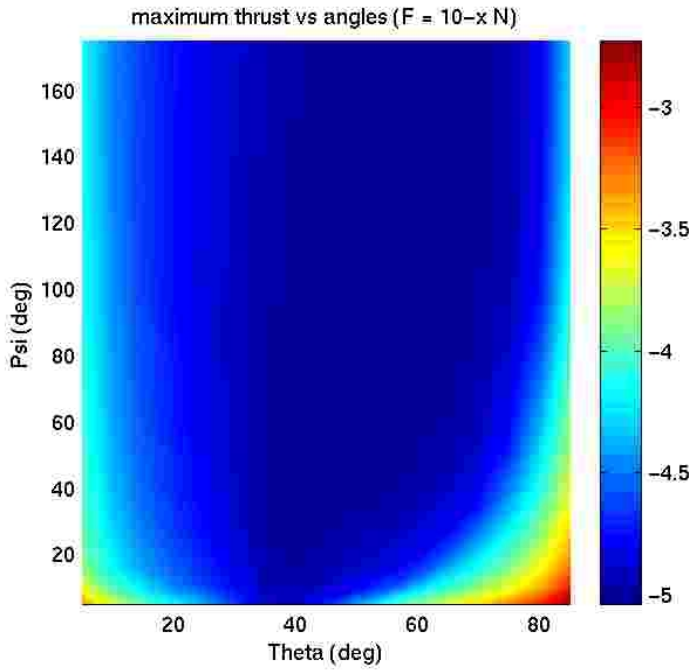

Figure 5.4-8 Maximum thrust versus configuration angle

The selected angles are $\theta = 55°$ and $\psi = 115°$ For this configuration, the largest thrust required to an individual FEEP is **9 µN**. It has to be noticed on Figure 5.4-8 that the area around the optimum is in fact very flat, and therefore these optimum values could be easily modified for bulkiness or plume inpingement considerations.

A factor of two margin is considered on this preliminary evaluation, the maximum thrust of the LISA FEEP thruster is specified to 20 µN. This does not account for any needs for orbit maintenance, since Phase A orbit analyses concluded that the geometry of the LISA cluster does not need to be controlled. If this eventually happen to be necessary, the recommendation is to use dedicated thrusters, since the required thrust level would set unrealistic constraints on the FEEP dynamic range.

5.4.5 AOCS Sensors

5.4.5.1 Acquisition & safe mode sensors

As indicated in section 2.2.1, the sensors for acquisition and safe mode during transfer are two wide FOV Sun sensors for nearly full sky coverage (one on the bottom of the P/M and one on the top of the S/M), plus a magnetometer used for attitude determination around the Sun line during the initial attitude acquisition. In subsequent phases, it is expected that maximum spacecraft angular rates will be low enough to rely on the star sensor, so that there is no need for a gyro to complement the Sun sensor.

Optionally, a specific AAD (Attitude Anomaly Detector) can be implemented on the S/M in order to completely segregate the failure detection from the failure recovery (i.e. the sensor used in Safe Mode). This is however not mandatory, if as proposed the Safe Mode is performed using redundant star sensor, so that the AAD can simply be the Sun sensor of the S/M.

All theses sensors are standard off-the-shelf equipment, as shown in the following table:

Table: 5.4-1: Candidate acquisition/safe mode sensors

Item	Potential Suppliers	Comments
Sun sensor	MMS (BASS17) TPD/TNO	1 unit on SM, and 1 unit on PM for full sky coverage.
Magnetometer	IAI TAMA (TFM) Sextant Avionique (170S3E)	1 unit for initial angular rate reduction
Attitude Anomaly Detector	MMS SAS, …	TBC for improved failure isolation wrt safe mode

5.4.5.2 Star sensors

The star sensor requirements and configuration are actually driven by the Laser Beam Acquisition Mode, as further detailed in section 3. For the transfer phase, there is no specific performance requirements (1° coarse pointing is sufficient), the only concern might be to avoid blinding by the Sun or the Earth along the attitude guidance profile. This is obtained with the proposed STR configuration (1+1 red. unit aligned with each telescope LOS).

The LISA STR is to be selected among the number of new generation wide FOV autonomous star sensors currently under development in Europe. The major characteristics of the candidate STR models are summarised in the following table.

Table 5.4-2 : Candidate star sensors

Item	Potential Suppliers	Comments
Star sensor	MMS (SSM) DTU (ASC) Sodern (SED16) DJO (SETIS) TERMA STR	4 optical head and 2 electronic units. Other configurations are in options (3 units, 2 aligned with each telescope LOS and a third one in the –Z direction)

At this stage, the two best candidates, in terms of performance, appear to be the ASC (Advanced Stellar Compass) from the Denmark Technical University and the SSM (Senseur Stellaire Miniature, or Miniature Autonomous Star Tracker) currently under development at Matra Marconi Space (see Figure below).

The evaluation of the performances of the STR is not straight-forward in the case of LISA, since most of these sensors are designed for LEO. A detail performance analysis is presented in section 5-107.

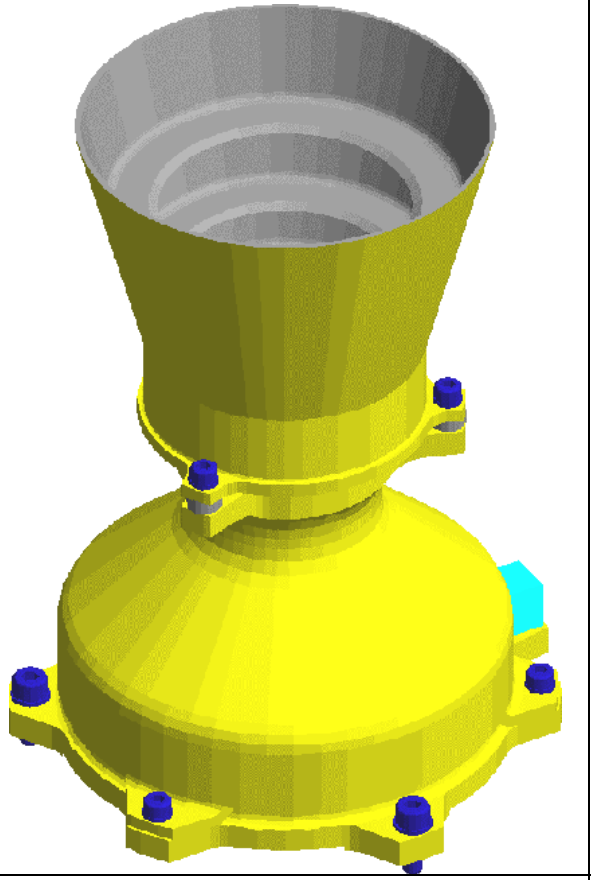

Senseur Stellaire Miniature

(MMS)

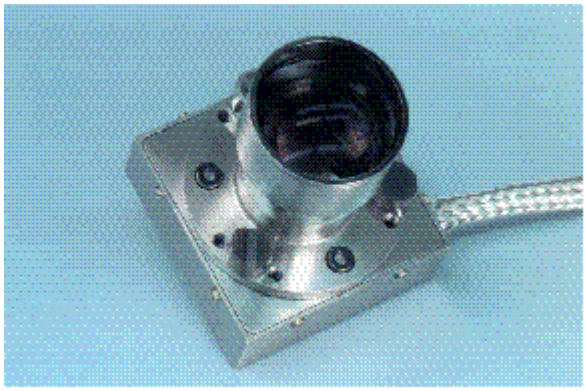

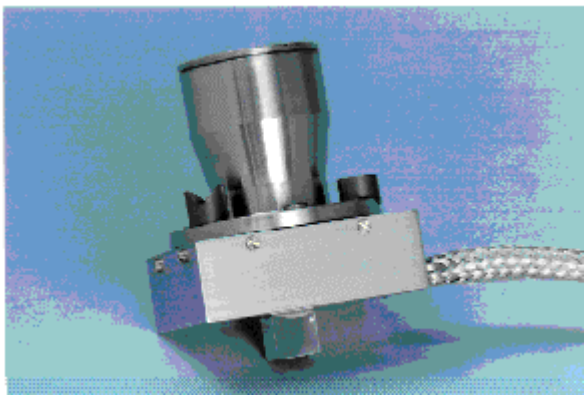

Advanced Stellar Compass

(Denmark Technical University)

Figure 5.4-9 Candidate star trackers for the LISA mission

The ASC is currently flown on the Oersted satellite, complete in-orbit results are expected in the very near future. As a consequence, the ASC is a very good candidate for a medium term technology demonstration mission for LISA.

For the more distant LISA mission, MMS recommend to consider a star tracker derived from the SSM, a sensor based on the latest detection and electronics technologies which is to be developed and qualified within a few years. The main features of this new generation of sensors are:

- APS (Active Pixel Sensor) detectors instead of CCDs, thus enabling major gains in the detector electronics mass, volume, power consumption and cost. The APS technology for space applications has reached a mature development status, which makes is suitable for the production of small and high performances star sensors.

- MCM (Multi Chip Module) fast processing calculators (already developed, to be used for ROSETTA mission) and ASIC electronics for a fast video chain.

The development and qualification of the SSM are to be completed by the end of year 2001, which is fully compatible with the LISA schedule.

In its current definition, the SSM is made of two distinct units, the optical head and the electronics unit. The electronics could then be integrated within an other electronic box, or remain self standing.

The following drawings gives and overview of the sensor in its current definition:

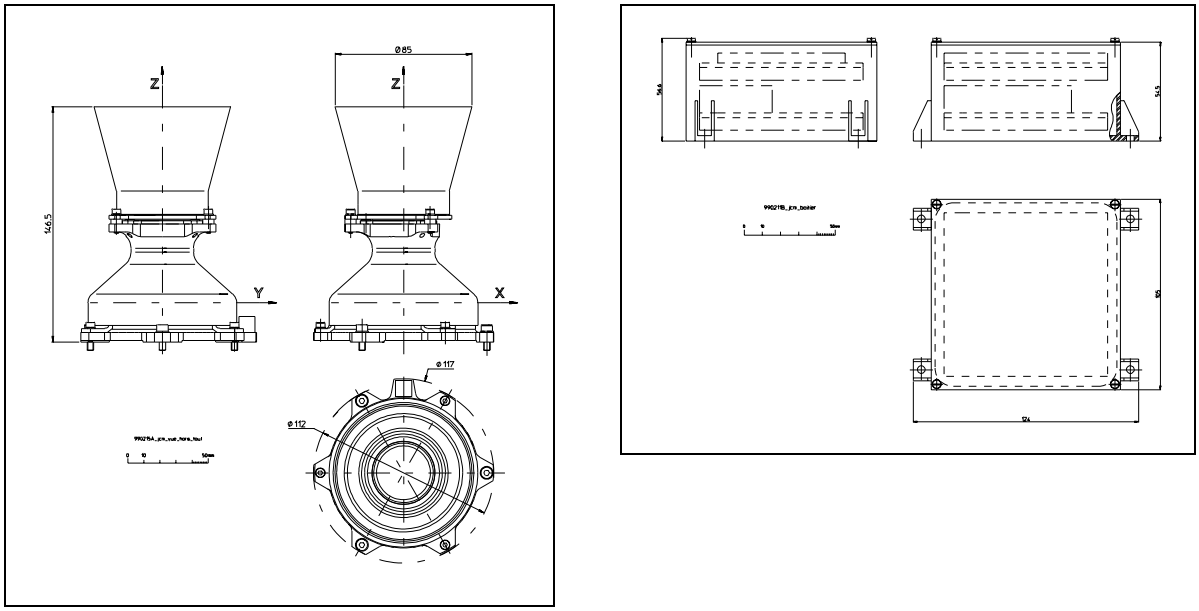

Figure 5.4-10 Optical head & electronics unit mechanical interfaces

The typical interfaces of a star tracker ensuring an 1 arcsec for the LISA mission and derived from the MMS SSM development are the following:

mass	2 kg
volume	
optical head	120 x 120 x 150 mm^3
electronics	125 x 105 x 120 mm^3
power consumption	8W.

5.4.5.3 Star tracker configuration

A single STR is not sufficient for LISA. Indeed, a STR cannot measure the attitude with the same accuracy on all directions. The error around the line of sight of the sensor is much larger than around the other two directions.

Therefore the nominal configuration for LISA is to have one STR working for the pointing of each telescope, which means 2 STR per satellite. Each sensor is aligned with its allocated telescope, so that it provides the best accuracy for the telescope pointing.

Several options exist to provide redundancy to the system.

The simplest idea is to put a spare STR for each telescope; then the total number of devices is 4 per S/C (12 total).

A very interesting alternative is to have a single spare sensor per S/C, pointing in the off-plane direction. After a failure, the pointing of the telescope with the failed STR would be performed by combining the measurements of the other nominal STR with the measurements of the spare. The drawback of this solution is the thermo-elastic biases that may affect the pointing accuracy due to the larger distance between the sensors and the telescope.

MMS recommend a third solution. It consists in having 2 +2 redundant optical heads (similar to the first solution), and only two electronic units, each one being able to compute the raw data coming from the optical head. This is possible with both the ASC and the SSM, which feature separate processing electronic boxes.

This last solution provides the required failure isolation capability, and limit the number of pieces of H/W.

5.4.6 Laser Beam Acquisition Strategy

5.4.6.1 Introduction

This section studies the mode during which the optical links between the three spacecraft are established. This of course is quite challenging since each spacecraft has to acquire narrow and very weak laser signal from its companions, which are located 5 millions km away.

A key aspect to realise these optical link acquisition is to have the best a priori pointing knowledge. The attitude is of course given by Star Trackers (STR, with an accuracy significantly better that in conventional LEO applications thanks to the very benign thermal & dynamic environment expected for LISA. The PAT (Pointing Acquisition & Tracking) strategy to explore the uncertainty cone and to obtain the two-way link is also a critical point, which hopefully benefits from the experience gained in the SILEX development.

This section intends to demonstrate the feasibility of this mode, and moreover to prove that the laser beam acquisition does not require additional cost-driving equipment.

5.4.6.2 Star Tracker performances

5.4.6.2.1 Introduction

The selection of this star tracker is a major trade-off. Indeed, very high attitude knowledge performances are requested, but highly accurate star sensors (e.g. SOHO STR from Galileo) also feature high cost, not compatible with LISA cost objectives.

The goal of this section is then to assess the possibility of using the so-called new generation star tracker (wide FOV & large number of tracked star allowing autonomous acquisition & very low probability of star hole), and to show how the standard performances of such sensors can be improved for the LISA mission.

The performances of a star tracker can be decomposed in bias, resulting from different contributions, and a white noise, called Noise Equivalent Angle (NEA). Both of them should be reduced to improve the overall pointing accuracy.

Roughly speaking, the bias of the STR will determine the attitude and the beam pointing knowledge, whereas the noise will have a direct impact on the attitude stability.

All new generation star trackers are able to provide a 3-axis attitude. However, the two axes transverse to the line of sight are always more accurate than the roll angle (around the line of sight). For LISA, we are only interested in the two “good” axes, since each telescope has his own star tracker for its own acquisition (the acquisition of one laser beam only requires 2 axis control).

5.4.6.2.2 Achievable STR performance

The overall performance (NEA, bias & thermo-elastic distortions) of the considered STR class is typically of 20 arcsec when it is operated at high frequency (several Hz) on conventional LEO platform

In the LISA very slow dynamic environment, a much lower measurement frequency can be accepted, and the NEA can then be decreased below 1 arcsec by :

- adequate measurements filtering and averaging,
- hybridisation with angular acceleration measurements from the inertial sensor.

The performance is then limited by

- the position knowledge of the stars used by the sensor (this error is small if the sensor field of view & sensitivity ensure that enough catalogued stars (10 to 50 typically) are always visible, which is the case for a typical 20° FOV),
- the “relativist aberration”, due to the spacecraft motion in an inertial reference frame. This effect is compensated internal star tracker processing of the measurements so only the small residual processing error is to be considered,
- the limitations of the optics and detector (matrix inhomogeneities and optics distortion aberration), which can however be minimised by a pixel by pixel initial characterisation.

Providing that the storage and processing capabilities of the STR are sufficient to enable measurements filtering and images correction, the contribution of the above errors can be low enough to achieve 1 arcsec accuracy through hybridisation (see section 3.2.4).

5.4.6.2.3 Bias Reduction

A lot of different sources will produce a bias of the attitude estimate : STR mounting bias, thermal effects, residual optic aberration, and distortion, star catalogue accuracy.

These biases can be reduced using the following techniques :

- Calibration of constant bias, by comparison with star sighting in the telescope
- Very stable thermal environment
- Simultaneous processing of a large number of stars (up to 50 stars is already possible).

To obtain a first assessment of the final bias for the LISA STR, we have chosen to consider the can SED-16 sensor, currently developed by SODERN for SPOT 5, for which very detailed bias budgets are available. This star tracker, almost “off-the shelf”, will probably not be selected eventually - it might be a good candidate for an earlier demonstration mission though - but it is understood that the same order of magnitude of bias can be expected for other sensors of the same class (e.g. the ASC or the SSM), if not better.

The figures given in the first column of Table 5.4-3 hereafter are SODERN preliminary noise budget (see[11]), the second column are figures estimated by MMS for LISA :

Table 5.4-3 : Expected STR performances for LISA *(arcsec,3σ; sensitive axes)*

	SED-16, Spot-5 orbit, 9 stars processed	**LISA STR, 50 stars processed**	**Comments**
Constant bias	11	~0	Removed by calibration using telescope
Thermal variation	2	~0	Thermal stability
Non-uniformity variation	3	1.3	Number of stars
Total	16	1.3	

Calibration

The constant bias will be in fact equal to the accuracy of the calibration using the telescope, which is basically the bias error of the incoherent detector, small compared to 1 arcsec accuracy objective.

The difficulty of the calibration is the ability to find a star in a ring defined by the rotation of the telescope around the direction of the Sun, so that no thermal distortion appears between the calibration and the acquisition phase. The width of this ring has to be defined in further study. It should be not to large, to keep an excellent thermal stability, but not too small, so that the incoherent sensor is able to work with the light of at least one star in the ring.

The non-uniformity error can only be reduced by processing more stars. It is also dependent of the Sun direction angle, which should not vary in the case of LISA.

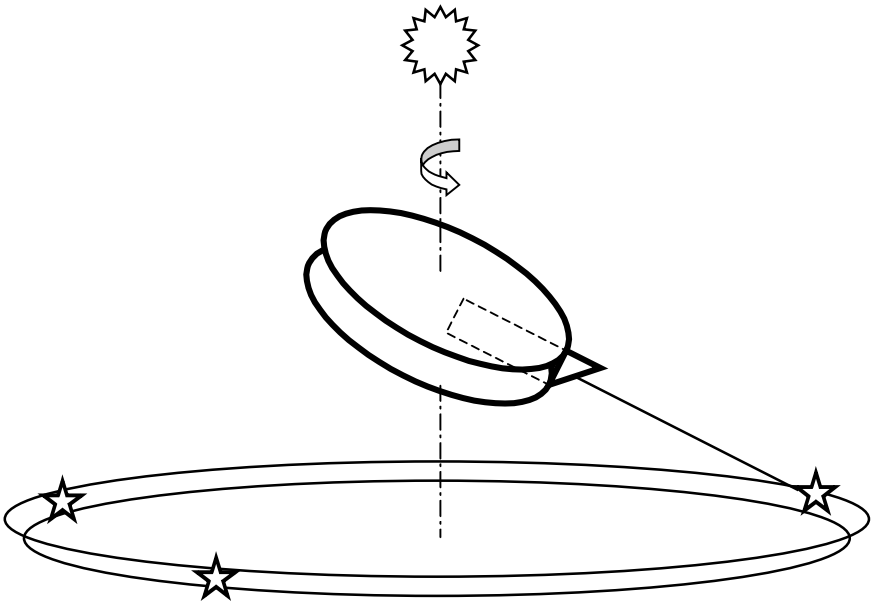

Figure 5.4-11 : Location of the stars compatible with STR alignment calibration

5.4.6.2.4 Reduction noise on the attitude estimate

The NEA of the star tracker is a function of the STR technology, of the sampling frequency and of the number of star processed. Nevertheless, like in the classical gyro-stellar estimation scheme, the attitude estimation accuracy can be largely improved by hybridising the STR information with the angular acceleration measurements from the inertial sensor Indeed, the latter will provide a low noise relative attitude reference that can be used to filter STR noise. Figure 5.4-12 compares the Power Spectrum Density (PSD) of the Star sensor and of the inertial sensor noises, demonstrating that the latter allows to filter the STR noise above 2 mHz.

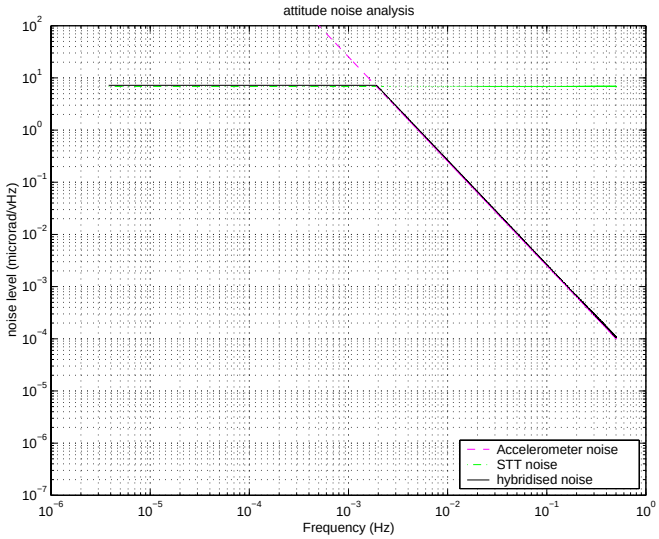

Figure 5.4-12 : Noise PSD of LISA sensors

The hybridisation consists in taking into account the information of the star tracker in the low frequency, and the low-noise information of the inertial sensor in the upper frequency band. Thus, with the resulting noise PSD, the pointing error is very stable, and will not exceed 0.5 µrad as shown on the following figure, which presents the evolution of the attitude estimation error as a function of time: the attitude estimate from the inertial sensor increases up to the upgrade with the filtered STR measurements every about 250 sec.

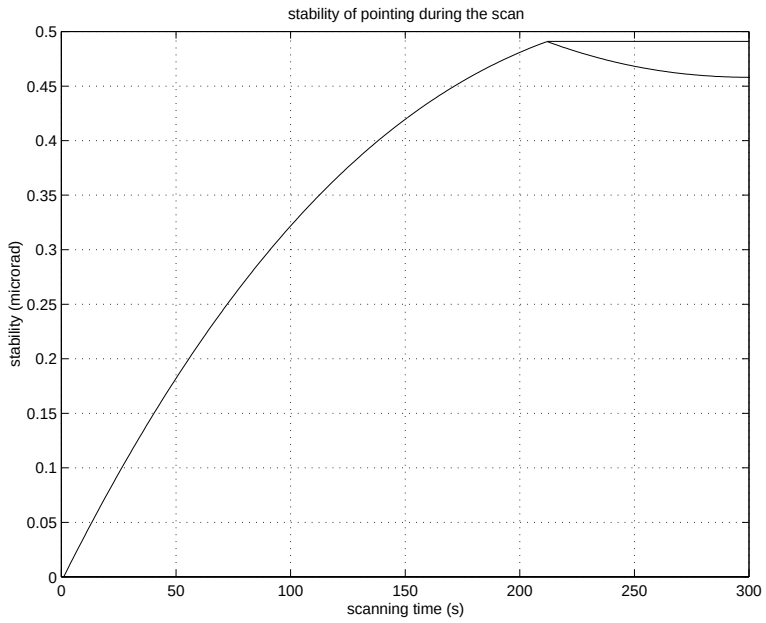

Figure 5.4-13 : attitude knowledge stability (standard deviation with time)

5.4.6.3 Acquisition cone budget

5.4.6.3.1 Acquisition cone definition

The acquisition cone corresponds to the angular sector that the emitting spacecraft will have to cover to be certain to illuminate the receiving spacecraft during the acquisition phase. It is also a contributor to the field of view of the receiving spacecraft incoherent optical channel.

The contributors to the acquisition uncertainty cone are:

- the knowledge of the spacecraft relative positions,
- the knowledge of each spacecraft emitted beam direction.

5.4.6.3.2 Spacecraft relative positions

Before the acquisition is performed, the position of each spacecraft can be determined with a ± 10 km accuracy using the NASA Deep Space Network (see Pre-Phase A report § 6.5, 1-sigma value estimated under the assumptions of X-band tracking). For the acquisition studies a value at 3σ is used, so we

consider that each spacecraft position is known with a ± 18 km error, leading to a ± 5 µrad contributor to the acquisition cone.

Remark: a ± 2 µrad may be achievable using the DSN because most of the uncertainties in the spacecraft position knowledge come from uncertainties in the Earth ephemeris, which have been improved since the Pre-Phase A report redaction. The Pre-Phase A report figure is however maintained in the budgets until an updated figure is provided by JPL.

5.4.6.3.3 Knowledge of each spacecraft emitted beam direction

The spacecraft attitude is determined before the acquisition using star trackers. The performance of a star tracker is determined by both its intrinsic accuracy and the knowledge of its orientation with respect to the optical payload line of sight.

5.4.6.3.3.1 Star tracker vs. payload alignment knowledge

The biases between the star tracker axes and the optical assembly line of sight are due to the initial sensor alignment, to the launch effects (vibrations, gravity release) and the long term in-flight thermo-elastic distortions. Relying on an on-ground calibration would have a dramatic impact (more than ± 100 µrad) on the bias between the star tracker axes and the instrument lines of sight knowledge. An in-flight calibration before the initial acquisition is necessary. Only the calibration accuracy is then to be considered for the performance budget.

The proposed co-alignment calibration principle is the following:

1) a selected star is imaged and then centred on the Optical Assembly acquisition sensor,

2) the spacecraft orientation is determined, using the same star or other catalogue stars within star tracker FOV.

The accuracy of step 2) is driven by the limitations of the STR optics and detector, and step 1) accuracy depends on the Optical Assembly acquisition sensor performance.

The following table gives an estimation of the star tracker vs Optical Assembly LOS in-flight calibration contributors.

1) acquisition sensor performance (barycentring on CCD)	< 1 µrad
2) star position determination by star tracker	± 3 µrad
Total (quadratic sum)	< ± 4 µrad

This calibration gives a knowledge of the Optical Assembly acquisition sensor LOS co-alignment with respect to the star tracker reference. The co-alignment between the Optical Assembly acquisition sensor and its emission path is also to be considered. It will be calibrated on-ground, and then be affected by the Optical Bench long term stability.

The calibration of the on-ground co-alignment between the emission and reception paths can be achieved with a ± 2 arcsec accuracy using a commercially available high quality retro-reflector and optical densities.

The main contributor to the long term drift is the fibre lateral stability. The fibre positioner lateral displacements will enable an in-flight compensation of the emission path misalignments, so an allocation of 1 µm for the fibre displacement is considered for the budget, corresponding to the re-alignment accuracy. This induces a 40 µrad co-alignment drift at optical bench level.

Co-alignment between acquisition sensor LOS and emission direction	
On-ground calibration accuracy allocation	± 10 µrad
Long term drift compensation accuracy	± 40 µrad
In-flight co-alignment at Optical Bench level	± 42 µrad
Telescope magnification	g_α=60
Co-alignment at telescope output	± 0.7 µrad

5.4.6.3.4 Acquisition cone budget

The contributors identified in the previous paragraphs are independent, and are therefore summed quadratically to obtain the acquisition cone budget.

Spacecrafts relative positions knowledge	± 5 µrad
Star tracker intrisic accuracy	± 5 µrad
Star tracker LOS calibration accuracy	± 4 µrad
Acquisition LOS vs emission direction	± 0.7 µrad
Acquisition cone budget (quadratic sum)	± 9 µrad (± 1.8 arcsec)

The knowledge of the acquisition cone budget associated with the emitted beam FWHM (2.6 µrad) enables to define the acquisition strategy.

5.4.6.4 Candidate acquisition strategies

From the budgets presented in the previous paragraph,

- the emitted beam FWHM is 2.6 µrad,
- the acquisition cone width is ± 9 µrad.

The acquisition cone corresponds to the angular sector to be covered by the emitting spacecraft to illuminate the receiving one during the acquisition phase. If the acquisition cone is larger than the

emitted beam FWHM the acquisition cannot be direct. Two possibilities have been considered to perform the acquisition, defocus of the emission beam or scan of the uncertainty cone. Both options are discussed in par. 4.3.2.

5.4.6.5 Acquisition sequence

The aim of this sequence is to enable the start of the mission measurement by ensuring a mutual acquisition of the spacecraft optical beams, their centring on the coherent detectors and the lasers frequencies synchronisation.

The important level of straylight generated by the emitted beams on the acquisition sensors lead to a strategy where one spacecraft laser has to be switched off when the use of the acquisition sensor is required.

During all the acquisition sequence, the spacecraft attitudes are controlled using the proof-mass as inertial sensor. Their attitudes can then be controlled in open loop with an accuracy better than 0.5 µrad over several hours, which makes possible the proposed sequence.

The acquisition sequence of event is described in Figure 5.4-14. The same scenario is then to be repeated twice to establish the link between spacecraft 1 and 2 with the spacecraft 3.

In addition to the nominal sequence, a « misalignment sequence » has been studied, which may occur for the first acquisition. This sequence shows how the acquisition may be possible in spite of unexpected launch effects inducing some optical bench misalignments.

If a mis-alignment has occurred between the emission and the reception paths, the beam may not be detected by the acquisition sensor. An additional scan is in this case necessary (see Figure 5.4-15), using the fibre positioner. This scan is to be initiated if no “answer” is received from the opposite spacecraft. This is presented in the “mis-alignment scenario”. A similar approach is to be applied if no beam detection occurs for the step 5 of the nominal scenario

	Nominal scenario	
	Spacecraft 1	Spacecraft 2
step 1	. Star tracker vs acquisition sensor calibration	. Star tracker vs acquisition sensor calibration
step 2	. Spacecraft stabilisation pointing toward opposite spacecraft within acquisition cone, using star sensor and NASA Deep Space Network data . Laser ON	. Spacecraft stabilisation pointing toward opposite spacecraft within acquisition cone . laser OFF
step 3	. Scan of acquisition cone - scan speed TBD according to acquisition sensor integration time	
step 4		. Beam detection on acquisition sensor . Determination of beam direction (barycentring on acquisition sensor CCD) . Orientation toward opposite spacecraft within emitted beam divergence angle (± 1.3 µrad) . Laser ON
step 5	. Laser OFF when scan completed . Beam detection on acquisition sensor . Beam centring on coherent sensor . orientation toward opposite spacecraft within emitted beam divergence angle (± 1.3 µrad) . laser ON	
step 6		. Laser OFF . Beam detection on acquisition sensor . Beam centring on coherent sensor . Orientation toward opposite spacecraft within ± 1 µrad accuracy (coherent sensor total FOV is 3 µrad) . Laser ON
step 7	. Frequency scan of the reference oscillator . Detection of the signal by the coherent sensor when both spacecrafts are synchronised . Emission at spacecraft 2 frequency	
step 8	Optimisation of emission vs reception channels co-alignments by signal flux optimisation (including fine focusing of emitted beams)	
Start of measurements		

Figure 5.4-14 Nominal Laser Beam Acquisition Sequence

	Mis-alignment scenario	
	Spacecraft 1	Spacecraft 2
step 1	. Star tracker vs acquisition sensor calibration	. Star tracker vs acquisition sensor calibration
step 2	. Spacecraft stabilisation pointing toward opposite spacecraft within acquisition cone . Laser ON	. Spacecraft stabilisation pointing toward opposite spacecraft within acquisition cone . laser OFF
step 3	. Scan of acquisition cone - scan speed TBD according to acquisition sensor integration time	
step 4		. Beam detection on acquisition sensor . Determination of beam direction . Orientation toward opposite spacecraft within emitted beam divergence angle (± 1.3 µrad) . Laser ON
step 4'	. Laser OFF when scan completed **NO beam detection on acquisition sensor**	
step 5'		. Laser OFF **NO beam received from opposite spacecraft** **=> mis-alignment compensation required** . Laser ON . Scan of acquisition cone using fibre positioner, the reception path remaining pointed toward opposite spacecraft . Laser OFF when scan completed
step 6'	. Beam detection on acquisition sensor . Beam centring on coherent sensor . Orientation toward opposite spacecraft within emitted beam divergence angle (± 1.3 µrad) . Wait t=scan duration . Laser ON	
step 7'		. Beam detection on acquisition sensor . Determination of co-alignment bias using detection datation wrt end of scan . Resume nominal scenario step 4

Figure 5.4-15 "Misalignment Scenario" for Laser Beam Acquisition Sequence

5.4.7 Budgets

5.4.7.1 Mass & power budgets

The mass and power budget of the DFACS and RCS system (without propellant) is given in Table 5.4-4.

Table 5.4-4 : Mass and power budget

Device	# of devices	Size (mm3)	Unit mass (kg)	Total mass (kg)	Unit Power (W)	Power (W)	Comments
Star sensor (MMS/SSM)	4 OH 2 EU	120 x 120 x 150 125 x 105 x120	0,74 0,7	2,96 1,4	1,5 7,9	3 7,9	Baffle included
Sun sensor (MMS/BASS)	1 on the SM 1 on the PM	19,5 x 70,5 x 72	0,08 0,08	0,08 0,08		0	
Ion thruster (DSS/RIT) Xenon Valves, piping, electronics, etc	x 2	Diam 165 x 185	2 15	4 22 35	588	588	
1 N Hydrazine thrusters (PRIMEX/MR-103) Hydrazine Tank, valves, piping, electronics, etc	x 8	34 x 148	0,33	1,32 10 4	13,7	0	Average power is almost null, when averaged over time.
magnetometer (IAI-TAMAM/TFM)	x 1	95 x 53 x 27	0,18	0,18		0,8	
FEEP micro-thrusters	6 x Pods of 2		1,77	10,62		16	ARCS data,
Mounting & baffles			2	8			Provision
Preliminary Total DFACS							
Total for the Science module				23,1		26,9	Margins are not included
Total for the Propu module				76,6		599,7	Margins are not included

5.4.7.2 Bus data and CPU load budgets

The DFACS system includes a lot of controllers, since 19 DOFs need to be controlled simultaneously. Fortunately the order of the controllers and the sampling rate can be kept low, so that DFACS-related bus data budget and CPU loads are not critical relative to current avionics performances. The estimated bus data budget is presented in Table 5.4-5, and the CPU load related to control algorithms in operational mode (FDIR & data management not included) is presented in Table 5.4-6. The critical aspect is likely to be the software size, because of the large number of AOCS modes (not evaluated here).

Table 5.4-5 : Bus data flow for DFACS

Device	# of operating devices	# of Inputs & Outputs	I/O Rate (Hz)	# of bits	Data Rate (bps)
Stiff suspension	10	1	2	18	360
Weak suspension	2	1	0.01	18	0.36
Input for DFC	3	2	2	18	216
Attitude	3	1	2	12	72
LOS actuation generation	1	1	2	16	32
FEEP command generation	1	7	2	12	168
TOTAL bus data budget for DFACS with no margins! (bit/sec)					**848**

Table 5.4-6 : Computation needs for DFACS

S/W modules	# of operating devices	# of floating operations	Rate (Hz)	Computation load (Flops)
Stiff suspension	10	11	2	220
Weak suspension	2	11	0.01	0.22
DFC	3	19	2	114
DFC command generation	3	5	2	30
Attitude	3	19	2	114
Attitude estimator	3	2	2	12
LOS actuation generation	1	15	2	30
LOS estimator	1	2	2	4
FEEP command generation	1	77	2	154
Software margins (100%)				**678**
TOTAL computation needs (kFlops)				**1.4**

5.4.7.3 Summary of Sensor & Actuator requirements

Star Trackers

NEA on transverse axes : < 1 arcsec/$Hz^{1/2}$.

Bias on transverse axes (other than mounting & thermal biases) : < 1 arcsec – 3σ.

FOV : shall allow 3-axis attitude determination without star measurement interruptio

Heterodyne sensor –

Attitude sensing noise : < 3 nrad/$Hz^{1/2}$.

Range : 3 µrad

Output frequency :2 Hz if no active damping of the telescope tilt mechanism oscillation (12 bits A/D conversion), 10 Hz if ctive damping performed with the heterodyne measurement

Telescope pointing mechanism

Range : 1°

Angular rate : 20 nrad/s

Absolute accuracy : < 1 µrad

Noise : 0.7 nm/$Hz^{1/2}$ above 40 mHz.

FEEP thrusters

Configuration : Pods of 2 thrusters with possible adjustment of the two thrust directions (+2 redundant emitters)

Range : 20 µN

Noise : <3 nN/$Hz^{1/2}$.

Scale factor : <5%

Thrust direction misalignment : <5°

5.4.7.4 Conclusions and critical areas

The AOCS/DFACS analyses (see par. 7.2) conducted in the frame of the LISA Phase A study have demonstrated the feasibility of the S/C & payload control for the considered configuration with two optical assemblies in each of the three spacecraft. In particular, the 10-DOF dynamic simulator has allowed to verify that the preliminary DFACS design meets all requirements in the MBW : PM acceleration along the principal axes, PM relative position w.r.t. the S/C, pointing stability.

If the overall feasibility of the very challenging control of this mission is now demonstrated, some areas need to be consolidated as detailed hereafter.

5.4.7.4.1 Sensor/actuator technology :

Four technologies deserve interest for the consolidation of the DFACS mission performance :

1. **Star tracker performance**. In this document, it was shown that new generation, and low-cost, star trackers should reach an accuracy of 1 arcsec in the favourable conditions of the LISA mission. This level of performance should be consolidated through a more detailed error budget for these sensors, which are generally designed for LEO operations.
2. **Inertial sensor** : Among all aspects related to the inertial sensor, one item has been shown in this document to be of primary interest for the control aspects : the inter-axis couplings due to electrostatic forces. Rough estimate of these couplings have been provided, but the accurate value (or an accurate model) for the final sensor configuration is necessary. Consolidation of the achievable minimum negative stiffness is also important for control design.
3. **FEEP thruster** : The most critical aspect for LISA DFACS design, to be covered by further studies is the level of noise in the MBW. MMS derived preliminary requirements from mission & control design constraints, which appear to significantly below (by a factor 2 to 3) first FEEP noise measurements at ARCS & Centrospazio. These requirements have to be consolidated/reviewed according to refined experimental results, which should be performed with FEEP drive electronics actually optimised to reduce thrust noise. Means to actually assess the thrust noise are also to be investigated..
4. **Mechanisms** : If the fibre positioner appears now as a nearly off-the-shelf mechanisms (thanks to the large descoping of its initial 3-DOF / wide range functionality), the telescope tilt mechanisms still deserves further attention. In particular the criticality of using a stepper motor should be further investigated and traded-off with a still-to-qualify piezo-driven motor .

5.4.7.4.2 Control Design

In terms of control, two major areas deserve further investigations : the drag-free acquisition modes, and the low frequency perturbation cancellation, as explained in the following paragraphs :

Drag-Free acquisition modes

During Phase A it was chosen to focus on the science mode, featuring a steady drag-free control, and on the laser beam acquisition mode, which appeared to be the most critical modes. In order to meet extreme mission requirements in the MBW, very large disturbance rejection ratios are requested from DFACS controllers, resulting in static gain up to 100 dB (i.e; reduction by a factor of 100,000 of quasi-static disturbances). In addition to sensor dynamic range issues, transient phases shall be analysed in depth, in order to define the drag-free acquisition sequence from uncontrolled dynamics to operational conditions. This need is reinforced by considerations on the inertial sensor : in drag-free mode, the proofmass is free-floating along the sensitive axis. During the Drag-Free Acquisition Mode, the suspension will be first stiff enough to allow release the proofmass without collision with the cage, and (progressively) softened in a second time, as the cancellation of the solar pressure by the FEEP thrusters becomes more accurate.

Low frequency perturbation attenuation

The very-low-frequency components of the forces (self-gravity mostly) acting on the PM will have to be cancelled out, because of the stringent requirement on the absolute variation of the distance between the PM and the cage. These aspects were only investigated at conceptual level during this phase A study, focused on the demonstration of the performance in the MBW. The proposed solution is to feed-forward a force command (either to the FEEP or to the CAESAR actuation system) to compensate for the estimated low frequency disturbance. The design & performance assessment of this estimation/feedforward scheme shall be further investigated in subsequent phases, with the support of a dynamic simulator, quite straightforward to develop from the existing 10-DOF noise analysis tool.

The simulator developed for this study could be completed by including all degrees of freedom, by improving the models describing every element of the DFACS architecture, and by utilising compiled versions of the simulator (automatic transformation from Matlab/Simulink environment toward a C program), so as to reduce the computation time, as required to assess performances in the very low frequency domain.

A demonstration mission on an Earth orbit is of course the best way to assess the performance of the DFACS for LISA, as well as to resolve the remaining control problems. In particular the viability of the strategy without electrostatic compensation along the principal axis, so-called “strategy 4” in Chapter 7.2, which was shown to improve the performances, could be demonstrated.

5.5 Propulsion Module

5.5.1 Configuration

5.5.1.1 Module Concept

The propulsion module is a relatively simple module. The only functions it has to perform are propelling the science module to the operational orbit from the near Earth trajectory, providing power to the science module for heating and navigation during transfer, and orienting and releasing the science module in its operational orbit and attitude.

Navigation control would be performed by the science module, and only the attitude forces, torques and propulsion is provided by the propulsion module. This means that only an RCS, the ion motor system and a power supply is necessary for this module.

5.5.1.2 Stack Height Limitations

This is indeed fortunate, because the available height in the stack of science and propulsion modules within the launcher has proved to be even less than originally envisaged in the Pre-Phase A study.

The restriction on height for any payload within any launcher always has two limits. The first and obvious one is the volume and shape of volume of the launcher fairing. The second is the maximum height of the centre of mass of the payload from the nominal launcher attachment interface plane.

This second factor varies according to the mass of the payload, as is illustrated for the baseline launcher here of Delta II by Figure 5.5-1.

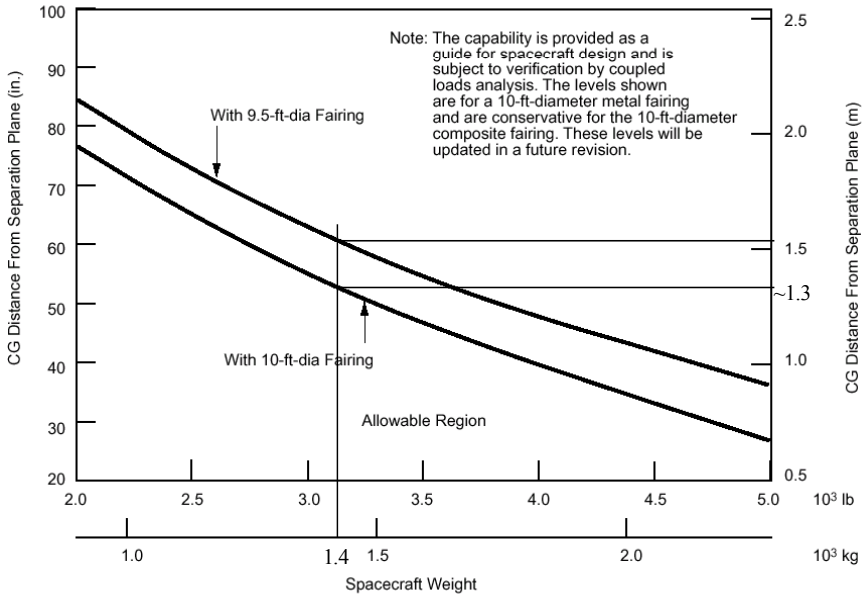

Figure 5.5-1: Payload mass versus centre of mass height for Delta II

For the originally assumed mass of 1407Kg in a 9.5ft fairing, the height is approximately 1.5m. This is less than the original configuration of Fig 5.2-1 indicates. For the 10ft composite fairing, the value is not

exactly defined, but is between the metal 10ft fairing shown in Fig 8 and the 9.5ft values. It can then be assumed around 1.4m.

This means the stack cannot be over 2.8m high even with a zero thickness launch adapter. For a stack of 3 module combinations, each combination cannot be deeper than 933mm. At 800mm, a launcher adapter of only 200mm height is allowed. This is too small for an adapter with one interface circular at 937mm diameter, and the other 3 points at 872mm radius (1745mm diameter circle). To keep the overall height within limits, the adapter must interface directly with the STAR 48 mounting ring, thus carrying some launcher equipment that is on the original adapter structure between the STAR 48 and the standard Delta II 937 interface (see Figure 5.5-2). This then involves development by the launcher supplier of a special adapter, a service they have offered elsewhere before.

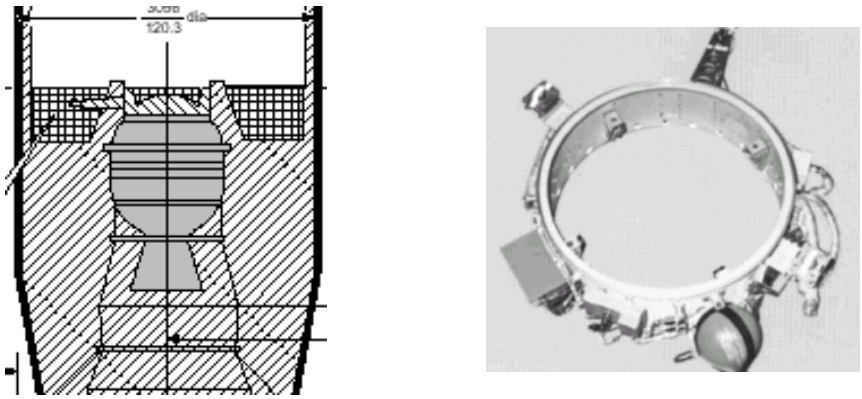

Figure 5.5-2: Delta II STAR 48 Adapter

The stack height for one combination of science and propulsion module, taken as 800mm, is shown in Fig 5.4-3. It is clear that only 203mm total height is available for the propulsion module.

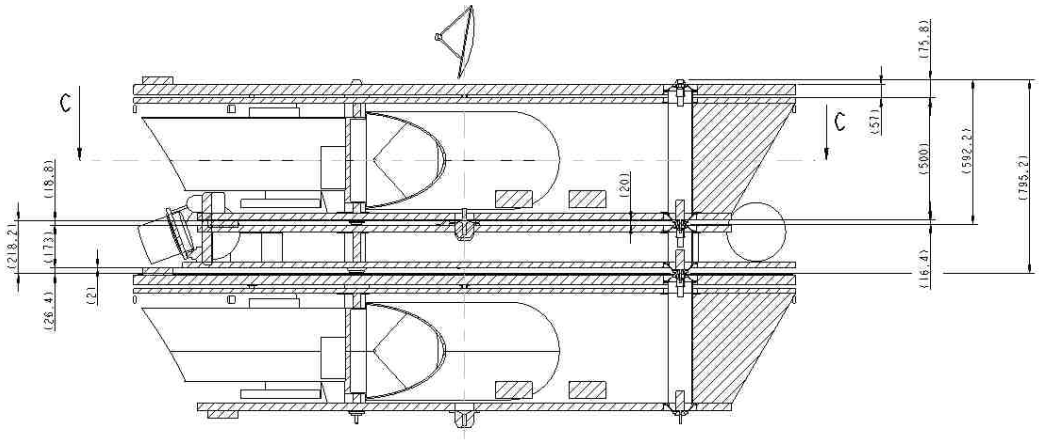

Figure 5.5-3: Stack height dimensions (repeat of Fig 5.2-9)

5.5.1.3 Propulsion Module Layout

The units to be accommodated in the module must therefore mostly be located around the periphery of the module structure, using the free volume created by the conical shape of the science module outer walls, but avoiding the science module antennas.

This also means the structure is not optimum for the module. it is effectively a large thick flat plate, supported only at 3 points some way inboard of the rim, and with the bulk of the mass at the rim in clumped masses. The structure can be reinforced locally to meet the eigenfrequency limits locally, but a heavy penalty is paid in mass and structural complexity. The resulting layout is seen in Figure 5.5-4.

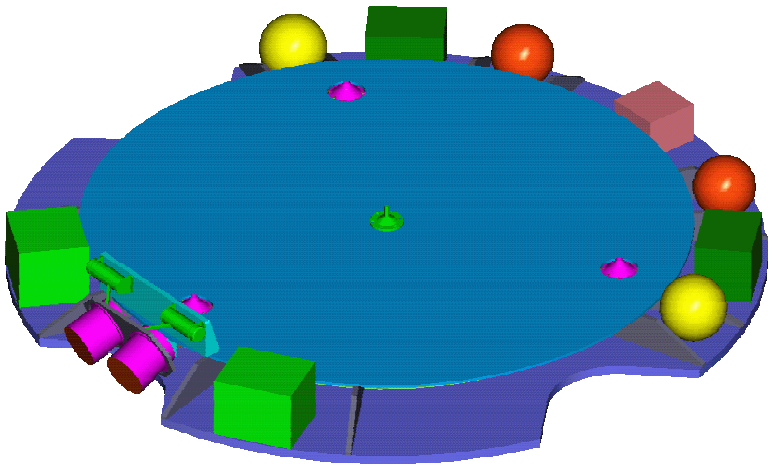

Figure 5.5-4: Propulsion Module layout.

It is seen from the internal detail illustration of Figure 5.5-5 that a return to the circular wall has been adopted, and this is to minimise the overhang distance of the clumped masses from the main structural elements.

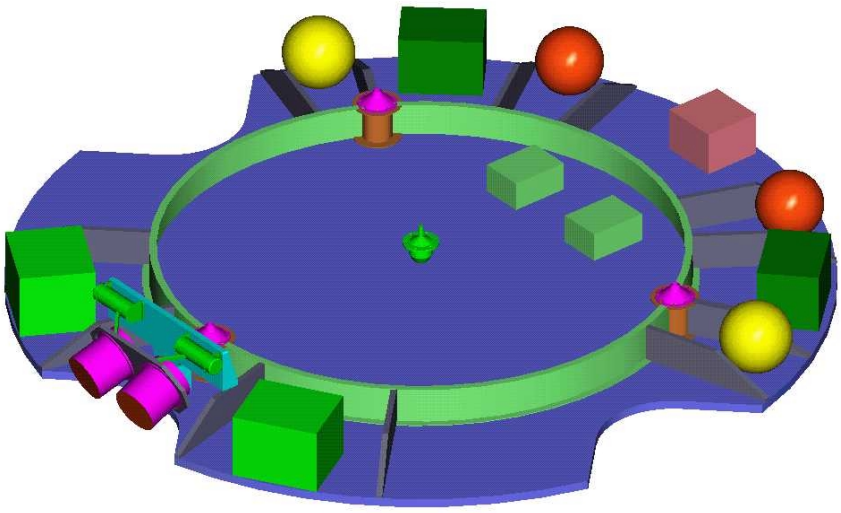

Figure 5.5-5: Internal detail of the propulsion module

Cutouts in the rim of the plate are to allow for the projection of the communications antennas of the science module into these spaces.

The heaviest element of the clumped masses is the ion thruster group on the tilt mechanism. This mechanism allows the thrust vector to be always aligned through the CoG of the science module/propulsion module combination during the transfer phase. There may be a possibility to be studied in the future of deleting the tilt mechanism if the RCS can provide enough counterbalancing torque without excessive fuel use.

The rear side of the main plate carries the propulsion module solar array, which will cover most of the surface. This will then provide power for both the propulsion and science modules during the transfer phase.

There are therefore a number of electrical interfaces between the modules, consisting of signal lines to operate the propulsion and RCS from the AOCS electronics in the science module, and power and signal lines for the propulsion module power subsystem, to allow control from the science module and power supply to it.

These connections must also have a separate and special separation unit, to ensure that separation of these connectors do not disturb the small separation velocity required at the operational orbit.

5.5.1.4 Review of the separable modules concept

When originally proposed, the concept of a separable propulsion module appeared full of advantages. It removed with one stroke all the problems of residual fuel slosh and allowed an optimised operational power subsystem for the science module functions.

What was then not expected was the severe limitation imposed by the centre of gravity height limitations of the stack within the launcher. This limitation has resulted in a flat disk propulsion module with significant structural and mass disadvantages, incorporation of special low velocity separation

mechanisms and connectors, and most significantly, removing any flexibility for minor growth changes in the telescope diameter should any detail design considerations in this area so require.

It may be therefore worthwhile in any subsequent study to quantify the disadvantages of reintegrating the propulsion functions into a single science/propulsion satellite, to allow comparison with the disadvantages of the present scheme. While the present layout does not appear to contain any show stoppers, the margin for refining the detail design could prove too small to prevent some restriction of science performance of the satellite as finally realised.

An alternative approach is to reconsider the selection of launcher. It is not clear that the Delta II will still be in production by the time of intended launch of this mission. In that case the newer generation launchers may provide just the margin that is at present lacking for the current selected baseline launcher.

5.5.2 P/M Electrical Architecture

The LISA electrical configuration is composed of the electrical subsystems on the Science Module and necessary add-ons on the Propulsion Module for ion- and chemical propulsion interface and for the power system (refer to Figure 5.3-2: Functional/Electrical Concept with Centralised Processor System and to Figure 5.3-4: Functional/Electrical Architecture).

The LISA specific electrical P/M functions are:

- providing the interface for the chemical propulsion and ion propulsion systems, if ion thrusters are mounted on optional gimbals the chemical propulsion could be deleted
- providing external and internal umbilical/harness for the stacked composites on the Launcher which shall allow for soft separation of the propulsion modules from the Science Modules
- providing the power and energy (from battery) during LEOP, the cruise phase, and the turning of the stack before separation of the propulsion module.

Design:

- The P/M power subsystem is realised by a Power Conditioning Unit (PCU) with some limited power outlets, and a solar array. The PCU and the solar array are designed for the selected power control concept (PPT).
- The PCU functional modules as the MPPT , voltage controller, and MEA and the Main bus voltage regulation are equivalent to the Science Module PCDU as described in section 5.3.2
- battery of Li-ION type
- charge and discharge regulators are located in and managed by the PCU. The design employs a highly efficient method with an extensive space proven heritage.

Table 5.5-1: Propulsion Module PCU Mechanical Characteristics

Module	Mass / g	No	Total Mass / g	Module Width / mm	Length / mm	
Input Module	1250	1	1250	50	50	MB-Filter 800u, 2 Batt-relay, 2 Curr. Sensors, 2 D*M 25 pol
SAR Module PPT-400W	900	3	2700	50	150	3 Power Regulator 400W, 2 aus 3 hot redundant
Propulsion Control Mod	530	2	1060	25	50	Switches for Prop Control
Discharge Regulators	1100	3	3300	50	150	2 aus 3 hot redundant
Charge Regulators	475	2	950	25	50	1 aus 2 cold redundant
Auxiliary Supply	650	1	650	25	25	Doppel-Supply 2*6W, 2*DxM
Interface	440	2	880	25	50	MIL STD 1553 I/F
HK-stage MEA,PPT	540	1	540	25	25	MEA Batt. Charge Control, HK-Erfassung (M+R) 2*DxM25, Peak Power Tracker
Housing			3300			
Total Mass			**14.63 kg**			
Dimensions:			**H x W x L (mm x mm x mm) 203 x 204 x 550**			

Solar Array

According to Table 5.3-4: Detailed Power Budget with Power Demand of the Solar Arrays' the SA of the Propulsion Module during the cruise phase is required to generated 938 W. This is only feasible with the application of dual junction GaAs solar cells (efficiency 23% at 28°C) or triple junction cells (efficiency 24.5% at 28°C, US source). Standard GaAs cells do not comply with the required performance (refer to Table 5.4.2-2).

During the cruise phase this SA is orientated to the sun under an aspect angle of some few (TBD) degrees. Up to an angle of +/- 34 degrees the SA of 5.2 m² delivers full power as given in the budget. At maximum illumination the required SA area is only 4.3 m².

Table 5.5-2: Potentially Available SA Power at EOL

Parameters	Propulsion Module	Propulsion Module
Available Area / m²	5.2	5.2
Applied GaAs cells	standard	triple junction
Efficiency of cells at 28°C	18.3	24.5%
Temperature Coefficient	0.19%/K	0.25%/K
Array Temperature /°C	110	110
Efficiency at ops temperature	15.45%	19.48%
Solar Aspect Angle	0°	0°
EOL	450 days	450 days
Required Power (SA area)	938 W	938 W (4.3m²)
Available SA Power at EOL	**(900 W)**	**1134 W**

Power Degradation: 2.75% per year, as for GEO application assumed for both types of cells

Battery:

There are no other requirements for the battery yet than for magnetic cleanliness and to serve for LEOP, cruise back-up, and turn-over manoeuvre.

Provisionally a hypothetical 10 kg Li-Ion battery is taken as reference for the budgets and mechanical configuration.

5.5.3 Ion Electric Propulsion Subsystem

5.5.3.1 Requirements

It was already decided at the beginning of the study based on the pre-phase a investigations that solar electric propulsion will be preferred against chemical propulsion due to the resulting mass saving. Electric propulsion systems generate the thrust by acceleration of a propellant by electric energy. The exhaust velocity is essentially higher than for chemical propulsion systems and thus is the specific impulse. The propellant necessary for transfer of the LISA spacecraft to their operational orbits decreases dramatically. Unfortunately is the propellant mass saving partially compensated by the high dry mass of the electric propulsion system mainly caused by the higher mass of the thrusters, the power conditioning units and the S/C power subsystem.

Two thrusters in cold redundancy will be installed on one side of the satellite thrusting in spacecraft X-axis through the c.g. of the satellite. Table 5.5-3 shows the main requirements on the performance of each thruster.

Table 5.5-3: Electric Thrusters Requirements

PARAMETER	REQUIREMENT
Maximum thrust	18 mN
Thrust level adjustable	Only on or off mode required
Total operation time	≤10,100 h
Thrust vector migration during the mission	± 0,5 °
Thrust vector stability	< 0.5 °
Thrust noise	5 mN,@ f < 2 mHz to 50 µN,@ f > 0.2 Hz 1/f slope in between

5.5.3.2 Suitable Electric Propulsion Systems

The important requirements for the thrusters along the orbital velocity axis (x-axis of the spacecraft) is the high specific impulse to decrease the propellant mass.

Different propulsions systems have been investigated with respect to their suitability to the requirements of the mission. Mainly thrusters with grids forming the ion beam are best suited for this application because they offer the most attractive data with respect to thrust stability and thrust accuracy. Out of the thrusters currently in development and/or in qualification in Europe 3 thruster types have been considered as applicable for this mission:

- Radio frequency Ion Thruster RITA, manufactured by Dasa in Germany
- Electron-Bombardment Ion thruster UK-10, manufactured by DERA (or MMS) in England
- Radio frequency with Magnetic field Thruster RMT, manufactured by Laben-PROEL in Italy

The first two developments are suitable for the application on LISA while the RMT is currently specified for 12 mN only. In the following the RITA and the UK-10 types are briefly described with respect to the LISA requirements.

5.5.3.3 The RF Ion Thruster RIT 10

The RF ion thruster (RIT) principle has been developed at the university Giessen, Germany. At Dasa the RIT thrusters are under development since many years. Discharge chamber diameters from 10 to 35 cm have been investigated. The most advanced thruster system RIT 10 is based on a 10 cm discharge chamber diameter. A thruster of this type has been flown on the retrievable carrier EURECA in 1992/93. Two thruster assemblies are qualified and delivered for the European telecommunication satellite Artemis, where they will perform north-south station keeping together with the UK-10 thrusters.

The design of RITA for Artemis has been mainly directed to its use for North/South station keeping of Geostationary satellites and the interfaces requirements of Artemis, but is considered to be adaptable to LISA without major changes. The thrust level is qualified at 15 mN but has already been demonstrated up to above 40 mN (RIT-evo grids). The LISA thruster will be equipped with the new grid design for lower power/thrust ratio.

Dasa has also started the development of a RIT ion thruster for commercial application for a nominal thrust level of 150 mN, which is expected to be qualified in 2001.

Operation Principle

The RF-ion thrusters achieve ionisation of the propellant gas by inducing energy by means of a high frequency generator coil positioned around a discharge chamber. The operational principle is illustrated in Figure 5.5-6.

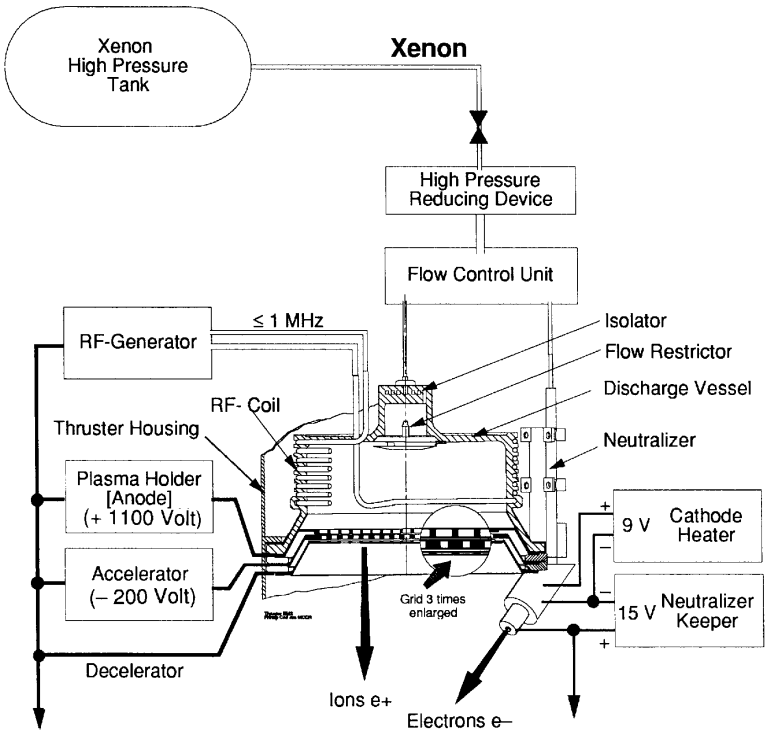

Figure 5.5-6: RF-Ion Thruster Operating Principle

The propellant Xenon enters the discharge chamber of the thruster through the isolator and a gas distributor. To start the ionisation of the Xenon the neutraliser is activated first. Electrons generated in the discharge at the neutraliser tip are drawn into the discharge chamber by application of positive potentials to the electrodes of the extraction system. The electrons in the discharge chamber accumulate energy from the RF-field of the induction coil and ionise the neutral propellant by inelastic collisions with the propellant atoms. Once the discharge has started it is self sustaining and the voltages on the grids can be switched off. The thruster is now in a state of Stand-by condition, ready for thrusting.

To generate thrust, a positive high voltage (900 to 1200 V) is applied to the plasma holder and a negative high voltage (-200 to -600 V) is applied to the acceleration electrode. The decelerator is kept on thruster ground potential. Under the influence of this electrostatic field positively charged propellant atoms (ions) are accelerated towards the thruster outlet at velocities in the range of 40 km/s.

The ion beam is neutralised by electrons from the discharge at the neutraliser tip, where the electrons are generated by ionisation of Xenon in a low voltage arc discharge between a cathode and the keeper of the neutraliser. The ion beam will act as potential wall for free electrons. The current drawn from the neutraliser thus match the needs for neutralising the ion beam automatically.

Thrust control can be realised easily and accurate by the control of the beam current via the density of the ions in the discharge chamber, which again is controlled by the energy of the RF-field via an automatic control loop.

Operational Characteristics

Figure 5.5-7 shows the total power input necessary for the RITA Evo (Evolution) thruster based on test results in 1998 and on calculations for the efficiencies of the electronics.

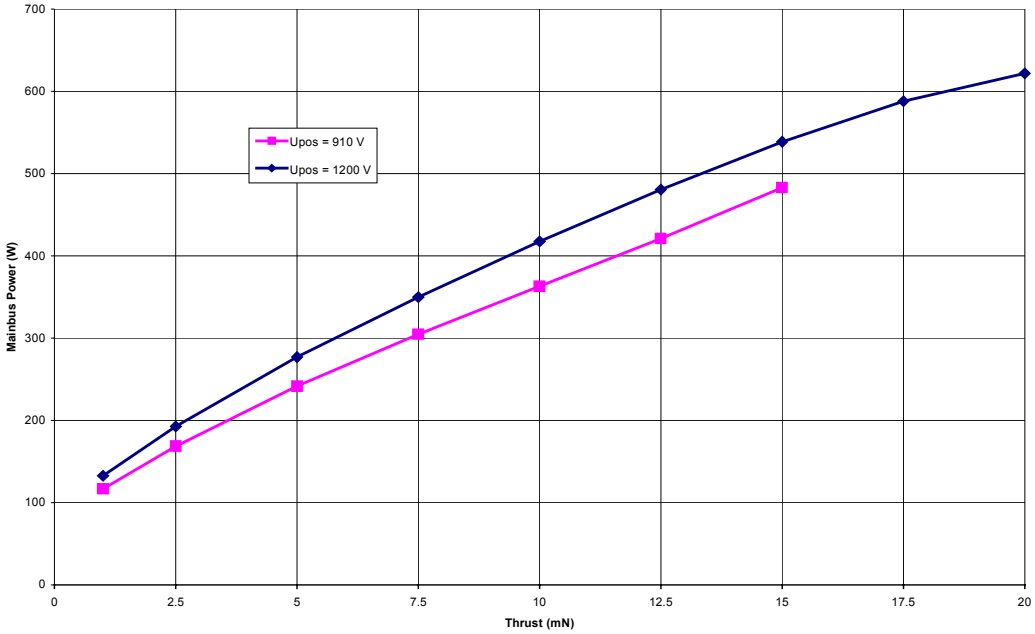

Figure 5.5-7: Total Power Input for RITA/Evo

Figure 5.5-8 shows the relevant optimised mass flow versus the thrust level. In both diagrams the thruster is operated at a screen grid voltage of 910 V up to a thrust level of 15 mN. Above 15 mN a screen grid voltage of 1200 V will be necessary to reach the required thrust level. This results in an increase of power input and in a decrease of required mass flow.

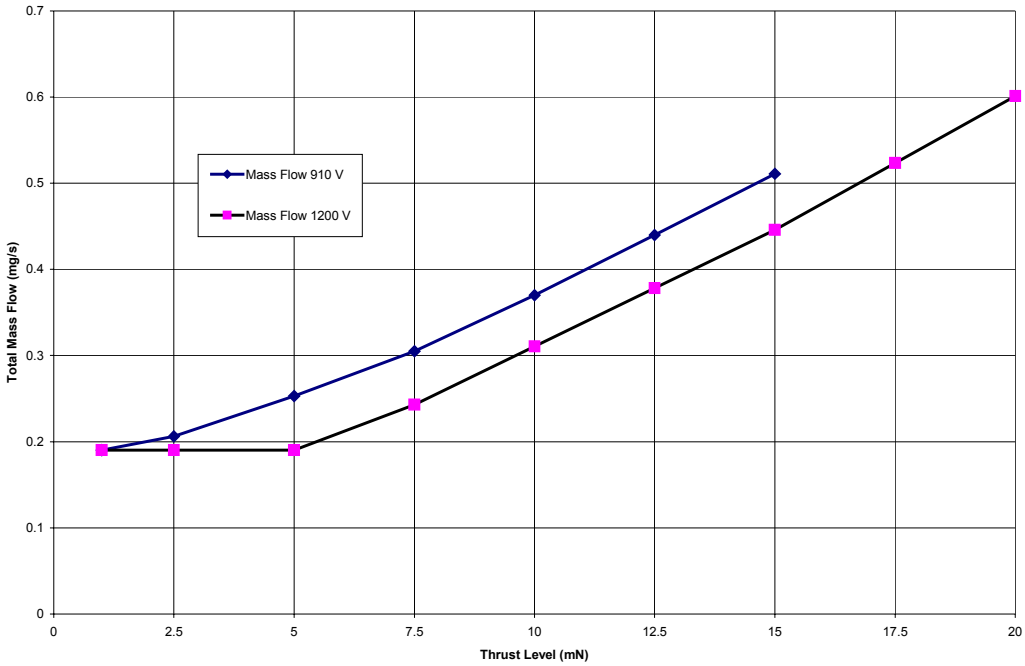

Figure 5.5-8: Total Mass Flow versus Thrust Level for RITA

Figure 5.5-9 shows the beam current control loop for RITA.

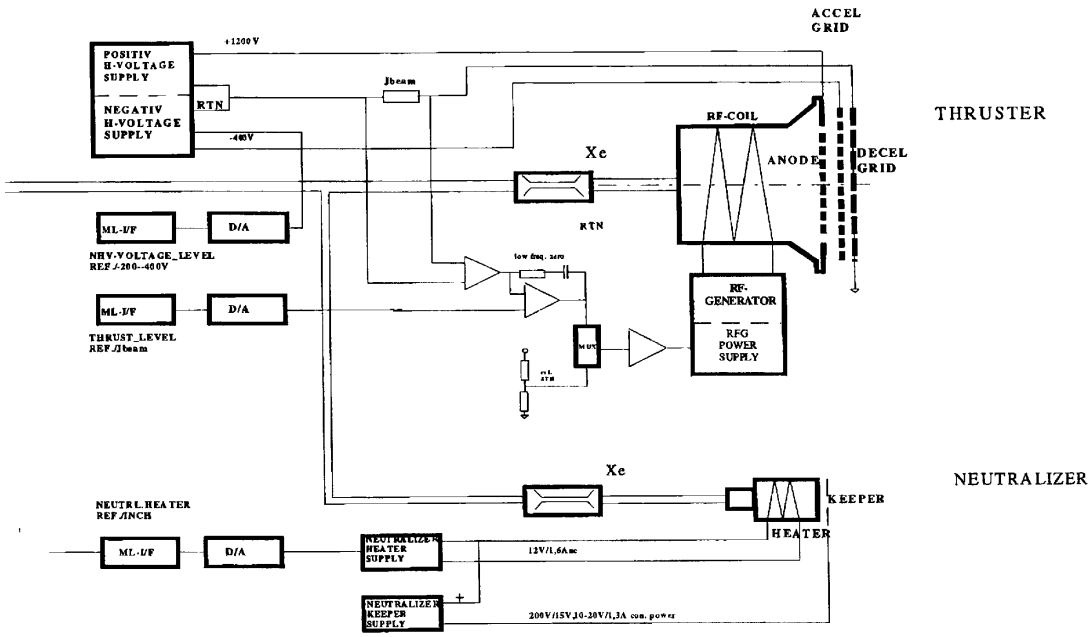

Figure 5.5-9: Beam Current Control Loop for RITA

The beam current is measured in the return line as a result of the current to the screen grid and to the accel grid. It will be compared with the given thrust value, which may come from ground commands or from a source in the satellite. Deviations will be regulated by the adaptation of the power of the RFG Power Supply.

Fast changes can be realised at constant mass flow through the thruster having some impact to the specific impulse. For slow variations the mass flow through the thruster can be adapted which will allow to run the thruster at optimum specific impulse conditions.

5.5.3.4 The UK-10 Thruster

Development Activities over many years in the UK have culminated in the development of a 10 cm beam diameter gridded ion thruster (UK 10, also referred to as T5) which has been developed for tasks requiring moderate thrust below about 30 mN. The UK 10 is also used for station keeping on ESA's Artemis. The UK-10 thruster system and the pressure reduction device have been qualified within the Artemis program to the same requirements and interfaces as RITA Thrust levels above 20 mN have been demonstrated

Operation Principle

The gridded ion systems developed in the UK are based on Kaufman-type ion thrusters. Each thruster must be supplied with propellant gas at accurately regulated flow rates from a propellant supply and monitoring equipment (PSME), and with appropriately controlled voltages and currents by a power conditioning and control equipment (PCCE).

The thruster schematic is shown in Figure 5.5-10. Propellant gas – originally mercury, now Xenon – is fed from the PSME into the cylindrical discharge chamber via an axial hollow cathode and a by-pass distributor mounted on the soft iron backplate. This gas is ionised in a DC discharge between the cathode and a concentric cylindrical anode. The efficiency of this discharge process is enhanced considerably by the application of an azimuthally symmetrical magnetic field to the discharge chamber. This field is generated by solenoids distributed around the outside of the discharge chamber. The magnetic field links two cylindrical pole pieces, the one bolted to the backplate being of much smaller diameter than that at the exit from the discharge chamber. The tip of the inner pole piece surrounds a non-magnetic baffle disc, which effectively separates the hollow cathode region (the coupling plasma) from the main discharge plasma.

The design of these critical components is such that the primary electrons from the cathode gain the correct amount of energy in passing through the annular gap between this disc and the pole piece to achieve optimum ionisation in the discharge chamber.

The resulting highly ionised plasma drifts toward a set of closely spaced, perforated grids at the downstream end of the discharge chamber. The positive ions are extracted and accelerated to a high velocity by electric fields applied to these grids. This velocity is determined totally by the applied potentials, and is typically 30 to 50 km/s.

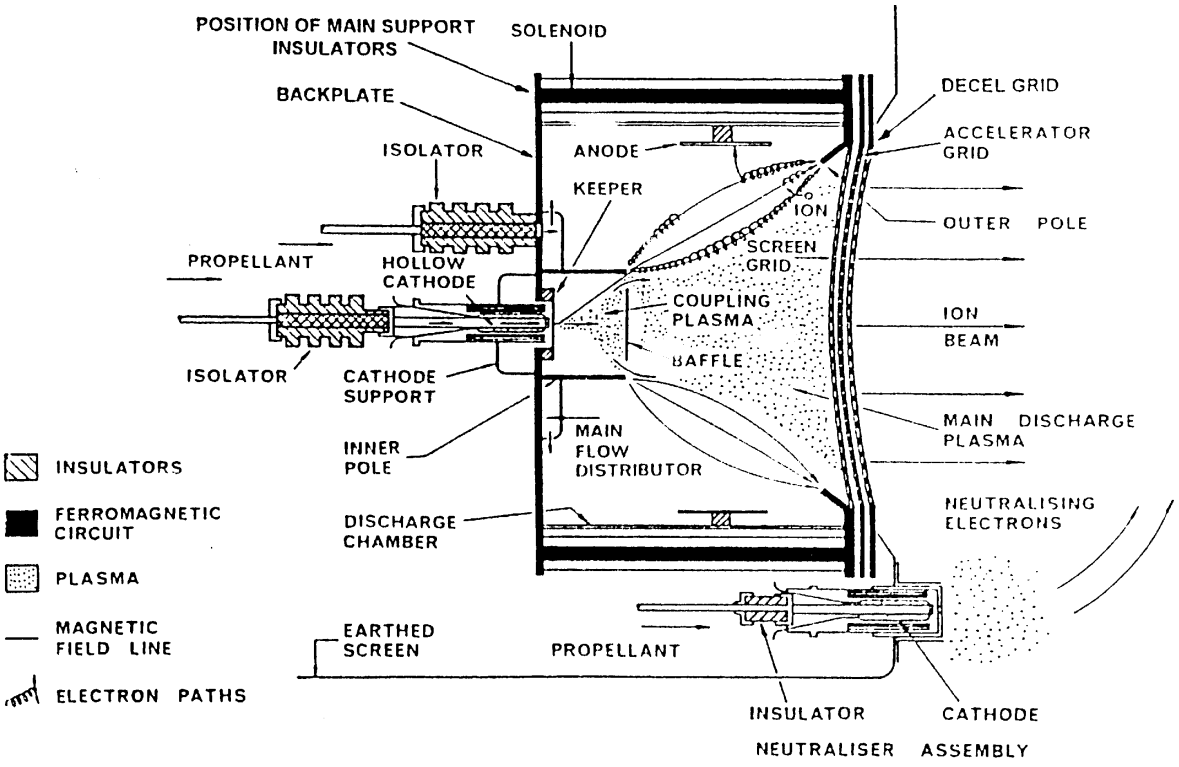

Figure 5.5-10: Schematic View of the UK Kaufman-Type Ion Thruster

The positive space charge of the emerging ion beam is neutralised by electrons emitted from an external cathode, which is essentially identical to that in the discharge chamber. The neutraliser is fed with Xenon at a very low flow rate, and a plasma is created adjacent to its tip by a discharge between it and a nearby keeper electrode. Electrons are extracted automatically from this plasma to maintain the spacecraft at close to space potential.

Operating Characteristics

Figure 5.5-11 shows the relation between power to the ion thruster and thrust level. The thrust level can be adapted to the requirements by influencing the operational parameters.

Numerous measurements have been performed at thrust levels between 0.2 to 22 mN by DERA in the course of the GOCE study. This included specifically thrust vector stability at different thrust levels, beam divergence and transient response. As an outcome of those tests it is mainly necessary to change the current to the magnets to change the thrust level. The mass flow of the hollow cathode can be kept nearly constant over the whole thrust range. The main mass flow has to be adapted to thrust level accordingly.

The UK-10 thruster system and the pressure reduction device have been qualified within the Artemis program to the same requirements and interfaces as RITA.

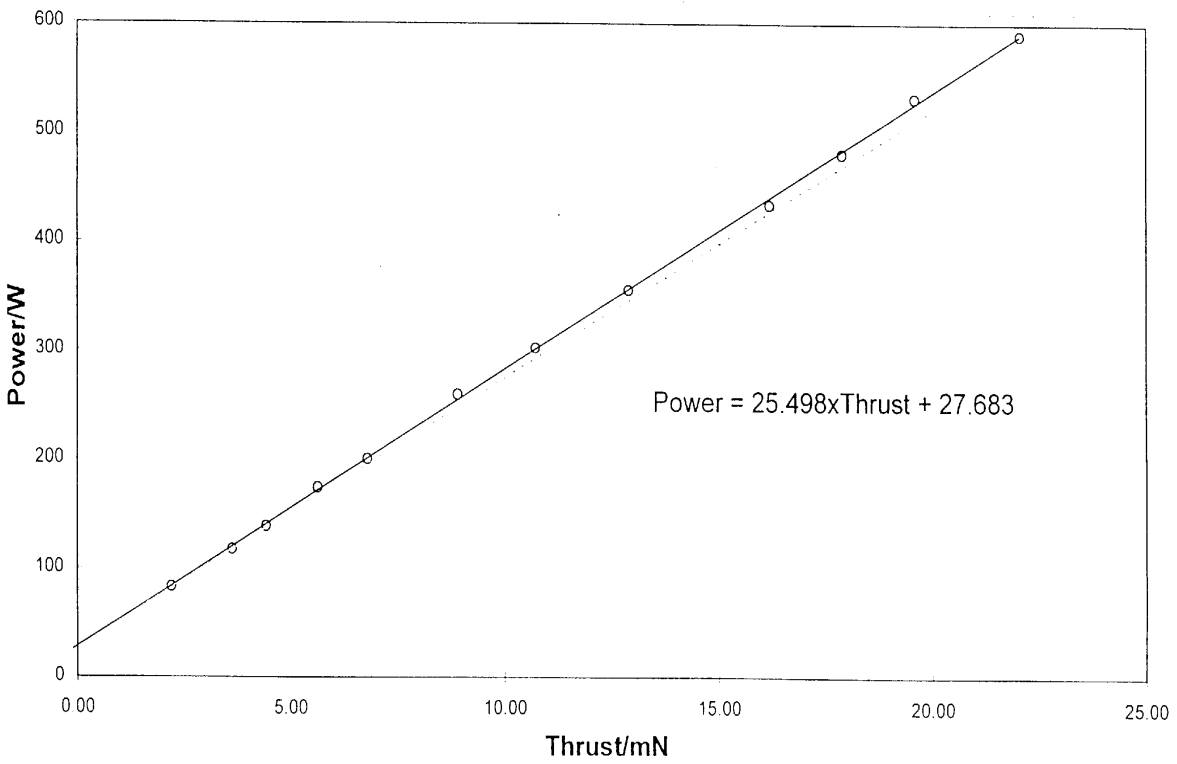

Figure 5.5-11: UK-10 Ion Thruster Power in Relation to the Thrust Level

5.5.3.5 Propulsion System Evaluation

Due to the 18 mN thrust requirement only 2 of the 3 European propulsion systems can be considered:

- The RITA, manufactured by Dasa in Germany
- The UK-10, manufactured by DERA (or MMS) in the UK.

A comparison of the system masses of RITA and UK-10 is shown in Table 4-1.

Table 5.5-4: Masses for RITA and for UK-10 based on Artemis

Unit	**RITA**			**UK-10**		
	Mass per Unit [kg]	Number of Units	Total Mass [kg]	Mass per Unit [kg]	Number of Units	Total Mass [kg]
Thruster	1.8	2	3.6	1.9	2	3.8
Mounting Bracket	1.0	1	1.0	1.0	1	1.0
Flow Control Unit	2.0	2	4.0	2.0	2	4.0
Pressure Reducer	0.6	2	1.2	0.6	2	1.2
Power Supply Unit	9.8	2	19.6	11.5	2	23.0
Harness, Tubing, Valves	2.3	1	2.3	2.3	1	2.3
Total Mass			**31.7**			**35.3**

The masses of the two systems are comparable within the accuracy of the estimations. Both ion thruster systems can be used for the application on LISA, the RITA being included in current baseline.

5.5.3.6 Thruster System Design and Interfaces

As a final selection of the ion propulsion system for the application to LISA will be done later the design and interfaces have been done using the RITA as an example. Same or similar solutions can be found for the UK-10 system.

Figure 5.5-12 shows the block diagram of the ion propulsion system for LISA for 2 RIT thrusters which can be operated alone or in parallel. 2 pressure reducers are mounted, one in operation and one in redundancy. Table 5.5-5 shows the main dimensions and constraints of the RITA components. The two thrusters shall be mounted as close as possible side by side, both thrusting through the COG of the spacecraft. Figure 5.5-13 shows a view on the RIT 10 thruster. Figure 5.5-14 shows the arrangement of the thrusters on the –x side of the spacecraft.

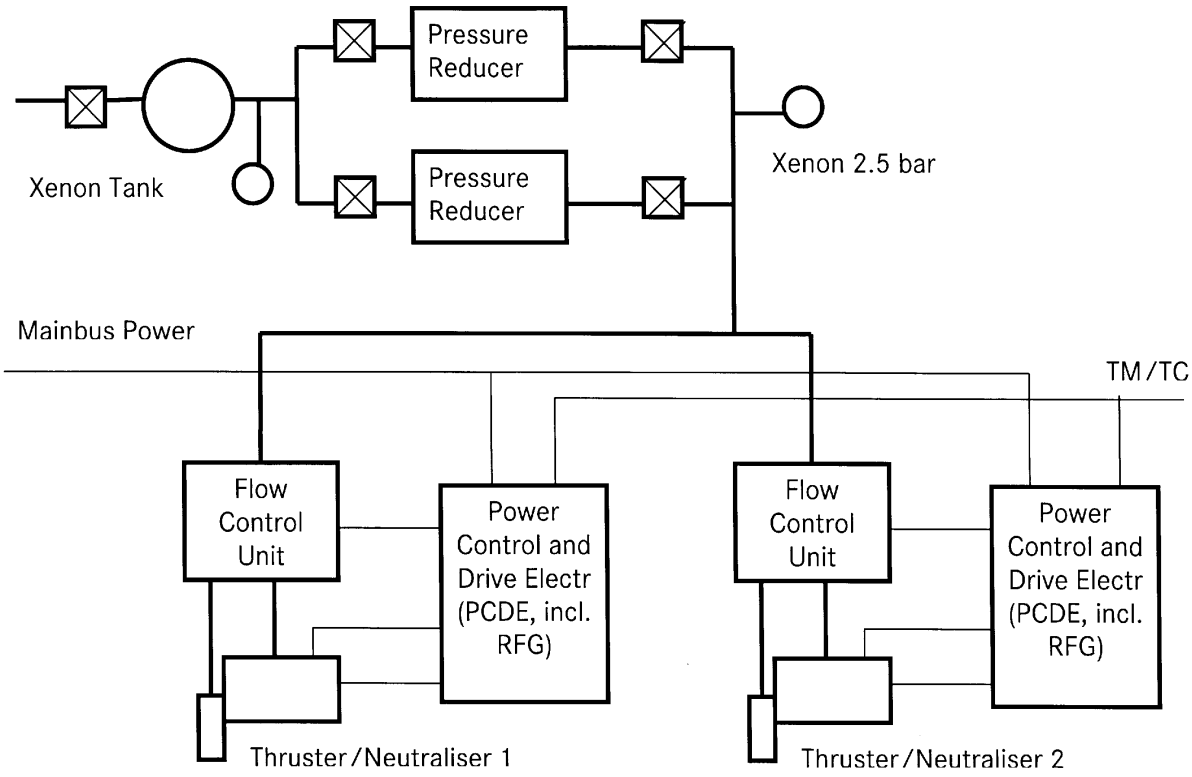

Figure 5.5-12: Ion Propulsion System RITA for GOCE

Table 5.5-5: Dimensions and constraints of the RITA Components

Equipment	Dimensions	Constraints
Thruster/Neutraliser	185 x 165 x 185 mm	Thermally decoupled from S/C structure ? Radiation of heat loss directly into space by thruster case ?
PCDE (includes RFG)	290 x 250 x 220 mm	Mounted inside the satellite, thermally coupled to S/C structure
Flow Control Unit	200 x 150 x 100 mm	Mounted inside the satellite, thermally coupled to S/C structure

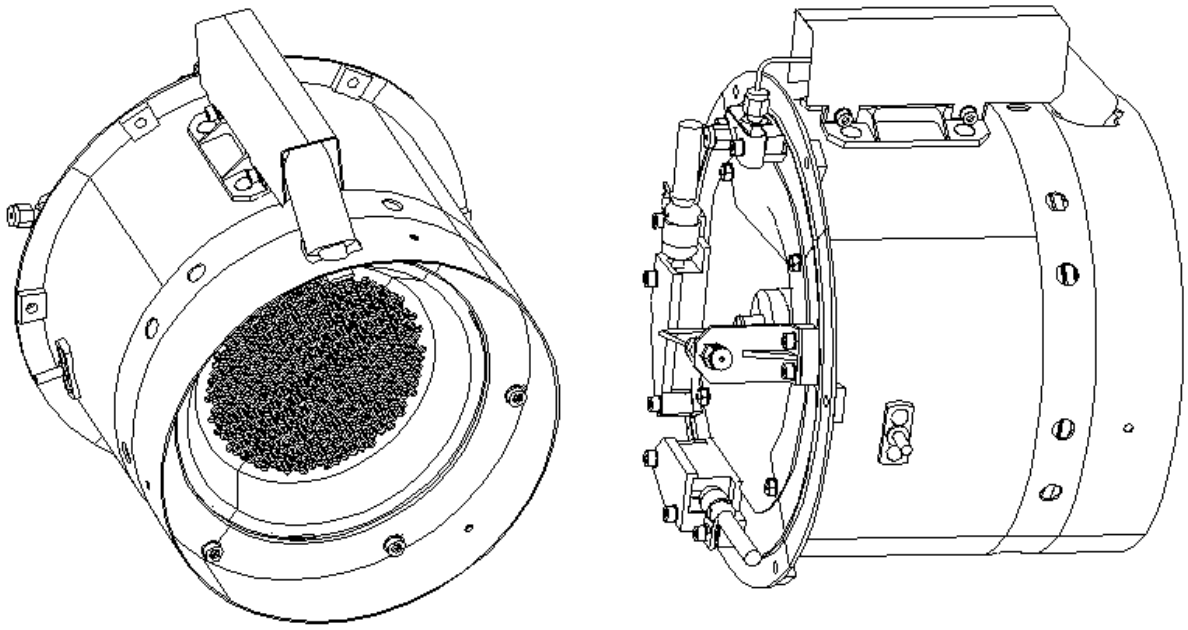

Figure 5.5-13: View on the RIT 10 Thruster

One of the two thrusters will be in operation at a time to decrease the power requirement on the solar arrays.

The thrusters will be arranged as close as possible to minimise the angle between the thrust vector and the x-axis in order to minimise the thrust component vertical to the x-axis. Figure 5.5-14 shows that for the RITA a minimum distance of 170 mm can be achieved considering cut-outs at the mounting flange.

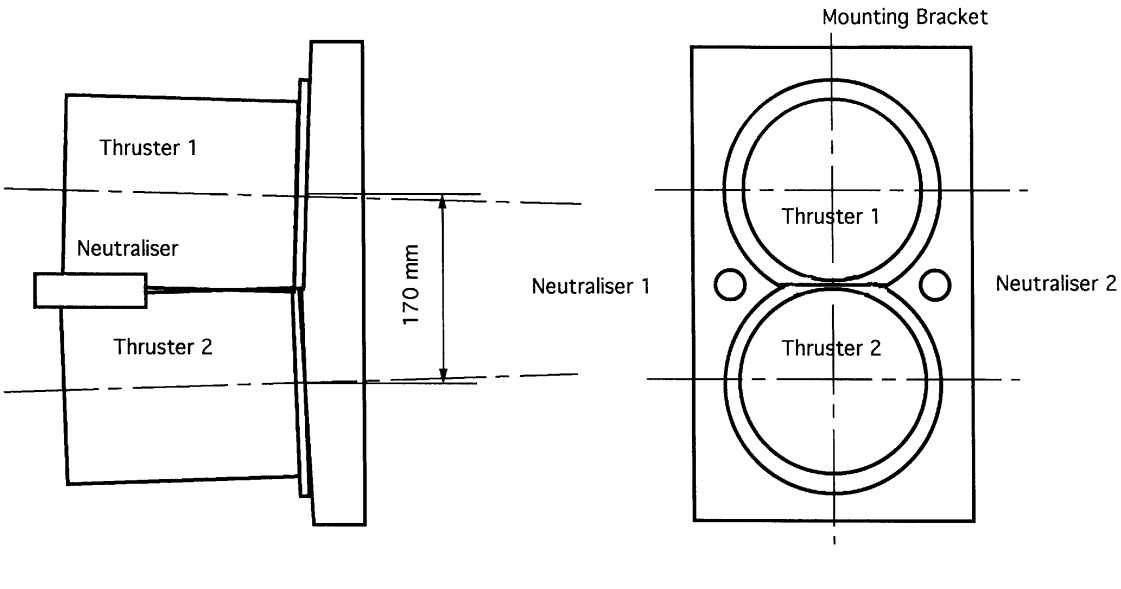

Figure 5.5-14: Mounting of the two Thrusters Side-by-Side

This arrangement guaranties full redundancy of the two thruster systems. If one thruster fails, the other thruster will be set in operation. In addition there is the possibility to operate one thruster with any of the two neutralisers if this situation is considered in the design of the electronics.

Regarding the thrust vector migration the current assumptions are:

- There will be a migration of the thrust vector by thermal expansion of the grid system during heating up of the thruster for the first hour of operation of maximum 1° over the total mission time. Measurements performed up to now show ± 0.2° for a few cycles.
- During steady state operation a migration of the thrust vector is very low.
- Unsymmetrical erosion in the grid system may cause an additional migration of the thrust vector of 1° over the total mission time which, in the worst case, can have the same direction as for heating up and could therefore increase the migration to 2°. Measurements for this migration have not been performed yet.
- The offset of the thrust vector with respect to the mounting plane will be measured during qualification- and acceptance tests.
- The thruster will be mounted on the satellite in a way which minimises the 3 reasons for thrust vector migration by shimming. This could help to achieve the required limitation of the migration to ± 0,5° under the operating conditions on LISA.

It is recommended that special tests of the thrust vector migration will be performed to measure the deviation during start-up, constant operation and change of thrust level on a real thruster in the lay-out for GOCE to get detailed information on this phenomenon.

5.5.3.7 Conclusions

Ion thrusters are under development world-wide since about 30 years. Since 5 years detailed experience in orbit operations exists. Application on commercial satellites (Hughes) and scientific missions (Deep Space 1) did show that this thruster technology is mature enough to be used on future programs.

The two thrusters currently under consideration have undergone a detailed qualification program for its application on Artemis, which will be launched this year. Both can be used with minor modifications for the LISA mission. The main modification concerns the thrust level of 18 mN.

Tests must also clarify if the thrust vector migration specified with ± 0.5 ° during the total mission can be achieved with the existing thruster design. The thrusters will be mounted on the satellite thrusting through the c.g. of the spacecraft. As deviations of the thrust vector direction increase the need for attitude control propellant, the thrust vector migration during the whole mission is an important issue for the spacecraft design. Test on a real thruster with detailed measurements on the thrust vector direction shall therefore be performed at an early stage of this program.

5.5.4 Hydrazine Propulsion Subsystem

During the transfer phase to the operational orbit the propulsion module provides the propulsion using Ion thrusters and attitude actuators are proposed using a conventional Hydrazine RCS system. The Ion thruster assembly can form part of the attitude control system in so far as the assembly can be mounted on a one axis gimbal to ensure the propulsion thrust is always through the predicted centre of gravity of the science module plus propulsion module combination. The alternative is to fix the Ion thruster assembly, and use the RCS to correct for the torques caused by the offset thrust axis of the Ion thrusters. In the latter case the RCS will be the same but with a larger fuel tank.

5.5.4.1 Requirements

The minimum number of thrusters to control 3-axis torques is 4, when no constraint is set on the resulting disturbance force. In a first configuration, it is proposed to place these thrusters regularly spaced on the outer border of the propulsion module plate (see Figure 5.5-15). This is a good configuration to create torques in all directions, with a large lever arm, but it could be re-optimised in later phases, taking into account other issues, such as bulkiness, etc...

With this preliminary configuration, the direction of thrust of each thruster that minimises the hydrazine consumption with respect to the expected spatial distribution of the disturbance torques can be found.

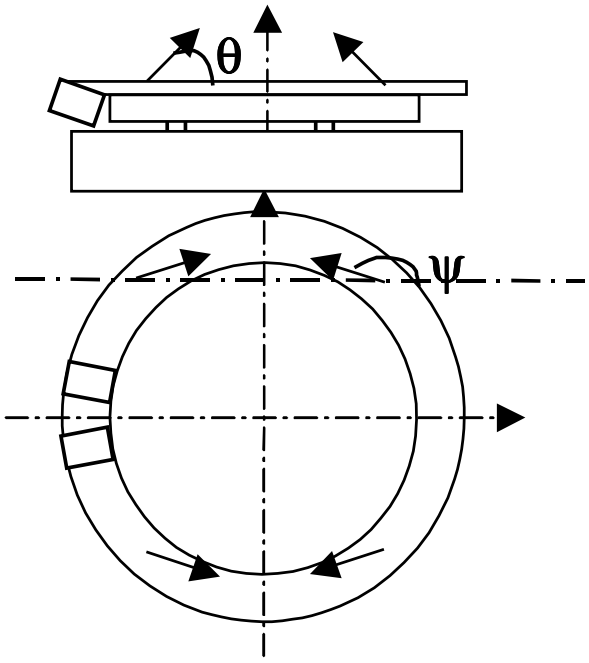

Figure 5.5-15: Thrust-direction-optimised configuration

The optimisation programme shows that the optimum angle for θ and Ψ (With Θ the off-plane angle, and Ψ the angle between X and the projection of the thrust in the plane) are $\theta = 45°$ and $\Psi = 160°$.

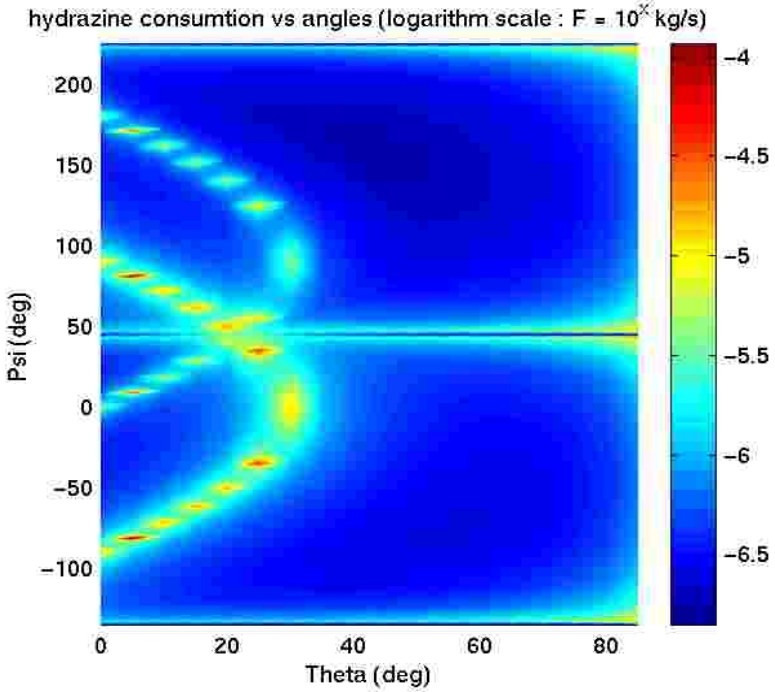

Figure 5.5-16: Thrust direction optimisation result

These results correspond to the case without gimbals for the IPS so only solar disturbing torques are accounted for.

Since there is only 4 thrusters, it is not possible to control the torques without creating parasitic forces. These are small, less than 400µN compared to IPS thrust. , so the effect on the transfer orbit is negligible.

The recommended configuration is therefore 4 thrusters, plus a redundant branch for failure isolation in Safe Mode.

5.5.4.2 Subsystem Description

As a typical example for a Hydrazine mono-propellant RCS fulfilling the requirements for attitude control of LISA during the transfer phase, the 'LEO ONE' module developed on basis of the Globalstar Spacecraft is shown in Figure 5.5-17 and Figure 5.5-18 summarised in Table 5.5-6. The tank size is representative of that expected for the fixed Ion thruster case and would be reduced for the mass optimised gimballed version.

The hardware presented will also be used as reference for the baseline cost estimate.

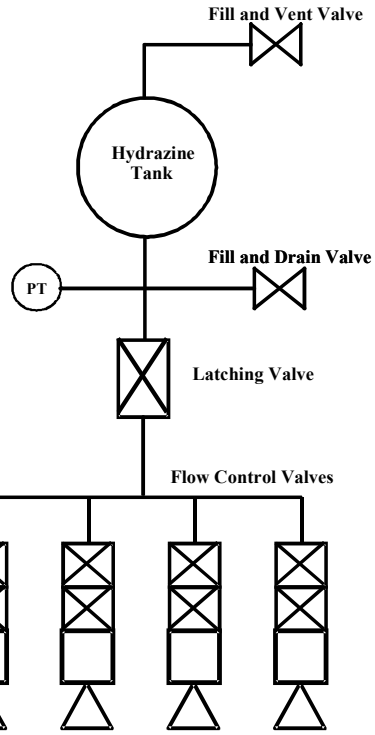

Figure 5.5-17: Schematic of the LEO ONE Mono-Propellant RCS

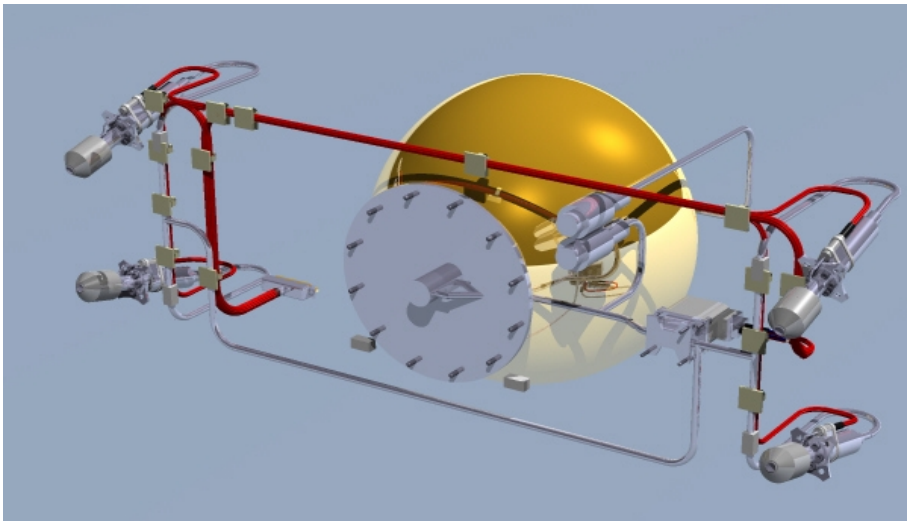

Figure 5.5-18: LEO One Hydrazine RCS

Table 5.5-6: Summary of a LEO ONE based RCS

Subsystem comprises:	4 Thrusters, 1 Propellant Tank, 2 Fill and Vent Valve, 1 Latching Valve, 1 Pressure Transducer, Tubing
Operational temp.:	+10°C to +50°C
Thruster:	1N with Isp of min. 211s and max. 222s
Supplier:	Dasa-RI / Moog (Valve)
Model:	CHT 1
Heritage:	GlobalStar
Operation mode:	blow down
Tank:	Ø=320mm
Capacity:	up to 12 kg Hydrazine
BOL pressure:	22bar @ 20°C, EOL >5.5bar
Supplier:	Pressure System Inc
Model:	80342-1
Operation	Propellant expelled by pressurant gas separated by rubber diaphragm
Tubing:	1/4 inch Titanium
Further Equipment:	
Latching Valve	Moog/Vacco
Pressure Transducer	Paine
Fill and Vent Valve	DSS (GlobalStar)

5.6 System Budgets

In the following tables the detailed figures estimated for the dimensioning of all units is listed. For the detailed power figures and other electrical system budgets please refer to section 5.3.

Table 5.6-1: LISA Subsystem Mass and Dimensions

H/W No.	*15-Feb-00* **DESCRIPTION**	QTY Sys/ Mod.	Mass [kg] p. unit	Mass [kg] p. S/C	Dimensions p. unit Length [mm]	Dimensions p. unit Width [mm]	Dimensions p. unit Height [mm]	Power p. unit / SS [W] average	Power p. unit / SS [W] peak
0	**LISA Satellite System**								
1000	**Science Module**	**3**		**273.9**					
1100	**Structures & Mechanisms**	1		69					
1200	**Thermal Control**	1		14					
1300	**Electrical Power**			18.4					
1310	PCDU	1		12.4	450	204	203	6	
1320	Solar Array	1		6					
1400	**Data Handling**			15.9					
1410	CPS	1		15.9	410	243	185	25	35
1500	**Radio Frequency**			19.6					
1510	Transponder	2	3.5	7	184	220	165	12	
1520	RFDU	1	1	1	160	60	80	1	
1530	SSPA	2	1.4	2.8	227	63	110	30	
1540	TWT	0	0.75	0	321	58	36		
1550	HG Antenna	2	3	6		300 Ø			
1560	LG Antenna	4	0.2	0.8					
1570	Cabling	set		2					
1600	**Cable harness**	1		21					
1700	**Attitude Control**			**16.9**				**65**	
1710	Star Camera Assembly	1		4.36				9.4	
1711	*SC Optical Head*	4	0.74	2.96	120	120	150	1.5	
1712	*SC Electronics*	2	0.7	1.4	125	105	120	7.9	
1720	Sun Sensor	2	0.08	0.16	72	71	20	0	0
1730	Att. Anomaly Detector	1	0.2	0.2					
1740	Magnetometer	1		0.18	95	53	27	0.8	0.9
1750	FEEP Assembly	1		9				49.8	74.4
1751a	*FEEP El. Clusters*	6	1.5	9				8.3	12.4
1760	HGA Drive	2	1	3				5	
1761	*HD Mechanism*	2	0.5	1					
1762	*HD Electronics*	2	1	2				5	
1800	**Science Instrument**			**99.1**					

Table 5.6-2: LISA Instrument Units Mass and Dimensions

H/W No.	DESCRIPTION (16-Feb-00)	QTY Sys/ Mod.	Mass [kg] p. unit	Mass [kg] p. S/C	Dimensions p. unit Length [mm]	Dimensions p. unit Width [mm]	Dimensions p. unit Height [mm]	Power p. unit / SS [W] average	Power p. unit / SS [W] peak
1800	**Science Instrument**			**99.1**					
1810	**Instrument Electronics**			**28.3**				**115.6**	
1811	Laser Assembly	2		12				37	
18111	*Laser Head*	4	2	8	165	130	60		
18112	*Laser Electronics*	2	2	4	200	200	100	37	
1813	USO	2	0.4	0.8	100	100	170	0.6	0.6
1814	Interferometer Electronics	2		10				13.2	
18141	*IE Front Unit*	2	1.5	3	200	100	100	5.2	11.9
18142	*IE Digital Unit*	2	3.5	7	200	200	150	8	10
1815	UV Discharger	2	0.5	1	100	150	70	3	
1816	Instrument Control Electronics	1	4.5	4.5	250	180	180	8	
1820	**Instrument Opto-mechanics**			**70.8**				**19**	
1821	*Telescope*	2	6.5	13					
1822	*Optical Bench*	2	5.6	11.2				4.5	4.5
1823	*Inertial Reference Sensor*	2		17				5	
18231	*Inertial Sensor*	2	6.5	13	200	200	200		
18232	*IRS Electronics*	2	2	4	200	100	100	5	
1824	*Fibre Positioner*	2	0.3	0.6					
1825	*OA Structure*	2	5	10					
1827	Y-Structure	1	13	13					
1826	*Mechanisms*	2	2	4					
1828	Thermal Control	1	2	2					

Table 5.6-3: LISA Propulsion Module Mass and Dimensions

H/W No.	DESCRIPTION (15-Feb-00)	QTY Sys/ Mod.	Mass [kg] p. unit	Mass [kg] p. S/C	Dimensions p. unit Length [mm]	Dimensions p. unit Width [mm]	Dimensions p. unit Height [mm]	Power p. unit / SS [W] average	Power p. unit / SS [W] peak
2000	**Propulsion Module**	**3**		**142**				**599**	
2100	**Structure & Mechanisms**	1		51					
2200	**Thermal Control**	1		6					
2300	**Electrical Power**	1		41				11	
2310	PCU	1		15	550	204	205	6	
2320	Battery	1		10				5	
2330	SA structure	1		4					
2340	Solar Cells	set		4	5.05 m²				
2350	Cable Harness	1		8					
2400	**Electric Propulsion**	1		36				588	
2410	Ion Thruster Assembly	1	4.6	4.6	185	165	185	-	-
2420	Xenon tank	2	2	4				-	-
2430	Pressure Reducer	2	0.6	1.2				-	-
2440	FCU	2	2	4	200	150	100	-	-
2450	ITPU	2	9.8	19.6	290	250	220	588	588
2460	Tubing, Valves, Harness	set	2.6	2.6					
2500	**Chemical Propulsion**			8				0	
2510	Fuel tanks	2	2	4					
2520	Valves & pipework	set		2					
2530	Thrusters & brackets	4	0.5	2					

Table 5.6-4: LISA Launch Mass Budget

Item		Mass [kg]
Science Module		274
Propulsion Module		142
Spacecraft dry		416
Propellant Xenon		18
Propellant Hydrazine		4
Spacecraft wet		438
3 Spacecraft		1314
System Margin	5%	66
Launch Mass		1380

6 System Configuration Analyses

Structure and thermal analysis have been performed initially at system level with a very much simplified model of the payload. In the established system level mechanical and thermal mathematical models, the payload models were then implemented. Since the system level models contained all performance relevant load cases, the implementation of the payload models provided the complete set of required mechanical and thermal results. Therefore, the system level results are described in the Annexes and the focus here is on the payload mechanical and thermal analysis under the loads induced on system level.

6.1 Structure Analysis

A FEM comprising about 70000 nodes has been established. It was used to perform the structural dimensioning and serves to analyse the thermo-elastic deformation.

A detailed description of the model and analysis is given in Annex A. It is demonstrated that the proposed design can fulfil the minimum stiffness requirement of 35 Hz in thrust axis and 15 Hz in the lateral axes for a spacecraft hard-mounted at the spacecraft separation plane .

6.2 Thermal Analysis

6.2.1 Applicable Documents

AD1 LISA Phase A Thermal Study Draft Final Report, Dr. Lutz Morgenroth, DORNIER, 17.11.1999 (c.f. Annex D of this report)

AD2 LISA Payload Pre-Phase A Thermal Study (WP03), Dr. Simon Peskett, RAL

AD3 LISA Phase A Study-PM3 Meeting (30/11/99), Various Contributors

AD4 LISA Telescope - Thermal Inputs e-mail Olivier Pierre -MMS (02-12-99)

AD5 LISA Optical Bench Power Fluctuations e-mail Iain Butler –BU (28-01-00)

6.2.2 Introduction

The results of the LISA Pre-Phase A study demonstrated that the steady-state requirements for the optical bench could be met under ‘Nominal’ conditions. However, the payload electronics boxes were running somewhat hot at up to 34°C. Optical bench stability requirements were shown to be feasible, given certain limitations on fluctuations in power dissipations and spacecraft temperature.

During Phase A, the following modifications have been made to the LISA payload thermal model.

- Geometric and thermal models updated by incorporating Dornier’s Spacecraft model.

- Y-Shaped Tube and Payload Tube surface properties modified, to improve steady-state results, whilst maintaining high stability.
- Telescope thermal model updated to be fully representative of the current SiC design.
- Power dissipations of all components updated.
- Analysis cases modified to agree with those run at spacecraft level.

6.2.3 Payload Thermal Requirements

The requirements for the payload are as follows:

- Optics Bench stability to be above 10^{-6} K/Hz$^{1/2}$ at 1mHz (AD2).
- Optics Bench temperature shall be maintained at 20°C +/-10°C (AD2).
- Electronics box temperature ranges not specified, therefore 'sensible' operational target range of -10°C to +30°C assumed.
- Analogue Electronics stability to be greater than 1.2E-03K/Hz$^{1/2}$ (AD3-BU).
- Phasemeter Electronics stability to be greater than 1.2E-03K/Hz$^{1/2}$ (AD3-BU).
- FEE stability to be greater than 2.2E-03K/Hz$^{1/2}$ (AD3-BU).

6.2.4 Payload Thermal Design

The thermal design of the Payload is similar to that described in the Pre-Phase A report (AD2). As a result of the very high stability requirement, it is necessary to isolate the payload from any temperature fluctuations due to spacecraft temperature changes. This may be due to power fluctuations, solar constant fluctuations or surface property degradation.

Therefore to achieve maximum conductive and radiative isolation, the payload is housed within two sets of goldised, CFRP, Y-shaped tubes. The outer and inner tubes are referred to as the 'Y-Shaped Tube' and the 'Payload Tube' respectively. The Optical Bench and Telescope are mounted from the Payload Tube on low conductance mounts. All possible surfaces on the telescope are goldised, including the Secondary Mirror Support Mast and the rear surface of the both the mirrors. This minimises heat losses to Space and provides further decoupling of the telescope from its surroundings.

Electronics boxes within the Payload Tube are housed at opposite ends to the OB and Telescope. Heat from these boxes is dissipated conductively into the Payload Tube and radiatively to the Tube's internal surface and Deep Space. To improve the radiative coupling, the Payload Tube is blackened on its internal surfaces around the electronics boxes.

6.2.5 Geometric Mathematical Model

6.2.5.1 Geometry

The current spacecraft GMM (AD1) has been converted into ESARAD and integrated with the RAL Pre-Phase A payload GMM to form a complete GMM of the spacecraft (LISA46_g).

The telescope model has been updated to represent the SiC design (AD3- MMS). This includes the addition of the mirror Baseplate and the Secondary Mirror Support Mast.

6.2.5.2 Surface Properties

Tubes

To achieve stability requirements, the Y-Shape Tube remains goldised on both internal and external surfaces, as defined in Pre-Phase A.

The gold internal and external surfaces on the Payload Tubes are also retained, with the exception of the area between the E-Box plates and the end of the Tube. This has been made black on the internal surface, to assist heat rejection from payload electronics, and hence reduce their temperature (see Figure 6.2-4 and Figure 6.2-5).

Electronics Boxes

The Analogue, Digital and USO electronics boxes and all electronics plates are painted black on external surfaces, to maximise radiative heat rejection.

Optical Bench

The Optical Bench surface properties are the natural surface properties of the materials (ULE Bench and Titanium box).

Telescope

The Primary and Secondary Mirror rear surfaces and baseplate are goldised. The Support Mast is also goldised, to reduce radiative heat leaks to deep space.

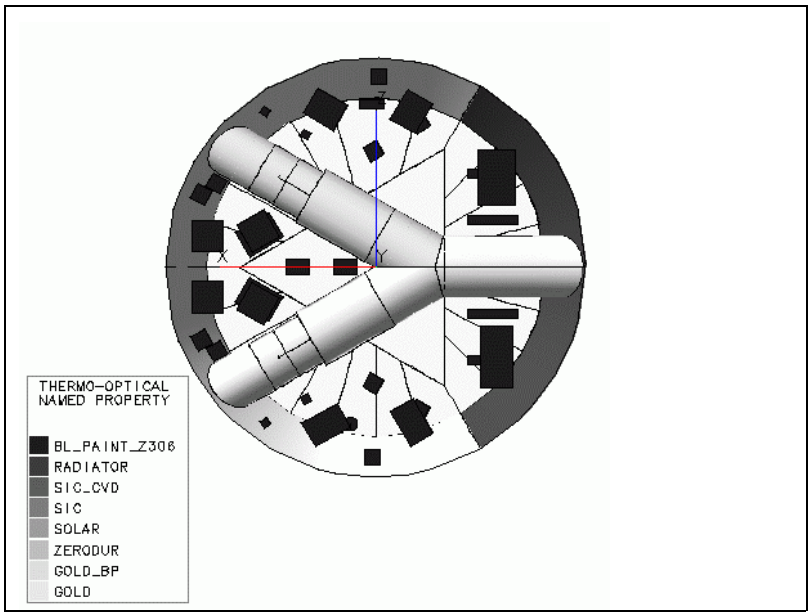

Figure 6.2-1- Overall LISA GMM (w/o Panels and S/A)

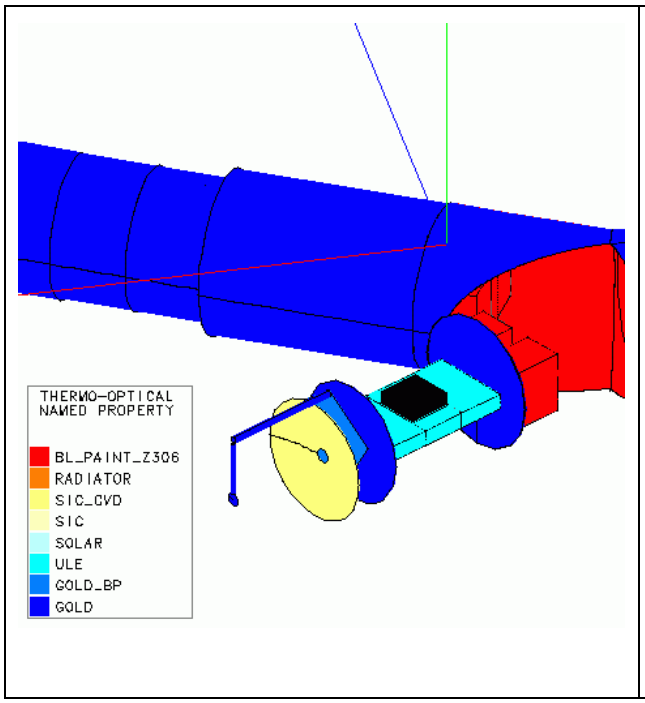

Figure 6.2-2: Telescope Assembly, Optical Bench and Electronics Boxes on Plate in Payload tubes

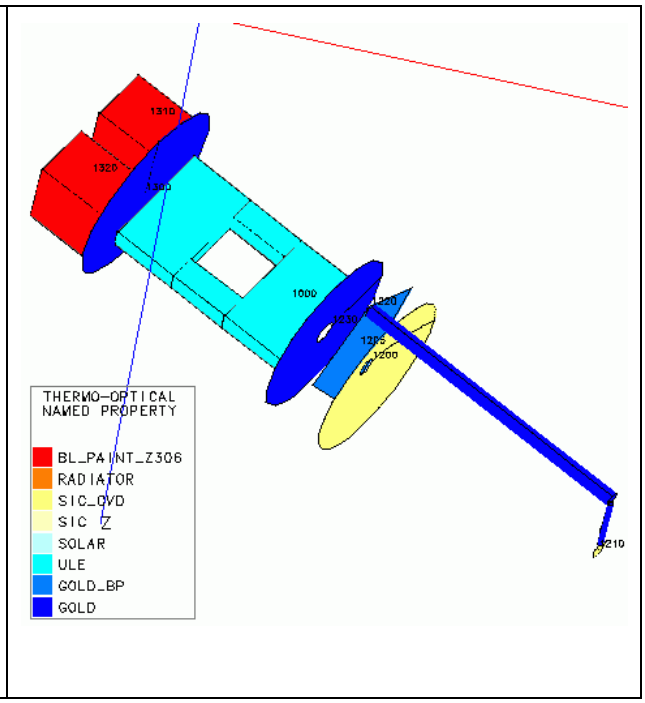

Figure 6.2-3: Telescope Assembly, Optical Bench and Electronics Boxes on Plate

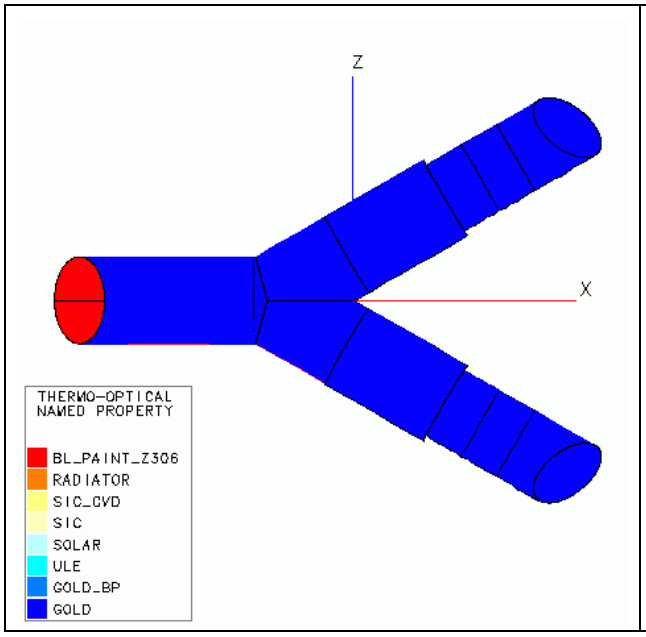

Figure 6.2-4: Payload Tubes

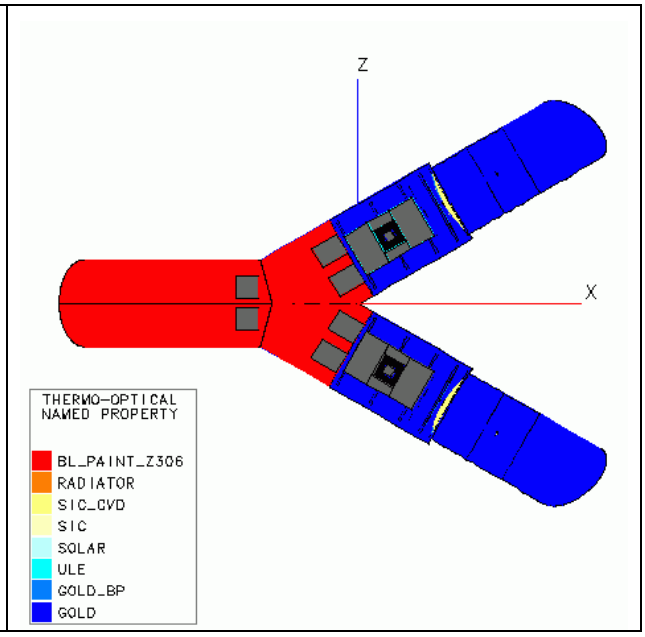

Figure 6.2-5: Payload Tubes (Cut Away)

6.2.5.3 Thermo-Optical Properties

The following thermo-optical properties are assumed for the spacecraft, the payload and the telescope (ref. AD4):

Table 6.2-1: Thermo-Optical Properties

Surface	Emissivity	Absorbtivity
CHEMZ306	0.90	0.95
ULE	0.80	0.20
Titanium	0.12	0.20
Gold	0.05	0.24
Gold - base-plate and primary mirror rear surface	0.02	0.24
SiC (bare material)	0.65 to 0.70	0.80
SIC CVD with AL deposit - Mirrors	0.03	0.06

6.2.6 Thermal Mathematical Model

6.2.6.1 Payload Nodal Breakdown

The Thermal Mathematical Model LISA42.d was created using ESATAN software. The nodal breakdown of the spacecraft and tubes is as defined in AD1. Additional nodes used to represent the payload are listed in the table below.

Table 6.2-2: Payload Nodal Breakdown

Location	Node Number(s)
Y-shaped tube arm A	81-90
Y-shaped tube arm B	170-180
Y-shaped tube base	3000
Payload Tube (A/B)	1400-1485/2400-2485
Sensor (Arm A/B)	1110/2110
Titanium housing (Arm A/B)	1120/2120
Primary mirror (Arm A/B)	1200/2200
Baseplate (Arm A/B)	1205/2205
Secondary mirror (Arm A/B)	1210/2210
Mast (Arm A/B)	1220/2220
Telescope thermal shield (Arm A/B)	1230/2230
Electronics plate (Arm A/B)	1300/2300
Analogue electronics box on plate (Arm A/B)	1310/2310
Digital electronics box on plate (Arm A/B)	1320/2320
USO box plate	3100
USO box A	3120
USO box B	3130

6.2.6.2 Conductive Couplings

Tube Support

The Y-Shaped Tube is mounted from the spacecraft using isolating CFRP supports.

The Payload Tubes are in turn mounted off the Y-Shaped Tube on insulating GFRP reinforced bands.

Telescope

The Mirror Baseplate is supported from the Payload Tube on three isostatic mounts, with a total conductance of 0.0234W/K (AD4).

The Primary Mirror is mounted from the Fixation Ring using three bolts. The Fixation Ring is in turn mounted to the Mirror Baseplate using three bolts. This gives a calculated overall conductance of 0.30W/K.

The Secondary Mirror is supported off the Baseplate on a SiC cylinder (the 'Mast') of diameter 23 mm and length 520mm, giving a total conductance of 0.1358W/K.

Optical Bench

The Optical Bench is mounted from the Payload Tube using a system of Pyroceram struts, followed by two titanium bolts with Delrin washers, as described by Alenia in AD3. This is calculated to produce a conductance of 0.004W/K.

The Inertial Sensor Housing is mounted from the OB using four titanium bolts with Delrin washers, producing a conductance of 0.0459W/K.

Electronics

The electronics boxes are hard mounted onto electronics plates with an assumed conductance of 0.5W/K per box. The Analogue and Digital Boxes in each arm are located on the same plate, the two USO boxes are mounted to a third plate. These plates are supported from the Payload Tube using low conductance Pyroceram Struts producing a conductance of 0.00322W/K per plate.

6.2.6.3 Radiative Couplings

All radiative coupling are calculated in ESARAD.

6.2.6.4 Heat Capacities

The masses of the telescope components are taken from AD4.

Table 6.2-3: Telescope Heat Capacities

Items	Material	Mass (kg)	Heat Capacity (J/K)
Primary Mirror (PM)	SiC	3.20	2176
Secondary Mirror (SM)	SiC	0.02	14
Mast and SM support	SiC	0.70	476
Baseplate, Mounts, Bolts etc	SiC/Titanium	2.70	1733
TOTAL	-	6.62	4399

The masses of the optical bench and components are taken from AD3 (Alenia-FEM).

Table 6.2-4: Optical Bench Heat Capacities

Item	Material	Mass (kg)	Heat Capacity (J/K)
Base plate, optics and detectors	ULE	5.532	4542
Test Mass	Gold alloy	2.561	341
Sensor	Aluminium	3.939	3151
Housing	Titanium	1.0	800
TOTAL	-	12.0	8209

Table 6.2-5: Electronic Boxes Heat Capacities

Item	Mass (kg)	Heat Capacity (J/K)
Analogue Electronics Box	1.0	800
Digital Electronics Box	1.0	800
USO A Electronics Box	1.3	1040
USO B Electronics Box	1.3	1040
TOTAL	4.6	3680

6.2.6.5 Power Dissipation

The most significant change to power dissipation since Pre-Phase A is an increase from 0.9W to 1.46W in the dissipation on the Optical Bench (AD3 - Alenia). A listing of all assumed payload power values is given in the tables below.

Table 6.2-6: Optical Bench Power

Component	Power (W)
qp1	1.1457
p1	0.260
p2	0.0007
p3	0.0162
CCD	0.024
FP	0.010
Total Optical Bench (each)	1.46373
Total 2 Optical Benches	2.93

Table 6.2-7: Electronics Power

Component	Power (W)
Analogue Electronics Boxes	4.0 x 2
Digital Electronics Boxes	4.5 x 2
USO A	3.0
USO B	1.3
TOTAL	21.3

Table 6.2-8: Overall Spacecraft Power

Component	Power (W)
Payload Power Dissipation	24.2
SVM Power Dissipation	154.2
Total	178.4

6.2.7 Analysis Cases

6.2.7.1 Steady-State Cases

Two extreme steady-state cases were established for the overall model. These were set up to agree with the analysis performed at Spacecraft level (AD1).

Table 6.2-9: Steady-State Cases

Property	Case	
	Hot	**Cold**
Solar Constant (W/m^2)	1247 (1187.5 + 5%)	1128 (1187.5 - 5%)
Solar Panel Absorbtivity	0.68	0.64

6.2.7.2 Transient Cases

The transient analysis was performed for the six load cases defined in AD1 together with an additional case in which only the Payload electronics power was fluctuated. These represent three cases of Solar Constant fluctuations, three cases of sinusoidal power fluctuation, and a single step case representing the switch on-off of three components. It should be noted that the first and third cases, with all units oscillating in synchrony, are not realistic, but will be used to establish a budget for allowable fluctuations in unit dissipation.

Table 6.2-10: Solar Constant Fluctuation Cases

Parameter	Case 1	Case 2	Case 3
Frequency (Hz)	10^{-1}	10^{-3}	10^{-4}
Fluctuation (%)	0.03	0.13	0.3
Fluctuation (W/m2/Hz1/2)	0.3	1.6	3.5

Table 6.2-11: Power Fluctuation Cases

	Case 1	Case 2	Case 3	Case 4
Components	All SVM EUs	CPS	All Payload EUs	Transponder, RFDU, EPC
Power (W)	154.2	35.0	21.3	36.0
Fluctuation (%)	1.0	20.0	1.0	Switch on for 3 hours.
Frequency (Hz)	10^{-4}	10^{-1}	10^{-4}	

6.2.8 Steady State Analysis Results

Table 6.2-12 summarises the predicted temperatures of the Spacecraft and Y-Shaped Tube, and compares them with the DORNIER predictions (AD1). Any differences are due primarily to the effects of the inclusion of the payload model (spacecraft level analysis considered the payload as a black boundary node at 20°C).

Table 6.2-13 summarises the results for the Optical Bench, the Telescope assembly and the payload electronics, and compares them with the Pre-Phase A temperatures (AD2).

The results demonstrate the following:

- All electronics box temperatures are within the range –10°C to +30°C, around 10 °C lower than Pre-Phase A (due to blackening of the Payload Tubes in this area).

The Optical Bench temperature is approximately 10 °C and varies by only 2.1°C throughout the mission. The temperature is ten degrees lower than in Pre-Phase A due to lower heat leaks from the cooler payload electronics. The cold case temperature is one degree below the required minimum. Heater power could be used to increase this temperature if necessary.

- Due to the use of high conductivity SiC, the telescope assembly is virtually homogenous, with temperatures between –11° C and –14°C. This is approximately 15 °C warmer than Pre-Phase A results, due to goldising of the Telescope surfaces which reduces heat leaks to space.
- The temperature gradients have been significantly reduced along the front sections of the Y-Shaped Tubes (gradients of 35°C compared to 80°C in the Pre-Phase A analysis). This is caused by the reduction of heat leaks to Space from the ends of the Payload Tube due to goldising the inner surface of the Tubes around the Telescope.

Table 6.2-12: Spacecraft Steady-State Temperatures

Location	Node Number	COLD Case		HOT Case	
		Phase A DSS	Phase A RAL	Phase A DSS	Phase A RAL
		T (°C)	T (°C)	T (°C)	T (°C)
Y-shaped tube arm A inner (between USO plate and electronic plate)	81	19.8	16.6	20.0	19.0
Y-shaped tube arm A middle (between electronic plate and primary mirror)	82-83	18.2	12.2	18.4	15.2
Y-shaped tube arm A front (in front of primary mirror, aft end)	86-87	17.0	-2.0	-15.8	0.8
Y-shaped tube arm A front (in front of primary mirror, middle)	88-89	-51.2	-11.5	-49.8	-8.7
Y-shaped tube arm A outer (in front of primary mirror, front end)	90	-78.9	-19.0	-77.7	-16.5
Y-shaped tube arm B inner (between USO plate and electronic plate)	171	19.8	16.3	19.9	18.7
Y-shaped tube arm B middle (between electronic plate and primary mirror)	172-173	17.9	9.9	18.1	13.0
Y-shaped tube arm B front (in front of primary mirror, aft end)	176-177	20.7	-6.5	-19.5	-3.6
Y-shaped tube arm B front (in front of primary mirror, middle)	178-179	-56.1	-17.3	-54.6	-14.5
Y-shaped tube arm B outer (in front of primary mirror, front end)	180	-83.3	-25.1	-82.0	-22.4
YBase / Toptube (surrounding USO Boxes)	3000	-2.6	-26.3	- 0.8	-24.4
Top Plate Centre	111	23.1	24.1	27.3	29.1
Bottom Plate Centre	121	15.0	17.1	17.4	20.4
Solar Sheet out Centre	311	81.8	81.8	96.4	96.4
Solar Sheet in Centre	321	44.8	45.7	53.2	54.4
Solar Core Centre	331	60.8	61.3	72.2	72.8
Radiator –X	512	-89.0	-89.2	- 89.0	-87.7
Radiator –Z	513	-122.9	-147.0	-122.9	-145.4
Radiator +Z	514	-118.9	-144.0	-118.9	-142.6

Table 6.2-13: Payload Steady-State Temperatures

Location	Node No.	Pre-Phase A	Phase A RAL	
			COLD Case	HOT Case
		T (°C)	T (°C)	T (°C)
Optical bench	1000	21.0	9.1	11.2
Proof mass	1100	20.4	8.4	10.6
Sensor	1110	20.4	8.4	10.6
Titanium housing	1120	20.4	8.4	10.6
Primary mirror	1200	-19.7	-14.0	-12.0
Baseplate	1205	-	-13.2	-11.1
Secondary mirror	1210	-45.3	-13.6	-11.6
Mast	1220	-	-13.6	-11.5
Telescope thermal shield	1230	4.4	-0.3	1.9
Electronics plate	1300	32.1	24.2	26.3
Analogue electronics box on plate	1310	33.6	25.6	27.8
Digital electronics box on plate	1320	33.8	26.0	28.1
P/L Tube A - Section 1 (aft end) - top	1400	N/A	7.55	10.01
P/L Tube A - Section 1 (aft end) - bottom	1405	N/A	7.83	10.28
Payload Tube A Stiffening ring 1 - top	1410	18.6	7.51	9.97
P/L Tube A Stiffening ring 1 - bottom	1415	18.6	7.79	10.24
Payload Tube A - Section 2 - top	1420	N/A	6.98	9.44
Payload Tube A - Section 2 - bottom	1425	N/A	7.27	9.73
Payload Tube A Stiffening ring 2 - top	1430	16.0	5.66	8.12
Payload Tube A Stiffening ring 2 - bottom	1435	16.0	6.10	8.55
Payload Tube A - Section 3 - top	1440	N/A	4.41	6.86
Payload Tube A - Section 3 - bottom	1445	N/A	4.99	7.44
Payload Tube A Stiffening ring 3 - top	1450	9.7	2.37	4.79
Payload Tube A Stiffening ring 3 - bottom	1455	9.7	3.30	5.72
Payload Tube A - Section 4 - top	1460	N/A	0.90	3.30
Payload Tube A - Section 4 - bottom	1465	N/A	2.09	4.50
Payload Tube A Stiffening ring 4 - top	1470	2.2	-0.65	1.72
Payload Tube A Stiffening ring 4 - bottom	1475	2.2	0.98	3.36
Payload Tube A - Section 5 (front end) - top	1480	N/A	-0.83	1.54
Payload Tube A - Section 5 (front end) - bottom	1485	N/A	0.76	3.14
Y-shaped tube base	3000	19.8	-26.3	-24.4
USO box plate	3100	24.7	-3.4	-1.3
USO box A	3120	26.6	-5.6	-3.7
USO box B	3130	26.6	-7.4	-5.5

6.2.9 Transient Analysis Results

6.2.9.1 Solar Constant Fluctuation Cases

The TMM was used to calculate the transfer functions, and hence temperature responses of the payload, due to fluctuations in the Solar Constant. The results are shown in Table 6.2-14 to Table 6.2-16 below.

The resulting temperature responses of the optical bench are 1.6×10^{-6} K/Hz$^{1/2}$ at 10^{-4} Hz, and 3.8×10^{-11}K/Hz$^{1/2}$ at 10^{-3} Hz. Therefore the requirement of 10^{-6} K/Hz$^{1/2}$ at 10^{-3} Hz is met by a factor greater than 10^{4}.

Table 6.2-14: Case 1 Solar Constant Fluctuation Results

Case 1: 10^{-1} Hz, 0.03 %						
Component	**Pre-Phase A**		**Phase A**			
	Temperature Response [K]/[Hz]$^{1/2}$	Ratio to 1E-06 [K]/[Hz]$^{1/2}$	Semi-Amplitude [K]	Transfer Function [K]/[W/m^2]	Temperature Response [K]/[Hz]$^{1/2}$	Ratio to 1E-06 [K]/[Hz]$^{1/2}$
Optical Bench	N/A	N/A	<1.0E-12	<3.3E-12	<1.0E-12	1.0E-06
Primary Mirror	N/A	N/A	<1.0E-12	<3.3E-12	<1.0E-12	1.0E-06
Payload E-Boxes	N/A	N/A	<1.0E-12	<3.3E-12	<1.0E-12	N/A

Table 6.2-15: Case 2 Solar Constant Fluctuation Results

Case 2: 10^{-3} Hz, 0.13 %						
Component	**Pre-Phase A**		**Phase A**			
	Temperature Response [K]/[Hz]$^{1/2}$	Ratio to 1E-06 [K]/[Hz]$^{1/2}$	Semi-Amplitude [K]	Transfer Function [K]/[W/m^2]	Temp. Response [K]/[Hz]$^{1/2}$	Ratio to 1E-06 [K]/[Hz]$^{1/2}$
Optical Bench	4.3E-07	0.43	3.8E-11	2.4E-11	3.8E-11	3.8E-05
Primary Mirror	4.5E-08	0.045	3.5E-11	2.2E-11	3.5E-11	3.5E-05
P/L E-Boxes	3.4E-05	N/A	3.5E-11	2.2E-11	3.5E-11	N/A

Table 6.2-16: Case 3 Solar Constant Fluctuation Results

Case 3: 10^{-4} Hz, 0.3 %						
Component	**Pre-Phase A**		**Phase A**			
	Temperature Response [K]/[Hz]$^{1/2}$	Ratio to 1E-06 [K]/[Hz]$^{1/2}$	Semi-Amplitude [K]	Transfer Function [K]/[W/m^2]	Temp. Response [K]/[Hz]$^{1/2}$	Ratio to 1E-06 [K]/[Hz]$^{1/2}$
Optical Bench	9.9E-05	99	1.1E-06	3.1E-07	1.1E-06	1.1
Primary Mirror	1.2E-05	12	9.9E-07	2.8E-07	9.9E-07	1.0
P/L E-Boxes	4.8E-03	N/A	2.2E-05	6.3E-06	2.2E-05	N/A

6.2.9.2 Electronic Dissipation Fluctuation Cases

The results of the first three electronics power fluctuation cases are shown in Table 6.2-17, Table 6.2-18,and Table 6.2-19. The results show that the calculated Y-Shaped Tube fluctuations are significantly higher in the payload analysis then in the spacecraft level analysis. This is due to the damping effect of a good radiative coupling assumed between payload and Payload Tube in the spacecraft level analysis.

With a 1% total power fluctuation in all SVM units at 10^{-4} Hz, the temperature fluctuations are in the order of:

-4.2E-05 K/W for the optical bench

-3.2E-05K/W for the telescope

-6.5E-03 K/W for the payload electronic boxes

With a 1% total power fluctuation in the payload electronics units of 0.213W at 10^{-4} Hz, the temperature fluctuations are in the order of:

-10^{-4} K for the optical bench

-10^{-6} K for the telescope

-10^{-2} K for the payload electronic boxes

The dissipation fluctuation of the CPS causes only a negligible response in the payload (i.e. <1E-12K).

Table 6.2-17: Temperature Response to Spacecraft Power Fluctuation

10^{-4} Hz, 1% (all SVM Electronics Box Powers –154.2 Watts)				
Thermal Model		**DORNIER Spacecraft Level Analysis**	**RAL Payload Analysis**	
Name	**Node Number**	**Temperature Fluctuation [K]**	**Temperature Fluctuation [K]**	**Transfer Function [K] / [W]**
Y-Shaped Tube Arm A Inner	81	1.2E-04	1.9E-03	N/A
Y-Shaped Tube Arm A Middle	82	2.5E-04	3.0E-03	N/A
Y-Shaped Tube Arm B Inner	171	1.1E-04	1.9E-03	N/A
Y-Shaped Tube Arm B Middle	172	1.6E-04	1.9E-03	N/A
Optical Bench	1000	N/A	6.5E-05	4.2E-05
Titanium Housing	1120	N/A	2.0E-05	1.3E-05
Primary Mirror	1200	N/A	3.0E-05	1.9E-05
Secondary Mirror	1210	N/A	5.0E-05	3.2E-05
Payload Analogue E-box	1310	N/A	1.0E-03	6.5E-04
Payload Digital E-box	1320	N/A	1.0E-03	6.5E-04
USO box A	3120	N/A	8.5E-03	5.5E-03
USO box B	3130	N/A	8.5E-03	5.5E-03

Table 6.2-18: Temperature Response to CPS Dissipation Fluctuation

10^{-1} Hz, 20 % (CPS Power –35 Watts)				
	DORNIER Spacecraft Level Analysis		RAL Payload Analysis	
Name	**Node Number**	**Temperature Fluctuation [K]**	**Temperature Fluctuation [K]**	**Transfer Function [K] / [W]**
Y-Shaped Tube Arm A Inner	81	0	N/A	N/A
Y-Shaped Tube Arm A Middle	82	0	N/A	N/A
Y-Shaped Tube Arm B Inner	171	0	N/A	N/A
Y-Shaped Tube Arm B Middle	172	0	N/A	N/A
Optical Bench	1000	N/A	<1.0E-12	<1.4E-13
Titanium Housing	1120	N/A	<1.0E-12	<1.4E-13
Primary Mirror	1200	N/A	<1.0E-12	<1.4E-13
Secondary Mirror	1210	N/A	<1.0E-12	<1.4E-13
Payload Analogue E-box	1310	N/A	<1.0E-12	<1.4E-13
Payload Digital E-box	1320	N/A	<1.0E-12	<1.4E-13
USO box A	3120	N/A	<1.0E-12	<1.4E-13
USO box B	3130	N/A	<1.0E-12	<1.4E-13

Table 6.2-19: Temperature Response to Payload Electronics Power Fluctuation

10^{-4} Hz, 1 % (Payload Electronics Box Powers -21.3 Watts)			
		RAL Payload Analysis	
Name	**Node Number**	**Temperature Fluctuation [K]**	**Transfer Function [K] / [W]**
Y-Shaped Tube Arm A Inner	81	N/A	N/A
Y-Shaped Tube Arm A Middle	82	N/A	N/A
Y-Shaped Tube Arm B Inner	171	N/A	N/A
Y-Shaped Tube Arm B Middle	172	N/A	N/A
Optical Bench	1000	3.3E-04	1.5E-03
Titanium Housing	1120	1.0E-04	4.7E-04
Primary Mirror	1200	4.0E-06	1.9E-05
Secondary Mirror	1210	3.5E-06	1.6E-05
Payload Analogue E-box	1310	5.2E-02	2.4E-01
Payload Digital E-box	1320	5.4E-02	2.5E-01
USO box A	3120	3.0E-02	1.4E-01
USO box B	3130	2.0E-02	9.4E-02

6.2.9.3 Electronic Power Step Change Case

The results of the step change in power dissipation are shown in Table 6.2-20. The Payload Tube time constant is significantly longer than those in AD1. However this is predictable, given the better isolation between the payload and the fluctuations sources.

The parameters $dT_{on\text{-}off}$, $dT_{3h,max}$, $t_{98\%}$, $t_{1e\text{-}4,}$ as defined in AD1, have been estimated for the main parts of the payload.

The calculation was stopped after 2,000,000 s (556 h), therefore the limit $t_{1e\text{-}4}$ was not reached at the optical bench.

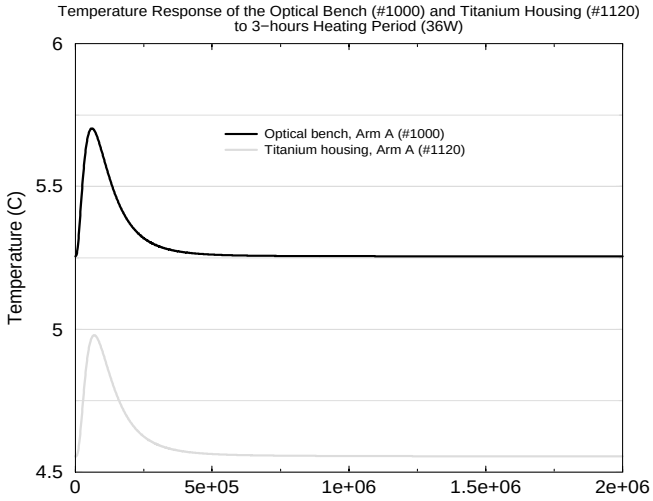

Figure 6.2-6: Response To Step Change in Power

Table 6.2-20: Temperature Response to Switch On-Off of Transponder 1, RFDU and EPC1

Name	Node Number	Steady State Temp. [K]		$dT_{on\text{-}off}$ [K]	$dT_{3h,max}$ [K]	$t_{98\%}$ [h]	$t_{1e\text{-}4}$ [h]
		Power On	Power off				
Y-Shaped Tube Arm A Inner	81	19.0	12.2	6.8	1.046	75.0	353.3
Y-Shaped Tube Arm A Middle	82	15.3	7.4	7.9	1.284	70.6	331.7
Y-Shaped Tube Arm B Inner	171	18.7	12.0	6.7	0.992	76.1	351.1
Y-Shaped Tube Arm B Middle	172	13.1	6.6	6.5	0.914	78.1	328.1
Optical Bench	1000	11.2	5.3	5.9	0.448	126.4	>555.6
Titanium Housing	1120	10.6	4.6	6.0	0.425	139.7	>555.6
Primary Mirror	1200	-12.0	-17.6	5.6	0.258	179.2	513.6
Secondary Mirror	1210	-11.6	-17.2	5.6	0.261	178.1	512.5
Payload Analogue E-Box	1310	27.8	21.7	6.1	0.886	77.5	347.8
Payload Digital E-Box	1320	28.1	22.0	6.1	0.889	77.5	346.7
USO E-box A	3120	-3.7	-10.5	6.8	1.664	58.3	303.9
USO E-box B	3130	-5.5	-12.4	6.9	1.680	58.6	305.0

Table 6.2-21: Residual Temperature Difference

Name	Node Number	T_1-T_0 after 278h	T_2-T_0 after 556h
Optical Bench	1000	1.8E-04	1.3E-04
Titanium Housing	1120	1.7E-03	2.9E-04

Note: T_0 is the initial steady-state temperature. T_1 and T_2 are the last temperatures calculated when the simulation stopped at 278 hours and 556 hours respectively.

For the temperature response shown in Figure 6.2-6 a spectral analysis was performed. The result is shown in Figure 6.2-7

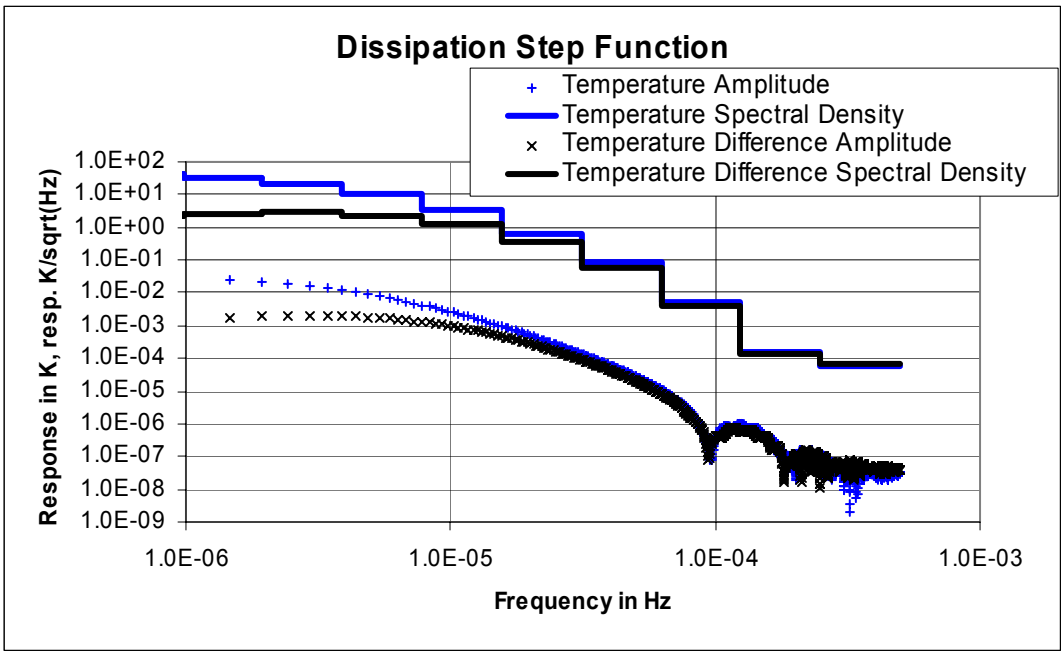

Figure 6.2-7 : Spectral Density of Temperature Response to Step in Dissipation

6.2.10 Telescope Optical path length Changes

It is necessary to minimise the thermal expansion/contraction of the Secondary Mirror Support Mast, in order to minimise the optical path length changes. The overall budget for optical path length change is 40 pm/$Hz^{1/2}$. The following tables give results for the predicted change in separation between the two mirrors, assuming a CTE for SiC of 2.0E-6/K and a Mast length of 0.52m.

Table 6.2-22: Telescope Path Length Changes Due To Solar Fluctuations

Solar Constant Fluctuations				
Component	Case 2: 10^{-3} Hz, 0.13 %		Case 3: 10^{-4} Hz, 0.3 %	
	Temperature Response [K]/[Hz]$^{1/2}$	Thermal Expansion/ Contraction [pm]/[Hz]$^{1/2}$	Temperature Response [K]/[Hz]$^{1/2}$	Thermal Expansion/ Contraction [pm]/[Hz]$^{1/2}$
Mast	4.7E-11	0.000049	1.3E-06	1.4

Table 6.2-23: Telescope Path Length Changes Due To Power Fluctuations

Power Fluctuations						
Component	Case 1: 10^{-4} Hz, 1% (all SVM EUs)		Case 2: 10^{-1} Hz, 20 % (CPS)		Case 3: 10^{-4} Hz, 1% (all P/L EUs)	
	Transfer Function [K]/[W]	Thermal Expansion/ Contraction [pm]/ [W]	Transfer Function [K]/[W]	Thermal Expansion/ Contraction [pm] /[W]	Transfer Function [K] /[W]	Thermal Expansion/ Contraction [pm] /[W]
Mast	3.2E-05	33.3	<1.4E-13	<0.00000015	1.6E-05	16.6

6.2.11 Optical Bench Detailed Analysis

6.2.11.1 Optical Bench Nodal Breakdown

The results obtained for the cold case and hot case have been applied to a detailed model of the optical bench. The detailed thermal model consists of 24 nodes as shown in Figure 6.2-8 and the nodal distribution across the baseplate is presented in Figure 6.2-9.

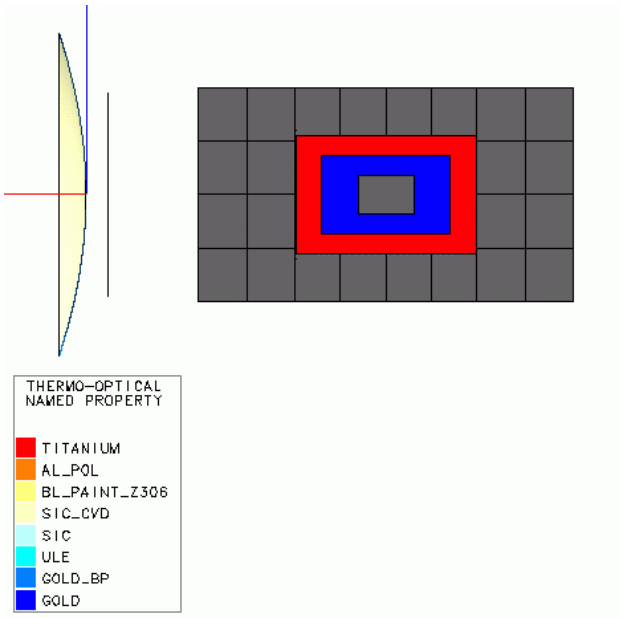

Figure 6.2-8: ESARAD Thermal Model of Optical Bench (Cut away)

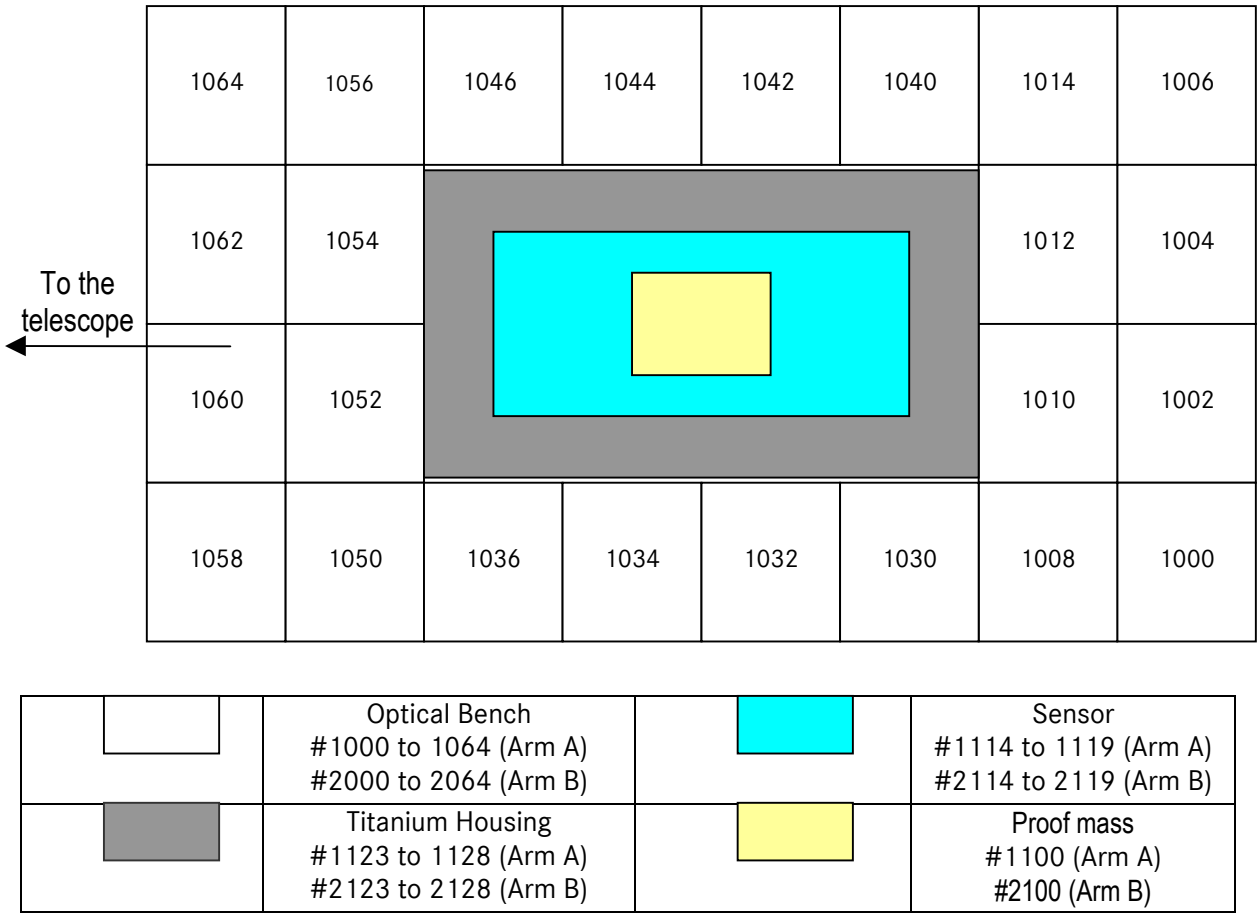

Figure 6.2-9: Optical Bench Nodal Distribution

6.2.11.2 Power Dissipation

The power distribution over the optical bench is based upon Alenia's power budget for the dissipating equipment, as follows:

Electronics:

Table 6.2-24: Optical Bench Electronics Power Dissipation

Item	Element	Location	Dissipated Electrical Power (mW)
Quadrant photodiode	qp1	1050	1145.7
Photodiode	p1	1014	260.12
Photodiode	p2	1008	0.7
Photodiode	p3	1058	16.2
Charge-coupled device	CCD	1064	24.0
Total	-	-	**1446.72**

Miscellaneous:

Table 6.2-25: Optical Bench Miscellaneous Power Dissipation

Item	Element	Location	Dissipated Electrical Power (mW)
Fiber Positioner	FP	1056	10.0
power circulating in the reference cavity	-	1100	6.4
Total laser power dissipated inside the optical elements	-	Evenly distributed across the bench	0.01
Power scattered through the bench	-	Evenly distributed across the bench	0.6
Total	-	-	**17.01**

Total:

Optical Bench	1.4467 + 0.017 **= 1.4637 W**

6.2.11.3 Steady-State Analysis

Table 6.2-26 and Table 6.2-27 give the predicted temperatures across the Optical Bench and Inertial Sensor respectively. Figure 6.2-10 shows a map of the predicted temperature distribution within the bench housed in Arm A. Results are given for cold and hot extreme cases experienced throughout the Mission.

A maximum temperature of 19.0 °C in the hot case is predicted in the region of the quadrant photodiode amplifier (Node 1050 of the optical bench). The minimum temperature predicted in the cold case is 7.4 °C in the region of the CCD (Node 1064 of the optical bench).

The maximum temperature gradient across the bench is 9.6 °C. This can be compared to the maximum temperature difference of 2.9 °C derived in Pre-Phase A, where the sources of power were more evenly distributed across the bench.

Table 6.2-26: Optical Bench Steady-State Temperatures - Arm A

Location	Node Number	Pre-Phase A	Phase A RAL	
		Nominal Case	COLD Case	HOT Case
		T (^{o}C)	T (^{o}C)	T (^{o}C)
Optical Bench	1000	-	8.70	10.90
Optical Bench	1002	-	8.88	11.08
Optical Bench	1004	-	9.15	11.35
Optical Bench	1006	-	9.56	11.76
Optical Bench	1008	-	8.76	10.95
Optical Bench	1010	-	8.94	11.13
Optical Bench	1012	-	9.39	11.58
Optical Bench	1014	-	10.57	12.76
Optical Bench	1030	-	8.90	11.08
Optical Bench	1032	-	9.30	11.46
Optical Bench	1034	-	10.28	12.41
Optical Bench	1036	-	12.39	14.49
Optical Bench	1040	-	9.21	11.40
Optical Bench	1042	-	8.38	10.56
Optical Bench	1044	-	7.88	10.06
Optical Bench	1046	-	7.67	9.84
Optical Bench	1050	-	16.98	19.05
Optical Bench	1052	-	10.91	13.02
Optical Bench	1054	-	8.52	10.65
Optical Bench	1056	-	7.65	9.80
Optical Bench	1058	-	12.03	14.12
Optical Bench	1060	-	9.70	11.81
Optical Bench	1062	-	8.08	10.21
Optical Bench	1064	-	7.45	9.60
Mean temperature	-	21.0	9.55	11.71
Tmin	-	20.1	7.45	9.60
Tmax	-	22.9	16.98	19.05
Tmax - Tmin	-	2.8	9.53	9.45

Table 6.2-27: Inertial Sensor Steady-State Temperatures - Arm A

Location	Node Number	Pre-Phase A	Phase A RAL	
		Nominal Case	COLD Case	HOT Case
		T (°C)	T (°C)	T (°C)
Proof mass	1100	20.4	11.69	13.80
Sensor	1114	20.4	8.70	10.87
Sensor	1115	20.4	8.70	10.87
Sensor	1116	20.4	8.70	10.87
Sensor	1117	20.4	8.70	10.87
Sensor	1118	20.4	8.70	10.87
Sensor	1119	20.4	8.70	10.87
Titanium Housing	1123	20.4±0.7	8.70	10.87
Titanium Housing	1124	20.4±0.7	8.81	10.99
Titanium Housing	1125	20.4±0.7	8.87	11.04
Titanium Housing	1126	20.4±0.7	8.83	10.99
Titanium Housing	1127	20.4±0.7	8.73	10.90
Titanium Housing	1128	20.4±0.7	8.69	10.86

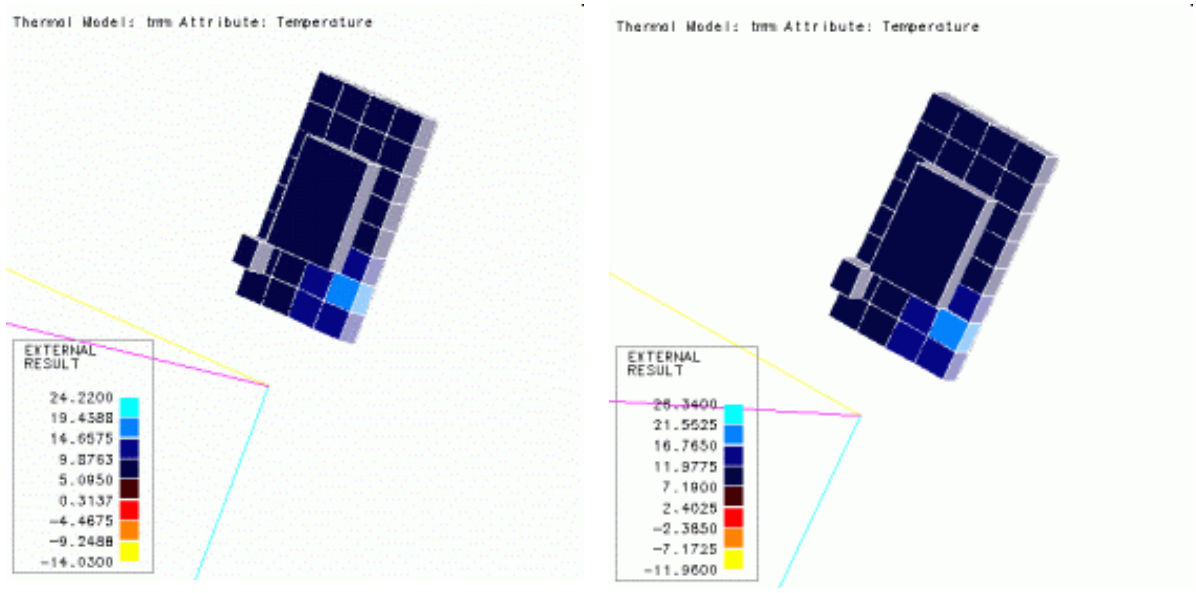

Cold Case Hot Case

Figure 6.2-10: Optical Bench Steady-State Temperatures - Arm A

6.2.11.4 Transient Analysis

Information provided (AD5) on the predicted maximum power fluctuations for the Optical Bench electronics is shown below.

Components	Main Photodiode qp1 Photodiode p1, p2, p3 Acquisition sensor qp2 M3, M4 & M5
Component Power Fluctuation	5.57μW/[$Hz^{1/2}$]
Frequency (Hz)	10^{-3}

Figure 6.2-11: Power Fluctuation Case Definition

Table 6.2-28: Temperature Responses to Trans-Impedance Amplifiers Power Fluctuation At 1mHz

POWER FLUCTUATION (optical bench components)		
Component	**Transfer Function [K] / [W]**	**Temperature Response [K] / [$Hz^{1/2}$]**
Optical Bench – N1000	3.258	1.8E-05
Optical Bench – N1006	3.245	1.8E-05
Optical Bench – N1064	4.187	2.3E-05
Optical Bench – N1030	3.771	2.1E-05
Optical Bench – N1036	6.370	3.5E-05
Optical Bench – N1040	3.457	1.9E-05
Optical Bench – N1046	3.899	2.2E-05
Optical Bench – N1008	3.415	1.9E-05
Optical Bench – N1014	3.314	1.8E-05
Optical Bench – N1050	9.408	5.2E-05
Optical Bench – N1058	6.533	3.6E-05

6.2.12 Summary

The study has shown that the current thermal design of the LISA Spacecraft and Payload is close to meeting the stringent thermal requirements in terms of both absolute temperature and temperature stability. In addition, the Y-Shaped Tube temperature gradients are significantly lower than those presented at Pre Phase A.

Steady-state temperatures are predicted within the following ranges:

- Optical Bench: 9.1 to 11.2°C [Requirement: 20°C +/-10]
- Telescope: -11 to –14°C [Requirement: non stated]
- Electronics: -7 to +28 °C [Requirement: -10°C to +30°C]

These steady state temperatures are based on a radiator trimming of 20% open, thus ample margin with respect to required radiator area is available.

Transient temperature variations due to Solar Constant fluctuations have been calculated for the Optical Bench, Telescope and Electronics Boxes. Optical Bench fluctuations have been significantly reduced since Pre-Phase A. The fluctuation at 1mHz is 3.8E-11K/$Hz^{1/2}$ compared to the requirement of <1.0 E-06 K/$Hz^{1/2}$.

Transient temperature variations due to fluctuations in power dissipations have been analysed. The cases run are not based on realistic predictions of power fluctuation, but are used to calculate transfer functions between power fluctuation and resulting temperature fluctuation. Analysis assumes synchronised variations of power in several different e-boxes. Power fluctuation in spacecraft and payload electronics boxes produces responses of 4.2E-05K/W and 1.5E-03W/K respectively on the Optical Bench. These transfer functions may be used to calculate budgets for allowable electronics power fluctuations in both payload and spacecraft units.

The results of the transient analysis have also been used to calculate the change in separation between the Telescope's primary and secondary mirrors. The values obtained may be used as input for the optical path length variation budget. The worst case variation due to Solar Constant fluctuations is 1.4pm/[$Hz^{½}$], which is well below the 40pm/[$Hz^{½}$] total budget.

Localised power fluctuations and gradients on the optical bench have been analysed for their effect on temperature stability. Again, the transfer functions obtained may be used to calculate an allowable power fluctuation for these components.

The spectral analysis result depend on the selected bandwidth which needs to be considered in the definition of the temperature stability requirement.

6.3 Gravitational Analysis

6.3.1 Method

The aim of this analysis is to determine the residual acceleration at the centre of one of the test masses as a consequence of the gravitational forces produced by the mass of spacecraft and payload components. The analysis lends itself to a finite element approach in which the spacecraft and payload components are divided into a large number of small elements and the required result is then a simple vector sum of the accelerations produced by each element. A spread sheet program is a convenient way to carry out the vector sum as each axis can be handled individually until a final summation to produce the acceleration magnitude and direction cosines. The input data is formed from the node matrix of a standard structural engineering finite element program such as the as the small example below.

NODE	MASS(KG)	X(MM)	Y(MM)	Z(MM)
1	9.35E-03	-124.0856637	-235	-318.0705404
2	1.15E-02	12.46878199	-310	-431.5513025
3	9.35E-03	-78.56751515	-260	-355.8974611
4	9.35E-03	-33.04936628	-285	-393.724382
5	9.35E-03	12.46878199	-160	-431.5513025
6	9.35E-03	-78.56751515	-210	-355.8974611
7	9.35E-03	-33.04936628	-185	-393.724382
8	9.35E-03	179.0232277	-235	-493.0705404
9	9.35E-03	67.98693025	-285	-452.057715
10	9.35E-03	67.98693025	-185	-452.057715
12	9.35E-03	123.5050794	-210	-472.5641279

The input information was created from the Spacecraft finite element model supplied by Dornier (39220 elements), the Optical bench finite element from Alenia and payload elements from Alenia and the RAL thermal model. (A total of 3310 elements)

6.3.2 Modelled cases

The following cases were calculated:

1) An undistorted model using the supplied nodal matrices.
2) A model to representing the on orbit case of the release of 1 g. Modelled by applying -g load to the undistorted case.

3) A model in which the nodal positions have been distorted by thermo-mechanical effects at the thermal model cold extreme

4) A model in which the nodal positions have been distorted by thermo-mechanical effects at the thermal model hot extreme

5) A model in which the elements and nodal positions have been distorted by dimensional change and mass loss of the CFRP components due to outgassing effects of the notional undistorted case.

6) A model in which the elements and nodal positions have been distorted as 5 above of the on orbit 1 g release case .

7) Mesh checking model

8) Variation due to solar fluctuations.

The spreadsheet has been used to calculate the acceleration magnitude and direction at the centre of the test mass location of payload 1 for each of the above cases.

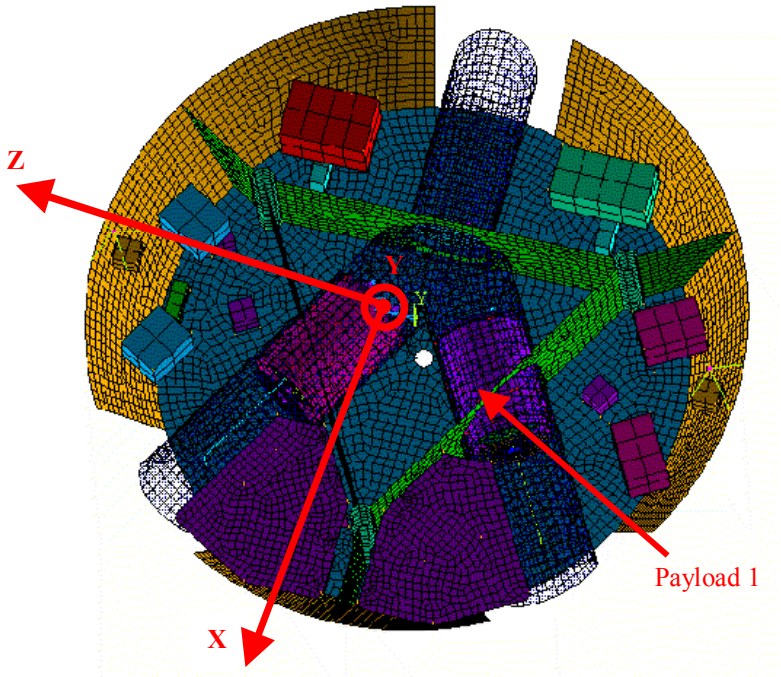

Figure 6.3-1: The Spacecraft finite element model and co-ordinate system which has been used throughout.

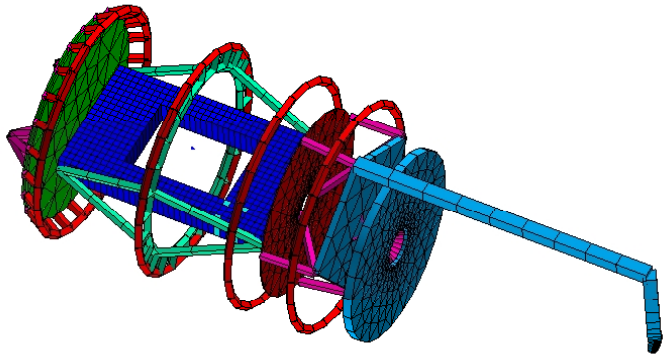

Figure 6.3-2: The payload components which have been added to the Spacecraft model). The co-ordinates of 2 such models are correctly positioned in terms of spacecraft co-ordinates and vectorally added to the spacecraft model results of figure 1.

The payload model consisted of a number of data files for various elements of the payload as described in the table below.

Table 6.3-1: Data Files use for Payload Model

Segment name	Number of nodes	Total Mass (kg)
Optics bench	1180	11.0668417
Bench support beams	144	1.7555217
Payload 2 proof mass	1	6.5
Point masses (electronics)	8	0.6742848
Thermal shield	408	0.3990935
Baseplate	92	3.8674790
Primary mirror	344	5.9340362
Secondary mirror	110	0.0443375
Mast	32	1.3664047
Electronics plates	220	2.4473098
Electronics boxes	4	4.0
Cylinder	767	7.3373246

As might be expected from an analysis that involves around models of 40000 elements there is a large quantity of available output information. However to keep a clear view of the prime objective the data is summarised only in terms of the final value of the acceleration and its direction cosines for each of the cases analysed.

Table 6.3-2: Summary results for acceleration at centre of Payload 1 test mass.

Case	Acceleration Magnitude (ms^{-2})	Direction Cosines		
		x	y	z
Undistorted	7.50761×10^{-9}	0.457340905	-0.599820223	0.656547787
1g Release	7.51525×10^{-9}	0.455684805	-0.60166181	0.656014043
CFRP mass loss	7.18234×10^{-9}	0.283679391	-0.683035326	0.673044387
CFRP loss + 1g release	7.19157×10^{-9}	0.282016483	-0.684392479	0.672364215
Thermal cold extreme	7.15476×10^{-9}	0.283010771	-0.680267786	0.676121766
Thermal hot extreme	7.15669×10^{-9}	0.283223277	-0.679997413	0.676304734

6.3.3 Gravitational Gradients

The gravitational acceleration was also established at intervals along the spacecraft axes and the gradient calculated. Shown here the acceleration magnitude at 2mm intervals for the 1g release case.

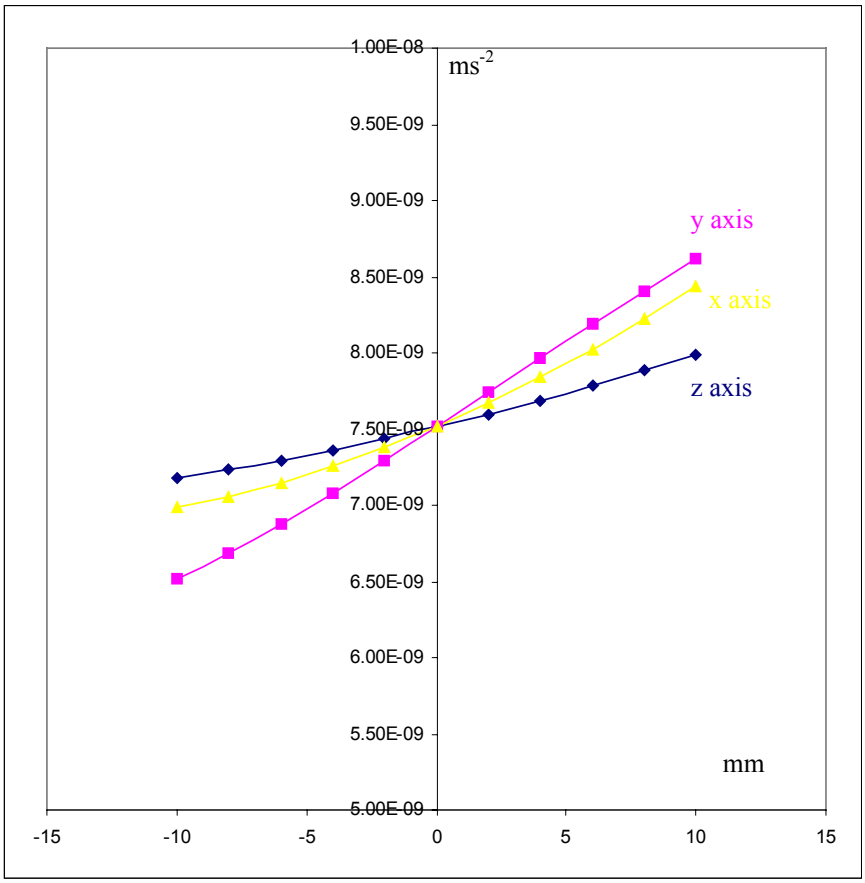

Taking a straight line approximation the gradients in each of the three spacecraft axis are :

X	7.27028×10^{-11} ms^{-2}/mm	=	7.27028×10^{-8} s^{-2}
Y	1.05311×10^{-10} ms^{-2}/mm	=	1.05311×10^{-7} s^{-2}
Z	4.04512×10^{-11} ms^{-2}/mm	=	4.04512×10^{-8} s^{-2}

6.3.4 Model mesh density considerations

The density of nodal elements in the model is a compromise between too few to give confidence in the result and too many such as to make the calculation unwieldy. As a check that sufficient were used in this analysis we have taken just one segment, the payload 2 optical bench, and calculated the acceleration it causes at the centre of payload 1 test mass location for a modelling density of 589 nodes and 1147 nodes.

Number of nodes	Acceleration magnitude (ms^{-2})	Direction cosines		
		x	y	z
589	8.62154×10^{-10}	-0.0168632	-0.00441803	0.998881
1147	8.62166×10^{-10}	-0.0168300	-0.00441795	0.998882

The mesh density change is responsible for a dc acceleration difference of ~ 1.2×10^{-14} . If we assume this is equivalent to an error of ~ $\pm 5 \times 10^{-15}$ ms^{-2} and further assume that a similar level of error is applicable to the other segments this implies an overall potential error in our analysis for dc accelerations of order 2×10^{-14} ms^{-2}.

6.3.5 Solar fluctuations

The thermal model was used to investigate thermal effects of solar constant intensity fluctuations. The worst case condition determined from that investigation was for solar constant fluctuation of

3.74 $W.m^{-2}$ $Hz^{-1/2}$ at a frequency of 10^{-4} Hz. The temperatures derived for the maximum and minimum of this fluctuation were used as the input temperatures to derive thermomechanical distortions in the FEM as in the hot and cold extreme cases above. The accelerations at the centre of the payload 1 test mass were calculated for both of these cases and the difference taken to be the acceleration due to solar fluctuations at the frequency of the wrest case fluctuations.

Giving a result of 1.3×10^{-16} $ms^{-2}.Hz^{-1/2}$ at 10^{-4} Hz. We believe this to be a worst case analysis as it intrinsically assumes that all of the nodes respond thermomechanically in phase.

6.3.6 Conclusions

The requirements set out for the LISA spacecraft and payload self-gravity are

- DC acceleration at centre of test mass $<10^{-9}$ ms^{-2}
- Gradient at centre of test mass $<5 \times 10^{-8}$ s^{-2}
- Dynamic - parasitic accelerations (over measurement band) $<1.2 \times 10^{-15}$ ms^{-2} Hz$^{-1/2}$

The results from this analysis are:

Case	DC acceleration (ms^{-2})	Maximum Gradient (s^{-2})
Undistorted	7.50761×10^{-9}	1.051×10^{-7}
1g release	7.51525×10^{-9}	1.053×10^{-7}
Mass loss due to CFRP outgas	7.18234×10^{-9}	
As above + 1 g release	7.19157×10^{-9}	
Thermal model hot case	7.15476×10^{-9}	
Thermal model cold case	7.15669×10^{-9}	

Clearly some mass balancing is required to fine tune the DC and gradient gravitational performance of the LISA system. The implication of such payload design is discussed in section 7.3.2.

The dynamic situation appears to be on the safe side with the analysis result of 1.3×10^{-16} ms^{-2} Hz$^{-1/2}$ being well within specification.

7 Payload Design

7.1 Payload Electro-Optical Design

7.1.1 Optical performance and budgets

7.1.1.1 Link budget and derived allocations

This paragraph presents the inter-spacecraft optical link budget as well as the results of the sensitivity analyses showing the criticality of the main contributors to the link budget.

7.1.1.1.1 Link budget

The link budget and all the related hypotheses are detailed in the following table.

Table 7.1-1: LISA link budget

		Value	Unit	Comments
1	wavelength	1.06	µm	
2	laser output power	1.00	W	laser power at fibre intput
3	optical transmission of emission path	0.63		from optical bench transmission budgets
4	telescope diameter	0.30	m	
5	maximum theoretical emitted intensity	$3.9\ 10^{10}$	W/sr	for a perfect, un-obstructed optical system
6	obscuration and truncature losses	0.80		gaussian beam truncature and obscuration impact
7	emission path wfe - lambda/n @ 1.06 µm	20		wfe = λ/20 rms @ 1.06µm
8	emission path optical quality - Strehl ratio	0.90		
9	pointing error	0.50	µrd	
10	off-axis attenuation due to pointing error	0.95		far field pattern diffraction limited
11	**emitted intensity in pointing direction**	**$2.7\ 10^{10}$**	**W/sr**	
12	distance between two spacecrafts	$5\ 10^{6}$	km	
13	received irradiance	$1.1\ 10^{-9}$	W/m^2	
14	telescope collecting area	0.07	m^2	
15	optical transmission of measurement path	0.85		from optical bench transmission budgets
16	**received power on detector**	**$6.5\ 10^{-11}$**	**W**	
17	optical transmission of acquisition path	0.04		from optical bench transmission budgets
18	**received power on detector**	**$3.4\ 10^{-12}$**	**W**	

Comments to the link budget:

line 5: maximum axial gain of an optical antenna is $4\pi A/\lambda^2$ (A is the antenna area).

line 6: the optimisation of the emitted beam radius (noted ω at $1/e^2$) with respect to the telescope aperture radius (noted a) is obtained for a $\approx 1.1\ \omega$. This, associated with the central obscuration and spider effects, leads to a 0.8 transmission factor.

line 8: for small aberrations, the Strehl ratio gives the emitted beam attenuation due to the aberrations (this therefore includes both optical bench emission path and telescope aberration).

$I/Io = 1 - 4\pi^2\sigma^2/\lambda^2$ (σ is the wfe rms)

line 9: the pointing error considered in the link budget is conservative.

line 10: the attenuation of the emitted beam for an off-axis angle is approximated by:

$I/Io = [2\ J_o(2\pi a\varepsilon/\lambda) / (2\pi a\varepsilon/\lambda)]^2$ (a is the telescope aperture radius)

7.1.1.1.2 Link budget and optical quality

All hypotheses are those of Table 7.1-1, but for the emission path optical quality.

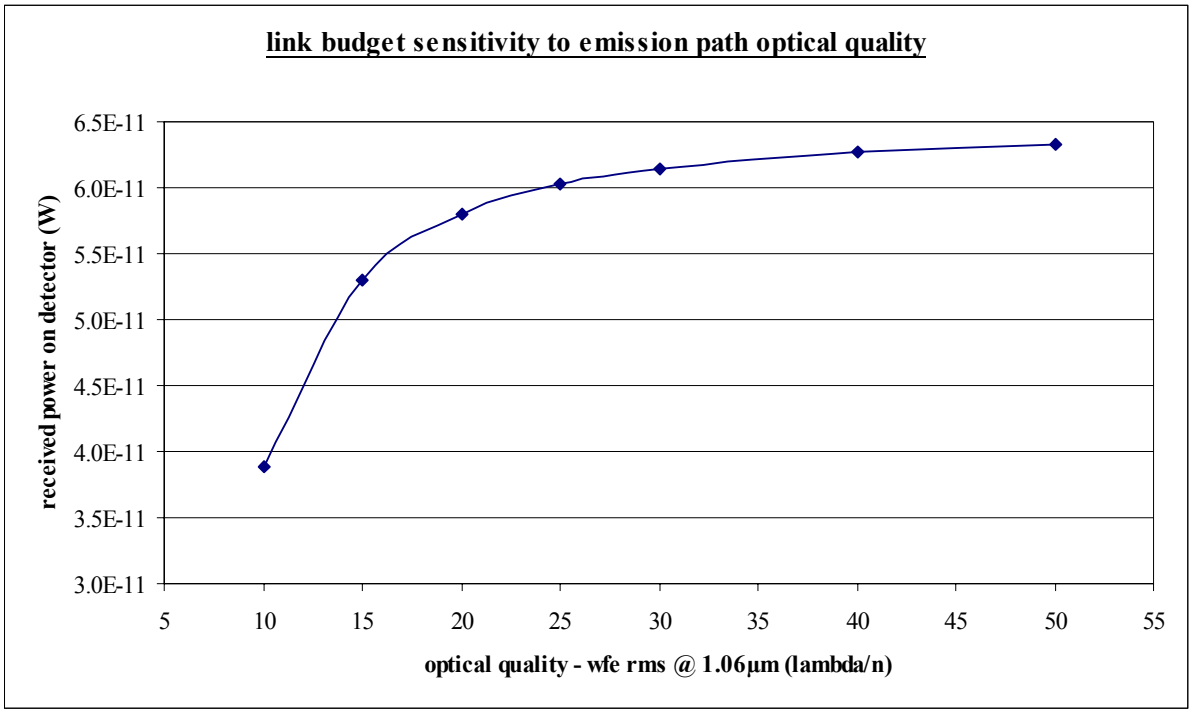

Figure 7.1-1: Link budget sensitivity to optical quality

A global emission path wfe of λ/20 rms @ 1.06µm appears as a good compromise between the optics feasibility and the performance.

This allocation covers all optical aberrations, including defocus. The maximum λ/10 defocus required to meet the measurement accuracy is therefore superseded by the link budget need on the emission path.

This allocation has then to be further apportioned between the telescope and the optical bench components. the following a priori allocation has been performed:

telescope on-axis wfe allocation λ/30 wfe rms @ 1.06µm (including defocus),

optical bench wfe allocation λ/30 wfe rms @ 1.06µm (including defocus).

The imaging quality achieved for the telescope and optical bench designs meet the global allocation, and is detailed in § 7.1.1.2.

7.1.1.1.3 Sensitivity to pointing error

All hypotheses are those of Table 7.1-1, but for the pointing error.

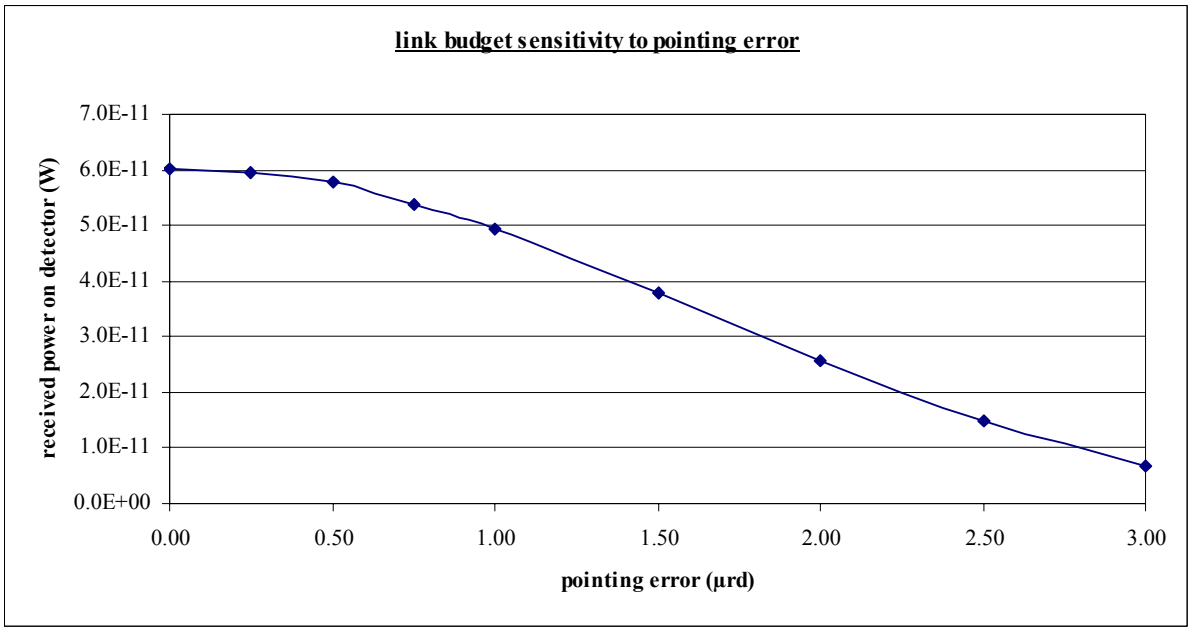

Figure 7.1-2: Link budget sensitivity to pointing error

The half angle of the far-field emitted cone is of 1.8 µrad.

The above figure shows that the emitted beam has to be maintained pointed toward the opposite spacecraft with a ± 0.5 µrad accuracy. The reception beam is therefore received off-axis on the

telescope because of the PAA angle (3.5 µrad), which has a negligible impact on the performance as the telescope field of view is sufficient.

7.1.1.1.4 Sensitivity to telescope diameter

The current link budget with the baselined 30 cm diameter telescope enables to meet the required scientific measurement performances.

If a major link budget increase were required, alternative telescope designs could be considered, as the telescope diameter D is the parameter which has the greatest impact on the link budget (D^4 sensitivity), as its influence is twofold. A larger telescope diameter:

- reduces the emitted beam diffraction, which results in a narrower emitted cone,
- increases the energy collected by the receiver.

An increase from 30 cm diameter to 50 cm diameter would improve the link budget by a factor 7.

An other solution to improve the link budget without increasing the spacecraft volume could be to use rectangular telescope (a 30 x 50 cm^2 telescope would increase the link budget by a factor 3.5). Such a solution should not raise major manufacturing obstacles, as non-circular optics can be polished using ion beam techniques to a high quality level. In this case, a cylindrical optics may be necessary to obtain an optimum fit between the laser beam and the telescope pupil and minimise truncature losses. The impacts on such a beam shape alteration on the emitted beam far field pattern and on the heterodyne detection efficiency would then have to be studied before this solution can be considered as valuable.

7.1.1.2 Imaging quality – allocations and budgets

7.1.1.2.1 Imaging quality allocations

Reception path: the imaging quality requirement is driven by the measurement noise budget. A wfe allocation of $\lambda/10$ rms @ 1.06 µm is derived from that budget.

Emission path: the imaging quality requirement is driven by the link budget. A wfe allocation of $\lambda/20$ rms @ 1.06 µm is derived from that budget.

The following apportionment of the imaging quality allocations has been made between the telescope and the optical bench, assuming a quadratic summation of their individual contributions and taking into account feasibility estimations:

	Emission path (WFE rms)	Reception path (WFE rms)
Optical bench imaging quality	35 nm ($\lambda/30$ @ 1.06 µm)	55 nm ($\lambda/20$ @ 1.06 µm)
Telescope imaging quality	35 nm ($\lambda/30$ @ 1.06 µm)	90 nm ($\lambda/12$ @ 1.06 µm)
Total (quadratic sum)	53 nm ($\lambda/20$ @ 1.06 µm)	106 nm ($\lambda/10$ @ 1.06 µm)

It is to be noted that the refocalisation ensured by the fibre positioner enables to compensate for the long term defocalisations on the emission path only, which explains the difference of allocation and performance between the telescope emission and reception paths.

7.1.1.2.2 Imaging quality budget

The figures hereafter are from the optical bench study and from the telescope study.

	Emission path (WFE rms)	Reception path (WFE rms)
Optical bench imaging quality	41 nm	52 nm
Telescope imaging quality	31 nm	69 nm
Total (quadratic sum)	51 nm	86 nm
Allocation	53 nm	106 nm
Compliance status	OK	OK

The phase A baseline optical design meets the imaging quality requirements on both the emission and reception paths.

7.1.1.3 Instrument FOV analysis

7.1.1.3.1 FOV definition

Several telescope fields of view can be defined according to the mission phase:

- telescope fields of view required for the measurement phase,
- telescope fields of view required for the acquisition phase.

The required telescope imaging quality also depends on the considered phase.

Definition: the telescope being afocal, the following paragraphs only consider the input field of view. The output FOV corresponds to the input FOV multiplied by the afocal magnification.

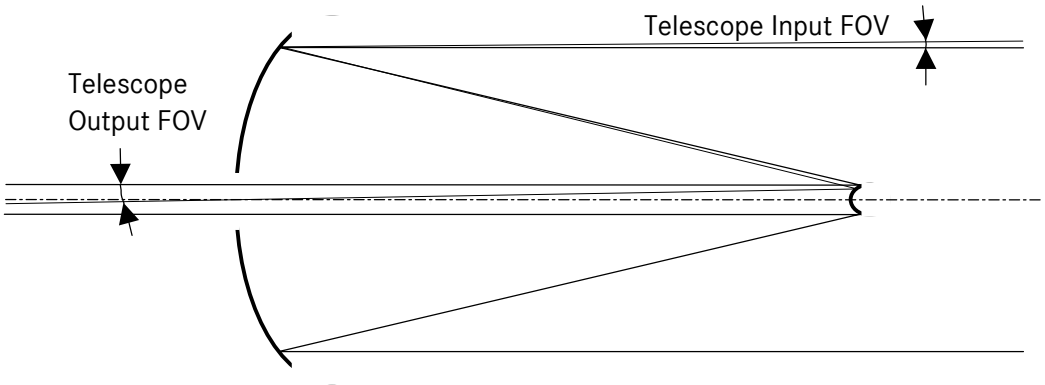

7.1.1.3.2 FOV required for the measurement phase

During this phase, the angle between the emitted beam and the received beam is the Point Ahead Angle (3.3 µrad constant bias ± 55 nrad sinusoidal variation in the constellation plane, 85 nrad constant bias ± 5.7 µrad sinusoidal variation in perpendicular, leading to a 6.6 µrad maximum PAA angle). All misalignments and long term opto-mechanical drifts shall therefore be compensated so that the PAA angle is maintained.

- A misalignment θ occurring between the optical bench and the telescope is compensated by an optical assembly rotation of θ/g_α, (g_α is the telescope angular magnification) which has a θ/g_α contribution on the telescope FOV. This is valid for both the initial OB / telescope alignment and the long term drifts.

Both the optical bench and the telescope are mounted on a Ø 360 mm CFRP tube. A 1µm shift at the interface induces a 3 µrad θ angle. The following allocations are proposed:

- initial telescope / optical bench co-alignment ± 100 µrad,
- long term telescope / optical bench drift ± 150 µrad.

The long term drift allocation covers the optical assembly thermal and moisture release contributions, estimated to 50 µrad by the RAL, as well as the gravity release and launch microsettling effects.

- The misalignments and drifts occurring inside the optical bench on the emission path will be compensated using the fibre positioner, and do not impact the telescope FOV. The compensation of the misalignments on the reception path will be performed by tilting the proof-mass, without FOV impact.

- The pointing accuracy of each spacecraft contributes to the telescope FOV. The current allocation for this contributor during the measurement phase is 0.1 µrad.

Telescope measurement Input FOV budget		
Telescope magnification hypothesis	$g_\alpha = 30$	$g_\alpha = 60$
Contributors:		
- Telescope / OB initial alignment 100 µrad	3.3 µrad	1.7 µrad
- Telescope / OB initial long term drift 150 µrad	5.0 µrad	2.5 µrad
- Pointing accuracy 0.1 µrad	0.1 µrad	0.1 µrad
- PAA max angle 6.6 µrad	6.6 µrad	6.6 µrad
Total (quadratic summation)	8.9 µrad	7.3 µrad

The PAA angle is the major contributor to the measurement FOV budget.

On the basis of this estimation, a ± 10 µrad (± 2 arcsec) FOV has been considered for the telescope optical definition, without distinction between the $g_\alpha = 30$ or $g_\alpha = 60$ study cases.

7.1.1.3.3 FOV required for the acquisition phase

During the acquisition phase, the beam emitted by the opposite spacecraft is imaged on the acquisition sensor. The telescope FOV required during this phase is the same as for the measurement phase, except for:

- the PAA is not to be considered for that phase,
- the acquisition sensor FOV, corresponding to the acquisition cone angle (± 9 µrad) is to be covered.

This leads to a ± 11 µrad acquisition FOV, therefore similar to the measurement FOV hypothesis.

7.1.2 Telescope

7.1.2.1 Telescope design drivers

7.1.2.1.1 Performances and interface requirements

The design drivers considered for the telescope definition are the following:

- afocal design,
- imaging quality (performance to be met at end of life in-orbit over the full field of view)
  - emitted beam: wavefront error better than 35 nm rms ($\lambda/30$ rms @ 1.06 µm)
  - received beam: wavefront error better than 90 nm rms ($\lambda/12$ rms @ 1.06 µm)
- straylight minimisation on both acquisition and coherent sensors,
- mechanical interface (Ø 360 mm cylinder), overall mechanical envelope minimisation.
- afocal magnification g_α=60 (g_α=30 acceptable if the performance requirements can not be met with a g_α=60 design),

The FOV considered for telescope optical design is ± 10 µrad, according to the § 7.1.1 analysis.

7.1.2.1.2 Telescope thermal environment

The main characteristics of the telescope thermal environment are :

- an operational temperature estimated to –15°C,
- an important longitudinal gradient between the primary mirror, located close to the optical bench thermal shield, and the secondary mirror close to the space aperture,
- an expected change over life time of 5°C (from pre-phase A study).

The telescope will therefore work far from its alignment temperature and in presence of important gradients. This is of major importance for the determination of the structure and mirrors materials.

The telescope short term thermal stability will depend on its discoupling from the environment. A high discoupling shall be preferred to improve the telescope intrinsic stability performances.

7.1.2.2 Review of possible optical and mechanical telescope designs

7.1.2.2.1 Possible optical designs

This paragraph presents the possible optical designs a priori compatible with the LISA telescope requirements. The next paragraph will then review the materials and technologies available to manufacture the mirrors and structures corresponding to the possible optical designs, and assess their performances.

A two mirrors design enables to meet the required imaging performance over the narrow FOV. Optical designs with convex or concave secondary mirrors can be considered:

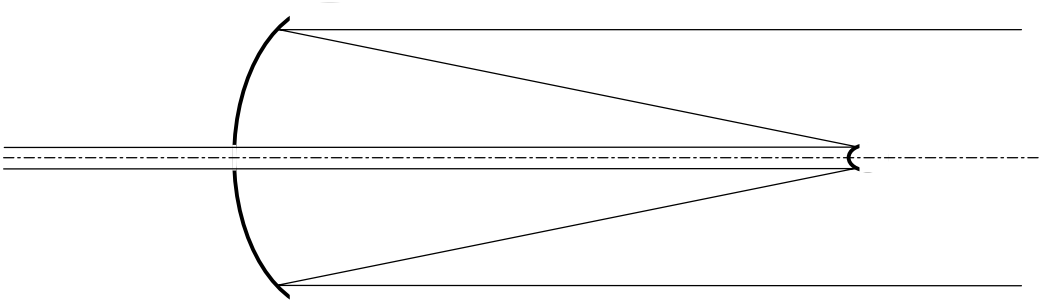

Figure 7.1-3: Telescope design with convex secondary mirror

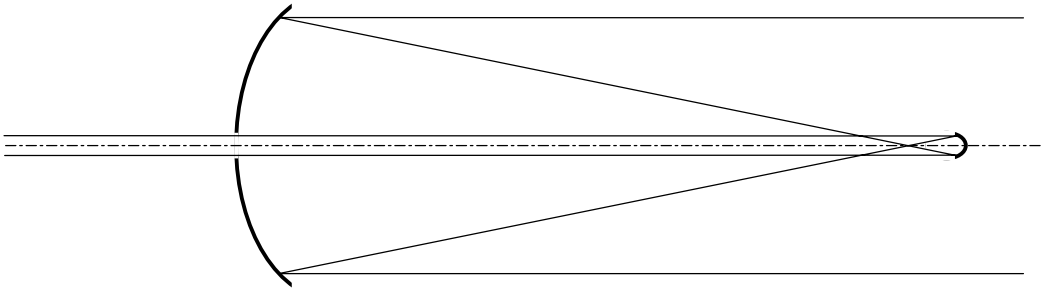

Figure 7.1-4: Telescope design with concave secondary mirror

Remark: because of the afocal design, the primary and the secondary mirrors have the same numerical aperture.

Two optical combinations can be considered to meet the required performance:

. Cassegrain type design:

- both PM and SM are parabolic,
- design corrected of all primary order aberrations but field curvature.

. Dall-Kirkham type design:

- quasi parabolic PM (K ≈ - 0.97),
- spherical SM,
- design corrected on-axis from spherical aberration, coma in FOV.

The Cassegrain telescope features the best imaging quality for a two mirrors afocal design. The small LISA telescope FOV however enables to consider a design not corrected from field aberrations. The main advantage of the Dall-Kirkham design is its spherical SM, which enables an easy and cost effective high quality manufacturing.

The performances achievable with both designs will be compared in the next paragraphs, taking into account the mirrors achievable WFE and roughness as well as the imaging quality sensitivity to aberrations induced by initial alignment and long term effects.

7.1.2.2.2 Primary mirror technologies and related performance

The primary mirror will be aspherical (parabolic or elliptical).

7.1.2.2.2.1 Zerodur mirrors

A 25 nm WFE rms can be considered as the best achievable quality for a 300 mm diameter parabola of 1.2 to 1.5 numerical aperture made of Zerodur or ULE. Such a performance requires a final polishing step using ion beam figuring. A 10 Å roughness can be obtained.

The SILEX terminals primary mirrors are representative of the ultimate polishing performance obtained on Zerodur. The mirrors are 250 mm diameter, 1.5 numerical aperture parabola, which have been polished using ion beam figuring to a 28 nm rms WFE and feature a 10 Å roughness (performances at mirrors delivery).

7.1.2.2.2.2 SiC-100 mirrors

The polishing of SiC-100 is comparable to glass polishing. A thin layer of SiC CVD (50 to 100 µm) is applied on the SiC-100 grinded substrate in order to overcome the residual intrinsic porosity of the bulk material and obtain low scattering performances. The achieved polishing equals the one achieved on glass and overpasses it when ion beam figuring is used for the final polishing. A 8 nm rms WFE is achievable with a 10 Å roughness for a 300 mm diameter parabola of 1.2 to 1.5 numerical aperture.

The DetelSiC primary mirror (diameter 200 mm, numerical aperture 1.46, asphere K=-0.96) is representative of the polishing quality achievable with ion beam figuring for the LISA telescope primary mirror. A WFE of 5.4 nm rms has been obtained, corresponding to $\lambda/196$ @ 1.06 µm (see figures hereafter).

Remark: this higher efficiency of the SiC ion beam polishing is due to the material high thermal conductivity which prevents local surface distortions.

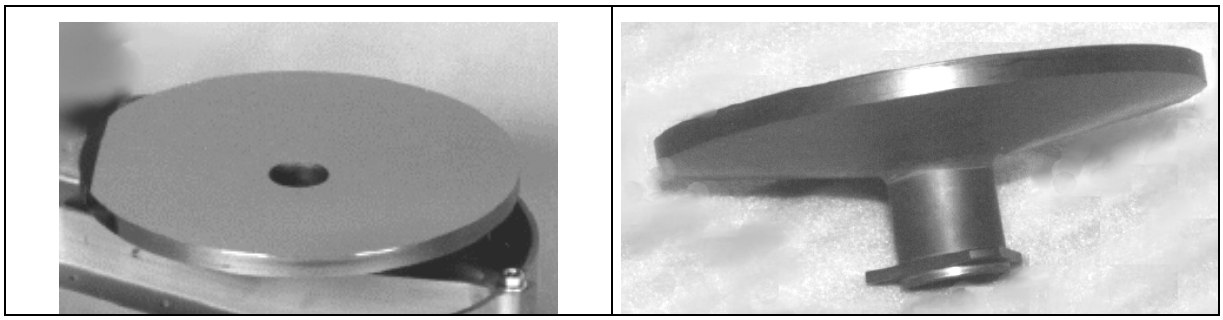

Figure 3-3 : The ϕ 200 mm aspherical primary mirror for the DetelSiC telescope

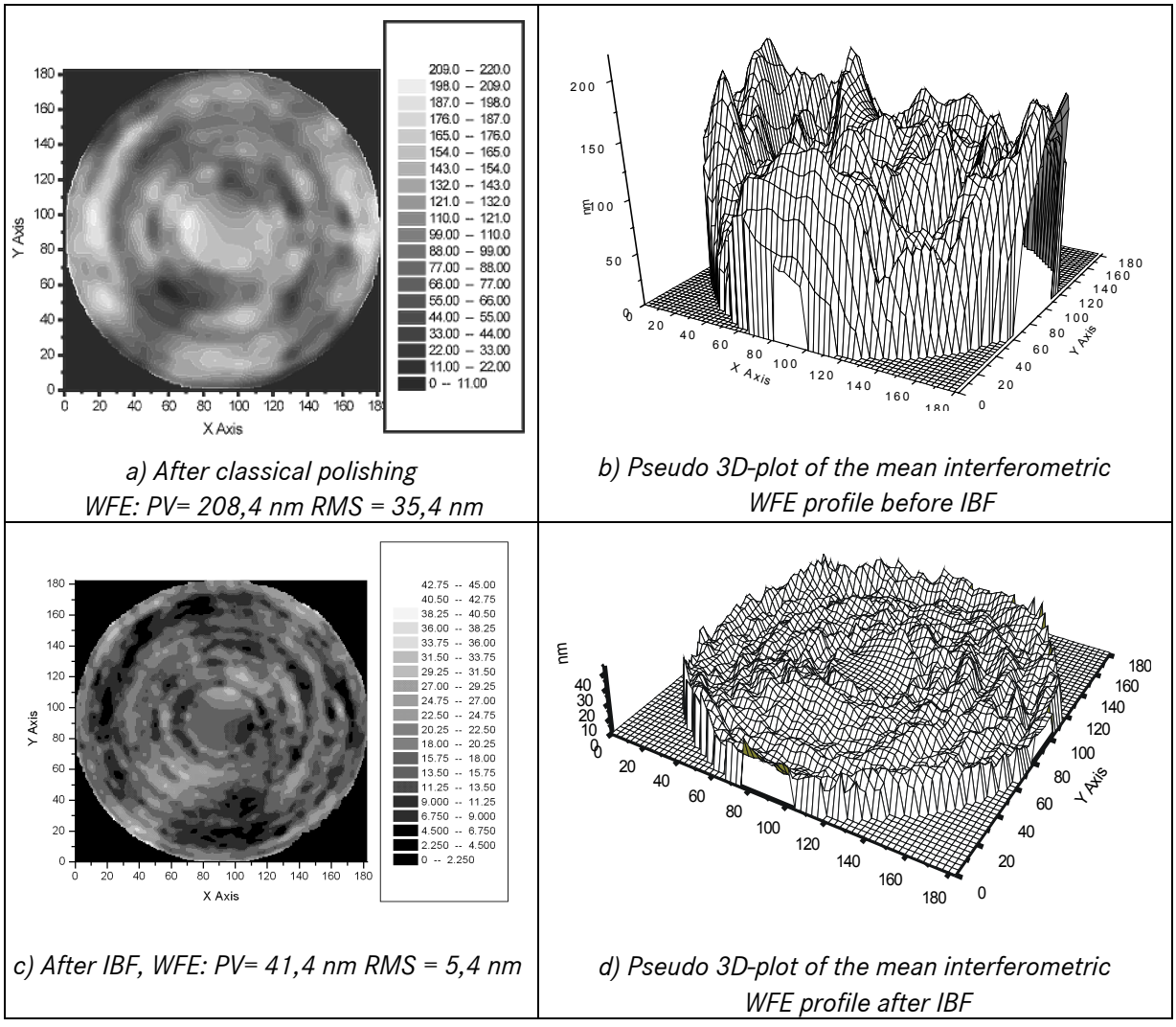

a) After classical polishing
WFE: PV= 208,4 nm RMS = 35,4 nm

b) Pseudo 3D-plot of the mean interferometric WFE profile before IBF

c) After IBF, WFE: PV= 41,4 nm RMS = 5,4 nm

d) Pseudo 3D-plot of the mean interferometric WFE profile after IBF

Figure 7.1-5: Data maps of the ϕ 200 mm DetelSiC primary mirror:

a,b) WFE mean value out of 12 individual measurements after classical polishing
c,d) final WFE error of the ion beam figuring processing

7.1.2.2.3 Secondary mirror achievable performance

The secondary mirror achievable polishing quality depends on the selected optical design as well as on the mirror material.

- the secondary mirror can be either convex or concave. For a small parabola, discussions with mirrors manufacturers show that there is no major feasibility difference between a convex and a concave shape. The concave shape requires an additional optics to be tested (Hindel sphere), which manufacturing is not challenging nor cost driving for a small mirror. A concave secondary mirror is therefore preferred, as it enables to minimise the telescope overall mechanical envelope.

- in the case of a Dall-Kirkham design, the secondary mirror is spherical. There is then no diameter limitation, and a 8 nm WFE rms polishing quality is achievable on Zerodur or SiC with a surface roughness of 5 to 10 Å.

- in the case of a Cassegrain design, discussions with optics manufacturers have enabled to estimate the feasibility limits of a 1.2 to 1.5 numerical aperture high quality parabolic mirror:

  . a 10 mm diameter mirror (required in the g_α=30 option) can be manufactured with a 15 nm rms WFE and 10 Å roughness (challenging but achievable target for a Zerodur or SiC mirror),

  . a 5 mm diameter mirror (required in the g_α=60 option) can be manufactured with a 25 nm rms WFE and 15 Å roughness.

Remark: ion beam figuring can not be used for the secondary mirror polishing as the mirror is too small with respect to the ion beam diameter (about 10 mm).

7.1.2.2.1 Structure design and performances

7.1.2.2.1.1 Main structure requirements

The telescope structure shall:

- ensure constraints-free interfaces to the mirrors so that their initial WFE and alignment is not jeopardised by mechanical stresses,
- minimise external straylight (due to sun illumination) and internal straylight (retro-reflection of the emitted beam toward detectors).
- provide a high long term relative stability between both mirrors, as well as between the telescope and the payload structure, taking into account the LISA mission environments (thermal interfaces, launch loads etc...),
- feature low mass / high stiffness performances,
- minimise costs.

7.1.2.2.1.2 Selection of the structure material

A high long term stability is required to maintain the imaging quality performance over the life time, which limits the choice of the structure material to the followings:

- CFRP, associated with Zerodur or ULE mirrors,
- Carbon-carbon, associated with Zerodur or ULE mirrors,
- SiC, associated with SiC mirrors,
- Beryllium, associated with beryllium mirrors,
- Zerodur, associated with Zerodur mirrors.

SiC has been preferred after comparison of the figure of merits of these materials, taking into account their mechanical and thermal properties, as well as the cost aspects.

The major advantages of the SiC are :

- The cost, the SiC solution being the cheapest of the five listed here above.
- The high specific stiffness (Young modulus over mass density or E/ρ= 420Gpa/3250Kg.m^{-3}) which allows a high level of alleviation, thus important mass savings. With respect to classical materials such as Zerodur, the mass saving is about 2 for the primary mirror. Only Beryllium alloys meet the SiC performance to this respect, but it shows out several drawbacks in terms of health hazard during manufacture and overall manufacturing costs.
- The high thermal distortion figure of merit (thermal conductivity over thermal coefficient of expansion or λ/α=160W/mK over 2.10^{-6}°C^{-1}). This ratio quantifies the impact of a thermal gradient on the deformation of the optical surface in steady state conditions. There again, the high thermal conductivity of the SiC coupled to a very low thermal expansion coefficient makes the SiC the best optical material, far above Beryllium alloys.
- The impacts of thermal transient can be quantified through an additional figure of merit which takes into account the specific heat of the material and the mass of the mirror, through the material mass density and its thermal conductivity. This figure is expressed as the ratio of the mass density times the specific heat times the thermal conductivity over the CTE (ρ Cp λ/α). The higher the figure, the best the material can either spread the heat in its bulk or store it with a minimum temperature change, thus minimum distortion. For this figure again, the SiC features the best behaviour.

The SiC exhibits the best overall behaviour, as indicated by its first ranking for all figures of merit (for specific stiffness it is second to Beryllium alloy, but the SiC low CTE of 2.10^{-6}°C^{-1} and high conductivity allows outstanding stability performances). Other fields of interest brought by SiC are the following:

- Total insensitivity to hygroelastic phenomena (moisture desorption) wrt CFRP materials,
- Ability to be polished to the highest WFE performance using ion beam figuring,
- Good compressive holding and high friction coefficient (SiC/SiC) used for direct linkage compatible with stability criteria under launch environment (enabling mirrors central mount, thus minimising parts number),

- Possible suppression of surface coating such as black painting due to high thermo-optical coefficient (ε=0.8).

Table 7.1-2: Relative materials mechanical properties

MATERIAL	DENSITY (kg/m^3)	YOUNG'S MODULUS (Gpa)	STIFFNESS-TO-WEIGHT RATIO (E+6Nm/kg)	THERMAL CONDUCTIVITY (W/m°K)	CTE (E-6/°K)
SiC	3200	420	131	170	2
Aluminium (2024)	2800	70	25	225	24
Beryllium	1850	304	164	220	11
Titanium (TA-6V)	4430	110	25	7.2	8.6
CFRP (GY70 Isotropic)	1800	100	56	35	0.02
ZERODUR	2530	91	36	1.6	0.05

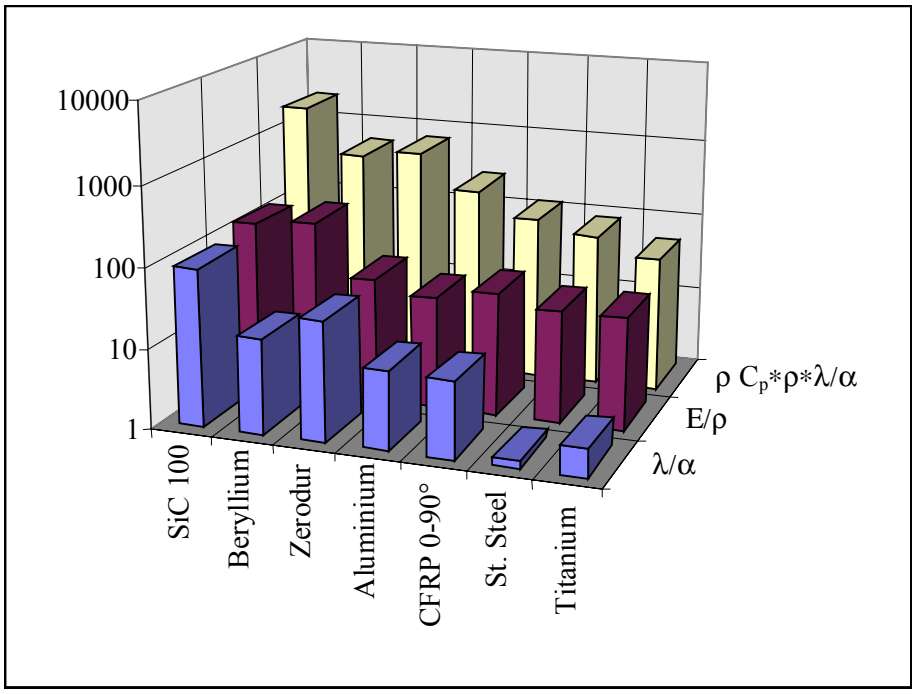

Figure 7.1-6: Relative figures of merit of the most space usual materials

7.1.2.2.1.3 Identification of an alternative structure material

The all Zerodur design has been successfully used for the Silex program. It is however discarded for the LISA telescope as more recent materials enable to reach equivalent or better performances at lower costs.

The carbon-carbon solution is also discarded for its much higher cost.

A telescope with a CFRP structure and Zerodur mirrors would feature high mechanical performances and excellent thermal stability, which makes this solution a technically valid alternative to the SiC design. But though cheaper than the above listed solutions, it remains more expansive than the all SiC design. The CFRP + Zerodur design is therefore considered as a back-up for the telescope design.

7.1.2.2.1.4 Selection of the mechanical design

7.1.2.2.1.4.1 Primary mirror design

Designs based on a structural primary mirror are rejected, as they are not compatible with high WFE performances. The telescope design will instead include a baseplate supporting the primary mirror as well as the secondary mirror spider structure. The primary mirror is linked to the baseplate by a central attachment, which is a compromise between several opto-mechanical aspects:

- mechanical stress under quasi-static load,
- mechanical stress under interface default and bolts preload,
- impact of mounting default on the WFE optical quality,
- impact of thermo-elastic effects due to local thermal gradient on the WFE optical quality.

This design enables to limit the impact of mounting distortion on mirror WFE to 5 nm rms (verified on the representative Ø 200 mm DetelSiC demonstrator).

In a conservative approach, the lightweighting ratio proposed for the primary mirror is of 0.4, which leads to a quite massive mirror and takes a maximum benefit of the SiC conduction to minimise potential thermal gradients impact on WFE. According to the result of detailed thermal analyses, a 60% lightweighted primary mirror could be considered, enabled by the SiC stiffness.

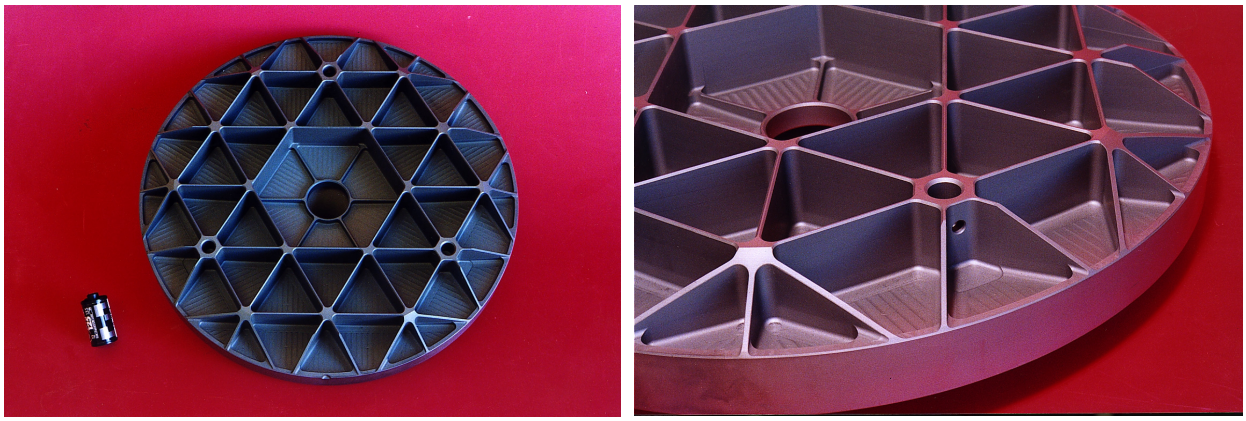

Figure 7.1-7: Example of a lightweighted (∅352 mm, 1,8 kg) SiC mirror (SOFIA - NASA/DLR program)

7.1.2.2.1.4.2 Secondary mirror support

The low mass of the secondary mirror (≈ 20 g) enables to consider two solutions for the SM supporting structure:

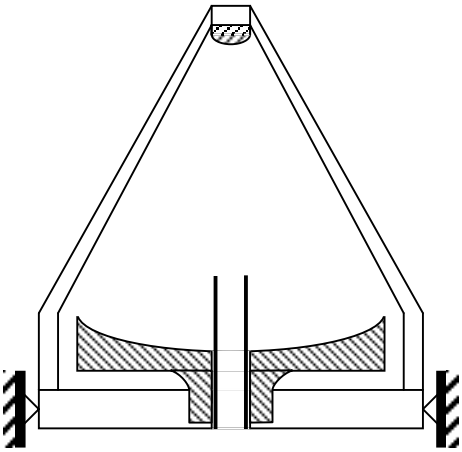

Concept 1: three spiders

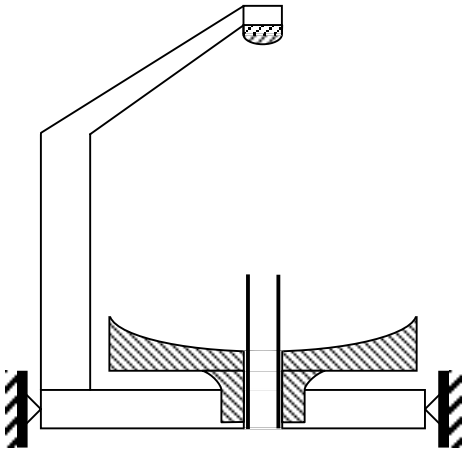

Concept 2: one mast

Both concepts are compatible with a SiC structure. The mast design however features the following advantages with respect to the spider one:

- reduction of the number of structure elements inducing costs saving,
- straylight minimisation.

The mast design is therefore preferred.

Remark: a classical three spiders design is also compatible with the SiC design and remains a possible back-up if strong short term thermal fluctuations shift the optical axis and induce pointing bias and jitter. The high SiC thermal conductivity should however minimise this type of effect.

7.1.2.2.1.4.3 Telescope baffling

In addition to the interface tube preventing any direct solar illumination on the telescope, an internal baffle is foreseen to minimise the straylight that could reach the optical bench after diffusion on the interface tube. The length of this internal baffle is set a priori to 70 mm from PM apex, this value being to be optimised according to detailed optical assembly straylight studies. The internal baffle will be made of black painted aluminium, and be attached to the interface plate.

7.1.2.2.1.5 Structure stability and alignment performances

7.1.2.2.1.5.1 Alignment principle and performances

The proposed alignment principle aims at reducing the number of components. For that purpose, all alignments are performed at the secondary mirror assembly level:

- the primary mirror will be mounted on the telescope baseplate. There are no alignment capabilities at this level, but tight PM interfaces manufacturing tolerances will be required (typically 0.05 mm),
- the secondary mirror will be aligned with respect to the PM using appropriate focus shims and step by step eccentrics. The angle of the focus shim will enable to adjust the mirror tilt.

During the alignment, the telescope will be in auto-collimation in front of an interferometer (for example Zeiss D100 featuring a $\lambda/100$ resolution), and the imaging quality will be monitored for each iteration. The alignment criteria will be the minimisation of focus and coma aberrations.

The following alignment accuracy can be achieved:

- adjustment of the inter-mirrors distance	± 3 µm
- SM / PM centring resolution	± 10 µm
- SM / PM tilting resolution	± 300 µrad

It is to be noted that SM / PM tilt and decentring both induce coma aberration. The residual SM tilt will therefore be compensated by a SM decentring (within centring resolution).

7.1.2.2.1.5.2 Long term stability

The long term stability of the telescope imaging quality covers all WFE evolutions from end of on-ground alignment to in-flight end of life.

The effects to be considered for the long term stability performance are the following:

- microsettling due to launch loads,
- thermal effects (impact of homogeneous temperature variations and gradients),
- gravity release (alignment under 1g, operation at 0g),
- radiations.

. Microsettling: though no detectable microsettling has been observed on the available SiC structures, an allocation corresponding to a 0.5 µm IMD variation and a 2 µm SM/PM lateral shift is considered for the telescope performance analyses. These figures, conservative in the case of a all-SiC telescope, are deduced from the maximum displacements observed at the optical equipments interfaces for both SILEX and GOMOS instruments.

. Thermal stability: the all-SiC telescope has a homothetic dilatation under homogeneous temperature changes which has no impact on the imaging quality. The influence of gradients is minimised thanks to

the material high thermal conductivity. Both homothetic behaviour and gradients resistance have been experimentally verified on the DetelSiC telescope:

- no WFE impact over a –100°C/+ 60+C uniform temperature range,
- ΔT of 5°C between PM and SM in a 100°C gradient environment (see drawing).
-

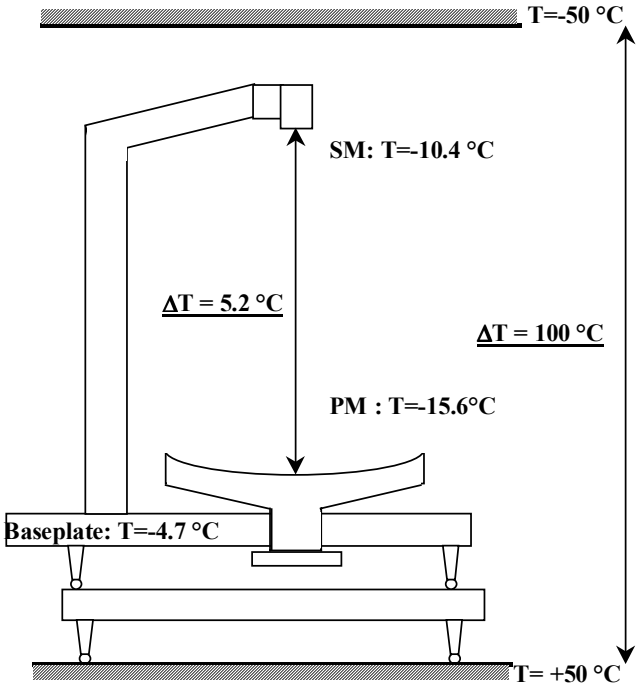

Figure 7.1-8: Gradient test result on DetelSiC demonstrator

A conservative allocation of 1 µm IMD variation, 5 µm SM/PM lateral displacement is however considered for the stability estimation, to be replaced by the results of a detailed thermo-elastical analysis when thermal data are available.

. Gravity release: a FEM mechanical analysis of DetelSiC telescope enables to estimate the gravity release worst case influence on the LISA telescope alignment and imaging quality:

- IMD variation 1 µm
- SM/PM lateral displacement 6 µm
- PM WFE distortion 5 nm rms

The gravity release impact on IMD will be compensated by refocalisation on the emitted path, which is not the case for the lateral displacements. A vertical telescope orientation during the alignment however enables to minimise the lateral displacements induced by gravity release.

. Radiations: it has been verified experimentally that a SiC telescope imaging quality shows no sensitivity to radiations. A SiC-100 mirror has been irradiated (200 Mrad of gamma rays) without showing a measurable WFE distortion.

The long term telescope structural stability taken into account for the performances assessment is then the following (quadratic summation of contributors):

- IMD variation 1.6 µm
- SM/PM lateral displacement 8 µm
- PM WFE distortion 5 nm rms

The refocalisation capability implemented on the emitted beam optical path enables to correct the IMD errors due to the initial alignment and to the long term stability. An allocation of 1 µm for a residual IMD error is however considered for the performances evaluations, which covers the accuracy of the focus correction as well as the acceptable focus evolution between two focus corrections.

7.1.2.3 Selection of the telescope optical design

This paragraph proposes a performance analysis of both Cassegrain and Dall-Kirkham designs according to the mirrors f-numbers, assuming the following hypotheses (from above paragraphs):

	Hypotheses summary			
	Cassegrain		Dall-Kirkham	
	g_α=30	g_α=60	g_α=30	g_α=60
Achievable primary mirror WFE	8 nm	8 nm	8 nm	8 nm
Achievable secondary mirror WFE	15 nm	25 nm	8 nm	8 nm
Design intrinsic aberrations	none		according to numerical aperture and FOV	
Input field of view	± 2 arcsec			
PM / SM errors (alignment + stability)				
- decenter	15 µm *			
- inter-mirrors distance	1 µm (emission) / 3,5 µm (reception) **			

* quadratic sum of the independent alignment and stability contributors.

** emission: residual IMD error after refocalisation

reception: quadratic sum of the independent alignment and stability contributors

All optical performances have been computed using the CodeV software.

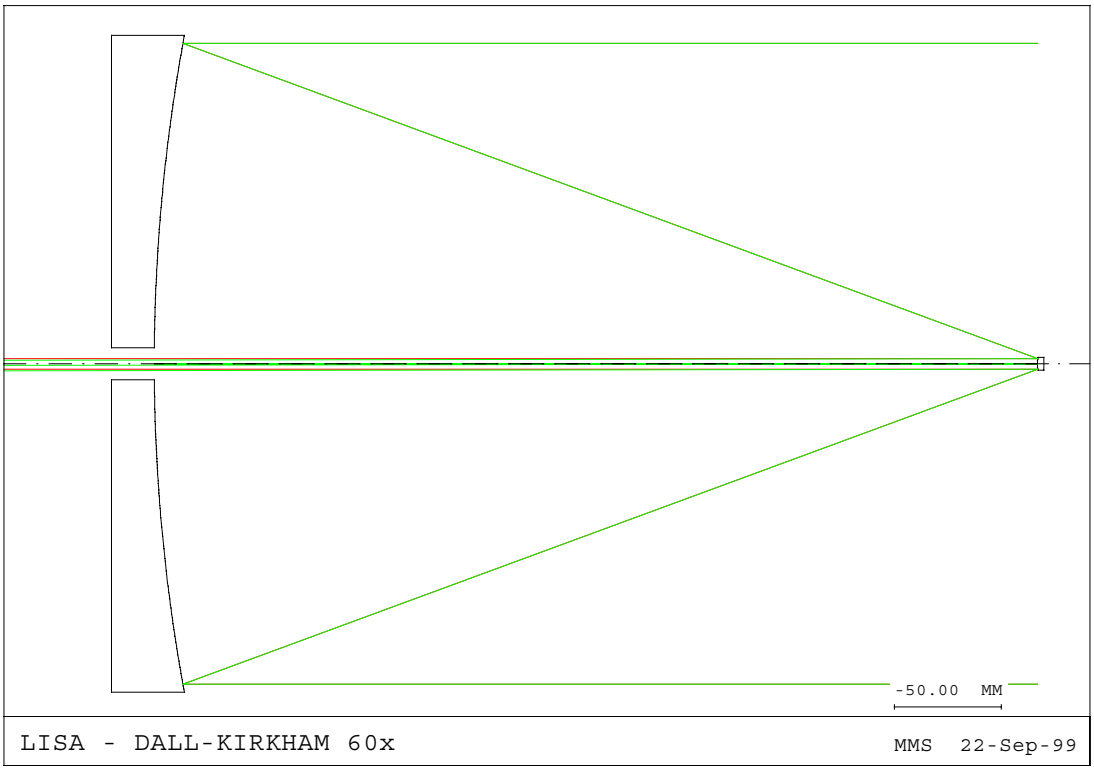

Figure 7.1-9: CodeV telescope modelisation

The imaging quality requirement being more stringent on the emission path, the reception path is not taken into account for the design versus performance trade-off. The performance on the reception path will only be computed for the selected design. It is therefore assumed for all following performances computations that the focalisation is optimised with a residual 1µm error.

The optical aberrations and sensitivities to PM/SM decentring depend only on the mirrors numerical apertures so the only distinction between the g_α=30 and g_α=60 designs is the mirrors manufacturing limits. This is why the same performance is achieved whatever the g_α in the case of the Dall-Kirkham design.

Cassegrain g_α=30 vs mirrors f-number	N=1.2	N=1.3	N=1.4	N=1.5
Achievable primary mirror WFE	8 nm	8 nm	8 nm	8 nm
Achievable secondary mirror WFE	15 nm	15 nm	15 nm	15 nm
PM mounting	5 nm	5 nm	5 nm	5 nm
PM long term distortion	5 nm	5 nm	5 nm	5 nm
15 µm SM decentring	30 nm	24 nm	19 nm	16 nm
1 µm IMD variation	25 nm	21 nm	18 nm	16 nm
Design aberrations within 2” FOV	0 nm *	0 nm *	0 nm *	0 nm *
Total (quadratic sum)	43 nm	37 nm	32 nm	29 nm
Allocation	35 nm	35 nm	35 nm	35 nm
Design compliance	NOK	NOK	OK	OK

* the only aberration of this design is field curvature compensated by refocusing.

Cassegrain g_α=60 vs mirrors f-number	N=1.2	N=1.3	N=1.4	N=1.5
Achievable primary mirror WFE	8 nm	8 nm	8 nm	8 nm
Achievable secondary mirror WFE	25 nm	25 nm	25 nm	25 nm
PM mounting	5 nm	5 nm	5 nm	5 nm
PM long term distortion	5 nm	5 nm	5 nm	5 nm
15 µm SM decentring	30 nm	24 nm	19 nm	16 nm
1 µm IMD variation	25 nm	21 nm	18 nm	16 nm
Design aberrations within 2” FOV	0 nm	0 nm	0 nm	0 nm
Total (quadratic sum)	48 nm	42 nm	38 nm	35 nm
Allocation	35 nm	35 nm	35 nm	35 nm
Design compliance	NOK	NOK	NOK	Marginal

Dall-Kirkham vs mirrors f-number	N=1.2	N=1.3	N=1.4	N=1.5
Achievable primary mirror WFE	8 nm	8 nm	8 nm	8 nm
Achievable secondary mirror WFE	8 nm	8 nm	8 nm	8 nm
PM mounting	5 nm	5 nm	5 nm	5 nm
PM long term distortion	5 nm	5 nm	5 nm	5 nm
15 µm SM decentring	30 nm	24 nm	19 nm	16 nm
1 µm IMD variation	25 nm	21 nm	18 nm	16 nm
Design aberrations within 2" FOV	11 nm	9 nm	7 nm	6 nm
Total (quadratic sum)	43 nm	36 nm	31 nm	27 nm
Allocation	35 nm	35 nm	35 nm	35 nm
Design compliance	NOK	NOK	OK	OK

The choice of the telescope mirrors aperture is made taking into account the imaging performance as well as the telescope overall mechanical envelope.

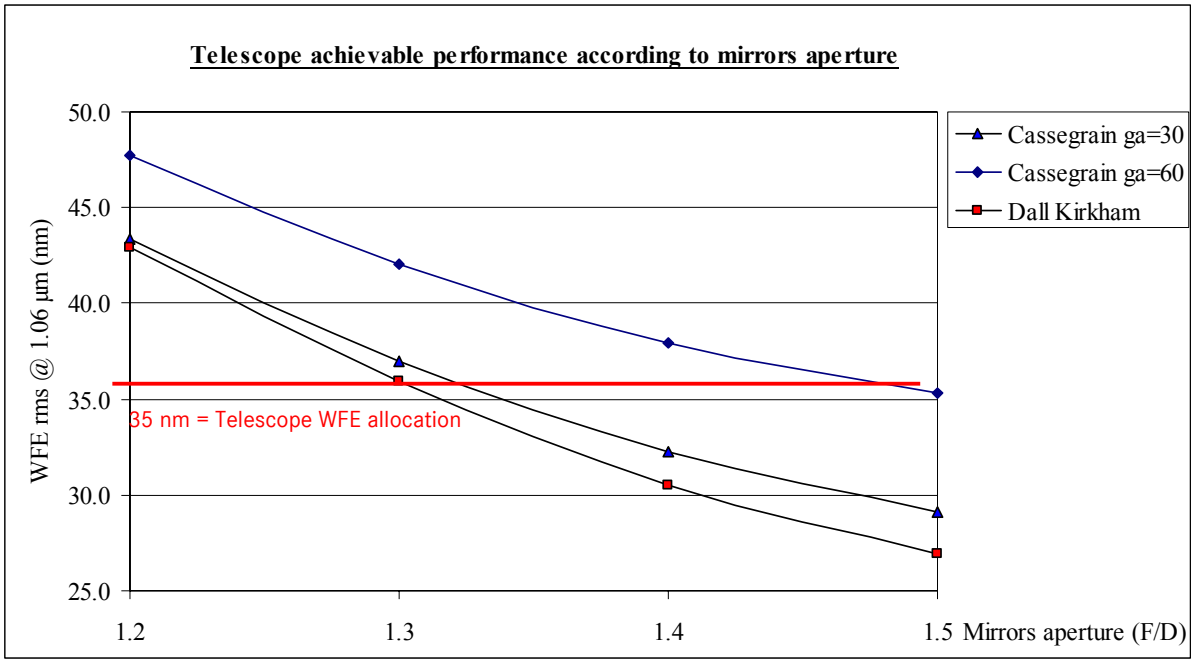

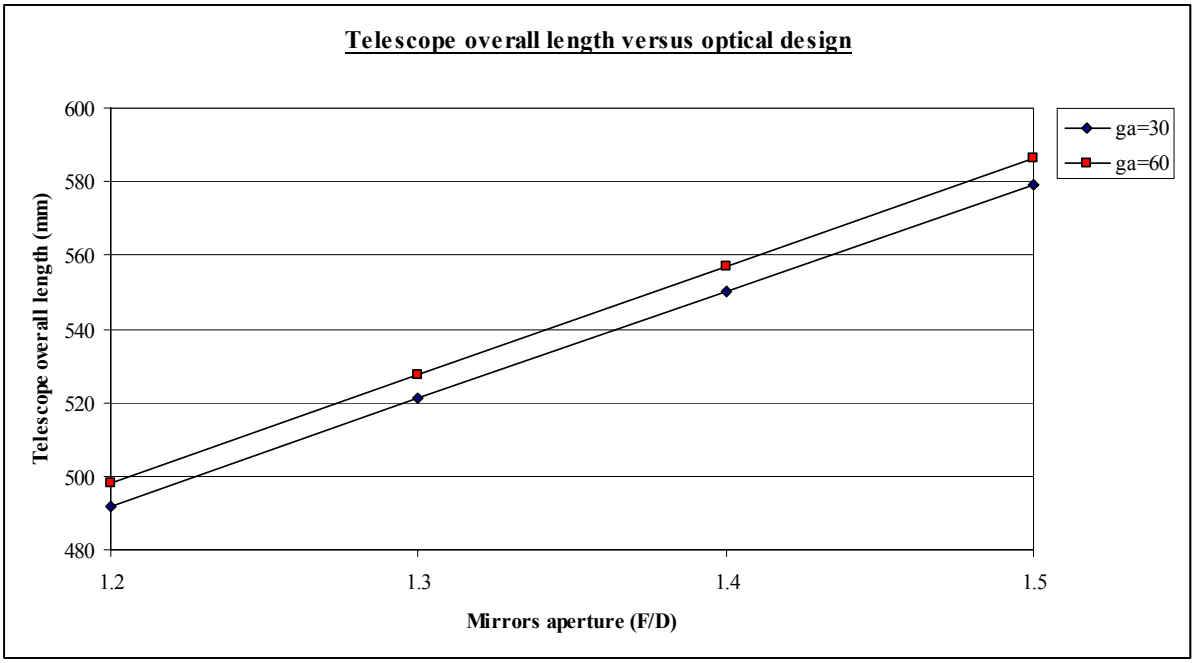

The Dall-Kirkham design is preferred for its simpler and cheaper secondary mirror. It enables to reach a 60 magnification ratio with the required performances for a telescope numerical aperture set to N=1.4, which leads to a design in line with the telescope envelope current hypotheses (550 mm).

7.1.2.4 Design and performance summary

7.1.2.4.1 Optical design and performance

The baseline telescope optical design is a Dall-Kirkham lay-out, with g_α=60 and N=1.4 mirrors apertures.

Primary mirror	Concave Elliptical	R = 840 mm K = -0.9837	Useful diameter mm Total diameter mm	300 305
Secondary mirror	Convex Spherical	R = 14 mm	Useful diameter Total diameter	5 mm 7 mm
Inter-mirror distance IMD = 413.0 mm				

	Performance on emission path	Performance on reception path
PM WFE manufacturing limit	8 nm	8 nm
SM WFE manufacturing limit	8 nm	8 nm
PM mounting	5 nm	5 nm
PM long term distortion	5 nm	5 nm
15 µm SM decentring	19 nm	19 nm
IMD variation	18 nm	65 nm
Design aberrations within FOV	7 nm	7 nm
Total (quadratic sum)	31 nm	69 nm
Allocation	35 nm	100 nm
Compliance	OK	OK

7.1.2.4.2 Mechanical design and mass budget

The following drawings correspond to the baseline SiC design described here above.

The telescope interfaces with the payload structural tube using tangential titanium blades featuring an isostatic interface. This blades also provide a high conductive discoupling with respect to the tube (the mechanical and thermal design of these fixations has been validated on the Meteosat SEVIRI telescope). If the tube diameter is to be maintained at 360 mm, a slight decentring (27 mm) between the tube axis and the optical beam is necessary. This decentring is suppressed it the tube diameter can be increased to 400 mm. The following drawings take into account the 360 mm diameter hypothesis.

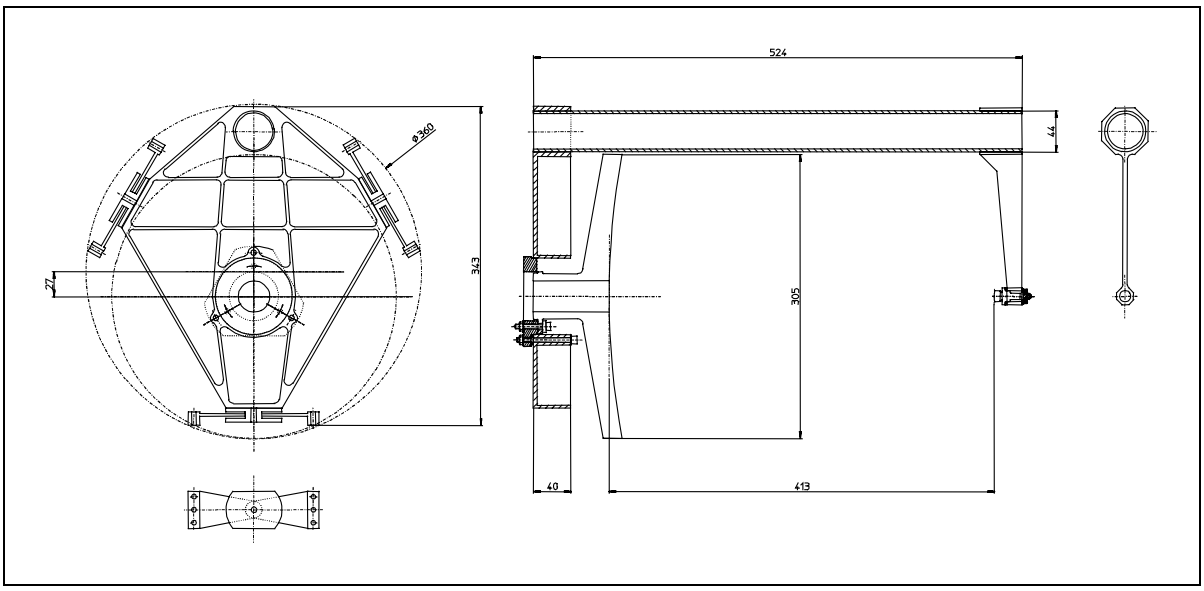

Figure 7.1-10: LISA telescope interface drawing

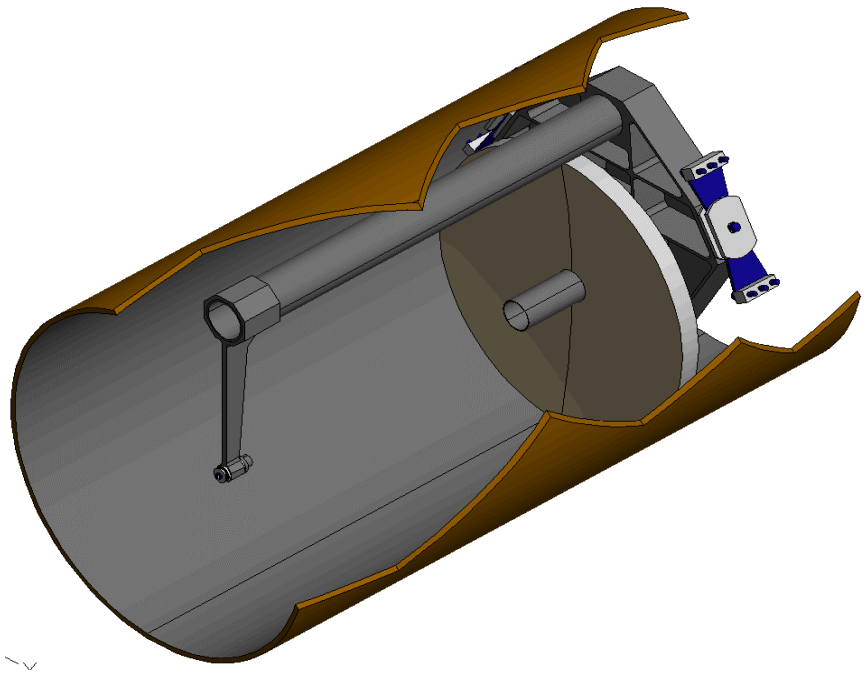

Figure 7.1-11: LISA telescope – view 1

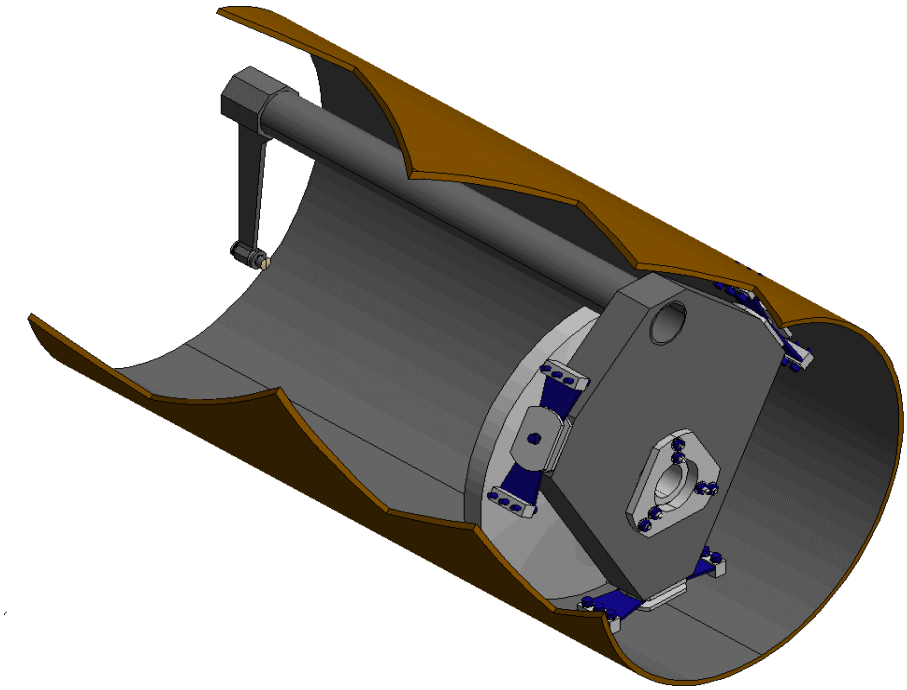

Figure 7.1-12: LISA telescope – view 2

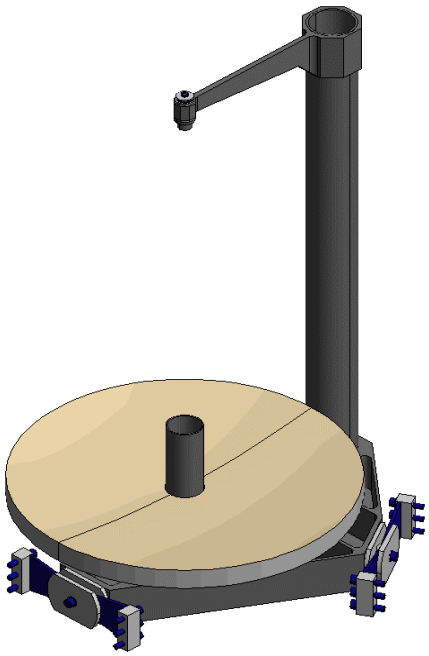

Figure 7.1-13: LISA telescope – view 3

On the basis of the here above mechanical design, a telescope mass budget has been estimated:

	Baseline: 40% lightweighted PM	60% lightweighted PM hypothesis
Primary mirror	3.2 kg	2.1 kg
PM fixation ring	0.2 kg	0.2 kg
Secondary mirror	0.02 kg	0.02 kg
Mast and SM support	0.7 kg	0.7 kg
Baseplate	1.6 kg	1.6 kg
Isostatic mountings	0.6 kg	0.6 kg
Baffle, bolts etc…	0.3 kg	0.3 kg
Total	6.6 kg	5.5 kg

7.1.3 Optical Bench

Each Optical Bench (OB) consists of a 350x200x40 mm baseplate made of ULE™ and of the optical elements (mounted on this baseplate) which form part of the interferometer for the detection of the gravitational waves and constitutes the reference resonant cavity for the stabilisation of the laser frequency.

The central part of the OB hosts the Inertial Sensor head containing the proof mass, which defines the reference point for the measurement of the distance variation between the S/C by means of the laser interferometers.

The photodiodes for the detection of the signals produced by the interferometer, the resonant cavity, the beat of the two local lasers, the laser amplitude variation, and the CCD for the initial acquisition of the incoming laser beam are also accommodated on the OB.

The general requirements applicable to the OB are:

- maximisation of the dimensional stability of the optical assembly and minimisation of the thermal power dissipated on the OB so that:
- the stability frequency of the laser locked to the reference cavity is maximised (Pre-phase A target $\delta\nu \leq 30$ Hz/$\sqrt{\text{Hz}}$ in the frequency range from 10^{-3} Hz to 10^{-1} Hz [1];
- the differential variation of the optical path length (OPL) between the local and in the incoming laser beams and between the two local laser beams do not exceed 5 pm/$\sqrt{\text{Hz}}$ in the frequency range from 10^{-3} Hz to 10^{-1} Hz [1];
- maximisation of the power transmitted to the other satellites and minimisation of the wavefront error (WFE) of the outgoing beam (overall allocation = 53 nm rms) and of the incoming beam (overall allocation = 106 nm rms);
- minimisation of the straylight level on:
- the photodiode for the detection of the interferometer signal, in order not to spoil the heterodyne efficiency;
- the CCD for the initial acquisition of the incoming laser beam, to allow, if possible, the execution of this operation without blocking the local laser beam (and thus its transmission to the other S/C's).

More specific requirements applicable to the single elements of the OB are provided and discussed in the following sections, together with the detailed description of the OB layout, optical design, mechanical design and budgets.

7.1.3.1 Optical Bench layout

The final layout of the OB is shown in Figure 7.1-14.

The linearly polarised light generated by the active laser source is routed via a polarisation maintaining mono-mode optical fiber (fiber 1) to the OB, where a motorised positioner allows to adjust its in-line and lateral displacements. The fiber is suitably rotated about its axis, so that the outgoing beam is nominally linearly polarised in a plane perpendicular to the OB (S polarisation). After being collimated to a size that matches the 60x magnification of the telescope, the beam arrives the at the polarising beamsplitter ps1, which deviates 99.5% of the power outside the bench, towards the telescope, where it arrives with

circular polarisation. The remaining portion (0.5%) leaks through the ps1 and is squeezed by the beam compressor bc1 to match the active area of the quadrant photodiode qp1, the sensor that detects the beat signal between the local beam and the incoming beam from the remote S/C. The latter is collected by the telescope and sent on the OB where it is partially deviated (5%) by the beamsplitter s2 towards the CCD utilised for the initial detection of the remote beam (the polarising beamplitter in front of this sensor reduces partially the - unpolarised - star light and scattered straylight). The remaining part bounces off the proof mass and is routed by ps1 towards qp1, where it overlaps the local laser beam. The polarisation of the outgoing and incoming laser beam on the OB and their selective routing through the polarising beamsplitters is shown in Figure 7.1-15.

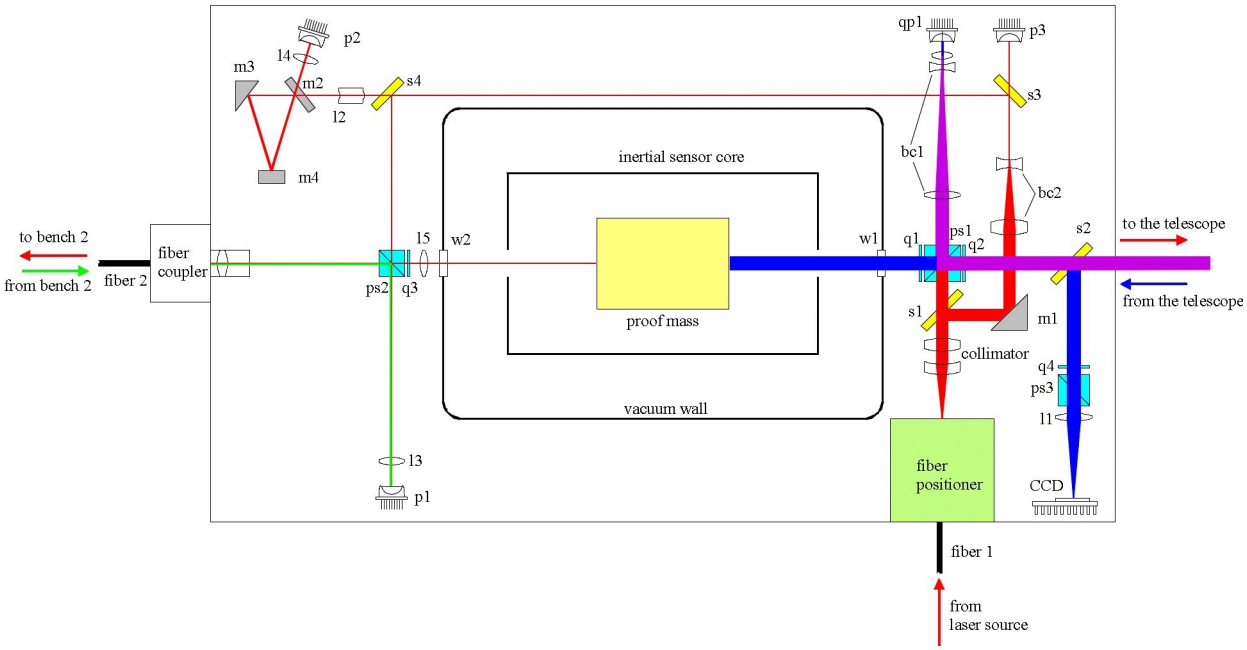

Figure 7.1-14 - Optical Bench layout

Between the collimator and ps1, a small portion of power (0.25%) is separated from the main beam by the beamsplitter s1 (the beamsplitter s2 is not utilised for this purpose to avoid possible backreflections on the CCD from the following optics), is passed through the beam compressor bc2 and is separated in two parts by the beamspitter s3. The beam crossing s3 is intercepted by the photodiode p3 that provides the signal for the stabilisation of the laser power. The beam reflected by s3 towards the rear part of the OB is in turn divided in two parts by the beamsplitter s4. One part is focused in the reference optical cavity constituted by the three mirrors m2, m3, m4, and then reaches the photodiode p2 that provides the signal for the stabilisation of the laser frequency. The other part is mostly reflected (99%) towards the back of the proof mass by the polarising beamsplitter ps2, while the remaining 1% leaks through this element and goes to the photodiode p1. The beam reflected off the back of the proof mass is focused, with polarisation P, in the optical fiber (fiber 2) that brings it to the second OB of the S/C, where it comes out with polarisation S thanks to a 90° twist of the fiber. In turn, the beam of the local laser that feeds the OB 2 comes through fiber 2 on OB 1 and is deflected almost completely by ps2 on the photodiode p1 that detects the beat signal of the two local lasers. This signal is utilised for phase locking the two lasers and to detect the motion of the proof masse relative to the OB (to be removed from the interferometric signal between the local and the remote laser).

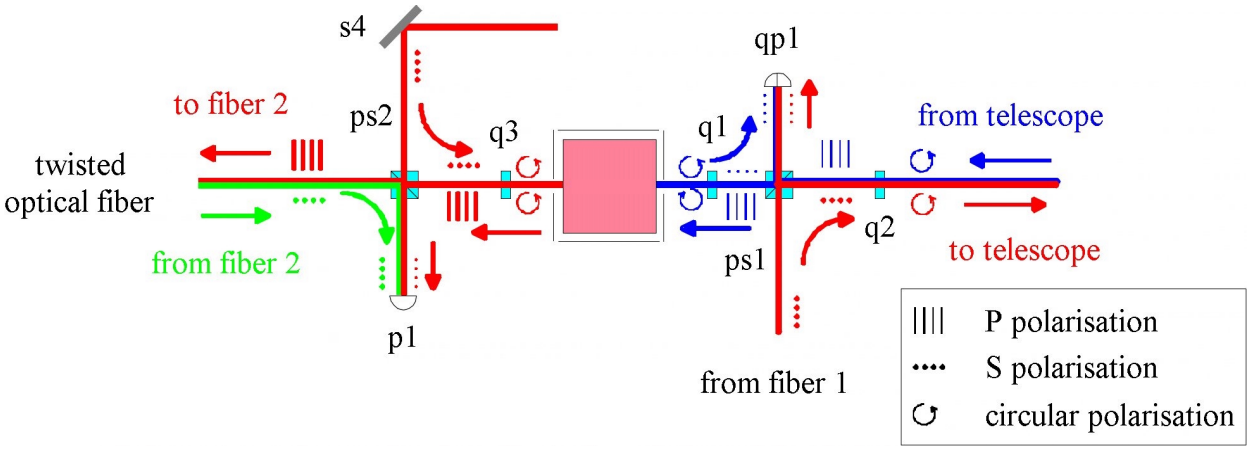

Figure 7.1-15 - Polarisation of the laser beams on the optical bench

The principal characteristics of the optical elements of the OB are summarised in Table 7.1-3. More details about the lenses are provided in section 7.1.3.2. The reflectivity of the beamsplitters s1, s3, s4 ps2 has been chosen so to:

- provide a minimum power of 1 mW to the photodiode p3, as required for the laser amplitude stabilisation;
- provide a minimum power of 0.5 mW to the reference cavity as required for the laser frequency stabilisation;
- limit to a maximum of 100 µW the power bounced off the back of the proof mass [1];
- provide a sufficient power to the photodiode p1;
- minimise the power subtracted to the main beam.

Table 7.1-3 - Main features of the optical elements of the Optical Bench

Element	Main features
Lenses	Material: Fused Silica (n = 1.4496, dn/dT = $9.6 \cdot 10^{-6}$ K^{-1}, CTE = $5.2 \cdot 10^{-7}$ K^{-1}, absorptance = $5 \cdot 10^{-4}$ m^{-1})
Beamsplitter (s1, s2, s3, s4)	Material: Fused Silica Thickness: 3 mm Reflectivity: 0.25% (s1), 5% (s2), 40% (s3), 15% (s4)
Polarising beamsplitter (ps1, ps2, ps3)	Material: Fused Silica Thickness: 15 mm (ps1), 10 mm (ps2), 10 mm (ps3) Reflection & Transmission efficiency: R_S = 99.5% T_P = 95% (ps1), R_S = 99% T_P = 90% (ps2), R_S = 99.5% T_P = 90% (ps3)

Quarter waveplate (q1, q2, q3, q4)	Material: Crystal Quartz (n_o = 1.5341, n_e = 1.5428, dn/dT = $5 \cdot 10^{-6}$ K^{-1}, CTE = $13.2 \cdot 10^{-6}$ K^{-1}) Thickness: 1 mm Retardation tolerance: $\lambda/100$ ($\pm 1.8°$)
Mirror (m1, m2, m3, m4)	Material: Fused Silica (m2), ULE™ (m1, m3, m4) Thickness: 3 mm (m2), 4 mm (m4), 15 mm side length (m1), 10 mm side length (m3) Reflectivity: 99.96% (m1), 99.995% (m2), 99.792% (m3), 99.792% (m4)
Window (*) (w1, w2)	Material: Fused Silica Thickness: 3 mm (sufficient to withstand a 1 bar pressure difference)
Optical fibers (fiber 1, 2)	Core material: Fused Silica Mode field diameter: 8.6 μm Numerical Aperture: 0.12 Length: ~1 m Attenuation 3 dB/km Polarisation extinction ratio: 35 dB (for 1° misalignment about the fiber axis) Minimum bend radius: 12.5 mm

(*) The windows are mounted on the walls of the vacuum vessel of the Inertial Sensor

7.1.3.2 Optical Design

The design of all the OB lenses has been performed using the Code V ray tracing software.

Collimator

The collimator is a two-lens system designed according to the following requirements:

- produce, in combination with the 60× telescope, a transmitted laser beam with a waist close to the telescope primary mirror having a radius ***r* = 133.8 mm** (= 0.446×telescope diameter), so to maximise the transmitted power [1];
- minimisation of the WFE of the outgoing beam.

The laser beam transmission path is shown in Figure 7.1-16. At the telescope output, the WFE caused by the optical aberrations of collimator + telescope is **λ/330 rms** (computed considering the gaussian distribution of the energy in the beam). The WFE and the tilt of the outgoing beam can be adjusted by small longitudinal (δ_L) and transversal (δ_T) translations of the fiber tip by means of the fiber positioner:

$\delta_L = +10$ μm WFE = $\lambda/100$ rms , $\delta_T = \pm 10$ μm tilt = ±6 μrad (linear behaviour)

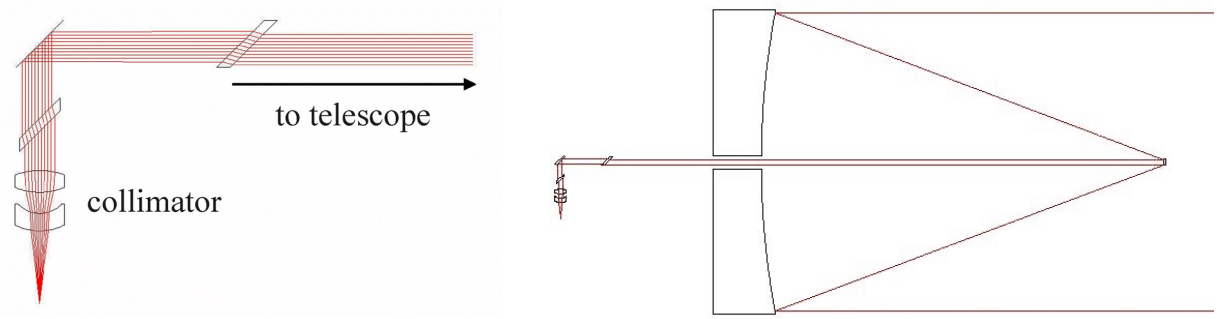

Figure 7.1-16 – Laser beam transmission path

Beam compressor bc1

The beam compressor bc1 is a three-lens afocal system with 10× magnification designed to:

- overlap the diameter of the incoming beam and of the local beam on qp1, with a diameter that matches the active area of this sensor ($\varnothing_{active}$ = 0.5 mm);
- minimise the WFE of the received and local beams at qp1;
- place the exit pupil of the receiving optical system as close as possible to qp1.

The last requirement is related to the compensation of the Point Ahead Angle PAA that separates the directions of the transmitted beams by an angle which has a maximum variation amplitude = ±5.7 μrad in the out-of-plane direction. The selected solution to cope with this effect is to transmit on-axis the outgoing beam and to receive the incoming beam off-axis by an amount = PAA; it has been preferred to the complementary option (outgoing beam transmitted off-axis) because of its lower impact on the OB. Since the two beams overlapping on qp1 must be kept parallel within 1.8 μrad in order not to blur the phase measurement, the off-axis angle of the incoming beam must be compensated by a counter-rotation β of the proof mass: for PAA = **±5.7** μrad **β = ±177** μrad. Under these conditions, the receiving optical system must minimise the incoming beam lateral shift at qp1 under the variation of its off-axis angle.

The path of the incoming beam from the telescope to qp1 and of the local beam from the fiber output to the same photodiode is shown in Figure 7.1-17. The incoming beam has a top-hat profile on qp1 with a diameter = **0.44 mm**, when it is received on-axis, and = **0.48 mm** with **22 μm** shift from the photodiode centre, when it is received off-axis by PAA = ±5.7 μrad and the proof mass is tilted by ±177 μrad. So, also in this case, the remote beam is almost completely inside the active area of qp1, with just ~1.2% of the power falling out of this sensor. The local beam has instead a gaussian profile with diameter at $1/e^2$ intensity = 0.395 mm (see Figure 7.1-17).

The WFE at qp1 is **λ/40 rms** for the remote laser beam and **λ/23 rms** for the local laser beam (computed considering the gaussian distribution of the energy in the beam).

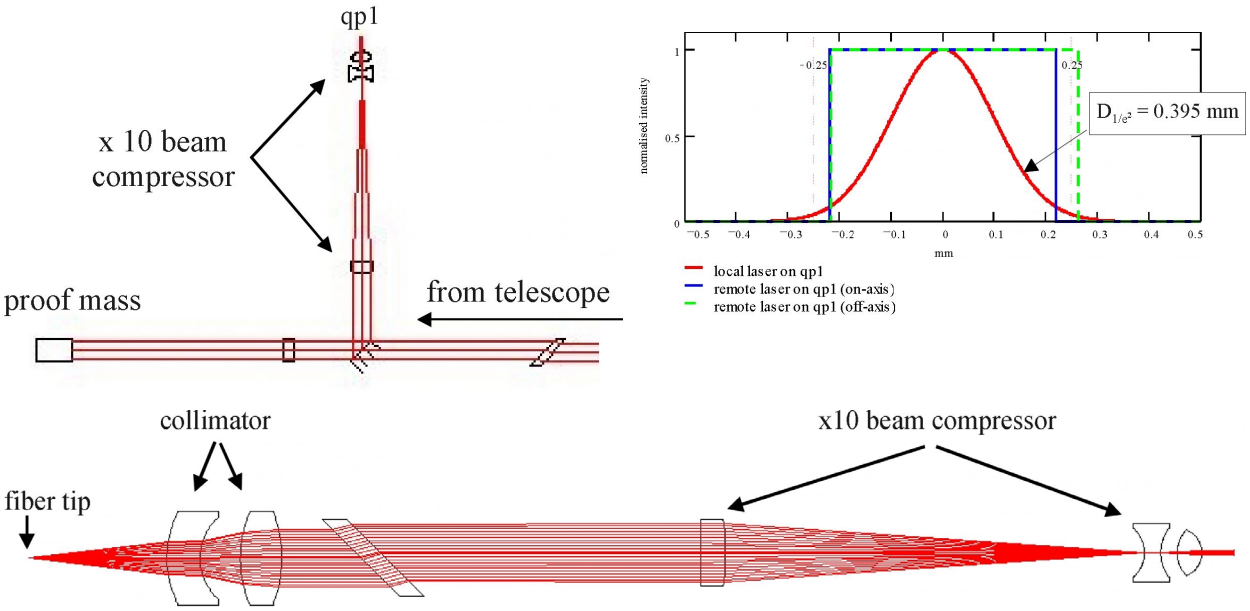

Figure 7.1-17 - Incoming beam and local beam path to qp1 and energy distribution on this sensor

Path to the Acquisition Detector (CCD)

The CCD02-06 deep depletion CCD manufactured by EEV has been identified as reference sensor for the initial acquisition of the remote laser beam. Its main features are:

- 385×578 22 µm square pixels;
- sensitive area = 12.7×8.5 mm;
- spectral range 420 – 1080 nm (quantum efficiency ≈ 3% @ 1064 nm);
- dark current = 60,000 e/pixel at room temperature;
- radiation tolerant up to 10 krad.

It has been preferred to InGaAs photodiodes or Silicon avalanche photodiodes because it enables a larger signal-to-noise ratio, and to other kind of CCDs because of its better sensitivity to the 1064 nm wavelength and/or its simpler accommodation on the OB.

The lens l1, which focuses the received beam on this CCD, has been designed in order to have the image spread over the extension of four pixels (the minimum required for the image centroid computation with a sub-pixel resolution). The path of the received laser beam from the telescope to the CCD is shown in Figure 7.1-18, together with the Point Spread Function on the CCD of the optical system telescope + l1: **90%** of the energy falls inside a **∅ = 42 µm** circle. When the incoming beam is received off-axis by a PAA = ±5.7 µrad, the image shift on the CCD is **±10.6 µm**, while the energy distribution doesn't change significantly with respect to the on-axis case.

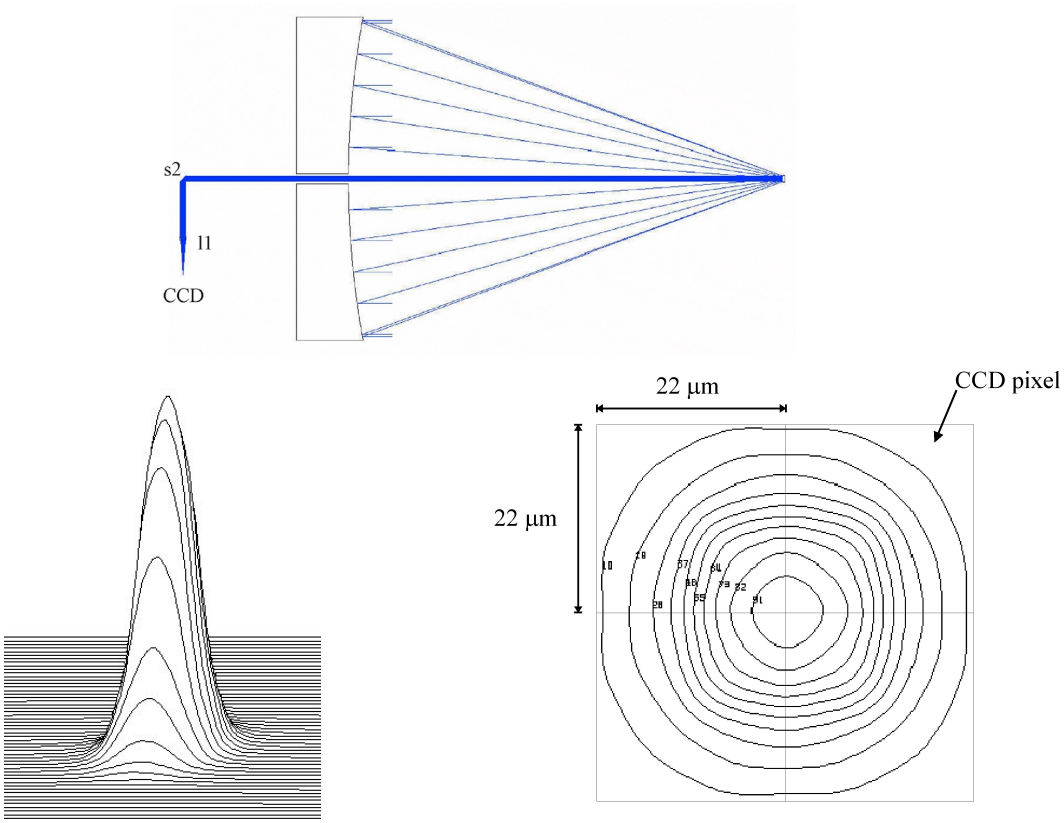

Figure 7.1-18 - Laser beam receiving path to the CCD and energy distribution on this sensor

Laser routing to the back of the bench and coupling to the rear fiber (fiber 2)

After being split from the main beam by s1, the portion of the laser routed to the back of the bench is passed through the two-lens afocal beam compressor bc2. The beam compressor is designed to reduce the full-power diameter of the laser from 10.3 mm to 2.8 mm, which allows the use of smaller size optical components. The portion of the laser that bounces off the back of the proof mass passes through the lens l5, designed to focus the beam on the proof mass surface (see Figure 7.1-19). This minimises the beam tilt at the fiber coupler when the proof mass is tilted by up to 177 μrad to compensate the PAA.

The fiber coupler lens is designed in order to match the beam waist to the fiber Mode Field Diameter (∅ = 8.6 μm). The resulting coupling efficiency into the fiber is **0.705** (computed by using a step-index model of the fiber, with fused silica core and core-cladding δ-index corresponding to numerical aperture 0.12). When the proof mass is tilted by ±177 μrad the coupling efficiency changes by **0.014%**.

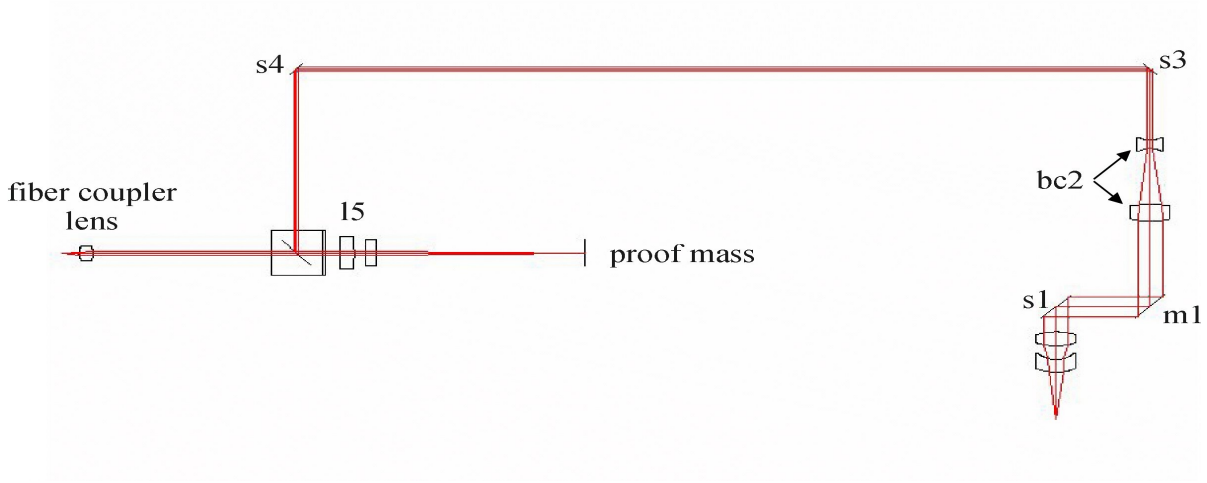

Figure 7.1-19 - Path to the backside of the proof mass and to the rear fiber

Coupling to the photodiode p1

Lens l3 is designed to match the full power diameter of the two local lasers (the laser of the OB 1 and the laser coming from the OB 2 through the fiber 2) overlapping on the photodiode p1 to the sensitive area of this sensor ($\varnothing_{active}$ = 0.5 mm). The path of these two lasers to p1 is shown in Figure 7.1-20, together with the energy distribution on this sensor. The full-power diameter of the two lasers on p1 is D_1 = 0.487 mm and D_2 = 0.109 mm, thus **41%** of laser 1 power overlaps laser 2 power. This overlapping is not optimal, but is still acceptable due to the relatively large amount of power contained the two beams.

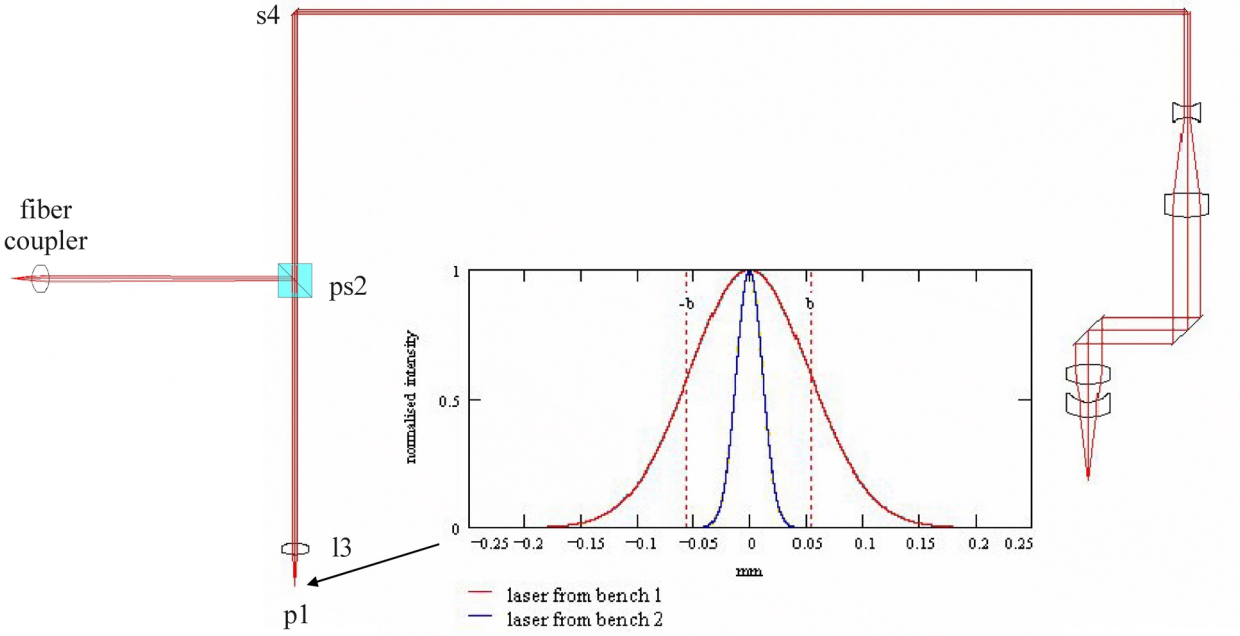

Figure 7.1-20 - Path to photodiode p1 and energy distribution of the two local lasers on p1

Reference cavity mode matching

The reference resonant cavity has been designed with the features listed in Table 7.1-4, according to the needs coming from the laser frequency stabilisation. The lens l2 is a toroidal lens designed so to match the laser to the cavity mode. This is achieved by placing the beam waist between the two flat mirrors with radii w_x = **173 µm** (in plane) and w_y = **196 µm** (out of plane). The lens l4 has been then designed so that full-power diameter of the beam coming out from the cavity at the photodiode p2 is smaller than the sensitive area of this sensor ($\varnothing_{active}$ = 0.5 mm): D_x = **0.34 mm** and D_y = **0.41 mm**. The path of the laser beam in the reference cavity is shown in Figure 7.1-21.

Table 7.1-4 - Main features of the reference cavity

- spherical mirror at the cavity vertex with curvature *r* = **30 cm** and reflectivity R_4 = **99.792%**
- 2 flat mirrors with R_2 = **99.995%** (input mirror) and R_3 = **99.792** (other mirror)
- overall optical length : **77.72 mm**
- finesse : **1490** (requirement ≈ 1500)
- linewidth : **2.6 MHz**
- free-spectral-range : **3.9 GHz**
- frequency difference between fundamental and higher order modes > 5 MHz. For the current design the two modes which are nearer to the fundamental one are (the modulation frequency ν_{EOM} has been assumed equal to 200 MHz):

- $TEM_{00}(q) - TEM_{24}(q+1)$ = **6 MHz**
- $TEM_{00}(q) - TEM_{52}(q+1) - \nu_{EOM}$ = **5.5 MHz**

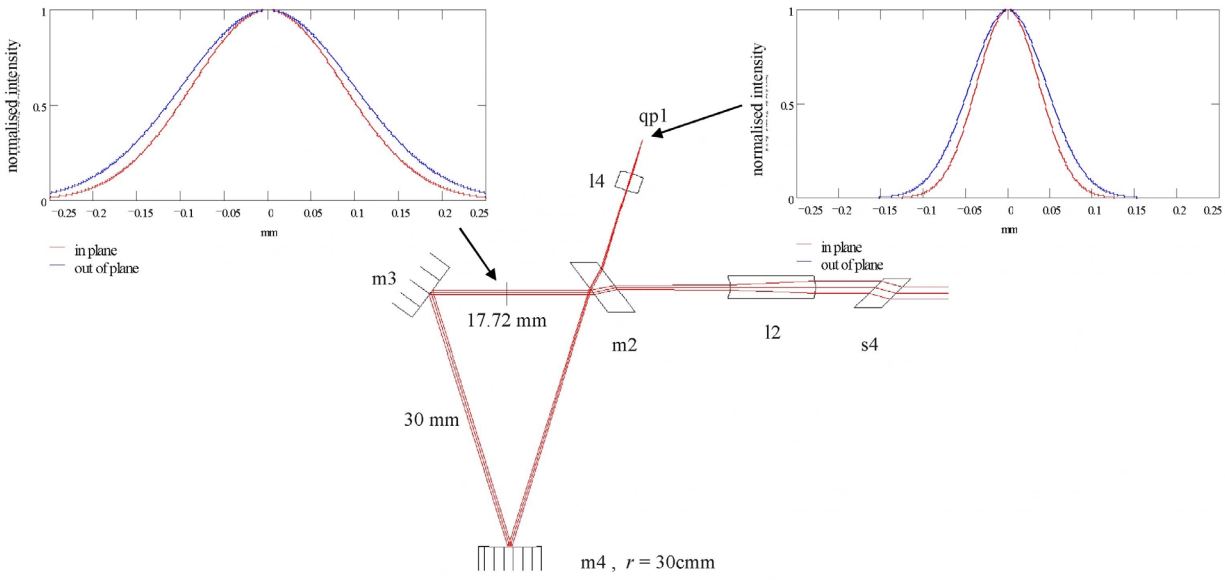

Figure 7.1-21 - Reference cavity and energy distribution at the waist position and on p2.

Path to photodiode p3

Because of the large active area of photodiode p3, no additional lens after bc2 is required to match the beam diameter to this sensor. The full power diameter of the laser beam produced by the beam compressor bc2 on p3 is D = **2 mm** (see Figure 7.1-22).

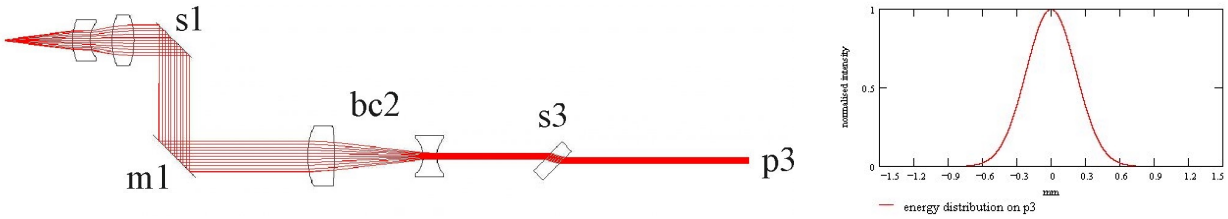

Figure 7.1-22 - Path to photodiode p3 and energy distribution of the local laser on this photodiode

The parameters of all lenses included in the OB are listed in Table 7.1-5.

Figure 7.1-23 provides the relationship between the polishing and figuring quality of the surfaces of the OB optical elements along the transmission path (collimator, s1, ps1, q2, s2) and the beam WFE at the OB output. The surface quality is expresses as wavelength fraction at λ = 1064 nm (the laser wavelength) and at λ = 633 nm (the usual wavelength at which the optical surface quality is specified). A polishing/figuring quality = $\lambda/40$ polishing and figuring @ 633 nm is a target achievable with the current techniques (feedback from optical manufacturers). This corresponds to a WFE of the outgoing beam at the OB output ≈ **$\lambda/26$** @ 1064 nm (this clearly dominates the WFE of the transmitted beam, since the optical aberrations of the collimator + telescope system give a WFE = $\lambda/330$ rms).

The same optical quality contributes to a WFE ≈ **$\lambda/24$** @ 1064 nm of the received beam at qp1.

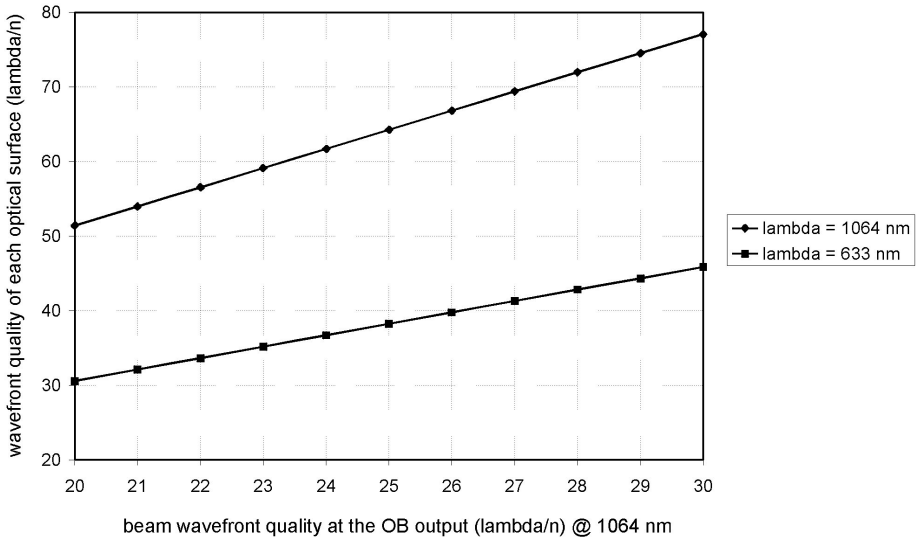

Figure 7.1-23 – Relationship between optical quality and WFE at the OB output

Table 7.1-5: Optical Bench Lens Parameters

Lens	Central Thickness (mm)	Curvature Radii (mm)	Conic Constant	4^{th} Order Aspherics	6^{th} Order Aspherics
1. (coll. 1)	4	R1 = 12.56 R2 = 6.74	- -	- -	- -
2. (coll. 2)	5	R1 = 14.84 R2 = -15.55	C1 =0.11876 C2 =-0.66528	A1 =$0.584\cdot10^{-5}$ A2 =$-0.224\cdot10^{-4}$	A1 =$-0.669\cdot10^{-6}$ A2 = $0.531\cdot10^{-6}$
3. (bc1 1)	3	R1 = 30.01 R2 = -106.68	- -	A1 =$-0.404\cdot10^{-4}$ A2 =$-0.398\cdot10^{-3}$	A1 =$-0.241\cdot10^{-4}$ A2 = $-0.146\cdot10^{-4}$
4. (bc1 2)	2	R1 = -4.00 R2 = 5.00	- -	- -	- -
5. (bc1 3)	3	R1 = 4.00 R2 = -3.00	- -	- -	- -
6. (bc2 1)	6	R1 = 17.12 R2 = -56.74	C1 =-1.92884 C2 =20.11013	A1 =$-0.433\cdot10^{-4}$ A2 =$-0.938\cdot10^{-4}$	A1 =$0.213\cdot10^{-5}$ A2 = $0.281\cdot10^{-5}$
7. (bc2 2)	3	R1 = -5.55 R2 = 5.78	- -	- -	- -
8. (l1)	3	R1 = -18.85 R2 = 83.72	- -	- -	- -
9. (l2)	9.5	R1x = -4.88 R1y = -4.92 R2x = -2.00	- -	- -	- -
10. (l3)	3	R1 = 9.00 R2 = -10.50	- -	- -	- -
11. (l4)	2	R1 = 7.00 R2 = -7.00	- -	- -	- -
12. (l5)	4	R1 = 91.19 R2 = -40.94	- -	- -	- -
13. (fiber coupler)	4	R1 = 5.04 R2 = -4.59	C1 =-4.81466	- -	- -

7.1.3.3 Optical Elements Mounting

All the optical elements are mounted on top of the ULE™ baseplate (see Figure 7.1-30); a **7.5 mm** offset between the plane where the laser beams lies and the top of the optical bench ensures no interference between the laser and the bench (at its maximum expansion, all the power of the laser beam is contained in a r = 5.15 mm cylindrical envelope). Before the beam compressors, the full-power diameter of the laser beam is 10.3 mm, so a larger clear aperture is required for s1, s2, ps1, q2, m1, and for some lenses of the collimator, bc1, bc2. The selected physical size for these optical elements is 15 mm. After the beam compressors, the full-power diameter of the laser beam is $\leq$ 2.8 mm. Thus smaller optical elements can be used. In particular, a physical size of 10 mm has been selected for the elements after bc2.

For the maximum dimensional stability, the optical elements must be bonded directly to the OB surface without using mechanical fixations. For this purpose, the hydroxy-catalysis bonding technique, originally developed at the Stanford University for the GP-B programme. This technique requires a good polishing ($\sim\lambda/10$) of the surfaces to be bonded, like for the optical contacting. Chemical elements like sodium silicate or sodium or potassium hydroxide are then applied to the surfaces to catalyse the bonding, that requires a curing time of the order of one month. The fact that, contrarily to the optical contacting, the bonding is not "instantaneous" allows the repositioning of the pieces after they are placed on the bench: this is an essential feature to achieve a fine alignment. The resulting bond is characterised by a high strength, compared to optical contacting: shear strength between **11 MPa** and **28 MPa**, depending on the bonding material. Tests are in progress at the University of Glasgow to verify the performance of this bonding technique with the optical materials planned to be used on the LISA OB, and its behaviour when the bonded elements are submitted to vibrations and large thermal gradients. An example of two optical elements of dissimilar material joined with the hydroxy-catalysis bonding is shown in Figure 7.1-24.

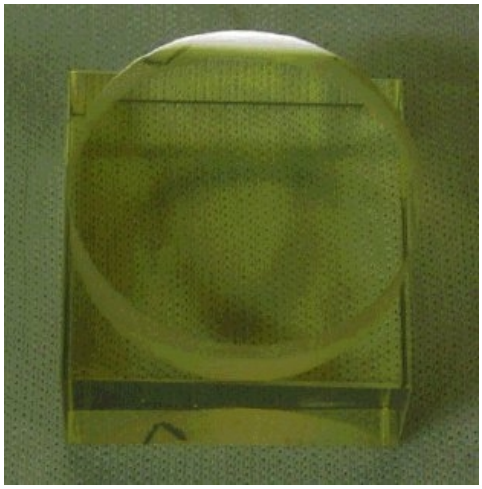

Figure 7.1-24 - Fused Silica element joined to a Zerodur® base with the hydroxy-catalysis bonding at the University of Glasgow

For a direct bonding of the optical elements to the OB they must have a contact surface area of $\approx$ 1 cm^2, also to achieve a good polishing of the surfaces to be bonded. This is straightforward for the polarising beamsplitter and for the mirrors. For the lenses this can be achieved by producing their surfaces in parallelepiped Fused Silica blocks with a thickness of some millimetres area (see Figure 7.1-25). The quarter waveplate, that have a thickness of about 1 mm, can be bonded to the side of the polarising

beamsplitter (they are always close to these elements). Using a spacer with a central hole it is possible to preserve the AR coating on the mutually facing sides of the polarising beamsplitter and the waveplate (see Figure 7.1-26). If needed, the spacer can be manufactured with a wedge angle of few degrees in order to tilt the quarter waveplate so to avoid backreflections on the detectors from these elements. The wedge cannot be included in the polarising beamsplitter itself, because this would increase the outgoing wavefront error. The required parallelism and perpendicularity for each of the polarising beamsplitter, beamsplitters and waveplates surfaces is **≤ 0.5 arcsec**

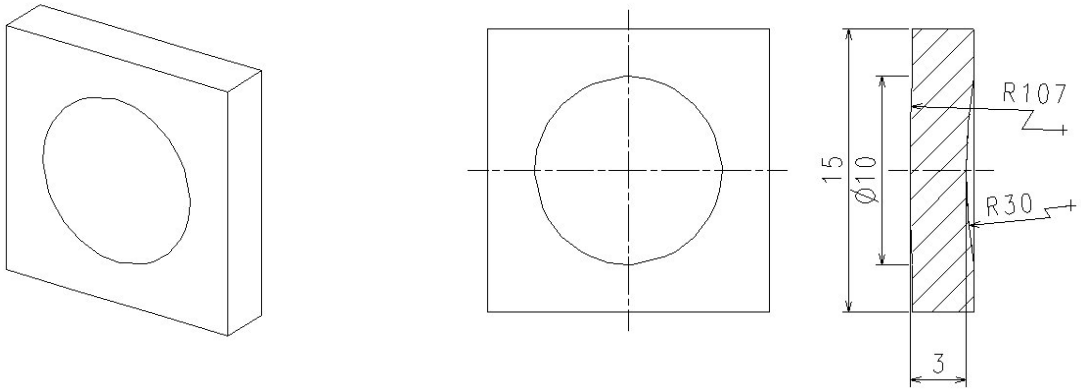

Figure 7.1-25 - Example of a lens (bc2 1) produced in a parallelepiped Fused Silica block

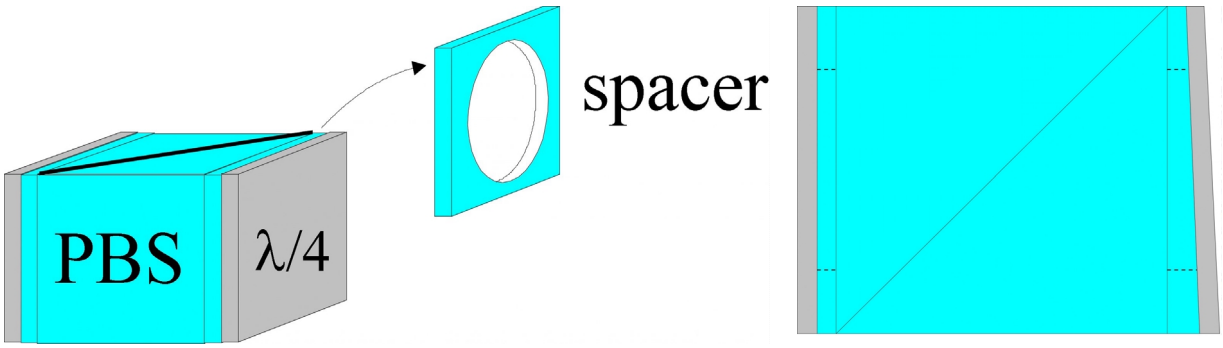

Figure 7.1-26 - Bonding of a quarter waveplate on the polarising beamsplitter side through a spacer

The other elements (detectors with proximity electronics, fiber positioner and fiber coupler) are planned to be bonded using a glass-metal glue (shear strength ≈ **14 MPa**, tensile strength ≈ **24 MPa** for a typical glue), to avoid additional holes in the ULE™ for the passage of bolts that can increase the stress in the material under the launch loads and can interfere with the mechanical interface with the OB support structure. Estimated maximum shear and normal tension on the OB elements due to launch loads are about **2.9 MPa** and **1.6 MPa** respectively. The relevant safety factors are hence **4.7** and **15**.

A possible packaging of the photodiode qp1 is shown in Figure 14. The sensor is enclosed with its proximity electronics (transimpedence amplifier) and its connectors in a metallic housing that provides the radiation shielding. The box protrudes in front of the sensor to form a baffle that partially shields the straylight. The focusing lenses (in this case the lenses 2 and 3 of bc1), for which the stability is less

critical are integrated in the baffle. The overall metallic housing is provided with a flat base that is bonded to OB surface. A similar mounting is adopted for the CCD (see Figure 7.1-28).

The fiber coupler in the rear part of the bench is also configured to permit its gluing on the OB surface (see Figure 7.1-29). It includes the matching lens and focus-tilt adjustment screws to fine tuning the fiber alignment after the OB's have been integrated on the S/C and the fiber is connected to the bench pairs. The coupler can be derived from commercial devices like e.g. the pigtail-style laser to fiber couplers from OZ Optics or from Optics For Research.

Engineering drawings of the OB showing the optical elements, the detectors, the inertial sensor and the support structure are shown in Figure 7.1-30.

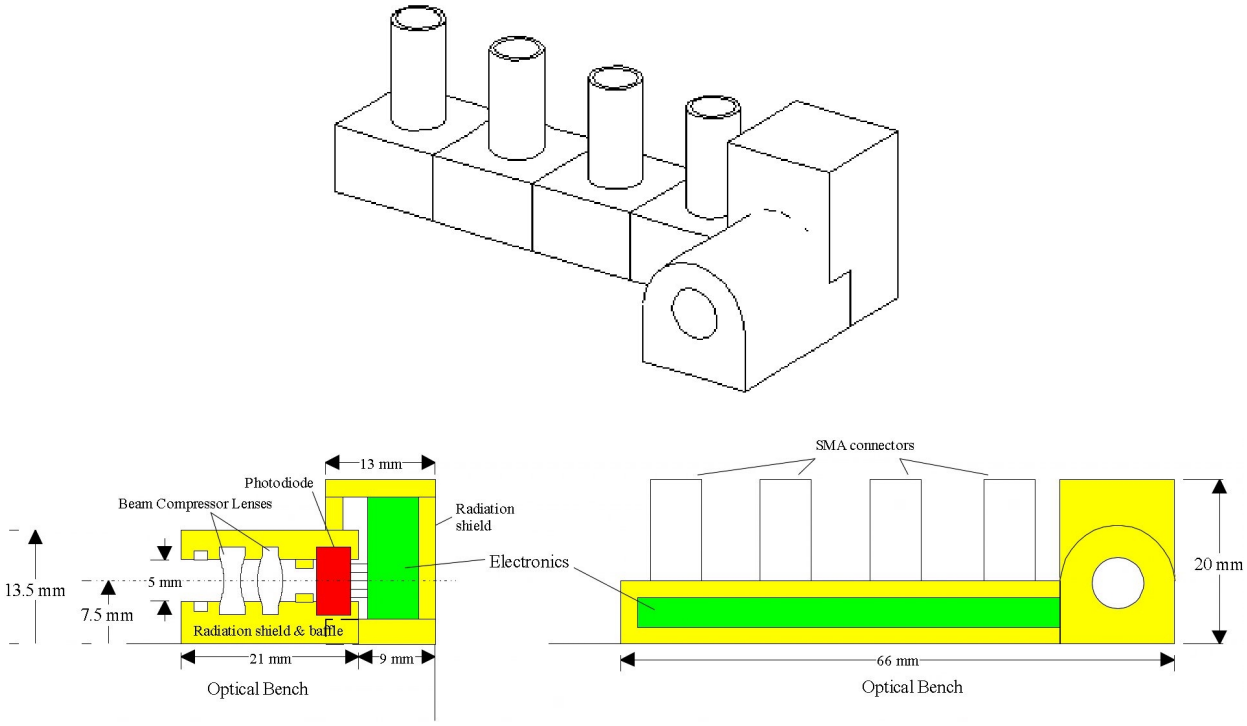

Figure 7.1-27 - The quadrant photodiode (qp1) assembly

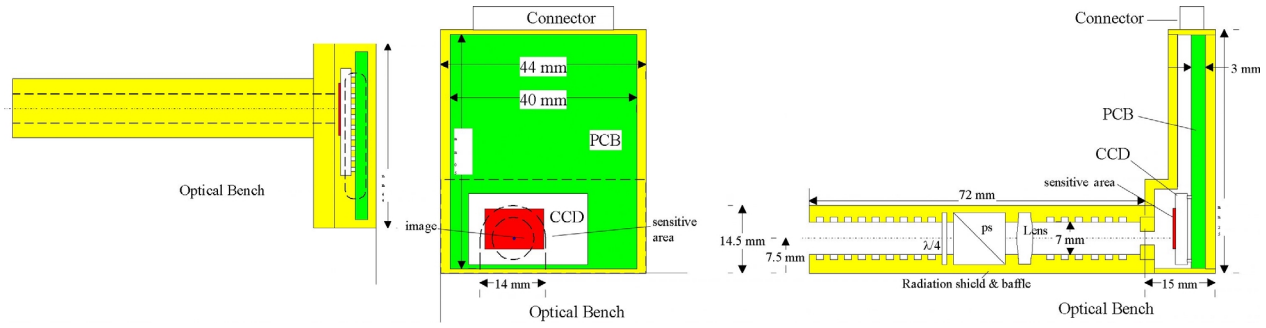

Figure 7.1-28 - The CCD assembly

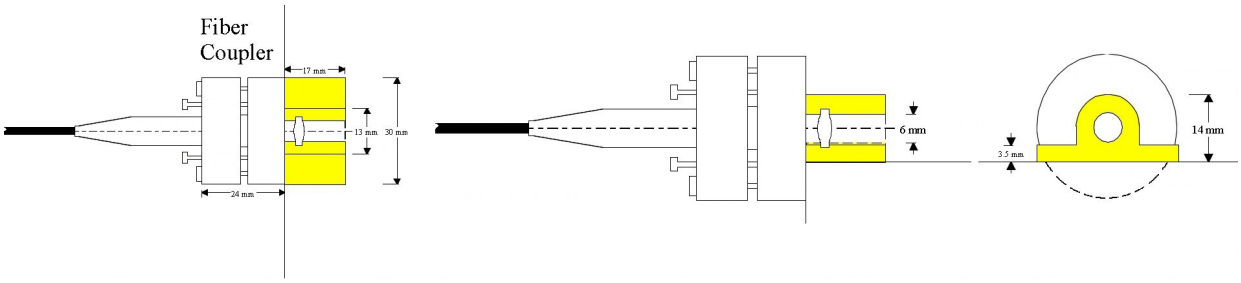

Figure 7.1-29 - The fiber coupler configuration

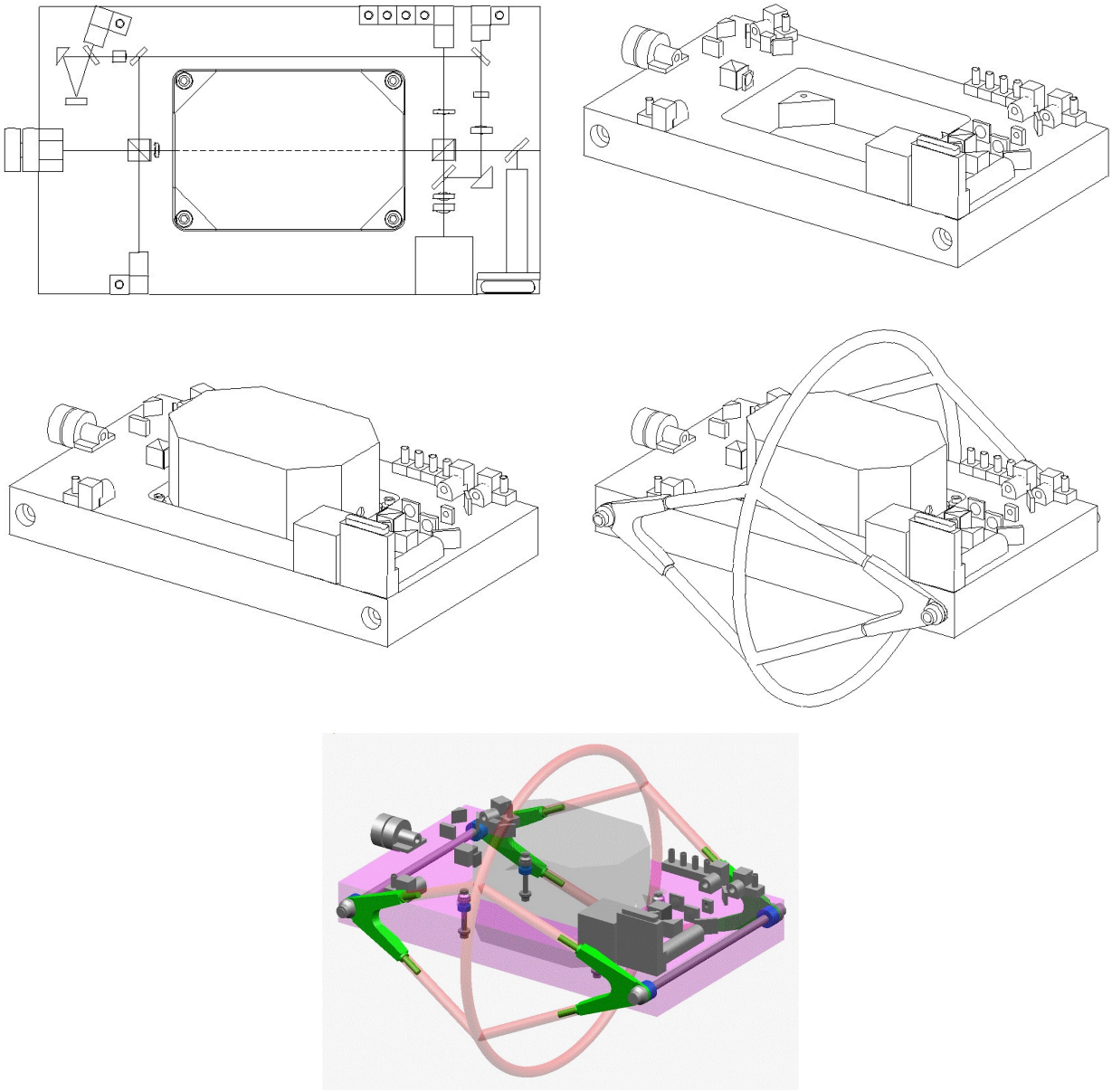

Figure 7.1-30 - Top and perspective views of the OB
showing the optics and detectors (top) plus the Inertial Sensor (middle left)
plus the support structure (middle right and bottom)

A first tolerance analysis has been performed in order to assess the requirements for the initial alignment of the various elements during the OB integration and the tolerable displacements during launch.

The parameters checked for are:

- the wavefront error (WFE) of the outgoing beam at the telescope output: maximum WFE degradation = $\lambda/100$ rms considered for the tolerance analysis (to get a negligible contribution of the optics misalignment w.r.t. optical surface polishing and figuring error);
- the variation of the position δp and of the size δs of the laser beam waist in the reference cavity: maximum δp = 10% (w.r.t. to the position of the input mirror) and maximum δs = 10% considered for the tolerance analysis.

The most critical elements are the lenses of the collimator and of the beam compressor. Their tolerances, in terms of maximum allowed shift and tilt w.r.t. the nominal design position compatible with the above criteria, is summarised in Table 7.1-6.

Table 7.1-6 - Alignment tolerances

Element	Maximum allowed shift (Δ) and tilt (Φ) w.r.t. the nominal position			
	WFE = $\lambda/100$ rms (*)		δp = 10% , δs = 10%	
Collimator lenses	Δ = 5 μm	Φ = 3.5 mrad	Δ = 1 μm	Φ = 1 mrad
Beam compressor 2 lenses	-		Δ = 1 μm	Φ = 1 mrad

(*) computed considering a gaussian distribution of the light in the beam

From this preliminary tolerance analysis it turns out that the lenses must be mounted with a positioning resolution of the order of 1 μm. This resolution is achievable by means of a μm linear translators (motor driven linear translators with 0.1 μm resolution over 300 mm stroke are available on the market).

The variation of the optical path length (ΔOPL) inside the optical elements mounted on the OB due to residual thermal fluctuations has been investigated, assuming for the thermal fluctuations the value $\Delta T = \mathbf{10^{-5}}$ K/√Hz. The critical elements are those which are crossed only by the received laser beam before the quadrant photodiode qp1 (s2, ps1, q1, q2, w1 impact on detection of the GW signal) and only by the local laser 1 before the photodiode p1 (bc2, ps2, q3, l5, w2 impact of phase locking of local laser 2 to local laser 1). Results are summarised in Table 7.1-7. The contribution to ΔOPL of the variation of the relative distances (0.1 m max.) between the optical elements is negligible because of the very low thermal expansion of the ULE™ baseplate where the elements are mounted (CTE = 10^{-8} /K between 5 and 35 °C).

Under the same thermal stability, the length l of the reference resonant cavity maintains a relative stability $\delta l/l = 10^{-13}/\sqrt{\text{Hz}}$, that corresponds to a laser frequency stability of 30 Hz/√Hz

Table 7.1-7 - Optical path length variations

Element	Material	CTE (1/K)	n	dn/dT (1/K)	Thickness crossed by the light (mm)	ΔOPL (pm/√Hz)
s2	Fused Silica	$5.2\ 10^{-7}$	1.4496	$9.6 \cdot 10^{-6}$	4.3	0.4
ps1					15×1.5	2.3
ps2					10×1.5	1.6
w1					3×2	0.6
w2					3×2	0.6
bc2					9	0.9
l5					4×2	0.8
q1	Crystal Quartz	$13.2\ 10^{-7}$	n_o = 1.5341	$5 \cdot 10^{-6}$	1×2	0.4
q2			n_e = 1.5428		1	0.2
q3					1×2	0.4
ΔOPL(s2 + ps1 + q1 + q2 + w1) = **3.9 pm/√Hz**						
ΔOPL(bc2 + ps2 + q3 + l5 + w2) = **4.3 pm/√Hz**						

7.1.3.4 Straylight Analysis

A preliminary straylight analysis has been performed for:

- the quadrant photodiode qp1 (impact on the gravitational wave signal detection);
- the CCD sensor (impact on the initial acquisition of the remote laser beam).

The two main sources of straylight are:

- the specular backreflection by the surfaces of the optical elements crossed by the laser beam;
- the scattering by the dust particulates which are on surfaces of the optical elements.

The specular backreflection analysis is based on the following assumptions:

- the surfaces of the lenses, polarising beamsplitters, quarter waveplates, optical windows, as well as the mirror and beamsplitter back surfaces, are covered by AR coatings with reflectivity **0.1%**, which is the ensured performance of different available AR coatings, e.g. from CVI, OptoSigma, Balzers (0.05% is also declared achievable). Possible degradation of the coating performances with radiations is TBV;
- the quarter waveplate q2 is tilted by an angle of about 3° (as shown in Figure 7.1-26) to ensure that the backreflected light from q2 doesn't hit qp1 (and the proof mass too).

The scattering analysis is based on the following assumptions:

- a cleanliness level of the optics corresponding to **0.03%** dust coverage areal fraction. This cleanliness level is achievable if the optics are effectively cleaned for the last time about 3 months before the launch and kept from then on, launch included, in a controlled environment equivalent to a cleanroom class 500 [13]; this is a realistic target for the OB, which is protected inside the payload Y-shaped tube;
- Bidirectional Reflectance Distribution Function of the scattered light modelled using the Harvey-Shack approximation:

$$BRDF(\theta) = b\,(100\ |\sin(\theta_i) - \sin(\theta)|\ )^m$$

where θ_i is the incidence angle, θ is the output angle w.r.t. surface normal, b = 0.15 and m = -1.9 (selected according to a 1064 nm wavelength and to a 0.03% of dust coverage). The Total Integrated Scatter results in $\mathbf{1.5 \cdot 10^{-3}}$ for normal incidence.

Straylight on qp1

The main source of backreflection towards qp1 is the polarising beamsplitter ps1 (see Figure 7.1-31 and Table 7.1-8). Note that in case the quarter waveplate q2 were not tilted, it would be the main source of bakreflected light on qp1, with an amount of about 591 µW (due to the backreflection of the outgoing beam on the second surface of q2).

Table 7.1-8 - Straylight by backreflection on qp1

Contributor	Total power on **qp1**	S polarisation	P Polarisation
Polarising Beamsplitter (ps1)	182 nW	24 nW	157 nW
Other optical elements	<1 pW	<1 pW	<1 pW
Total	**182 nW**	24 nW	157 nW

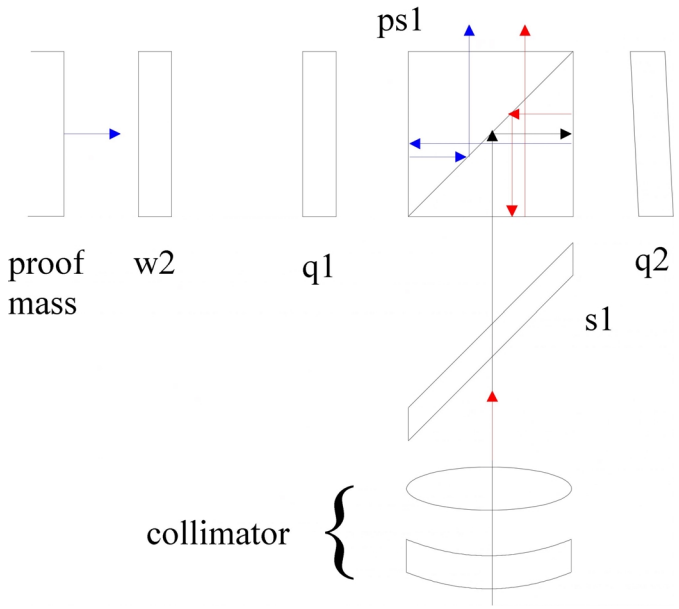

Figure 7.1-31 - Backreflection main paths to qp1 from ps1

The main contribution to the light scattering towards qp1 is instead the residual dust on q2 that intercepts part of the outgoing beam. The energy scattered in the solid angle subtended by the photodetector qp1 at the position of quarter waveplate q2 is ≈ **20 nW**.

Note however that the optical path variation of the straylight generated by the OB elements on qp1 is few picometers for a thermal stability $\Delta T = 10^{-5}$ K/√Hz. In addition, any signal on qp1 produced by the beat of the local laser with this straylight occurs at a different frequency than the beat signal between the local laser and the remote laser. The beat signal of the straylight with the remote laser is instead about 20 dB smaller than the main beat signal and is therefore negligible.

Straylight on the CCD

The main source of backreflection towards the CCD is the beam compressor bc2, and, in particular, the surfaces of the lenses shown in Figure 7.1-32. The total power entering the baffle aperture is 0.14 pW for the first surface of the first lens of bc2, and 290 pW for the second surface of the second lens of bc2. However, no ray reaches the CCD directly or even after a single reflection inside the baffle. Thus, considering any reflection on the internal walls of the baffle further reduces the reflected power by a factor ≈ 100, a negligible level of straylight by backreflection from the OB elements is expected to reach the CCD.

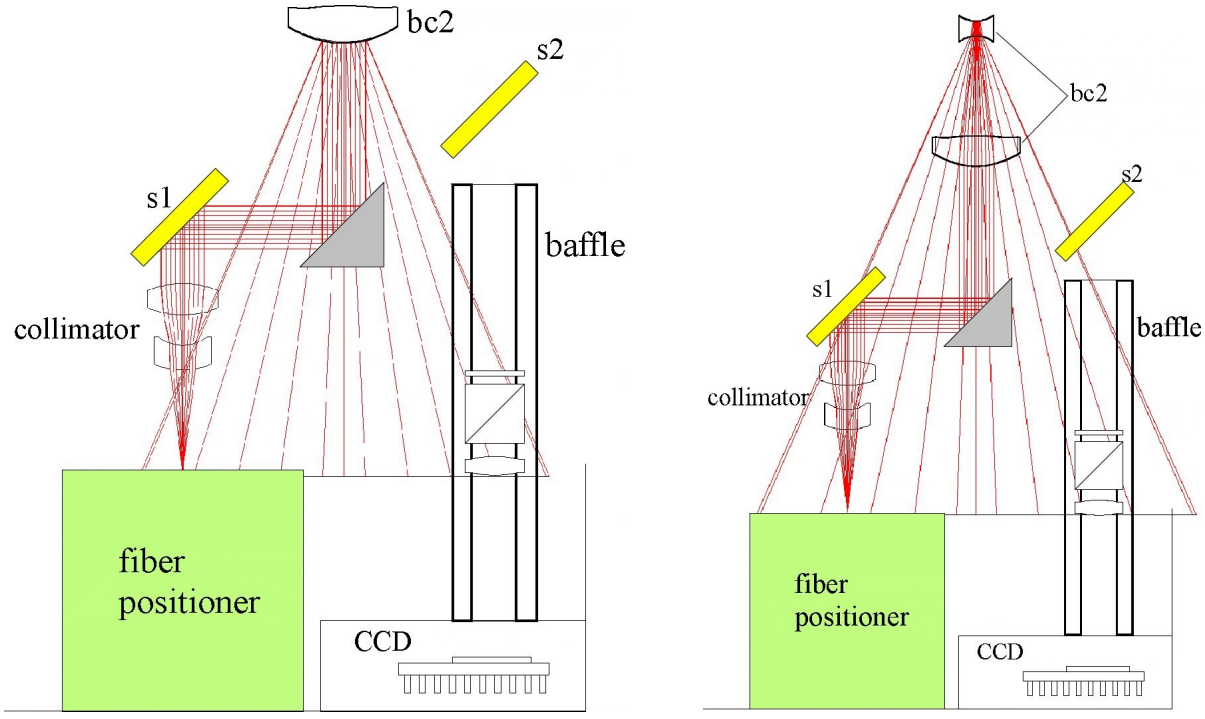

Figure 7.1-32 - Straylight by backreflection on CCD

The main contribution to the light scattering towards the CCD is the residual dust on the surface of the beamsplitter s2 (see Figure 7.1-33). The energy of the outgoing beam scattered in the solid angle Ω subtended by the lens l1is 80 nW. This energy is distributed almost uniformly by the lens l1 over a ∅ = 3.9 mm circle on the CCD (see right side of Figure 7.1-33). Thus, considering a further factor 2 reduction due to the polarising beamsplitter, the energy scattered on each pixel of the CCD is **1.6 pW**.

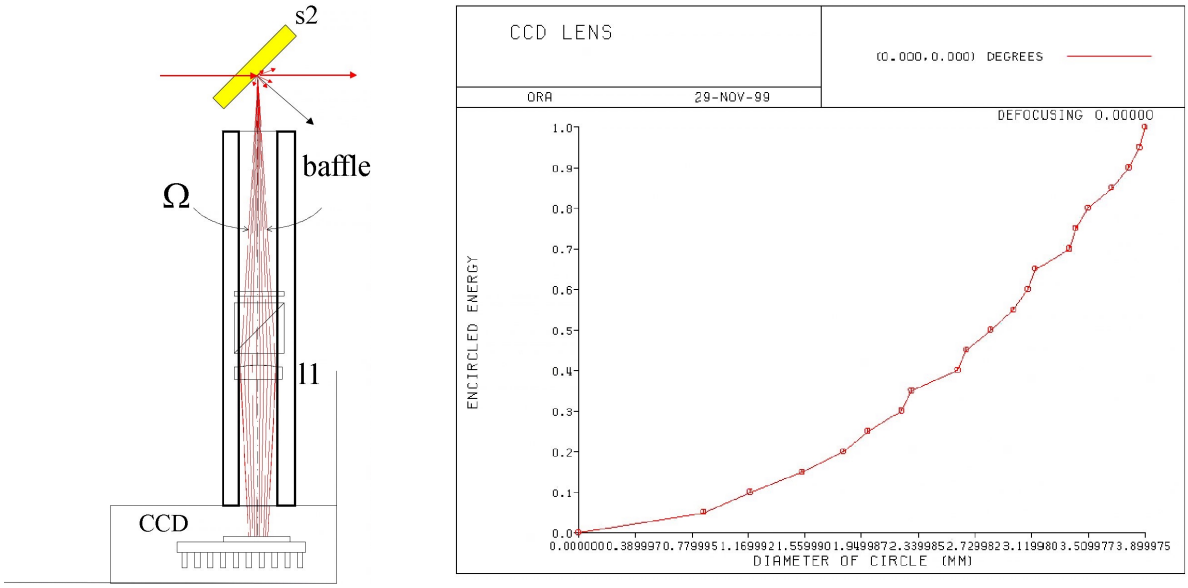

Figure 7.1-33 - Straylight by scattering on CCD

7.1.3.5 Mechanical Design

The ULE™ baseplate of the OB is shown in Figure 7.1-34. Its outer dimensions are 350×200×40 mm. A large cutout (170×120 mm) at the centre of the OB allows the accommodation of the Inertial Sensor head (this interface solution requires that the corners of the sensor vacuum vessel are removed at about 3 cm from the edge). The cutout corners are rounded to reduce the ULE™ stress concentration.

The OB is interfaced to the support structure, made by 8 Pyroceram rods joined to a stiffening ring [1], by two titanium bolts inserted through holes (∅ = 9 mm) lying on the bench middle plane and parallel to the short side (see Figure 7.1-35, and Figure 7.1-36). With this arrangement the entire top surface is available for the optics and detectors accommodation. The bolts are in contact with the ULE™ only at their ends by means of suitable bushes (∅ = 18 mm) made of Delrin (a material more elastic than the titanium and with small thermal conductivity) to partially absorb the launch loads and to increase the thermal cut.

The Inertial Sensor is joined to the OB by four titanium bolts (∅ = 5 mm) with the interposition of thermal washers made of Delrin (see Figure 7.1-35 and Figure 7.1-36). The Inertial Sensor is mounted with an offset of 27.5 mm from the centre of the OB, so to bring the proof mass centre at the level of the laser beam.

Two FEM's of the OB have been produced using the ANSYS v5.3 software. The first one is built by means of 1-D and 2-D elements and has been used to evaluate the global dynamics behaviour of the OB connected by the 8 Pyroceram rods to the stiffening ring (assumed as a rigid element). The second one is built by means of 3-D elements (thanks to the symmetry of the OB, only a portion of it has been modelled) and has been used to compute the stress state in the material under the quasi-static design loads. The analyses are described in detail in the Annex 11-1 Optical Bench Mechanical Analysis. From the dynamic analysis it turns out that the first vibration mode takes place in the lateral direction (along the short side of the OB, see Figure 7.1-37) and has a frequency of about **105 Hz**. The requirement of a 60 Hz minimum frequency [1] is then fulfilled with good a margin.

The quasi-static design loads prescribed by [4] for an equipment around 15 kg (which is approximately the total mass of OB + inertial sensor + mechanical interfaces) is 35 g's along the worst spatial direction. However, in consideration of the position of the OB with respect to the launcher thrust direction, the following design loads have been applied to the 3-D FEM:

- - 35 g's perpendicular to the OB plane (i.e. along the launcher X-axis, where the maximum acceleration is expected)
- - 15 g's on the OB plane

According to the prescriptions of [4], the two loads have not been applied simultaneously.

The results of the static analysis have been expressed in terms of maximum principal strains. In fact, for a brittle material like ULE^{TM}, the De Saint-Venant/Grashop resistance criterion applies: the material breaks as soon as one of the principal strains (taken in absolute value) exceed its Ultimate Tensile strain (ε_{ult} = 0.72 10^{-3} for ULE^{TM}). The static analysis gives a maximum value of **$-0.26 \cdot 10^{-3}$** for the principal strain vector components, located in the interface zone between the OB and the inertial sensor (see Figure 7.1-38). There is therefore a safety margin of **2.77** with respect to ε_{ult}, above the prescription of 1.5 (see [4]), but not excessive considering brittle nature of the ULE^{TM}. More detailed analyses are therefore advisable in order to consolidate the results and acquire the sufficient confidence about the absence of cracks generation risks during the launch phase.

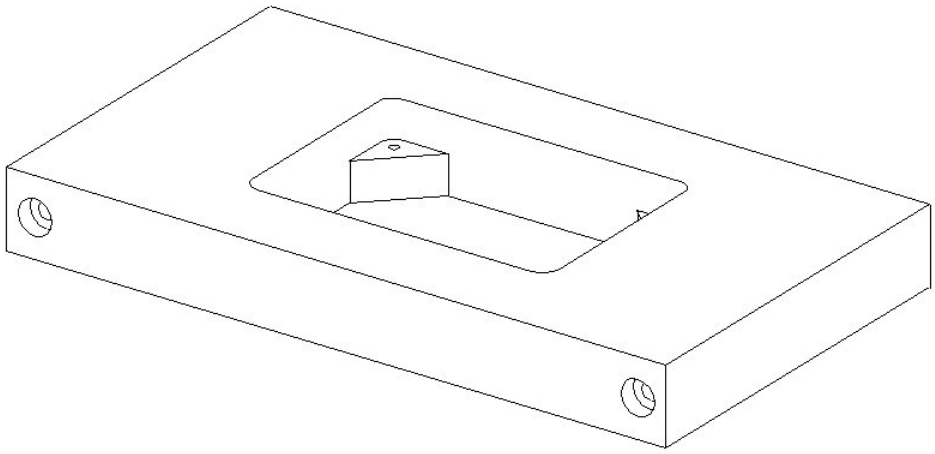

Figure 7.1-34 - Optical Bench ULE^{TM} baseplate

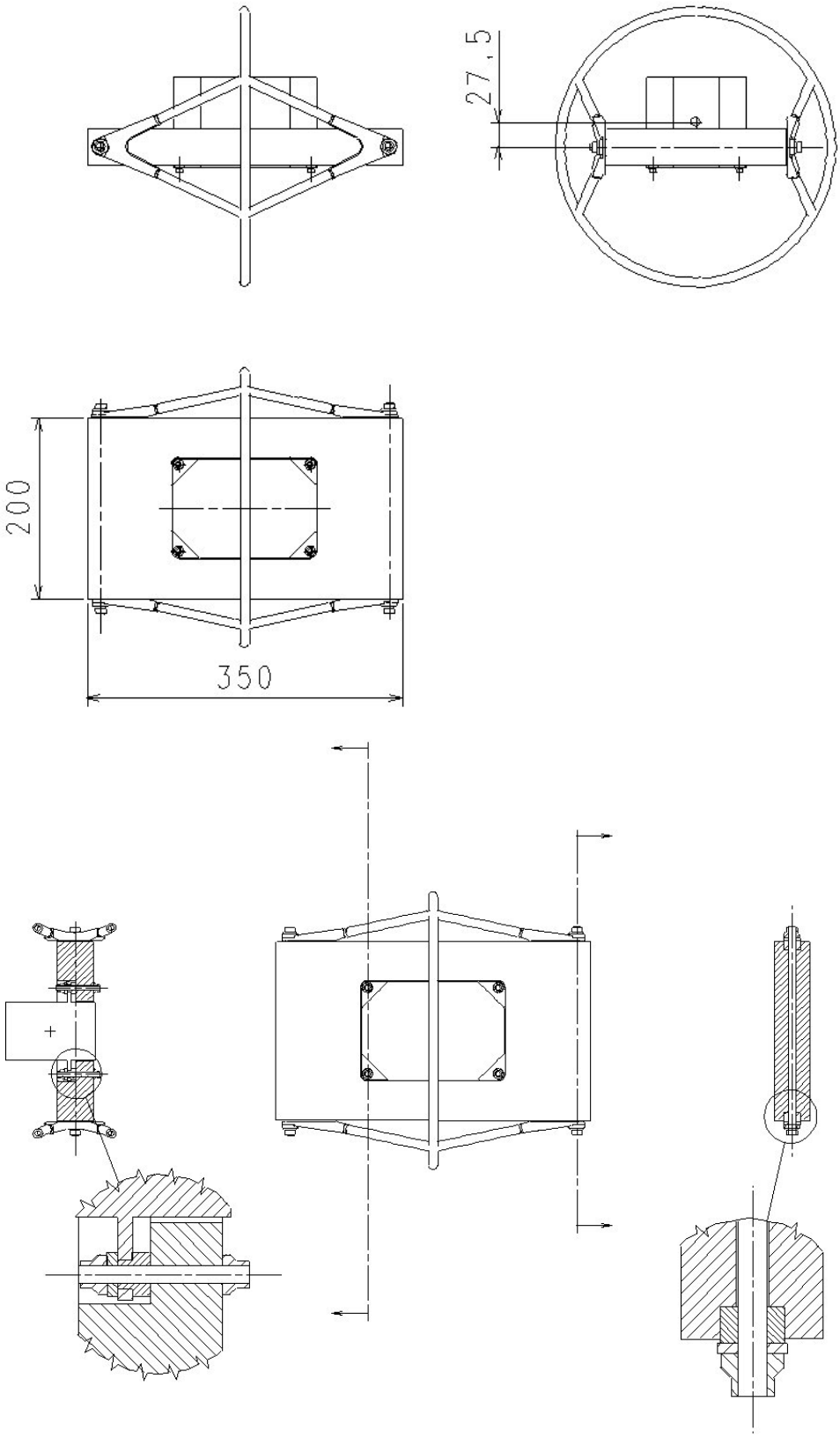

Figure 7.1-35 - OB interfaces with the Inertial Sensor and the support structure

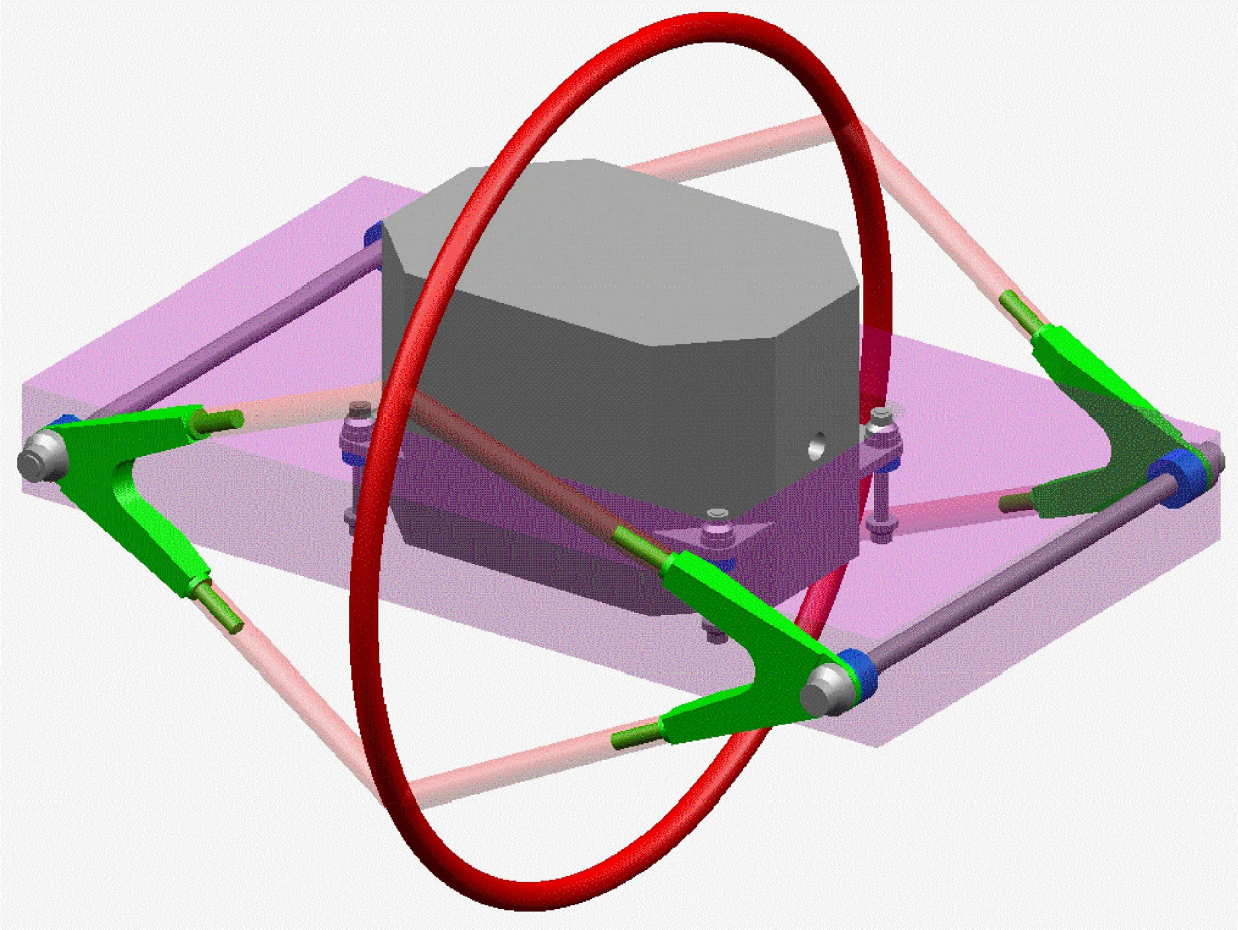

Figure 7.1-36 - Perspective view of the OB showing the interfaces with the Inertial Sensor and the support structure

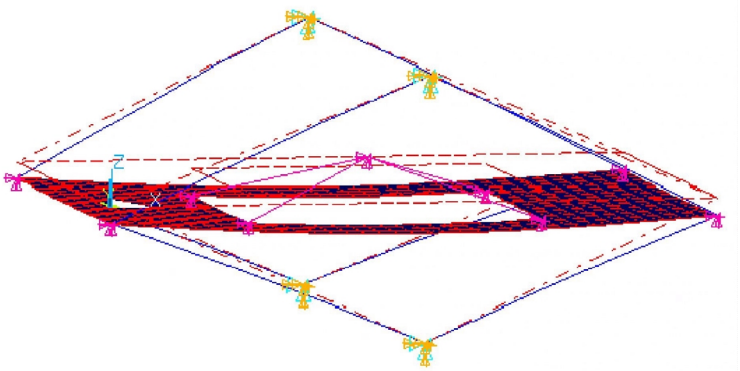

Figure 7.1-37 - Eigenshape of the first vibration mode of the OB

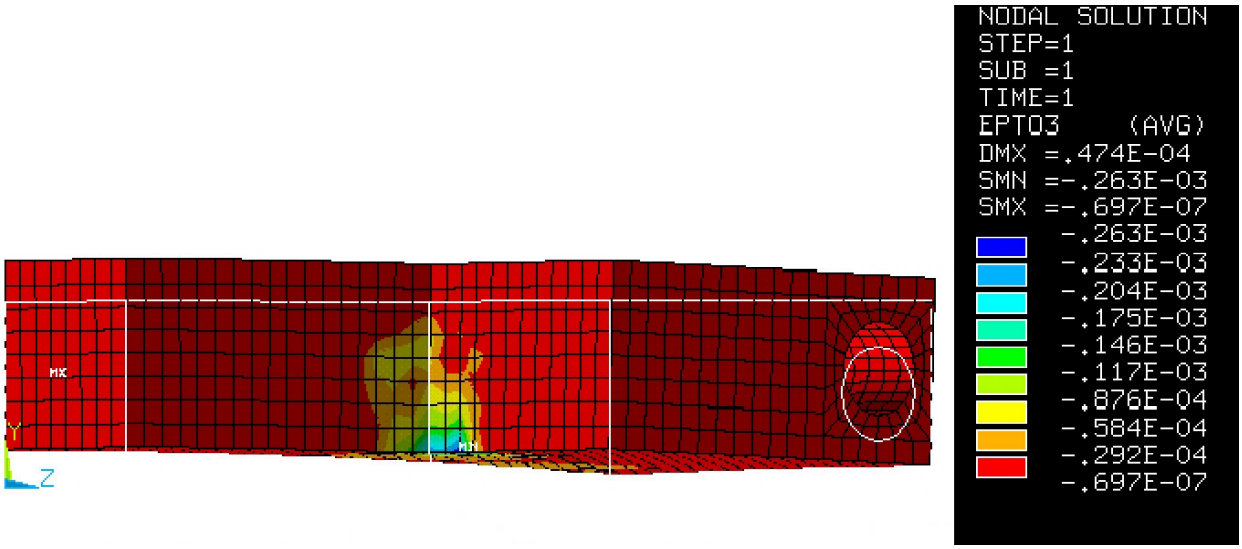

Figure 7.1-38 - Third component of the OB principal strain under an axial load of 35 g's

7.1.3.6 Optical Bench Budgets

The amount of power that local laser delivers to the telescope and to all the detectors distributed on the OB is provided in Table 7.1-9. It is computed under the following main assumptions

- output power of the laser source = 1 W in S polarisation;
- bulk phase modulator before the fiber coupler;
- laser-fibre coupling efficiency = 70%;
- surfaces of the all refractive optics are AR coated, and AR coatings reflectivity = 0.1%;
- proof mass (90% Au + 10% Pt) surface reflectivity = 96.67%;
- 0.8 loss factor for the transmitted beam truncation and partial obstruction by the telescope.

The amount of power of the incoming laser beam that arrives on the OB detectors is provided in Table 7.1-10.

The power dissipated inside the material of the OB elements is provided in Table 7.1-11. It is computed considering an internal absorptance = $5 \cdot 10^{-4}$/m for the Fused Silica. Other sources of optical power dissipation on the OB volume are:

- the power circulating in the reference cavity for the laser frequency stabilisation: 6.4 mW;
- the power scattered through the bench (mainly by backrefections) and eventually absorbed by the walls of the Inertial Sensor vacuum vessel, of the detectors' housings and of Y-shaped cylinder enclosing the bench: ~600 μW.

The mass budget of the OB (excluding the fibre positioner and the Inertial Sensor) is provided in Table 7.1-12.

Table 7.1-9 - Optical link budget (transmission path)

Element	Total power	Power in S polarisation	Power in P polarisation	Note
Laser source	**1000 mW**	**1000 mW**	**-**	Laser output power, assumed linearly polarised
Phase modulator	959.4 mW	959.4 mW	-	0.18 dB insertion loss
Laser-fiber coupler	671.6 mW	671.6 mW	-	70% coupling efficiency
Optical fiber	671.1 mW	670.3 mW	0.8 mW	35 dB polarisation extinction ratio
Collimator	668.4 W	667.6 mW	0.8 mW	1° orientation error around fiber axis
Main photodiode qp1	**4.056 mW**	**3.293 mW**	**0.763 mW**	Considering a ps1 with R_S = 99.5%, T_P = 95%
OB output	625.8 mW	312.9 mW	312.9 mW	Power sent to the telescope
Telescope	**500.6 mW**	**250.3 mW**	**250.3 mW**	Power transmitted to satellite B (C)
Beamsplitter s1	1.671 mW	1.669 mW	0.002 mW	Power to the back of OB (s1 with R = 0.25%)
Reference cavity	**564.1 µW**	**563.4 µW**	**0.700 µW**	Power entering the reference cavity
Photodiode p3	**997.5 µW**	**996.2 µW**	**1.300 µW**	Utilised for the laser power stabilisation
Proof Mass	**97.96 µW**	**48.98 µW**	**48.98 µW**	Power reflected off the back of the proof mass (a)
Photodiode p1	**1.102 µW**	**0.993 µW**	**0.109 µW**	Power of laser A1 on the photodiode p1 (b)
Fiber coupler, OB 1	59.18 µW	0.02 µW	59.16 µW	Power sent to OB 2
Fiber coupler, OB 2	59.02 µW	58.95 µW	0.07 µW	Power received by OB 2
Photodiode p1	**58.13 µW**	**58.12 µW**	**0.01 µW**	Power of laser A2 on the photodiode p1

(*a*) Considering a ps2 with R_S = 99%, T_P = 90% ; the power of the laser from the OB 2 on the proof mass is about 65 nW

(*b*) The power of the local laser on photodiode p1 is limited because of the 100 µW constraint for the power on the proof mass

Table 7.1-10 - Optical link budget (receiving path)

Element of the optical chain	Total power	Power in S polarisation	Power in P polarisation	Note
Telescope, S/C A	500.6 mW	250.3 mW	250.3 mW	Power transmitted to S/C B (C)
Telescope, S/C B (*a*)	76.32 pW	38.08 pW	38.24 pW	Power received by S/C B (C)
Beamsplitter s2 (*b*)	3.816 pW	1.904 pW	1.912 pW	Power sent to the CCD
CCD (*c*)	**3.414 pW**	-	**3.414 pW**	Power available for initial acquisition
Waveplate q2	72.28 pW	0.14 pW	72.14 pW	Power towards the PBS
Proof Mass	68.12 pW	34.06 pW	34.06 pW	Power reflected off the front of the proof mass
Main photodiode qp1	**64.94 pW**	**64.94 pW**	**≈ 0**	Remote laser power at qp1

(*a*) A 1° rotation about the optical axis of the two mutually facing OB's on the S/C's A and B has been assumed.

(b) A beamsplitter s2 with RP = RS= 5% @ 45° incidence has been considered, in order to have more power on the acquisition sensor

(c) Corresponding to about 1.8·107 photons per second.

Note: no alignment error has been assumed in the orientation of the quarter waveplates

Table 7.1-11 - Optical power dissipation inside the material of the OB elements

Element	Dissipated optical power	Element	Dissipated optical power
Collimator	2.679 µW	Lens l3	89.03 pW
Beamsplitter s1	1.418 µW	Fiber coupler	287.4 pW
Mirror m1	335 nW	Lens l2	1.130 nW
Beam compressor bc2	7.506 nW	Reference cavity	1.080 nW
Beamsplitter s3	4.956 nW	Lens l4	537.6 pW
Beamsplitter s4	1.412 nW	Beam compressor bc1	16.31 nW
Polarising beamsplitter ps2	1.265 nW	Polarising beamsplitter ps1	5.006 µW
Quarter waveplate q3	96.75 pW	Quarter waveplate q2	330.3 nW
Lens l5	385.7 pW	Beamsplitter s2	1.399 µW
Window w2	289.3 pW	**Total**	**11.20 µW**

Note: dissipation due to the optical power coming from the remote laser has been neglected

Table 7.1-12 - OB mass budget

Element	Number of units	Total Mass (g)	Contingency	Total Mass + contingency (g)
ULE™ baseplate		4590.0	10%	**5049.0**
Optics				
- Lenses	13	14.4		
- Mirrors	4	7.6		
- Beamsplitter	4	6.8		
- Polarising beamsplitter	3	14.0		
- Quarter waveplates	4	3.4		
Total Optics		46.2	30%	**60.1**
Fiber Coupler		53.0	30%	**68.9**
Detectors (*)				
- Quadrant photodiode	1	25.0		
- Photodiode	3	54.0		
- CCD	1	90.0		
Total Detectors		169.0	30%	**219.7**
Mechanical Interface				
- Titanium bolts	6	160.0		
- Thermal washers	8	17.0		
Total Mechanical I/F		177.0	10%	**194.7**
Grand Total		**5035.2**		**5592.4**

(*) The detector mass includes the proximity electronics and the radiation shield/light baffle (assumed to be made in Aluminium, with a thickness in the range 2 - 3 mm).

7.1.4 Laser Assembly

As described in section 4.3.1.4 the laser concept trades resulted in the selection of a non-planar ring oscillator (NPRO) with Neodymium doped Yttrium Aluminium Garnet as the active medium as the baseline concept for the LISA laser system. The laser components trades thereafter resulted in the laser head design as it is described here.

7.1.4.1 Optical Design

The laser head consists of a Nd:YAG crystal pumped by two aluminium-free 3000 mW GaAsP laser diodes (e.g. S-81-3000c-200H manufactured by Coherent Inc.). The nominal single-mode output power of the NPRO in this configuration is ~3500 mW, but this is downrated for LISA to ~1700 mW to improve reliability properties of the laser diodes (50 % pump power) and to simplify the thermal management.

The nominal constant power consumption for the 1700 mW (1100 mW on the optical bench) of output power of the complete laser system (including supply unit) is approximately 37 W.

The pump light from each laser diode is transferred into the crystal by imaging the emitting area of 1µm x 200µm at unit magnification into the TEM_{00} mode volume of the crystal, using two identical, aspherical lenses with plano-convex surfaces to minimise spherical aberration (best form lens shape). A polarising beamsplitter is inserted between the two lenses to combine the pump light from the two laser diodes, which are orthogonal in polarisation.

Two strong permanent magnets are mounted above the crystal to establish a magnetic field of 0.3 T inside the NPRO crystal. That field is required in direction of beam propagation to maintain single frequency operation by implementing an optical diode in the crystal. Another element of the laser head is a fibre coupler, which under current design is a standard OZ Optics non-contact (-60dB back reflection from fibre end) pigtail style coupler with an aspherical focusing lens permanently glued to the fibre end.

Two options for the laser head design have been discussed in section 4.3.1.4:

1. A Faraday isolator for suppression of back-reflection to the laser crystal and an electro-optical modulator for laser phase modulation are part of the laser head.
2. A Faraday isolator for suppression of back-reflection to the laser crystal and an electro-optical modulator for laser phase modulation are fibre-optic devices that are located outside the laser head.

The first has been selected as the baseline and will be presented in detail, whereas only a conceptual design of the second fall-back option is presented in the next section.

7.1.4.2 Mechanical Design

For Both options the laser head components are incorporated into a quasi-monolithic monoblock design (cf. Figure 7.1-40 and Figure 7.1-43). This means the individual constituent parts are glued to a solid fused silica spacer to ensure mechanical stability. Also glued to that spacer are heat sinks, which serve as the mechanical and thermal interface to the radiator plate, which is part of the satellite structure.

Baseline Option

The spacer is made of a single block of fused silica with dimensions 165 x 130 x 60 mm^3, a volume of 1080 cm^3 and therefore a mass of 2700 g. The components will have an additional mass of

approximately 800 g. Holes are drilled into the spacer for the optical path of the pump radiation and the infra-red radiation and spacings are milled for the laser components.

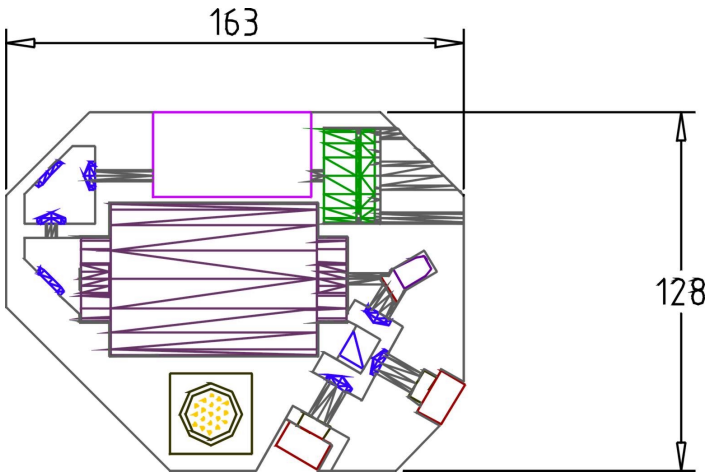

Figure 7.1-39: Dimensions of the baseline fused silica laser head spacer. *(height is 60 mm)*

The permanent magnets for the optical diode, all optical elements and the laser crystal are mounted to the inside walls of the respective spaces with a high strength epoxy (e.g. Araldit AY103+AY256). Adjustment of the lenses, to maximise the laser output power or the fibre coupling efficiency, is done during the thermal curing phase of the epoxy.

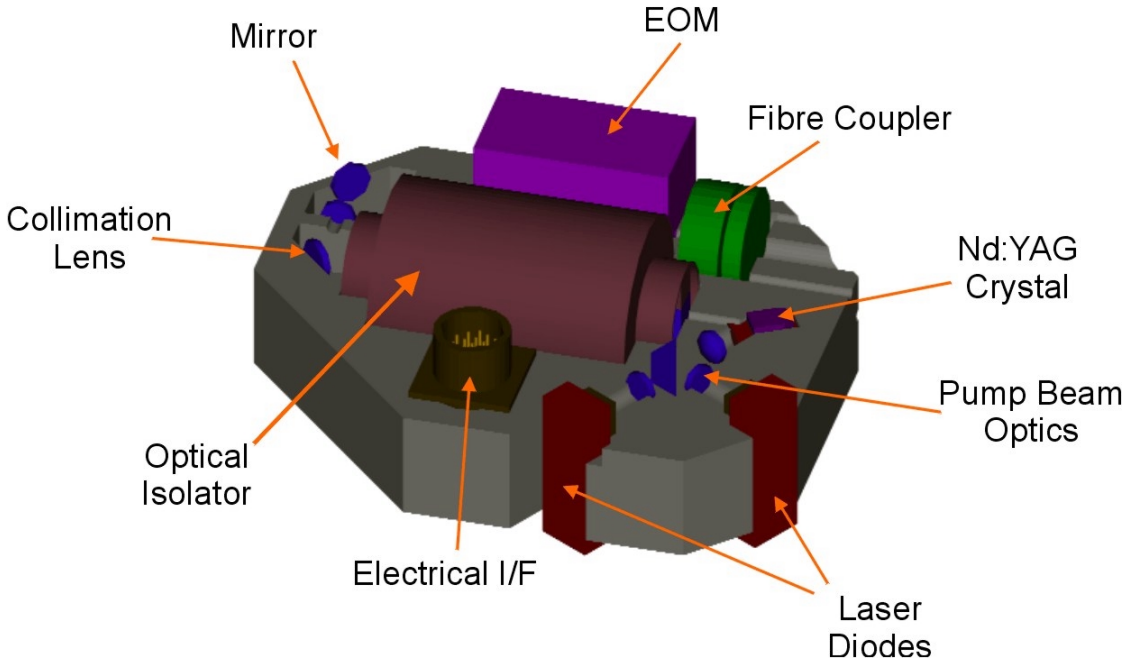

Figure 7.1-40: Schematic layout of the baseline fused silica laser head spacer.

(All components are glued to the spacer)

The optical isolator is located in a spacing in the centre of the spacer. It consists of a TGG crystal with a non-zero Verdet-constant that is surrounded by a Neodymium-Iron-Boron permanent magnet in a configuration based on the model IO2-YAG-VHP from OPTICS FOR RESEARCH (OFR). Due to its size and mass, the isolator is one of the design drivers of the laser head. The isolator is glued to the spacer and adjustment for maximum throughput is done during the thermal curing phase of the glue.

Two folding mirrors direct the laser beam to the EOM (electro-optic modulator), which is based on the commercial design of the model 4003 by NEW FOCUS. Fixation and adjustment of the modulator is done as for the optical isolator.

Two lenses are mounted on the walls of the spacer in the beam path. These lenses are for collimation and focusing of the laser radiation into the fibre coupler. The lenses are spherical optics made of synthetic fused silica.

Adjustment of the coupler to maximise in-coupling efficiency is again done during the curing phase by exact positioning of the complete coupling device. Fine adjustment is done with three fine thread screws, which are arrested with epoxy afterwards to avoid later misalignment (see Figure 7.1-41). The fibre is lead to the top surface of the spacer where a PM-FC fibre connector is fixed.

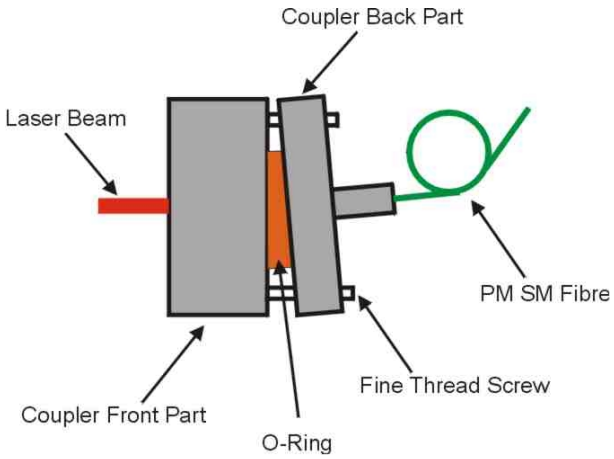

Figure 7.1-41: Schematic drawing of the fibre coupler.

The pump laser diodes are mounted into the respective spacings on the outside walls of the spacer, the current supplies leading to the top where a multipin connector is fixed. In its spacing the crystal is cemented with its top surface to the fused silica. A piezo-electric crystal (PZT) for the frequency fine tuning is located in a gap between the spacer and the crystal.

Heat sinks are to be glued to the backsides of the diodes and the bottom of the crystal, respectively. The heatsinks are used for the temperature control of these parts and do also serve as the mechanical interfaces to the S/C, as they are srewed onto the radiator disk. Temperature transducers are glued to the heat sinks for precise temperature readout.

Fallback Option

The fallback option for the laser head as identified in section 4.3.1.4 is a smaller design with the EOM and the optical isolator located outside the head and connected with fibres. The laser head design in this case is a cylindrical spacer with a diameter of < 100 mm and height < 50 mm. The total mass of this

laser head (including components) is below 1000 g. The individual components, except for the isolator and the modulator, are mounted as in the baseline option.

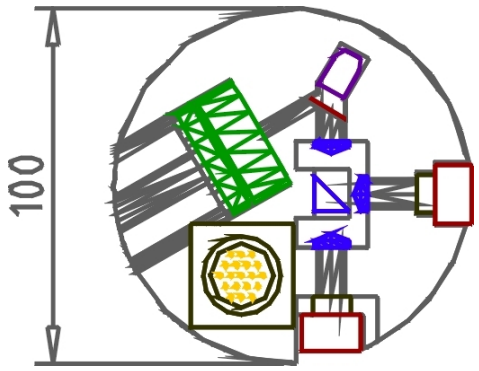

Figure 7.1-42: Diameter of the laser head fallback design. The height is 40 mm.

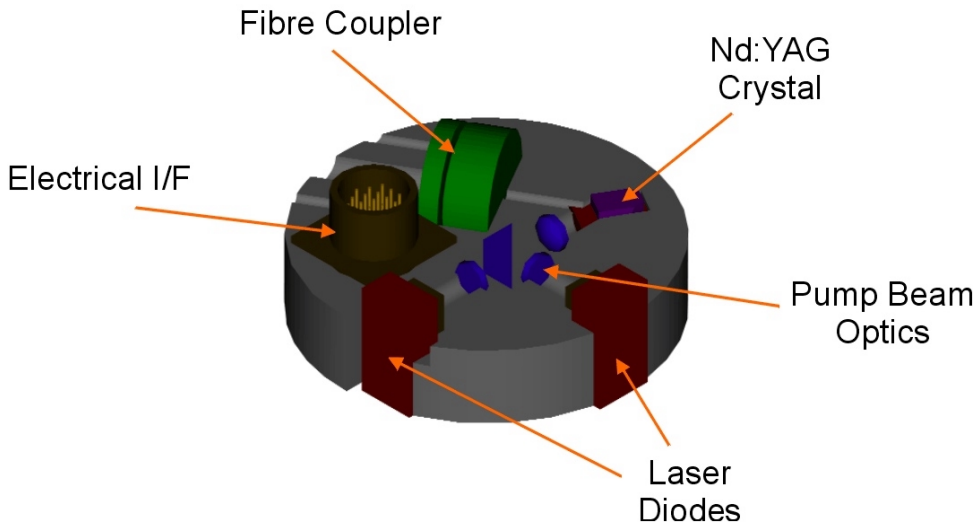

Figure 7.1-43: Schematic layout of the fallback design.

(The cylindrical fused silica spacer with all components glued to the spacer)

7.1.4.3 Thermal Design

For the desired 1000 mW light power on the optical bench 1700 mW light power out of the crystal is required. The loss is due to diffraction limited 75 % incoupling efficiency into the 6 µm core diameter polarisation maintaining mono-mode fibre and 6 % total loss at the optical isolator and the PM modulator, respectively. The heat flux of the total amount of 700 mW is conducted away by thermally connecting all components to the crystal heat sink.

The slope efficiency and threshold pump power of Nd:YAG in the described resonator design, 65 % and 130 mW respectively, are leading to a total optical to optical efficiency of 56 % at 1700 mW output

power. Therefore a pump power of 3000 mW is required and 1100 mW heat is dissipated in the crystal (minor losses due to reflection). The optical power budget table summarises these findings.

The threshold current of the photodiodes is 600 mA and the differential efficiency is 1 W/A. For a pump power of 3000 mW per diode a current of 3600 mA is required, corresponding to 7200 mW electrical power per diode or 14.4 W total electrical power. Therefore the nominal heat dissipation of each laser diode is 4200 mW.

Heat sinks are glued to the back of the laser diodes and to the bottom of the crystal to conduct the heat away. There is a heater in each heat sink to control the operating temperature of the corresponding component. In order to maintain the possibility to heat and cool their device (even in case of failure of one diode), the diode heaters are designed so that in normal operation they produce half the heat load due to the current above threshold. The crystal heater is operated at half the expected maximum heater dissipation. The total dissipation due to the heaters amounts to approximately 10 W.

The bottom of each heat sink is glued to a block of pyroceram of appropriate thickness to provide the desired heat resistance to the radiator plate. For the two laser diode heat sinks the heat resistance is determined by the required operating temperature, which is set to center the emission spectrum of the diodes on the absorption maximum of Nd:YAG at 808 nm.

Pump Power [mW]	3000

Component	Lens 1	Mirror 808	Lens 2	ETR Thershold	ETR Slope	Faraday Isolator	Modulator	Fibre Coupler	Total System
Transmission T [%]	99	98	99	95	65	94	94	75	(91 % -150 mW) * 11 %
Transmission T [mW]				-130					
Reflection R [%]	1	1	1	5	0	1	1	1	27% (Sum)
Power Losses L [%]	0	0	0		35	5	5	24	120 % (Sum) + 150 mW
Power Losses L [mW]				130					

Optical System [mW]									
Transmission T [mW]	2970.00	2910.60	2881.49	2607.42	1694.82	1593.13	1497.55	1123.16	1123.16
Reflection R [mW]	30.00	29.70	29.11	144.07	0.00	16.95	15.93	14.98	280.74
Power Losses L [mW]	0.00	0.00	0.00	150.00	912.60	84.74	79.66	359.41	1586.41

Table 7.1-13: Laser Optical Power Budget

7.1.4.4 Laser Power Supply

Overview

The main functional parts of the supply unit are two current sources for the laser diodes, three temperature controllers, the mixer and feedback servo for the frequency stabilisation and the feedback circuit for intensity stabilisation.

The basic functional principle of the current sources foresees that the nominal output current is set by taking a certain voltage from a very stable voltage reference with a digital potentiometer. The signal from the intensity stabilisation circuit is added with a summing amplifier. The resulting voltage signal is sent to a transconductance current source, which is a modified Howland current source with an additional bipolar Darlington transistor to amplify the current. The set point is controlled remotely via the spacecraft bus through adjustment of the digital potentiometer. In case of failure, say a breakdown of supply voltage or temperature stabilisation failure or on demand, a safety logic is implemented that shortcuts the laser diode anode.

The temperature controller gets its error signal from a comparison of the signal from the temperature transducer with a very stable reference voltage, remote controlled with a digital potentiometer. That signal is amplified with a PID-stage, which is a proportional amplifier, an integrator and a differentiator in parallel, and then sent to a simple transistor current source.

The feedback circuit for the frequency stabilisation consists of a double-balanced mixer and a high gain servo. Most of the signal from the USO oscillator is directed to the EOM, but some is coupled to the mixer, where it is used to demodulate the Pound-Drever dispersion signal (cp. Section laser performance) from the stabilisation photodiode. The demodulated error signal is amplified in the servo, which consists of four stages of integrators with adjustable gain (remotely via the satellite bus). The unity gain frequency is approximately 10 kHz with a 1/f roll off to assure stability. The highest adjustable dc-gain (below 1 Hz) is 120 dB for good noise rejection at the measurement frequency.

The feedback circuit for the intensity stabilisation consists of a two stage servo that amplifies the ac-signal from the photodiode, which will be added to the voltage determining the laser diode current in the current drivers. The unity gain frequency is 100 Hz with a 1/f-rolloff to assure stability, and the dc-gain (below 1 Hz) is 60 dB.

Laser Diode Current Source

For the LISA laser system a slightly modified version of the current source for the commercial NPRO systems manufactured by the Laser Zentrum Hannover/InnoLight GmbH will be used. The key parameters of this laser diode current source are

Parameter	Value
Max. current	3 A
Max. voltage	4 V
Supply Voltage	12 V
Current noise	30 nA/Hz1/2
Current stability	9x10-6 Arms over 3 hours
Appr. Mean input power	3 W

The current stability is of major interest as any pump power fluctuations, either caused by wavelength shifts or by current instabilities, directly affect the frequency stability of the NPRO. The following graph displays the current driver stability in the time domain.

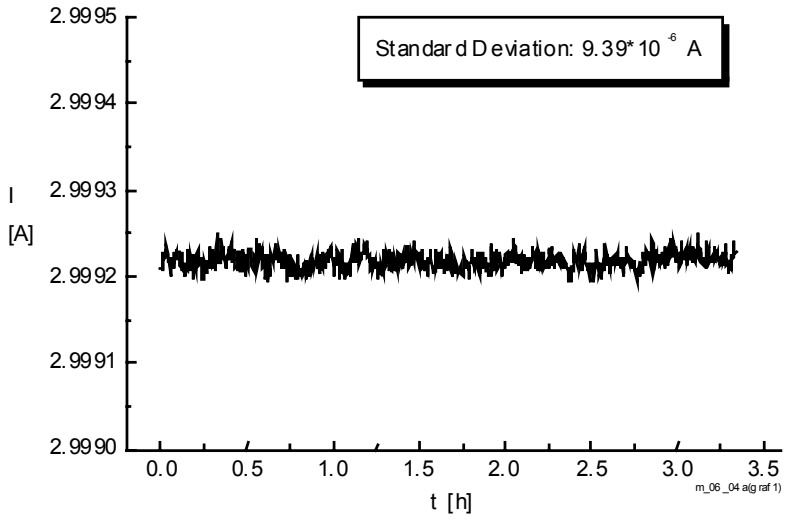

Figure 7.1-44: Long term stability of the laser diode current driver

Temperature controller

Also for the temperature controller a slightly modified version of the controller for the commercial NPRO will be used. Under present design the signal from the temperature controller drives peltier elements to control the temperature. These peltier elements can be easily replaced by passive resistors, as preliminary investigations have shown. The key parameters of the temperature controller are (driving peltier elements):

Parameter	Value
Set point temperature	20oC – 50oC
Set point resolution	10 mK
Max. current	3 A
Max. power throughput @ dT=0	5 W
Supply Voltage	+/- 8 V
Appr. mean power dissipation	3 W

The performance of the temperature controller directly affects the frequency stability of the free running laser output with a tuning coefficient of approximately 3 GHz/K. Therefore a very high stability of the crystal temperature stabilisation is required. The following graph displays the measured residual temperature fluctuations of the stabilised crystal

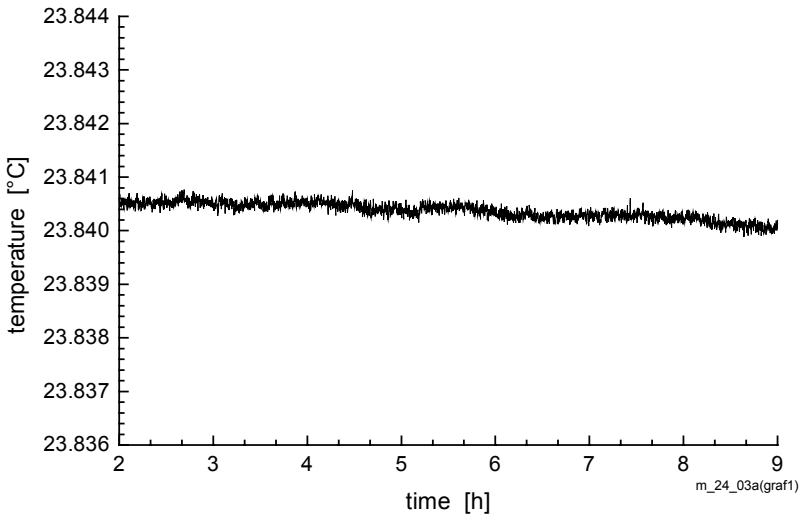

Figure 7.1-45: Long term stability of the crystal temperature controller

7.1.4.5 Laser performance

Power Stability

The desired sensitivity in the LISA metrology requires a high signal-to-noise ratio of the laser light source. The fundamental limit of the power noise for a free-running laser is set by the quantum properties of light. In principle diode-pumped solid-state lasers offer the potential to reach this quantum

noise limit (QNL). However, in real systems the power fluctuations are many orders of magnitude larger. This is mainly due to relaxation oscillations at intermediate frequencies (> 100 kHz) and due to pump noise transfer at low frequencies.

Substantial power noise reduction has been demonstrated for monolithic non-planar Nd:YAG ring lasers by application of electronic feedback loops. A fraction of the laser light is detected with a photo diode and the AC components are appropriately amplified to generate an error signal. This signal is fed back to the pump diodes. For the LISA mission the requirement on relative power noise is 4 x 10^{-4} $Hz^{-1/2}$ at frequencies between 10^{-4} Hz and 1 Hz. This noise reduction goal has already been experimentally demonstrated within an order of magnitude (see figure).

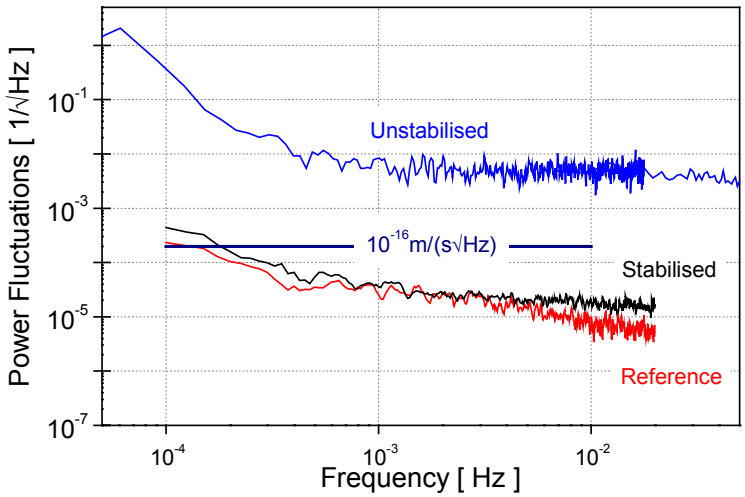

Figure 7.1-46: Relative power noise of the stabilised NPRO and the unstabilised NPRO (1mW optical power detected).

Frequency stability

The monolithic structure of the nonplanar Nd:YAG ring laser and the low technical noise of the supply electronics offer a high intrinsic frequency stability of this laser system. But the LISA interferometry requires even lower frequency noise, namely 30 $Hz/Hz^{-1/2}$ at frequencies between 10^{-3} Hz and 1 Hz. Therefore the laser is stabilised to a resonance of a reference cavity, making use of a rf-reflection locking scheme known as Pound-Drever-Hall scheme.

About 5 mW of the light from the fibre is mode-matched into a reference cavity. That cavity consists of three mirrors optically contacted to the optics bench that form an optical resonator of approximately 1,000 finesse. The light reflected from the cavity is detected on the stabilisation photodiode, tuned to the modulation frequency. The signal from the photodiode is amplified and then demodulated, producing a bipolar error signal for the feedback servo. Fast correction signals are fed back to the piezo-electric transducer mounted on top of the Nd:YAG crystal. Slow frequency adjustment is done with feedback to the laser crystal temperature.

The Pound-Drever-Hall scheme has been investigated stabilising a NPRO to a rigid optical resonator of 10,000 finesse. That resonator was placed in a vacuum chamber and shielded by multiple layers of active and passive thermal isolation to simulate the very stable environment inside the LISA spacecraft.

The result of the laser stabilisation is shown in Figure 7.1-47. The residual frequency fluctuations have been reduced within an order of magnitude to what is required for the LISA mission.

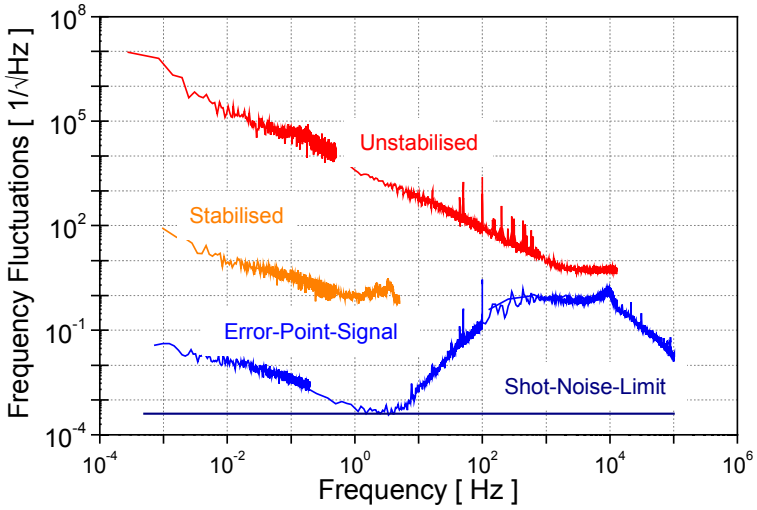

Figure 7.1-47: Frequency noise of NPRO.

Top trace shows the noise spectrum of the free running laser, middle trace shows the frequency noise of the stabilised laser measured with an independent reference system. Bottom trace is the stability relative to the optical resonator

7.1.5 Ultra Stable Oscillator

A frequency reference provided by an Ultra Stable Oscillator (USO) is required on each LISA P/L in order to:

- reduce to a manageable level the Doppler shift frequency (up to 15 MHz) in the beat signals over the interferometer arms;
- drive the ~200 MHz phase modulator of the laser beams on each OB;
- drive the phase locking (with offset frequency ~10 kHz) of the various lasers with the master laser A1.

Each P/L will be equipped with two USO's, one for each OB. All USO's on the three S/C are locked to a single reference clock, whose frequency is corrected for by locking it to a delay line (interferometer arm). The maximum Doppler frequency is the driving parameter for the sidebands' frequency (~200 MHz).

Figure 7.1-48 is a schematic block diagram showing the functional relationship between the USO and the various users on board of the P/L (the nomenclature of the components is consistent with the definitions of par. 7.1 and par. 7.1.3)

On each S/C six phase measurements are taken and compared using a multiple input phase comparison unit:

- beat between the carriers of the transmitted and received beam on qp1, used for the laser phase noise compensation and gravitational wave detection (the four individual quadrants are used for attitude control);
- beat between the transmitter carrier and sideband of received beam, used for the USO phase noise compensation;
- beat between the laser carriers from the backside of each proof-mass, used for the identification of the relative motion between the S/C and the proof mass.

All the frequencies used on-board the spacecraft are derived from the USO. The frequencies in the audio range (like the 10 kHz needed for the laser offset locking) are obtained by Numerically Programmed Oscillators (NPO's), operated as Digital Direct Synthesisers, fully maintaining the stability of the USO.

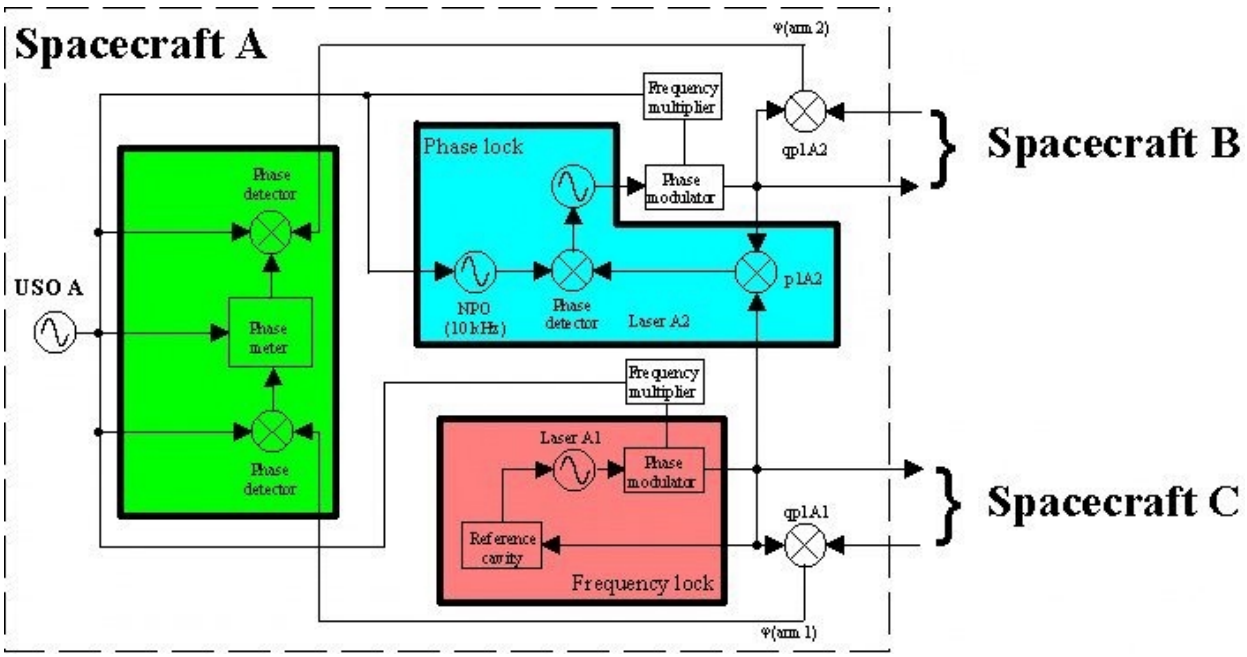

Figure 7.1-48: Functional relationship between the USO and the various users on board of a S/C
(the nomenclature of the components is consistent with the definitions of par. 7.1 and par. 7.1.3)

As for the laser, the main and most critical requirement of the USO concerns its frequency stability. The USO is a key element in the phase measurement chain, and a relative frequency stability $\delta\nu/\nu = 8\cdot10^{-16}/\sqrt{\text{Hz}}$ (much less than the performances of the state of the art systems) would be required to keep its contribution to the phase noise below $\sim 4\pi\cdot10^{-6}$ rad/$\sqrt{\text{Hz}}$ [1]. However, the USO phase noise can be determined by the same technique utilised for the laser phase noise measurement, and compensated for in the measurement processing [1]. This relaxes the requirement for the USO to a frequency stability (Allan standard deviation) of $\boldsymbol{\sigma_y(\tau) = 2\cdot10^{-13}\,\tau^0}$ for an integration time $\boldsymbol{1\text{ s} < \tau < 10^4\text{ s}}$ [2]. This results, for the selected 5 MHz oscillator, in a PSD of phase noise $S_\varphi(f) = 7.21\cdot10^{-13}\,f^{-3}$ rad^2/Hz [13]; thus the phase noise will be $2.7\cdot10^{-2}$ rad/$\sqrt{\text{Hz}}$ @ 1 mHz.

Table 7.1-14: Requirements and rationales for the USO.

Requirement	Rationale
Allan variance $\leq 2\cdot10^{-13}$, 1 s < τ < 10^4 s	Contribution to optical path noise ≤10 pm/$\sqrt{\text{Hz}}$ (after phase noise measurement and correction)
Phase modulator driving @ ~200 MHz	Doppler frequency shift ≤15 MHz, and signal transmission at 100 bit/s data rate

The reference oscillator identified in the Pre-Phase A study is based on the Mars Observer USO [1], but several other USO's for space application exist or are currently under development. The next paragraph compares the performances of some available oscillators.

7.1.5.1 Ultra Stable Oscillator market survey

A review of the available Ultra Stable Oscillator has been performed during the study in order to identify the unit that better meet the LISA needs. Three ultra-stable, space qualified crystal oscillators have been identified: the first is the baseline USO, manufactured by Syntonics LLC; the second is manufactured by Datum; the third was developed by Temex under an ESA contract. Table 7.1-15 reviews the frequency performances of the identified ultra-stable oscillators.

Table 7.1-15: Frequency performances for some ultra-stable crystal oscillators.

Model	Mars Observer	FTS 9500	MO4C-SC (*)
Manufacturer	Syntonics LLC	Datum	Temex
Frequency (MHz)	5	4 - 60	5 or 10 or 16
Frequency control range	NA	$\pm 2 \cdot 10^{-7}$	1.5 Hz
Ageing per day	$7 \cdot 10^{-13}$	$5 \cdot 10^{-11}$	$3 \cdot 10^{-11}$
Ageing per year	$1 \cdot 10^{-7}$ (**)	$1.5 \cdot 10^{-8}$	$3 \cdot 10^{-8}$
Temperature coefficient (1/K)	$4 \cdot 10^{-13}$	$3 \cdot 10^{-10}$	$3 \cdot 10^{-12}$
Magnetic coefficient (1/gauss)	$2 \cdot 10^{-12}$	NA	NA
Static acceleration coefficient (1/g)	$3 \cdot 10^{-9}$	$2 \cdot 10^{-10}$	NA
Radiation coefficient (1/rad)	$1 \cdot 10^{-11}$	NA	NA

(*) ESA GSTP-1 qualification

(**) per 5 years

NA: Not Available

Figure 7.1-49 shows the relative frequency stability, expressed as the square root of the Allan variance, of the crystal oscillators listed in Table 7.1-15. For comparison, a Cesium clock, a Rubidium clock and a Hydrogen maser have been added. It is clear that the frequency stability of the Mars Observer USO is one order of magnitude better than that of any of the identified oscillators, with the exception of the H-maser, in the LISA measurement bandwidth.

Table 7.1-16 shows the phase specifications for the identified USO's.

Table 7.1-16: Phase specification for the identified USO's

Model	Mars Observer	FTS 9500	MO4C-SC
Manufacturer	Syntonics LLC	Datum	Temex
Phase noise (dBc)			
@ 1 Hz	-137	NA	-100
@ 10 Hz	-149	NA	-130
@ 100 Hz	-155	NA	-140
@ 1 kHz	-158	NA	-150
@ 10 kHz	-160	NA	-155
Harmonics (dBc)	-60	-40	-30
Spurious (dBc)	-80	-100	-120

NA: Not Available

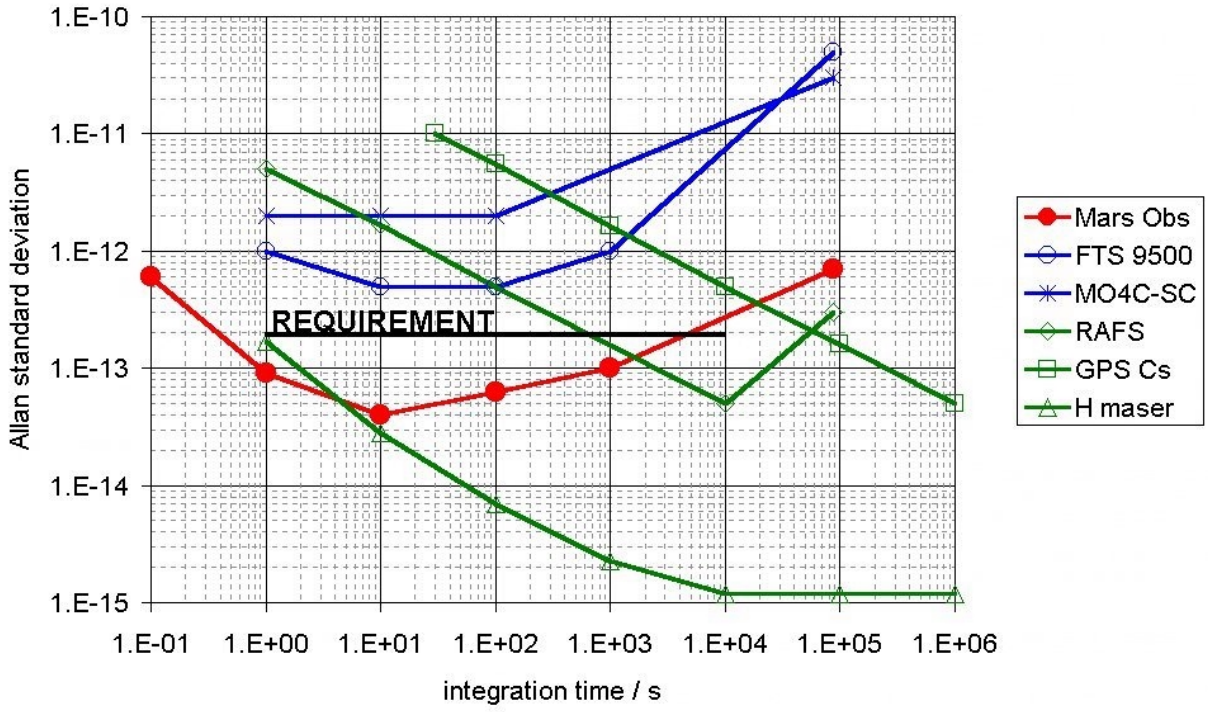

Figure 7.1-49: Frequency stability for the crystal oscillators listed in Table 7.1-15 and for some atomic clocks.

Table 7.1-17 shows the mass, the dimensions and the power consumption of the oscillators listed in Table 7.1-15.

Table 7.1-17: Mass, dimensions and power consumption for the identified USO's

Model	Mars Observer	FTS 9500	MO4C-SC
Manufacturer	Syntonics LLC	Datum	Temex
Mass (kg)	0.4	2.7	0.2
Dimensions (mm)	102×102×168	108×152×219	44×54×57
Temperature range (°C)	NA	-20 to 60	-15 to +60
Storage temperature range (°C)	NA	-40 to +100	-40 to +70
DC Power (W)	0.6 @ 25°C	2.9 @ 25°C (*)	3 (4.5 max)
Heat-up power (W)	NA	8	5
Heat-up time (min)	NA	120	5

(*) in vacuum

NA: Not Available

7.1.5.2 USO choice and specifications

The crystal oscillator produced by Syntonics LLC, identified as a baseline for Phase A, is the only one which meets the specified frequency stability $\sigma_y(\tau) = 2 \cdot 10^{-13}\ \tau^0$, $1\ s < \tau < 10^4\ s$ [2].

No viable alternatives to this oscillator have been identified.

It should be noted that the upward conversion process by frequency multiplication which is needed to obtain the required ~200 MHz frequency from the USO, which operates at 5 MHz, increases the PSD of phase noise by the square of the multiplication factor: this results in a 1600-time increase of the PSD. Syntonics LLC is capable of manufacturing a device equipped with a frequency multiplication stage, thus meeting the ~200 MHz specification for the output frequency.

In the following the characteristics of the selected oscillator are summarised.

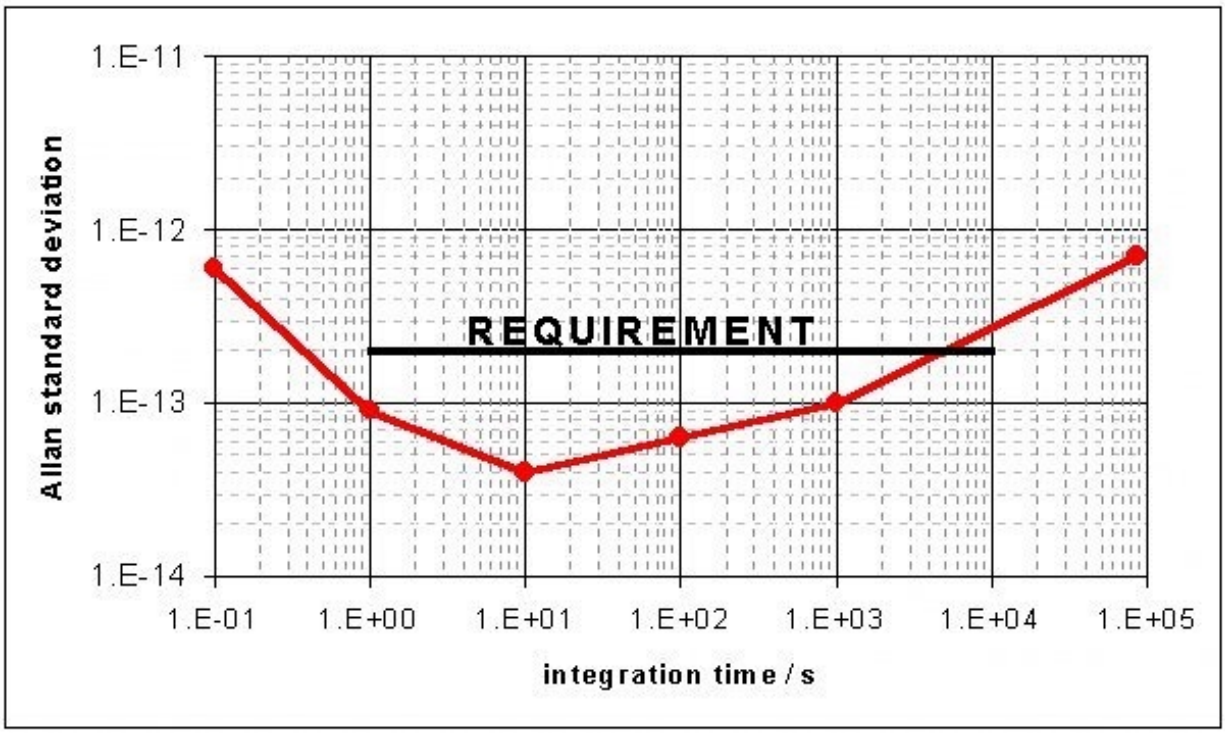

Figure 7.1-50: Relative frequency stability of the Syntonics LLC oscillator

Table 7.1-18: Characteristics of the Syntonics LLC oscillator.

Frequency (MHz)	5
Ageing per day	$7 \cdot 10^{-13}$
Ageing per year	$1 \cdot 10^{-7}$ (*)
Temperature coefficient (1/K)	$4 \cdot 10^{-13}$
Magnetic coefficient (1/gauss)	$2 \cdot 10^{-12}$
Static acceleration coefficient (1/g)	$3 \cdot 10^{-9}$
Radiation coefficient (1/rad)	$1 \cdot 10^{-11}$

(*) per 5 years

Phase noise (dBc)	
@ 1 Hz	-137
@ 10 Hz	-149
@ 100 Hz	-155
@ 1 kHz	-158
@ 10 kHz	-160
Harmonics (dBc)	-60
Spurious (dBc)	-80

Power consumption (W)	0.6 @ 25°C
Mass (kg)	0.4
Dimension (mm)	102×102×168

7.1.6 Interferometer Electronics

7.1.6.1 Design Specification

To attain the desired gravitational wave sensitivity the interferometer electronics should measure the differences in round trip path length between the two arms to less than 40pm/ $\sqrt{Hz}$, over a frequency range from 10^{-3} to 10^{-1} Hz. This suggests that the limitation due to photoelectron shot noise in each detector should not exceed about 10 pm/ $\sqrt{Hz}$, corresponding to $1x10^{-5}$rad/ $\sqrt{Hz}$. The expected laser phase noise will exceed the shot noise level at low frequencies. The expected laser frequency noise was estimated earlier to be roughly 30Hz/ $\sqrt{Hz}$ at 1mHz (see 7.1.4) which translates roughly to $2x10^{4}$rad/ $\sqrt{Hz}$ for the phase noise at 1 mHz. Thus a phase measurement dynamic range of roughly 10^{9} is required in order to perform the laser phase noise cancellation scheme.

The laser phase noise will decrease with measurement frequency such that there is a point at which the laser phase noise would drop below the shot noise from the quadrant photodiode. Taking into account the behaviour of the reference cavity this cross over would be expected to occur at about 10 kHz. Any measurement of the phase at a frequency below 10 kHz will have the problem of aliasing of the laser noise into the measurement band. To remove this problem the phase measurement should be performed at a frequency above this cross over, or analogue filtering should be included to reduce the noise which could be aliased into the measurement band to below the photodiode shot noise level. It is not obvious that the laser noise at these high frequencies is correlated, hence this noise can not be removed by any subtraction algorithm and therefore must not enter the measurement band.

It is proposed that the USO noise is removed in a similar way to the laser phase noise. Two 200 MHz sidebands will be added to the transmitted laser beam, these sidebands will contain both the laser and USO phase noise contribution, thus in combination with the Doppler data it should be used to subtract the USO noise. Since the USO frequency noise scales the frequency multiplication factor squared, the measurement of the 200 MHz sideband can be obtained to a lower accuracy. Thus for a maximum Doppler shift of 15 MHz and a sideband frequency of 200 MHz the sideband signal needs to be measured to less than $1x10^{-2}$ rad/ $\sqrt{Hz}$, with a dynamic range of 10^{9}.

The difference in the round trip path length between the two arms is extracted from the beat signal as a time series of phase measurements. The phase of the beat signal between the received and transmitted beams is measured with the time base provided by the on-board USO in each of the S/C. The two laser beams being beat together have different frequencies because of gradual changes in arm length and because of the roughly 10 kHz offset frequencies used in the locking scheme. The expected Doppler shifts for arms 1 and 2 are of the order of 1 MHz, and for arm 3, the Doppler shifts may be as high as 15 MHz.

The orbits of the S/C, combined with the very long arm length of the interferometer and the finite speed of light, give rise to an angle between the incoming and transmitted beams in the main telescope. This ‘point ahead’ angle (PAA) would lead to the two interfering beams having an angle between them at the main photodiode. (This angle is the PAA multiplied by the angular magnification of the telescope.) Thus the wavefront of the received beam is tilted. The interferometer electronics must measure this tilt and any fluctuations to the tilt angle.

The specifications to enable the measurement of a gravitational wave strain of $\frac{\delta l}{l} = 10^{-23}$ in one year are set out below.

Table 7.1-19 - Interferometer electronics system specification

Requirement	
Single Arm Distance Measurement	11 pm/ $\sqrt{\text{Hz}}$
Dc wavefront tilt	20 nrad
Wavefront tilt jitter	~7 nrad/ $\sqrt{\text{Hz}}$
200 MHz Sideband	$2\text{x}10^{-3}$ rad/ $\sqrt{\text{Hz}}$
Laser Frequency Locking	$1\text{x}10^{-13}$/ $\sqrt{\text{Hz}}$
Dynamic Range	10^9
Optical Telemetry	1400 bits/s

On the master S/C the interferometer electronics will measure the difference in the arm lengths. On the far S/C the interferometer electronics will monitor the outgoing laser beam for slow fluctuations in the frequency lock. This information can either be used to drive an actuator to remove this additional noise source, or this information could be passed back to the master S/C for use in the laser noise subtraction algorithm.

It is expected that communication between the three S/C's will be via the laser beams with a bandwidth sufficient to transmit 1400 bits/s. Thus the interferometer electronics should be able to handle these signals and pass them onto the S/C controller.

7.1.6.2 System Design

The interferometer electronics needs to measure the beat signal produced by the incoming laser beam and the local reference to a high precision and with a wide bandwidth. The highest quantum efficiency of commercially available photodiodes at 1064 nm is provided by an InGaAs photodiode. Other materials may become available before the launch of LISA, which could improve the quantum efficiency slightly but InGaAs will be taken as the baseline in this study.

The interfering beam will be detected by a wide bandwidth InGaAs quadrant photodiode. The diameter of the photodiode is limited by the internal capacitance, which for a 200 MHz bandwidth limits the photodiode to 0.5 mm diameter. The quadrant structure is required to measure the tilt of the received wavefront.

The signals from the four quadrants of the photodiode are then amplified. The baseline design is to use four wide bandwidth transimpedance amplifiers. As wide bandwidth electronics are not readily available for space applications this has limited the number of available devices. At present a Maxim MAX3266 amplifier is the baseline, but this device is less than ideal and alternatives are still sort. The signals are then passed through a series of low noise amplifiers to provide a signal of about 1 V peak to peak for the

phase measurement electronics. At this point the signals are split off into the various measurement channels. The basic design of the front-end electronics is shown below.

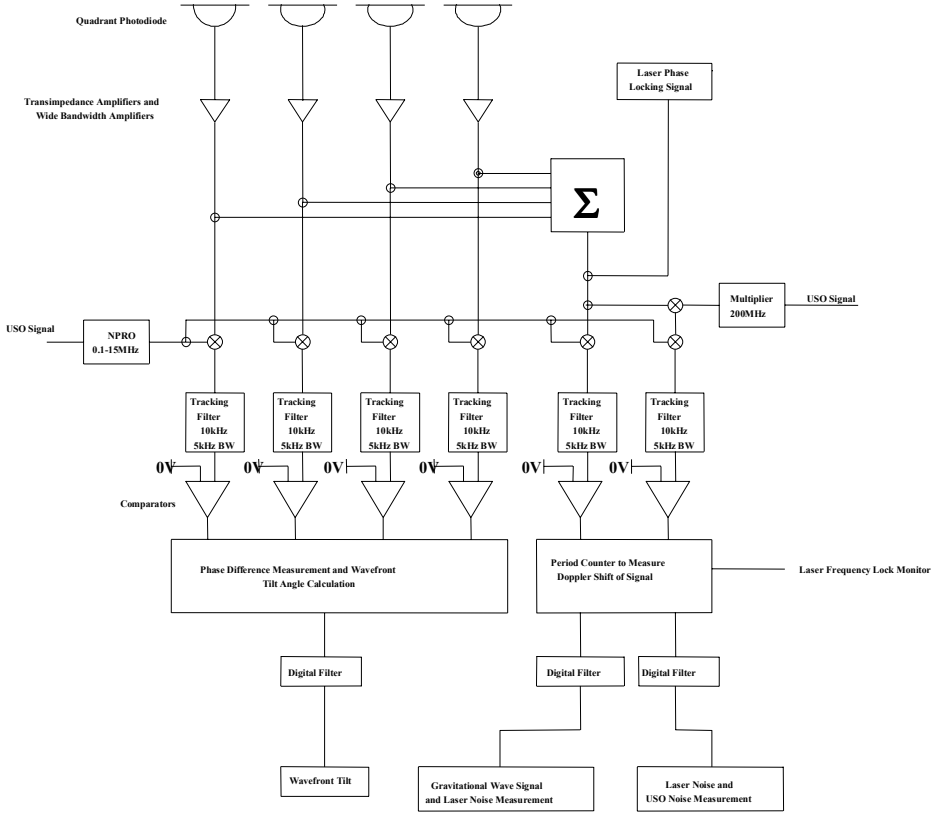

Figure 7.1-51 - The schematic layout of the interferometer electronics.

In order to measure the phase to the necessary accuracy and with the desired dynamic range, the signal from each optical heterodyne detector is beat again against a suitable reference frequency, which are generated from the USO using Direct Digital Synthesis. The reference frequencies are chosen to remove the variation in the Doppler frequency and to place the final beat frequencies in the range 8 to 12 kHz. This beat frequency is chosen to minimise the clock frequency required for the phase measurement, and to enable the laser frequency noise to be reduced with a filter to below the photodiode shot noise. The performance of a 32-bit Direct Digital Synthesiser (DDS) limits the precision with which the Doppler frequency can be removed, hence a comb of frequencies is used rather than trying to lock to the incoming signal. A tracking filter is then used to remove phase noise above 1 kHz in order to prevent aliasing of the laser phase noise into the measurements. Anti-aliasing filters will be required before and after the tracking filter. This design is shown schematically in Figure 7.1-51.

The resulting signals are then passed through a comparator and turned into digital signals. The phase meter then measures the number of the USO clock pulse between successive zero-crossings giving the total number of clock pulses per period. This makes the phase measurement the phase electronics insensitive to gain variations in the front-end electronics. The results are then digitally filtered to remove phase variations at frequencies above about 1 Hz, and the data set is reduced to a set of periods every 0.5 s. The baseline phase meter design is shown below. The phase meter must also calculate the current

Doppler frequency and send a feedback signal to the Numerically Programmable Oscillator (NPO), to ensure that the beat frequency doesn't deviate outside the measurement bandwidth.

Alternative Phase Measurement Schemes

To minimise the sensitivity of the phase measurement to temperature variations a zero-crossing measurement must be employed. Otherwise the measurement would be voltage sensitive and this would introduce errors due to changes in gain.

Thus there seem to be two options, a totally digital phase lock loop, or a combination of digital and analogue phase lock loop. Both of these options need to be studied to assess the sensitivity of the measurement to thermal or voltage drifts, but they may prove to have some qualities that are advantageous.

7.1.6.3 Noise Budget

Additional noise can be added into the measurement in a number of ways, for example excessive dark current in the photodiode, or thermally driven phase changes in the analogue electronics. The shot noise from the quadrant photodiode is equivalent to a time delay of 5 ns any thermally driven time delay must not vary by more than 0.1 ns. A detailed noise budget for the full phase meter has been calculated. The calculations showing what error contributions can be expected from the different components of the interferometer electronics are presented below.

Photodiode Error Budget

Errors in the measurement of the distance of the arm length can be introduced in a number of ways in the photodiode. Since the signal levels are relatively low care must be taken that the thermal dark current noise in the photodiode does not increase to a level where it is comparable to the shot noise. The 0.5 mm diameter quadrant photodiode will have low dark currents, <1 nA, at the begin of life, which will increase to about 100 nA after exposure to 10 krad of radiation. In both cases the thermal noise is well below the shot noise from the received radiation.

The transimpedance amplifier is also a very low noise one at beginning of life, but radiation test need to be performed to see have this behaviour alters with exposure to radiation. The contributions from the later stages of gain have little effect once the signal has been initially amplified. The noise budget for the front-end electronics is shown below.

Table 7.1-20 - Interferometer front-end electronics error budget.

Noise Component	Measurement Noise pm/$\sqrt{\text{Hz}}$
Shot Noise	10.05
Photodiode	0.03
Transimpedance Amplifier	0.5
Additional Gain Stages	0.01
Total	**10.06**

The calculated error budget has highlighted a number of requirements that must be met if the interferometer electronics is to measure the distance in one arm to 11 pm/$\sqrt{\text{Hz}}$.

If the wavefront on the interfered beam is tilted by a large angle the beat signal will become blurred. To stay within the distance measurement error budget a maximum beam tilt of 1.5 μrad is allowable.

The thermal and electrical requirements for the interferometer electronics can be split into two sections, thus items on the optical bench and thus items contained inside the electronics box. These requirements are shown below.

Table 7.1-21 - Thermal and electrical requirements for the optical bench environment.

Component	Voltage Requirement @ 1mHz	Temperature Stability @ 1mHz
Photodiode	$8.0\text{x}10^{2}$ V/$\sqrt{\text{Hz}}$	$6.0\text{x}10^{2}$ K/$\sqrt{\text{Hz}}$
Transimpedance Amplifier	$2.8\text{x}10^{-6}$ V/$\sqrt{\text{Hz}}$	$2.2\text{x}10^{-3}$ K/$\sqrt{\text{Hz}}$

Analogue Electronics Error Budget

If a filter of 100 Hz bandwidth were to be used the signal would have to be reduced by a factor of 100 at 100 Hz to keep the noise level at the level of the quadrant photodiode shot noise. This modest level of filtering must imply that noise introduced due to changes in the shape of the pass band must be ignorable in comparison to thermally driven phase changes or time delays.

The typical thermal behaviour of an analogue filter is that the centre frequency of the pass band will change by ±5 ppm/°C. The temperature stability for the electronics to be specified such that any phase shifts introduced by changing the centre frequency are much less than the phase measurement sensitivity.

Care is need when altering the centre frequency of the tracking filter as this could introduce phase errors. The centre frequency is determined by a 32-bit DDS chip clocked with the 10 MHz USO signal. If there is one change in frequency bit this corresponds to a change of $3\text{x}10^{-8}$ rad, which at 1 mHz corresponds to $9.8\text{x}10^{-6}$ rad/$\sqrt{\text{Hz}}$. This could be more of a problem for the demodulation of the received signal. If the reference frequencies were separated by less than about 160 Hz, the demodulation reference signal would have to be altered with a period less than 1000 s. This could introduce an error signal into the measurement band.

Table 7.1-22 - Interferometer analogue electronics error budget

Noise Component	Measurement Noise pm/$\sqrt{\text{Hz}}$
Mixer	0.0
Filter	0.5
Total	**0.5**

Table 7.1-23 - Thermal and electrical requirements for the components in the electronics box.

Component	Voltage Requirement @ 1mHz	Temperature Stability @ 1mHz
Filter	$2.4\text{x}10^{-5}$ V/ $\sqrt{\text{Hz}}$	$1.2\text{x}10^{-3}$ K/ $\sqrt{\text{Hz}}$
Comparator	$4.0\text{x}10^{-6}$ V/ $\sqrt{\text{Hz}}$	$1.0\text{x}10^{0}$ K/ $\sqrt{\text{Hz}}$
Phase Electronics	$4.0\text{x}10^{-1}$ V/ $\sqrt{\text{Hz}}$	$4.0\text{x}10^{0}$ K/ $\sqrt{\text{Hz}}$

Phase Measurement Error Budget

The present design for the phase electronics measures the time between zero crossing. To provide the timing signals the input sinewave is converted into a digital signal via a comparator. If there are changes in the reference voltage or temperature driven changes in the time delay they will introduce additional noise into the measurement. Also it is assumed that the input sinewave will have an amplitude of 0.5 V peak to peak. Thus the following specifications for the comparator can be derived.

Table 7.1-24 - Phasemeter requirements.

	Voltage Stability @ 1mHz	Temperature Stability @ 1mHz
Propagation Delay	0.1 V/$\sqrt{\text{Hz}}$	0.2 K/$\sqrt{\text{Hz}}$
Reference Voltage	$2\text{x}10^{-5}$ V/$\sqrt{\text{Hz}}$	—
Offset Voltage Drift	—	0.5 K/$\sqrt{\text{Hz}}$

The period of the incoming signal is then obtained by counting the time between the zero-crossings, the time base being supplied by the USO clock. If the signal being measured is at 10 kHz and the timing clock is operating at 10 MHz, then the incoming signal should be measured to $6\text{x}10^{-5}\text{rad}/\sqrt{\text{Hz}}$, which is equal to the quadrant photodiode shot noise level. This situation is unacceptable. Thus either the USO clock must be multiplied up to so higher frequency, about 100 MHz, or the incoming signal must be measured at a lower frequency like 1 kHz. The former option is consider the baseline at the moment as the lower measurement frequency may cause aliasing problems.

Table 7.1-25 - Interferometer electronics error budget

Noise Component	Measurement Noise pm/ $\sqrt{\text{Hz}}$
Wide-bandwidth Front-end	10.06
Analogue Electronics	0.5
Phasemeter	1.0
Total	**10.12**

200 MHz Signal Error Budget

Assuming that 20% of the transmitted laser signal is contained in the two 200 MHz sideband. If a single sideband is measured the phase of this signal can be measured to $4.8\times10^{-4}\,\mathrm{rad}/\sqrt{\mathrm{Hz}}$, which should be sufficient for the USO noise cancellation scheme. Though it is assumed that this first order calculation is sufficient, a full model of the laser and USO noise extraction scheme is required.

Pointing Stability Error Budget

Taking the signals from the four quadrants of the photodiode they can be combined in such a way that the tilt angle of the incoming wavefront can be measured. The minimum tilt that can be measured is limited by the shot noise on the individual quadrants, assuming a telescope magnification of 600 an angle jitter of 0.1 nrad/$\sqrt{\mathrm{Hz}}$ can be measured. The DC component must be measured at a lower frequency, but not so low that the measurement is dominated by the laser phase noise, e.g. at 1 Hz the laser phase noise would limit this measurement to 1 rad rms. So taking 500 Hz as the measurement frequency, i.e. inside the tracking filter bandwidth, a minimum DC pointing of 20 nrad rms can be observed.

7.1.6.4 Power Budget

The power requirements for the interferometer electronics have been estimated, and the dissipations at the optical bench and inside the electronics box are presented below. An estimate of the maximum power dissipation, for example during data transfer, and the minimum dissipation are presented. The significant difference in powers would need to be confirmed once the electronics hardware has been built, and this data can then be input into the thermal design to assess the impact of the variable dissipation.

Table 7.1-26 - Interferometer Electronics Power Budget

Component	Number	Power Dissipation per Component (W)		Total Dissipation (W)	
		Max	Min	Max	Min
Quadrant Photodiode	1	0.01	0.01	0.01	0.01
Transimpedance Amp.	4	1.13	1.13	4.52	4.52
Wide band amp.	4	0.30	0.30	1.20	1.20
Splitter 2:1	6	0.0	0.0	0.0	0.0
Combiner 4:1	1	0.0	0.0	0.0	0.0
Filter	7	0.12	0.12	0.84	0.84
Comparator	7	0.08	0.08	0.56	0.56
FPGA	5	1.00	0.10	5.00	0.50
Multiplier	1	0.10	0.10	0.10	0.10
NPO	1	1.46	1.46	1.46	1.46
Data Link	2	1.18	0.10	2.36	0.20
Voltage Reference	10	0.03	0.03	0.30	0.30
Total Optical Bench (W)				4.5	4.5
Total Electronics Box (W)				11.9	5.2
DHU (W)				10	8
Total (W)				26.4	17.7

7.2 Payload Control Design

Scope

The general description of the spacecraft AOCS is contained in section 5.4 of this report, including the definition of the AOCS overall architecture, modes, sensors/actuators, and the pointing acquisition and tracking.

This section presents the results of the study activities addressing the Instrument's Inertial Sensor, the payload control mechanisms and the Drag-free & Attitude Control (DFAC) aspects, i.e. specifically:

- The review of the Inertial Sensor requirements and alternative design options and description of the proposed baseline design and expected performance of the ONERA CAESAR device
- The design and analysis of the payload control mechanisms, the fibre positioner and the telescope steering mechanism
- The assessment through detailed simulation of the Drag-free & Attitude Control System (DFACS) performance during the operational phase, one of the key contributors to the scientific performance.

7.2.1 Inertial Sensor

7.2.1.1 General overview

In the LISA mission, three spacecraft orbit in a triangle formation with a dedicated interferometric Laser link between them. Each spacecraft contains two inertial sensors, at the end of each laser from/to the two other LISA spacecraft. The proof-masses of the inertial reference sensors reflect the light coming from the YAG laser and define the reference mirrors of the interferometer arms. The same proof-masses are also used as inertial references for the drag-free control of the spacecraft which constitutes a shield to external forces.

The proposed sensor (commonly called CAESAR: Capacitive And Electrostatic Sensitive Accelerometer Reference) can be derived from existing space qualified electrostatic accelerometers already developed for the ESA projects, like the GRADIO accelerometer [13] or the ASTRE sensor delivered to ESTEC for the micro-gravity spacelab survey [14]. The last one has flown successfully three times on board the COLUMBIA shuttle in 1996 and 1997.

A first optimisation [15] of the inertial sensor has been performed under the ESA contract 12563/97/NL/MS in 1998 by taking into account in one hand the mission requirements and in the other hand the expected quality of the sensor mechanical core and the electronics function performances. From this design, the evaluation of the performance was detailed. The instrument interfaces and budgets (mass, volume, power) were also derived. However this design was performed without the study of the drag-free system and the implementation constraint considerations.

In the present study, some design assessment has been performed to take into account the study of the spacecraft drag-free control with two sensors performed by Matra Marconi Space and the design of the optical bench performed by Alenia.

7.2.1.2 Inertial sensor description

The sensor is composed of a Gold-Platinum alloy Proof-mass of 1.3 kg kept at the centre of a set of electrode plates (Figure 7.2-1) by the mean of electrostatic forces. Four plates are used for the proof-mass position and attitude measurements and control with respect to the cage mechanically linked to the satellite frame. The two other plates have an hole at their centre to allow the passage of the laser beam towards the proof-mass.

Six capacitive sensors are used to finely measure the position and attitude of the proof-mass. The capacitive sensors are derived from previous space qualified sensors developed in ONERA. A specific digital controller ensures the servo-loop of the suspended proof-mass by driving the control voltages applied on the electrodes (Figure 7.2-2). During the LISA measurements, the position and attitude of each proof-mass (six data) and its acceleration in translation (except for the Laser beam direction) and rotation(five data)are available on the serial bus of the instrument linked to the micro-controller of the satellite.

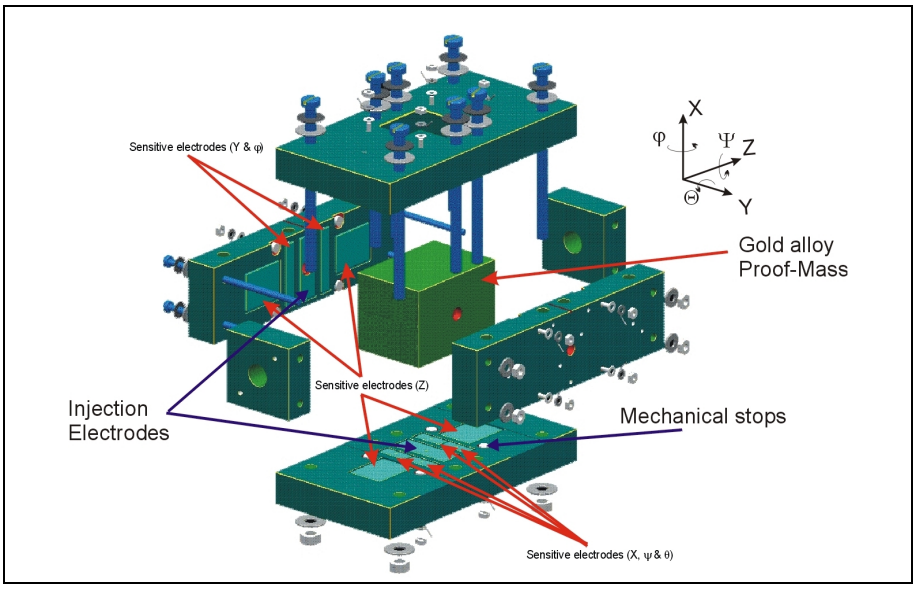

Figure 7.2-1: Core of LISA Inertial Sensor

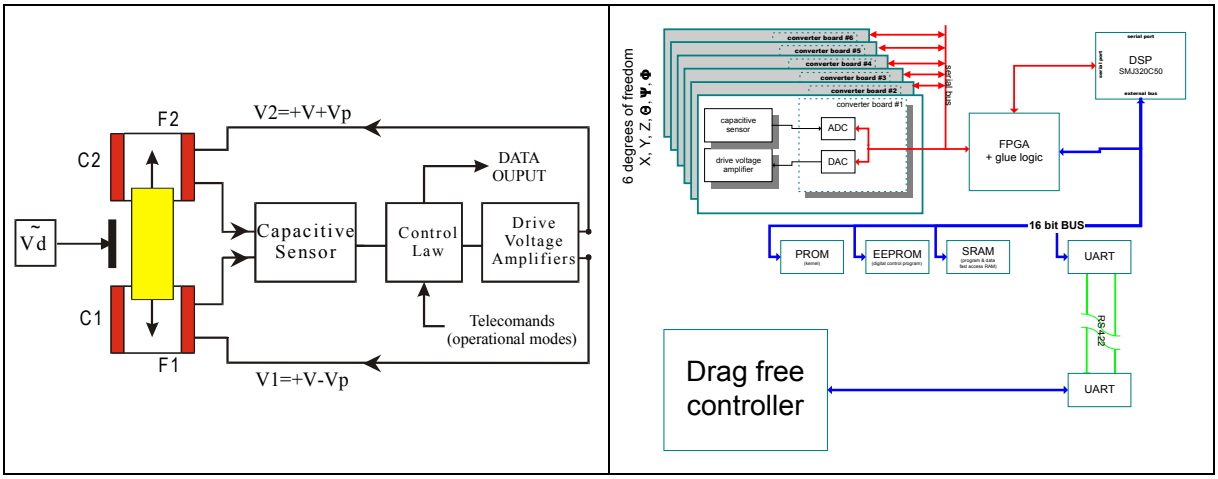

Figure 7.2-2: One sensor control loop channel and digital controller architecture.

Thanks to the digital control loop, the sensor can provide several type of operational mode with increased sensitivity :

- Initial Mode (IM) : for the initialisation of the proof-mass suspension when the drag-free controller is off.
- Accelerometer Mode (AM) : for the acquisition of the Drag-free Mode and s/c attitude control, on flight calibrations.
- Drag-Free Sensor Mode (DM) : intermediary mode, like AM with reduced control loop bandwidth.
- Measurement Mode (MM): for the LISA experiment, the drag-free controller must be on in this mode.

7.2.1.3 Design Assessment study

7.2.1.3.1 Low back-action readout system

In view of minimising the disturbance forces on the proof-mass, the proof-mass motion readout system must provide a low back-action and stiffness to the inertial sensor. The possibility of an all-optical has been discussed because of its promising “no back-action” potential.

However, concerning the actuation with light pressure, the induced complexity of the device increases its risk. Moreover the initialisation of the sensor needs forces far beyond the possibility of the pressure induced by the envisaged Laser light (roughly a dc value of a few $10^{-8}ms^{-2}$ has to be applied on the Proof-Mass before DFAC operation).

Now, concerning the all or partial optical read-out, the absolute position of the proof-mass, at least at the initialisation, must still be measured by an external device like a capacitive position read-out. Also, the position resolution is quite a challenge at very low frequency (typically 10^{-4}Hz) for the classic interferometric devices where a nanometer/$\sqrt{}$Hz is needed. Another difficulty appears with the ground calibration or the test of such a sensor. Because the proof-mass cannot be levitated and is then a few tens of µm far from its centred flight position, the reflecting proof-mass cannot be used for the adjustment of the interferometers elements and mirrors. At last, the optical read-out needs additional electronics and then additional power, mass and volume.

As a baseline the capacitive read-out must be considered for the normal operation and a measurement mean of acceleration for the Drag-Free and Attitude Controller (DFAC). However the possibility of a complementary Proof-Mass position readout in the main direction of the Laser light might be analysed in future studies by using the available data output from the existing Laser beam in the optical bench.

Other solutions to reduce the electrostatic back-action on the sensor have been envisaged in this study with a main concern coming from the DFAC operation during the mission. The considered stiffness (see Table 7.2-1 and Table 7.2-2) in the Pre-Phase A study didn’t seem to give sufficient margins for the stability of the loops. The adopted philosophy here is to use the information coming from both sensors to control the s/c. At very low frequency, typically bellow the lowest frequency of the measurement bandwidth (10^{-4} Hz), the Proof-Mass is electrostatically suspended along the laser beam direction for each sensor. Above 10^{-4}Hz, the Proof-mass is free floating. For the transverse direction, the control

bandwidth can be greater in order to include the higher intrinsic electrostatic negative stiffness frequency and to damp its effect. To summarise there is a “slow-damping” of the Proof-mass.

Table 7.2-1 : Inertial Sensor Performances in position sensing (Pre-Phase A design).

Measurement Mode		
Position	**Gain**	**Max Range**
X	0.5 V/µm	20 µm
Y	0.5 V/µm	20 µm
Z	0.08 V/µm	50 µm
	Resolution	**Stiffness**
X	$5\times10^{-12}\,mHz^{-1/2}\sqrt{1+\frac{5\times10^{-2}\,Hz}{f(Hz)}}$	$5x10^{-3}$N/m
Y	$5\times10^{-12}\,mHz^{-1/2}\sqrt{1+\frac{5\times10^{-2}\,Hz}{f(Hz)}}$	$5x10^{-3}$N/m
Z	$2\times10^{-10}\,mHz^{-1/2}\sqrt{1+\frac{10^{-3}\,Hz}{f(Hz)}}$	$3x10^{-7}$N/m

Table 7.2-2: Inertial Sensor Performances in attitude sensing (Pre-Phase A design).

Measurement Mode		
Attitude	**Gain**	**Max Range**
θ , ψ, φ	~ $5x10^{-3}$ V/µrad	2 mrad
	Resolution	**Stiffness**
θ , ψ, φ	$<10^{-9}\,radHz^{-1/2}\sqrt{1+\frac{5\times10^{-2}\,Hz}{f(Hz)}}$	$4x10^{-5}$N.m/rad

From this design, there is enough flexibility to enlarge the gaps between the Proof-Mass and the electrodes (2mm instead of 1.5mm for the main axis, 2mm for the transverse axis instead of 300 µm) in order to reduce the stiffnesses (see Table 7.2-3 and Table 7.2-4).

Table 7.2-3: Rough estimation of the Inertial Sensor position performances with a slight modification of the design.

Measurement Mode		
Position	**Gain**	**Max Range**
X or Y	0.07 V/µm	50 µm
Z	0.06 V/µm	50 µm
	Resolution	**Stiffness**
X or Y	$4.5\times10^{-10}\,mHz^{-1/2}\sqrt{1+\frac{3\times10^{-4}\,Hz}{f(Hz)}}$	3x10^{-5}N/m
Z	$5\times10^{-10}\,mHz^{-1/2}\sqrt{1+\frac{3\times10^{-4}\,Hz}{f(Hz)}}$	5x10^{-8}N/m

Table 7.2-4: Rough estimation of the Inertial Sensor attitude performances with a slight modification of the design.

Measurement Mode		
Attitude	**Gain**	**Max Range**
θ , ψ, φ	~ 7x10^{-4} V/µrad	10 mrad
	Resolution	**Stiffness**
θ , ψ, φ	$<10^{-7}\,radHz^{-1/2}\sqrt{1+\frac{3\times10^{-4}\,Hz}{f(Hz)}}$	3x10^{-7}N.m/rad

Thanks to the concept used for the capacitive sensing with sliding electrodes instead of gap varying electrodes, the main axis remains much less stiff than the transverse axis although with the same electronics parameters and performances. Increasing the gaps raise then the problem of coupling between axis and of non-linearities. The larger is the gap, higher is the non-linear term of the electrostatic actuator in the transverse direction (not the case for sliding electrodes schema) and then greater is the sensitivity to out of band frequency disturbances (i.e aliasing) [16]. A trade-off should be addressed in future studies to optimise the sensor configuration with respect to the DFAC operation and the minimisation of stiffnesses, couplings and non-linearities. This trade-off has also to consider new constraints coming from the laser acquisition for which a tilt and a displacement of the Proof-Mass should be envisaged. In the on-going Phase A study the needs coming from the laser acquisition are of the order of 175µrad for the Proof-Mass tilt and of 10µm for its displacement. This huge value of 175µrad is actually greater than the estimated coupling factor. Such biases of the Proof-Mass position and attitudes are of course possible with CAESAR but has to be analysed with respect to its compatibility with the required performances.

7.2.1.3.2 Material choice considerations

In the optimal design, the material choice for each part of the inertial sensor should be important. This choice can be mainly made at two levels : at the Proof-Mass level and at the electrode level. For the Proof-Mass, a specific alloy of Gold and Platinum (10% of Pt) is preferred because of its high density, allowing a better rejection of disturbing forces, and because of its low magnetic susceptibility. This last one can be an important issue if some ferromagnetic materials are used nearby the sensor.

For the electrodes, ONERA has a long experience of using both metallic or non-metallic materials. In fact in the case of high sensitive accelerometers, it is preferable to use materials with very low CTE in order to preserve the geometry stability and in particular the scale factor stability. That's why ULE has been preferred for the last developed sensors. For Lisa, as no measurement is required for the main axis, only the geometry stability is required and can be matched with various materials thanks to the good thermal environment.

However, ULE material can be machined with much better accuracy than metallic materials. A specific ultrasonic tool was developed in ONERA in order to produce very accurate 3-D machining of ULE pieces (~a few microns) on the contrary of metallic pieces machined with one order of magnitude less accurate.

Actually, three options can be considered for the electrode supports (see Figure 7.2-3): a gold coated ULE, a metallic support with ceramic and metallic coatings or a metallic assemblage.

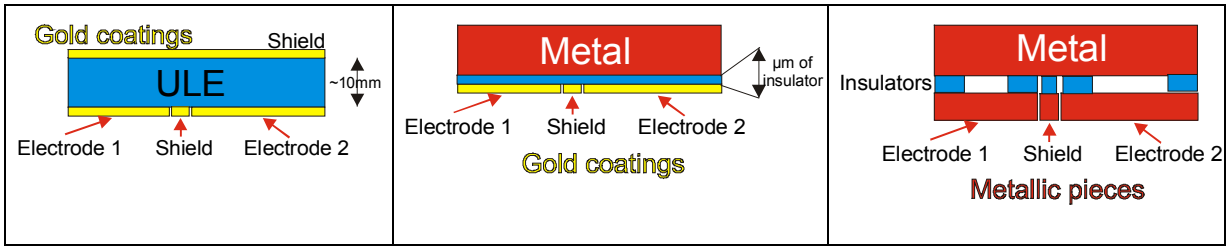

Figure 7.2-3: Schema of possible electrode implementations

Concerning the last one, although a good thermal material, in order to minimise all thermal gradients, the metallic electrode assembly appears to be more complex to accommodate. For example, in the case of CAESAR 48 electrodes are necessary to control the Proof-Mass 6 degrees of freedom and its electrical charge. With ULE plates, a metallic coating is deposited and grooved to realise several electrodes per plate. Here only 4 plates are necessary for the mounting. With metallic electrodes, some insulate spacers and metallic shields are needed between the electrodes. It is then nearly 60 metallic and non-metallic pieces which must be assembled instead of 4 with very high accuracy. The parallelism and orthogonality of the pieces can generate couplings and biases in the position measurements. Moreover the default of symmetry of the geometry induced directly by the accuracy of the mounting gives rise to electrostatic stiffnesses. A geometry achievement default of nearly 5µm has been assumed for the design of CAESAR giving a few 10^{-4} coupling factor between the axes or dissymetry defect. This requirement of 5 µm can be easily met by ULE ultrasonic machining and polishing. At last one of the advantage of metallic material over insulators is the low charging property. But this advantage could be a little bit reduced by the use of the necessary insulate spacers.

The alternative design with metallic pieces coated with a ceramic insulator appears to be simpler to accommodate. As for the gold coated ULE, the techniques and quality of deposition are quite the same

enabling good achievement accuracies. However one of its major draw back is the important parasitic stray capacitance and its stability which can reduce excessively the capacitive sensor performances.

7.2.1.3.3 Mechanical update

From the Phase A study on the Optical Bench performed by ALENIA, some new constraints for the integration of the sensor have to be taken into account :

- Mechanical interfaces
- Mass of the sensor to be minimised with respect to mechanical stress at launch
- Compatibility of the sensor housing volume with the Optical Bench
- Implementation of Electrical interfaces
- Discharging device interface (optical fibre)
- Vacuum system
- Blocking mechanism
- Gravity balance masses to be integrated on the Optical bench

The main modification of the design with respect to the pre-Phase A study is the reduction of the volume of the sensor housing placed in the dedicated Optical Bench hole. The size of the box should be of the order of 170x120x120 mm^3 (see Figure 7.2-4, Figure 7.2-5 and Figure 7.2-6).

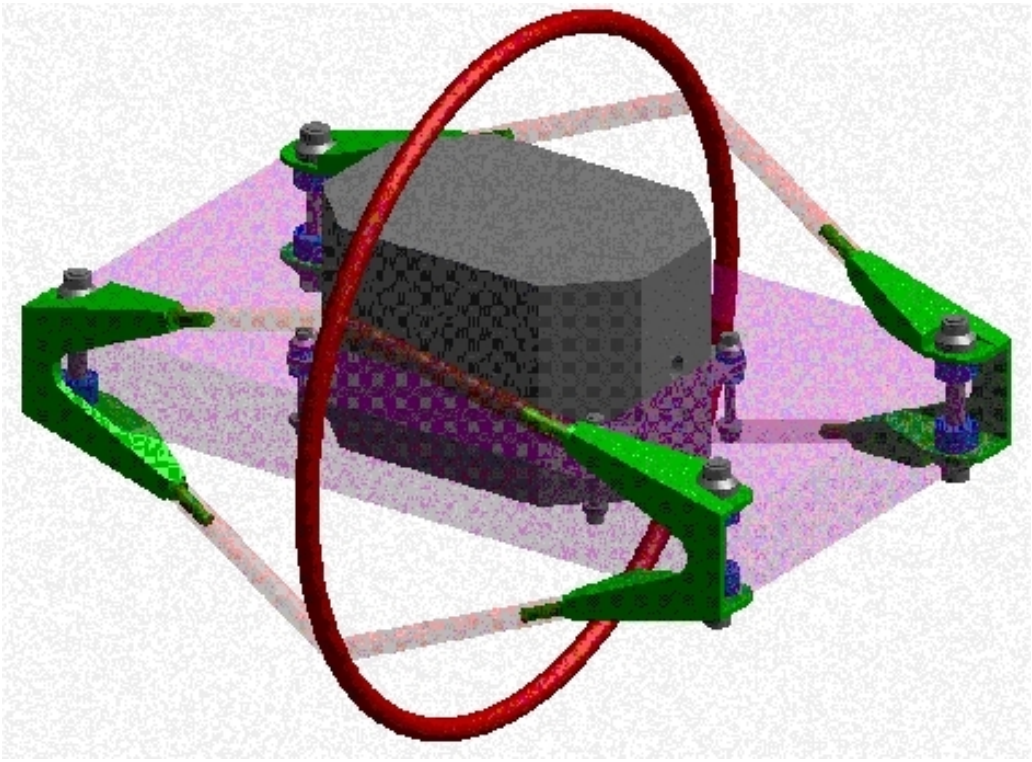

Figure 7.2-4: Sensor implementation in the optical bench

A first LISA sensor prototype has been produced under CNES contract with reduced performances compatible with a ground operation of the sensor. The sensor core has been designed and produced with the LISA concerns for the electrode repartition and function, the Proof-Mass sizes, the implementation of a discharging optical fibre and the implementation of a re-usable caging mechanism (Figure 7.2-6). This prototype is still compatible with the new constraints brought by the Phase A study and should help in future experiments to test the coupling and Proof-Mass tilt and displacement bias impact on performances.

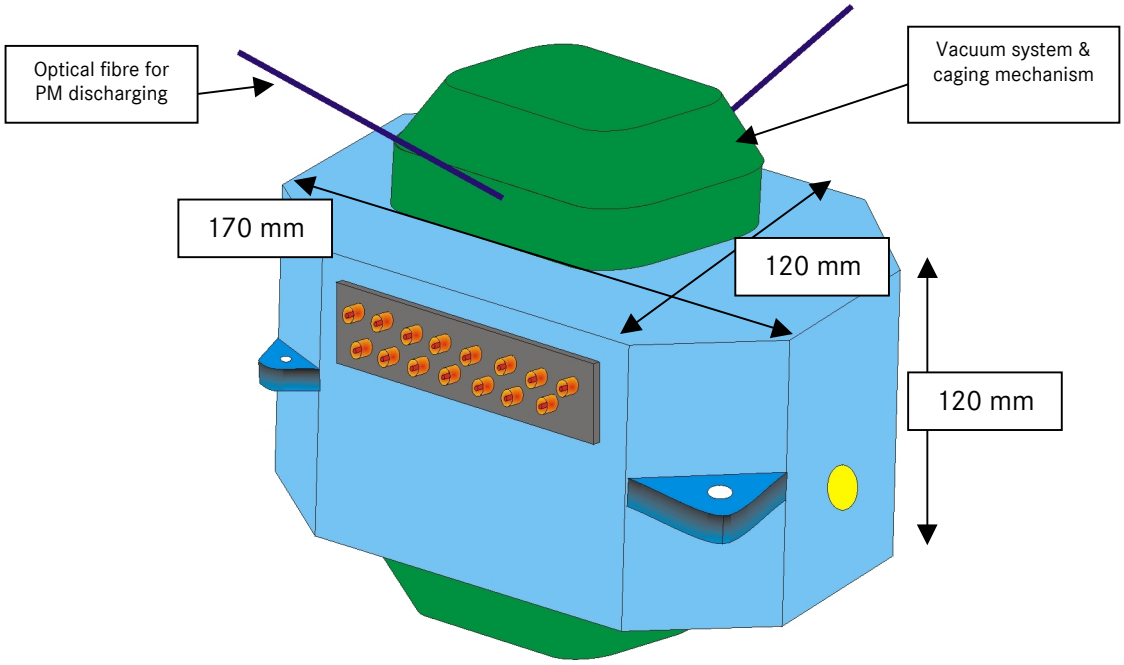

Figure 7.2-5: Sensor vacuum housing overview

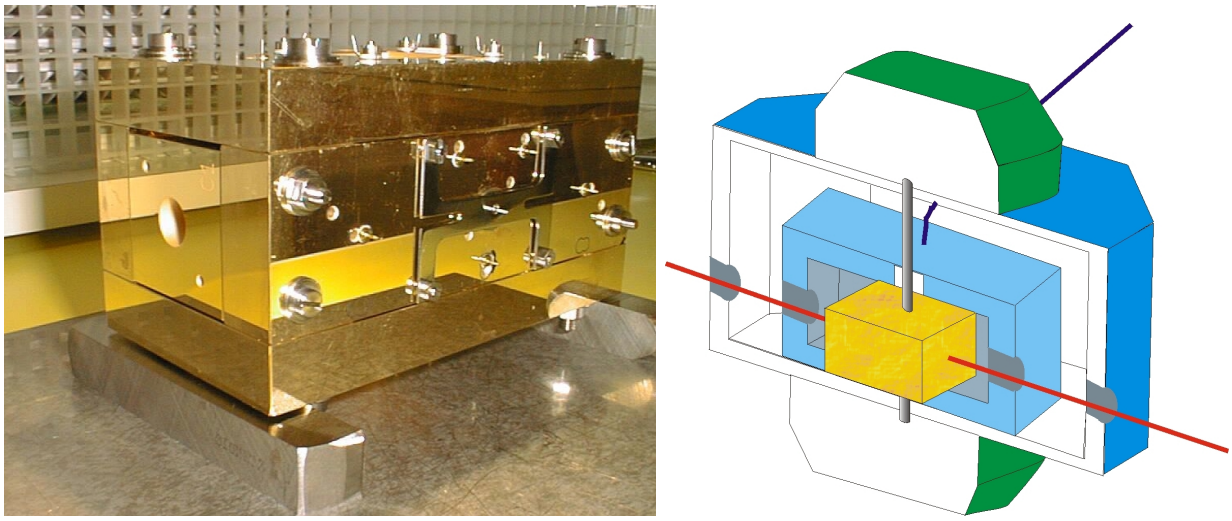

LISA sensor prototype (ONERA's proprietary) Sensor core overview

Figure 7.2-6: Sensor Core

7.2.1.4 Proof-Mass caging mechanism

The optimal design must take care of the caging mechanism and of the charging device. On the contrary of the previous developed accelerometers, ASTRE [14], STAR or SuperSTAR, the proof-mass of the sensor must be clamped during the launch phase to prevent damages on the sensor core with a moving proof-mass.

The caging mechanism was also envisaged to be used during unexpected events, such as solar flares producing excessive charging. In fact the occasional mass-recaging should not be necessary. In case of an increased external force, it would be better to switch the sensor to a safe mode (DM, AM or IM) depending on the acceleration which should however not exceed the range of the sensor Initialisation Mode. There are several advantages. The sensor doesn't need to be restarted and the laser focusing could not be totally lost. Second, the re-acquisition of the full Drag –free operation could be easier and quicker. In the case of excessive charging of the proof-mass not sustained by the discharging device, it could be envisaged to discharge the Proof-mass by contact on the mechanical stops.

The design drivers for this system should be the damping of launch vibrations, the minimisation of eventual parasitic forces induced for example by electric field distortions. This last one is achieved if the clamping mechanism is far from the Proof-Mass. This system must also ensure that the proof-mass properties are not spoilt during the launch or other mission phase.

A first study has been undertaken to evaluate different systems for the Proof-Mass caging. Two of them are well suited for the LISA needs: the paraffin actuator and the jack screw stepper motor. The last one is being tested on the LISA sensor prototype developed for CNES.

Metallic bellows

This is the simplest system. A bellow linked to the vacuum housing (Figure 7.2-7) is pushing a finger on the Proof-Mass on ground because of the differential pressure between the housing and the external. It is then possible to dimension a hole in order to liberate the bellow with a calibrated delay when the outside pressure goes down to space vacuum after the launch. The main drawback is the difficulty to re-cage the proof-mass on flight as it is needed to foreseen a pressurised reservoir to rearm the mechanism. However this system is compatible with 4°K operation.

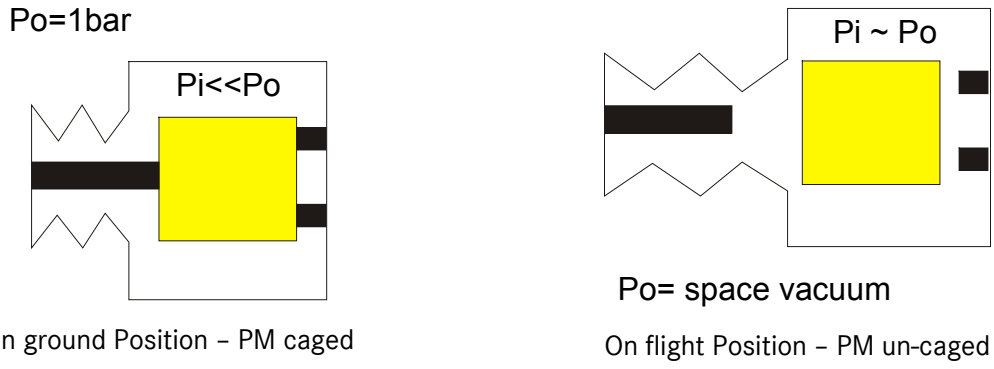

Figure 7.2-7: Principle of Proof-Mass caging with metallic bellows

Shape memory alloy

This system is “space qualified”. Most of the system are nevertheless “one shot” system unless a bulky rearming dedicated tool is implemented. If no re-caging is necessary, this system could be used with minimum mass/power/volume requirements.

Piezoelectric actuator

This system can be re-used and can be found in a space qualified version. Its simplest version enables only little displacement. The main drawback is in fact the electrical power consumption in the blocked position.

Paraffin actuator

- This one is already produced for space applications and is used for example with the FEEP thrusters developed by CENTROSPAZIO (see Figure 7.2-8). The two position latching actuator version of this device doesn’t need electrical power to maintain a position (blocked or un-blocked) but only some to go forward or backward.

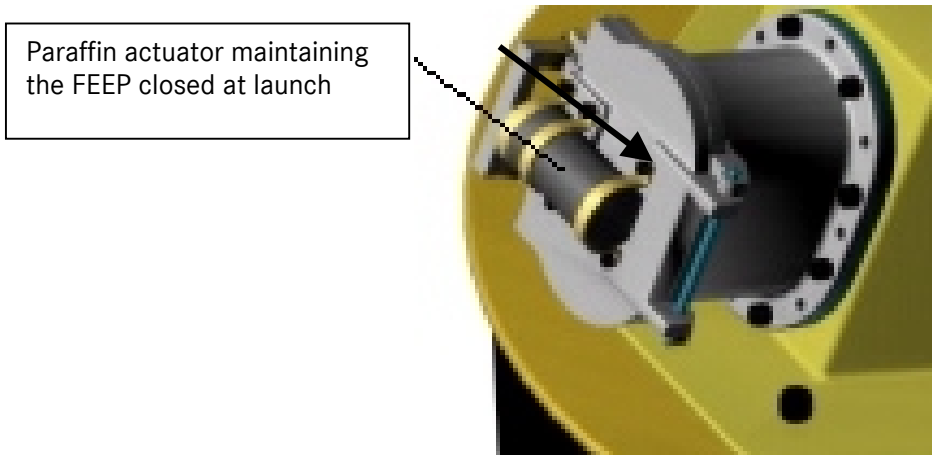

Figure 7.2-8 : Paraffin actuator used for the FEEPS of Centrospazio

Electrical Jack screw stepper motor:

This motor enables large displacement capability (11mm) with high accuracy (few microns): see Figure 7.2-9. Developed by Newport, it can be provided with vacuum compatibility operation. With 9kg maximum load, no power consumption at rest and reversible actuation, this system fulfils the needs of the LISA sensor. The main drawback could be its size in the direction of the load force (120mm). A laboratory version of the actuator is being tested within CNES contract in order to define the necessary loads preventing Proof-Mass damages under simulated launch vibrations. The LISA sensor prototype has been defined to allow a 5 mm pin to cage the Proof-Mass (Figure 7.2-10).

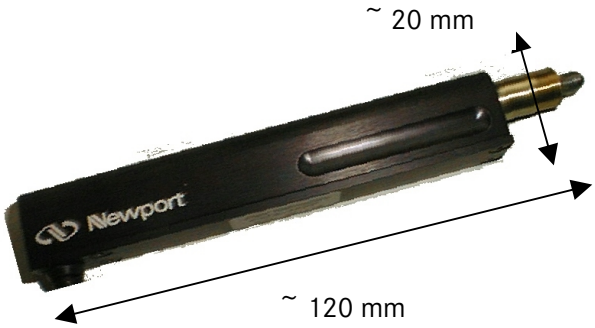

Figure 7.2-9: Stepper actuator

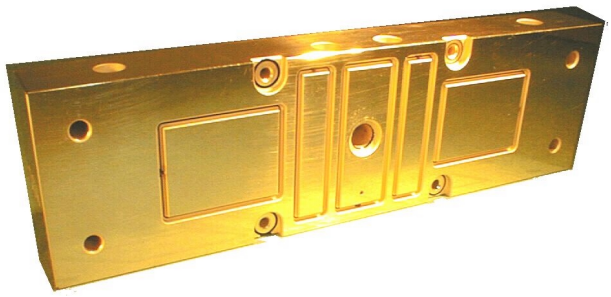

Figure 7.2-10 : Electrode plate with a hole for the caging mechanism finger (LISA sensor produced under CNES contract)

7.2.1.5 Measurement available output modes

The CAESAR sensor is derived from the previous developed electrostatic accelerometers with the benefits of technology improvements concerning the reduction of stiffness and of electronics improvements concerning the use of a digital controller for the sensor loops.

From the designed LISA inertial sensor configuration, it is possible to estimate the performance of such a sensor when it is used as an accelerometer. Due to the good space environment the sensor can enhance acceleration measurements with good resolutions (see Table 7.2-5). This kind of operation can be useful to the initialisation of the DFAC or to the laser focussing adjustment. The following Table 7.2-5 shows a non exhaustive list of possible modes of operation for this type of sensor.

These modes are necessary to start the operation of the sensor as the Drag-free compensation can only operate with the inertial sensor output. At the initialisation or levitation of the Proof-Mass, the s/c is then submitted to dc forces and torques that must be sustained by the sensor :

- 32µN normal to the orbital plane ($Z_{s/c}$ axis)
- 4.5µN in the plane ($X_{s/c}$ or $Y_{s/c}$ axis)
- Transverse torque(about $X_{s/c}$ or $Y_{s/c}$ axis) : 4.2 µNm

The acceleration range and resolution have been estimated on the basis of the Pre-Phase A design and could be revised with the definitive design of the sensor in one hand and with the DFAC needs in the other hand.

The Table 7.2-6 summarises the performances of the inertial sensor in the Measurement Mode by taking into account the Pre-Phase A design configuration. Further studies should deal with optimising the design by taking into account the couplings (intrinsic and through the DFAC), the stiffness and the maximum acceleration range (in translation and in rotation). The Table 7.2-6 gives also the gains and resolution for the angular acceleration actuation and measurement. This last information is useful for the DFAC, which can couple the outputs from the STAR sensors for the attitude measurement and from the inertial sensor for the angular acceleration measurement. The use of a gyro turns to be then not mandatory in the MM phase.

Table 7.2-5: CAESAR modes for DFAC initialisation and operations

Mode	Observation	Function
IM	*Operation as a 6-axis accelerometer* • Max Acc Range ~ 10^{-8} ms^{-2} • Acc Resolution ~ 10^{-12} ms^{-2} $Hz^{-1/2}$ within [10^{-3} Hz - 1 Hz]	• *Initialisation of the Proof-Mass levitation,* • *Drag free controller is off*
ϑ AOCS "ON" to improve s/c attitude stability		
AM	*operation as a 6-axis accelerometer* • Max Acc Range ~ 10^{-9} ms^{-2} • Acc Resolution ~ 10^{-13} ms^{-2} $Hz^{-1/2}$ within [10^{-4} Hz - 0.1 Hz]	• *Drag-free controller initialisation and fine s/c attitude control* • *Calibration of payload sub-systems (feeps, Laser focusing, ...)*
ϑ Drag-Free Controller "ON"		
DM	*operation as a 6-axis accelerometer* • Performances to be defined with respect to DFAC needs	• *Intermediary mode between AM and MM* • *Can be like AM with reduced bandwidth of control*
ϑ Reduction of spurious accelerations within the measurement bandwidth		
MM	*operation as an inertial sensor (5 axis accelerometer)* • Max Acc Range ~ 10^{-10} ms^{-2} • Acc disturbance reduction ~ $3x10^{-15}$ ms^{-2} $Hz^{-1/2}$ within [10^{-4} Hz - 0.1 Hz]	• *Drag-free controller is on with maximum sensitivity*

Table 7.2-6: Accelerometric Performances for the Sensor used as "a free-fall proof-mass".

Measurement Mode	
Acceleration in translation	
Gain of control	
X & Y	$5 \times 10^{-9} ms^{-2}/V$
Z	$6 \times 10^{-11} ms^{-2}/V$
Noise	
X	$10^{-13} ms^{-2} Hz^{-1/2} \sqrt{1 + \frac{10^{-2} Hz}{f(Hz)}}$
Z	$10^{-15} ms^{-2} Hz^{-1/2} \sqrt{1 + \frac{10^{-3} Hz}{f(Hz)}}$
Acceleration in rotation	
Gain of control	
θ , ψ, φ	$5 \times 10^{-7} rads^{-2}/V$ [(1)]
Noise	
θ , ψ, φ	$< 10^{-10} rads^{-2} Hz^{-1/2} \sqrt{1 + \frac{10^{-2} Hz}{f(Hz)}}$ rough estimation to be confirmed

[(1)] The control of all degrees of freedom supposed that it must be applied to the same electrode a voltage composed of one part for the translation control and one part for the rotation control. If the DC applied linear acceleration is $10^{-10} ms^{-2}$ with a $10^{-7} rads^{-2}$ DC angular acceleration, the sensor controller will applied to one couple of electrodes 1.86 Volts (0.2 volts for the rotation and 1.66 volts for the translation) at DC and to other one couple of electrodes the difference 1.46 volts. All rotations are controlled by lateral electrodes.

7.2.1.6 Conclusions

The present study has shown that the proposed design during the Pre-Phase A study [15] was compatible with the Drag Free and Attitude Control System. However, due to the very little margin of the servo-loops stability, it appears preferable to make some slight changes on the sensor core in order to reduce the electrostatic stiffness to values lower than 10^{-7}N/m. This requirement on the stiffness applies also on other sources of stiffness like the gravity gradients.

It was also shown that some modifications of the sensor housing design are necessary in order to accommodate the sensor on the optical bench. Some complementary future studies should be performed to implement the Proof-Mass blocking mechanism and the vacuum system in this new design of the housing.

At last, the study has underlined the interest to use extended functions of the inertial sensor like the operation as an accelerometer for the initialisation of the DFAC system, the biasing of the Proof-Mass position and attitude for the adjustment of the laser focussing or the use of angular accelerations for optimisation of the DFAC.

7.2.2 Payload Optical Control Mechanisms

7.2.2.1 Introduction

Two mechanisms are investigated in this analysis :

- the Fibre Positioner Unit (FPU)
- the Telescope Orientation Mechanism (TOM)

For each mechanism, the following aspects are addressed :

- recall of the main requirements. Based on intermediate recommendations and iterations performed at instrument level, the requirements were updated in the course of the study, mainly concerning the ‘Fibre Positioner Unit’.
- Identification of candidate architectures and technologies
- Identification of key issues
- Selection of promising candidates and illustration of the associated conceptual design.

7.2.2.2 Fibre Positioner

7.2.2.2.1 Initial Configuration

7.2.2.2.1.1 Requirements

The Fibre Positioner Unit (FPU) is requested to provide the following functions :

- scan of the acquisition cone and/or beam defocusing during the acquisition phase.
- switch-off the laser during the acquisition, in order to avoid pollution of the receive signal by the emit signal straylight)
- co-alignment between emission and reception paths, including :
  - correction of long term relative displacement
  - Pointing Ahead by implementing a bias
- Emission path focus correction
- Switch between laser 1 and laser 2.

The FPU is implemented directly in the optical bench. As such, key requirements apply :

- minimize volume ; target is 40 x 40 x 40 mm^3.
- No thermal perturbation to the optical bench. In that respect, permanent dissipation is preferable compared to transient dissipation. In case of permanent dissipation, only very small variations are acceptable ; in case of transient dissipation, only very small power shall be commuted.
- No jitters inducing pointing perturbations.

The performance requirements are summarized figure 4-/1. Based on the telescope optical properties, ±0.05 µrd lateral and vertical motions resolution - output space - correspond to ±0.1 µm at FPU level.

The power dissipation requirements is a key parameter for the mechanism actuators selection :

- for non-backdriveable mechanism, the actuator drive power is applied only when a motion is requested. During rest period, the power is switched off and the fibre position remains constant due to the irreversibility of the actuator (no motion, even under parasitic forces : fibre stiffness, etc.)
- for backdriveable mechanism, the actuator drive power can not switched off : parasitic forces would lead to non deterministic motion of the fibre. So, for such technologies, the drive power shall be maintained permanently.

Table 7.2-7: Fibre Positioner Unit initial requirements.

Function	Range (µm)	Resolution (µm)	Motion dynamics	Motion class	Knowledge (µm)
Lateral motion :		(*)			(repeatability)
- 2 positions	1 mm	± 0.1 µm	10 000	'Ultra-fine'	± 0.2 µm
- 3 positions	2.5 mm	± 0.1 µm	25 000		± 0.2 µm
Possible apportionment		± 1 %			50/50 :
- coarse motion	1 or 2.5 mm	(± 25 µm)	100	'Coarse'	± 0.1 µm
- fine motion : overall	**150 µm**	± 0.1 µm			± 0.1 µm
• alignment	± 30 µm				
• long terme	± 20 µm				
• coarse resolution	± 25 µm		1500	'Fine'	
Vertical motion	100 µm	± 0.1 µm	1000	'Fine'	± 0.2 µm
Focus	500 µm	10 µm	50	'Coarse'	10 µm

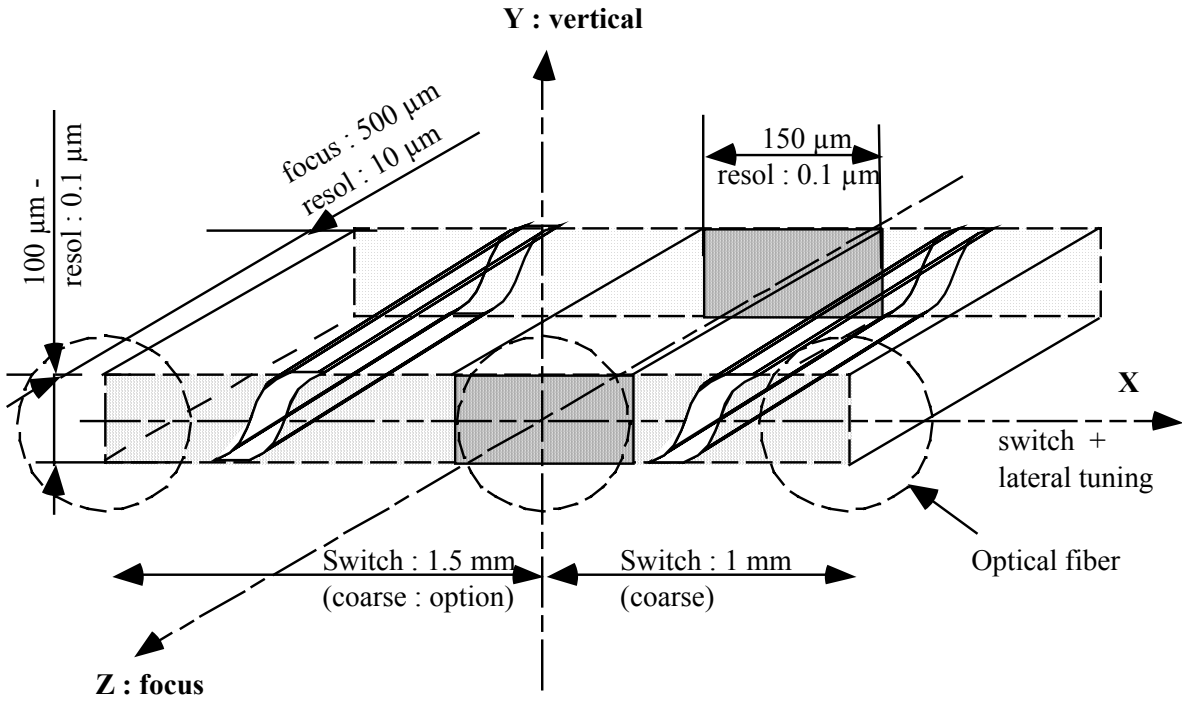

Figure 7.2-11: Fibre Positioner Unit initial requirements (3D illustration).

The force associated to the fibre stiffness is a design driver wrt the actuator selection, in terms of :

- actuator force capability (including standard uncertainty and safety margins)
- actuator non-backdriveability (if preferred solution)

Other performance requirements are related to :

- motion coupling between axes : shall be less than TBD.
- parasitic rotations ; few mrad parasitic rotations during translation are acceptable.

7.2.2.2.1.2 Mobile mass

The mobile load is mainly composed of the fibre(s) and associated mounts (interface with the mechanism mobile plate).

The mass to be translated by the Fibre Positioner Mechanism is estimated to less than 0.1 kg.

7.2.2.2.1.3 Mechanical environment

The mechanism shall withstand the launch loads. Applying margins, the mechanical loads to be considered are :

- launch : 20 g (TBC)
- qualification : launch * 1.25 = 25 g (TBC)
- sizing : qualification * 1.25 = 31 g (TBC)

With a mobile mass of 0.1 kg, the sizing load is : 0.1 * 31 g = **31 N** (any direction).

To minimise volume & complexity, a launch locking device shall be avoided (if possible). In that case, both the guiding elements and the actuators shall designed in accordance with this ‘sizing load’.

7.2.2.2.1.4 Mechanism components

The main components and functions of the mechanism are :

- the guidance : provides the capability to block the DOF not controlled by the actuator.
- The actuator(s)
- The sensing (if necessary) : provides the explicit information concerning the position of the mobile load.

7.2.2.2.1.5 Candidate actuators

A survey of candidate actuators and technologies was performed in the frame of the study, considering sub-µm resolution capabilities. The main candidate classes are :

- inch-worm : combines nanometre motion resolution with millimetre range capabilities. The main reference supplier is Burleigh (USA). The actuator accommodates piezo-electric components.
- Piezo electric, with different design options : direct, amplified, friction drive.
- Screw-jack actuator combined with 'elastic' reducer. In general, a first crew-jack provides a millimetre range ; a second screw-jack, through an 'elastic' reducer provides the nanometre motion resolution.
- Hybrid rotary and translation stages: a rotary actuator provides the 'coarse' motion ('large rang') capability, with a millimetre resolution (rod-type kinematics). A piezo actuator is accommodated in series (for instance in the rod) and provides the sub-µm resolution.

The candidate actuators are illustrated table 4-5/1, indicating the main elements :

- motion range and resolution
- basic technologies
- mass and dimensions
- force capabilities : powered and non powered.
- Stiffness
- Development status.

Candidates / ***Characteristics***	Burleigh Inchworm IW- 710-00	Burleigh NGST type Inchworm II	Direct	Piezo Amplified	Friction	AEH Angstrom actuator	AEH Rubicon actuator	Micro-LS ACME	Rotary motor & piezo rod.
Range	± 3 mm	± 5 mm	100 µm	500 µm	3 mm	± 5 mm	± 5 mm	± 3 mm	± 5 mm
Resolution	4 nm	4 nm	10 nm	40 nm	10 nm	4 nm	2.7 nm	10 nm	2 nm
Technology	Piezo /piezo clamps	Piezo with piezo clamp	Piezo stack	Piezo plus mech ampli	Piezo with vibration	Screw/stepper & 'elastic' red	Screw/stepper & 'elastic' red	Screw & P110 motor	motoreducer & piezo rod
Mass	≈ 180 g	≈ 240 g	≈ 300 g	≈ 300 g	≈ 350 g	180 g	280 g	≈ 180 g	300 g
Length	85 mm	40 mm	140 mm	150 mm	60 mm	100 mm	95 mm	100 mm	60 mm
Section	Φ 25 mm	50 * 36 mm	Φ 25 mm	50 * 20 mm	square 60 mm	50 mm	Φ 35 mm	22 mm	40 mm
Axial force op.	10-15 N	5 N	2000 N	300 N	20 N	10 N	4 N	10 N	10 N
Blocked non-operational.	Friction (stability ?)	**YES** : stable with preload	**NO** : rest in OFF position	**NO** : rest in OFF position	**YES** : stable with preload	Yes	Yes	Yes (lead scew)	100 N(*)
Axial stiffness		5.5 N/µm	30 N/µm	< 1 N/µm		1.2 N/µm	1.0 N/µm	9 N/µm	2 N/µm
Power consumption	Capa : ?	Capa : ?	Capacitance : ≈ 30 µF	Capacitance : ≈ 30 µF		10 mW	0.16 mW	2 W (motor rotation)	2W (motor rotation)
Status	Industrial	Prototype. Position glitch 250 nm	Industrial & space : PI, Cedrat DPA)	Industrial & space : PI, Cedrat APA	Industrial & space : Cedrat LPM 20-3	Proto	Proto	Lab proto	concept with mature technos.
Ball bearings	No	No	No	No	No	Yes	Yes	Yes	Yes

(*) : near the 'dead point'

Table 7.2-8: Sub-micrometre candidate actuators survey

The candidate actuators compared in Table 7.2-2 are shortly described hereafter.

1) Burleigh Instrument.

Burleigh provide industrial-rated hardware : classical inchworm IW-710-00. The corresponding design and operation sequence are illustrated figure 4-5/2.

The extension of an accurate ceramic is achieved with nanometre resolution. The clamp-extend-clamp-retract operation dramatically increases the achievable stroke, up to millimetres. The performances are limited by the lack of internal preload, without reliable holding force (power off).

A prototype design improves the following aspects :

- preloaded flexures
- push force greater than 40 N – which is proportional to the preload.
- stable off-power holding force
- reduced clamp glitch : ≈ 50 nm

The final prototype of the inchworm II was built and tested and demonstrated. However the amount of preload was limited due to the rail deflection under flexure preload.

2) AEH Angstrom actuator.

The actuator consists of a coarse and a fine stage adapted for NASA NGST Primary Mirror Phasing. Both stages are a stepper motor and lead screw mechanism. The nanometre resolution is obtained by combining a screw-jack (identical to the 'coarse' stage one) with an 'elastic reducer'.

3) CEDRAT Recherche LPM20-30 actuator.

The unit illustrated Figure 7.2-13 has a resolution of 10 nm with a stroke of 3 mm. Two contact points are excited by vibration displacement, inducing translation motion of the 'rotor'. Preload prevents for backlash and standard piezo ceramic is implemented.

4) NASA LaRC linear stepper motor.

This concept accommodates magnetostrictive shaft. Two clamping mechanisms hold the rod when unpowered. In that respect, this concept is similar to the Burleigh Inchworm. Patents are under process, thus very limited performance data are available.

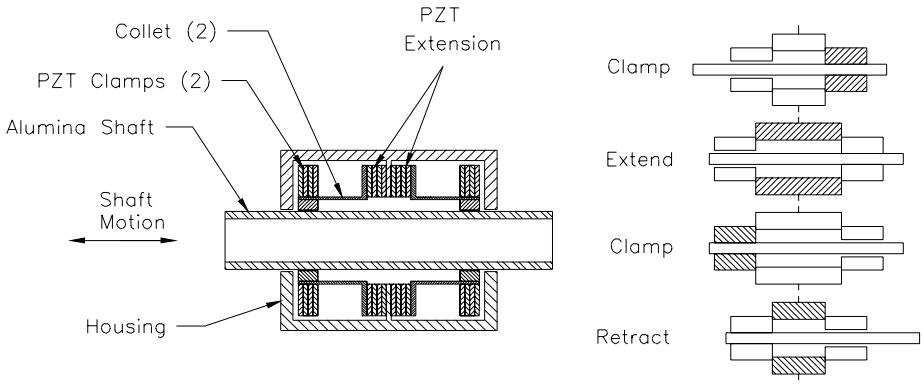

Figure 7.2-12: Burleigh - Classical inchworm IW-710-00 Design and operations illustration.

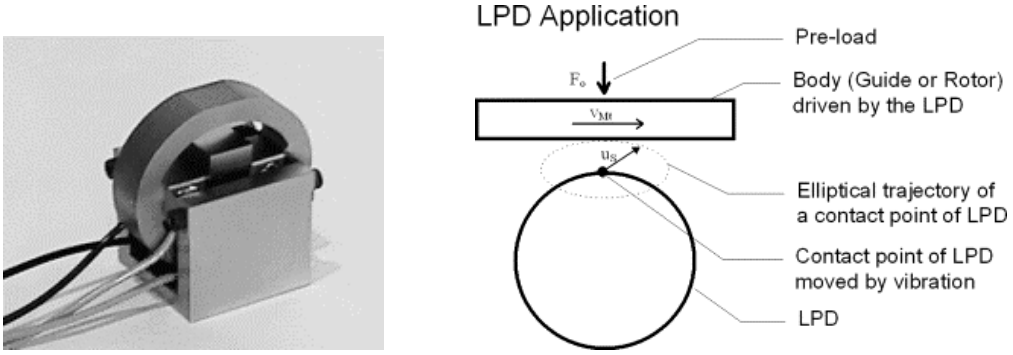

Figure 7.2-13: CEDRAT – LPM 20-30 actuator.

5) Micro-LS ACME lead screw & motor.

The device is based on the lead screw principle, accommodating a piezo nut made of stack of ceramic disks. The motor driving the screw shall exhibit sufficient torque to overcome the friction torque induced by the backlash-free nut.

6) Left Hand design linear actuator.

The stroke can be up to 100 mm, with a resolution less than 10 nm. The voice coil is friction-free/non-contacting action. The force is proportional to the current, with a single phase (commutation not needed). The associated drawback is the zero holding force when powered-off.

7) Electromechanical & piezo actuator.

Compared to the state-of-the-art survey, alternative concept can be proposed. Large stroke/low resolution can be obtained with a two stage mechanism :

- 'coarse' stage, made with a moto-reducer assembly, driving a rod ; resolution : 500 nm typ
- 'fine' stage, obtained by accommodating a 'classical' piezo actuator in the rod.

This concept is illustrated figure 4-5/4 (MMS concept).

The stroke depends on the rod-foot/moto-reducer axis distance. With a distance of 3 mm, a stroke of 6 mm is achievable. The piezo ceramic- including preload device – provides the nanometre resolution. The rod kinematics includes two 'dead-points', corresponding to non-backdriveable positions (even if the moto-reducer unpowered holding torque is small). This characteristics can be used to avoid launch locking device and is very favourable for the positioner unit where the coarse motion is executed between two extreme positions (optic fibre switching). These two positions can be closed to the rod 'dead points'.

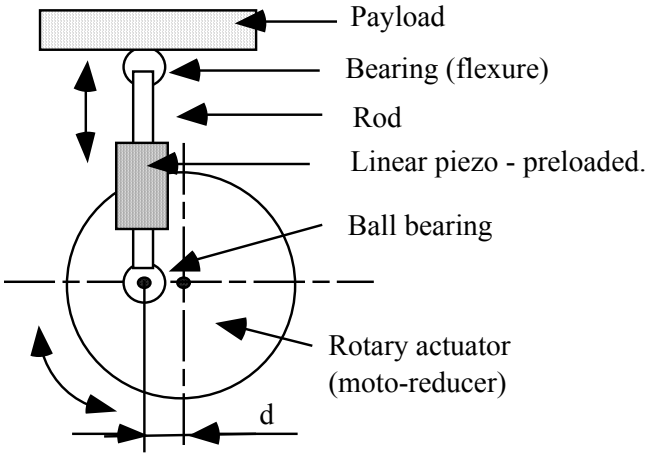

Figure 7.2-14: Illustration of hybrid rotation/translation stages : moto-reducer (coarse stage) plus piezo (fine stage) – MMS concept.

8) Alternative concepts can be envisaged :

- lead screw ('coarse' stage) plus linear piezo with preload.

- electrostatic actuator : idem voice coil with very low force capability
- differential lead-screw plus linear piezo with preload.

Based on the candidate actuator survey, one can conclude that :

- the FPU resolution requirement (100 nm) is large compared to the nanometre-type technologies (10 nm typ.). That means that ultimate resolution capabilities (10 nm) is neither necessary nor adequate wrt the FPU requirements
- the FPU motion range is not accessible with 'direct' piezo actuators
- inch-worm can provide the required motion range and delivers very (too !) small motion resolution. By principle, they are stable after power switch-off ; this leads to a transient dissipation when actuating the system. This transient can be detrimental to the thermal stability of the optical bench. In addition, position glitch can be observed when actuating the piezo clamps. This characteristics is under improvement in the frame of the NGST but is not completely validated today.
- the 'amplified' piezo actuators can deliver the required motion range. However, permanent supply would be necessary, as the piezo retrieves its initial/rest length when the supply is switched-off. This aspect is not a 'killing' criteria, as the dissipated power in the piezo in static conditions (no motion) is negligible and that a permanent/very stable dissipation is compatible with the optical bench thermal stability requirements.
- The 'amplified' piezo features long term drift, as any piezo actuator. A stable position can be obtained by implementing a local position control loop. Capacitive sensors are well adapted to the required motion range and resolution and have been used in a large number of applications, including space applications.

7.2.2.2.1.6 Guiding.

The Fibre Positioner Unit shall provide small translations with a high resolution. Utilization of flexural elements is both adequate and recommended for such applications, featuring :

- ♦ no friction : favorable for fine motion resolutions
- ♦ excellent linearity
- ♦ low resistance force : related to the flexures stiffness
- ♦ high stiffness in the directions perpendicular to the 'free' motion.

Flexural elements are usually obtained from a plain/homogeneous part (Aluminum, steel). 'Hinges' are manufactured by machining the material, keeping small section/reduced length 'beams'. The 'beams' are articulated at both sides (compliant local rotation) but are stiff in traction/compression.

It is possible to combine hinges, leading finally to :

- ♦ either rotation (see Figure 7.2-15)
- ♦ or translation (see Figure 7.2-16)

of the mobile part with respect to the fixed part.

For small motion, a translations δx can be obtained from a rotation $\delta\theta$, assuming that a sufficient lever arm R is used : $\delta x = R\,\delta\theta$ to minimise the disturbing tilting. Based on a specified translation δx and a maximum disturbing tilt angle $\delta\theta$ of the payload, the level arm shall be : $R > \delta x / \delta\theta$.

The Fibre Positioner Units requires 3 translations. Two approaches can be considered :

- 'stacked' translations : the 3 translations are obtained by stacking three elementary translation, with perpendicular axes
- parallel architecture : two translations can be directly obtained, for instance with a '3 feet' table architecture.

An hybrid architecture is attractive for the FPU, implementing a single translation atop a dual-translation stage.

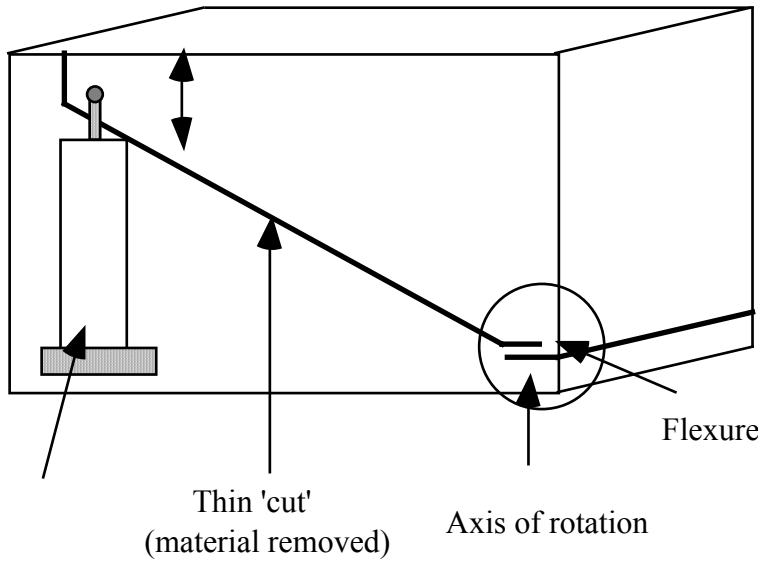

Figure 7.2-15: rotational hinge obtained with flexural element.

Quasi-translation of the payload is obtained for small motions (adequate if the application is compatible of the induced tilt).

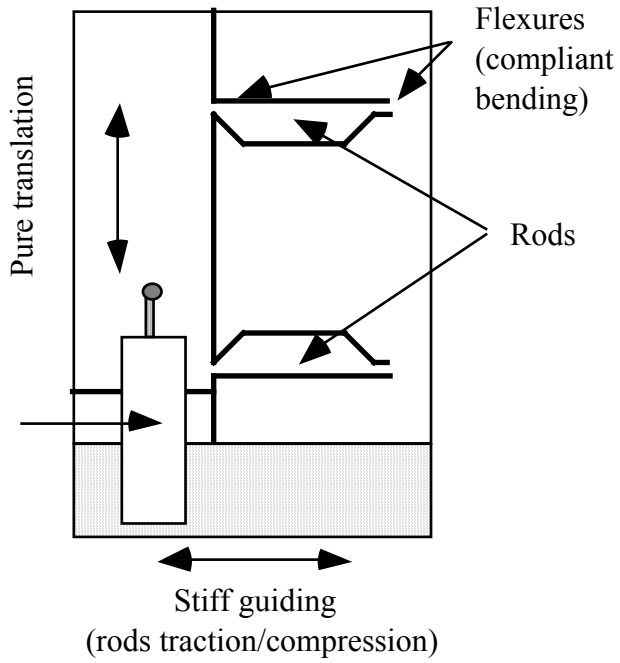

Figure 7.2-16: translation guiding – Combination of 'rods'.

7.2.2.2.1.7 Synthesis

The FPU is implemented in the optical bench, leading to severe dissipation stability requirements but is very favourable with respect to the mechanism performances and technologies. By principle of the LISA instrument, a very high temperature stability is achieved at the focal bench level. So, thermo-elastic disturbances at the mechanism level cannot degrade the mechanism positioning stability performances.

The performance tests which will be performed on-ground will be representative of the operational thermal environment, without requiring performance tests under high or low temperatures.

The operational temperature is identical to 'ambient', making possible the implementation of 'ambient' temperature technologies (near 20°C), such as piezo-electric actuators.

The utilisation of piezo-based actuators (inch-worm or 'amplified' piezo) is adequate for the FPU application. The utilisation of the piezo in a static way leads to very small power dissipation inside the piezo actuator (high quasi-static electrical impedance : MΩ). The main source of dissipation is the drive electronics, which shall be located outside the optical bench.

Considering the technological aspects, mature technologies can be selected for the FPU :

- flexural elements for the guidance
- piezo-electic based actuator ('amplified' piezo or improved inch-worm : NGST-type with internal preload). However, the lateral motion requires a motion range larger than 1 mm (up to 2.5 mm for the three-position option), incompatible of an 'amplified' piezo and making mandatory the implementation of an inch-worm.
- capacitive sensors for position knowledge and actuators long term drift and non-linearities compensation.

Based on the initial FPU specification, the **mechanism volume is the major concern** due to :

- the 3 translation guiding (up to 2.5 mm motion in the lateral direction)
- **the 'state-of-the-art' actuators (inch-worm), not compatible of the overall allocated volume** : cube 40 mm side. The volume of a single inch-worm actuator exceeds the allocated volume. The accommodation of a inch-worm actuator would require a dramatic improvement in size of the actuator ; the feasibility can not be extrapolated today, based on the existing experience.

Finally, a high level of integration would be mandatory to minimise the mechanism overall volume. The main consequence is related to the mechanism development efforts (feasibility, technology improvement) and cost.

7.2.2.2.2 Reduced Functionality FPU

7.2.2.2.2.1 Requirements

Based on the previous conclusions and recommendations, the functions and performances allocated to the Fibre Positioner evolved in the course of the study.

This concerns in particular the two functions :

- avoid straylight by switching-off the laser – in fact by lateral motion of the fibre.
- Exchange laser 1/laser 2

These two functions, if accommodated at the FPU level, lead to very stringent requirements hardly compatible of the actuators technology state-of-the-art. Alternative solutions were investigated at instrument level to complete these functions independently of the FPU.

A new set of FPU requirements was derived, in accordance with the instrument updated functional allocation. The fibre commutations (switch-off position and laser 1/laser 2 commutation) is no more performed at FPU level but 'up-stream'. The FPU updated requirements are indicated in Figure 4-8, including in particular a dramatic reduction of the lateral motion range requirement.

The motion dynamics (ratio : motion range/motion resolution) becomes smaller than 200 for all the axes. Such dynamics is not a design driver, many technologies being able to fulfil such requirement.

Table 7.2-9: updated Fibre Positioner requirements.

Function	Range (µm)	Resolution (µm)	Motion dynamics	Motion class	Knowledge (µm)
Lateral motion	**10 µm**	± 0.1 µm	200	'Medium'	± 0.1 µm
Vertical motion	**10 µm**	± 0.1 µm	200	'Medium'	± 0.2 µm
Focus	**100 µm**	10 µm	10	'Coarse'	10 µm

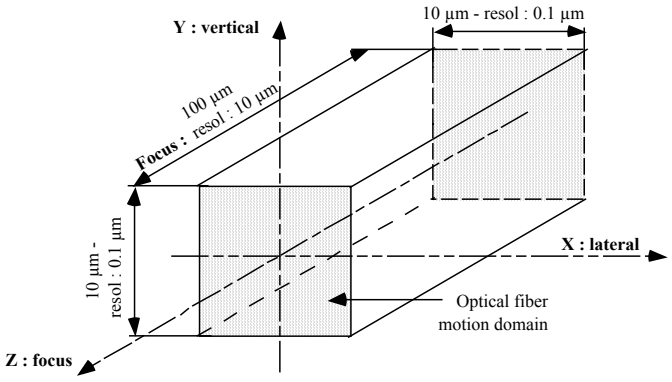

Figure 7.2-17: updated Fibre Positioner requirements (3D illustration).

7.2.2.2.2.2 Reference concept

The reference concept for the Fibre Positioner is illustrated Figure 7.2-18. The guidance is ensured by flexural elements, with the following accommodation :

- a first stage providing two-axis capabilities : lateral and vertical motions (10 µm motion range each direction)
- a second stage, providing the focus function

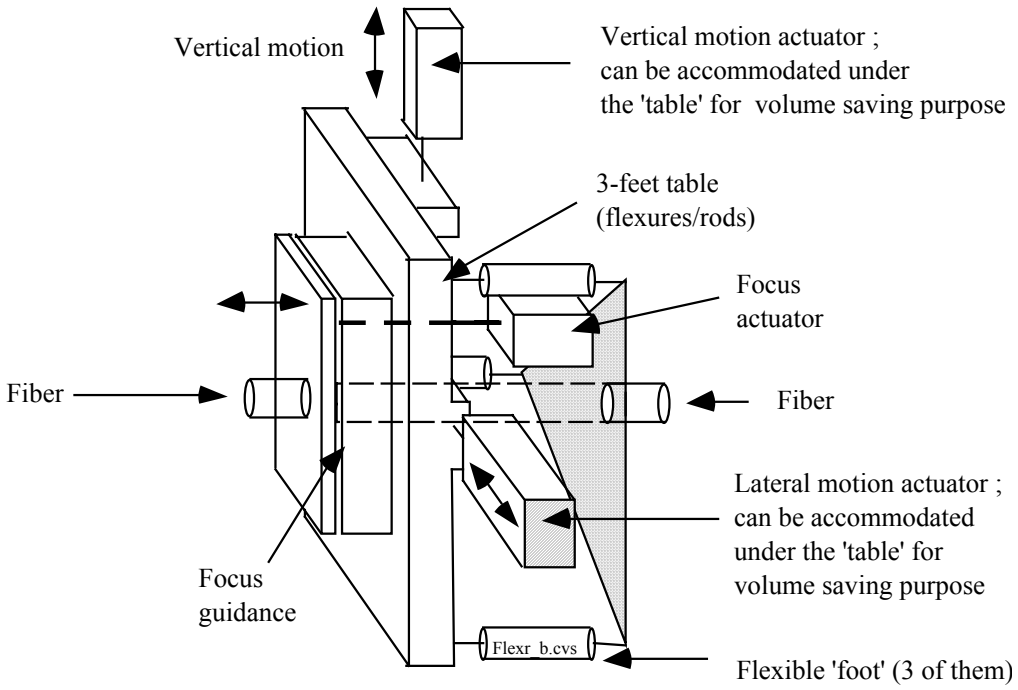

Figure 7.2-18: Fibre Positioner mechanism : reference concept illustration.

The selection of the actuator is updated considering the following trade-off criteria :

- volume/bulkiness
- launch load capabilities (no locking device preferred)
- stiffness – wrt the parasitic force and stiffness induced by the fibre to be moved
- power consumption : small/permanent consumption versus small transient
- glitch motion : to be avoided
- long-term position stability
- non-linearities (hysteresis)
- tribology : avoid sliding surface requiring coating or special process.
- position knowledge

The candidate actuators illustrated in the previous section ('Initial Configuration') are compared with respect to these criteria. For the first stage, the direct drive piezo is the most promising candidate, featuring a length of 10 mm for both lateral and vertical motion. Low voltage piezo (0-100 V) are recommended. The focus motion range is more demanding ; a direct drive piezo would be too bulky (length : 100 mm). For the focus, an amplified piezo is preferred, with a magnification between 3 and 5. This magnification is a compromise between the volume, the stiffness and the compatibility with the launch loads.

The utilisation of piezo actuators requires permanent supply to keep the fibre is the requested position. This corresponds to quasi-static supply of the piezo ; in that case, the dissipation in the piezo is very small (1 mW at full extension).

The long-term drift and the hysteresis of the piezo are compensated by the utilisation of the capacitive sensors. These sensors are necessary for the position knowledge and are used in local control loops, one per axis. A control bandwidth in the range of 0.1 Hz to 1 Hz is sufficient.

7.2.2.2.2.3 Conclusion

The high temperature stability of the focal plane is a constraining requirement with regards to the mechanism power dissipation. Conversely, the operating temperature is identical to 'ambient', making possible the implementation of mature technologies. In addition, the thermo-elastic distortion of the mechanism is very small and can not disturb the positioning performance.

The positioning performance validation of the mechanism with regards to the temperature will not be a key issue : testing conditions (clean room) are similar to the in-orbit operational conditions.

The first design run based on the initial requirements allowed to identify critical aspects, in particular the mechanism volume budget. The reallocation of functions was performed, based on the conclusions and recommendations of the first run.

The requirements were updated accordingly, allowing to identify promising mechanism design.

Further activities are necessary for detailing the proposed concept and consolidating the budgets. The implementation of the guiding elements and the actuators will require design optimisation to fulfil the 40 x 40 x 40 mm^3 allocated volume. This effort shall be taken into account in the programmatics (planning/cost impacts).

7.2.2.3 Telescope Orientation Mechanism

7.2.2.3.1 Configuration

The fine pointing of the two telescopes can be realised :

- either by combining a single-axis mechanisms controlling the angle between the telescope with the FEEP thrusters controlling the attitude of the entire spacecraft,
- or by dedicated two-axis mechanisms for each telescope

Indeed, a mechanism is at least required to control the angle between the telescopes ; this angle is a DOF not controllable by the S/C attitude. Indeed the geometrical configuration of the three LISA satellites is not a constantly perfect equilateral triangle. The spacecraft constellation slowly evolves versus time, demanding a fine control of the relative angle between counter spacecraft LOS'.

For LISA, the proposed telescope pointing architecture is the following :

- Use of the attitude control to realise a complete pointing of 1 telescope - let's call it telescope A - and of the off-plane angle of the second telescope (telescope B).
- Use of a mechanism to control the in-plane angle of telescope B.
- Implement a spare mechanism on telescope A, so that the roles of telescope A & B can be switched in case of failure.

The resulting architecture is illustrated Figure 7.2-19.

This choice is based on the ability to perform the fine pointing with the thrusters, without inducing any new or more stringent requirement on the FEEP propulsion. Then, three of the four DOF will be maintained through the 3-axis attitude control.

The objectives of this section is to present the mechanism controlling the fourth DOF, independent from the S/C attitude. The following aspects are addressed :

- short synthesis of the requirements applicable to the mechanism
- review of the candidate architectures and design drivers
- identification of a mechanism reference concept : architecture, components
- identification of the component achievable performance
- dynamic simulation, implementing the mechanism components characteristics
- assessment of the overall pointing performances and verification of the adequacy of the mechanism and its control schema with respect to the performance requirements.

All these points will indicate to which extent the telescope orientation system is feasible and what are potential key issues.

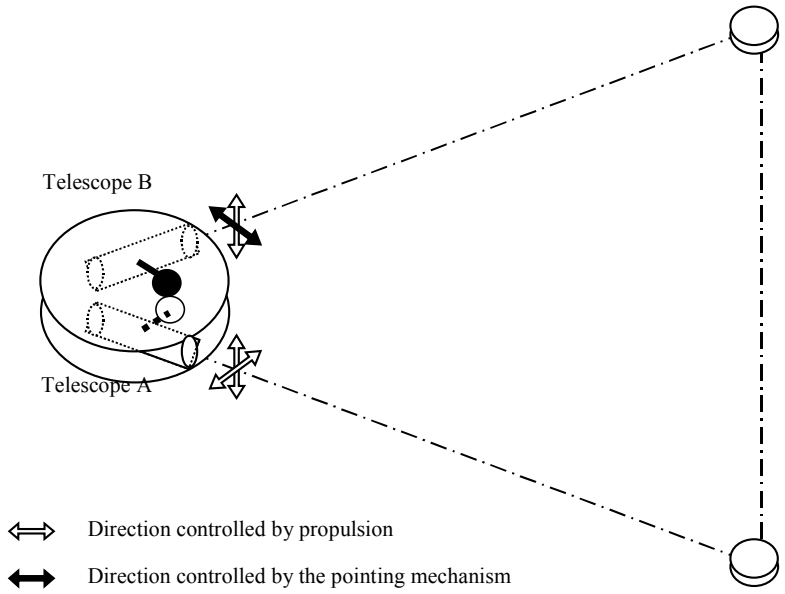

Figure 7.2-19: Control of the telescope pointing DOF

7.2.2.3.2 Pointing mechanism requirements

The main mechanism requirements are indicated hereafter :

- Angular range :
  - overall angular range : 1°. This is driven by the seasonal variations of the three spacecraft constellation.
  - scanning range : ± 6 µrad for the counter spacecraft LOS acquisition
- Angular rate :
  - acquisition : ≥ ±20 nrad/s. This is driven by the capability to scan the 12 µrad acquisition angle in less than 10 min
  - operational : up to ±3.5 nrad/s. This corresponds to the maximum constellation seasonal deformation rate (sine motion ; magnitude 1° ; period : 1 year).
- Absolute accuracy : better than 1 µrad. This contributes to the scan angle extension. The current allocation to the mechanism is 10% of the overall scan angle.
- Angular resolution and noise : 0.5 nrad
- Stability/noise : based on the instrument performance template
  - allocation : 0.7 nm/√Hz above 40 mHz
  - rms : TBD (20 nrad)
- stiffness in operational configuration : around 0.5 Hz. This requirement is selected in order to set the first mechanism resonance higher than the MBW. Conversely, it is selected low enough for allowing active damping by the control loop if required. A priori, such a value is

consistent with the heterodyne detector bandwidth. This assumption would need further evaluation and analysis at sensor level.

- Life time : 2 years. Provision for 10 years is considered.

Telescope mass properties

The mechanism steers the whole telescope. The following telescope mass properties are assumed:

- mobile mass : 36 kg
- telescope inertia around the Centre Of Mass : 15 kg.m^2.

Mechanical environments.

The mechanism shall survive to the launch loads and shall be fully operational in orbit, with the performances specified before.

The assumptions considered with regards to the launch environment are :

- launch : 20 g quasi-static
- qualification level : 25 g
- sizing level : 30 g

In the frame of the study, the critical components of the mechanism are sized considering 30g quasi-static load, assuming that the random levels will not be more critical.

Combined with the telescope mass (36 kg), the mechanical loads are :

30 g * 36 kg = 11 000 N

7.2.2.3.3 Mechanism design drivers

Mechanism complexity.

In general, the launch loads can not be withstood by the critical elements (guiding), requiring the accommodation of a launch locking device (LLD). The main purpose of the LLD is to avoid the launch loads to pass through the critical elements. Conversely, such accommodation leads to more complex mechanism design, both in terms of analysis (hyperstatic configuration) and hardware : the LLD is in fact a second mechanism. The cost impact is important.

Despite of the large mass of the telescope (36 kg), a design without LLD is identified, as shown in the following feasibility assessment.

i) Location of the rotation axis.

The location of the rotation axis with respect to the centre of mass has two main impacts :

- static unbalance : generates disturbing torques during launch
- self gravity, considering the proof masses sensitivity during in-orbit operations.

ii) Actuation resolution.

The actuation resolution and noise (0.5 nrad typ.) is very demanding, compared to the angular motion range required (1°). This corresponds to a motion dynamics of :

$$0.5 \text{ nrad} / 1° = 35\,000\,000$$

This is far from the 'usual' pointing mechanisms, even for the most constraining applications. This can be compared to high performance steering mechanisms (mirror steering), requiring resolution of few µrad over 30° typ (motion dynamics = 100 000). The LISA telescope pointing requires motion dynamics three order of magnitude larger than 'state-of-the-art mechanisms) ; LISA is a very challenging application.

7.2.2.3.4 Location of the centre of rotation.

Three configurations were considered and compared :

- remote centre of rotation
- balanced configuration : rotation axis near the telescope Center Of Mass
- minimum self-gravity oriented : rotation axis near the proof-mass location.

The static unbalance is the separation distance between the rotation axis and the telescope centre of mass. Considering the launch environment, static unbalance generate torques to be compensated to avoid the rotation of the telescope. The selection of small static unbalance is favourable with regards to the design of the device aiming at blocking the telescope rotation during the launch.

i) *Architecture 1 : remote centre of rotation.*

This configuration, illustrated Figure 7.2-20 does not feature decisive advantages. The drawbacks are:

- the large static unbalance generates high torques during the launch. Assuming a static unbalance of 0.5 m, this corresponds to a torque of : 11 kN * 0.5 m = 5 500 Nm
- generates large self-gravity variations
- corresponds to higher telescope inertia

The large unbalance will require the accommodation of a LLD to withstand high torques during launch.

ii) Architecture 2 : balanced configuration

This configuration is illustrated Figure 7.2-21. The rotation axis is selected to include the telescope centre of mass. The purpose is to minimise the static unbalance, ideally down to 0. Residual unbalance in the range of few mm (d = 3 mm for instance) is easily achievable, leading to torques during launch of :

$$C = F \cdot d = 11\ kN * 0.003\ m = 33\ Nm$$

Assuming the accommodation of a blocking element at 0.5 m, this leads to a blocking force of 70 N, which can be provided by a lot of available/simple/small volume devices. All the launch load passes through the rotation axis (11 kN). The design of the spacecraft structure shall provide ‘hard’ points at that location.

The possible drawback is related to the self-gravity if the proof mass is not located at the vicinity of the telescope centre of mass. By design, the separation between the proof mass and the telescope center of mass shall be limited to few cm

iii) Architecture 3 : centre of rotation near proof mass

This configuration is illustrated Figure 7.2-22. The rotation axis crosses the proof mass, minimising the self-gravity variations. This configuration corresponds to a static unbalance of TBD (10 cm maxi), generating torque during launch of 1 000 Nm (TBC). Loads of 2 000 N shall be withstood by the rotational blocking device. Such value is less favourable compared to the architecture 2 but does not lead to unfeasibility nor severe extra-complexity.

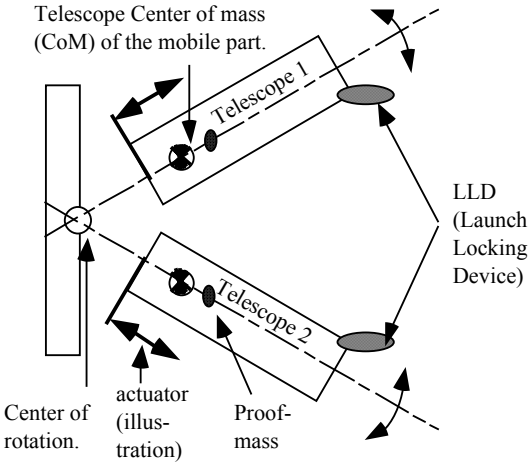

Figure 7.2-20: 'remote centre of rotation'

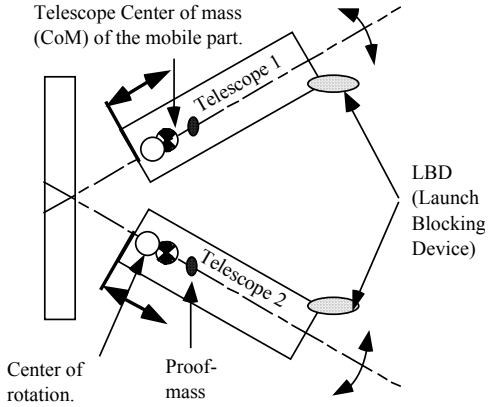

Figure 7.2-21: 'balanced configuration'.

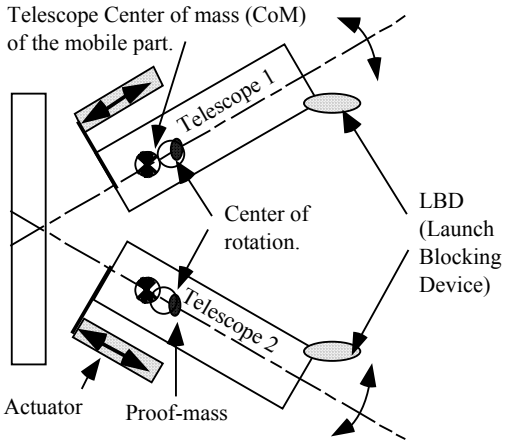

Figure 7.2-22: self-gravity oriented : minimum variations.

Conclusion

Considering the telescope internal architecture (proof mass location with respect to the telescope centre of mass), the architectures 2 and 3 seem equivalent. Architecture 2 is recommended and considered as the reference in the following.

7.2.2.3.5 Candidate technologies

i) Actuators

The review of candidate actuators performed for the 'Fibre Positioner Unit' (see section 4.2) is fully applicable and relevant for the Telescope pointing application.

ii) Bearings (guidance)

Considering the bearing (guidance) aspects, the selection of flexural pivots is mandatory due to the very small motion resolution required ; for nanometer applications, guiding elements with friction shall be disregarded.

In order to assess the feasibility of the Telescope pointing mechanism, standard components are first considered. In case key issues are identified, improvement areas of such components will be listed.

The usual procurement source for flex pivots is the Lucas company (US). R&T efforts were completed in Europe in the past years, allowing to have now alternative European procurement sources.

Considering the Lucas products, high load capability pivots are available, for instance Lucas 5032-400. The characteristics are :

- load capability : 7 000 N per pivot
- torsional stiffness : ≈ 50 Nm/rd

The telescope guiding can be ensured by implementing a pair of such pivots. Such a pair is able to withstand the launch loads without additional support (LLD for instance). The torsional stiffness of the pair of the guiding element is 100 Nm/rd. Combined with the telescope inertia (15 $kg.m^2$), this leads to a mechanical eigenfrequency of : 0.4 Hz. This resonance frequency is higher than the scientific measurement bandwidth and will not be detrimental to the measurement performance.

iii) Sensing

A priori, no local sensing device is necessary at mechanism level. The LISA instrument delivers directly the LOS measurement which can be used by the controller to drive the mechanism. Sufficient sensor measurement bandwidth is expectable and can be used for actively damping the telescope eigenfrequency.

7.2.2.3.6 Mechanism concept

i) Performance apportionment

The mechanism design is driven by the very large motion dynamics requirement (40 000 000):

- resolution : 0.5 nrad
- range : 20 mrad (1°)

A single stage mechanism can not fulfil such a requirement. A two-stage design is mandatory, with some operational overlapping of the two stages. The apportionment is the following :

Stage	Motion range	Resolution	dynamics
'Fine' stage	[0.5 nrad -> 5 µrad]	0.5 nrad	10 000
'Coarse' stage	[0.5 µrad -> 20 mrad]	0.5 µrad	40 000
Overlapping zone	[0.5 µrad -> 5 µrad]		1 'coarse' stage step = 10% of the 'fine' stage range

The resolution and overlapping allocation aims at ensuring that the 'coarse' stage resolution corresponds to 5 to 10% of the fine stage range capability. The allocation is illustrated Figure 7.2-23.

ii) Mechanism concept.

The utilisation of direct drive (not amplified) piezo is compatible of the 'fine' stage specification, both in terms of resolution and range.

The telescope overall geometry indicates that a translation mechanism can drive the Telescope rotation via a lever arm R. This is possible in accordance with the overall angular range (1°).

The lever arm selection is limited by the following aspects :

- bulkiness : the lever arm shall remain smaller than 300 to 400 mm maxi
- telescope diameter : does not allow accommodation of the mechanism at less than 150 mm of the telescope axis.

Therefore, the selected lever arm is R = 200 mm (TBC).

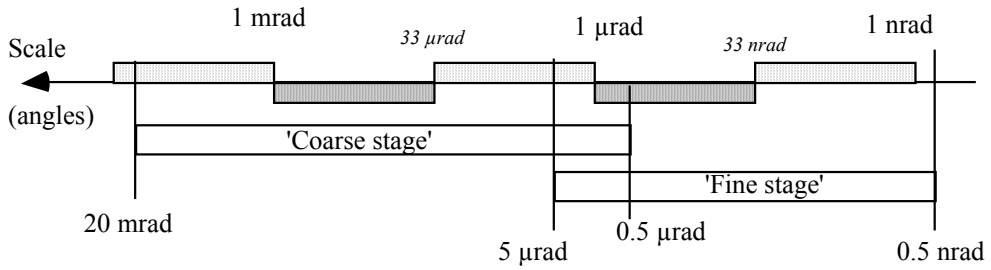

Figure 7.2-23: performance allocation between the 'fine' and the 'coarse' stages.

After selection of the lever arm, the performance apportionment between the two stages (rotation) can be translated into translation requirements, relevant for translation actuators.

For R = 0.2 m, it comes :

Stage	Motion range	Resolution	dynamics
'Fine' stage	[0.1 nm -> 1 µm]	0.1 nm	10 000
'Coarse' stage	[0.1 µm -> 4 mm]	0.1 µm	40 000
Overlapping zone	[0.1 µm -> 1 µm]		1 'coarse' stage step = 10% of the 'fine' stage range

Various mechanism architectures were reviewed and compared.

The two main candidate families are :

- 'fine' and 'coarse' stages in series
- 'fine' and 'coarse' stages in parallel.

Concerning the 'coarse' stage, the main candidate solutions are :

- spindle-nut
- voice-coil

The voice-coil solution would require a linear sensor, as the voice coil generates a force and not directly a position. In that respect, the spindle-nut candidate is the most promising one and its feasibility is further analysed. The coarse 'stage' motion resolution is very small : 0.1 µm, not directly achievable with a spindle-nut assembly ; a linear motion reducer shall be added.

Classical reducer with gears and friction (at least in the guiding elements) shall be disregarded. The 'elastic' reducer principle is very attractive for the application.

Finally, the reference mechanism principle is illustrated figure 4-15. It includes the two actuators :

- direct drive piezo for the 'fine' stage
- spindle-nut drive for the 'coarse' stage, driven by a stepper motor

combined with mechanical compliance/stiffness :

- flex pivots, supporting the telescope and featuring torsional stiffness : k_{flex} =100 Nm/rd typ.
- Piezo transmission : k_{fine}.
    - Spindle-nut head transmission : k_{head}.

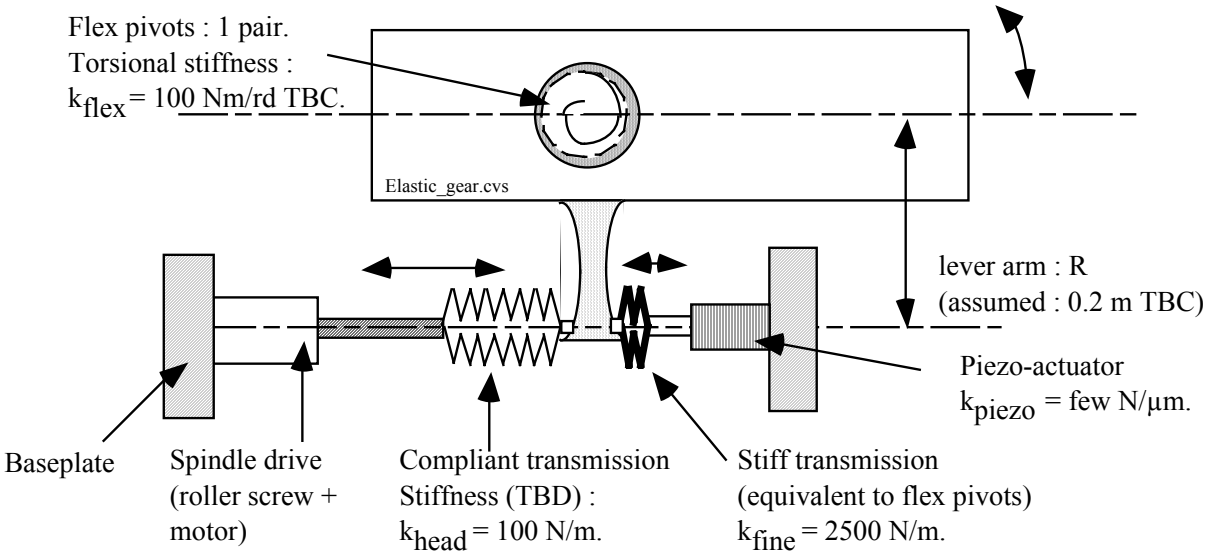

Figure 7.2-24: Telescope pointing : reference mechanism principle.

The flex pivot torsional stiffness can be translated into equivalent translation stiffness at actuators level:

- k_{flex} =100 Nm/rd
- R = 0.2 m
- Equivalent to : $k'_{flex} = k_{flex} / R^2 = 2500$ N/m

In order not to require large increase of the piezo motion range, the following is selected :

- piezo transmission : stiff, equivalent to the flex pivots stiffness - k_{fine} = 2500 N/m
- Spindle-nut head transmission : compliant in order to ensure both :
  - a large reduction ratio of the screw-jack motion.
  - a negligible reduction of the piezo motion efficiency

  Selected value : 100 N/m

Based on these values, the requirements at stage level can be translated into actuator requirements, considering :

- for the piezo : motion ratio $\approx k_{fine} / (k_{fine} + k'_{flex}) \approx 0.5$

  $\rho_{fine} \approx 1/0.5 = 2$
- for the spindle-nut : motion ratio $\approx k_{head} / (k_{fine} + k'_{flex}) \approx 0.02$

  $\rho_{head} \approx 1/0.02 = 50$

By applying ρ_{fine} and ρ_{head} to the fine stage and the coarse stage specification respectively, one can derive the actuators specifications :

Actuator	Motion range	Resolution	dynamics
'Fine' stage : piezo	[0.2 nm -> 2 µm]	0.2 nm	10 000
'Coarse' stage : spindle-nut	[5 µm -> 200 mm]	5 µm	40 000

A piezo of few mm length provides the 2 µm range capability. Longer piezo stacks can be accommodated, in combination with the reduction of the k_{fine} stiffness. For instance, k_{fine} = 1000 N/m can be associated to a piezo motion range of 5 µm ; including casing, the piezo actuator overall length is then 30 mm.

The motion resolution (and noise) depends mainly on the piezo drive electronics. With low voltage ceramics (100 V maxi), the dynamics requires a resolution/noise of 10 mV. The command covering the 10 000 dynamics corresponds to a 16 bit coding.

Concerning the 'coarse' actuator, the motion range of 200 mm drives the choice of the spindle length, leading to 250 mm typ. This aspect is not a severe design driver and is well in accordance with the state of the art.

The 5 µm resolution is achievable with a roller screw device ; one can consider the following combination :

- spindle pitch : 1 mm
- stepper motor : 200 steps/rev

leading to a motion resolution in full step command : 5 µm.

Other combinations can be envisaged, typically :

- spindle pitch : 1.2 mm
- stepper motor : 360 steps/rev

leading to a motion resolution in full step command : 3.33 µm

This indicates that the proposed design includes margins and can be further optimised, based always on the utilisation of well demonstrated components for space applications. For instance, a resolution of 3.33 µm instead of 5 µm can reduce the spindle motion range down to 133 mm (= 200 mm * 3.33 µm /5 µm).

In order to validate the adequacy of the proposed mechanism concept, a dynamic simulator was developed, including the mechanism components (stiffness, actuators), the telescope inertia and the control loop (LOS control). The results are presented hereafter.

7.2.2.3.7 Dynamic simulations

The simulator has been developed in the MATLAB/SIMULINK environment to assess the overall dynamic performance, including the mechanism. This simulator, modelling the behaviour of the mechanism, has also been integrated in the overall DFACS simulator presented in section 7.2.3.3.

The plots that will be presented hereafter correspond to the following assumptions :

- Telescope arm inertia : J_{zz} = 15 kg.m².
- Stepper motor in full step mode. One full step corresponds to 3 µm of elongation.
- System damping : structural type - ξ = 2%.
- Heterodyne sensor noise : 3 nrad/$Hz^{1/2}$.
- Piezo resolution : 0.2 nm
- S/C attitude jitter : 6 nrad/$Hz^{1/2}$.

The strategy used to reduce the effect of the motor steps is a feed-forward command to the piezo, synchronous with the motor stepping. With this strategy, the system does not see anymore steps, but just impulses, resulting from the error between the motor step and the piezo compensation.

The time history of the pointing error obtained in this simulation and its PSD are plotted on Figures 4-16 and 4-17. We can see on this last plot that in terms of PSD level, the requirement is met with margins. However two points of concern remain :

1. The harmonic peaks due to the periodic steps of the motor are marginally larger than the requirement. In the time domain, it means that the measurement might be too corrupted for scientific use in the couple of seconds after each step of the motor.
2. The oscillating mode at 0.5 Hz, with very small damping, induces large pointing errors, up to 50 nrad. This might not be acceptable

To improve these two points, which are marginally critical, MMS recommend the following solutions:

- Utilisation of the stepper motor in ministepping mode. A division by a factor 8 or 16 of the steps is easily achievable, without severe constraints nor real increased complexity.
- Better damping of the oscillations. This can be done by several means : either passively or actively. Passive damping remains an open issue, because it is difficult to guarantee that a technology compatible with the jitter magnitude exists. Active damping with the piezo seems to be the most promising solution. It depends on the heterodyne sensor output frequency : to be faster than 10 Hz. If confirmed, the 0.5 Hz oscillation can be damped with the attitude controller.

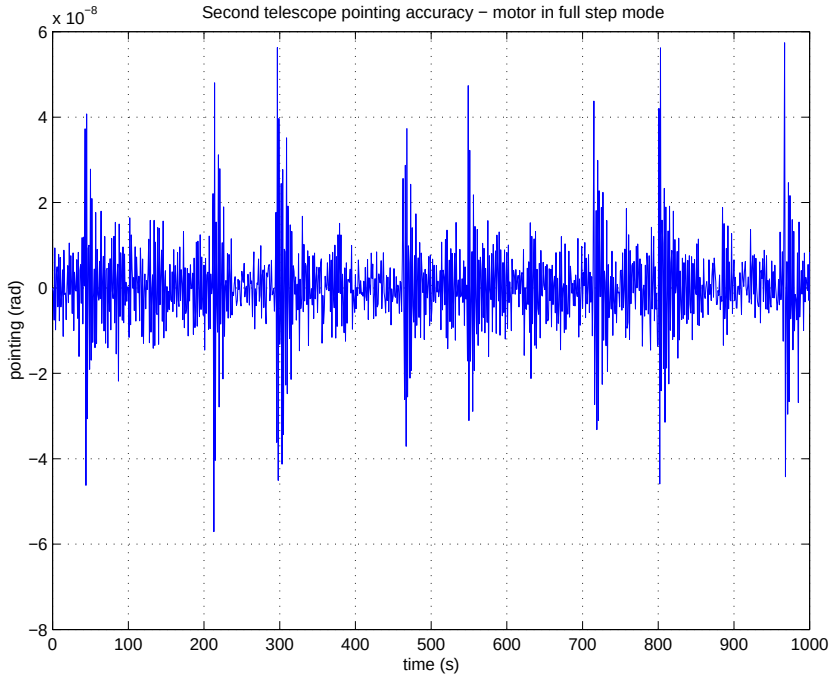

Figure 7.2-25: Time history of the pointing error

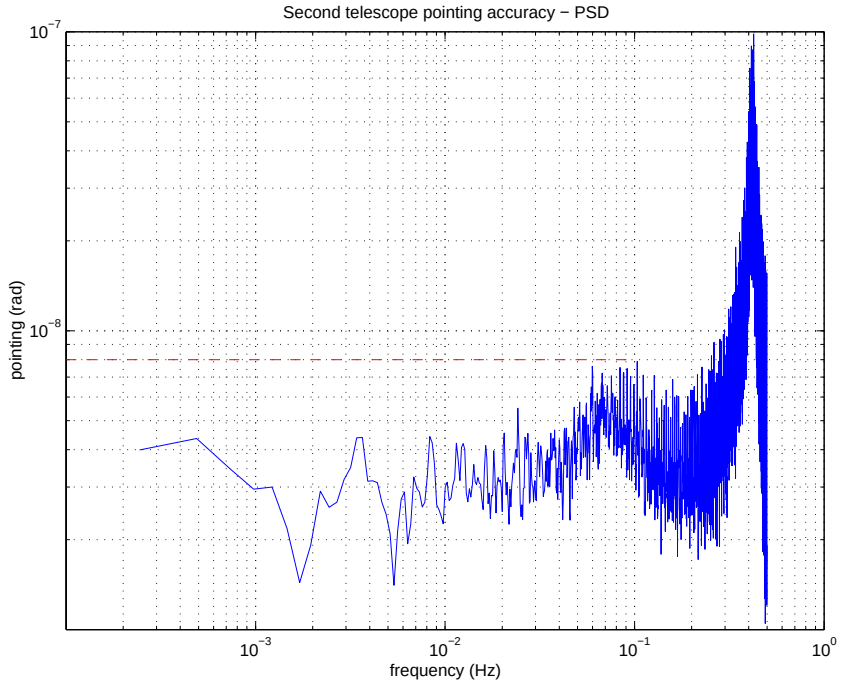

Figure 7.2-26: pointing error PSD.

7.2.2.3.8 Conclusion

During the Phase A, MMS has demonstrated the feasibility of a telescope pointing mechanism meeting both constraints of high range and high accuracy. A two-stage mechanism is proposed, relying on very mature technologies, such as stepper motor, roller screw and piezo actuators. The design of the spindle-nut drive is flexible, allowing to separate the resolution (defined by the spindle pitch and the motor step) and the motion range capabilities (defined by the spindle length).

The number of cycles can be estimated from the analysis. The motor stepping rate correspond to one full step every 100 s, worse case S/C constellation seasonal deformation rate. This correspond to 0.6 Msteps for 2 years (3 000 rev), with an extension to 3 Msteps (15 000 rev) for 10 years. The life time is not a critical issue, as the roller-screw components provide Mrevs capability.

This reliable mechanical design can be further improved in different directions.

The performances obtained with full step command of the spindle drive are acceptable but feature no sufficient pointing margins. Simple improvement of the motor drive – ministepping instead of full step command - will significantly reduce the magnitude of the disturbance induced by the 'coarse' stage and the mechanism eigenfrequency excitation (ratio of 10).

The control strategy including active damping is an other promising solution, boosting the mechanism performances at low cost.

The classical stepper motors include permanent magnets and generate magnetic field (stator windings). This can lead to an open issue with regards to the PM magnetic requirements. Alternative technologies exist, based on rotary piezo actuators. Such technology is under development under ESA funding, preparing the validation of this type of motors for future missions. Only a limited torque capability is requested for the motor, as a large reduction ratio/torque magnification is provided by the screw-jack device. The volume and the reliability of the motor is improved accordingly.

The analyses performed indicate that the telescope pointing mechanism requirements can be fulfilled with mature technologies. The concept relies in particular on the 'elastic' gear principle, which is theoretically simple. Further design activities up to breadboarding deem necessary to consolidate the feasibility statement and refine the component specification, selection and definition.

7.2.3 Drag-Free & Attitude Control

7.2.3.1 Introduction & Requirements

This section is dedicated to the study of the Drag-Free & Attitude Control System (DFACS) in charge of high accuracy pointing & translation control during the science mode, one of the most challenging control issues of this mission.

The demonstration of the ability of the DFACS to achieve the very stringent pointing & translation stability in the Measurement Bandwidth (MBW) is of primary importance since the quality of the realised control has a direct impact on the final mission performance. For this reason, the Phase A analyses were focused on the verification of the DFACS performance in the MBW, control of long-term effects (below the MBW) and initialisation aspects being covered at conceptual level only.

The challenging goal of DFACS is to keep the two different proofmasses onboard the S/C inertially fixed (at least along each line of sight), while achieving a very accurate pointing of each telescope toward the companion satellites. The complete DFACS requirements, as derived at system level from scientific mission objectives are given hereafter :

Table 7.2-10 : Summary of DFACS Requirements

PM acceleration noise along the sensitive axis in the MBW.	$3.10^{-15}\left[1+\left(\frac{f}{5.10^{-3}}\right)^2\right]$ m/s²/Hz$^{-1/2}$
Relative displacement between the S/C (Spacecraft) and the PM (Proofmass) on the sensitive axis, in the MBW	2.5 10^{-9} m/Hz$^{-1/2}$
Relative displacement between the S/C and the PM on the transverse axes in the MBW	10 10^{-9} m/Hz$^{-1/2}$
Absolute value of the relative displacement between the S/C and the PM	5 µm
Telescope pointing stability in the MBW	8 nrad//Hz$^{-1/2}$
Absolute telescope pointing error	30 nrad

DFACS relies on the inertial sensors and the heterodyne detectors of the two optical assemblies for sensing, while the actuators for both the drag-free and the attitude control are FEEP thrusters plus the telescope steering mechanisms (to adjust the angle between the two telescope LOS. The proofmass suspension control, which cannot be designed independently from the S/C control loops, will also be discussed in this section.

In Phase A1 (ref [4]) MMS's approach was to study a simplified 1-axis problem, in order to identify the critical points, specify the equipment, perform preliminary design of controllers, and evaluate first-order performance budgets. One of the major conclusion was to point out the very complex interactions between drag-free and attitude issues, and the potential criticality of coupling between DOFs (Degrees Of Freedom).

It was therefore an absolute necessity to analyse the problem in a multi-axis environment. However, since the total number of DOFs is as large as 19 (6 for each PM, 6 for the S/C and 1 for the angle between the telescopes), it was proposed to simplify the analysis in this phase, and concentrate in planar problem which allows to investigate all potential interactions between control loops (10-DOF problem: 2 translation and one rotation for each PM and for for the S/C and the angle between the telescope).

This study relies on a Matlab/SIMULINK simulator, that make possible both transfer function analyses, and also time simulations.

7.2.3.2 External disturbances analysis

7.2.3.2.1 Solar Pressure Perturbation

Constant perturbation

The solar pressure is the main external disturbance on the S/C. Its constant value can be roughly calculated considering the S/C as a disk with normal 30° away from the Sun direction:

With Lo = 1358 W/m² the mean solar flux

$$F_0 = -\frac{Lo.A_{S/C}}{c}.\cos\theta.\left[(1-Cs).S + 2(Cs.\cos\theta + Cd/3).Z\right]$$

$$T_0 = GP \otimes F_0$$

C = 3 10^8 m/s² the speed of light

Asc ~= 6 m²

Cs = 0.19 the coefficient of specular reflection for solar cells

Cd = 0.02 the coefficient of diffuse reflection for solar cells

The resulting force is $F_0 = {}^t[9.5\ 0\ -24]$ µN in the S/C frame.

This order of magnitude is consistent with the solar pressure calculated by DSS using a more refined geometrical model of the S/C:

Fxmax = 4.6 E-6 N Fxmin = -4.6 E-6 N

Fymax = 4.5 E-6 N ..... Fymin = -4.5 E-6 N

Fzmax = -3.24 E-5 N Fzmin = -3.24 E-5 N

These last values will be taken as reference values from now on.

DSS has also calculated the associated torques :

Txmax = 1.0 E-6 Nm Txmin = -1.0 E-6 Nm

Tymax = 4.2 E-6 Nm Tymin = 2.2 E-6 Nm

Tzmax = 4.5 E-7 Nm Tzmin = -4.5 E-7 Nm

In the MBW

In the MBW, the solar pressure variations are also expected to be the main external perturbation.

The solar lux variations consist in an incoherent noise and in harmonics of the so-called 5-minute acoustic oscillation (i.e. @ 3.5 mHz). A first assessment (See phase A1 report) shows that the PSD (Power Density Spectrum) level of the force in the MBW, and in the plane defined by both LOS, is the following:

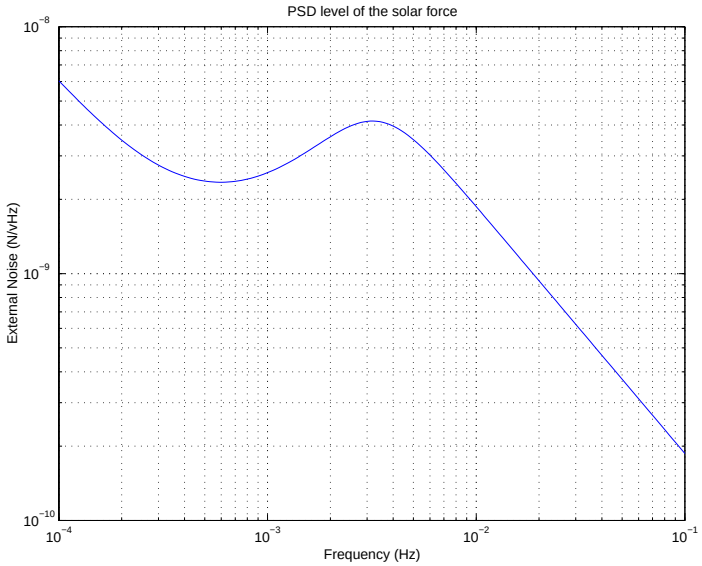

Figure 7.2-27 : PSD level of the solar force in the MBW (rough estimation by MMS)

This curve has to be compared with the PSD given by SOHO flight measurements:

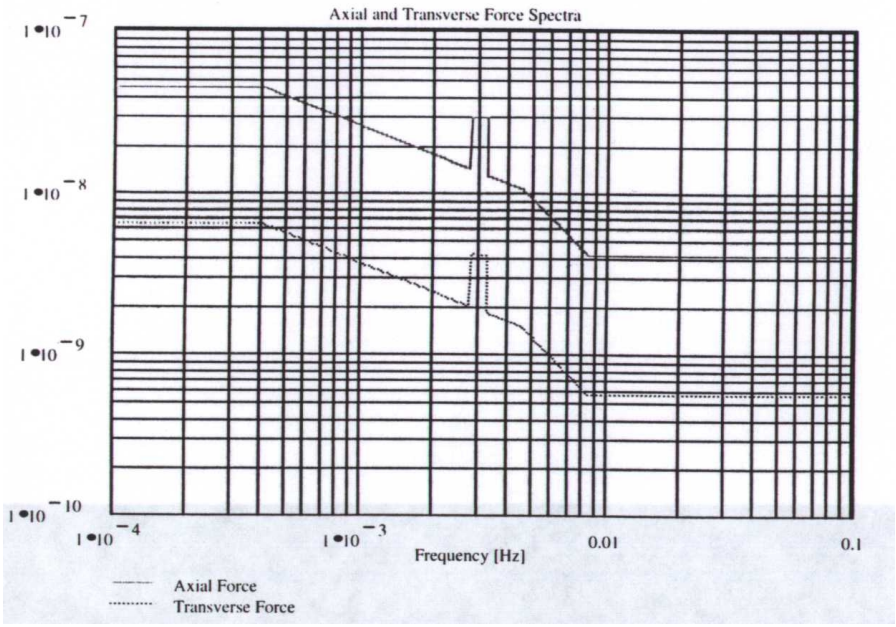

Figure 7.2-28 : PSD of the solar forces (from SOHO source)

Even though the curves have different shapes, it must be noticed that the experimental PSD for the transverse axis (bottom curve), and the PSD assumed by MMS during the study are more or less at the same level. The largest difference is around 5 10^{-4} Hz : at this frequency the experimental curve is a factor 3 larger than for MMS assumption.

However the level are close enough to validate MMS's study using the PSD of Figure 7.2-27.

7.2.3.2.2 Effect of micrometeorites

7.2.3.2.2.1 Introduction

Impacts of micrometeorites would result in transient DFACS errors with the following risks, ordered in increasing severity (depending on impact strength)

- Temporary degradation of the measurement quality (a few seconds typically)
- Transient interruption of scientific measurement because of inertial sensor saturation
- Loss of optical link between the spacecraft because of excessive pointing error or of collision between the inertial proofmasses and their cages.

This short study is based on the statistical data on the velocity, density and mass distributions of micrometeorites used in the ESABASE tool developed by MMS to analyse the impact of meteoroids and debris on space structures.

The meteoroids mass repartition is given by Figure 7.2-29:

In the neighbourhood of the Earth, the velocity of micrometeorites ranges from 11 to 72 km/sec with an average of 18 km/s (in an Earth frame), as shown in Figure 7.2-30. Since LISA spacecraft dynamics relative to the Earth is small, these figures can be directly considered as the impact velocity distribution.

7.2.3.2.2.2 Assumption about the impact

It is assumed that the momentum of an impacting particle is entirely transmitted to the S/C with no reflection (the meteorite is absorbed by the S/C structure). The effect of the impact on the S/C is a nearly instantaneous acceleration. Hence; the shock is modelled as an impulsive velocity increment on the S/C which can be calculated by writing the conservation of the momentum :

Linear momentum : $m.V = (M+m).\Delta V$

Angular momentum : $m.\mathbf{l}x\mathbf{V} = (J+m.l^2).\boldsymbol{\Delta\omega}$

where : m is the particle mass

M is the S/C mass (250 kg)

V is the velocity of the particle relative to the S/C

ΔV, $\Delta\omega$ are the linear and the angular velocity increment of the S/C due to the impact

l is the distance between the impact location and the S/C centre of mass.

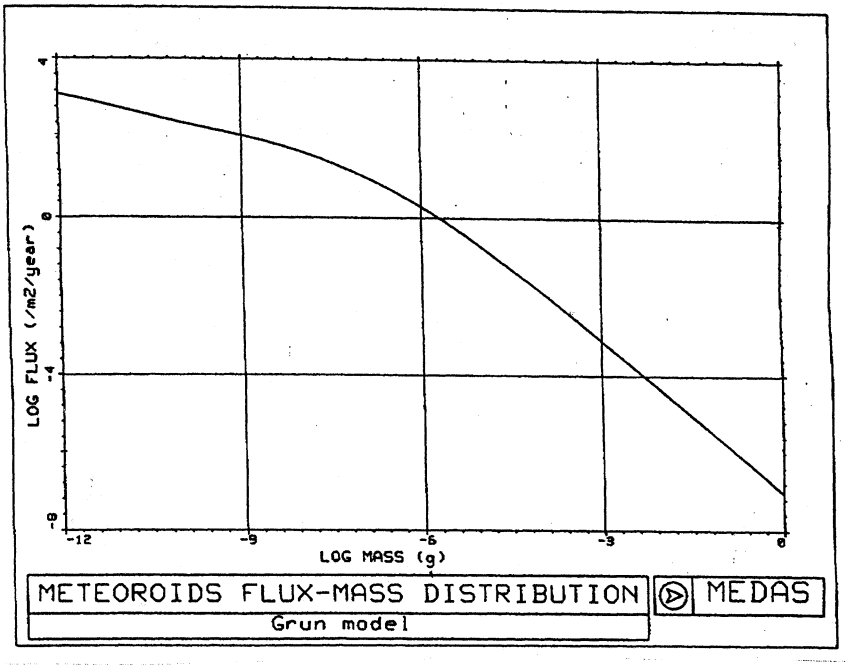

Figure 7.2-29 : Meteorites flux-mass distribution

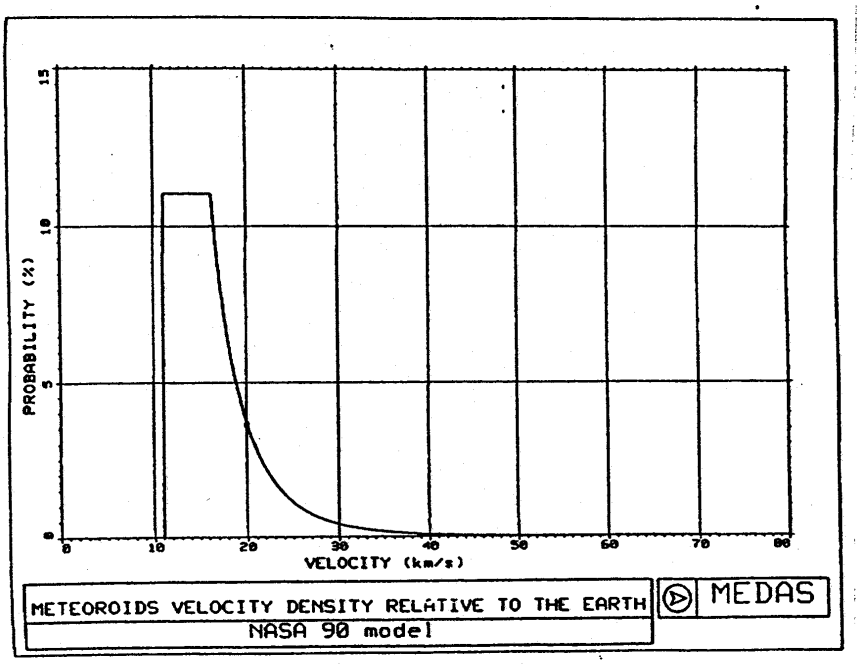

Figure 7.2-30 : Meteorites velocity density

7.2.3.2.2.3 Maximum allowed linear & angular velocity increment

We can assume as a first approximation that the maximum values that can be handled without long mission interruption (i.e. loss of the of the optical links and/or of the inertial reference) are :

- 10 µm for the distance between PM and cage
- 10 µrad for the laser beam pointing.

Furthermore, an impact will significantly disturb the scientific measurement during a few seconds if it results in more than 1 nm variation of the distance between the PM.

The impulse response of the DFACS are given in Figure 7.2-31 & Figure 7.2-32.

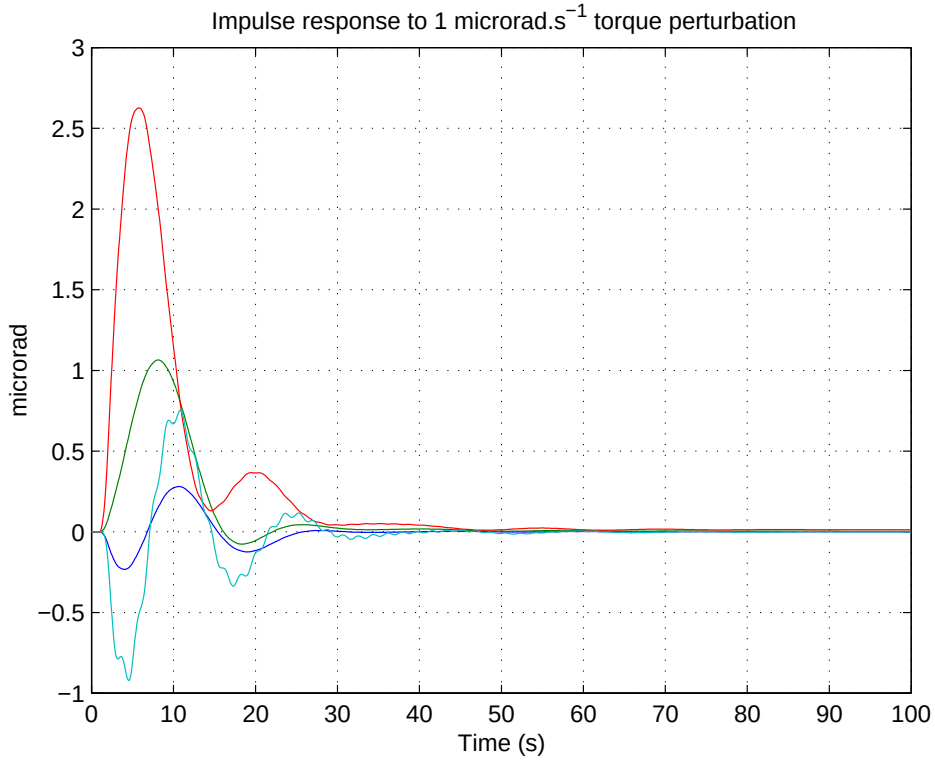

Figure 7.2-31 : rotational impulse responses of the DFACS

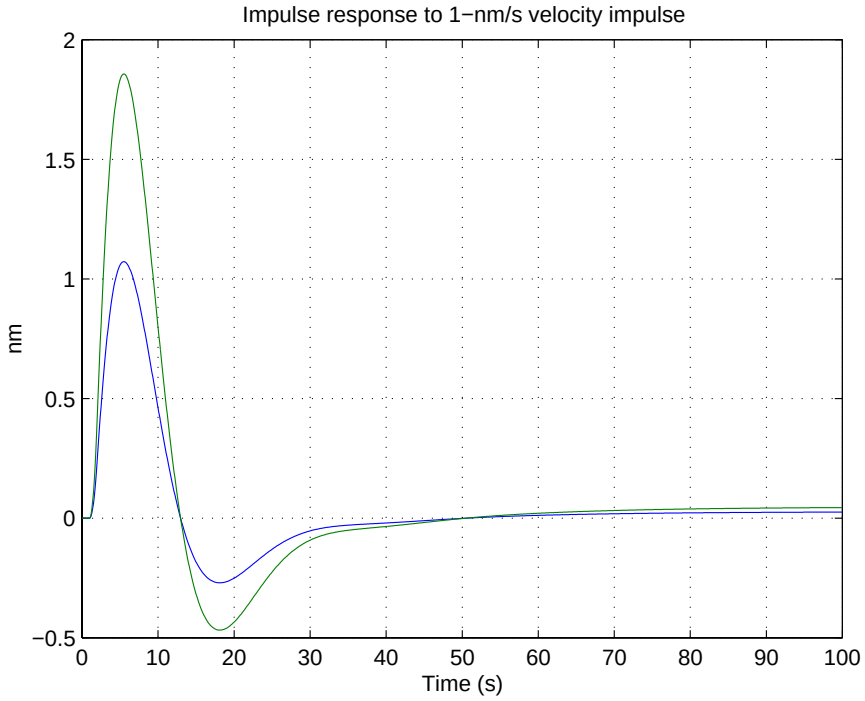

Figure 7.2-32 : Translation impulse responses of the DFACS

From these impulse responses, we can deduce that the maximum speed step for the S/C are :

Δv_{max} = 5.4 µm/s

$\Delta \omega_{max}$ = 4µrad/s

These values correspond to a particle linear momentum of :

Δv_{max} = 5.4 µm/s P = m.V = 1.3 mNs

$\Delta \omega_{max}$ = 4µrad/s P = m.V = 0.8 mNs (50 cm lever arm assumed)

Therefore both conditions are of the same order of magnitude, but the limiting condition is the pointing needs.

Similarly, the maximum velocity increment and the maximum linear momentum of a meteorite that will not disturb the scientific measurement are :

$\Delta v_{invisible}$ = 0.54 nm/s

Δv_{max} = 0.54 µm/s P = m.V = 0.13 µNs

7.2.3.2.2.4 Probability of impact resulting in a mission interruption

The number of impacts with meteorites resulting in the interruption of the science data collection and transition to the back-up stellar mode (i.e. with a linear momentum larger than P_{min} = 0.8 mNs) is given by:

$$N \leq \int_0^{\infty} p(V > \frac{P_{\min}}{m}).fl(m).A.dm$$

where fl(m) is the flux of particle of weight between m and m+dm, and A is the satellite cross-section. V < 72 km/s, so a large over-estimate of N is

$$N \leq A. \int_{\frac{P_{\min}}{72 km/s}}^{\infty} .fl(m).dm$$

$fl(m) = c_0.m^{-0.694}.(c_1 m^{0.306} + c_2)^{-5.38}$ with $c_0 = 1.2537\ 10^6$, $c_1 = 2200$, $c_2 = 15$ (see [10])

N< 1.2 impacts per year for the 3 LISA satellites together.

Considering this number is an over-estimate (especially on the meteorite velocity), it is expected that collision of micrometeoroids will not cause a mission interruption over the two-year nominal mission time . However the loss of optical link between the satellites is still possible, so the laser beam acquisition sequence has to be possible at any moment of the mission.

7.2.3.2.2.5 Number of impact per year corrupting the scientific measurement

The same formula is applied with P = 0.13 µNs. The resulting estimated frequency of scientific measurement degradation by meteoroid impacts is then:

N < 625 impacts per year for the 3 satellites together.

The estimated frequency is therefore about 2 impacts per day corrupting the measurement for typically a few seconds (the response time of the DFACS). As a consequence, it is not a critical issue but should probably takent into account in the data post-processing to remove the corrupted data.

7.2.3.3 DFACS Dynamic Simulator

7.2.3.3.1 Simulator architecture

The verification of the DFACS performance in the MBW is conducted with a multiple DOF dynamic simulator, developed in the Matlab/SIMULINK environment. This software is able to model the behaviour of all S/C DOFs in the plane defined by the LOS of the two telescopes:

- 2 in-plane translation axe for the S/C and the two proof masses (PM1, PM2)
- 1 rotation about the normal to the LOS plane for the S/C, PM1, PM2
- 1 rotational DOF between the telescopes LOS

The model is fully linear at this point, so that transfer function analyses are possible. This simulator could easily be refined if necessary in subsequent phases, with a more accurate modelling, including non-linearity; so as to allow time simulations of the transient phases..

The bloc diagram of the simulator is the following :

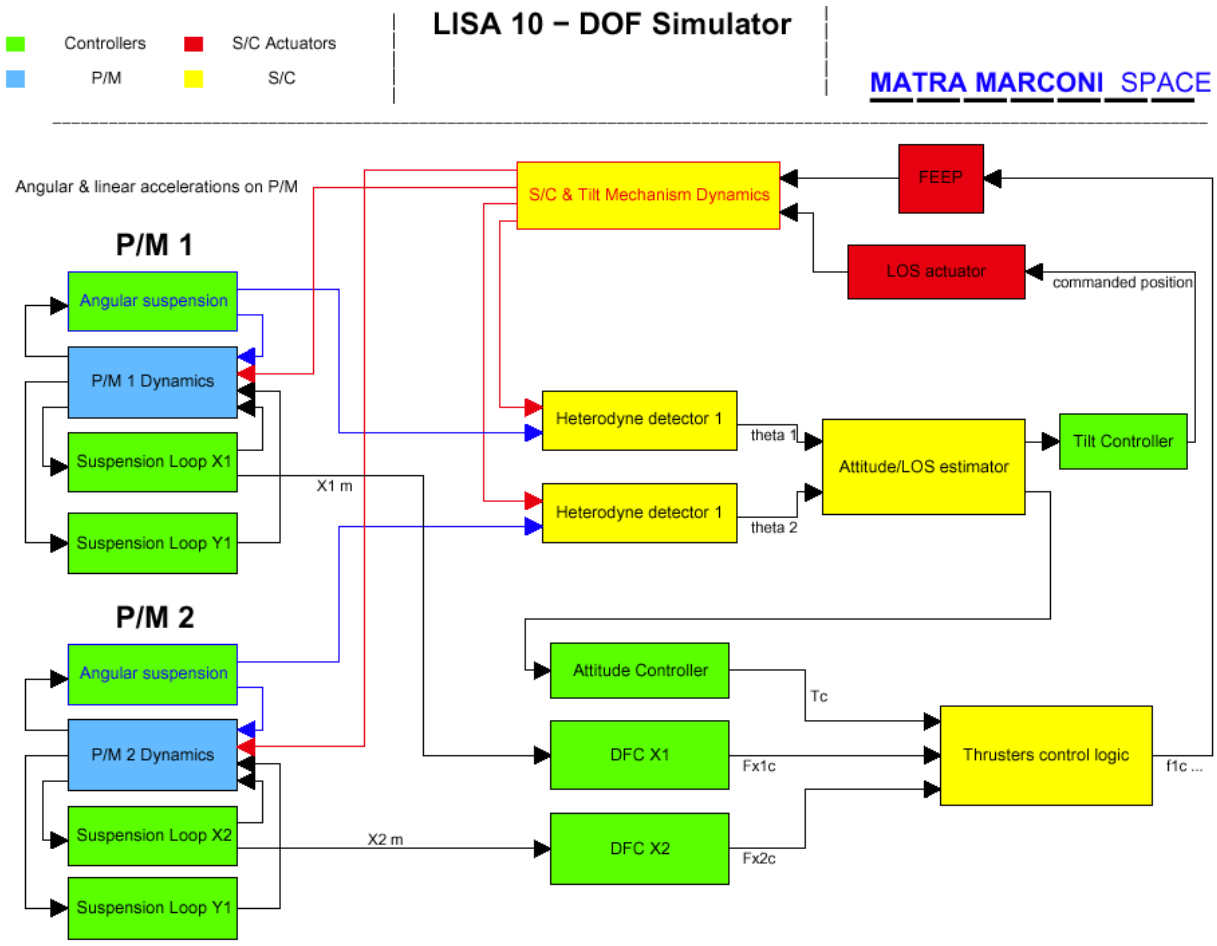

Figure 7.2-33 : LISA simulator bloc-diagram

7.2.3.3.2 Summary of simulation hypotheses :

- CAESAR : 2 soft axes
- Overall negative stiffness : 1. 10^{-7} N/m ("reasonable" objective agreed during Phase A2)
- CAEASAR measurement noise : 6.10^{-10} m/$Hz^{1/2}$ @ 10^{-4} Hz, 1/f slope
- CAESAR actuation noise : 7.10^{-16} m/s²/$Hz^{1/2}$ @ 10^{-4} Hz, 1/f slope
- FEEP thruster noise : 3.10-9 N/$Hz^{1/2}$ over the MBW.
- Heterodyne sensor attitude noise : 3 nrad/ $Hz^{1/2}$ for a sampling at 2 Hz.
- Distance between PM1 PM2 : 40 cm is used in the simulation, this small inconsistency with the latest design (50 cm) oes not affect the conclusions of the following analyses.

Remarks on these hypotheses :

- CAESAR characteristics are given by ONERA.
- Negative stiffness : During phase A1, MMS has identified that this unstable stiffness s a control design driver. This negative stiffness has two contributors : the electrostatic forces due to the inertial sensor operation, and the self-gravity forces, which are also unstable. It was agreed during Phase A2 that maximum efforts must be spend to minimise both sources of negative stiffness. In particular, in the mechanical design, the mass repartition around each PM must be optimised in this goal.
- The FEEP thruster noise specification is derived from both the solar perturbation and the controller performance : The idea of this specification is to keep the actuator (= FEEP here) noise smaller than the perturbation to be controlled. 3 10^{-9} N/$Hz^{1/2}$ corresponds roughly of the level of solar pressure at the controller cut-off frequency (to be described later on in this section). Even though the thrust noise level have never been directly measured on any FEEP thruster at this stage, this level seems to be an achievable objective, by comparison to the required thrust range of 20 µN.

7.2.3.4 Control Design

7.2.3.4.1 Candidates strategies

The goal of the drag-free control is to make inertial the two proof masses, which mirrored sides are used to reflect the laser beams, defining the interferometer arm length. This is obtained by the following complementary actions:

1. reducing as far as possible the linear/angular acceleration experienced by the S/C (role of the DFACS)
2. providing best possible isolation of the PMs relative to the S/C (optimisation of the inertial sensor servo loops in close relation with DFACS "outer loops")
3. making sure the PM are "quiet" in the MBW (acceleration< 2.5 10^{-15} $m/s^2/Hz^{1/2}$).

Point 3. is independent of any control strategy, whereas the first two points are really the core of MMS's task in this project.

Various drag-free missions in which MMS has been involved in the past (Gravity Probe-B, STEP, GOCE) relied on the concept of "drag-free reference point". This point is the point chosen on the S/C to ideally follow a purely gravitational motion.

This concept could be applied to LISA, but the selection of this point is not trivial at all, since we would ideally like to have two drag-free points on the S/C (at each mirror location), which is not physically possible. A trade-off is then necessary to select the best DFRP. This trade-off is presented in Appendix 1. Two candidates are retained for the discussion here : the intersection of the LOS, and one of the PM location.

But this concept of drag-free reference point can be bypassed in the case of LISA. Indeed, for each proofmass, only one axis must be inertial, while there are only requirements on the PM-cage relative position on the other two axes.

Therefore another family of strategies consists in performing the drag-free control using only the "sensitive" axis of each PM (i.e. in the telescope LOS direction), while the other axes of the PM are only suspended, through the electrostatic suspension loops

Thus, four strategies can be preliminarily selected for a detailed trade-off :

- **Strategy 1** : DFRP located at one of the proofmasses. In other words, one PM is the only reference for the DFC (master PM), the other one has no role in DFC (slave PM).
- **Strategy 2** : DFRP located at the intersection of the LOS. DFC measurement is reconstructed from measurements of both PM to be fed into the DFC controllers.
- **Strategy 3** : Strategy without any defined DFRP : The DFC is performed with the raw measure of each sensitive axis.
- **Strategy 4** : Same strategy as 3, but no suspension is implemented along the sensitive axis. The cancellation of instability effects, constant forces (self-gravity), etc, is handled by the DFC loop.

7.2.3.4.2 Controller design

The LISA DFACS is quite complex since a large number of DOFs need to be controlled, so many different controllers are required. Since the dynamics are to large extent decoupled (nearly inertial pointing), the design is conducted axis-by-axis as SISO (Single Input, Single Output) control filters. Interactions between loops because of the sensor/actuator system are accounted for in the control filter design and verified a posteriori through the multi-DOF simulator. The control filters are described hereafter, following an ascending order, from the PM suspension to the LOS pointing.

It must be noticed that these controllers have been designed for the strategies with DFRP (strategies 1 & 2) to meet the requirements or to be as close as possible to them. The same controllers will be applied for strategies 3 & 4 (which will turn out to be better - see 7.2.3.5) to provide consistent comparison between the strategies. As a consequence, the control filters might appear to be over-designed for these last two options, but there is no point decreasing the performances of these controllers, since they already feature low order, relatively low cut-off frequency, and therefore are fully compatible with the computational capacity of standard space-qualified processors.

7.2.3.4.2.1 Suspension controller

The suspension loop is made to restrain the PM relative motion under the effect of low frequency disturbances (below the MBW). Above the suspension bandwidth, in the MBW, the PM is isolated from the S/C accelerations. The minimum possible value for the suspension bandwidth is constrained by the natural instability frequency f_s (5 10^{-5} Hz including self gravity and electrostatic field effects), so that, when accounting for stability margins and robustness to uncertainty on the instability, the suspension cut off moves slightly in the MBW. The suspension controller has an order of two and the following structure:

$$Controller = \frac{3.w_s{}^2 + 2.\xi.\sqrt{2.w_s}.s}{\left(1+\frac{s}{15.ws}\right)\left(1+\frac{s}{160.ws}\right)} \quad \xi = 1;\ w_s = 2.\pi.f_s$$

The controller is conceived to be adapted to the instability frequency while keeping good stability margins. With the considered negative stiffness effect, suspension main features are:

- Cut off frequency : 1.3 10-4 Hz
- Gain margin : 9.5 dB
- Phase margin : 57°
- Sampling frequency (objective): 0.01 Hz

These margins are very sensitive to errors on the instability frequency, as illustrated in Figure 7.2-34. The gain margin becomes equal to only 6 dB for a frequency increased by 25%. The proportional derivative in the numerator is tuned to have a gain margin of 9 B; which determines the cut off frequency. Because of the positive eigenvalue of the unstable dynamics the Nyquist diagram must used to study the stability of the suspension loop. The denominator is implemented to decrease the electrostatic noise contributions in the MBW. The final open loop transfer function is presented in Figure 7.2-35

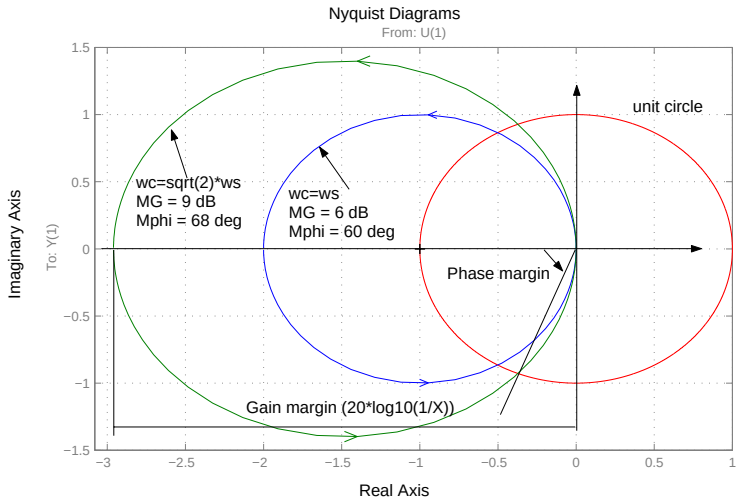

Figure 7.2-34 Nyquist diagram of the open loop (controller numerator only)

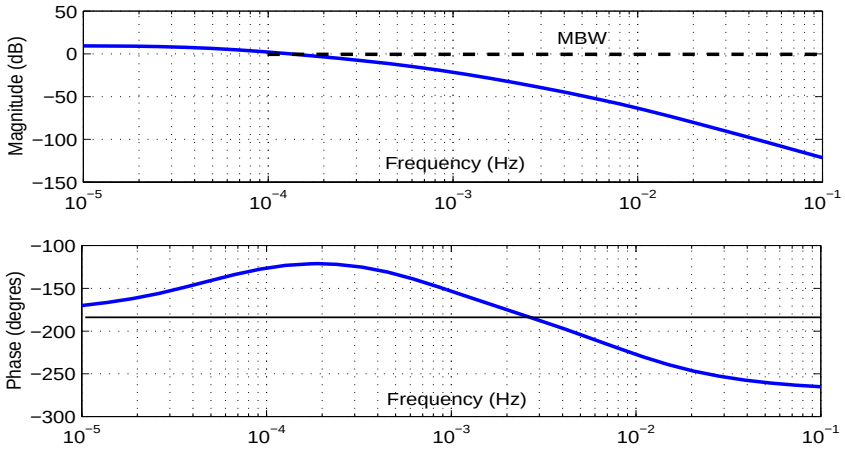

Figure 7.2-35 Transfer function of the open suspension loop

This describes the controller that is used in the simulation of the performance in the MBW. In reality, the suspension control scheme will have to be more complex to provide the very high rejection of the almost-constant forces applied on the PM (mainly self-gravity forces) required to meet the PM centring requirements. This rejection gain has to be at least 100 times larger than the low frequency gain provided by this controller to meet the specification of 5 µm of absolute displacement of the proofmass in its cage.

Several solutions could be considered, such as simply adding an integral term to have a high gain at low frequency. Such a solution would probably lead to numerical problems, since the frequencies of interest for this high rejection is around 10^{-7} Hz, to be compared to the 10^{-2} Hz sampling frequency forecast for this controller.

The most promising idea consist in implementing a feed-forward compensation of the constant forces, as conceptually described below :

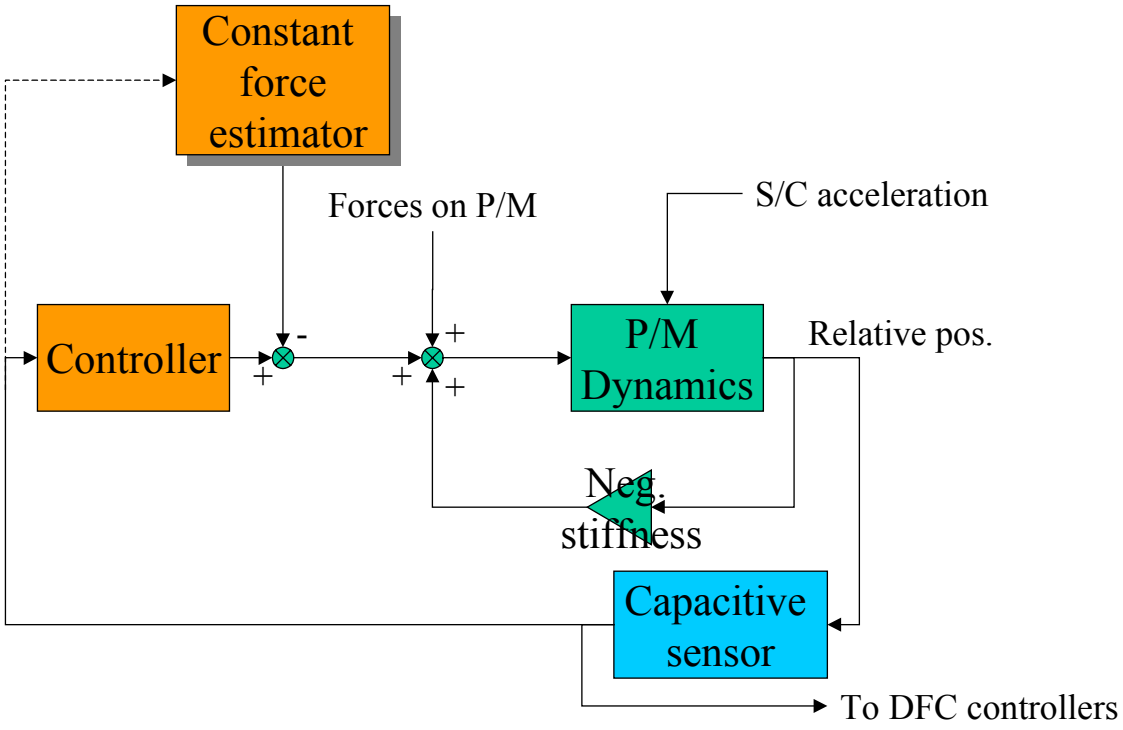

Figure 7.2-36 : control architecture including constant force rejection blocks

This estimator of the DC disturbances will be initialised with an a priori estimate of the forces to be compensated and will operate on the capacitive sensor measurements. Its refreshing frequency could several orders of magnitude lower than the controller frequency. The validation of such an estimator requires to simulate the system during several days, a task to be performed during the detailed design phase.

7.2.3.4.2.2 DFC controller

The DFC controller is used on the three translation axes of the S/C to reject the external perturbations like solar pressure and FEEP noise. The rejection needs are driven by the acceleration and the position requirements and depends on the control strategy (master slave, no DFRP...). The structure of the considered 4th-order controller is the following:

$$Controller = \frac{10^{\frac{-36}{20}} \cdot \left(1+\frac{s}{w_1}\right)^2 \cdot \left(1+\frac{a.s}{w_4}\right) \cdot \left(1+\frac{s}{w_5}\right)}{\left(1+\frac{s}{w_3}\right) \cdot \left(1+\frac{2.\varsigma.s}{w_2}+\frac{s^2}{w_2{}^2}\right) \cdot \left(1+\frac{s}{w_4}\right)} \qquad w_i = 2.\pi.f_i \quad \begin{cases} f_1 = 3.4\,10^{-4}\,Hz \\ f_2 = 2\,10^{-3}\,Hz \quad \varsigma = 0.7 \\ f_3 = 1\,10^{-3}\,Hz \\ f_4 = 0.2\,Hz \quad a = 8 \\ f_5 = 1\,10^{-2}\,Hz \end{cases}$$

The characteristics of the open loop transfer function (with the suspension loop closed) are:

- Cut off frequency : 6 10-2 Hz
- Gain margin : 8 dB
- Phase margin : 44°
- Sampling frequency : 1 Hz

The open-loop transfer function is presented in Figure 7.2-37. The major feature of this controller is the very large frequency range of operation, resulting in a static gain of about 100 dB. Numerical implementation will need to be carefully addressed in subsequent phases, so as the acquisition strategy.

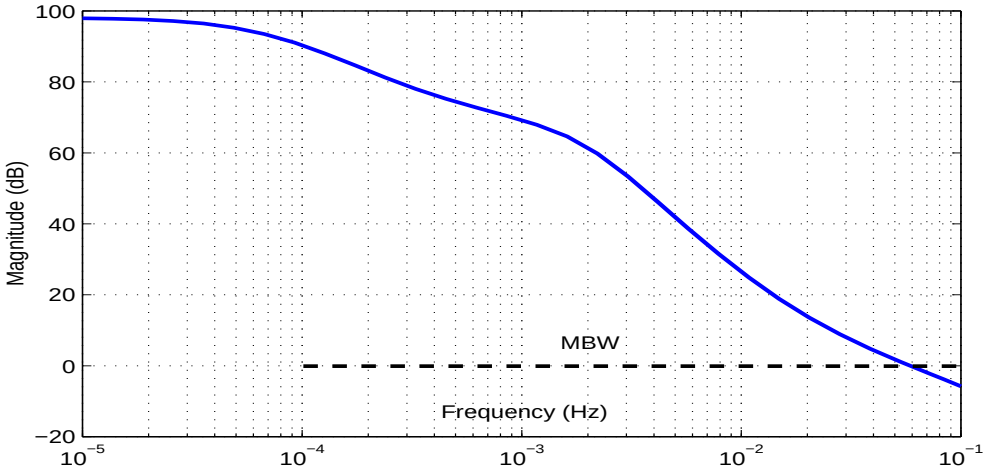

Figure 7.2-37 Open-loop transfer function of the DFC

7.2.3.4.2.3 Attitude controller

The attitude controller is implemented to have a good absolute pointing stability of the S/C in the MBW despite external perturbations. The proposed controller has an order of two and the following structure:

$$Controller = \frac{10^{\frac{-32.5}{20}}.\left(1+\frac{a.s}{w_1}\right).\left(1+\frac{s}{w_3}\right)}{\left(1+\frac{s}{w_1}\right).\left(1+\frac{s}{w_2}\right)} \quad w_i = 2\pi.f_i \quad \begin{cases} f_1 = 0.1\ Hz \\ f_2 = 110^{-4}\ Hz \\ f_3 = 2\,10^{-4}\ Hz \end{cases} \quad a = 6$$

Characteristics of the open loop transfer function :

- Cut off frequency : 6.3 10-2 Hz
- Gain margin : 9 dB
- Phase margin : 45°

The transfer function is presented in Figure 7.2-38. As for the DFC, the low cut off frequency requires a sampling frequency of about 1 Hz

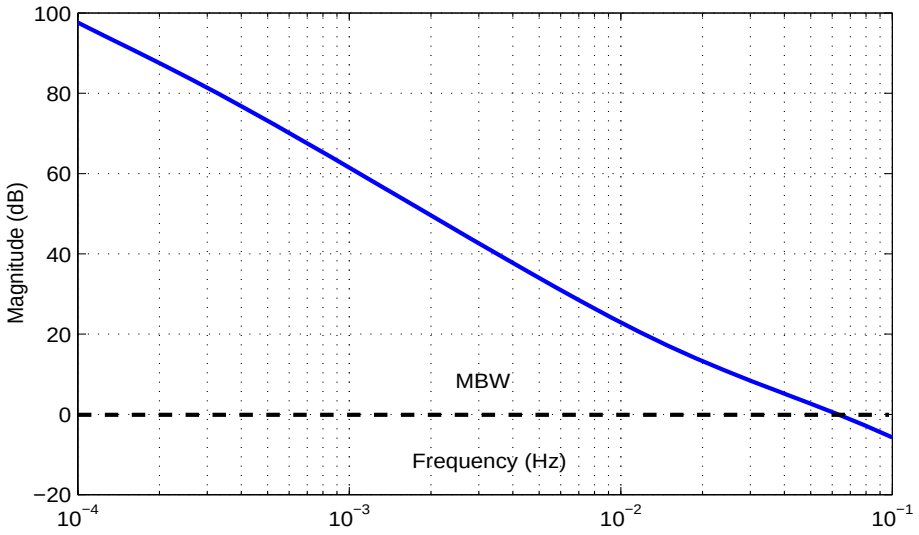

Figure 7.2-38 Open-loop transfer function of the attitude control

7.2.3.4.3 Tilt mechanism controller

The tilt mechanism controller is implemented to correct the angle between the two telescopes. The proposed 2nd order controller is tuned to meet the requirements in position and in acceleration.

$$Controller = \frac{10^{\frac{12}{20}}.\left(1+\frac{a.s}{w_1}\right)}{\left(1+\frac{s}{w_1}\right).\left(1+\frac{2.\varsigma.s}{w_2}+\frac{s^2}{{w_2}^2}\right)} \qquad w_i = 2\pi.f_i \qquad \begin{cases} f_1 = 6\,10^{-2}\,Hz & a = 6 \\ f_2 = 1\,10^{-2}\,Hz & \varsigma = 0.7 \end{cases}$$

Characteristics of the open loop transfer function :

- Cut off frequency : 6.8 10^{-2} Hz
- Gain margin : 21 dB
- Phase margin : 45°

The stability margin is important and insures robustness to variations of the mechanism dynamic (e.g. uncertainty on the resonance of the optical assembly suspended on flexible bearings).

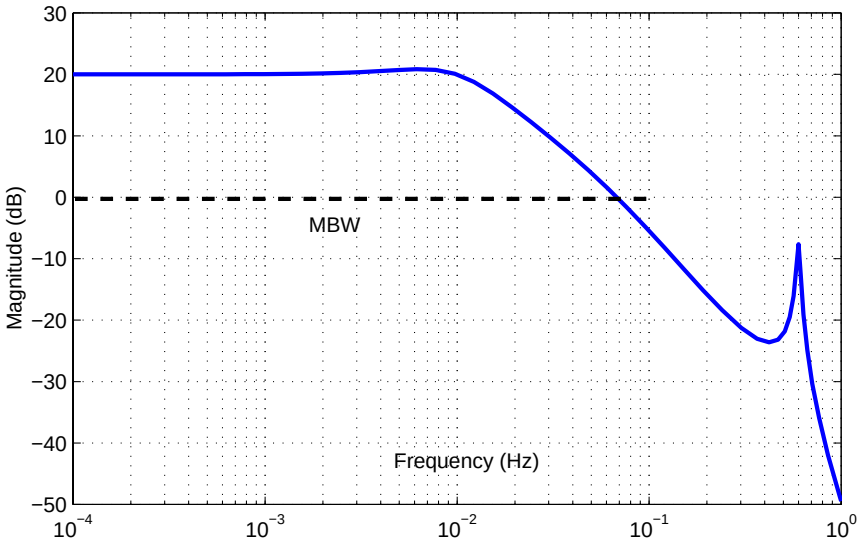

Figure 7.2-39 Open-loop transfer function of the tilt mechanism control

7.2.3.5 Control Strategy Trade-off

7.2.3.5.1 Performance in the MBW

The various strategies have been compared using the dynamic simulator used to compute the closed-loop transfer functions. The results presented here are in the frequency domain, obtained by multiplication of the closed-loop transfer functions by the input disturbances & sensor noise PSD. Computed PSDs have been validated by time simulations with noise-only inputs.

Two plots are presented : The first one compares the residual PM acceleration on the principal axis for each strategy to the requirement. In the second one, the disturbing forces acting directly on the PMs (on which DFACS has no effect) were removed so that the contribution of each DFC strategy can be compared more easily.

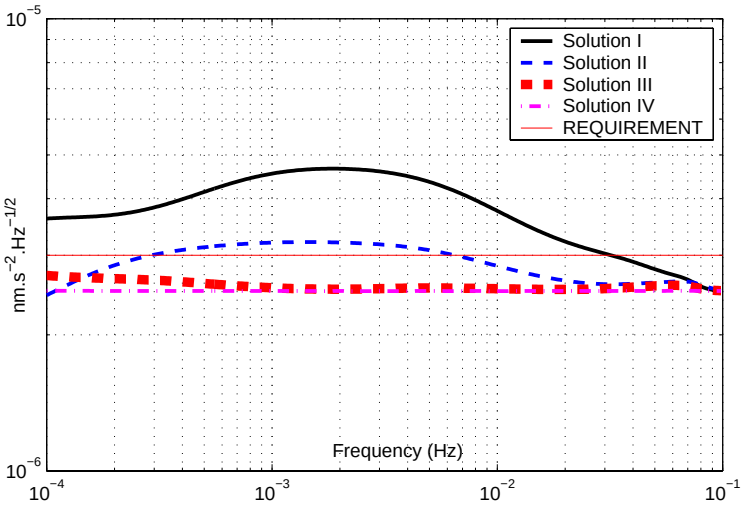

Figure 7.2-40 : Residual PM acceleration along the sensitive axis

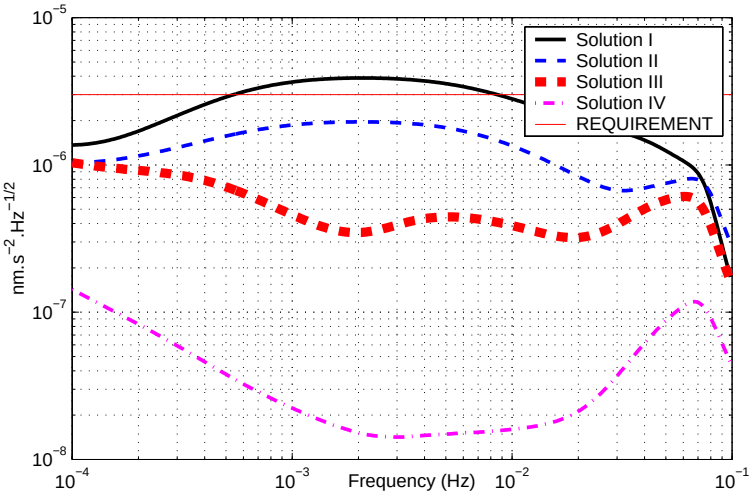

Figure 7.2-41 : Residual DFACS-related acceleration of the PM.

For each strategy, the contribution of all PM disturbing forces was assumed to be flat in the MBW with a level of 2.5 10^{-15} $m/s^2/Hz^{1/2}$. This is the main contributor to the final acceleration performance. The additional DFC contribution is analysed below for each strategy :

Strategy 1 : The plots of course correspond to the performances of the slave PM (worst case). The noise is dominated by the transmission of the heterodyne sensor noise (effect of angle jitter transmitted with the lever arm and the suspension loop). The acceleration is 2 times larger than the requirement in the middle of the MBW. It will probably be difficult to further optimise the suspension loop, and the requirement will hardly be met, unless the heterodyne sensor noise is significantly improved.

Of course on the master PM (not shown here), the performance is much better since it is not sensitive to attitude jitter. Therefore this solution should be selected for the failure mode, when only one optical assembly is operated.

Strategy 2 : The noise is dominated by the heterodyne sensor noise as well. But for this strategy, it is due to the reconstruction of the measurement at the DFRP. Marginal violation of. the requirement appears with this solution (20%).

Strategy 3 : No dominant contributor. Impact of measurement noise, actuator noise, and FEEP noise have the same order of magnitude. The requirement is met with factor 2 to 5 margin. This is then a nice solution.

Strategy 4 : The performance is further improved by a factor more than 10. These margins could be used to relax the sensor noise requirements, and also the FEEP thruster noise.

Note on coupling effects : These plots do not take into account any kind of parasitic coupling between CAESAR axes. These couplings have a minor, but non negligible effect, presented in section 7.2.3.6.

7.2.3.5.2 Conclusion & Recommendation

Strategies 3 & 4, without DFRP, allow to meet requirements with margins (this is also the case for other requirements, such as PM position, not detailed here).

Strategy 3 is recommended by MMS to be the baseline for this phase A, with the possibility of preferring strategy 4 in subsequent phases, provided that constant force cancellation does not rise the complexity of the control scheme, which still needs to be demonstrated for strategy 4.

7.2.3.5.3 Discussion on CAESAR's configuration

Two options have been discussed with DSS, ONERA, and the Science team. A short description of each one , as well as a quick summary of advantages and drawbacks is presented hereafter :

The baseline for the inertial sensor is to feature two equivalent soft axes, and one stiff direction (off-plane direction):

+ Some redundancy in case of loss of sensitivity of one sensor (TBC)
+ Possibility to measure the noise on one PM using the other PM transverse axis.
− Some bulkiness and implementation concerns.

Another option is to design a sensor with one soft axis and two stiff axes (it corresponds to ONERA's prototype configuration):

+ Nice implementation of sliding capacitive sensor.

− Stiff axes implies coupling from the transverse axes toward the main axis

Both configurations are equally feasible in terms of control, with some preference to the "2-soft axis" solution, since it minimises the coupling effects.

This trade-off is interesting for mission performance optimisation, but it is not a critical issue.

7.2.3.6 Detailed Analysis of the Performance in the MBW

This paragraph draws a detailed description of the performances of the DFACS designed by MMS for the selected strategy, through transfer function analyses. Effects of inter-axis couplings will be described in the last paragraph of this section (7.2.3.6.5), and are not accounted for before.

7.2.3.6.1 Acceleration performance

PM acceleration on the principal axis

The quadratic sum of all the contributors is under the requirement of 3 $10^{-15}.s^{-2}.Hz^{-1/2}$

The parasitic forces on the PM are, as can be expected, completely transmitted to the PM acceleration. It is the major contributor to the residual acceleration (the assumption is a white noise of 2.5 $10^{-15}.s^{-2}.Hz^{-1/2}$). This error source is almost completely non correlated to the control strategy. It must be noticed that the contributors related to the DFACS are **significantly lower** than these perturbations. Therefore the performance here are mainly driven by direct perturbations on the PM, which should be carefully evaluated in subsequent phases.

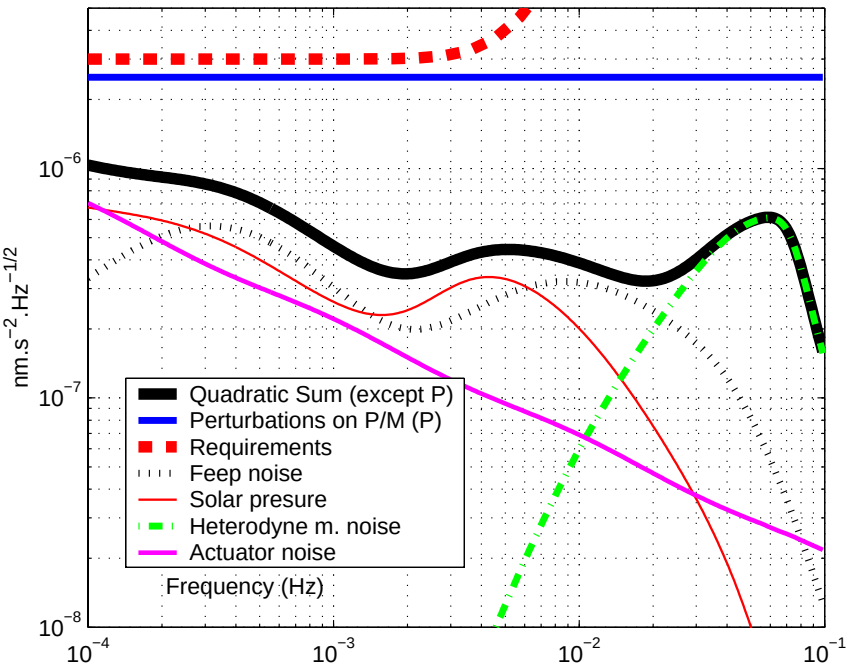

Figure 7.2-42 : PM acceleration PSD in the MBW (principal axis)

As expected, there is a good rejection of the noise due to attitude jitter on the principal axis, providing design margins and for the equipment specifications. In particular, the electrostatic measurement noise and the heterodyne measurement noise appear not to be critical, and some relaxation of the FEEP noise requirement could be considered in further phases.

PM acceleration on the transverse axes

Of course, the very good isolation on the principal axes is paid by a very poor acceleration isolation on the transverse axes. This is not a problem, since the scientific performance is not correlated to the mirror transverse acceleration. In particular, the angle jitter, visible on Figure 7.2-43 as the heterodyne sensor noise is fully transmitted.

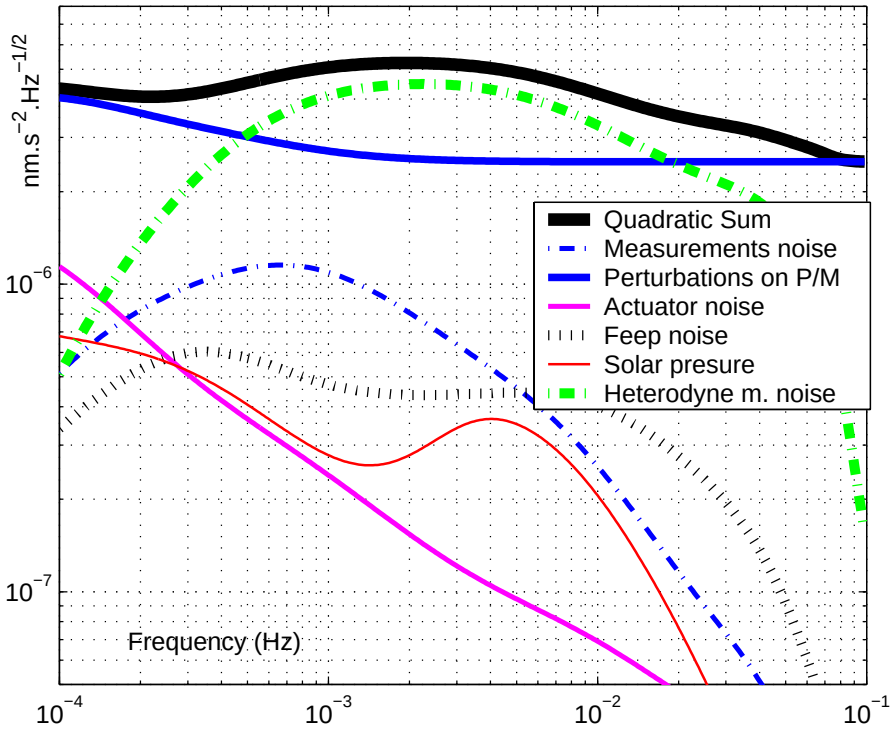

Figure 7.2-43 : PM acceleration on the transverse axis

7.2.3.6.2 Relative position

7.2.3.6.2.1 Relative position on the principal axis

The requirement 2.5 nm.Hz$^{-1/2}$ on the distance between the PM an the cage is fulfilled with some margins, as shown in the following plot.

The major contributors are the external perturbations on the S/C and the angle jitter. The inertial sensor measurement noise is also an important contributor, but only at the beginning of the MBW (0.6 nm.Hz$^{-1/2}$ @ 10^{-4} Hz f $^{-1/2}$ slope). Here again, there is some design margins, in particular in the middle of the MBW, that may ease the final control design.

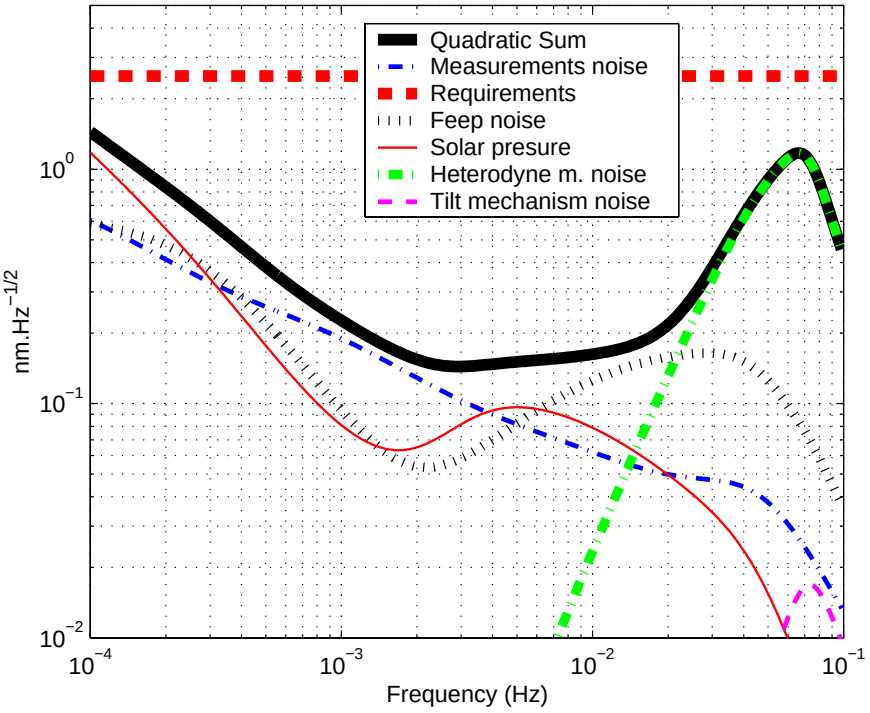

Figure 7.2-44 : Relative position in the MBW on the principal axis

Relative position on the transverse axes

The requirement on the transverse axis, relaxed to 10 nm.Hz$^{-1/2}$, is fulfilled.

The major contributor at the beginning of the MBW is the PM perturbation. In fact, this contributor is really the perturbation on the sensitive axis of the other PM. This can be easily understood : the first proofmass – let's call it PM A – is free-floating along its principal axis. It means that the S/C is following PM A along its principal direction. On PM B, the transverse axis is not free-floating, but suspended to the S/C. Therefore the motion of the S/C to follow PM A can be read on the transverse axis of PM B.

Therefore measurements on this axis makes possible the indirect knowledge of the PM perturbation along the principal axes. This is in fact the only way to sense during the flight if the assumptions on the level of perturbation on the PM are correct or not (at least in the beginning of the MBW).

The angle jitter contribution is very important after 0.5 mHz.

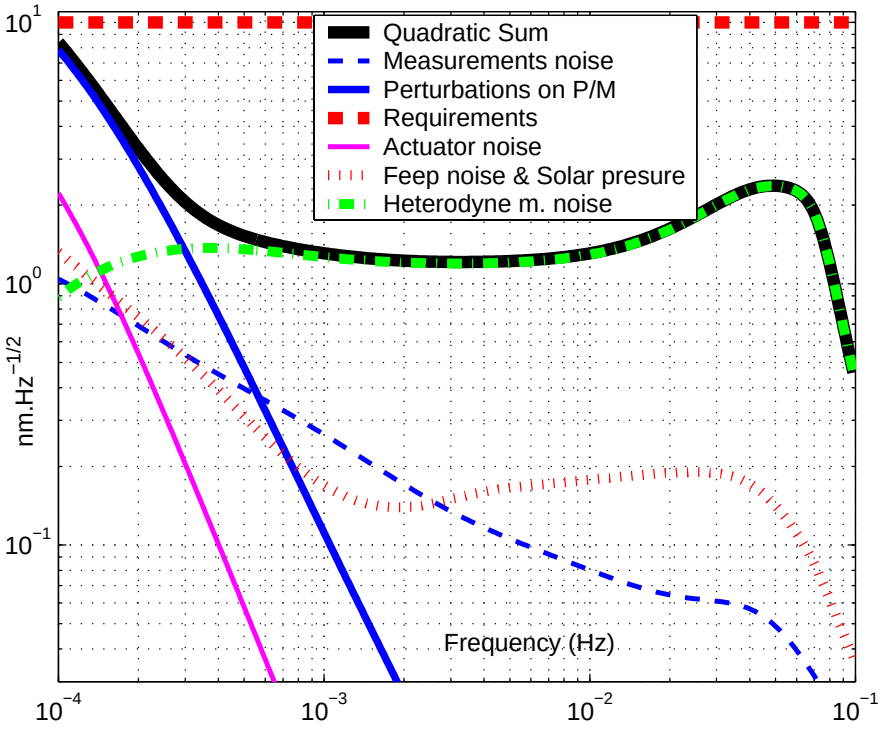

Figure 7.2-45 : Relative position in the MBW on the transverse axis

7.2.3.6.3 Attitude performance

With the pointing strategy presented in chapter 4, the attitude performance is directly the pointing stability of one of the telescope LOS, specified to 8 nrad/$Hz^{1/2}$.

With the current design, this requirement is met with some margin (Figure 7.2-46). It is relatively easy to implement here high control rejections (control bandwidth is not critical, and the dynamic range compatible with a standard 12-bit A/D converter). As a consequence, disturbance torques can be very efficiently rejected, so the major contributor is the heterodyne sensor noise over the entire MBW.

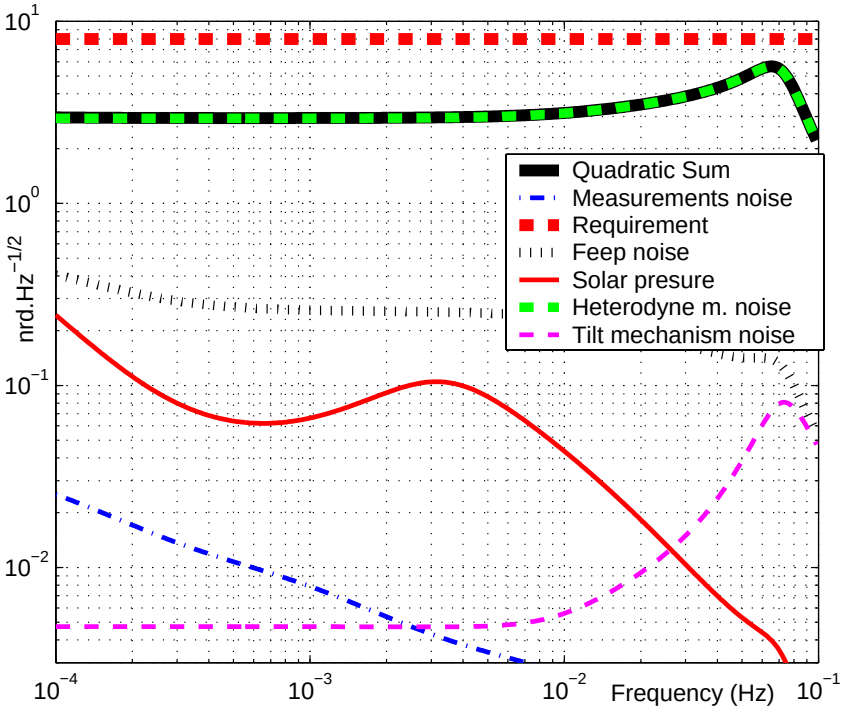

Figure 7.2-46 : Attitude performance

7.2.3.6.4 Cross validation through time simulations

All the results found by transfer function analysis have been verified with time simulations. The PSD of the simulated signals are fully consistent with the frequency domain analysis , as illustrated in. Figure 7.2-47 .

In subsequent phases, the same simulator (with possibly some refinement of the error models) can be used to validate the through time simulations the low frequency (below the MBW) performances, the transient phases (drag-free & fine pointing acquisition) and the laser beam acquisition.

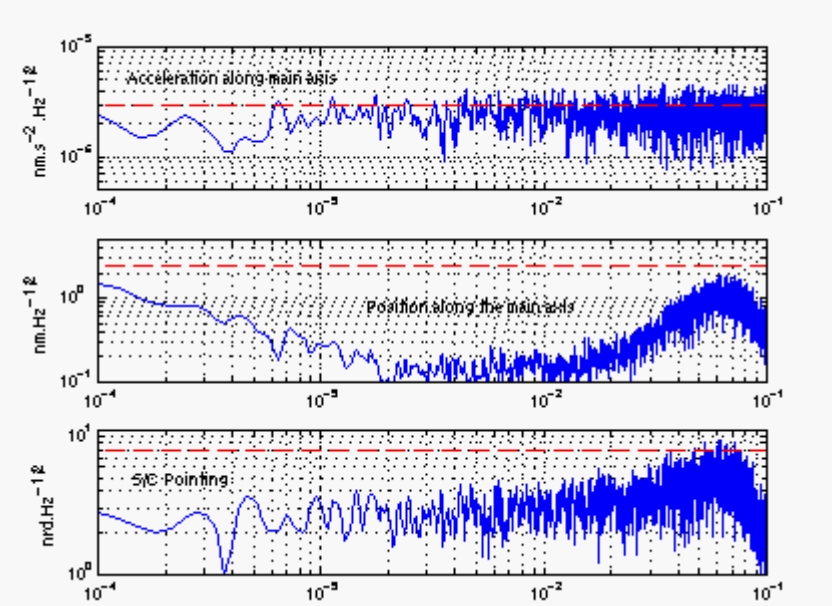

Figure 7.2-47 : Typical time simulation results

7.2.3.6.5 Effect of couplings

The coupling aspects have been studied separately. Indeed, the most important couplings are due to the projection of electrostatic forces in the inertial sensor, and only in the case of stiff suspension. In the current baseline for CAESAR configuration, there is only one stiff-suspended axis, and this is the off-plane direction, which is not modelled in this simulator. This explains why these couplings could not be simply included in the previous analyses. Their impact is carefully assessed in this paragraph.

The possible sources of couplings are :

- Couplings by FEEP errors. The misalignments & scale factors related to the thrusters could be roughly estimated to 5° & 5% (3σ) . It appears in fact that this source of coupling has a negligible effect on the PM acceleration. It is fully compensated by closed-loop control .
- Couplings due to the electrostatic sensing and actuating system. The values of these coupling effects are 10^{-4} between longitudinal axes and $5\ 10^{-6}$ between longitudinal & rotation (in

acceleration). These values are the result of a very preliminary assessment by ONERA. They need to be carefully consolidated in subsequent phases, considering the final configuration for CAESAR.

- Coupling due the PM tilt : 2 10^{-4} if the option of using the PM to realise the point ahead angle is selected. It is actually an additional electrostatic coupling.

To assess the impact of these coupling effects, the simulator has been modified so that the in-plane transverse axis of each PM is now suspended with a stiff control. This is done to assess the impact of the off-plane transverse axis. But this is also an option for the design of the inertial sensors.

The acceleration performance with coupling is compared to the performance without coupling on Figure 7.2-48.

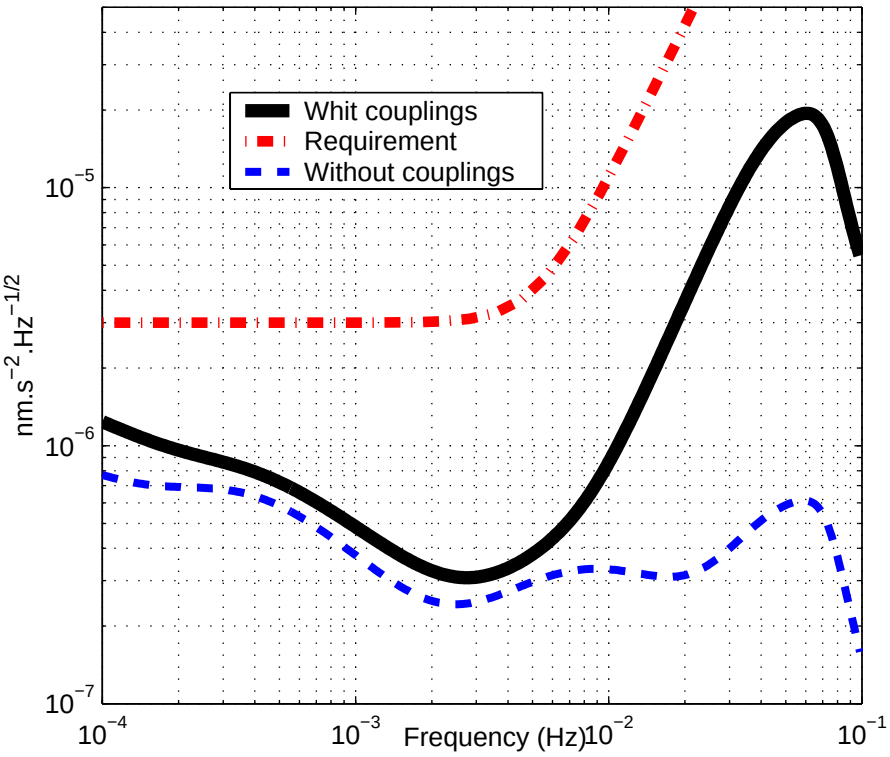

Figure 7.2-48 : Comparison of the noise level with and without coupling

The impact of couplings is quite significant in the upper part of the MBW, but the residual acceleration remains below the requirement, relaxed in this frequency range. At lower frequencies, couplings induce a degradation by about a factor of two, well within the design margins.

7.2.4 Synthesis & Recommendation

The AOCS subsystem budgets of mass, power are summarised in the section 5.4 of this report. The Bus data and CPU load budgets of the DFACS are summarised below. The DFACS system includes a lot of controllers, since 19 DOFs need to be controlled simultaneously. Fortunately the order of the controllers and the sampling rate can be kept low, so that DFACS-related bus data budget and CPU loads are not critical relative to current avionics performances. The estimated bus data budget is presented in Table 7.2-11, and the CPU load related to control algorithms in operational mode (FDIR & data management not included) is presented in Table 7.2-12. The critical aspect is likely to be the software size, because of the large number of AOCS modes (not evaluated here).

Table 7.2-11 : Bus data flow for DFACS

Device	# of operating devices	# of Inputs & Outputs	I/O Rate (Hz)	# of bits	Data Rate (bps)
Stiff suspension	10	1	2	18	360
Weak suspension	2	1	0.01	18	0.36
Input for DFC	3	2	2	18	216
Attitude	3	1	2	12	72
LOS actuation generation	1	1	2	16	32
FEEP command generation	1	7	2	12	168
TOTAL bus data budget for DFACS with no margins! (bit/sec)					**848**

Table 7.2-12 : Computation needs for DFACS

S/W modules	# of operating devices	# of floating operations	Rate (Hz)	Computation load (Flops)
Stiff suspension	10	11	2	220
Weak suspension	2	11	0.01	0.22
DFC	3	19	2	114
DFC command generation	3	5	2	30
Attitude	3	19	2	114
Attitude estimator	3	2	2	12
LOS actuation generation	1	15	2	30
LOS estimator	1	2	2	4
FEEP command generation	1	77	2	154
Software margins (100%)				**678**
TOTAL computation needs (kFlops)				**1.4**

7.2.4.1 Summary of Sensor & Actuator requirements

Star Trackers

NEA on transverse axes : < 1 arcsec/$Hz^{1/2}$

Bias on transverse axes: < 1 arcsec – 3σ (other than mounting & thermal biases)

FOV : 3-axis attitude determination without star measurement interruption

Heterodyne sensor –

Attitude sensing noise : < 3 nrad/$Hz^{1/2}$.

Range : 3 µrad

Output frequency : 2 Hz if no active damping of the telescope tilt mechanism oscillation (12 bits A/D conversion), 10 Hz if active damping performed with the heterodyne measurement

Telescope pointing mechanism

Range : 1°

Angular rate : 20 nrad/s

Absolute accuracy : < 1 µrad

Noise : 0.7 nm/$Hz^{1/2}$ above 40 mHz.

FEEP thrusters

Configuration : Pods of 2 thrusters with possible adjustment of the two thrust directions (+2 redundant emitters)

Range : 20 µN

Noise : <3 nN/$Hz^{1/2}$.

Scale factor : <5%

Thrust direction misalignment : <5°

7.2.4.2 Conclusions and Critical Areas

The AOCS/DFACS analyses conducted by MMS in the frame of the LISA Phase A study have allowed to demonstrate the feasibility of the S/C & payload control for the considered configuration with two optical assemblies in each of the three spacecraft. In particular, the 10-DOF dynamic simulator has allowed to verify that the preliminary DFACS design proposed by MMS meets all n the MBW : PM acceleration along the principal axes, PM relative position w.r.t. the S/C, pointing stability.

While the overall feasibility of the spacecraft control concept appears to be demonstrated now by this study, some areas need to be further consolidated as detailed hereafter.

Sensor/actuator technology :

Four technologies deserve interest for the consolidation of the DFACS mission performance :

1. **Star tracker performance**. In this document, it was shown that new generation, and low-cost, star trackers should reach an accuracy of 1 arcsec in the favourable conditions of the LISA mission. This level of performance should be consolidated through a more detailed error budget for these sensors, which are generally designed for LEO operations.
2. **Inertial sensor** : Among all aspects related to the inertial sensor, one item has been shown in this document to be of primary interest for the control aspects : the inter-axis couplings due to electrostatic forces. Rough estimate of these couplings have been provided, but the accurate value (or an accurate model) for the final sensor configuration is necessary. Consolidation of the achievable minimum negative stiffness is also important for control design.
3. **FEEP thruster** : The most critical aspect for LISA DFACS design, to be covered by further studies is the level of noise in the MBW. The preliminary requirements derived from mission & control design constraints appear to be significantly below (by a factor 2 to 3) the first FEEP noise measurements at ARCS & Centrospazio. These requirements have to be consolidated/reviewed according to refined experimental results, which should be performed with FEEP drive electronics actually optimised to reduce thrust noise. Means to actually assess the thrust noise are also to be investigated.
4. **Mechanisms** : If the fibre positioner appears now as a nearly off-the-shelf mechanism (thanks to the large descoping of its initial 3-DOF / wide range functionality), the telescope tilt mechanisms still deserves further attention. In particular the criticality of using a stepper motor should be further investigated and traded-off with a still-to-qualify piezo-driven motor .

Control Design :

In terms of control, two major areas deserve further investigations : the drag-free acquisition modes, and the low frequency perturbation cancellation, as explained in the following paragraphs :

Drag-Free acquisition modes

During Phase A it was chosen to focus on the science mode, featuring a steady drag-free control, and on the laser beam acquisition mode, which appeared to be the most critical modes. In order to meet extreme mission requirements in the MBW, very large disturbance rejection ratios are requested from DFACS controllers, resulting in static gain up to 100 dB (i.e; reduction by a factor of 100,000 of quasi-static disturbances). In addition to sensor dynamic range issues, transient phases shall be analysed in depth, in order to define the drag-free acquisition sequence from uncontrolled dynamics to operational conditions. This need is reinforced by considerations on the inertial sensor : in drag-free mode, the proofmass is free-floating along the sensitive axis. During the Drag-Free Acquisition Mode, the suspension will be first stiff enough to allow release the proofmass without collision with the cage, and (progressively) softened in a second time, as the cancellation of the solar pressure by the FEEP thrusters becomes more accurate.

Low frequency perturbation attenuation

The very-low-frequency components of the forces (self-gravity mostly) acting on the PM will have to be cancelled out, because of the stringent requirement on the absolute variation of the distance between the PM and the cage. These aspects were only investigated at conceptual level during this phase A study, focused on the demonstration of the performance in the MBW. The proposed solution is to feed-forward a force command (either to the FEEP or to the CAESAR actuation system) to compensate for the estimated low frequency disturbance. The design & performance assessment of this estimation/feedforward scheme shall be further investigated in subsequent phases, with the support of a dynamic simulator, quite straightforward to develop from the existing 10-DOF noise analysis tool.

The simulator developed for this study could be completed by including all degrees of freedom, by improving the models describing every element of the DFACS architecture, and by utilising compiled versions of the simulator (automatic transformation from Matlab/Simulink environment toward a C program), so as to reduce the computation time, as required to assess performances in the very low frequency domain.

A demonstration mission on an Earth orbit if of course the best way to assess the performance of the DFACS for LISA, as well as to resolve the remaining control problems. In particular the viability of the a strategy without electrostatic compensation along the principal axis, so-called “strategy 4” in Chapter 7.2.3, and which was shown to improve the performances could be demonstrated.

7.3 Payload Configuration

7.3.1 Payload Structural and Thermal Design

The payload structural and thermal concept has been analysed in pre-phase A and is described in [1] and [2], respectively. The concepts have been briefly reassessed in this study in order to simplify system design and to avoid potential interface problems to the spacecraft structure and thermal control. No major design changes have been found to be necessary at this level of investigation. The conceptual alternatives identified are:

- Replacement of the Y-cylinder shaped thermal shield by an integral structural element of the spacecraft, i.e. a rectangular box, capable of carrying the launch loads and allowing easier access to the optical assemblies and hinges during AIVT.
- Removal of hinge mechanisms from the back of the optical assemblies (line of sight intersection) to the normal to plane proof masses axes intersection with the Y-cylinder structure.
- Additional thermal shields in the telescope baffle are required for the SIC telescope option (section 7.1.2).

The first alternative presents no real advantage after all over the spacecraft configuration finally selected as baseline. In addition, separate spacecraft and payload verification would be more complicated.

A major driver for considering a change of hinge mechanisms had been the possibility, to keep the proof mass centre of mass at the same position during the annular variation of the in-plane line of sight intersection angle. However, the gravity analysis has shown, that self-gravity induced accelerations are acceptable in the pre-phase A configuration, where the centre of mass is moving a few mm relative to the spacecraft surroundings (section 7.3.3).

There is another advantage in removing the hinge mechanisms from the back of the assemblies and employing flex pivots for placing the rotation axis in the centre of mass of the optical assemblies, namely the avoidance of static imbalance and the possibility to employ simpler launch locks. Hence, DSS has requested MMS to recommend this modified configuration as baseline concept.

The baseline payload structural and thermal design specified in the payload definition document [2] is described in the following. The mechanical interfaces between cylinder, payload support structure and optical bench/telescope have been analysed in sections 7.1.1-3. Section 6.4 deals with the baseline payload thermo-elastic analysis.

Payload thermal shield. The payload thermal shield is a Y-shaped assembly of graphite-epoxy cylinders that surround the optical assemblies to thermally isolate them from the spacecraft. The cylinders are gold-coated on both the inside and the outside to have an emissivity of 0.05 or less. The payload thermal shield is reinforced by stiffening rings at the places where the optical assemblies are supported from the shield.

The optical assemblies are supported at the front by pointing devices, which steer the input and output beams with respect to the spacecraft, and at the aft end by flexures that are attached to a structure which is suspended from the payload thermal shield by stressed fibreglass bands. The payload thermal shield is also reinforced by stiffening rings where the payload thermal shield is attached to the spacecraft structure by stressed fibreglass bands.

The payload thermal shield could be made up of half-pipes to allow access to and ease the mounting of the payload support structure inside the payload thermal shield.

Payload thermal shield mass (to surround both optical assemblies):

Front cylinder	4.0 kg
Middle tube	4.5 kg
Transition section	3.0 kg
Aft tube	0.8 kg
Stiffening rings	0.8 kg
Flexure support & fittings	0.7 kg
Total	13.8 kg

Payload support structure. The payload cylinder constitutes the main payload support structure, a graphite-epoxy cylinder 360 mm in diameter, 500 mm long, with a wall thickness of 2 mm.

The payload cylinder is gold-coated to have an emissivity of 0.05 or less, in order to isolate the telescope, optical bench, and sensitive electronics from external temperature fluctuations. The payload cylinder is reinforced at four points along the length by toroidal stiffening rings. The stiffening rings are made of graphite epoxy with a cross-section of 10 mm by 10mm and 2mm wall thickness. The rings are gold-coated to have emissivity 0.05 or less. The rings are bonded to the payload cylinder.

The telescope support is attached to the front stiffening ring. This telescope support is a graphite-epoxy or alternatively an all SiC spider that suspends the primary mirror at three attachment points. In the first case, the primary support is compliant under differential thermal expansion of the ULE primary mirror and the graphite-epoxy payload cylinder; the all SiC design secures the homothetic behaviour..

The telescope thermal shield is mounted from the second stiffening ring. This shield is to reduce radiative transfer between the telescope primary mirror, which will reach an equilibrium temperature of below 250 K, and the optical bench, which needs to be at a temperature of about 290 K. The thermal shield is a disk of graphite-epoxy 300 mm in diameter, 1 mm thick, with hole 40 mm diameter in the middle for passage of the laser beam. The thermal shield is supported by 4 ceramic tubes, 5 mm in diameter, 1 mm wall, 60 mm long, which are attached to the thermal shield and the stiffening ring by aluminium fittings into which the tubes are glued.

The optical bench is supported from the third stiffening ring, by 8 ceramic rods, which are ceramic cylinders 10 mm in diameter, 250 mm long, with 2 mm wall thickness. The support arrangement has been chosen to reduce the tendency of thermal gradients in the payload cylinder to cause thermal gradients in the optical bench. Figure 1.5 gives a top view of the support arrangement. One ceramic support rod is attached to each of the eight corners of the optical bench. Four rods on each side of the optical bench meet at a single point on the payload cylinder stiffening ring. An electronics plate accommodating circuits that need to be near the optical bench (accelerometer and photo detector preamplifiers) is supported from the fourth stiffening ring.

The structural interface between the optical bench optics and the telescope optics is a compromise between optical alignment requirements, thermo-elastic stability, mechanical load bearing capability and

thermal insulation requirements. Potential detrimental effects are long term creeping and optical path changes within the measurement band induced by structural thermo-elastic deformations, primarily within the payload support cylinder. However, due to the very stable thermal environment in combination with the CFRP materials baseline, any changes in optics alignment can be expected to be within tolerable limits. In addition, the optical concept features an inherent re-alignment and re-focusing capability by using the transmitter fibre positioner. The received beam path is less sensitive in terms of alignment. The proof mass as an active mirror provides re-alignment capability for the heterodyne beam. As far as optical phase changes are concerned, an immediate effect detectable in the heterodyne signal can only be generated by the telescope back-reflected straylight, which is at sufficiently low level (section 7.1.2).

The electronics plate is 3 mm thick, 300 mm in diameter, with a 40 mm diameter hole in the middle for passage of laser signals. The electronics plate is made of graphite epoxy and gold coated on both sides. The electronics plate is supported by 4 ceramic tubes, 5 mm in diameter, 1 mm wall, 60 mm long, which are attached to the payload cylinder and the stiffening ring by aluminium fittings into which the tubes are glued.

The whole optical assembly is supported at the intersection of the rotation axis -with is located near the centre of mass- with the payload thermal shield by e.g. flex pivots bearings. The rotational degree of freedom is controlled by the optical assembly's actuator located about 0.5 m away between the payload support structure and the payload shield in the plane spanned by the line of sights. Details of the hinges mechanism and actuators are described in section 7.1.

Payload support structure mass budget (for one optical assembly):

Payload cylinder	2.8 kg
Stiffening rings (4)	0.5 kg
Telescope thermal shield	0.1 kg
Shield supports and fittings	0.2 kg
Bench supports and fittings	0.5 kg
Electronics plate	0.6 kg
Plate supports and fittings	0.2 kg
Flex pivots and fittings	0.5 kg
Launch locks	0.5 kg
Total	5.9 kg

7.3.2 Payload Gravitational Design

The LISA requirements related to self-gravity at proof-mass locations have been listed in section 5.2.4. In the following subsections we separately discuss the design issues related to achieving the required constant and time varying self-gravity on payload level.

7.3.2.1 Compensation of Constant Self-Gravity

In this section the needs and techniques for balancing of constant self-gravity on payload-level will be discussed.

In order to meet the requirements (listed in section 5.2.4) imposed on the constant part of self-gravity, additional balance masses will have to be foreseen, since the mass distribution of the Science Module yields according to section 6.4 a non-compliant level of self-gravity. As we will see the total weight of these balance masses crucially depends on their mounting location.

For the sake of simplicity we will consider the gravitational balancing at a single proof-mass location along a single axis only. It is essential to take into account for balancing both self-gravity and its gradient. In order to reduce both of them below allowable limits in general two balance masses will have to be foreseen. These balance masses need to be positioned on either side of the proof-mass. The arrangement considered is depicted in Figure 7.3-1

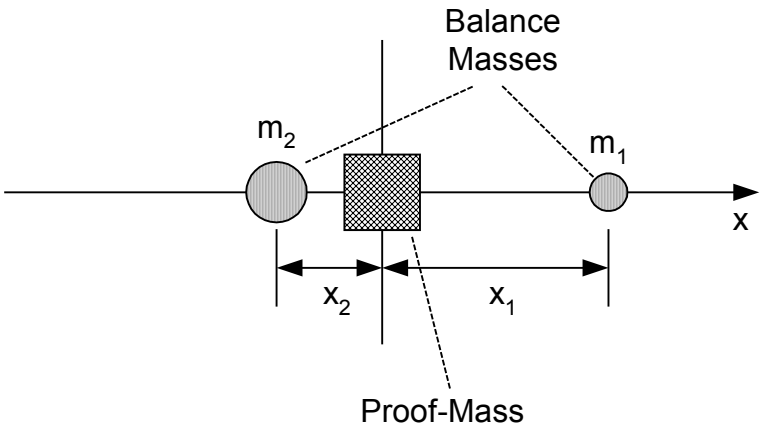

Figure 7.3-1: Single Axis Balancing of Self-Gravity and Its Gradient at Proof-Mass Location

The conditions for exactly balancing a given constant self-gravity induced acceleration **a** and its gradient along x $\partial\mathbf{a}/\partial x$ at proof mass location x=0 using two balance masses m_1, m_2 are:

$$G\cdot\left(m_1\cdot\frac{x_1}{\left|x_1^{\,3}\right|}+m_2\cdot\frac{x_2}{\left|x_2^{\,3}\right|}\right)+a(x=0)=0$$

$$G\cdot\left(\frac{m_1}{x_1^{\,3}}+\frac{m_2}{x_2^{\,3}}\right)+\left.\frac{\partial a}{\partial x}\right|_{x=0}=0$$

These two equations represent an inhomogeneous system of two linear equations in the unknown balance masses m_1, m_2 provided that their locations x_1, x_2 are known. Being given the self-gravity induced acceleration and its gradient at x=0 these equations can easily be solved after definition of a set of balance mass locations x_1, x_2. It only has to be made sure that solutions yielding negative balance masses are discarded.

For balancing along any two orthogonal axes x and y intersecting at the proof-mass centre, independent balancing along both axes is possible. For the non-orthogonal two-axis case a system of four linear equations has to be solved for the four balance masses.

We note that in the above equations we tacitly implied that proof-mass and balance masses can be considered as point masses. This assumption is supported by analysis presented in section 7.3.2.1.2.

7.3.2.1.1 Example for Orthogonal Two-Axis Balancing

For further insight we study an example for which we require to be compensated self-gravity acceleration and its gradient along two orthogonal axes x, y. For the sake of simplicity we assume the same imbalance values along both axes:

$$a(x=0) = 6\cdot 10^{-9}\left[\frac{m}{s^2}\right] \qquad \left.\frac{\partial a}{\partial x}\right|_{x=0} = 2.5\cdot 10^{-8}\left[\frac{1}{s^2}\right]$$

$$a(y=0) = 6\cdot 10^{-9}\left[\frac{m}{s^2}\right] \qquad \left.\frac{\partial a}{\partial y}\right|_{y=0} = 2.5\cdot 10^{-8}\left[\frac{1}{s^2}\right]$$

The x/y-plane is assumed to be parallel to the optical bench with an allowable range of balance mass locations between 5 and 20 cm off the proof-mass centre. This range is visualised wrt. the optical bench dimensions in the Figure 7.3-2. It can be seen from this figure that for an offset of only 5 cm the balance

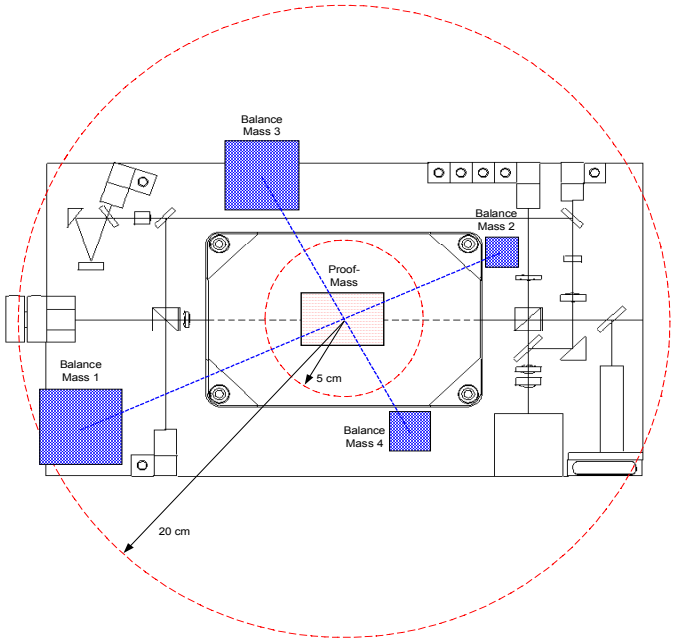

Figure 7.3-2: Possible Accommodation of Balance Masses on the Optical Bench

mass would interfere with the dimensions of the Inertial Sensor housing. In reality a balance mass offset of at least 7-10 cm will be mandatory. The resulting balance masses are shown in Table 7.3-1. Since we can assume that balancing is primarily required in the plane of the optical bench, a realistic balance mass arrangement has to take into account the remaining free space on the optical bench. A possible arrangement on its upper side[2] is shown in Figure 7.3-1. We would get for the sketched pair of balance masses 1 and 2 (located at about x=-16 cm and x=+10 cm, respectively, off the proof-mass centre)

Table 7.3-1: Example for Req'd Balance Masses [kg] Versus Position (Top: m_1, Bottom: m_2)
Balance mass positions yielding negative balance masses are marked with #####.

	0,05	0,06	0,07	0,08	0,09	0,10	0,11	0,12	0,13	0,14	0,15	0,16	0,17	0,18	0,19	0,20
-0,05	####	####	#####	#####	#####	#####	#####	#####	#####	######	######	######	######	######	######	####
-0,06	1,54	####	#####	#####	#####	#####	#####	#####	#####	######	######	######	######	######	######	####
-0,07	1,22	2,31	#####	#####	#####	#####	#####	#####	#####	######	######	######	######	######	######	####
-0,08	1,22	1,73	3,26	#####	#####	#####	#####	#####	#####	######	######	######	######	######	######	####
-0,09	1,30	1,64	2,32	4,37	#####	#####	#####	#####	#####	######	######	######	######	######	######	####
-0,10	1,42	1,69	2,12	3,00	5,62	#####	#####	#####	#####	######	######	######	######	######	######	####
-0,11	1,58	1,80	2,12	2,66	3,74	6,98	#####	#####	#####	######	######	######	######	######	######	####
-0,12	1,76	1,94	2,20	2,59	3,24	4,53	8,42	#####	#####	######	######	######	######	######	######	####
-0,13	1,96	2,12	2,33	2,63	3,09	3,84	5,35	9,88	#####	######	######	######	######	######	######	####
-0,14	2,17	2,31	2,50	2,74	3,08	3,60	4,46	6,17	11,31	######	######	######	######	######	######	####
-0,15	2,40	2,53	2,69	2,89	3,16	3,54	4,11	5,06	6,96	12,65	######	######	######	######	######	####
-0,16	2,65	2,76	2,90	3,07	3,29	3,58	3,99	4,60	5,63	7,67	13,81	######	######	######	######	####
-0,17	2,91	3,01	3,13	3,27	3,45	3,68	3,99	4,42	5,06	6,14	8,28	14,73	######	######	######	####
-0,18	3,19	3,28	3,38	3,50	3,64	3,82	4,06	4,37	4,81	5,46	6,56	8,74	15,30	######	######	####
-0,19	3,49	3,56	3,64	3,74	3,86	4,00	4,18	4,41	4,71	5,14	5,78	6,85	9,00	15,42	######	####
-0,20	3,80	3,85	3,92	4,00	4,09	4,20	4,33	4,50	4,71	5,00	5,40	6,00	6,99	8,99	14,99	####

	0,05	0,06	0,07	0,08	0,09	0,10	0,11	0,12	0,13	0,14	0,15	0,16	0,17	0,18	0,19	0,20
-0,05	####	####	#####	#####	#####	#####	#####	#####	#####	######	######	######	######	######	######	####
-0,06	0,84	####	#####	#####	#####	#####	#####	#####	#####	######	######	######	######	######	######	####
-0,07	0,40	1,38	#####	#####	#####	#####	#####	#####	#####	######	######	######	######	######	######	####
-0,08	0,25	0,65	2,06	#####	#####	#####	#####	#####	#####	######	######	######	######	######	######	####
-0,09	0,18	0,40	0,96	2,88	#####	#####	#####	#####	#####	######	######	######	######	######	######	####
-0,10	0,13	0,28	0,60	1,34	3,82	#####	#####	#####	#####	######	######	######	######	######	######	####
-0,11	0,10	0,21	0,42	0,83	1,78	4,87	#####	#####	#####	######	######	######	######	######	######	####
-0,12	0,08	0,16	0,31	0,58	1,09	2,25	5,98	#####	#####	######	######	######	######	######	######	####
-0,13	0,06	0,13	0,24	0,42	0,75	1,37	2,74	7,12	#####	######	######	######	######	######	######	####
-0,14	0,05	0,10	0,18	0,32	0,55	0,94	1,66	3,24	8,23	######	######	######	######	######	######	####
-0,15	0,04	0,08	0,14	0,25	0,41	0,67	1,12	1,94	3,70	9,25	######	######	######	######	######	####
-0,16	0,03	0,06	0,11	0,19	0,31	0,50	0,80	1,29	2,20	4,11	10,12	######	######	######	######	####
-0,17	0,03	0,05	0,09	0,15	0,24	0,37	0,58	0,91	1,44	2,40	4,43	10,74	######	######	######	####
-0,18	0,02	0,04	0,07	0,12	0,18	0,28	0,43	0,65	0,99	1,54	2,53	4,60	11,05	######	######	####
-0,19	0,02	0,03	0,05	0,09	0,14	0,21	0,31	0,46	0,69	1,03	1,58	2,56	4,60	10,93	######	####
-0,20	0,01	0,02	0,04	0,06	0,10	0,15	0,22	0,32	0,47	0,69	1,01	1,53	2,45	4,37	10,28	###

[2] It would be much easier to mount the balance masses on the lower side of the optical bench. Since the proof-mass centre of mass is located about 3 cm above the mid-plane of the optical bench, it is likely that there will be a net gravitational pull acting on the proof-mass which needs to be compensated by balance masses on the upper side.

balance masses as follows: m_1 = 3.58 kg and m_2 = 0.50 kg. For the balancing normal to the x-axis interconnecting balance masses 1 and 2 by means of the sketched balance masses 3 and 4 and assuming the same self-gravitational imbalance in this direction (y-axis) we get for the pair of balance masses 3 and 4 (located at about y=-11 cm and y=+8 cm, respectively, off the proof-mass centre) balance masses as follows: m_3 = 2.66 kg and m_4 = 0.83 kg. We hence easily end up in this example with considerable balance mass in the order of several kilograms which have to be accommodated on the optical bench. In principle it would also be possible to attach these masses to the payload Y-structure. In this case, however, a further dramatic increase in balance mass can be anticipated.

Table 7.3-2: Total Balance Mass Required for the Example of table 7.3-1

	0,05	**0,06**	**0,07**	**0,08**	**0,09**	**0,10**	**0,11**	**0,12**	**0,13**	**0,14**	**0,15**	**0,16**	**0,17**	**0,18**	**0,19**	**0,20**
-0,05	###	###	####	####	####	####	####	####	####	#####	#####	#####	#####	#####	#####	###
-0,06	2,38	###	####	####	####	####	####	####	####	#####	#####	#####	#####	#####	#####	###
-0,07	1,62	3,69	####	####	####	####	####	####	####	#####	#####	#####	#####	#####	#####	###
-0,08	1,46	2,37	5,32	####	####	####	####	####	####	#####	#####	#####	#####	#####	#####	###
-0,09	1,47	2,04	3,29	7,25	####	####	####	####	####	#####	#####	#####	#####	#####	#####	###
-0,10	1,56	1,97	2,72	4,34	9,44	####	####	####	####	#####	#####	#####	#####	#####	#####	###
-0,11	1,68	2,01	2,54	3,49	5,52	11,85	####	####	####	#####	#####	#####	#####	#####	#####	###
-0,12	1,84	2,10	2,51	3,17	4,33	6,78	14,40	####	####	#####	#####	#####	#####	#####	#####	###
-0,13	2,02	2,24	2,57	3,06	3,84	5,22	8,09	17,00	####	#####	#####	#####	#####	#####	#####	###
-0,14	2,22	2,41	2,68	3,06	3,63	4,54	6,12	9,41	19,54	#####	#####	#####	#####	#####	#####	###
-0,15	2,44	2,61	2,83	3,14	3,57	4,22	5,23	7,00	10,66	21,90	#####	#####	#####	#####	#####	###
-0,16	2,69	2,83	3,01	3,26	3,60	4,08	4,79	5,90	7,82	11,79	23,93	#####	#####	#####	#####	###
-0,17	2,94	3,06	3,22	3,42	3,69	4,06	4,57	5,32	6,50	8,54	12,71	25,47	#####	#####	#####	###
-0,18	3,22	3,32	3,45	3,61	3,82	4,11	4,49	5,02	5,80	7,01	9,08	13,35	26,34	#####	#####	###
-0,19	3,50	3,59	3,69	3,83	3,99	4,21	4,49	4,87	5,40	6,17	7,36	9,41	13,60	26,35	#####	###
-0,20	3,81	3,88	3,96	4,06	4,19	4,35	4,55	4,82	5,18	5,68	6,41	7,53	9,45	13,36	25,27	###

The situation improves if we take into account that we may not need to perform a *perfect* balancing of self-gravity at proof-mass location but balance only within the requirements listed in the beginning of section 7.3.2. In this case we find when balancing along the line connecting balance masses 1 and 2 in Figure 7.3-2 that balance mass 2 may vanish while balance mass 1 can be reduced to 2.29 kg which implies a mass saving of about 1.8 kg. A similar saving can be expected for balance masses 3 and 4.

7.3.2.1.2 Gravitational Field of Proof-Mass and Balance Masses

The example for balancing of self-gravity analysed in the preceding section showed that it is important to mount the balance masses close to the proof-mass. The question arises at which distance the near-field effects of a proof-mass or a balance mass may be rightfully disregarded. It is well known that the outer gravitational field of a homogeneous sphere can be perfectly represented by a point-mass located in the centre of the sphere and having the same mass. Now the proof-mass has the shape of a cube (more precisely: of a cuboid) and the shapes of the balance masses are unlikely to be spheres. We will therefore analyse in this section the gravitational potential in the vicinity of a homogeneous cuboid. The gradient of this potential gives the force of attraction on a particle of unit mass.

In : we have visualised the Newtonian gravity potential in one of the mid-planes of a homogeneous cube of unit edge length. The position and size of the cube is indicated on the figure. It is obvious from this figure that the potential is nicely similar to a radially symmetric field.

For a quantitative comparison in Figure 7.3-4 the relative difference in Newtonian potential between a homogeneous cube and a point-mass of the same weight is shown versus the distance from the cube centre. This distance is represented in multiples of the cube's edge length. It is easily recognisable from this graph that at a distance of greater than one edge length from the cube centre the point-mass approximation of the field is better than 1 percent.

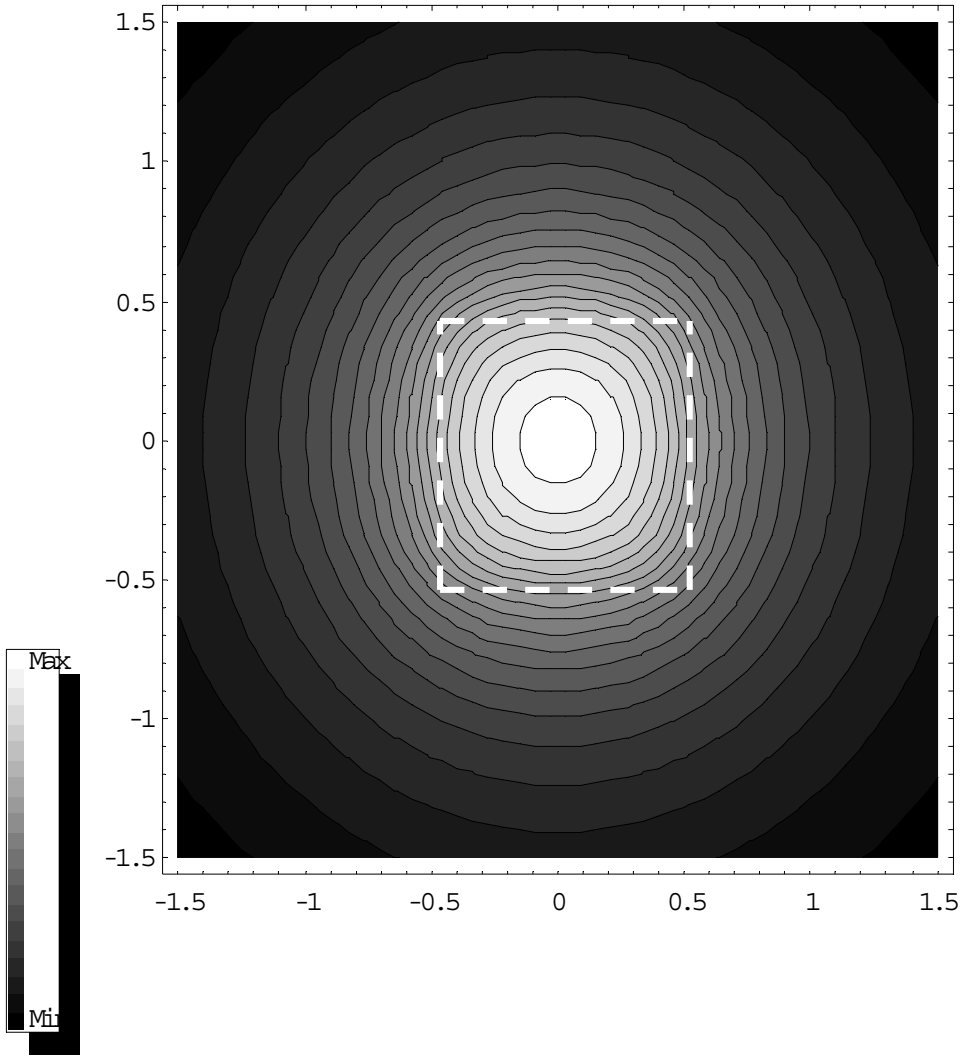

Figure 7.3-3: Contour Plot of Newtonian Potential in the Mid-Plane of a Homogeneous Cube[3]

This finding allows to conclude that for balancing purposes the gravitational field of a homogeneous cube may well be approximated by the one resulting from a point-mass with identical weight located at the cube's centre as long as the balancing takes place at a distance of at least one edge length. The shape presently foreseen for the proof-mass has the dimensions 35x35x50 mm. Since the Inertial

[3] The cube is centred at (0,0) and the cube's edges have unit length.

Sensor's dimensions exclude mounting of balance masses closer than 70 mm from the proof-mass centre, the balancing approach used in the preceding section remains valid.

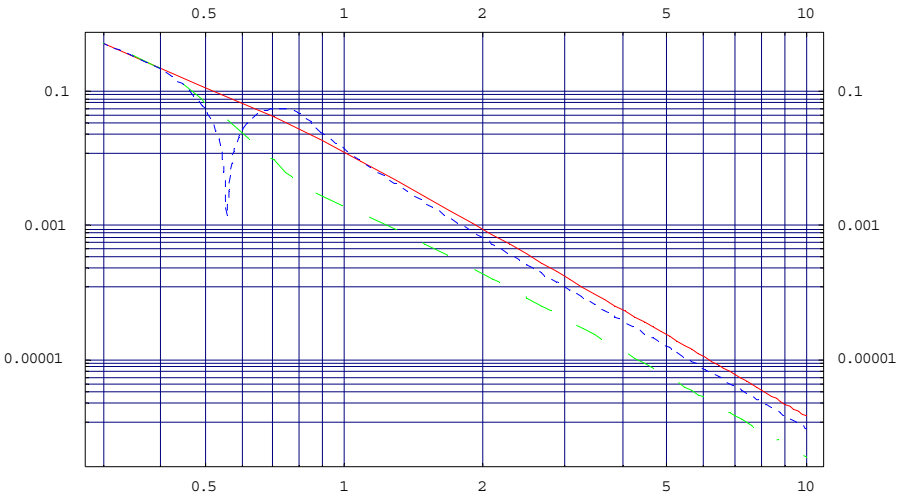

Figure 7.3-4: Relative Difference in Newtonian Potential of Point-Mass wrt. Homogeneous Cube[4]

[4] The abscissa represents the offset from the cube centre in multiples of the cube's edge length. The meaning of the curves is as follows:

- the solid (red) line represents the rel. difference in potential along the *mid-face* direction of the cube
- the dashed (green) line represents the rel. difference in potential along the *mid-edge* direction
- the dotted (blue) line represents the rel. difference in potential along the *vertex* direction.

7.3.2.1.3 Gravitational Interaction Between Proof-Mass and Cage

The proof-mass and its cage are shown in Figure 7.3-5. The gravitational attraction of the proof-mass by its cage in this arrangement should ideally vanish if the proof-mass is centred in its homogeneous cage. For small offsets in position and attitude the proof-mass will experience gravitational forces and torques due to the gravity gradient that will result in effective translational and rotational stiffnesses. These stiffnesses are of considerable importance for proof-mass control.

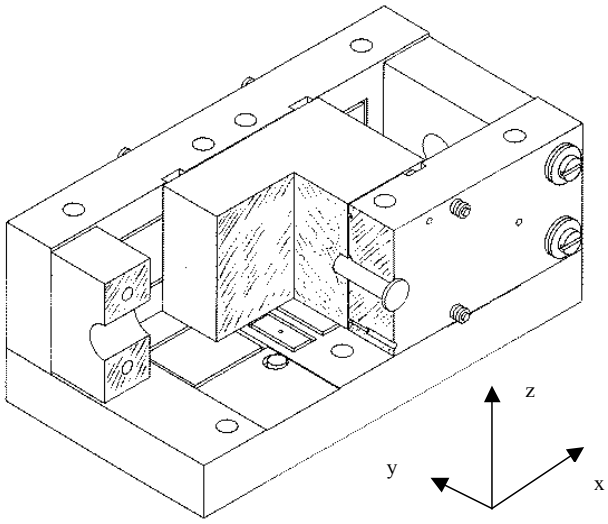

Figure 7.3-5: Geometry of Proof-Mass and Cage

In order to quantify these stiffnesses a model has been established allowing to study the gravitational interaction between a homogeneous proof-mass and a homogeneous cage of constant wall thickness.

Data used for this model are summarised hereafter:

Proof-mass dimensions	50 x 35 x 35 mm
Proof-mass density	21000 kg/m^3
Outer cage dimensions	150 x 80 x 80 mm
Inner cage dimensions	110 x 40 x 40 mm
Cage wall thickness	20 mm
Cage density	3000 kg/m^3

For the proof-mass in centred position these data imply gaps between proof-mass and cage of 30 mm along x and of 2.5 mm along y and z.

The gravitational potential of the cage alone is shown in Figure 7.3-6. The graphs in this figure show the Newtonian potential in the x/y-plane as well as in the y/z-plane. The interesting finding from these graphs is that only two of the three translational degrees of freedom are unstable: The x-axis which is acc. to Figure 7.3-5 the direction of the optical axis is in fact stable with the present design, since in

case of a non-zero x-position of the proof-mass the x-component of the force will always tend to re-centre the proof-mass. This property is due to the increased length of the cage along the x-axis compared to the other two.

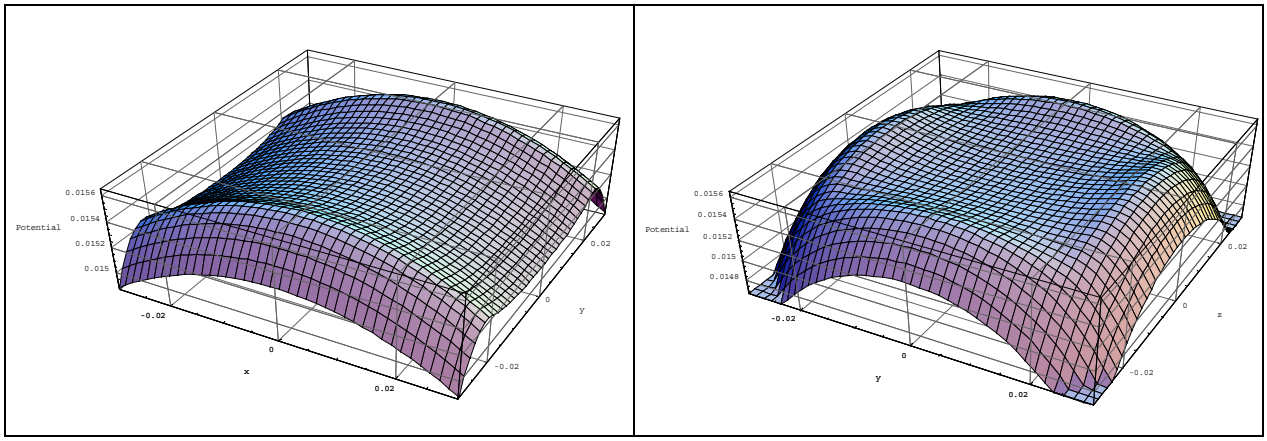

Figure 7.3-6: Gravity Potential in Planes Intersecting the Cage Centre
(left: x/y-plane, right: y/z-plane)

The translational gravitational stiffness of the proof-mass can be obtained from the gravitational potential by integrating its gradient over the volume of the slightly displaced proof-mass. Similarly, the rotational stiffness can be calculated. The resulting stiffnesses are summarised hereafter where positive stiffness is supposed to indicate stability of motion in this degree of freedom:

Translational stiffness along x	2.2 E-7 N/m
Translational stiffness along y	-1.1 E-7 N/m
Translational stiffness along z	-1.1 E-7 N/m
Rotational stiffness about x	-3.5 E-11 Nm/rad
Rotational stiffness about y	-4.1 E-11 Nm/rad
Rotational stiffness about z	-4.1 E-11 Nm/rad

Taking into account that for the electrostatic proof-mass control the total translational stiffness should not exceed a value of ±1.0 E-7 N/m in order to avoid interference with the MBW, it can be seen from this table that the calculation of gravitational stiffness is not only of academic interest. It appears that the gravitational stiffness due to the cage needs to be taken into account when designing the proof-mass sensor.

The internal geometry of the present proof-mass sensor indicates that it allows for high sensitivity only along the x-axis. It is beneficial that, due to the positive gravitational stiffness exactly along this axis, the negative stiffness of the electro-static suspension is partly compensated. For a two-axis sensor with an additional highly sensitive y-axis it can be shown that a different design of the cage allows to obtain gravitationally stable uncontrolled motion (positive stiffness) of the proof-mass in addition also along the y-axis – probably at the expense of larger dimensions and mass of the sensor, though.

For gravitational balancing at proof-mass locations the influence of the cage is found to be significant and has to be taken into account.

7.3.2.2 Compensation of Quasi-Constant Self-Gravity

This section discusses the need to compensate variations in self-gravity which exhibit a deterministic frequency content below the MBW. The design of LISA has been aimed at minimising movable items on the Science Module. The only major exceptions are: High Gain Antenna and Optical Assembly. These variations are quantified in section 6.4.2.

The results presented there are benign and indicate that there is no need for a dynamic compensation of quasi-constant self-gravity.

8 Summary and Conclusions

Starting from the results of Lisa Pre-phase A study mission concept, spacecraft and payload design have been refined and the corresponding analyses to assess measurement performance and to verify the underlying assumptions on payload properties have been carried out.

Mission Design

The basic outline of the mission concerning

- transfer and operational orbits
- simultaneous launch of 3 spacecraft with a single Delta 2 class carrier
- each spacecraft equipped with a separable ion thruster powered propulsion module

has been revisited and has been found still adequate when compared to a set of alternatives.

The application of spacecraft attitude constraints during transfer in order to enable fixed solar arrays were determined to be compatible with time and propellant requirements.

Spacecraft Design

Spacecraft design of propulsion module and science module has been performed. Specifically compatibility with Delta 2 class launcher has been achieved albeit with little margin in terms of mass and allowable height of the spacecraft stack.

While the present layout does not appear to contain any show stoppers, the margin for refining the detail design could prove too small to prevent some restriction of science performance of the satellite as finally realised.

Payload Design

The optical assembly system architecture has been validated in this study. The opto-mechanical and thermal control concept has not but slightly been modified relative to the pre-phase A status. Especially, the actuation axis has been moved close to the centre of mass for each assembly. The hinge mechanisms are flex pivot bearings and only one-dimensional actuation in the triangle constellation plane is recommended.

The optical design and on-bench beam size has been modified to match telescope magnification and detector size and to implement the variable point ahead compensation function.

For the telescope, a Dall-Kirkham afocal all-reflective optical design is recommended. Two valid candidate materials have been identified: an all SiC homothetic telescope concept and, alternatively, a composite Zerodur/CFRP. The latter having advantages in thermal stability while the former has manufacturing advantages.

The study has underlined the interest to use extended functions of the inertial sensor like the operation as an accelerometer for the initialisation of the DFAC system, the biasing of the Proof-Mass position and attitude for the adjustment of the laser pointing to compensate for the variable point ahead angle or the use of angular accelerations for optimisation of the DFAC.

Analyses

The design work performed within this study has been supported by analyses to ensure compatibility with mission performance requirements and the underlying assumptions on subsystem requirements.

Thermal analysis has shown that the current thermal design of the LISA Spacecraft and payload meets the thermal requirements in both steady-state and transient conditions as driven by fluctuations in solar irradiation. The Y-shaped tube temperature gradients are found to be significantly lower (≈35°C) than those presented at Pre Phase A. The effects of fluctuations of power dissipation of components on payload temperatures have also been analysed to determine requirements for allowable electronics power fluctuations.

The AOCS/DFACS analyses have demonstrated the feasibility of the S/C and payload control for the considered configuration with two optical assemblies in each of the three spacecraft. In particular a 10-DOF dynamic simulator has been developed and used to verify the DFACS design. All primary requirements (residual in band proof-mass acceleration) and secondary requirements (proof mass position) can be met. Consolidation of the achievable minimum negative stiffness has been identified as crucial for the control design because of the little margin of the servo-loops stability. It appears advisable to make some slight changes on the sensor core in order to reduce the electrostatic stiffness to values lower than 10^7N/m. This requirement on the stiffness applies also on other sources of stiffness like the gravity gradients.

The effect of the spacecraft's self-gravity on the proof-masses has been analysed in terms of static forces negative spring stiffness and in terms of transients resulting from thermoelastic deformation. Transient effects are well within requirements while the static effects of the present mass distribution exceed their allocation, however only to an extend that can likely be compensated by compensation masses without a mayor change of the configuration.

System measurement performance has been synthesised based on the results of the subsystem analyses. The predicted performance of the baseline design is compliant with the measurement requirements. The analyses demonstrate the consistence of the measurement set-up including all ancillary measurements needed to compensate for laser phase noise, clock instability and spacecraft to proof-mass relative motion. The measurement performance depends critically on the ability to compensate for laser phase noise. A reduction of laser phase noise in the measurement bandwidth is desirable. However, correct representation of the in-band phase noise in the phase meter read out is essential. Phase meter dynamic range and suppression of aliasing artefacts must therefore be carefully matched to the transmitter laser characteristics.

Recommendations

Evaluation of the analyses of the present design has identified the need of further refinement of design or demonstration of assumed component performance. In terms of spacecraft design, refinement on unit level is needed to implement requirements to magnetic field and stabilisation of dissipated power. Furthermore a system of compensation masses to achieve static self gravity requirements need to be worked out.

On functional level further refinement of the Drag-Free acquisition modes is needed covering coarse acquisition of the beam and transition from (relatively) uncontrolled dynamics to operational conditions.

In terms of components in particular the inertial sensor needs refinement. The inter-axis couplings due to electrostatic forces must be more accurately characterised as it is presently available. Furthermore a reduction of the negative spring stiffness resulting from electric forces is desirable as well as a demonstration of the sensor performance when applying the relatively large angular offsets needed for point ahead compensation.

Transmitter technology needs further development preferably in close connection with development of a phase meter matched to the effective phase noise performance.

A demonstration mission in an Earth orbit would be the best way to verify the performance of the DFACS for LISA, as well as to resolve the remaining control problems. In particular the initialisation sequence and the viability of the strategy without electrostatic compensation along the principal axis, which was shown to improve the performance, could be demonstrated.

9 References

[1] LISA Pre-Phase A Report, MPQ 233 (issue 2), July 1998

[2] LISA Payload Definition Document V 0.53, 3 November 1998

[3] LISA Advanced Projects Design Team Final Report, NASA JPL D-14350, 27 January 1997

[4] System Requirements Document, AO/1-3511/99/NL/MS, Appendix 1

[5] LISA Pre-Phase A Structural Study, M.S.Whalley (WP 01)

[5] Gravitational effects of payload components, B.J. Kent (WP 02)

[7] LISA Pre-Phase A Thermal Study, S. Peskett (WP 03)

[8] LISA Interferometer sensitivity to spacecraft motion, M. Peterseim (WP 08)

[9] Statement of Work for the Laser Interferometer Space Antenna, AO/1-3511/99/NL/MS

[10] Effect of Micrometeorites impacts on translation control, L. Vaillon, Fairchild Space, ref : GP-B-91-127

[11] Bilan de performance en attitude du SED16-A, SODERN, ref : LER 25.1499

[12] Drag-Free Satellite Control, Klotz, H., Marcuccio, S., Speake, C., Sumner, T., Strauch, H. Wolfsberger, W.,et al., , Final Report to ESTEC Contract 10016/93/NL/JG, 1998)

[13] Touboul P. et al. Continuation of the GRADIO accelerometer predevelopment; ONERA Final Report n° 51/6114 PY ESTEC Contract (1992); ONERA Final Report n° 62/6114 PY ESTEC contract (1993).

[14] Nati M.(ESTEC) and Bernard A., Foulon B., Touboul P.(ONERA); ASTRE-A highly preformant accelerometer for the low frequency range of the microgravity environment; 5th European symposium on Space Environmental Control Systems and 24th International conference on Environmental systems (June 20-23, 1994).

[15] M. Rodrigues, P. Touboul, Optimisation of the inertial sensor design for the LISA mission, ONERA final report RTS24/3815DMPH/Y, ESTEC contract 12563/97/NL/MS, July 1998

[16] D. Horrière, P. Touboul, Impact of the vibratory environment on GAMES accelerometer performance, ONERA final report FR8/3805PY, CNES contract 1/89/54888/05, October 1994

[17] LISA Phase A Payload Thermal Study, D. Hayoun, RAL, Draft 31 Jan. 2000

[18] G. Giamperi et al., Optics Communications 124 (1966) 669-678

[19] R. Hellings et al., Optics Communications 124 (1966) 313-320

10 Acronyms

AAD	Attitude Anomaly Detector
AC	Alternating Current
AD	Appl. Document / Attitude Determtn.
AIV	Assembly, Integration and Verification
AME	Absolute Measurement Error
AOCS	Attitude and Orbit Control Subsystem
APE	Absolute Pointing Error
ASC	Advanced Stellar Compass
AU	Astronomical Unit
AWG	American Wire Gauge
BER	Bit Error Rate
BOL	Begin Of Life
CAD	Computer Aided Design
CCD	Charge Coupled Device
CDMU	Central Data Management Unit
CFRP	Carbon Fibre Reinforced Plastic
COG	Centre Of Gravity
COM	Centre of Mass
CPU	Central Processing Unit
CTE	Coefficient of Thermal Expansion
DC	Direct Current
DDS	Digital Direct Synthesyser
DFACS	Drag-Free and Attitude Control System
DFC	Drag-Free Control
DFRP	Drag-Free Reference Point
DMA	Direct Memory Access
DMS	Data Management Subsystem
DOD	Depth of Discharge
DOF	Degree Of Freedom
DRAM	Dynamic Random Access Memory
DSN	Deep Space Network (NASA)
EDAC	Error Detection And Correction
EEPROM	Electrically Erasable Programmable ROM
EGSE	Electrical Ground Support Equipment
EID	Experiment Int erf ace Document
ELITE	European LISA Technology Demonstration Satellite
EM	Engineering Model
EMC	Electromagnet ic Compatibility
EOL	End Of Lifetime
EOM	Electro-Optic Modulator
ESA	European Space Agency
ESARAD	ESA Radiation
ESATAN	ESA Thermal Analyser
ESOC	European Space Operations Cent re
ESTEC	European Space Research and Technology Centre
FD	Flight Dynamics
FEEP	Field Emission Electric Propulsion
FEM	Finite Element Model
FFT	Fast Fourier Transform
FM	Flight Model
FMECA	Failure Modes, Effects and Criticality Analysis
FOV	Field Of View
FPAG	Fundamental Physics Advisory Group
FPGA	Field Programmable Gate Array
FS	Fight Spare
FSS	Fine Sun Sensor
GTO	Geostationary Transfer Orbit
GW	Gravitational Wave

H/W	Hardware
HGA	High Gain Antenna
HK	House Keeping
I/F	Interface
I/O	Input /Output
IEEE	Institute of Electrical and Electronics Engineers
IPS	Ion Propulsion System
IR	Infrared
IRU	Inertial Reference Unit
ISV	Independent Software Validation
IWDB	Interacting White Dwarf Binaries
JILA	Joint Institute for Laboratory Astrophysics
JPL	Jet Propulsion Laboratory
Kbits	Kilo-bits (thousand bits)
KHz	Kilohertz - (1000 Hertz)
LCDA	Launcher Coupled Dynamic Analysis
LCL	Latching Current Limiter
LGA	Low Gain Antenna
LISA	Laser Interferometer Space Antenna
LOS	Line Of Sight
LSC	LISA Science Centre
LSDAC	Lisa Science Data Archiving Centre
MBH	Massive Black Hole
Mbits	Mega-bits (million bits)
MBW	Measurement Bandwidth
MEU	Million Euro
MGSE	Mechanical Ground Support Equipment
MHz	Megahertz (Million Hertz)
MIPS	Million Instructions Per Second
MIPS	Million Instructions Per Second
MLI	Multi-Layer Insulation
MMH	Mono Methyl Hydrazine
MOS	Margin Of Safety
NASA	National Aeronautics and Space Administration (USA)
NdYAG	Neodymium-doped Yttrium-Aluminium Garnet
NEA	Noise Equivalent Angle
NPO	Numerically Programmed Oscillator
NS	Neutron Star
OB	Optical Bench
P/L	Payload
P/M	Propulsion Module
PAT	Pointing Acquisition & Tracking
PAA	Point Ahead Angle
PCU	Power Control Unit
PFM	Proto Flight Model
PI	Principal Investigator
PM	Proof Mass or Primary Mirror
PP	Program Plan
PROM	Programmable Read-Only Memory
PSD	Power Spectral Density
QM	Qualification Model
QNL	Quantum Noise Limit
RAM	Random Access Memory
RCS	Reaction Control Subsystem
RD	Reference Document
RF	Radio Frequency
RFDU	Radio Frequency Distribution Unit
RFS	Radio Frequency Subsystem
RMS	Root Mean Square
RPE	Relative Pointing Error
RSS	Root Sum Square
S/A	Solar Array
S/C	Spacecraft

S/M	Science Module
S/W	Software
SC	Star Camera
SEP	Solar Electric Propulsion
SEU	Single Event Upset
SF	Safety Factor
SM	Structural Model or Secondary Mirror
SNR	Signal-to-Noise Ratio
SPC	Science Program Committee
SSR	Solid State Recorder
STM	Structure / Thermal Model
STR	Star Tracker
TBC	To Be Confirmed
TBD	To Be Determined
TCS	Thermal Control Subsystem
TID	Total Ionising Dose
TMM	Thermal Mathematical Model
TOM	Telescope Orientation Mechanism
ULE	Ultra-Low Expansion glass
USO	Ultra-Stable Oscillator
UV	Ultra Violet
WFE	Wave Front Error
XIPS	Xenon Ion Propulsion System
XUV	Extreme Ultra Violet
YAG	Yttrium-Aluminium Garnet

A LISA Structure FE-Model and Analysis

A.1 Scope

This document describes the structural analysis of LISA in the conceptual design from 14.10.1999. This includes:

- Mathematical model description
- Dynamic Properties
- Preliminary Design Loads for Components

The LISA mission comprises three identical spacecraft. In launch configuration the satellites are stacked and the dynamic properties in this configuration are analysed.

The calculations have been performed by use of MSC / NASTRAN FE-Program System.

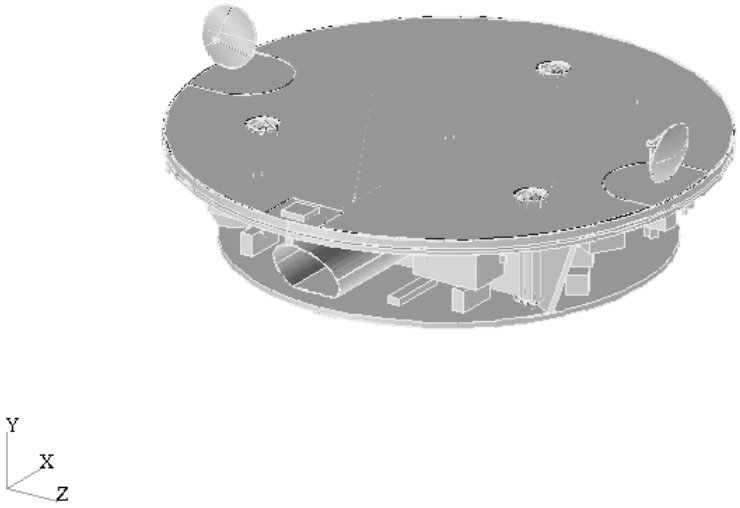

Figure A-1: LISA sciencecraft – conceptual design /3/

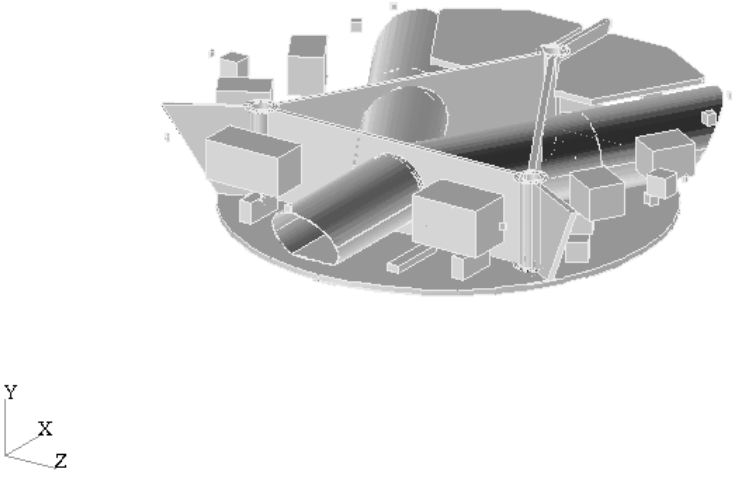

Figure A-2: Lisa sciencecraft without Solar Array and Upper Plate /3/

A.2 Reference Documents

/2/ DELTA II Payload Planners Guide; MDC H3224D; April 1996

/3/ Conceptual design of LISA; Status 14.10.1999; Kurt Gehbauer, DSS ST81

A.3 Requirements and Load Cases

The structural design of the satellites is driven by the launch environment /2/ and the requirements concerning the thermal distortions.

Stiffness requirement:
Minimum natural frequency has to be above 35 Hz in thrust axis and 15 Hz in the lateral axis for a spacecraft hard-mounted at the spacecraft separation plane /2/. The analytically predicted natural frequency shall be at least 5 % higher.

Note: The standard payload attach fitting of DELTA II for a three-stage mission is cylindrical and 940 mm in diameter. The LISA spacecraft in the actual design has an diameter at the interfaces of about 1760 mm. Therefore a special adapter should be provided by McDonnell Douglas, fitting to the interface dimensions of the satellite (Statement of Henry Faulks). The separation plane is the interface between special adapter and spacecraft. All analyses are based on hard mounted conditions at this separation plane .

Static design loads:
The DELTA II Payload Planners Guide /2/ provides Spacecraft CG Limit-Load Factors depending on the spacecraft weight. For a three-stage Delta vehicle, the maximum axial acceleration occurs at the end of the first-stage burn (MECO) for payloads above 885 kg. The Limit Load Factors are listed in the following table:

Axis	Three-Stage	MECO
Lateral	± 2.5	± 0.1
	± 3.0[1]	
Thrust	+ 2.8 / - 0.2[2]	+ 6.2 ± 0.6[3]

Table A-1: Spacecraft CG Limit-Load Factors (g) /2/

These loads should be taken as preliminary design loads for the primary load path.

The loads on the other components mainly depend the acoustic and random environment. The acoustic loads of DELTA II are comparable with the loads at ARIANE. Therefore the preliminary design loads are based on launch loads of ARIANE launchers. These preliminary design loads depend on the component mass, as shown in Figure A-3.

[1] Lateral load factor to provide correct bending moment at spacecraft separation plane.
[2] Plus indicates compression load and minus indicates tension load.
[3] Axial load factor at MECO consists of a static component which is a function of spacecraft weight and a dynamic component at a frequency of ≈ 17 – 18 Hz. The 6.2-g static value shown is based on a spacecraft weight of 1885 kg for a three-stage mission.

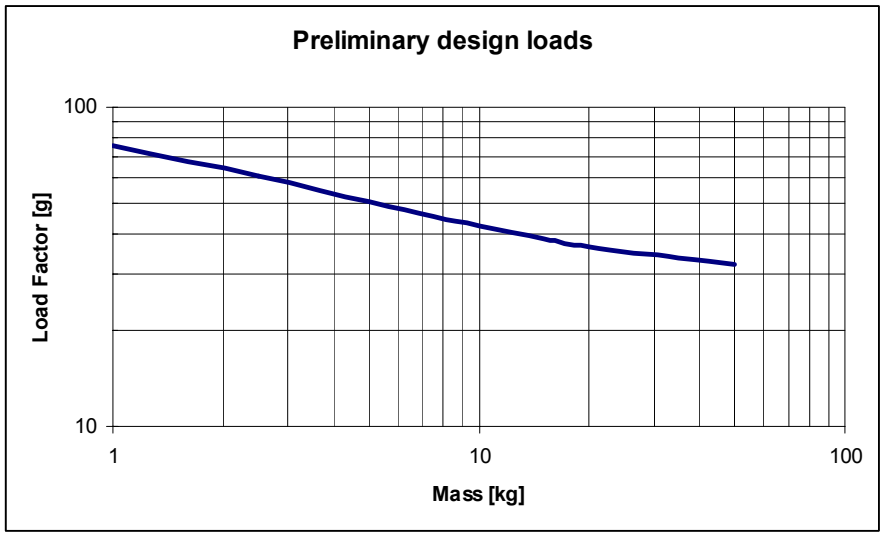

Figure A-3: Preliminary design loads

A.4 Description of FE-Model

The FE-model of the launch configuration is shown in the following figure. The launch configuration consists of three LISA spacecraft, each with attached propulsion module. The dimensions and masses are based on the conceptual design from 14.10.1999 /3/. The conceptual design has slightly been changed in order to improve stiffness of the satellite launch configuration. Outer panels at the Science Module have been introduced and the locations of units at the Propulsion Module have been modified.

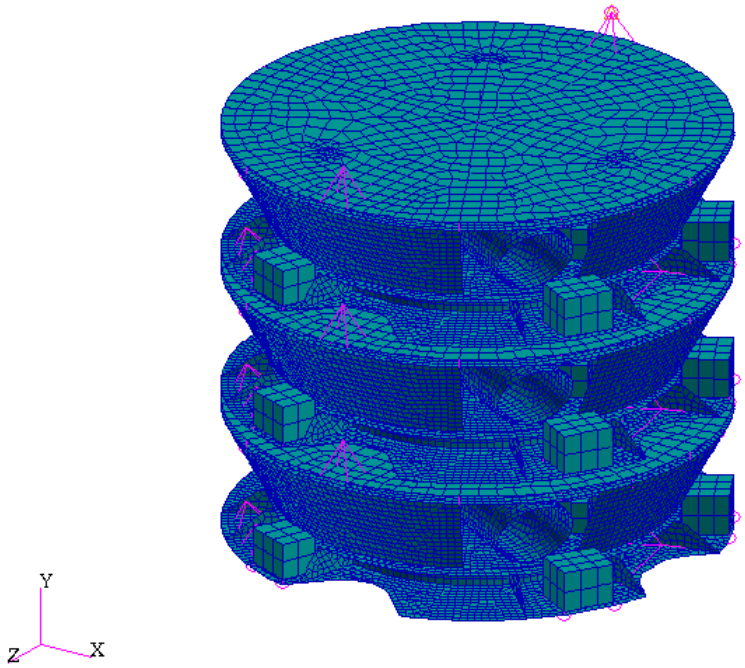

Figure A-4: FE-model of launch configuration

The model consists of the following number of nodes and elements:

Nodes	69873
QUAD Elements	69525
TRIA Elements	93
BAR2 Elements	24
POINT Elements	27
RBE2 Elements	828
RBE3 Elements	27

A.4.1 Units

The following units have been used for modelling:

Force:	Newton
Length:	Millimetre
Temperature:	° Celsius
Mass:	Tons
Time:	Second

A.4.2 Material Properties

Aluminium

Property	Value	Unit	Comment
E	70000	N/mm^2	Young's Modulus
G	26923	N/mm^2	Shear Modulus
ν	0.3	-	Poisson's Ratio
ρ	2.7 E –9	t/mm^3	Density
α	23.0 E –6	1/K	CTE
β	0.	1/%	CME

CFRP – M55 quasiisotropic layup

Property	Value	Unit	Comment
E	108000	N/mm^2	Young's Modulus
G	41130	N/mm^2	Shear Modulus
ν	0.32	-	Poisson's Ratio
ρ	1.7 E –9	t/mm^3	Density
α	0.1 E –6	1/K	CTE
β	150 E –6	1/%	CME

Honeycomb 3/16 – 5056 – 0.001

Property	Value	Unit	Comment
G_L	310	N/mm^2	Shear Modulus L
G_W	138	N/mm^2	Shear Modulus W
ρ	49.7 E –12	t/mm^3	Density

A.4.3 FE-Model – Science Module

In launch configuration there are three identical modules. The total mass of one Science Module amounts to 283 kg.

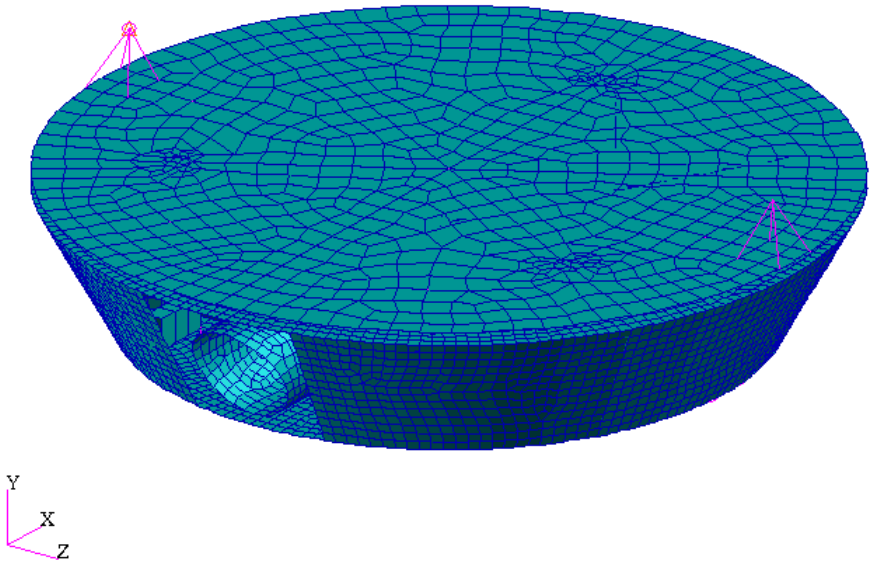

Figure A-5: FE-Model of Science Module

A short description of the components is given in the following paragraphs.

A.4.3.1 Primary Structure Science Module

Figure A-6 shows the Primary Structure except the Upper Plate. Properties of elements are shown with different colours.

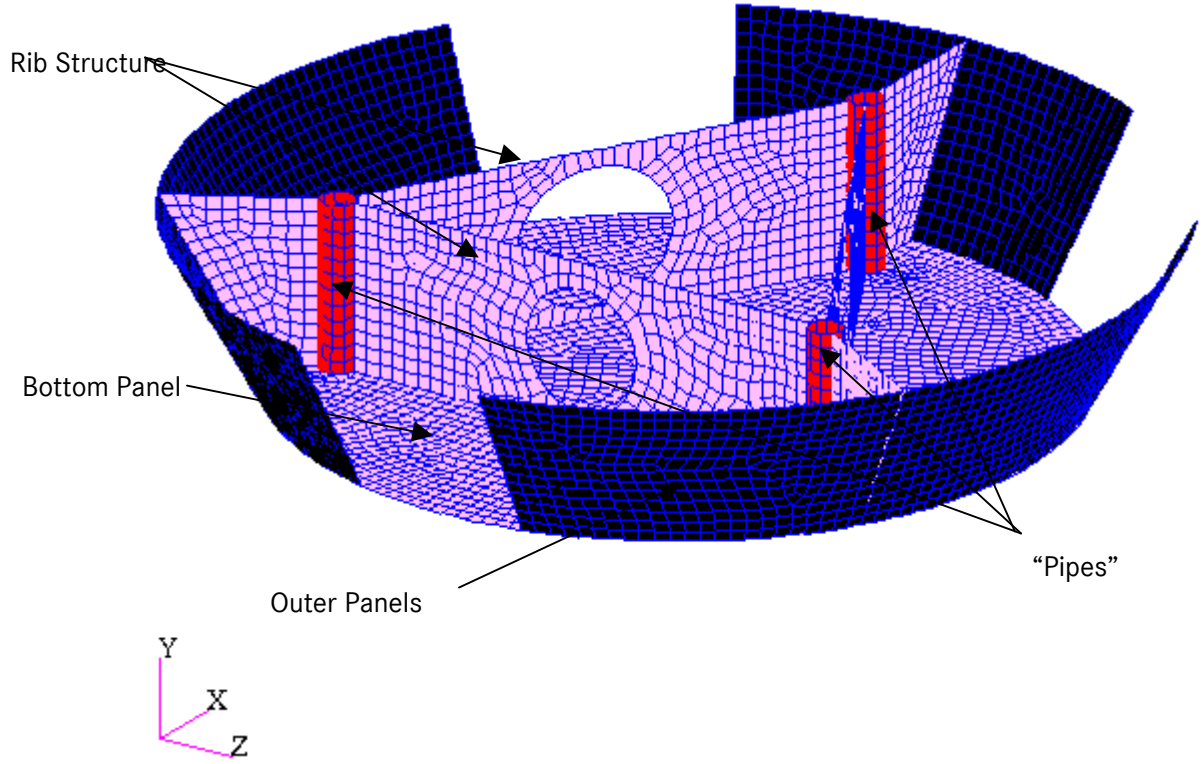

Figure A-6: Science Module Primary Structure without Upper Panel

Bottom Panel, Rib Structure and Upper Panel (not visible):

Sandwich Structure: Total height 30 mm

Face sheets 0,5 mm Aluminium

Core 29 mm honeycomb 3/16 – 50565 – 0.001

Pipes

Material: Aluminium

Thickness: 2,5 mm

Outer Panels:

Sandwich Structure:

Total height 30 mm

Face sheets 0,5 mm Aluminium

Core 29 mm honeycomb 3/16 – 50565 – 0.001

A.4.3.2 Payload with Thermal Shield

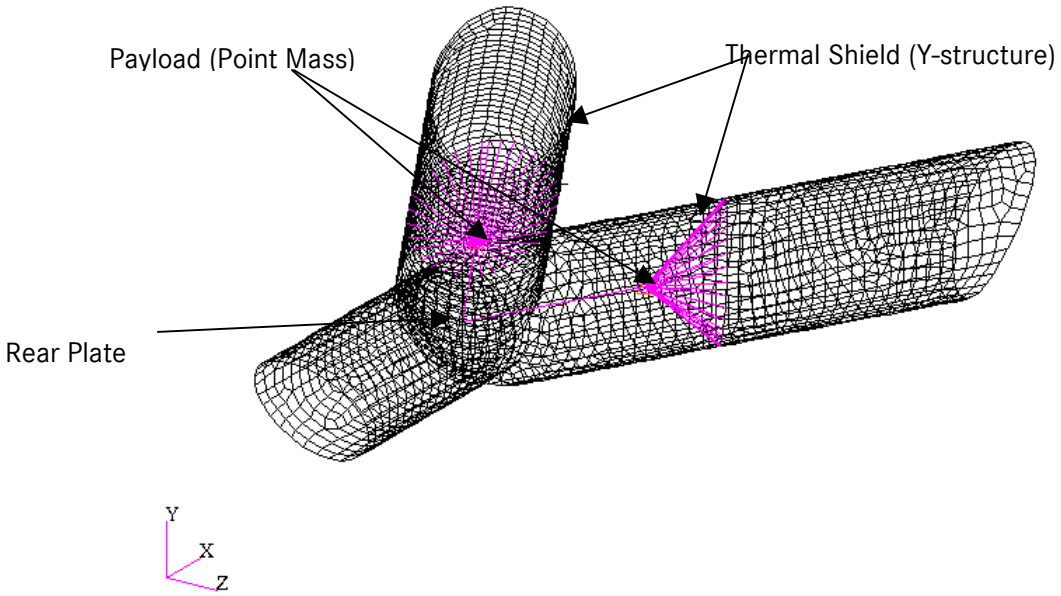

Figure A-7: Payload with Thermal Shield

Thermal Shield:

Material: CFRP – M55 quasiisotropic layup

Thickness: 2 mm

Rear Plate:

Sandwich Structure:

Total height 30 mm

Face sheets 1 mm CFRP – M55 quasiisotropic layup

Core 28 mm honeycomb 3/16 – 50565 – 0.001

Payload:

Point Mass 20 kg each

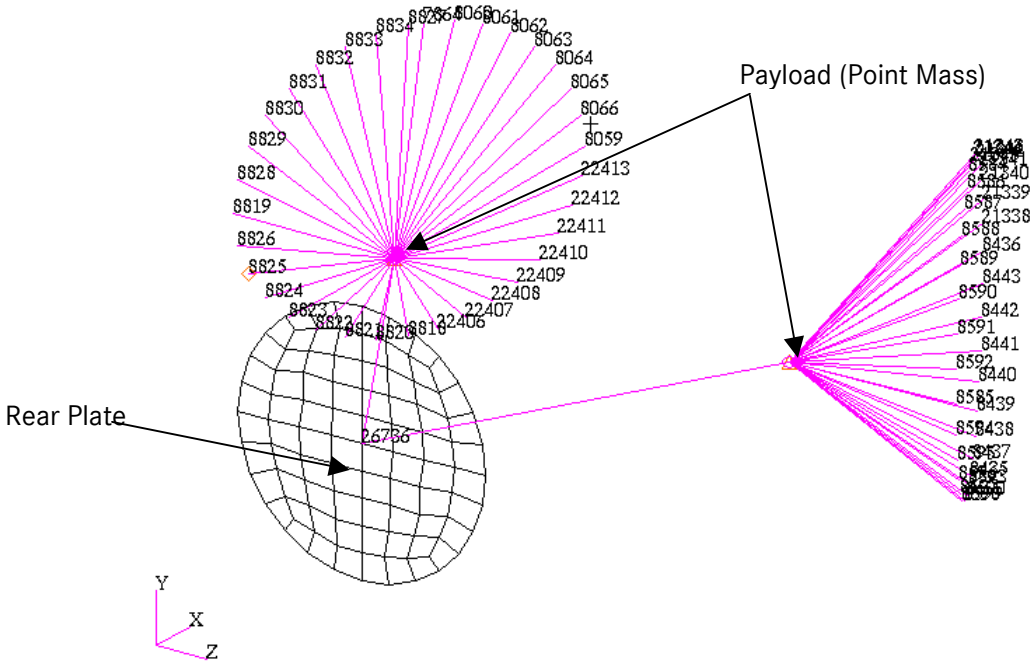

Figure A-8: Interface Nodes Payload to Thermal Shield and Rear Plate

Interface Nodes:

Rear Plate:	Node 26736
Thermal Shield – z:	Node 7864, 8059 – 8066, 8818 – 8834, 22406 - 22413
Thermal Shield + z:	Node 8435 – 8443, 8584 – 8600, 21338 - 21345

A.4.3.3 Solar Array

The isolating foam has been taken into account as additional mass and not as a structural component with stiffness.

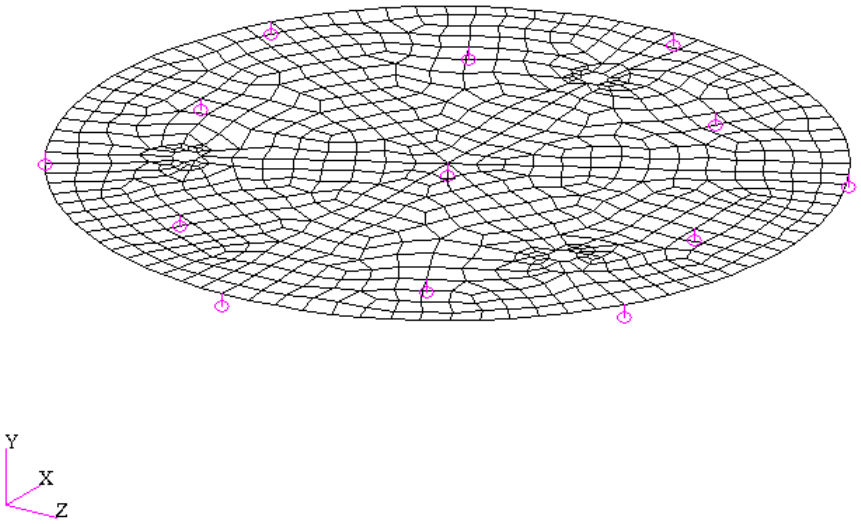

Figure A-9: Solar Array with IF-Elements

Solar Array:

Sandwich Structure (Support Structure):

Total height 40 mm

Foam 20 mm

Face sheets 0,6 mm CFRP – M55 quasiisotropic layup

Core 18,8 mm honeycomb 3/16 – 50565 – 0.001

A.4.3.4 Other Components

All components with a mass greater or equal 1 kg have been modelled. The masses of the other ones have been added to the panels they are mounted on. The weights are taken from /3/.

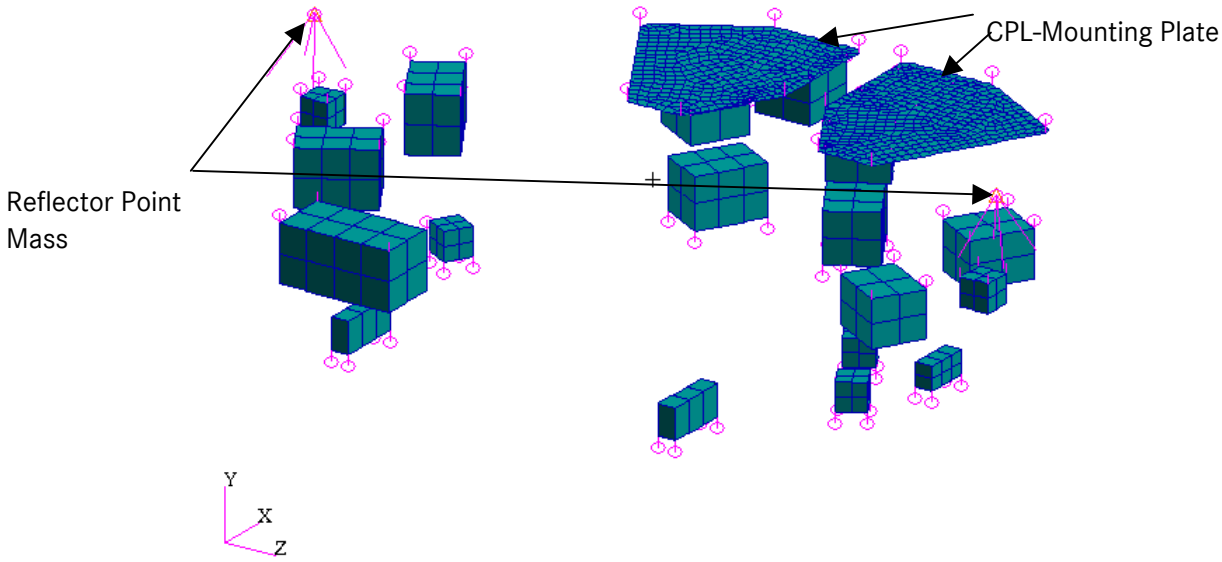

Figure A-10: Other Components Science Module

CPL-Mounting Plate:

Sandwich Structure:

Total height 30 mm

Face sheets 0,5 mm Aluminium

Core 29 mm honeycomb 3/16 – 50565 – 0.001

Reflectors:

Point Mass 3 kg each

All boxes are assumed to be made of aluminium and the housing having a constant thickness of 4 mm.

All boxes:

Material: Aluminium

Thickness: 4 mm

A.4.4 FE-Model – Propulsion Module

In launch configuration there are three identical modules. The total mass of the Propulsion Module with filled tanks amounts to 202 kg.

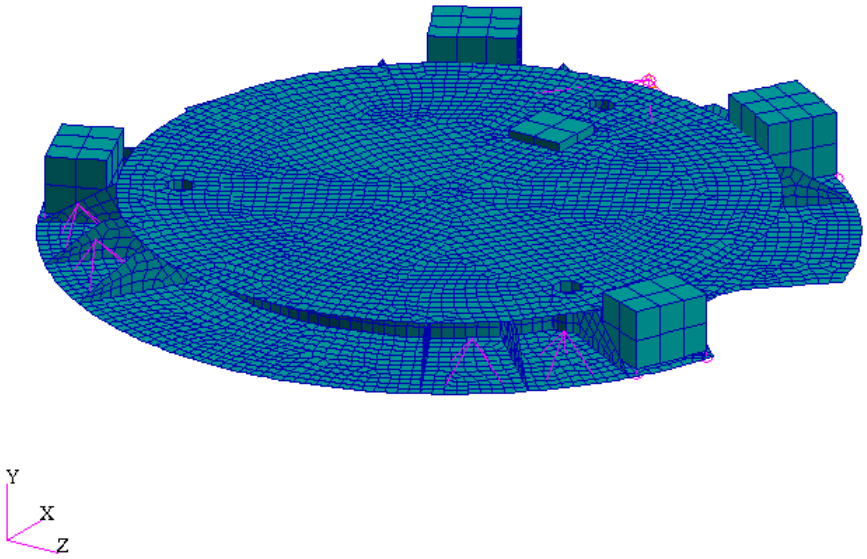

Figure A-11: FE-Model of Propulsion Module

A.4.4.1 Primary Structure Propulsion Module

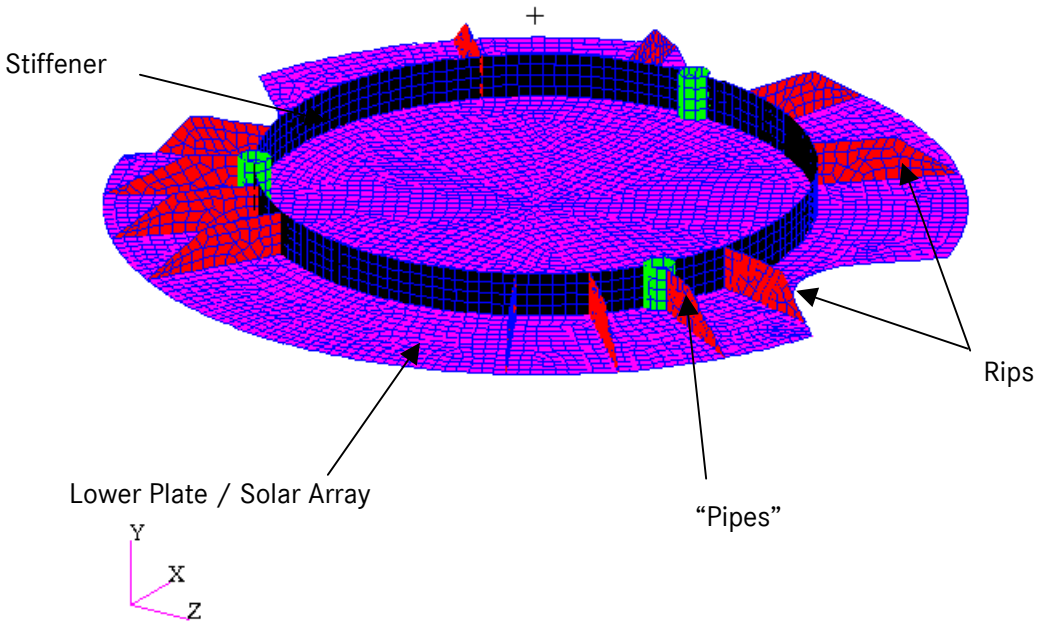

Figure A-12: Propulsion Module Primary Structure without Upper Panel

Lower Plate / Solar Array:

Sandwich Structure:

Total height 30 mm

Face sheets 0,5 mm Aluminium

Core 29 mm honeycomb 3/16 – 50565 – 0.001

Pipes

Material: Aluminium

Thickness: 2,5 mm

Rips:

Sandwich Structure:

Total height 20 mm

Face sheets 0,5 mm Aluminium

Core 19 mm honeycomb 3/16 – 50565 – 0.001

Stiffener

Material: Aluminium

Thickness: 3 mm

Upper Plate (not visible):

Sandwich Structure:

Total height 10 mm

Face sheets 0,5 mm Aluminium

Core 9 mm honeycomb 3/16 – 50565 – 0.001

A.4.4.2 Other Components Propulsion Module

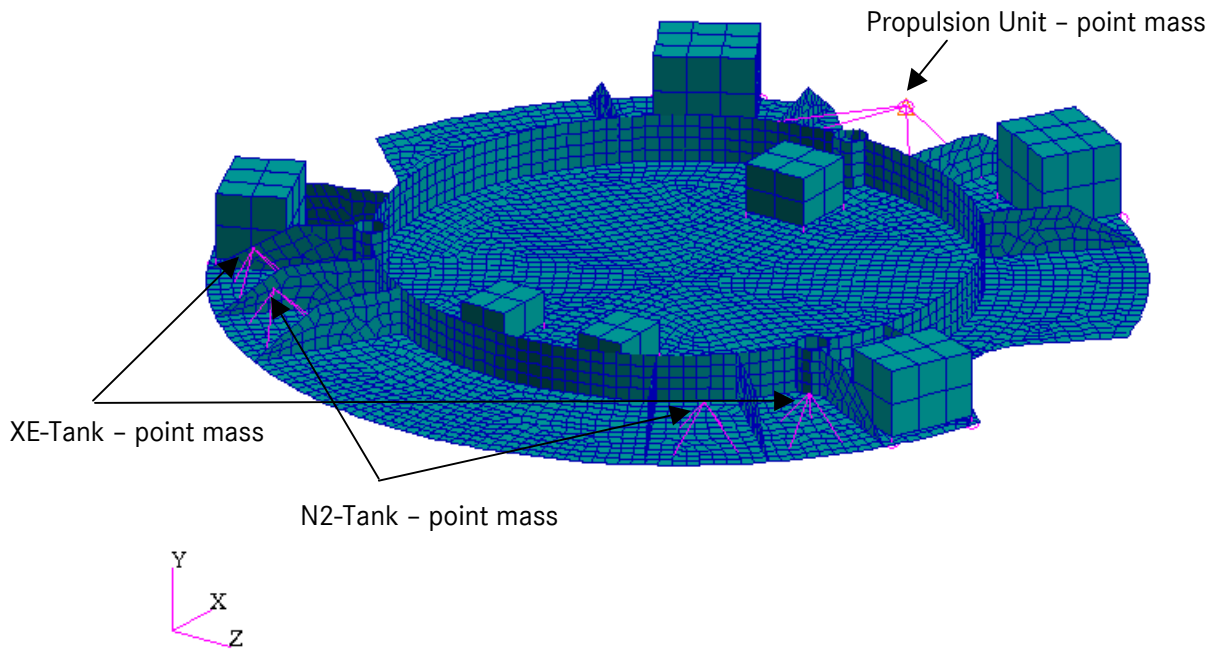

Figure A-13: Other Components Propulsion Module with Solar Array, Pipes, Rips and Stiffener

XE-Tank:	Point Mass 13 kg each
N2-Tank:	Point Mass 7,5 kg each
Propulsion Unit:	Point Mass 39,05 kg
All boxes:	Aluminium 4 mm

A.4.5 Launch Configuration – Interface Elements

Figure A-14 shows the launch configuration of LISA consisting of three Science Modules and the accompanying Propulsion Modules.

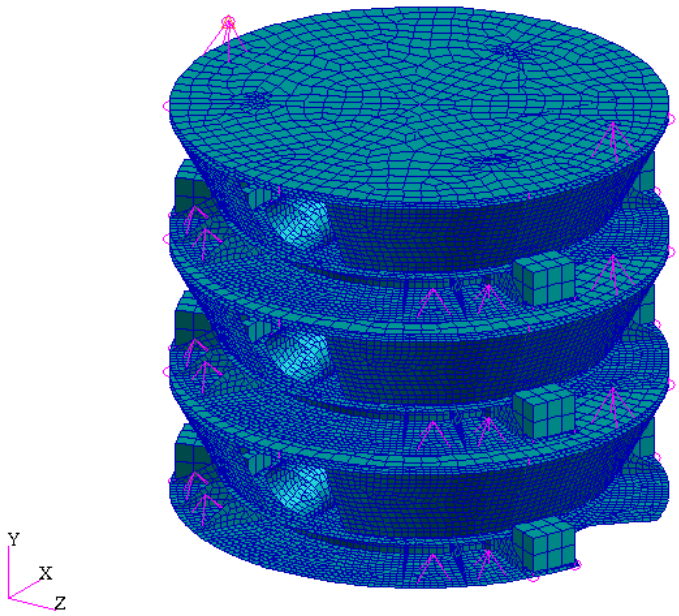

Figure A-14: LISA launch configuration

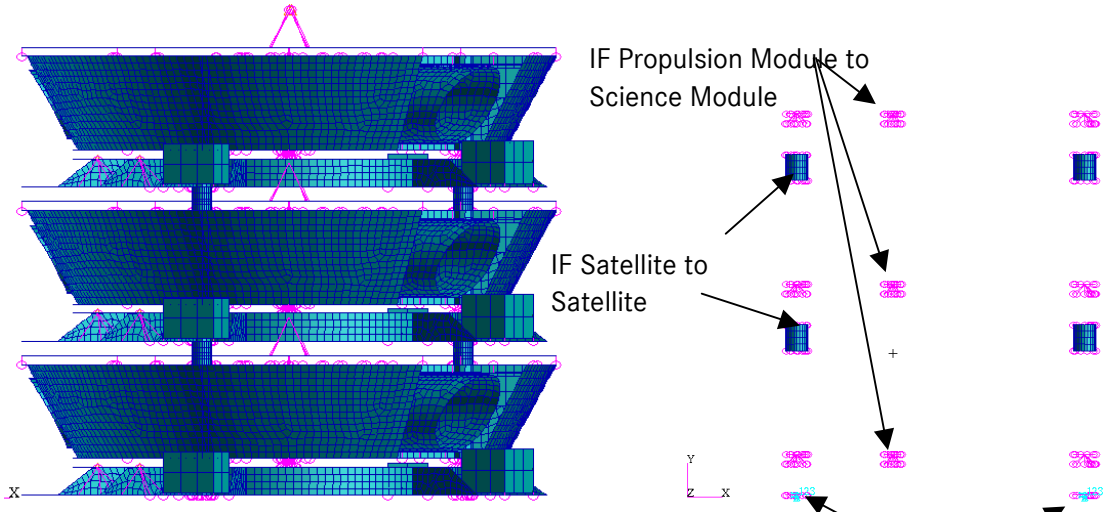

Figure A-15: Interface Elements

The stack of satellites is hard mounted at the launcher interfaces for dynamic analysis.

Propulsion Module and Science Module are joint by use of rigid elements (Type RBE2, MSC Nastran).

The interface structure satellite to satellite is modelled by use of rigid elements and beam elements. The beam elements have the same dimensions as the “Pipes” of the primary structure.

A.4.6 Model Verification

For dynamic model verification a Rigid Body Check has been performed, the results are listed below.

Strain Energies		KGG	KNN	KAA
Direction	1	1,55E-08	1,19E-08	1,19E-08
Direction	2	7,95E-09	2,62E-09	2,62E-09
Direction	3	2,17E-08	2,20E-08	2,20E-08
Direction	4	2,32E-02	2,01E-02	2,01E-02
Direction	5	1,98E-02	2,22E-02	2,22E-02
Direction	6	7,12E-03	5,64E-03	5,64E-03

Table A-2: Resulting strain energies from Rigid Body Check (Free-Free boundary conditions)

The resulting strain energies are well below the typical specification value of 1 Nmm. The natural frequencies of the model in Free-Free boundary conditions contains 6 rigid body modes for each degree of freedom.

mode no,	frequency [Hz]	m_eff (relative) [%] T1	T2	T3	R1	R2	R3
1	2,47E-05	1,1	88,5	0,1	2,3	0,5	7
2	3,26E-05	16,4	12	1,1	0,8	10	27,6
3	3,71E-05	0,9	1	0,1	73,6	3,8	0,4
4	3,82E-05	10,7	0	19,2	10,6	48,9	27,3
5	4,18E-05	8,5	0,7	77,1	13,3	6,2	16,7
6	4,78E-05	65,4	0	3,3	0,1	30,8	22,8
7	31,48	0	0	0	0	0	0
8	42,07	0	0	0	0	0	0
9	44,32	0	0	0	0	0	0
10	44,84	0	0	0	0	0	0

Table A-3: Resulting frequencies and effective masses from Rigid Body Check

```
O U T P U T   F R O M   G R I D   P O I N T   W E I G H T   G E N E R A T O R
0                                                REFERENCE POINT =       0
                                        M O
 1.455783E+00  0.000000E+00  0.000000E+00  0.000000E+00 -8.065556E+00 -6.641826E+02 *
 0.000000E+00  1.455783E+00  0.000000E+00  8.065556E+00  0.000000E+00  5.042359E+01 *
 0.000000E+00  0.000000E+00  1.455783E+00  6.641826E+02 -5.042359E+01  0.000000E+00 *
 0.000000E+00  8.065556E+00  6.641826E+02  1.611811E+06 -1.189210E+04  6.283104E+03 *
-8.065556E+00  0.000000E+00 -5.042359E+01 -1.189210E+04  1.354236E+06  6.198146E+03 *
-6.641826E+02  5.042359E+01  0.000000E+00  6.283104E+03  6.198146E+03  1.705441E+06 *
                                        S
                 *  1.000000E+00  0.000000E+00  0.000000E+00 *
                 *  0.000000E+00  1.000000E+00  0.000000E+00 *
                 *  0.000000E+00  0.000000E+00  1.000000E+00 *
      DIRECTION
 MASS AXIS SYSTEM (S)     MASS              X-C.G.        Y-C.G.        Z-C.G.
        X            1.455783E+00      0.000000E+00  4.562375E+02 -5.540358E+00
        Y            1.455783E+00      3.463676E+01  0.000000E+00 -5.540358E+00
        Z            1.455783E+00      3.463676E+01  4.562375E+02  0.000000E+00
                                       I(S)
                 *  1.308741E+06 -1.111303E+04 -6.003740E+03 *
                 * -1.111303E+04  1.352445E+06 -2.518336E+03 *
                 * -6.003740E+03 -2.518336E+03  1.400669E+06 *
                                       I(Q)
                 *  1.354789E+06                            *
                 *                1.305786E+06              *
                 *                              1.401280E+06 *
                                       Q
                 * -2.236116E-01  9.719495E-01  7.288454E-02 *
                 * -9.711748E-01 -2.285186E-01  6.781378E-02 *
                 *  8.256704E-02 -5.561968E-02  9.950323E-01 *
```

Table A-4: Output from Grid Point Weight Generator

Thermal model verification:

The thermal check has only been performed for one Science Module.

With a thermal check it has to be verified, that e.g. rigid body elements have no influence on the deformation of the model due to thermal loads. The resulting stresses in the model have to be small.

The main problem to pass the check is the warping of QUAD elements. Warping induces stresses into the model. This can be prevented by splitting each warped QUAD element into two TRI elements, because a TRI element cannot be warped.

Therefore the model of the Science Module has been modified, all warped QUAD elements have been replaced by two TRI elements. In addition, the same property definition has been assigned to all elements.

Material:	Aluminium	
	Young's modulus	$70000 N/mm^2$
	Coefficient of thermal expansion	$23 * 10^{-6}/K$
	Thickness	1 mm

Load case: uniform warming up about 100 K

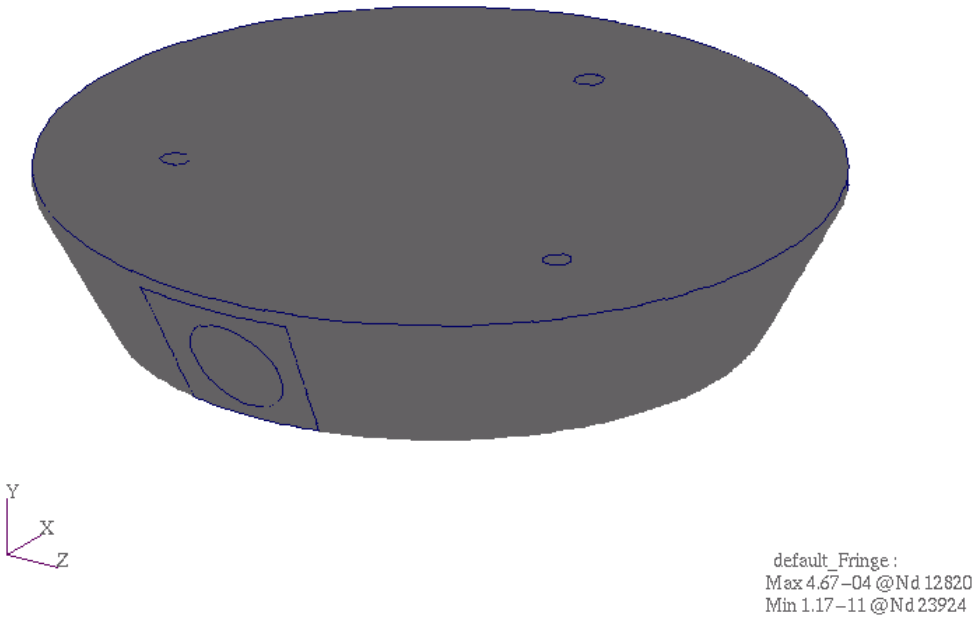

Figure A-16: Stress distribution due to thermal check load case

The maximum stress due to this load case amounts to 0,00046 MPa. The model is suitable for thermal distortion analysis.

A.5 Analyses Results

A.5.1 Dynamic Analysis

The following Table A-5 shows the resulting natural frequencies and the accompanying effective masses.

mode no,	frequency [Hz]	m_eff (relative) [%] T1	T2	T3	R1	R2	R3
1	15,9	71	0	0,2	0,2	0,3	65,8
2	16,37	0,4	0	55,1	49,1	18,4	0,4
3	18,32	0	0	15,4	17	54,6	0
4	37,72	8,7	0,3	0	0	0	9,3
5	40,67	0	0,1	8,4	9,9	0,1	0
6	44,71	0	0,1	0,4	0,2	3	0
7	46,58	0,5	7,3	0	0	0	0,2
8	46,68	0	1,2	0,8	0	0,1	0
9	47,01	0,1	21,3	0	0	0	0,2
10	47,64	0	0,3	0	1,5	0,3	0
11	48,03	0,1	0,2	0	0,1	0	0
12	48,48	0	1,8	0	0,3	0	0,1
13	49,84	0	26,1	0	0	0	1,7
14	51,25	0	0	0,3	0	0,2	0
15	52,6	0,8	5,9	0	0	0	4,4
16	52,83	0	0	0,3	0,2	3,1	0
17	55,88	0,2	2,2	0	0	0	0,4
18	56,11	0	0	0,3	0,1	0	0
19	56,48	0	0	0	0	0	0
20	56,91	0,1	0	0	0	0	0,5

Table A-5: Mode Shapes and Effective Masses in %

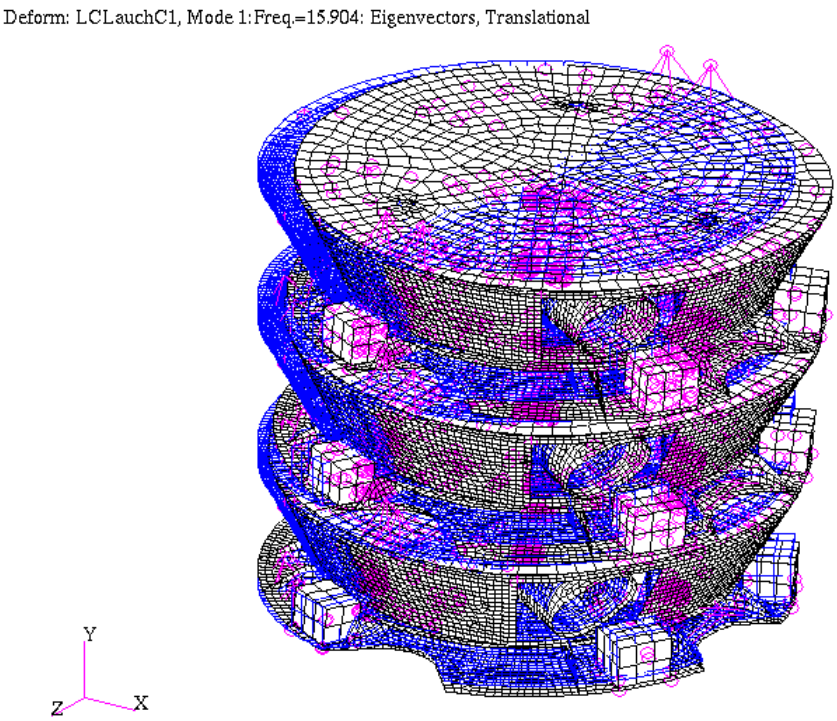

Figure A-17: Mode 1 – 15,9 Hz – Lateral Mode

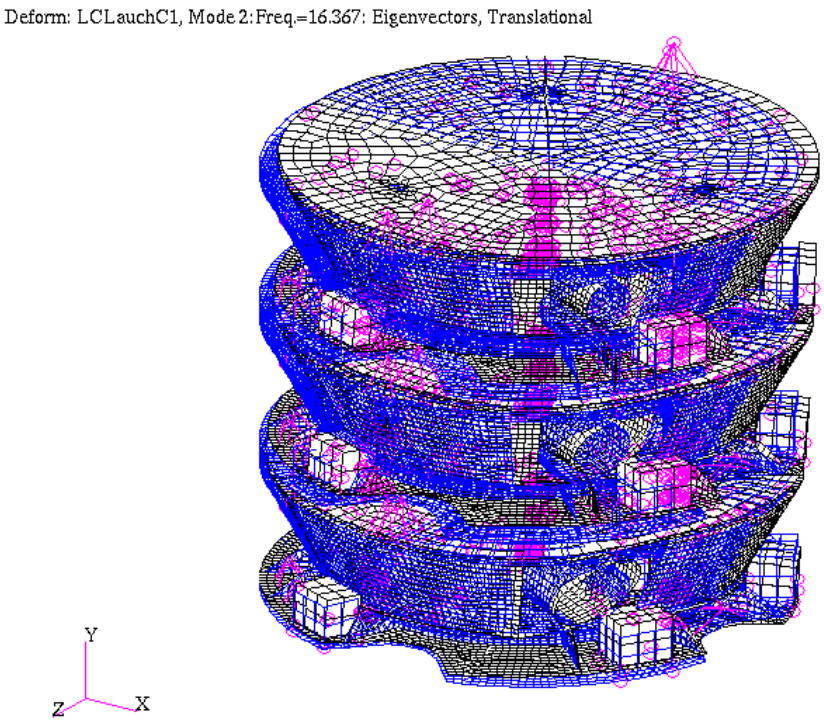

Figure A-18: Mode 2 – 16,4 Hz – Lateral Mode

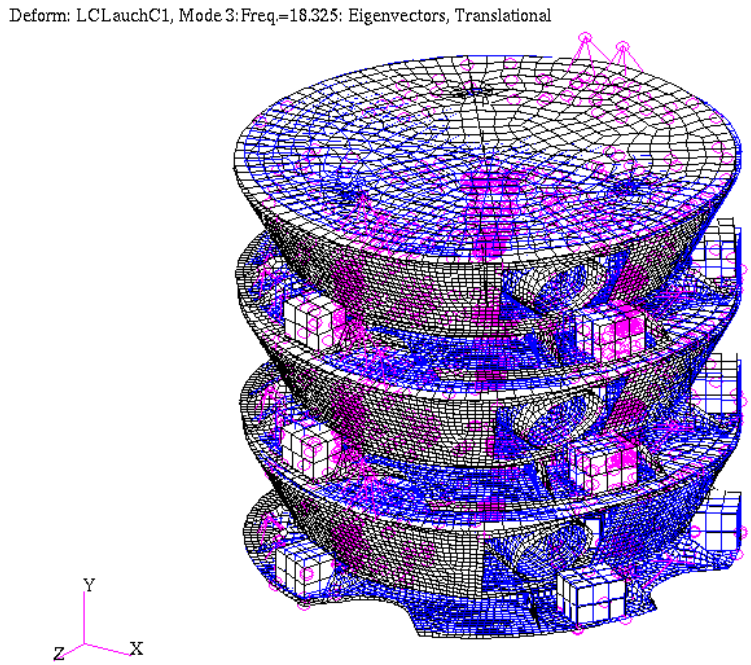

Figure A-19: Mode 3 – 18,3 Hz – Lateral Mode

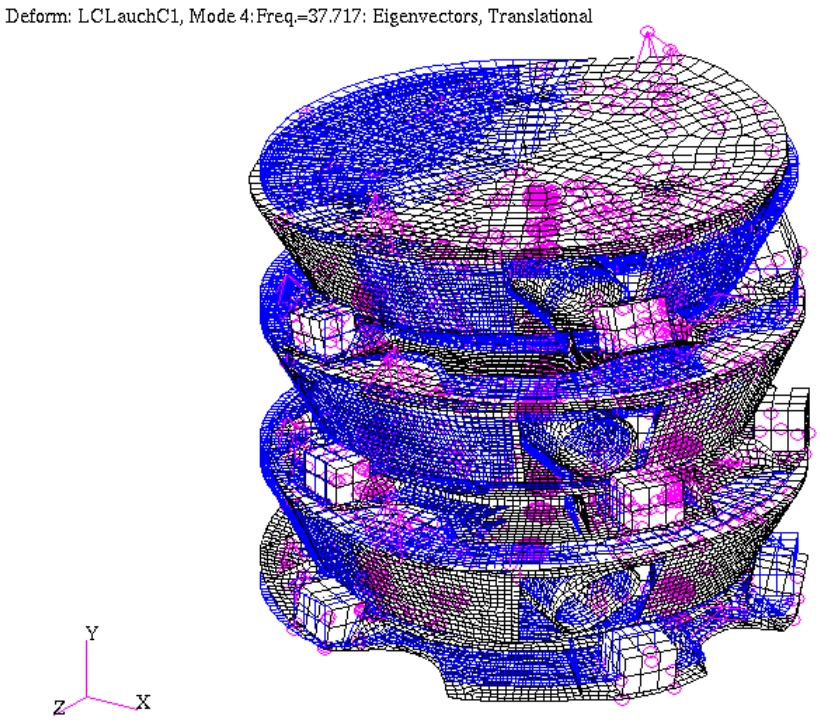

Figure A-20: Mode 4 – 37,2 Hz – Panel Mode

A.6 Summary

The analyses has demonstrated that the LISA spacecraft in launch configuration is able to cope with the stiffness requirements, described in chapter A.3.

B Optical Bench Mechanical Analysis

This annex describes the activities performed during the Phase A about the mechanical design of the OB. It includes:

- the selection of the OB baseplate material;
- the analyses relevant to the mounting options of the various components on the OB;
- the analysis relevant to the mounting options of the OB inside the S/C;
- the analyses relevant to the selected mechanical design of the OB.

B.1 Optical Bench Material Selection

The main requirement of the OB is an ultra high dimensional stability. This restricts the selection of the material for the OB baseplate to the ULE™, produced by Corning, and the Zerodur , produced by Schott, both characterised by a very small CTE. The properties of these two materials are summarised in Table B-1.

The ULE™ guaranteed maximum limit for the coefficient of thermal expansion is 40% lower than Zerodur® one, in the operational temperature range of the OB (20°C ± 10 °C).

On the other hand, the ULE™ thermoelastic stability (defined by the parameter CTE/thermal conductivity ≡ CTE/k) is 33% lower than ZERODUR® one.

The mechanical properties of the two materials are very similar (the Zerodur® specific elastic modulus is only 17% greater than ULE™ one).

Both the materials can be easily machined and polished.

In conclusion, since the important parameters for the dimensional stability are the CTE and thermoelastic stability (the lower the CTE, the higher the dimensional stability under a given temperature change; the lower the CTE/k, the higher the dimensional stability under a given thermal power dissipated in the element), the recommended material is the ULE™.

		ULE™	Zerodur®
Physical Properties			
Mean CTE		$0\pm1\cdot10^{-8}$/K (1)	$0\pm2\cdot10^{-8}$/K (2)
CTE guaranteed max. limit		$3\cdot10^{-8}$/K (1)	$5\cdot10^{-8}$/K (2)
Density (ρ)	Kg/m^3	2210	2530
Thermal Properties (3) (4)			
Thermal Conductivity (k)	W/m K	1.31	1.46
Mean Specific Heat (c)	J/Kg K	767	800
Thermoelastic Stability (CTE/k)	m/W	$2.29\cdot10^{-8}$ (5)	$3.42\cdot10^{-8}$ (5)
Mechanical Properties (3) (4)			
Elastic Modulus (E)	GPa	67.6	90.3
Specific Elastic Modulus (E/ρ)	m^2/s^2	$3.06\cdot10^7$	$3.57\cdot10^7$
Shear Modulus	GPa	29	36
Bulk Modulus	GPa	34.1	TBD
Poisson's Ratio (ν)		0.17	0.243
Ultimate Tensile Stress	MPa	49.8 (6)	30 - 65 (7)
Others			
Machinability		good	good
Surface Polishing		easy	Easy
Surface Coating		feasible	Feasible
Optical Contacting Compatibility		yes	Yes

(1) "Premium grade" ULE™, in the temperature range 5 - 35 ºC
(2) "Expansion class 0" Zerodur®, in the temperature range 0 - 50 ºC
(3) @ T_{ref} = 25 ºC for ULE™
(4) @ T_{ref} = 20 ºC for Zerodur®
(5) Computed for the maximum guaranteed CTE
(6) Samples average value
(7) Bending Strength vs. grit size with 0% failure

Table B-1- Comparison between ULE™ and Zerodur®

B.2 Components Mounting on the Optical Bench

Two concepts for the component mounting on the OB have been considered (see):

- components mounting on top of the OB - concept A;
- components embedded in insets machined into the ULE™ baseplate – concept B (solution proposed in the Pre-Phase A design [2]).

The main advantages of the first concept are an easier implementation and the possibility of mounting the components without removing material in the baseplate (using bonding techniques like the hydroxy-catalysis bonding), thus minimising the stress in the OB material under the launch loads. The main advantage of the second option is that the various elements lie on the mid plane of the OB, and the lack of offsets w.r.t. this plane improves the stability of the layout under thermal or mechanical loads applied to the bench. On the other hand, the insets for the accommodation of the elements and the holes (with diameters ranging from ~3 mm up to ~10 mm) for the passage of the laser beams weaken the OB baseplate and increases the risk of breaking during under the launch loads.

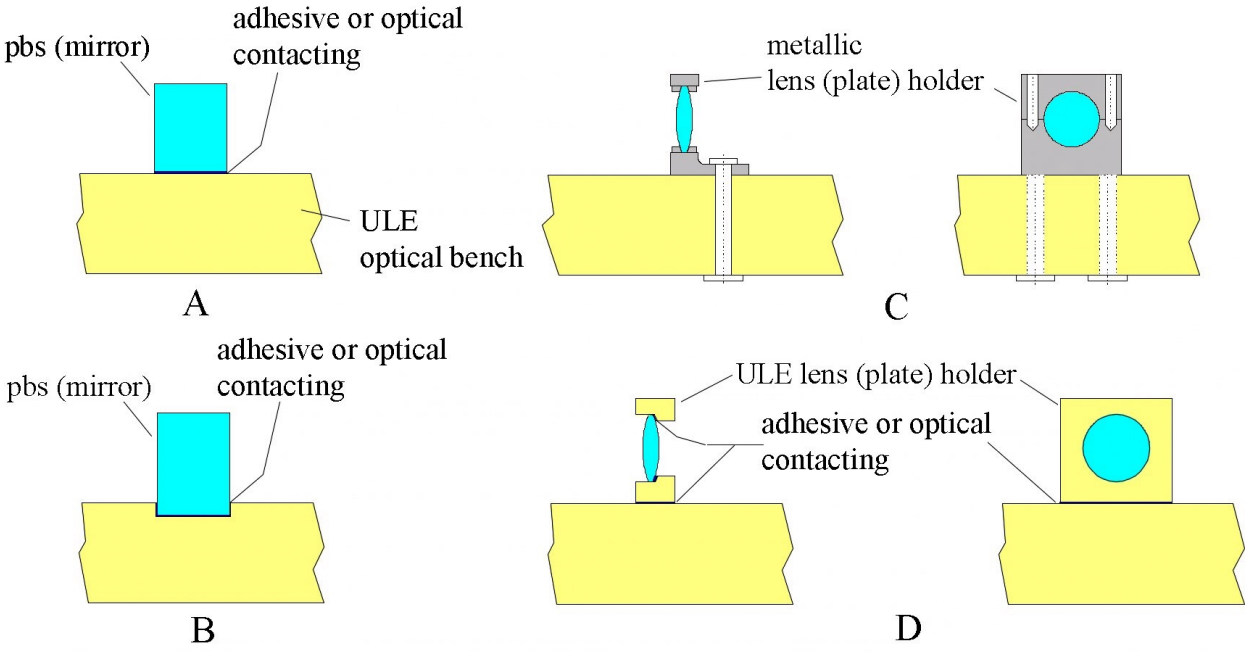

Figure B-1- Examples of optical components mounting on top of the OB (above) and inside the OB (below)

The two concepts for the optical component mounting constraint also the design of the OB mechanical interface with the support structure (made by 8 Pyroceram tubes departing from a stiffening ring converging two-by-two at the corners of the OB [1]) and with the Inertial Sensor head.

The solution devised for the concept A is shown in Figure B-2. The interface with the support structure is implemented by means of two special titanium bolts passing through holes (∅ = 9 mm) lying on the OB middle plane and parallel to its short side. The bolts are not in contact with the ULE™ all over their length but only at their ends by means of suitable bushes (∅ = 18 mm), to diffuse the loads and increase the thermal de-coupling. The connection of the bolts to the Pyroceram tubes is achieved by means of V-shaped machined elements. The interface with the inertial sensor is implemented in a similar way. This solution allows preserving the overall envelope of the vacuum vessel, but additional cutouts are needed

in the bench. On the OB side this kind of interface is very simple (cylindrical holes in the ULE™) and allows for a simple manufacturing and a high integration accuracy. Moreover, it leaves the upper surface available for the accommodation of the optics.

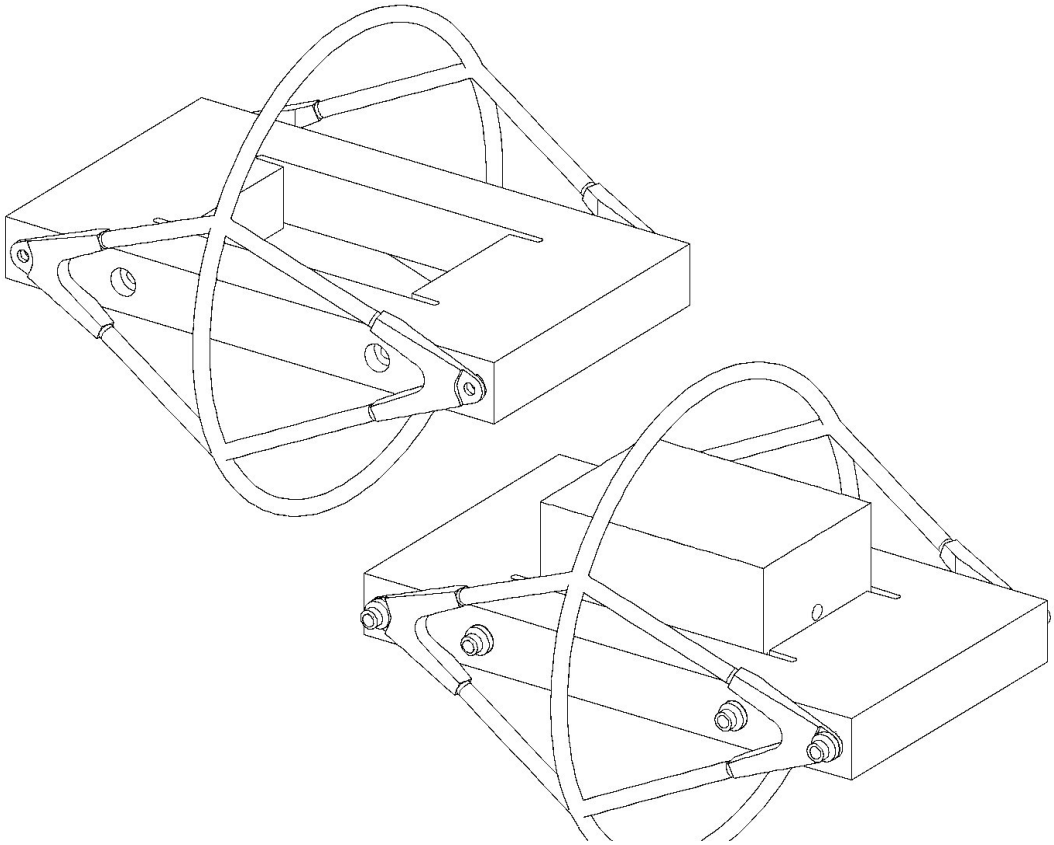

Figure B-2 - OB mechanical interface with support structure and inertial sensor: Solution A

The solution devised for the concept A is shown in Figure B-3. The interface with the support structure implemented by means of four bolts passing through holes with the axes perpendicular to the bench plane. The connection of the bolts to the Pyroceram tubes is achieved by means of machined elements that clamp the OB at its four corners. The interface with the Inertial Sensor is implemented in a similar way. This interface does not need additional cut outs in the bench, apart from the central one, but the vacuum vessel corners must be removed. This solution is tailored to the embedding of the optics inside the OB (minimum interference between the structural elements and the OB mid plane).

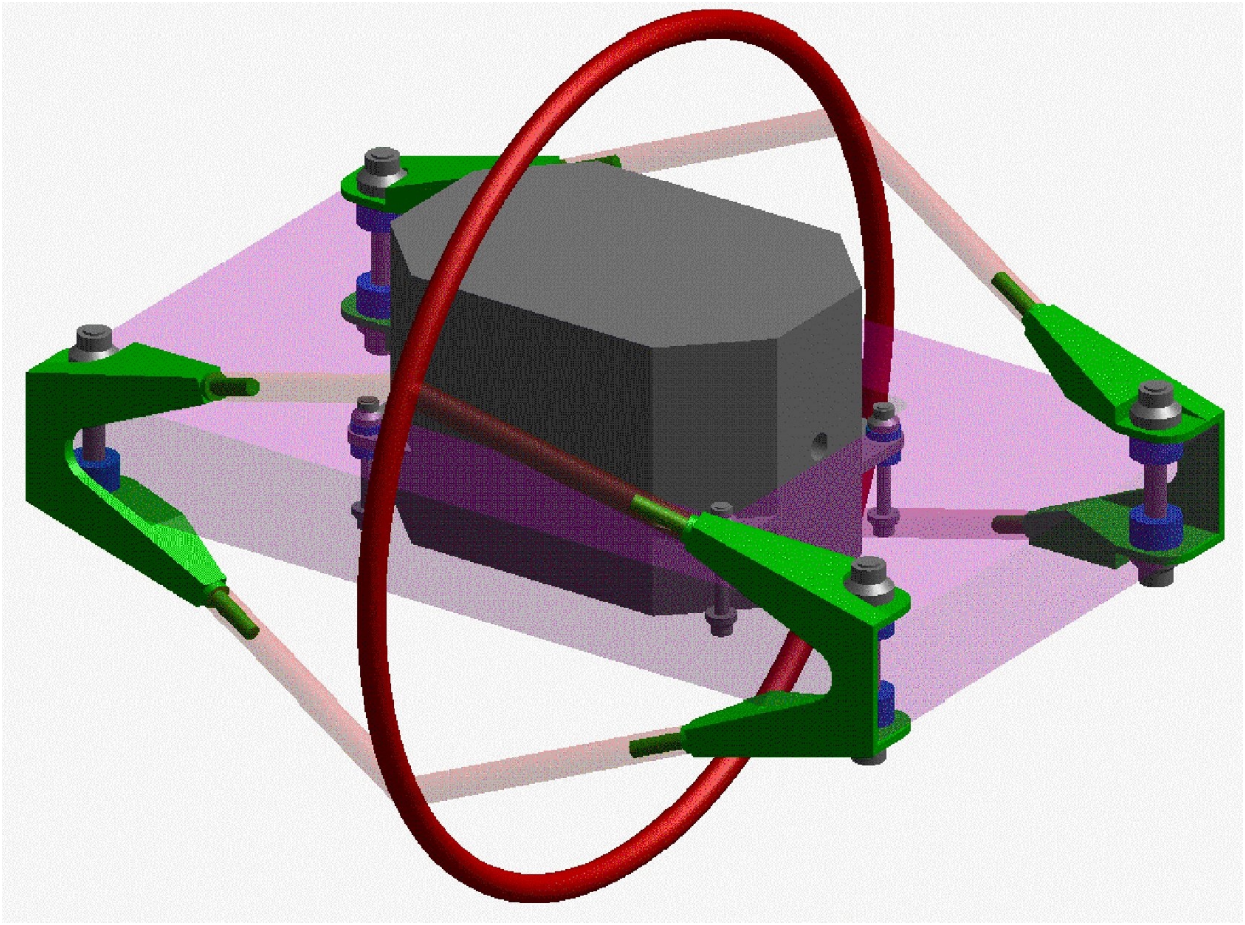

Figure B-3 - OB mechanical interface with support structure and inertial sensor: Solution B

The mass budget relative to the two mechanical solutions is provided in Table B-2.

Element type	Mass (kg)	
	Solution A	Solution B
OB ULE™ baseplate	4.40	4.61
Bolts	0.45	0.26
Thermal washers	0.03	0.03
Machined elements	0.19	0.43
TOTAL	**5.07**	**5.33**

Table B-2 - Mass budget for the two OB mechanical solutions (no contingency included)

A Finite Element Model (FEM) has been built for the two solutions, using the ANSYS® v5.3 software, in order to assess and compare their dynamic and static behaviour. It is shown in Figure B-4 and consists of 1-D elements (BEAM4) and 2-D elements (SHELL63) for a total of 615 nodes and 533 elements. The stiffening ring to which the Pyroceram rods are connected has been considered a rigid element. The rods have been modelled as flexible elements with a coefficient $A \cdot E = 6.72 \cdot 10^6$ N (corresponding to the Pyroceram tensile module and to the rods cross section area obtained from the data contained in [1]). The angle between the beams joined at the OB corners has been taken = 46°. The constraints between

the rods and the OB at the four corners have been modelled according to the mechanical design of the two options. In addition to the mass reported in Table B-2 (with a further 10% contingency) the following masses have been included in the OB FEM:

- Inertial Sensor head mass = 6.5 kg (modelled as a concentrated mass, MASS21, located in the middle of the OB with an offset of 0.027 m in the out-of-plane direction);
- fiber positioner mass = 0.5 kg;
- mass of the components mounted on the top of the bench (optics + detectors) = 0.33 kg.

The quasi-static design loads prescribed by [4] for an equipment around 15 kg is 35 g's along the worst spatial direction. However, in consideration of the position of the OB with respect to the launcher thrust direction, the following design loads have been applied to the OB FEM for the static analysis:

- 35 g's perpendicular to the OB plane (i.e. along the launcher X-axis, where the maximum acceleration is expected);
- 15 g's on the OB plane.

According to the prescriptions of [4], the two loads have not been applied simultaneously.

The results of the dynamic analyses, in terms of eigenfrequencies of the first vibration modes of the OB, are summarised in Table B-3. The results of the static analyses, in terms of maximum value of the equivalent stress distribution (Von Mises criterion), are summarised in Table B-4. The resulting map of the stress distribution for the OB Solution A under the application of a 35 g's load perpendicular to the OB plane is provided in Figure B-5.

From these analyses it turns out that there are small differences between the two solutions. However the static analysis highlights a relatively high level of stress in the material, with a small safety factor with respect to the ULE^{TM} ultimate tensile stress. This advises against the addition of further cutouts or insets in the OB baseplate for the accommodation of the various components (some of which, like the fiber positioner, are relatively large). Thus, the mounting of the elements on top of the OB is the preferred concept, also in consideration of its easier implementation (for instance, it is much more difficult to polish the internal surface of the insets at the quality required for the hydroxy-catalysis bonding), lower costs and risks. Consequently the Solution A is to be chosen for the OB interface with the support structure. On the other hand, since both Solutions A and B for the Inertial Sensor interface with the OB are in principle compatible with element mounting on top of the OB, the second one is to be preferred. In fact, Solution B, provided that the corners of the Inertial Sensor vacuum vessel can be removed, provides the maximum free area for the accommodation of the optical elements, the fiber positioner and the detectors.

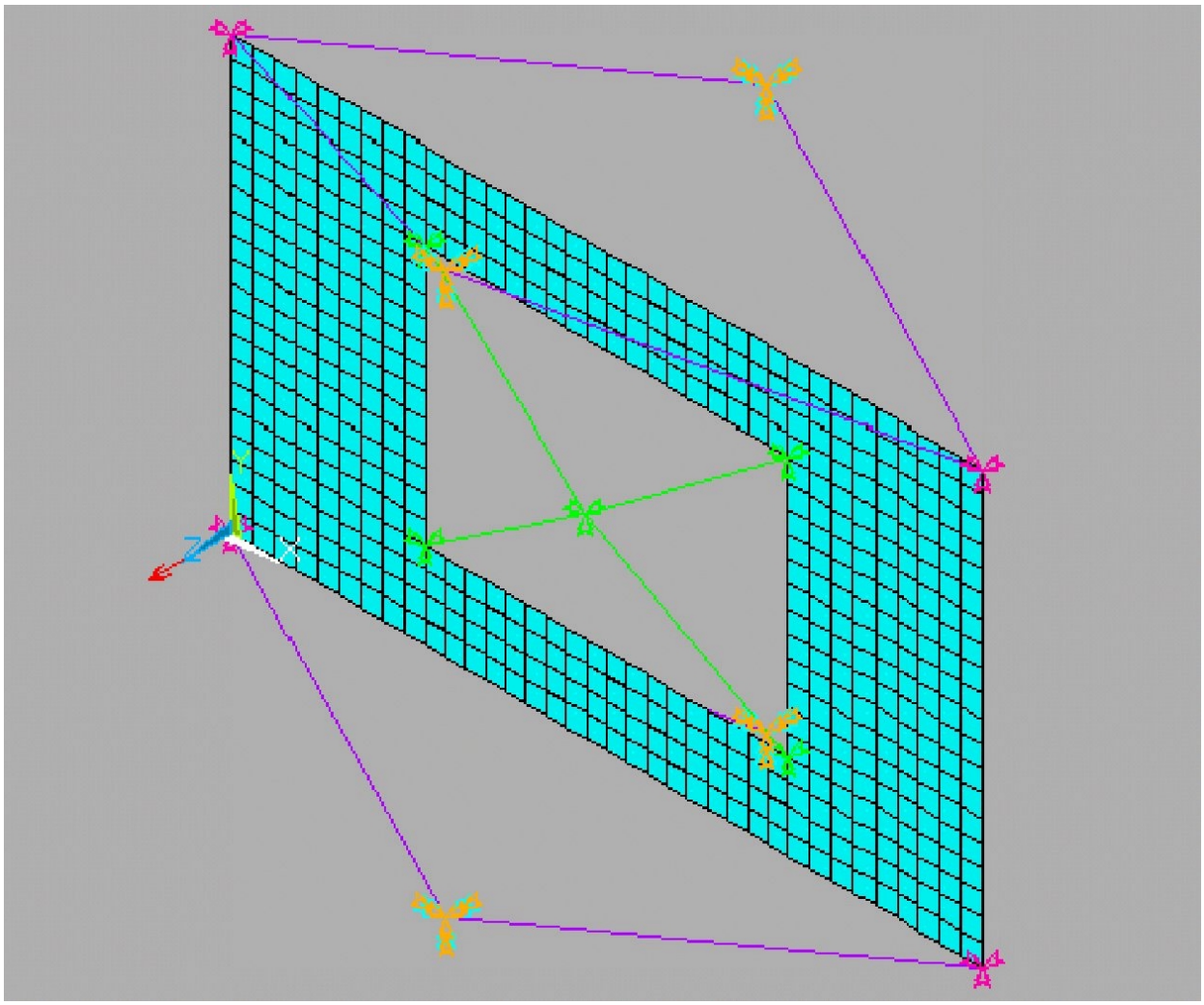

Reference frame: X-axis along long side, Y-axis along short side, Z-axis perpendicular to OB

Figure B-4 - FEM of the OB (undeformed shape)

	Frequency (Hz)	Mode
OB Solution A	106	Lateral Y
	240	Axial Z
	626	Lateral X
OB Solution B	106	Lateral Y
	276	Axial Z
	625	Lateral X

Table B-3 - Frequency of the first vibration modes of the OB

	Applied loads (g's)	Direction	Max Equivalent Stress (MPa)	S.F. (1)
OB Solution A	35	Z-axis	13	3.8
	15	X-axis	16	3.1
	15	Y-axis	35	1.4
OB Solution B	35	Z-axis	12	4.1
	15	X-axis	16	3.1
	15	Y-axis	35	1.4

(1) S.F. = Safety Factor (computed w.r.t. ULE™ Ultimate Tensile Stress = **49.8 MPa**)

Table B-4 - Maximum equivalent stress of the OB

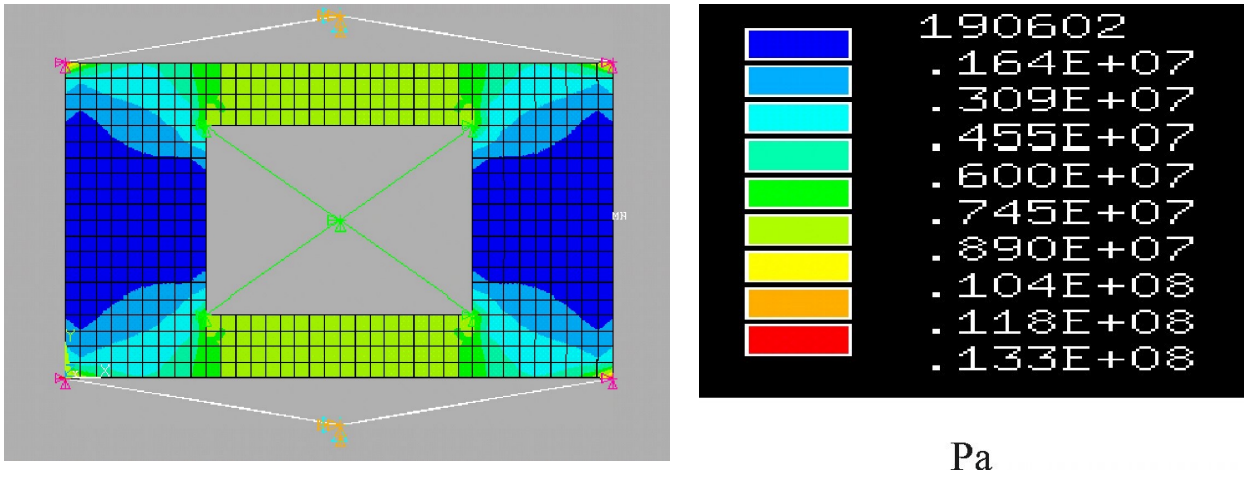

Figure B-5 - Equivalent stress distribution on the OB: Solution A (35 g's applied along the Z-axis)

B.3 Optical Bench Mounting Inside the Spacecraft

In the S/C configuration defined in the Pre-Phase A study [1] the OB is mounted horizontally (i.e. its plane is perpendicular to the S/C centreline). Nevertheless, the OB mounting with its plane rotated through an angle of 45° w.r.t. the horizontal plane (see Figure B-6) would introduce a simplification in the optical layout: the quarter waveplate that transform the linearly polarised outgoing beam in a circularly polarised beam can be removed. In this case, in fact, the light will leave one S/C in polarisation S and will be received by the other S/C in polarisation P, thanks to the relative rotation of 90° of the two, mutually faced OB's of the two S/C's. The advantages introduced by the removal of this quarter waveplate (beside have one less element to be accommodated) are:

- the possibility of working only with linear polarisation, for which it is easier to design and to predict the behaviour of the antireflection coatings of the optics;
- the removal of the main source of backreflection towards the quadrant photodiode for the detection of the beat signal between the remote laser and the local reference.

This OB mounting option has been then analysed from a mechanical point of view, to assess its viability. In particular the stress induced in the material by the launch loads have been computed using the OB FEM built for the Solutions A and B of the mechanical interfaces (see previous paragraph). The resulting map of the stress distribution for this configuration (Solution A) under the application of a 35 g's along vertical direction (45° from the normal to the OB plane) is provided in Figure B-7. The maximum equivalent stress is:

50 MPa for Solution A and **49 MPa** for Solution B.

In both cases they are considerably larger then the stresses obtained for the horizontal mounting case analysed in the previous chapter. Moreover they are very close or even larger than the ULE™ ultimate tensile stress. Thus this result advise against the adoption of the OB mounting with a 45° tilt from the horizontal plane.

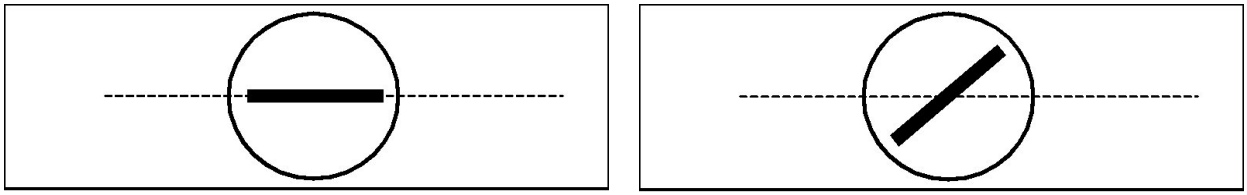

Figure B-6 - Concepts for the OB mounting inside the S/C

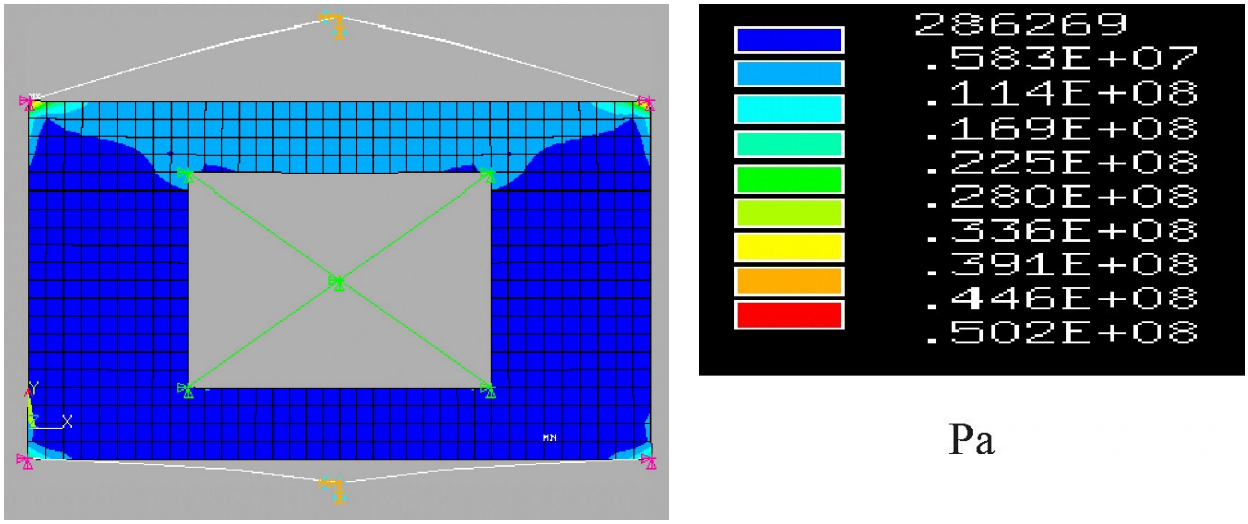

Figure B-7 - Equivalent stress distribution on the OB Solution A for α = 45° (35 g's in the vertical direction)

B.4 Analyses of the Selected Optical Bench Mechanical Design

The selected mechanical design of the OB is shown in Figure B-8. It is a combination of the Solution A for the OB-support structure interface and Solution B for the OB-Inertial Sensor interface. The mass budget for the selected solution is provided in Table B-5.

The selected material for the thermal bushes placed at the ends of the bolts is the homopolymer Delrin® which is compliant with the ESA out-gassing limits (see Table B-6).

Element type	Mass (kg)	Material	Notes
OB	4.59	ULE™	0.35×0.20×0.04 m
Hardware	0.16	Titanium	Bolts, etc.
Thermal bushes	0.017	Delrin®	
SUBTOTAL	4.77		
10% S/S contingency	0.48		
TOTAL	**5.25**		

Table B-5 - Mass budget for the selected OB mechanical solution

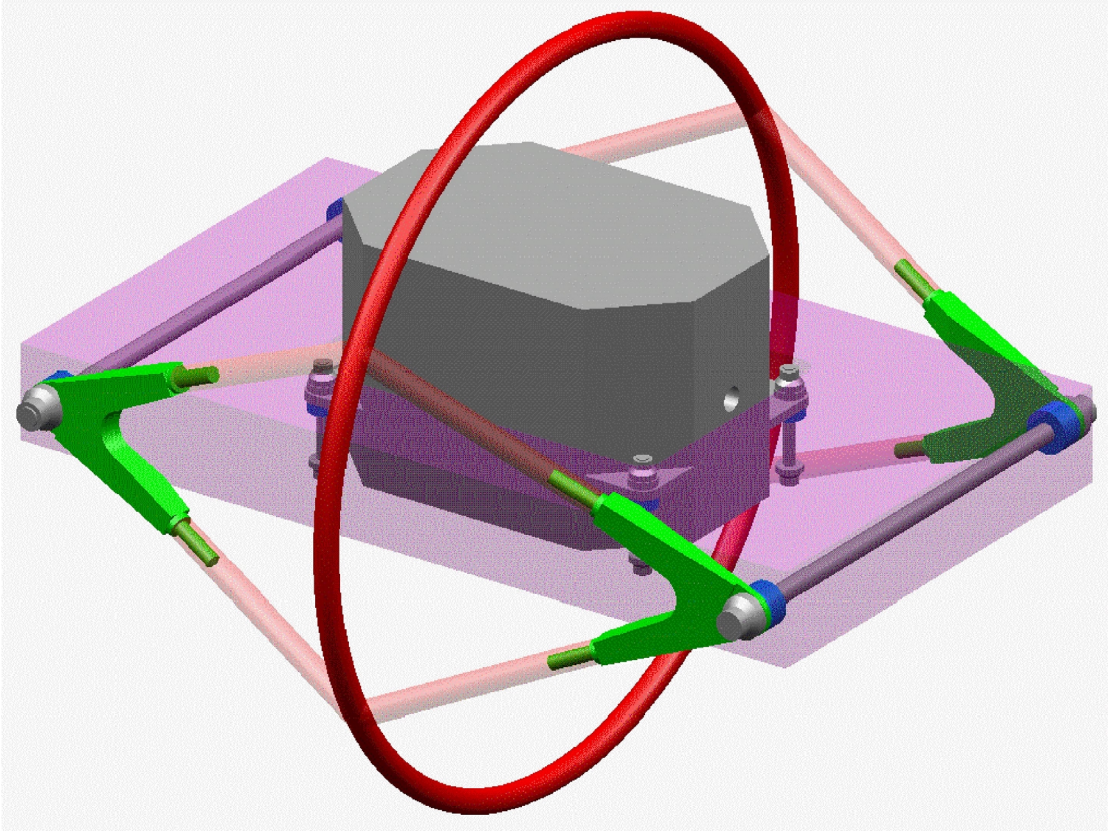

Figure B-8 - Perspective view of the OB showing the mechanical interfaces with the support structure and with the Inertial Sensor

Physical Properties			
Mean CTE		$122 \cdot 10^{-6}$	
Density (ρ)	Kg/m^3	1420	
Thermal Properties			
Thermal Conductivity (k)	W/m K	0.4	
Mechanical Properties			
Elastic Modulus (E)	GPa	2.8	T_{ref} = 20 ºC
Poisson's Ratio (ν)		0.35	
Ultimate Tensile Stress	MPa	69	
Others			
Outgassing specification	TML	VCM	
	0.49	0.02	*ESTEC/135*
	0.55	0.03	*ESTEC/140*
	0.49	0.02	*ESTEC/135*

Table B-6 - DuPont Delrin® 100 Main characteristics

Two types of FEM's have been built for this OB configuration. The first is similar to that utilised for the comparative analyses of the mechanical solutions A and B. It consists of 1-D and 2-D elements and has been, and has been used to evaluate the global dynamic behaviour of the OB (the eight support structure rods connected to the OB are included in this model). The second one consists of 3-D elements (SOLID45), utilised for modelling in details the interface zones, and has been used to compute the stress state in the material under the quasi-static design loads. This in order to have more reliable results about a parameter that was highlighted to be relatively critical by the analyses performed with the 2-D FEM's. Thanks to the symmetry of the OB, only portions of it have been modelled with the solid elements, and symmetry boundary conditions have been applied. In particular, two 3-D FEM's have been built:

- 3-D FEM 1, consisting of one quarter of the OB, with 5669 nodes and 4306 elements "SOLID45", utilised to compute the stress under loads applied perpendicular to the OB plane (see Figure B-9);
- 3-D FEM 2, consisting of one half of the OB, with 11144 nodes and 8612 elements "SOLID45", utilised to compute the stress under loads applied on the OB plane (see Figure B-10).

The masses included in the OB FEM's are summarised in Table B-7.

Element	Mass (kg)
OB structure (ULE™ plate, Titanium bolts, thermal bushes and washers)	5.25
Inertial Sensor Head (assumed inclusive of all contingencies)	6.50
Fiber Positioner (assumed inclusive of all contingencies)	0.50
Optical elements, detectors, baffles, fiber couplers	0.33
TOTAL	**12.58**

Table B-7 - Masses included in the OB FEM's

Two types of load have been considered for the static analysis:

- +Y gravity load of 35 g's (Type A), applied on the 3-D FEM 1. Two limit cases have been considered in order to verify the stress distribution sensitivity to the external constraints

- OB simply supported at I/F points worst case for the stress away from the interface zone, and

- OB partially clamped at I/F points (θ_z free) worst case (upper boundary) for the stress at the interface zone;

- +Z gravity load of 15 g's (Type B), applied on the 3-D FEM 2. The OB is simply supported at I/F points; for each external I/F one bush is axially loaded while the other is free.

Delrin® bushes models have been also implemented to evaluate the stress distribution at the support structure I/F points. The gravity load along X-axis has not been considered, as it is encompassed by Z-axis load case.

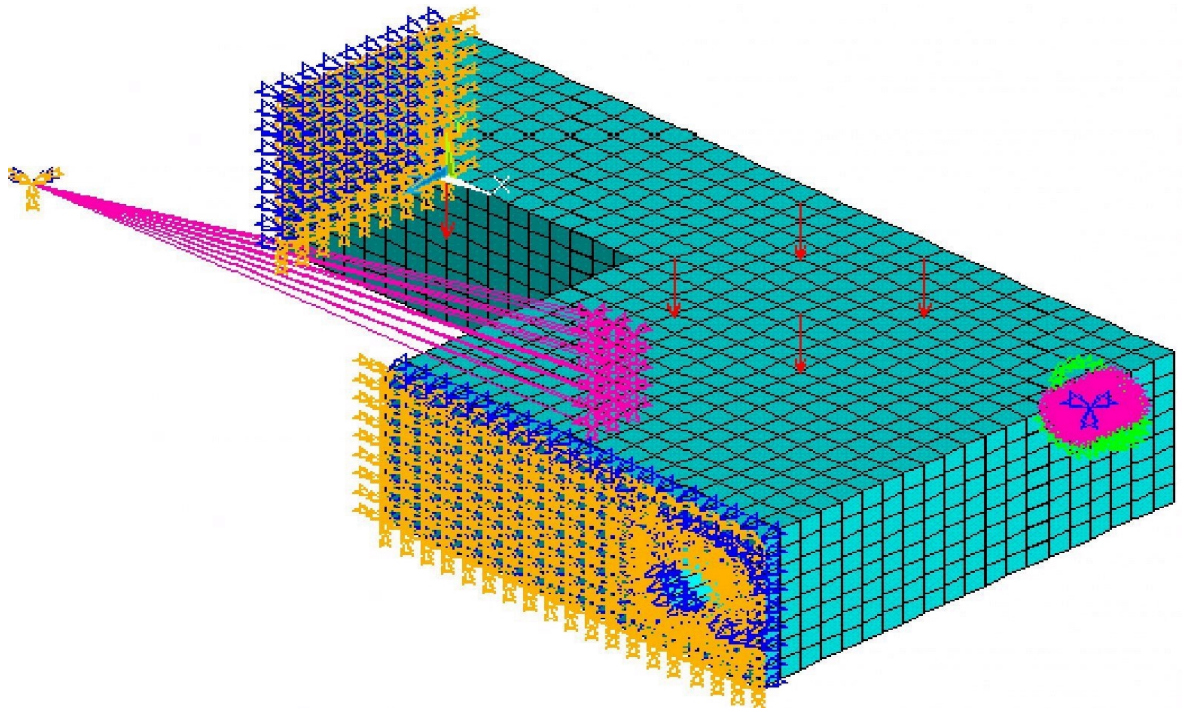

Reference Frame: X-axis along long side, Z-axis along short side, Y-axis perpendicular to OB

Figure B-9 - 3-D FEM 1, undeformed shape (utilised for +Y gravity load)

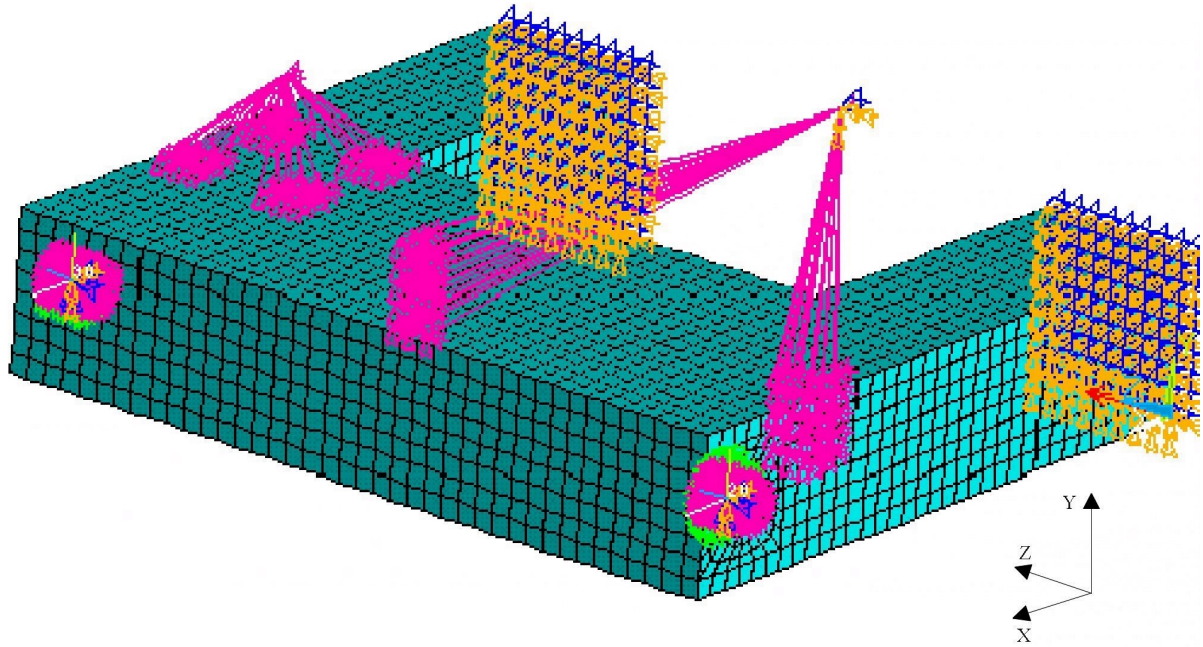

Reference Frame: X-axis along long side, Z-axis along short side, Y-axis perpendicular to OB

Figure B-10 - 3-D FEM 2, undeformed shape (utilised for +Z gravity load)

The OB eigenfrequencies obtained from the dynamic analysis are provided in Table B-8. The first eigenshape is shown in Figure B-11. The requirement for the vibration mode eigenfrequencies [1] is f_i **≥ 60 Hz**, and is fulfilled with a good margin.

Frequency (Hz)	Mode
104.9	Lateral Y
236.1	Axial Z
528.7	Combined

Table B-8 - Dynamic analysis output

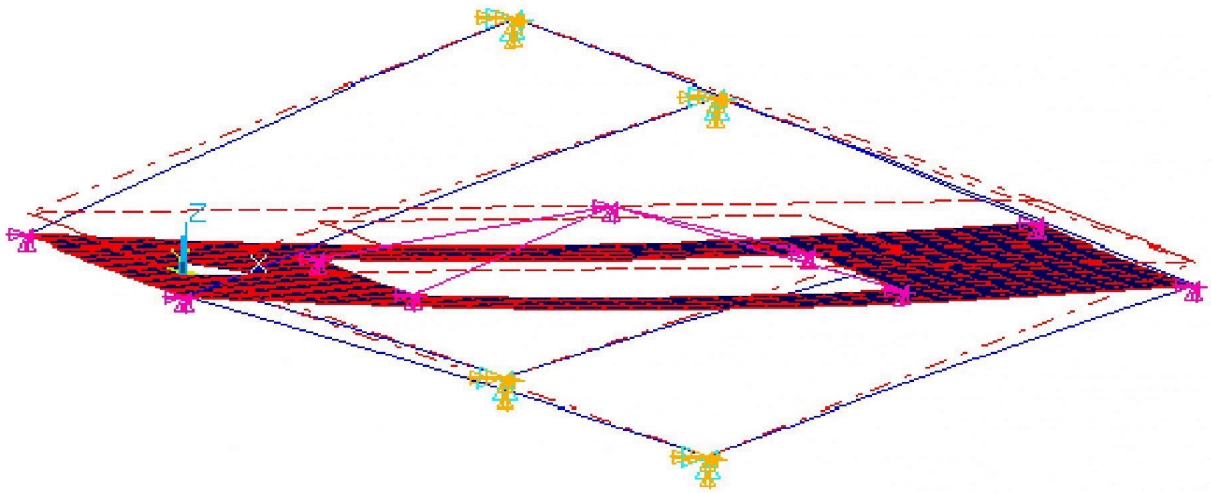

Figure B-11 - Dynamic FEM analysis eigenshape (104.9 Hz)

The results of the static analysis have been now expressed more appropriately in terms of maximum principal strains. In fact, for a brittle material like ULE™, the De Saint-Venant/Grashop resistance criterion applies: the material breaks as soon as one of the principal strains (taken in absolute value) exceed its Ultimate Tensile strain (ε_{ult} = 0.72 10^{-3} for ULE™).

Figure B-12 shows the ε_3 principal strain component distribution for the OB simply supported constraints and loaded out-of-plane.

Figure B-13 shows the ε_3 principal strain component distribution under +Z load.

Table B-9 summarises the results of the analysis in the static case.

The static analysis gives a maximum value of **$-0.26 \cdot 10^{-3}$** for the principal strain vector components, located in the interface zone between the OB and the inertial sensor (see Figure B-12). There is therefore a safety margin of **2.77** with respect to ε_{ult}, above the prescription of 1.5 [4], but not excessive considering brittle nature of the ULE™. More detailed analyses are therefore advisable in order to consolidate the results and acquire the sufficient confidence about the absence of cracks generation risks during the launch phase.

The maximum stresses in the Delrin thermal bushes located between the titanium bolts and the ULE™ baseplate are:

- **σ_{eq} = 2.3 MPa** for the axial load case (hand calculation);
- **σ_{eq} = 11.7 MPa** for the radial load case (FEM).

As the ultimate tensile stress for Delrin is **σ_{ult} = 69 MPa**, there are good positive margins.

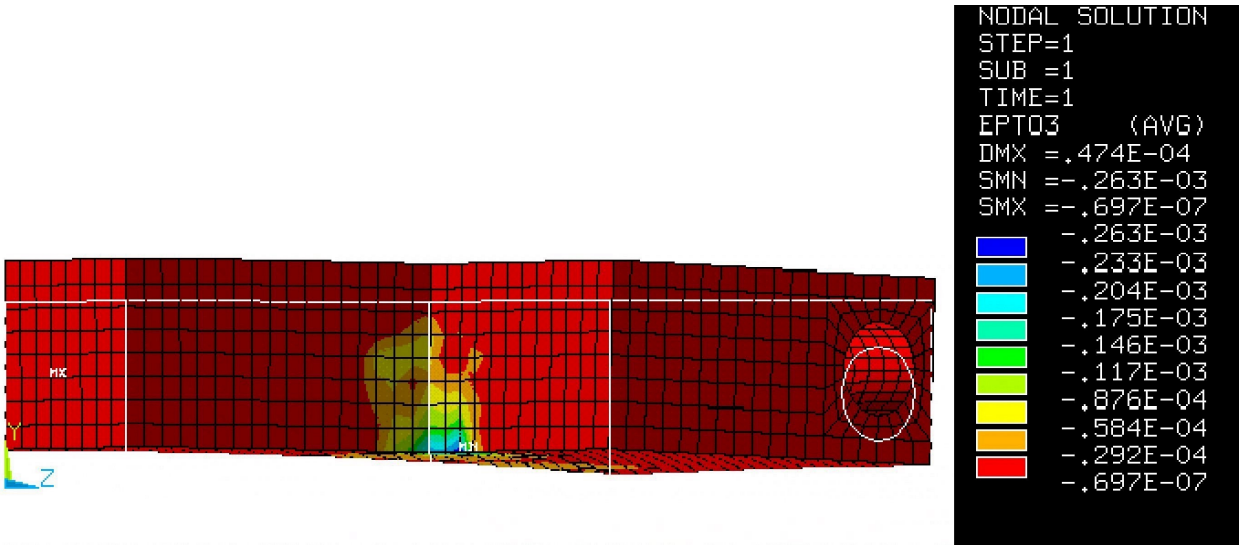

Figure B-12 - Static FEM analysis output (load Type A)

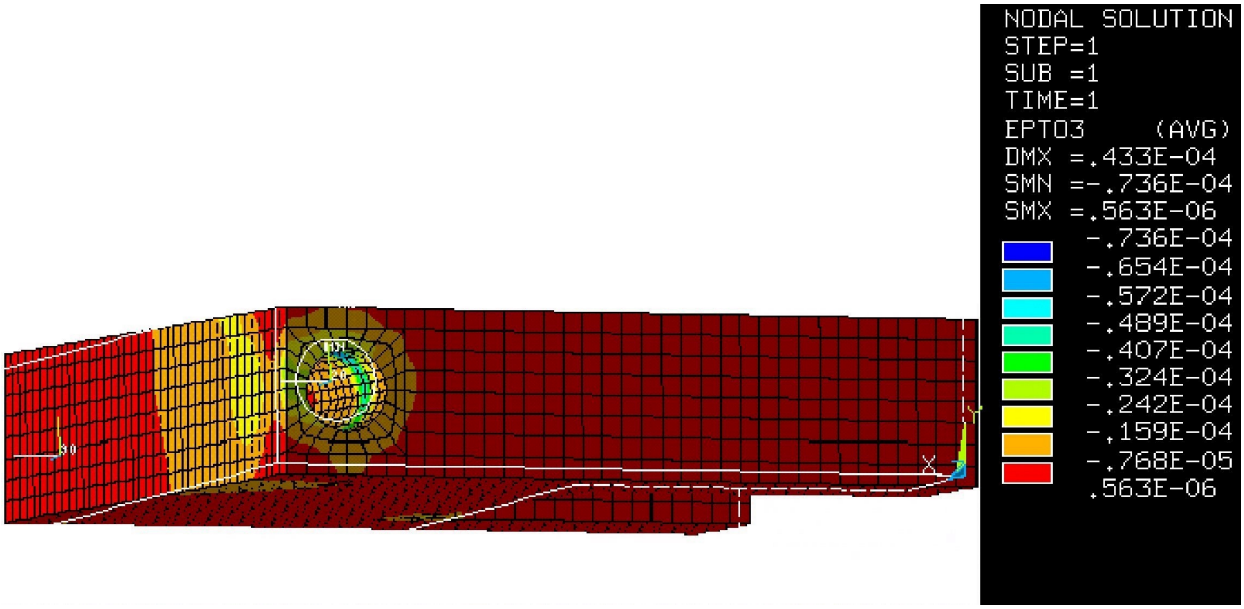

Figure B-13 - Static FEM analysis output (load Type B)

Load Type	Applied loads (g's)	Maximum Principal Strain	Location	Safety Factor
	35 Y-axis	$0.14 \cdot 10^{-3}$	Inertial Sensor area	5.14
A		$-0.31 \cdot 10^{-4}$		23.22
		$-0.26 \cdot 10^{-3}$		2.77
	15 Z-axis	$0.40 \cdot 10^{-4}$	Support structure I/F area	18.00
B		$-0.22 \cdot 10^{-4}$		32.73
		$-0.74 \cdot 10^{-4}$		9.73

Table B-9 - Static FEM results summary

C Temperature Stability Analysis Method

C.1 Scope

This TN describes an analytical method to determine the temperature fluctuations resulting from periodic disturbances due to solar constant and electronic unit dissipation fluctuations and their transfer into the spacecraft.

C.2 Introduction

In the LISA spacecraft extreme requirements on thermal stabilities down to 10^{-6}K have to be considered. The calculation of such small temperature fluctuations using finite difference models is difficult due to large time constants and the numerical representation. Since only temperature stabilities are of concern, it is possible to derive an analytical solution for a simplified model to circumvent the numerical problems. The following cases shall be considered:

- Solar array thermally decoupled from the spacecraft
- Electronics unit mounted on spacecraft structure
- Transfer of temperature fluctuation from one unit to the other

C.3 Analytical Solution

C.3.1 Solar array

A simple model of the solar array is shown in Figure C-1. The solar array with surface properties described by α and ε is irrradiated by solar radiation with an intensity described by $S(t)= S_0+\Delta S*\sin(\omega t)$.

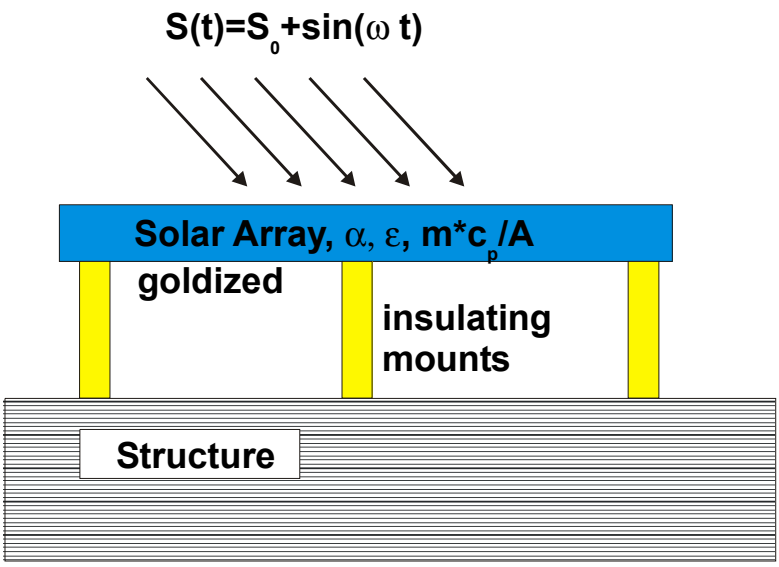

Figure C-1: Simplified model of solar array

The solar array is insulated on the rear side. Therefore the induced temperature fluctuations in the spacecraft structure will be orders of magnitudes smaller than those in the solar array and will not influence solar array temperature fluctuation. The heat balance for the solar array is thus:

$$m \cdot c_p \cdot \frac{dT_{S/A}}{dt} = \alpha \cdot A \cdot S(t) - \varepsilon \cdot \sigma \cdot A \cdot T_{S/A}^4$$

The radiative exchange with space can be linearized and with the use of the average temperature one gets:

$$\varepsilon \cdot \sigma \cdot {T_{S/A}}^4 \approx 4 \cdot \varepsilon \cdot \sigma \cdot (\overline{T}_{S/A})^3 \cdot T_{S/A} = 4 \cdot \varepsilon \cdot \sigma \cdot \left(\frac{\alpha \cdot S_0}{\varepsilon \cdot \sigma} \right)^{\frac{3}{4}} \cdot T_{S/A}$$

Thus the heat balance can be written as:

$$\frac{dT_{S/A}}{dt} = \frac{A}{m \cdot c_p} \cdot \left[\alpha \cdot (S_0 + \Delta S \cdot \sin(\omega \cdot t)) - 4 \cdot \varepsilon \cdot \sigma \cdot \left(\frac{\alpha \cdot S_0}{\varepsilon \cdot \sigma} \right)^{\frac{3}{4}} \cdot T_{S/A} \right]$$

The following constants will be used

$$\frac{A}{m \cdot c_p} \cdot \alpha \cdot S_0 = k_0; \qquad \frac{A}{m \cdot c_p} \cdot \alpha \cdot \Delta S = k_1; \qquad \frac{4 \cdot A \cdot \varepsilon \cdot \sigma \cdot \left(\frac{\alpha \cdot S_0}{\varepsilon \cdot \sigma} \right)^{\frac{3}{4}}}{m \cdot c_p} = r$$

This then gives the following first order linear differential equation

$$\frac{dT_{S/A}}{dt} + r \cdot T_1 = k_0 + k_1 \cdot \sin(\omega \cdot t)$$

Solutions can be found from the literature (e.g. Bronstein):

With $e^{-\int_0^t r \cdot dt} = e^{-r \cdot t}$; $\qquad T_{S/A}(t) = e^{-r \cdot t} \cdot \left[\int_0^t (k_0 + k_1 \cdot \sin(\omega \cdot t)) \cdot e^{r \cdot t} \cdot dt \right]$

$$T_{S/A}(t) = e^{-r \cdot t} \cdot \left[\frac{k_0}{r} \cdot e^{r \cdot t} - k_0 + k_1 \cdot \frac{e^{r \cdot t}}{r^2 + \omega^2} \cdot (r \cdot \sin(\omega \cdot t) - \omega \cdot \cos(\omega \cdot t)) \right]$$

$$T_{S/A}(t) = \frac{k_0}{r} - k_0 \cdot e^{-r \cdot t} + \frac{k_1}{r^2 + \omega^2} \cdot (r \cdot \sin(\omega \cdot t) - \omega \cdot \cos(\omega \cdot t)) + C$$

with the boundary condition $T_{S/A}(t \to \infty) = \overline{T}_{S/A} = \sqrt[4]{\frac{\alpha \cdot S_0}{\varepsilon \cdot \sigma}}$ one gets for the constant:

$$\frac{k_0}{r} + C = \overline{T}_{S/A} = \sqrt[4]{\frac{\alpha \cdot S_0}{\varepsilon \cdot \sigma}}$$

Thus: $\qquad T_{S/A}(t) = \overline{T}_{S/A} + \frac{k_1}{r^2 + \omega^2} \cdot (r \cdot \sin(\omega \cdot t) - \omega \cdot \cos(\omega \cdot t))$

This is a harmonic oscillation with:

Amplitude: $\Delta T_{S/A} = \frac{k_1}{\sqrt{r^2 + \omega^2}}$; Phase: $\varphi = \arctan\left(\frac{r}{\omega}\right)$

C.3.2 Electronic Unit

A simple model of a electronic unit is shown in Figure C-2.

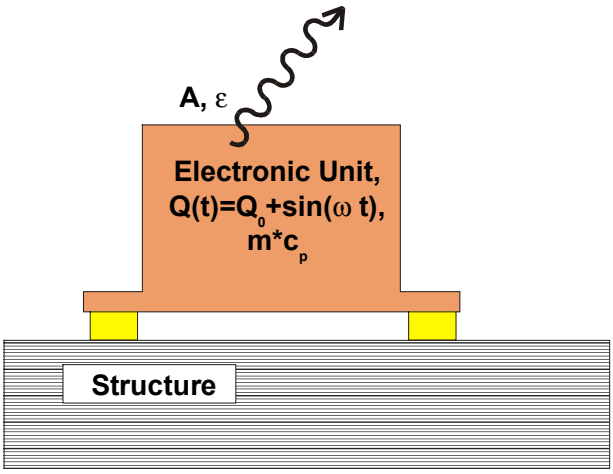

Figure C-2: Simple model of electronics unit attached to the structure

For the dissipating unit the dissipation can be represented by:

$$Q_{EU}(t) = Q^0_{EU} + \Delta Q_{EU} \cdot \sin(\omega \cdot t)$$

The heat balance is then as follows:

$$m \cdot c_p \cdot \frac{dT_{EU}}{dt} = Q^0_{EU} + \Delta Q_{EU} \cdot \sin(\omega \cdot t) - D_{EU,STR} \cdot (T_{EU} - T_{STR}) - R_{EU.space} * T^4_{EU}$$

If the unit is equipped with a radiator, it will be decoupled from the structure and the heat rejection will mainly occur via radiation to space. Therefore the radiated heat can be expressed as:

$$R_{EU,space} \cdot T^4_{EU} = 4 \cdot A_{EU} \cdot \varepsilon_{EU} \cdot \sigma \cdot \overline{T}^3_{EU} \cdot T_{EU}; \qquad \overline{T}_{EU} = \sqrt[4]{\frac{Q^0_{EU}}{A \cdot \varepsilon \cdot \sigma}}$$

Furthermore it can be assumed that the temperature fluctuations of the structure can be neglected compared with the temperature fluctuations of the unit. The following constants are introduced:

$$\frac{Q^0_{EU} + D_{EU,STR} \cdot T_{STR}}{m \cdot c_p} = h_0; \quad \frac{\Delta Q_{EU}}{m \cdot c_p} = h_1; \quad \frac{D_{EU,STR} + 4 \cdot (A_{EU} \cdot \varepsilon_{EU} \cdot \sigma)^{\frac{1}{4}} \cdot (Q^0_{EU})^{\frac{3}{4}}}{m \cdot c_p} = s$$

This then gives as before a first order linear differential equation

$$\frac{dT_{EU}}{dt} + s \cdot T_{EU} = h_0 + h_1 \cdot \sin(\omega \cdot t)$$

The solution can be found as above:

$$T_{EU}(t) = \frac{h_0}{s} - h_0 \cdot e^{-s \cdot t} + \frac{h_1}{s^2 + \omega^2} \cdot (s \cdot \sin(\omega \cdot t) - \omega \cdot \cos(\omega \cdot t)) + C$$

With the boundary condition for $t \to \infty$, the constant is found as:

$$\frac{h_0}{s} + C = \overline{T}_{EU} = T_{STR} + \frac{Q^0_{EU} + D_{EU,STR} \cdot T_{STR}}{D_{EU,STR} + 4 \cdot (A_{EU} \cdot \varepsilon_{EU} \cdot \sigma)^{\frac{1}{4}} \cdot (Q^0_{EU})^{\frac{3}{4}}}$$

The solution thus is:

$$T_{EU}(t) = \overline{T}_{EU} + \frac{h_1}{s^2 + \omega^2} \cdot (s \cdot \sin(\omega \cdot t) - \omega \cdot \cos(\omega \cdot t))$$

This is again a harmonic oscillation with

Amplitude: $\Delta T_{EU} = \frac{h_1}{\sqrt{s^2 + \omega^2}}$; Phase: $\varphi = \arctan\left(\frac{s}{\omega}\right)$

C.3.3 Transfer of temperature disturbances

The temperature disturbance created on solar array or dissipating units will be transferred to other spacecraft components as shown in Figure C.3-1 .

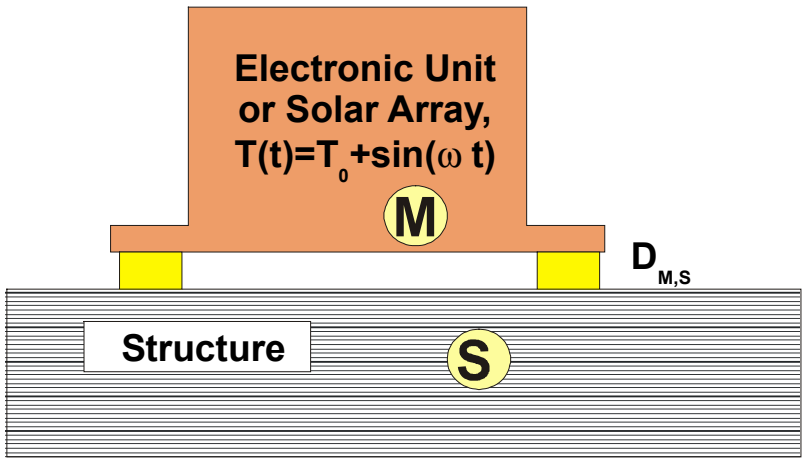

Figure C.3-1: Representation of electronic unit or solar array mounted on the structure

The heat balance is given by:

$$m \cdot c_p \cdot \frac{dT_S}{dt} = -D_{M,S} \cdot (T_S - T_M) - D_{S,j} \cdot (T_S - T_j)$$

By design, a rather good decoupling has to be achieved. Thus it can be assumed that the fluctuations of other components, T_j can be neglected compared with the fluctuations of T_S.

The temperature fluctuation is given by

$T_M = \overline{T}_M + \Delta T_M \cdot \sin(\omega \cdot t)$, the phase needs not to be considered. In case of more than 1 disturbance source, the root sum square of the individual contributions can be taken. The heat balance can thus be written as:

$$\frac{dT_S}{dt} = \frac{D_{M,S}}{m \cdot c_p} \cdot \left[\overline{T}_M + \Delta T_M \cdot \sin(\omega \cdot t) - T_S\right]$$

The following constants are introduced:

$$\frac{D_{M,S}}{m \cdot c_p} = p; \quad \frac{D_{M,S} \cdot \overline{T}_M}{m \cdot c_p} = g_0; \quad \frac{\Delta T_M \cdot D_{M,S}}{m \cdot c_p} = g_1 = \Delta T_M \cdot p$$

Again we get a first order linear differential equation:

$$\frac{dT_S}{dt} + p \cdot T_S = g_0 + g_1 \cdot \sin(\omega \cdot t)$$

with the solution

$$T_S(t) = \frac{g_0}{p} - g_0 \cdot e^{-p \cdot t} + \frac{g_1}{p^2 + \omega^2} \cdot (p \cdot \sin(\omega \cdot t) - \omega \cdot \cos(\omega \cdot t)) + C$$

with the boundary condition for $t \to \infty$ the constant is found as: $\frac{g_0}{p} + C = \overline{T}_S$

The solution thus is:

$$T_S(t) = \overline{T}_S + \frac{g_1}{p^2 + \omega^2} \cdot (p \cdot \sin(\omega \cdot t) - \omega \cdot \cos(\omega \cdot t))$$

Amplitude: $\Delta T_S = \frac{g_1}{\sqrt{p^2 + \omega^2}} = \frac{\Delta T_M \cdot p}{\sqrt{p^2 + \omega^2}}$; Phase: $\varphi = \arctan\left(\frac{p}{\omega}\right)$

The transmission of the temperature disturbance from T_M to T_S is then given by:

$$TR_{M,S} = \frac{\Delta T_S}{\Delta T_M} = \frac{p}{\sqrt{p^2 + \omega^2}}$$

D Thermal Study

D.1 Summary

D.1.1 Scope

The purpose of the thermal analysis of one LISA science module is to determine the response of the LISA payload to fluctuations in the solar constant and to changes in the dissipation of the electronic units.

D.1.2 Conclusion

- The selected configuration allows the rejection of the dissipated heat. The electronic units have to be thermally decoupled from the structure for temperature stability reasons. For some units doubler plates to enhance the heat rejection will be needed.
- Long term in-orbit temperature variation of the structure due to orbital position and degradation amount to about 4 K. Additional dissipation of 18 W (i.e. 12 % of the over all dissipation) leads to a local temperature increase of about 10 K.
- Solar fluctuation leads to temperature fluctuation of 8e-5 K at 1e-4 Hz in the payload tube. This can be compared with about 3e-3 K derived by RAL in pre phase A.
- Overall dissipation fluctuation has to be limited to 0.1 % in order not to exceed the effect of solar fluctuations.
- 20 % dissipation fluctuation of the CPS Central Electronic unit at 0.1 Hz is not critical due to the high heat-capacity of the unit.
- If a step function in dissipation is limited to 1 mW, the maximum temperature variation within 3 h is limited to 8e-5 K in the payload tube.
- The most effective way to improve the isolation between the payload and the fluctuation sources would be an additional radiation shield around the payload, and maybe also between the solar panel and the structure. The reduction of the conductive couplings is less effective, because the heat transfer is dominated by radiation.

D.1.3 References

RD1 LISA Payload Pre-Phase A Thermal Study (WP03) (RAL)

RD2 LISA Payload Mechanical/Thermal Design (DSS)

D.2 Thermal Requirements

The major science requirement is one of the temperature stability, with the optical bench fluctuations due to variations in the solar intensity and dissipation fluctuations kept below 1e-6 $K/Hz^{1/2}$ between 1e-1 and 1e-4 Hz.

This study is based on a detailed thermal model of the spacecraft down to the payload y-shaped thermal shield, but without any details of the inside of the tubes. Therefore this analysis can only give information of the temperature fluctuation in the payload thermal shield. Due to the thermal decoupling between the shield and the payload this fluctuations are allowed to be considerably higher. A coarse assumption for the allowable fluctuations is a limit of 1e-5 $K/Hz^{1/2}$.

The temperature field in the spacecraft shall comply with small thermal deformations from the on-ground to in-orbit conditions. Therefore the radiator properties shall ensure temperatures of the structure about 20 °C.

The temperatures of the electronics boxes shall not exceed their as yet unspecified limits. The standard acceptance temperature range of –10 °C to 50 °C is assumed.

D.3 Thermal Mathematical Model

For thermal analysis a mathematical model has been prepared using ESATAN. View factors have been determined by means of THERMICA.

D.3.1 Nodal Breakdown and Properties

The model consists of 110 thermal nodes: three boundary nodes, 17 for the payload, 20 for the structure, three for the conical radiator, twelve for the solar panel, 37 for the EU-boxes and 18 additional lumped mass structure nodes.

The nodal breakdown and the material properties are listed in the following tables. In Fig. 3-1 to Fig. 3-4 the nodal breakdown is shown for the structure, the payload and the EU. The node numbers of the top- and bottom plate and the solar panel (both facesheets and the core) are such, that nodes with identical last digit (1, 2, 3, 4) lay on top of each other. The node numbers of the payload are based on the thermal model of RD1. The top tube and the outer payload tube nodes are circular, whereas the other ring-shaped parts are divided into two nodes of equal size. The middle and the front payload tube nodes are divided parallel to the x-z-plane, the inner payload tube nodes are divided parallel to the x-y-plane

The MLI is located on the outer side of the bottom plate and is simulated with an effective emissivity of 0.003.

The conical area of the spacecraft is used as an radiator. Due to the inhomogeneous dissipation contribution in the spacecraft, the three thermal nodes of the radiator have two different medium emissivities on the inner side.

Model name: Lisa_1

File names: Lisa_1.d, Lisa_1.NOD, Lisa_1.QI, Lisa_1.CONST,

Lisa_199R.TAN, Lisa_1_Extra_R.TAN

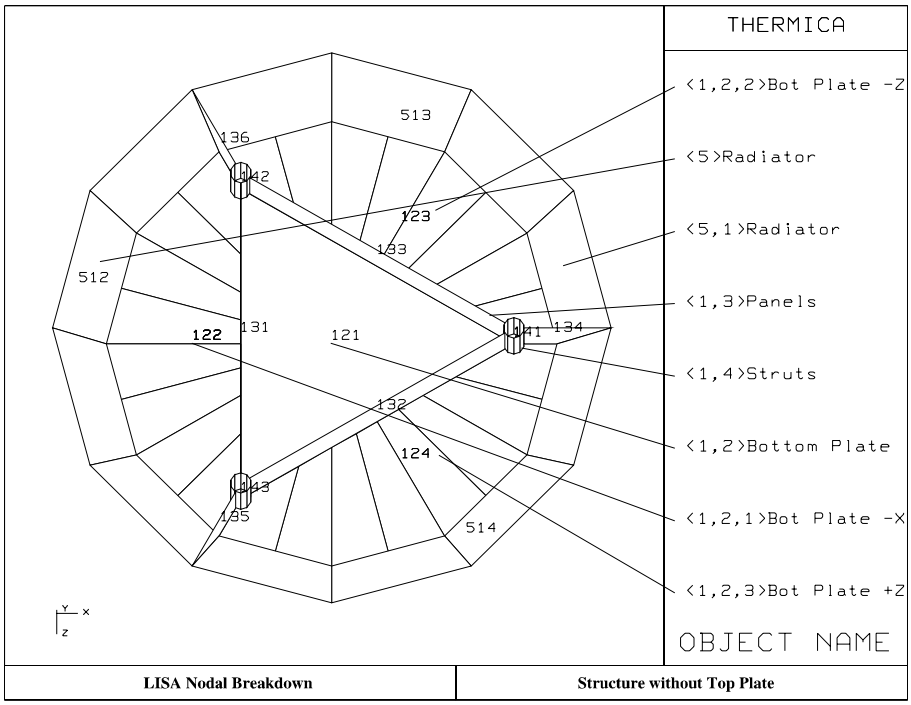

Fig. D-1: LISA Nodal Breakdown: Structure without Top Plate

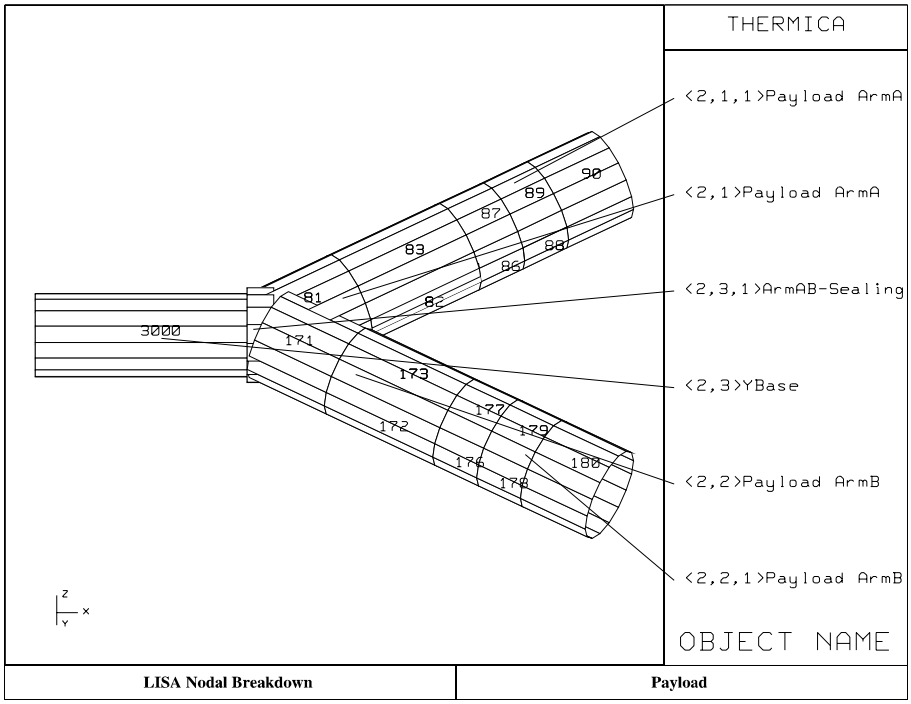

Fig. D-2: LISA Nodal Breakdown: Payload

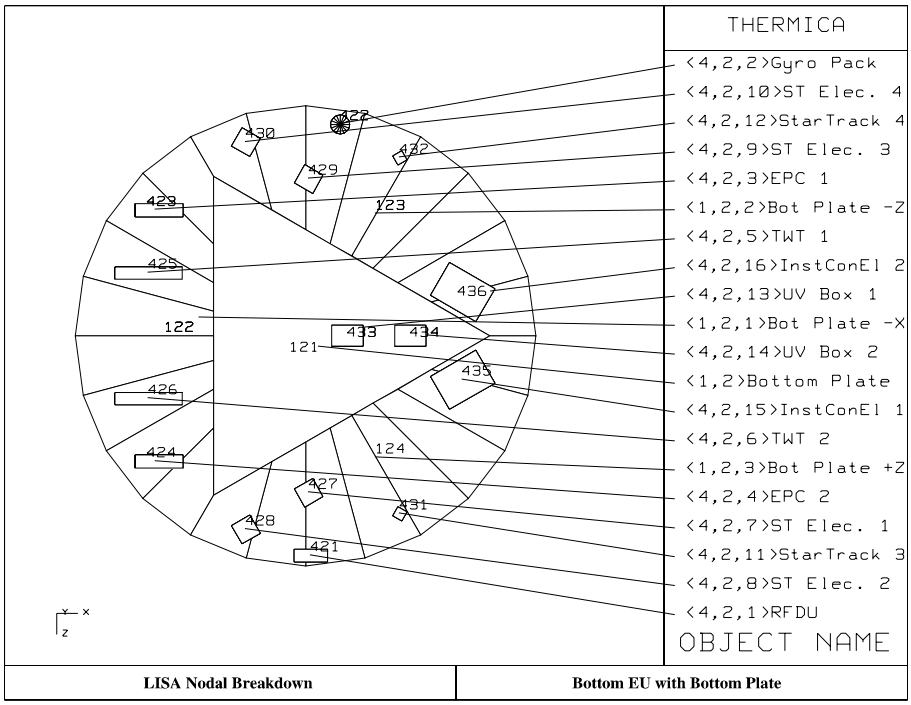

Fig. D-3: LISA Nodal Breakdown: Bottom EU with Bottom Plate

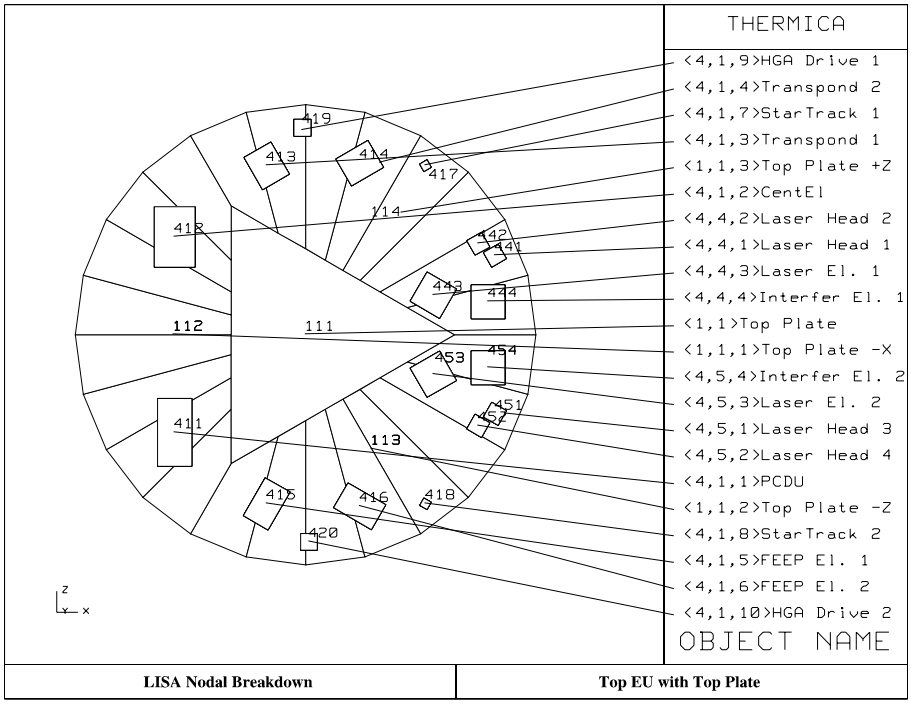

Fig. D-4: LISA Nodal Breakdown: Top EU with Top Plate

Tab. D-1: Material Properties

Material	λ [W/(mK)]	c_p [J/(kgK)]
Aluminium	125.0	900
Alu-Box	125.0	1000
Alu-Honeycomp	125.0 (in the facesheet)	900
CFRP	10.0	1000
Foam	0.0054	1050
Glass	2.0	1000

Tab. D-2: Coating Properties

Coating	ε	α
Solar Array	0.79	0.64 BOL 0.68 EOL
Alu polished	0.08	--
Gold	0.05	--
CHEMZ306	0.90	--
MLI (eff. emissivity)	0.003	--
Radiator	0.16	--

Tab. D-3: Nodal Breakdown of LISA TMM

Name	Node ID Range	Power [W]	Mass [kg]	Thickness [mm]	Material	Coating
Payload A+B Instrmt	80+170				Boundary	
Payload A+B Inner	81+171		3.5 x 2	5.0	CFRP	Gold (out) CHEMZ306 (in)
Payload A+B Middle	82+ 83 172+173		2.5 x 4	5.0		
Payload A+B Front	86- 89 176-179		0.3 x 8	1.5		
Payload A+B Outer	90+180		0.55x 2	1.5		
YBase Toptube	3000		2.0	1.5		
Top Plate	111-114		23.4	20.0	Alu-Honeycmb	Alu polished
Bottom Plate	121-124		27.4	30.0	Alu-Honeycmb	Alu pol. (in) MLI (out)
Panels	131-136		9.2	30.0	Alu-Honeycmb	Alu polished
Struts	141-143		2.9	2.5	Aluminium	Alu polished
Payload-Flange	151-153		0.0		Titan	Lump Node
Lump Top Panels	1131-1136		0.0		None	Lump Node
Lump Top Struts	1141-1143		0.0			
Lump Bottom Panels	2131-2136		0.0			
Lump Bottom Struts	2141-2143		0.0			
Solar Facesheet out	311-314		5.2 3.9	0.6 0.25	CFRP Glass	Solar Array
Solar Facesheet in	321-324		5.2	0.6	CFRP	Alu polished
Solar Core	331-334		5.8 23.4	20.0 20.0	Foam Alu-Honeycmb	
PCDU	411	19	12.0		Alu-Box	CHEMZ306
Central El. CPS	412	35	15.9			
Transpond 1	413	10	3.5			
Transpond 2	414		3.5			
FEEP El. 1	415	14	6.5			
FEEP El. 2	416		6.5			
StarTrack 1+2	417+418		0.3 x 2			
HGA Drive 1+2	419+420		1.0 x 2			
RFDU	421	1	1.0			
Gyro Pack	422		1.0			
EPC 1	423	25	1.4			
EPC 2	424		1.4			
TWT 1+2	425+426		0.75x 2			
ST Elec. 1	427	2	2.0			
ST Elec. 2-4	428-430		2.0 x 3			
StarTrack 3+4	431+432		0.3 x 2			
UV Box 1+2	433+434		0.5 x 2			
InstConEl 1	435	8	4.5			
InstConEl 2	436		4.5			
Laser Head 1	441	9	0.7			
Laser Head 2	442		0.7			
Laser El. 1	443		3.0			
Interfer El.1	444	10	3.5			
Laser Head 3	451	9	0.7			
Laser Head 4	452		0.7			
Laser El. 2	453	3	3.0			
Interfer El. 2	454		3.5			
FEEP Units 1-3	464+465	3 x 3	4.5 x 3		Alu-Box	Lump Node
Radiator	512		0.0		Kapton Foil	CHEMZ306 (out) Radiator (in)
Radiator	513+514		0.0		Kapton Foil	CHEMZ306 (out) Alu pol. (in)
SPACE	9999				Boundary	

D.3.2 GMM

In the following figures the GMM of the overall LISA model is depicted. The diameter of the spacecraft is 2700 mm and the high is 557 mm.

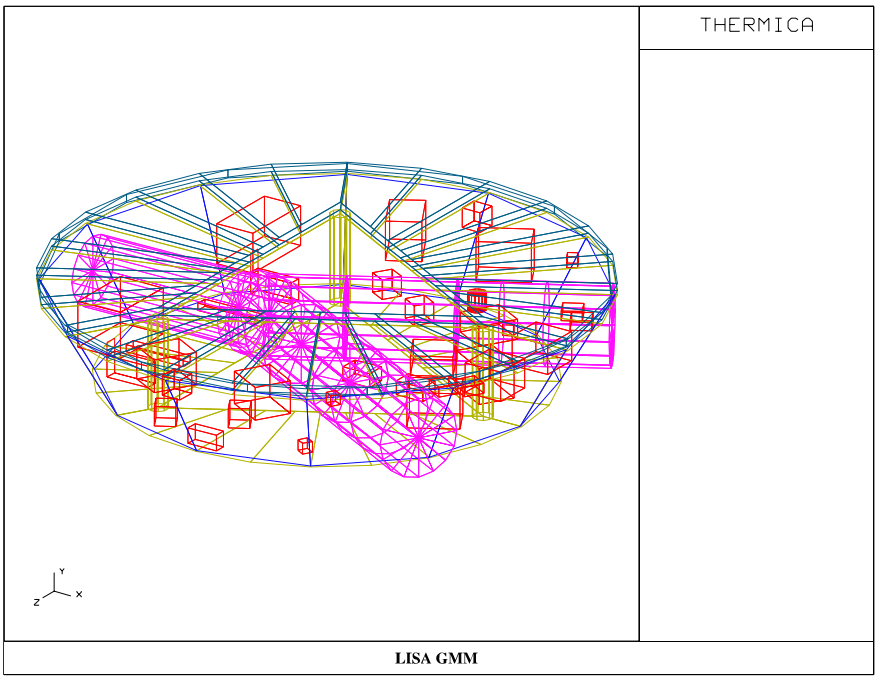

Fig. D-5: Overall LISA GMM

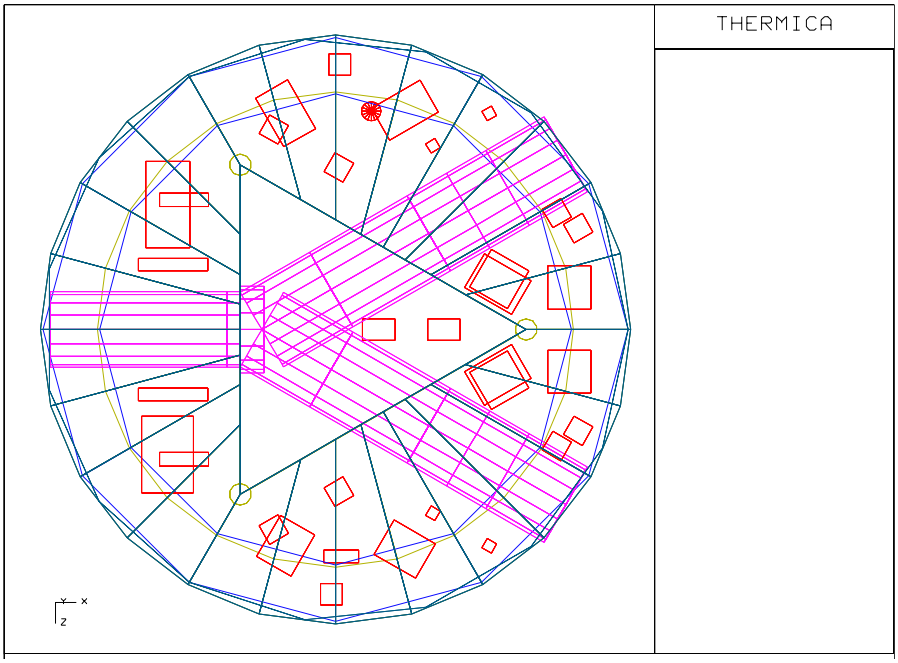

Fig. D-6: Overall LISA GMM Top View

D.3.3 Conductances

The detailed conductive couplings are listed in the appendix.

Couplings with thermal washers are simulated with 0.02 W/K for each washer.

Couplings with screws are simulated with 0.1 W/K for each screw.

The coupling between the different structural parts is assumed to be with twelve screws on every long side of the three big panels (# 131/132/133) and with six screws on every other side.

The coupling between the payload and the payload flange and also between the payload flange and the structure is simulated with eight screws at every flange. The thermal resistance of the flange is neglected.

The couplings from the EU-boxes to the structural plates are simulated with four thermal washers at each box.

The conductive coupling from the solar panel to the top plate is simulated with twelve thermal washers, three on each thermal node.

The conductivity of the honeycomb-structure is simulated only with the conductivity of the two facesheets (with 0.5 mm Aluminium each).

In order to reduce the high temperatures of the EU-boxes EPC and Laser Head Electronics, some additional couplings were introduced:

Due to the high dissipation and the small area of the EPC-boxes 1 and 2 (# 423 and 424) a Aluminium plate with additional radiative area and an assumed coupling of 0.3 W/K is introduced between them and the PCDU (# 411) or the Central Electronic (# 412) respectively.

For the Laser Head Electronics a doubler plate with two screws is introduced between Laser Head Electronic 1 and 2 and also between Laser Head Electronic 3 and 4. That enables the active unit to use the radiative surface area of the redundant one.

D.3.4 Assumptions and Uncertainties

The payload is simulated as a boundary node with a temperature of 20 °C and a good radiative coupling to the payload tube in order to get a realistic temperature level in this area. This assumption is damping the amplitude of the payload tube and therefore is not a conservative one.

A more detailed simulation of the inner part of the payload tube will be performed separately and will then consider the correct coupling between the payload and the optical bench.

The most critical transient load case with a fluctuation of 1 % and a frequency of 1e-4 Hz of all EU-boxes, with all boxes oscillating synchronous, is thermally a problem for the temperature fluctuation in the payload. This is not a realistic case, but the result will be used to establish a budget value for allowable fluctuations in unit dissipation.

D.4 Temperature Analysis

D.4.1 Steady State Analysis

The steady state temperature analysis was performed for three different load cases:

1) Cold Case: Maximum distance to sun (i.e. solar constant = 1371 W/m² - 5 %)

   BOL-properties for the solar panel (α=0.64)

2) Hot Case: Minimum distance to sun (i.e. solar constant = 1371 W/m² + 5 %)

   EOL-properties for the solar panel (α=0.68)

3) Hot Case 2: Additional dissipation in some EU-boxes:

Laser Head 1 + 3	(#441/451):	12.5 W each instead of 9 W
EPC 1	(#423):	30 W instead of 25 W
FEEP Units 1-3	(#464/465/466):	5 W each instead of 3 W

The structure temperature in the Hot Case is in the range of 10 to 28 °C.

In the Cold Case the structure temperature is reduced to 7.5 to 26 °C.

In the Hot Case 2 the structure temperature is increased to 14 to 38 °C.

The detailed results are listed in the following table.

Tab. D-4: Steady State Temperatures

		Temperatures [K]				
Name	NODE ID	Cold Case	Diff. to HC	Hot Case	Diff. to HC	HC 2
Payload ArmA Instrument	80	20.0	0.00	20.0	+ 0.00	20.0
Payload ArmA Inner	81	19.8	- 0.12	20.0	+ 0.16	20.1
Payload ArmA Middle	82	18.2	- 0.22	18.4	+ 0.31	18.7
Payload ArmA Middle	83	18.2	- 0.21	18.4	+ 0.31	18.7
Payload ArmA Front	86	-17.0	- 1.21	-15.8	+ 2.08	-13.7
Payload ArmA Front	87	-17.0	- 1.15	-15.9	+ 2.04	-13.8
Payload ArmA Front	88	-51.2	- 1.45	-49.8	+ 2.59	-47.2
Payload ArmA Front	89	-51.4	- 1.39	-50.0	+ 2.53	-47.4
Payload ArmA Outer	90	-78.9	- 1.24	-77.7	+ 2.35	-75.3
Payload ArmB Instrument	170	20.0	0.00	20.0	+ 0.00	20.0
Payload ArmB Inner	171	19.8	- 0.12	19.9	+ 0.16	20.1
Payload ArmB Middle	172	17.9	- 0.22	18.1	+ 0.31	18.4
Payload ArmB Middle	173	17.9	- 0.21	18.1	+ 0.31	18.4
Payload ArmB Front	176	-20.7	- 1.22	-19.5	+ 2.09	-17.4
Payload ArmB Front	177	-21.2	- 1.16	-20.1	+ 2.06	-18.0
Payload ArmB Front	178	-56.1	- 1.48	-54.6	+ 2.65	-52.0
Payload ArmB Front	179	-56.6	- 1.42	-55.2	+ 2.60	-52.6
Payload ArmB Outer	180	-83.3	- 1.29	-82.0	+ 2.44	-79.6
YBase / Toptube	3000	- 2.6	- 1.74	- 0.8	+ 3.63	2.8
Top Plate Center	111	23.1	- 4.15	27.3	+ 3.27	30.5
Top Plate -X	112	22.3	- 3.76	26.1	+ 3.51	29.6
Top Plate -Z	113	14.7	- 3.93	18.7	+ 4.26	22.9
Top Plate +Z	114	19.7	- 3.81	23.5	+ 4.09	27.6
Bottom Plate Center	121	15.0	- 2.36	17.4	+ 3.67	21.0
Bottom Plate -X	122	19.4	- 2.04	21.4	+ 4.55	26.0
Bottom Plate -Z	123	7.5	- 2.49	10.0	+ 4.24	14.2
Bottom Plate +Z	124	13.4	- 2.40	15.8	+ 4.08	19.9
Panels Panel -X	131	19.9	- 2.44	22.3	+ 3.71	26.0
Panels Panel +Z	132	17.9	- 2.56	20.5	+ 3.60	24.1
Panels Panel -Z	133	14.9	- 2.60	17.5	+ 3.66	21.2
Panels QUAD +X	134	23.8	- 2.82	26.6	+ 9.73	36.3
Panels QUAD +Z	135	24.3	- 2.62	26.9	+ 9.00	35.9
Panels QUAD -Z	136	25.8	- 2.58	28.4	+ 9.23	37.7
Struts CYL +X	141	19.0	- 2.85	21.9	+ 6.10	28.0
Struts CYL -Z	142	19.8	- 2.71	22.6	+ 5.76	28.3
Struts CYL +Z	143	21.2	- 2.68	23.8	+ 5.70	29.5
Payload-Flange -X	151	17.9	- 1.46	19.4	+ 2.29	21.7
Payload-Flange +Z	152	18.0	- 1.28	19.3	+ 1.80	21.1
Payload-Flange -Z	153	16.5	- 1.30	17.8	+ 1.83	19.7
Solar Sheet out Center	311	81.8	-14.54	96.4	+ 0.04	96.4
Solar Sheet out -X	312	81.6	-14.54	96.2	+ 0.04	96.2
Solar Sheet out -Z	313	81.6	-14.55	96.2	+ 0.04	96.2
Solar Sheet out +Z	314	81.6	-14.54	96.1	+ 0.04	96.2
Solar Sheet in Center	321	44.8	- 8.43	53.2	+ 1.63	54.8
Solar Sheet in -X	322	39.2	- 8.11	47.3	+ 1.48	48.8
Solar Sheet in -Z	323	36.7	- 8.22	44.9	+ 1.67	46.6
Solar Sheet in +Z	324	38.2	- 8.14	46.4	+ 1.66	48.0
Solar Core Center	331	60.8	-11.38	72.2	+ 0.83	73.0
Solar Core -X	332	57.4	-11.03	68.4	+ 0.75	69.2
Solar Core -Z	333	56.4	-11.08	67.5	+ 0.83	68.3
Solar Core +Z	334	57.0	-11.04	68.1	+ 0.82	68.9

Tab. 4-1 (continue): Steady State Temperatures

		Temperatures [K]				
Name	NODE ID	Cold Case	Diff. to HC	Hot Case	Diff. to HC	HC 2
PCDU	411	32.9	- 1.79	34.7	+ 5.17	39.9
Central El. CPS	412	31.9	- 1.82	33.7	+ 3.06	36.7
Transpond 1	413	20.3	- 2.45	22.8	+ 3.46	26.3
Transpond 2	414	8.6	- 2.72	11.3	+ 3.72	15.0
FEEP El. 1	415	18.8	- 2.44	21.2	+ 3.48	24.7
FEEP El. 2	416	4.3	- 2.77	7.0	+ 3.84	10.9
StarTrack 1	417	13.1	- 3.18	16.3	+ 3.80	20.1
StarTrack 2	418	8.5	- 3.29	11.8	+ 3.95	15.8
HGA Drive 1	419	11.0	- 2.86	13.9	+ 3.70	17.6
HGA Drive 2	420	7.2	- 2.94	10.1	+ 3.81	14.0
RFDU	421	13.3	- 2.44	15.7	+ 3.67	19.4
Gyro Pack	422	5.6	- 2.58	8.1	+ 3.93	12.1
EPC 1	423	51.3	- 1.59	52.9	+ 8.94	**61.9**
EPC 2	424	23.9	- 1.87	25.8	+ 3.34	29.1
TWT 1	425	21.5	- 1.96	23.5	+ 5.09	28.5
TWT 2	426	19.0	- 1.99	21.0	+ 3.73	24.8
ST Elec. 1	427	16.5	- 2.41	18.9	+ 3.61	22.5
ST Elec. 2	428	10.9	- 2.52	13.5	+ 3.84	17.3
ST Elec. 3	429	6.4	- 2.60	9.0	+ 3.91	12.9
ST Elec. 4	430	7.3	- 2.58	9.9	+ 3.97	13.9
StarTrack 3	431	10.6	- 2.45	13.1	+ 3.85	16.9
StarTrack 4	432	5.5	- 2.54	8.0	+ 4.01	12.1
UV Box 1	433	17.0	- 2.31	19.4	+ 3.10	22.4
UV Box 2	434	17.2	- 2.40	19.6	+ 3.15	22.7
InstConEl 1	435	28.9	- 2.31	31.2	+ 4.73	35.9
InstConEl 2	436	8.0	- 2.71	10.7	+ 5.51	16.2
Laser Head 1	441	43.7	- 2.57	46.3	+12.45	**58.7**
Laser Head 2	442	31.0	- 2.68	33.7	+ 8.25	42.0
Laser El. 1	443	22.8	- 2.64	25.5	+ 4.97	30.5
Interfer El. 1	444	31.4	- 2.40	33.8	+ 4.96	38.7
Laser Head 3	451	34.0	- 2.72	36.8	+13.11	**49.9**
Laser Head 4	452	21.3	- 2.84	24.2	+ 8.79	33.0
Laser El. 2	453	13.2	- 2.80	16.0	+ 5.23	21.3
Interfer El. 2	454	7.7	- 2.89	10.6	+ 5.92	16.5
FEEP Unit 1	464	39.3	- 2.82	42.1	+20.06	**62.2**
FEEP Unit 2	465	39.8	- 2.62	42.4	+19.34	**61.7**
FEEP Unit 3	466	41.3	- 2.58	43.9	+19.56	**63.5**
Radiator -X	512	- 89.0	- 1.23	- 87.8	+ 2.74	- 85.0
Radiator -Z	513	-122.9	- 1.46	-121.4	+ 2.49	-118.9
Radiator +Z	514	-118.9	- 1.39	-117.5	+ 2.36	-115.1

D.4.2 Transient Analysis

The transient temperature analysis was performed for six different load cases: three load case with solar constant fluctuation, two load case with electronic dissipation fluctuation and one load case with the temperature response to electronic switch on-off of some EU-boxes.

All transient calculations were based on the steady state hot case conditions.

Some investigations about the influence of numerical errors show, that fluctuations down to 1e-9 K can be reproduced with different computation time steps and different relaxation criteria, although the relative error can reach about 50 % with the smallest fluctuation values. Hence fluctuations smaller than 1e-9 K are neglected in the results tables.

D.4.2.1 Solar Constant Fluctuation

The solar constant fluctuation is given as $\Delta S = 1.3 \cdot f^{-\frac{1}{3}} \cdot S_0$ (RD2).

The temperature response was determined for three frequencies 1e-1 Hz, 1e-3 Hz and 1e-4 Hz with the associated fluctuation values 0.03 %, 0.13 % and 0.3 %.

The total solar input on the LISA spacecraft is 4883 W with hot case conditions.

The results are listed in Tab. 4-2. The temperature fluctuation of the payload tube is in the order of 1e-5 K with a 1e-4 Hz-input. With the other sun constant fluctuation frequencies the temperature fluctuation in the payload tube is negligible.

D.4.2.2 Electronic Dissipation Fluctuation

Three transient dissipation load cases were calculated:

1) Dissipation fluctuation of all EUs (154.2 W) with a frequency of 1e-4 Hz and a fluctuation of 1 %.
2) Dissipation fluctuation of the CPS Central Electronic (35 W, #412) with a frequency of 0.1 Hz and a fluctuation of 20 %.
3) The temperature response to the switch on-off of the Transponder 1 (10 W, #413), the RFDU (1 W, #421) and the EPC 1 (25 W, #423).

The results of the load cases 1 and 2 are listed in Tab. 4-3.

With the 1e-4 Hz-input from all units the temperature fluctuation of the payload tube is in the order of 1e-4 to 1e-3 K. Although the situation of all units oscillating synchronous is not a realistic case, this result can be used to establish a budget value for allowable fluctuations in unit dissipation.

In order not to exceed the effect of solar fluctuation on the inner and middle payload tube the fluctuation in the unit dissipation has to be limited to roughly 0.1 %.

The dissipation fluctuation of the CPS causes only negligible response in the payload tube.

The temperature response to the switch on-off of 36 W dissipation is summarised in Tab. 4-4.

The maximum temperature change, that can appear within a period of 3 hours is listed in the column $dT_{3h,max}$.

The time, after that the temperature change within a period of 3 hours has dropped back to 1e-4 K is listed in the column t_{1e-4}. The calculation stopped after 500,000 s (about 139 h), so that this limit was not reached for every node.

In the column $t_{98\%}$ the time, until 98% of the temperature-difference (power on-off) is reached is listed.

The temperature response of the middle payload tubes to a switch-on for 3 hours is depicted in Fig. 4-1. In this case the 3-hour-temperature-change in the middle payload tubes has dropped back to 1e-4 K after about 80 h; the limit of 1e-5 K is reached after 115 h.

Hence it follows, that step functions in dissipation lead to long term temperature fluctuations. Due to the non-linear radiation behaviour the result can not easily be scaled down to a allowable step size. A brief numerical calculation shows, that if a step function in dissipation is limited to about 1 mW, the maximum temperature variation within 3 h is limited to 8e-5 K in the payload tube.

Tab. D-5: Temperature Response to Solar Constant Fluctuation (Solar Input: 4883 W)

Load Case:		1e-1 Hz, 0.03 %		1e-3 Hz, 0.13 %		1e-4 Hz, 0.30 %	
Name	NODE ID	Temperature Fluctuation [K]	Phase[π/8]	Temperature Fluctuation [K]	Phase [π/8]	Temperature Fluctuation [K]	Phase [π/8]
Payload ArmA Inner	81	**0**	0	**2.0e-09**	-14	**2.7e-05**	-15
Payload ArmA Middle	82	**0**	0	**2.5e-09**	-14	**3.9e-05**	-14
Payload ArmA Middle	83	**0**	0	**1.2e-09**	-14	**3.0e-05**	-14
Payload ArmA Front	86	0	0	4.3e-09	-14	8.2e-05	-14
Payload ArmA Front	87	0	0	1.4e-09	-14	4.2e-05	-13
Payload ArmA Front	88	0	0	4.3e-09	-14	8.5e-05	-14
Payload ArmA Front	89	0	0	1.6e-09	-14	5.0e-05	-13
Payload ArmA Outer	90	0	0	3.5e-09	-14	7.3e-05	-14
Payload ArmB Inner	171	**0**	0	**2.0e-09**	-14	**2.7e-05**	-15
Payload ArmB Middle	172	**0**	0	**2.5e-09**	-14	**3.9e-05**	-14
Payload ArmB Middle	173	**0**	0	**1.2e-09**	-14	**2.9e-05**	-14
Payload ArmB Front	176	0	0	3.9e-09	-14	7.4e-05	-14
Payload ArmB Front	177	0	0	1.2e-09	-14	3.6e-05	-13
Payload ArmB Front	178	0	0	3.9e-09	-14	7.7e-05	-14
Payload ArmB Front	179	0	0	1.4e-09	-14	4.3e-05	-13
Payload ArmB Outer	180	0	0	3.3e-09	-14	6.7e-05	-14
YBase / Toptube	3000	0	0	3.1e-09	-14	7.0e-05	-14
Top Plate Center	111	0	0	2.5e-06	- 4	3.3e-03	- 2
Top Plate -X	112	0	0	2.0e-06	- 4	2.9e-03	- 2
Top Plate -Z	113	0	0	2.0e-06	- 4	2.7e-03	- 2
Top Plate +Z	114	0	0	2.0e-06	- 4	2.7e-03	- 2
Bottom Plate Center	121	0	0	5.0e-09	-14	1.8e-04	-13
Bottom Plate -X	122	0	0	1.3e-09	-14	6.1e-05	-12
Bottom Plate -Z	123	0	0	1.2e-09	-14	5.4e-05	-12
Bottom Plate +Z	124	0	0	1.3e-09	-14	5.9e-05	-12
Panels Panel -X	131	0	0	4.3e-08	-14	5.8e-04	-15
Panels Panel +Z	132	0	0	4.2e-08	-14	5.5e-04	-15

Panels Panel -Z	133	0	0	4.1e-08	-14	5.5e-04	-15
Panels QUAD +X	134	0	0	2.9e-08	-15	3.4e-04	-15
Panels QUAD +Z	135	0	0	3.1e-08	-15	3.6e-04	-15
Panels QUAD -Z	136	0	0	3.1e-08	-15	3.6e-04	-15
Payload-Flange -X	151	0	0	2.3e-08	-14	3.2e-04	-15
Payload-Flange +Z	152	0	0	2.0e-08	-14	2.7e-04	-15
Payload-Flange -Z	153	0	0	2.0e-08	-14	2.7e-04	-15
Solar Facesheet out	311-314	2.5e-04	-14	8.0e-02	-14	2.6e-01	-10
Solar Facesheet in	321-324	0	0	1.5e-04	- 7	2.4e-02	- 5
Solar Core	331-334	4.3e-08	-10	1.5e-03	-10	4.4e-02	- 6
EU-Boxes (Maximum)	411-454	0	0	7.8e-08	-14	5.0e-04	-12
EU-Boxes (Miniumum)	411-454	0	0	1.9e-09	-14	5.3e-05	-15

(Temperature Fluctuations <1e-9 K are set to 0)

Tab. D-6: Temperature Response to Electronic Dissipation Fluctuation

Load Case:		1e-4 Hz, 1 % (all EUs, 154.2 W)		1e-1 Hz, 20 % (only CPS, 35 W)	
Name	NODE ID	Temperature Fluctuation [K]	Phase [π/8]	Temperature Fluctuation [K]	Phase [π/8]
Payload ArmA Inner	81	**1.2e-04**	- 8	**0**	0
Payload ArmA Middle	82	**2.5e-04**	- 9	**0**	0
Payload ArmA Middle	83	**2.6e-04**	- 9	**0**	0
Payload ArmA Front	86	2.7e-03	- 9	0	0
Payload ArmA Front	87	3.1e-03	- 9	0	0
Payload ArmA Front	88	3.6e-03	- 9	0	0
Payload ArmA Front	89	3.8e-03	- 9	0	0
Payload ArmA Outer	90	4.1e-03	- 9	0	0
Payload ArmB Inner	171	**1.1e-04**	- 8	**0**	0
Payload ArmB Middle	172	**1.6e-04**	- 9	**0**	0
Payload ArmB Middle	173	**1.3e-04**	- 8	**0**	0
Payload ArmB Front	176	1.6e-03	- 9	0	0
Payload ArmB Front	177	1.1e-03	- 9	0	0
Payload ArmB Front	178	2.0e-03	- 9	0	0
Payload ArmB Front	179	1.5e-03	- 9	0	0
Payload ArmB Outer	180	2.4e-03	-10	0	0
YBase / Toptube	3000	5.8e-03	- 9	3.8e-08	- 8
Top Plate Center	111	2.0e-03	- 7	0	0
Top Plate -X	112	7.2e-03	- 9	6.3e-08	- 8
Top Plate -Z	113	6.1e-03	-10	0	0
Top Plate +Z	114	8.0e-03	-10	0	0
Bottom Plate Center	121	1.2e-03	- 6	0	0
Bottom Plate -X	122	6.9e-03	-10	1.9e-08	- 8
Bottom Plate -Z	123	9.3e-04	- 8	0	0
Bottom Plate +Z	124	2.8e-03	- 9	0	0

Panels Panel -X	131	5.3e-03	-10	4.0e-08	- 8
Panels Panel +Z	132	2.8e-03	- 9	0	0
Panels Panel -Z	133	1.7e-03	- 8	0	0
Panels QUAD +X	134	7.1e-03	-10	0	0
Panels QUAD +Z	135	7.2e-03	-10	7.1e-08	- 8
Panels QUAD -Z	136	8.7e-03	-11	5.1e-09	0
Payload-Flange -X	151	3.2e-03	- 9	2.4e-08	- 8
Payload-Flange +Z	152	1.4e-03	- 9	0	0
Payload-Flange -Z	153	8.4e-04	- 8	0	0
Solar Facesheet out	311-314	1.4e-05	- 5	0	0
Solar Facesheet in	321-324	1.7e-03	- 8	1.4e-09	0
Solar Core	331-334	2.9e-04	- 5	0	0
EU-Boxes (Maximum)	411-454	1.9e-01	- 5	7.0e-04	0
EU-Boxes (Miniumum)	411-454	8.1e-04	-14	0	-12

(Temperature Fluctuations <1e-9 K are set to 0)

Tab. D-7: Temperature Response to Switch On-Off of Transponder 1, RFDU and EPC 1

(together 36 W Dissipation)

Name	NODE ID	Steady State Temp. [K]		dT_{on-off} [K]	$dT_{3h,max}$ [K]		$t_{98\%}$ [h]		t_{1e-4} [h]	
		Power on	Power off		Power on	Power off	on	off	on	off
Payload ArmA Inner	81	20.0	19.6	0.4	7.0e-2	7.0e-2	49	52	88	92
Payload ArmA Middle	82	18.4	17.8	0.6	1.2e-1	1.2e-1	51	53	97	102
Payload ArmA Middle	83	18.4	17.8	0.6	1.1e-1	1.2e-1	51	53	98	102
Payload ArmA Front	86	-15.8	-19.6	3.8	7.8e-1	8.0e-1	50	52	123	129
Payload ArmA Front	87	-15.9	-19.7	3.8	7.6e-1	7.8e-1	50	53	124	129
Payload ArmA Front	88	-49.8	-54.3	4.5	9.2e-1	9.3e-1	50	53	126	132
Payload ArmA Front	89	-50.0	-54.6	4.6	9.0e-1	9.1e-1	50	53	126	132
Payload ArmA Outer	90	-77.7	-81.5	3.8	7.7e-1	7.7e-1	50	53	124	130
Payload ArmB Inner	171	19.9	19.6	0.3	6.5e-2	6.6e-2	50	53	88	92
Payload ArmB Middle	172	18.1	17.8	0.3	5.3e-2	5.3e-2	59	61	99	103
Payload ArmB Middle	173	18.1	17.7	0.4	5.4e-2	5.4e-2	59	61	99	103
Payload ArmB Front	176	-19.5	-21.0	1.5	1.6e-1	1.6e-1	66	68	126	131
Payload ArmB Front	177	-20.1	-21.6	1.5	1.6e-1	1.6e-1	66	68	126	131
Payload ArmB Front	178	-54.6	-56.4	1.8	1.9e-1	1.9e-1	66	69	129	134
Payload ArmB Front	179	-55.2	-57.0	1.8	1.9e-1	1.9e-1	66	69	129	134
Payload ArmB Outer	180	-82.0	-83.6	1.6	1.7e-1	1.6e-1	66	69	127	132
YBase / Toptube	3000	- 0.8	-13.2	12.4	3.0e+0	2.9e+0	41	45	130	137
Top Plate Center	111	27.3	21.5	5.8	1.1e+0	1.1e+0	52	55	131	137
Top Plate -X	112	26.1	16.3	9.8	2.5e+0	2.4e+0	44	47	129	137
Top Plate -Z	113	18.7	15.3	3.4	4.0e-1	3.9e-1	62	65	134	>139
Top Plate +Z	114	23.5	16.0	7.5	1.8e+0	1.8e+0	49	52	132	138
Bottom Plate Center	121	17.4	10.4	7.0	1.3e+0	1.3e+0	52	55	134	>139
Bottom Plate -X	122	21.4	7.2	14.2	3.9e+0	3.8e+0	42	46	133	>139
Bottom Plate -Z	123	10.0	5.6	4.4	5.3e-1	5.1e-1	62	65	138	>139
Bottom Plate +Z	124	15.8	7.1	8.7	1.7e+0	1.7e+0	51	54	135	>139

Panels Panel -X	131	22.3	13.1	9.2	2.1e+0	2.1e+0	46	49	131	138
Panels Panel +Z	132	20.5	13.8	6.7	1.3e+0	1.3e+0	51	54	132	>139
Panels Panel -Z	133	17.5	13.1	4.4	6.7e-1	6.5e-1	58	61	134	>139
Panels QUAD +X	134	26.6	21.3	5.3	6.3e-1	6.1e-1	64	67	>139	>139
Panels QUAD +Z	135	26.9	18.2	8.7	1.4e+0	1.4e+0	57	60	>139	>139
Panels QUAD -Z	136	28.4	18.5	9.9	1.8e+0	1.8e+0	55	58	>139	>139
Payload-Flange -X	151	19.4	13.4	6.0	1.4e+0	1.4e+0	45	49	124	131
Payload-Flange +Z	152	19.3	16.0	3.3	6.4e-1	6.3e-1	51	54	123	128
Payload-Flange -Z	153	17.8	15.6	2.2	3.3e-1	3.3e-1	58	61	124	129
Solar Facesheet out	311-314	96.2	96.1	0.1	1.2e-2	1.2e-2	54	56	70	73
Solar Facesheet in	321-324	47.9	45.2	2.7	5.2e-1	5.3e-1	53	55	121	126
Solar Core	331-334	69.1	67.7	1.4	2.5e-1	2.5e-1	54	56	112	117
Transpond 1	413	22.8	1.1	21.7	1.3e+1	1.3e+1	36	40	133	>139
RFDU	421	15.7	1.3	14.4	6.0e+0	5.9e+0	43	46	134	>139
EPC 1	423	52.9	7.2	45.7	3.5e+1	3.3e+1	24	29	128	>139
other EU-Boxes:										
Maximum	411-454	46.3	40.5	5.8	9.0e+0	8.5e+0	66	69	>139	>139
Minimum	411-454	7.0	0.4	6.6	3.0e-1	3.0e-1	34	38	129	137

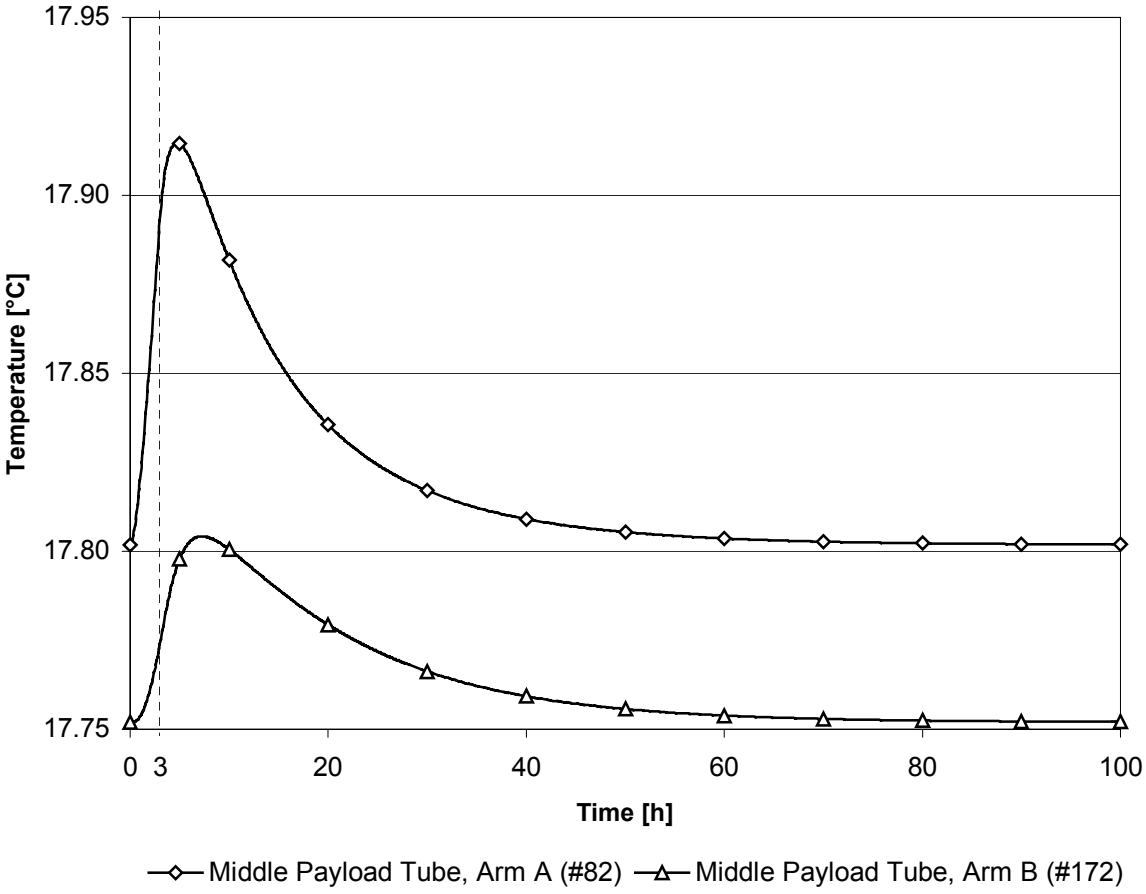

Fig. D-7: Temperature Response of the Middle Payload Tubes (#82 and # 172)
to a 3-h-Heating-Period (36 W)